Lower Hybrid Current Drive on Alcator C-Mod: Measurements with an Upgraded MSE Diagnostic and Comparisons to Simulation

by

Robert Thomas Mumgaard

B.S. Mechanical Engineering (2008)
B.S. Interdisciplinary Engineering- Physics (2008)
University of Nebraska-Lincoln

S.M. Nuclear Science and Engineering (2015)
Massachusetts Institute of Technology

Submitted to the Department of Nuclear Science and Engineering
in partial fulfillment of the requirements for the degree of

Doctor of Philosophy in Applied Plasma Physics

at the

MASSACHUSETTS INSTITUTE OF TECHNOLOGY

June 2015

Author .....
Department of Nuclear Science and Engineering
May 22, 2015

Certified by .....
Steven D. Scott
Principal Research Physicist, Princeton Plasma Physics Laboratory
Thesis Supervisor

Certified by .....
Ian H. Hutchinson
Professor, Department of Nuclear Science and Engineering
Thesis Reader

Certified by .....
Ronald R. Parker
Professor Emeritus, Department of Nuclear Science and Engineering and Department of Electrical Engineering and Computer Science
Thesis Reader

Accepted by .....
Mujid S. Kazimi
TEPCO Professor of Nuclear Engineering
Chair, Department Committee on Graduate Students

Lower Hybrid Current Drive on Alcator C-Mod: Measurements with an Upgraded MSE Diagnostic and Comparisons to Simulation

by

Robert Thomas Mumgaard

Submitted to the Department of Nuclear Science and Engineering
on May 22, 2015, in partial fulfillment of the
requirements for the degree of
Doctor of Philosophy in Applied Plasma Physics

Abstract

Lower Hybrid Current Drive (LHCD) is a promising technique to sustain tokamak plasmas and provide control over the current profile—two important capabilities required for the development of tokamak fusion reactors. Upgraded measurement capabilities on the ALCATOR C-MOD tokamak create a unique opportunity to study the plasma's toroidal electric current profile at magnetic fields, plasma densities, and magnetic geometries anticipated in future reactors in stationary discharges dominated by LHCD.

The Motional Stark Effect (MSE) diagnostic uses polarized light to infer the plasma's internal current profile. The MSE diagnostic deployed on the ALCATOR C-MOD tokamak previously experienced unacceptable calibration drift and sensitivity to partially-polarized background light that limited its ability to measure magnetic field pitch-angles. A comprehensive analytic study of the origin of polarization angle errors in MSE diagnostics and an experimental study using a robotic calibration system were conducted. Insight from this study guided the fabrication and installation of a first-of-a-kind in-situ calibration system for MSE diagnostics—a long sought capability—and the development of thermal isolation schemes for the periscope. An experimental study of the effect of partially polarized background light identified this as a significant source of systematic error. Partial-polarization upon reflection was identified as the mechanism that leads to polarized light in a tokamak. Visible bremsstrahlung, divertor emission, and blackbody emission were identified as the dominant sources of light. A new technique, MSE multi-spectral line polarization (MSE-MSLP), was developed to measure the polarization on a single sightline in multiple wavelengths simultaneously using a high-throughput polarization polychromator. Wavelength-interpolation of the background light polarization utilizing this hardware decreases the error from background subtraction by a factor of 5-10 relative to time-interpolation, drastically improving the measurement quality while eliminating the need for neutral beam pulsing. The method also allows for simultaneous measurement of multiple polarized transitions within the Stark multiplet.

The upgraded MSE diagnostic was used to measure the magnetic field pitch angle profile in plasmas with some or all of the plasma current driven by LHCD. Measurements were made across a range of single-parameter scans: LHCD power, loop voltage, plasma density, plasma current, and launched $n_{\|}$ spectrum. The current profile is observed to broaden during LHCD, but consistently has significant on-axis current density, even in fully non-inductive plasmas. The current profile and hard x-ray (HXR) profiles are observed to be most sensitive to plasma current, with higher current yielding broader profiles. The current and HXR profiles as well as global current-drive efficiency are insensitive to changes in $n_{\|}$ or loop voltage.

Numerical simulations by the ray-tracing Fokker-Planck GENRAY/CQL3D code reproduce the total measured current in non-inductive conditions but fail to accurately predict the current

and HXR profiles; the simulations consistently predict more current drive in the outer half of the plasma than is observed. This leads to a flattening of the HXR profile compared to the experimental profiles. These qualitative discrepancies persist across the range of plasma parameters scanned. Varying code inputs within their measurement uncertainties and adding experimentally-constrained levels of fast-electron diffusion do not reconcile profile discrepancies. Some qualitative profile trends in single parameter scans are reproduced by the simulations including broadening of profiles at higher current, and a weak dependence on the launched $n_{\|}$ spectrum. However, HXR profile self-similarity across different densities and powers is not reproduced. These new comparisons between profile measurements and simulation suggest that the simulations are missing important physics in this operational regime.

Thesis Supervisor: Steven D. Scott
Principal Research Physicist, Princeton Plasma Physics Laboratory

Thesis Reader: Ian H. Hutchinson
Professor, Department of Nuclear Science and Engineering

Thesis Reader: Ronald R. Parker
Professor Emeritus, Department of Nuclear Science and Engineering and Department of Electrical Engineering and Computer Science

"An expert is a person who has made all the mistakes that can be made in a very narrow field."
-Niels Bohr

ACKNOWLEDGMENTS

This work was not possible without the contributions of a very large number of people who initiated, contributed to, refined, executed, and critiqued the ideas and machinery inside this document. Special thanks is required for people whose technical and scientific efforts contributed directly to this thesis:

ALCATOR C-MOD

This work was not possible without the incredibly skilled and insightful team that built, operates, and maintains the tokamak. The fact that creating a star in the middle of Cambridge feels routine is a testament to the excellence of the scientists, engineers, technicians, students, and support staff. I am grateful to have been a part of such a wonderful team and am excited to glimpse what the future may hold.

MSE FOREFATHERS AND ACCOMPLICES

The foundations of this thesis rest on the efforts over the past decade plus of the team that has been diligently working to field such a complicated diagnostic in such a harsh environment. The work done by Steve Scott, Jinseok Ko, and Howard Yuh laid the foundations that enabled all the work in this thesis. It has been a long journey, against long odds, over much skepticism, with many heartbreaks, and many wrong turns, but it is done and everybody involved shares in the accomplishment. We have measured actual pitch angles, and they mean something! Thanks to fellow MSE enthusiast elsewhere, particularly Fred Levinton, Chris Holcomb, Maarten DeBock, Nick Hawkes, Niel Conway, and John Howard for insightful discussions about MSE minutia, help identifying important problems, and the occasional loan of hardware. Hopefully the work presented here can be of use in your MSE pursuits. Credit goes to Paul Geelen for a very fruitful, though too short, collaboration adapting the MSESIM code to C-MOD. His work expanded our understanding of the diagnostic and retired many open questions. Matthew Khoury's work on assembling and coding the new MSE-MSLP system has enabled future MSE on C-MOD and (hopefully) elsewhere.

THE BEAM TEAM

There would be no measurements without the operation of the diagnostic neutral beam. Bob Granetz, Mo Chung, and Edgar Rollins worked tirelessly on what can only be described as a fickle and unforgiving machine. Their persistence and optimism in the face of seemingly endless challenges pushed us to make

proper use of the neutrals they supplied when they were supplied. Igor Bespamyatnov was invaluable in helping to keep the beam a going concern, understanding its performance, and making the spectral measurements of the MSE filters.

RECONSTRUCTIONS

Thanks goes in particular to Syun'ichi Shiraiwa for his immense software development skills exemplified in the πSCOPE package which was used to process both the MK-EFITS and the GENRAY/CQL3D simulations in this work. The many discussions and permutations of magnetic reconstructions led to very capable and robust methodologies. Up next: real-time MSE-constrained reconstructions (wink). Steve Wolfe and Bob Granetz were also important for this effort, providing sage advice and magnetics data, respectively.

LHCD PHYSICS AND SIMULATIONS

The world-leading LHCD team at C-MOD let this diagnostician outsider into their realm, allowing me to explore physics that I'm sure they were interested in and capable of doing. Thank you for your faith while I interloped into your life's work. In particular, Syun'ichi Shiraiwa, Paul Bonoli, and Greg Wallace were invaluable for discussions of LHCD physics and instruction (and outright hand-holding while) running simulations.

PLASMA DATA

Specific thanks goes to Ian Faust for maintaining and operating the HXR camera that is an integral part of this thesis—typically a thankless job. Jerry Hughes and John Walk maintained and operated the Thomson scattering system while helping provide accurate profiles for reconstructions and simulations.

LOWER HYBRID TEAM

Greg Wallace, Dave Terry, Atma Kanojia, Dave Johnson, and Pat McGibbon maintained and operated a very impressive current drive system, driving current almost at will.

ENGINEERING TEAM

The engineering team at the PSFC was an incredible resource to draw on. Rui Vieria and Dave Terry helped me mature as an engineer, Bill Parkin taught me proper electronic design, Sam Pierson and Maria Silveria tolerated and aided my endless hours inside the vacuum vessel, and Paul Lienard helped me refine my drafting skills.

MACHINE SHOP

Ed Fitzgerald, Mark Iverson and Bill Forbes machined many of the doodads and pieces required to make it all work, often at a moment's notice.

The contributions of Steve Scott to this work and my professional development cannot be overstated. I am confident that nobody in the world knows more about the Motional Stark Effect, and he continues to produce insights everyday. It has been a pleasure to explore such a complex system with Steve, his levity and determination were invaluable when large setbacks were encountered, always offering support and encouragement (and often late-night pizza) during seemingly endless calibrations. Our time together cannot be described by anything less than a partnership. We were able to seamlessly collaborate on a body of work whose breadth could justify a small team of scientists (and does at other labs!). His tone as an advisor struck the perfect balance of engagement, guidance, and freedom. I am thankful he was hands-off except when needed and am grateful for his ability to wrench support from the bureaucracy to implement ideas that would be crazy coming from an established scientist or engineer let alone a lowly grad-student. I know that nobody is happier to see this diagnostic produce physics results than him. I look forward to continued collaborations utilizing the capabilities we have developed over the last seven (!) years.

I thank the readers of this thesis, Ian and Ron, for persevering through what was a daunting process, always working to make the draft better. Special thanks goes to Ian for his always correct comments on the most efficient way to make my point—the reader of this thesis should thank him for keeping the page count down (at least in this document). His insight into the physics was key at several junctures in MSE development and his un-biased approach to science was very clarifying. Others at the PSFC were invaluable for scientific direction, insight, discussion, and friendship. In particularly Matt Reinke, Zach Hartwig, Nathan Howard, Jerry Hughes, John Rice, Bob Granetz, Christian Theiler, Mike Churchill, Anne White, Martin Greenwald, Earl Marmar and Dennis Whyte.

In addition to those who gave their scientific support I thank my family and friends, particularly those who have made living in Boston a joy; Steve Renter, Chris Bolin, Tim Lucas, and the Migration Sailing team. I could not have gotten through this process without Geoff, Mike and Dan who I felt like I went to battle with. I guess I'm the last of the NW17-169'ers to get out (by a safe margin). I think we all saw that coming.

Last but not least, I thank my wife, Rachael, for putting up with this hair-brained idea and leaving her life behind to move to the big city and start over. Her tolerance, acceptance, love, humor, and especially patience made this, and anything, possible.

CONTENTS

LIST OF FIGURES

LIST OF TABLES

1 INTRODUCTION

Humanity will require more energy by the end of the century [1]. Meanwhile, concerns about global climate change motivate a migration from traditional carbon-intensive fossil fuels to alternate sources of energy. Ongoing concerns about safety and nuclear proliferation may limit global deployment of zero-carbon fission energy. Deploying wind, solar, and other intermittent renewable energy sources at scale remains challenging. The development of new energy sources that can be deployed at large scale is therefore recognized as an important pursuit for both the near-term and well into the future.

Fusion energy is one such long-sought energy source. Fusion—the process that powers the stars—offers tremendous benefits, including practically unlimited fuel, no long-term radioactive waste, inherent safety, zero-emissions, and dispatchable generation. The most promising reaction involves combining deuterium and tritium to produce a high-energy neutron and helium nucleus which then heat the walls of the reactor and further heat the fuel, respectively. The use of this reaction for energy generation requires the fuel to be thermalized at very high temperature ($\sim$ 10keV, $\sim$ 100,000,000°C) at sufficient density for an adequate length of time to be economically viable. At these temperatures the fuel is a plasma. The primary challenge to the development of fusion as an energy source has been confining the hot plasma and keeping it away from the walls of the reactor adequately in order to heat it to sufficient temperatures and confine the heat long enough for fusion to occur. The reader is referred to other texts for the details of this process [2].

1.1 MAGNETIC CONFINEMENT WITH TOKAMAKS

The plasma is a "soup" of positively charged ions and negatively charged electrons which allows a variety of novel schemes to confine the heat and particles using magnetic fields; the charged particles spiral around magnetic fields instead of crossing them. Magnetic confinement is being pursued actively in most major industrialized countries, typically funded by the government.

The most successful magnetic confinement configuration to date is the tokamak. This consists of a toroidal-shaped device containing the plasma. The history and important topics concerning these devices can be found in reference [3]. In this configuration, external magnetic coils create a toroidal magnetic field (the long way around a donut) while other external coils are used to provide control over plasma po-

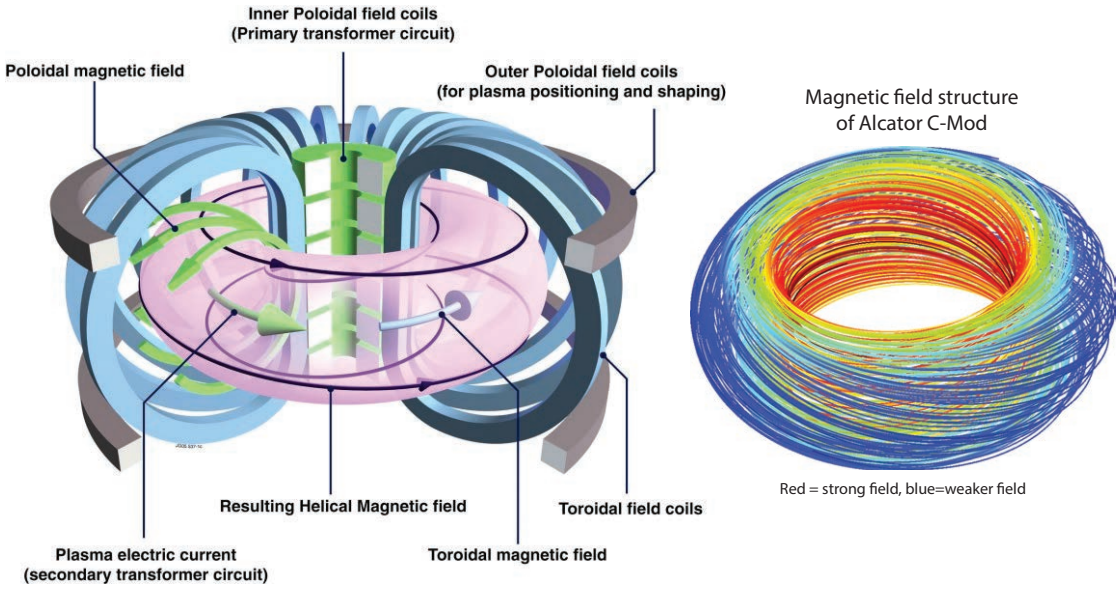

Figure 1: The tokamak concept is shown (left, source: https://www.euro-fusion.org/2011/09/tokamak-principle-2/. Strong external magnets create a toroidal field (blue) and provide control and shaping. A toroidal electrical current (green) is carried by the plasma, producing a poloidal magnetic field. This current is often driven inductively using a central transformer. The two magnetic fields create a helical magnetic field structure (right, a ALCATOR C-MOD equilibrium. Source: M. L. Garrett), which differs across the plasma minor radius depending on the details of the toroidal current profile.

sition, stability, and shape. The plasma itself caries a toroidal electrical current (I_p), typically of order MA in modern devices, that creates a poloidal magnetic field (i.e., looping through the hole in the donut). The combined field thus forms a helix shape, spiraling around the plasma. The configuration is shown schematically in Figure 1. The plasma is surrounded by a vacuum vessel (not shown) and is created in high vacuum. Various other engineering systems are used to heat the plasma, fuel it, control it, measure its properties, and extract heat from the system.

1.2 CURRENT DRIVE AND STEADY-STATE OPERATION

Some of the toroidal current in the plasma must be driven by an external source[1]. This current is usually driven inductively in existing devices by pulsing a central transformer (center green magnet in Figure 1) that induces a voltage, termed the "loop voltage" (V_{loop}, or alternatively, the parallel electric field), around the plasma toroidal; the plasma acts as the secondary winding of the transformer. This drives current in the plasma, and the process is called "Ohmic" current drive.

1 Some of the current is generated by the plasma itself, a phenomenon termed "bootstrap current."

The details of the radial distribution of current in the plasma is important for operation of the tokamak. The toroidal current density, termed J_{tor}, is uniform toroidally but has a profile as a function of the plasma minor radius. This current profile leads to a variable "twist" to the magnetic field as a function of location in the plasma. This twist is parameterized as the "safety factor" or "q-profile":

$$q(r) = \frac{1}{2\pi} \oint \frac{1}{R(s)} \frac{B_\phi(s)}{B_p(s)} ds \tag{1}$$

where R is the local major radius, B_ϕ is the local toroidal field, B_p is the local poloidal field, and the integral is taken while following a field line along a length ds for a single poloidal circuit around the device.

The q-profile plays an important role in the energy confinement and stability of the tokamak and is thus important to control—usually by controlling the toroidal current density. However, changes in q-profile change the plasma transport which changes the plasma profiles which changes the current drive ad infinitum. Thus the system is highly coupled. The challenge is then to drive the required current profile in a self-consistent manner. In a reactor design, the desired q-profile, typically non-monotonic, is prescribed to obtain good confinement, usually requiring a current density profile that is strongly peaked off-axis.

Ohmic current drive is inflexible in where it drives the current since it relies only on the profile of the plasma resistivity. This leads to the current being driven at the hottest parts of the plasma (i.e., the center), leading to monotonic q-profiles that are not attractive for reactor operation. Additionally, it is widely accepted that a fusion reactor must operate in steady-state to be viable from an engineering and economic perspective, but Ohmic current drive is inherently pulsed—eventually the transformer must swing the other direction. Therefore, a method to drive the current non-inductively in a continuous manner with a prescribed current density profile is desired for attractive tokamak fusion reactors. Because this method will require a non-negligible amount of power, which must be supplied by the plant itself, it is desirable chose the most efficient current drive scheme for a reactor.

The use of various sources of current drive, combined with the self-generated bootstrap current, to optimize the tokamak operation, is referred to as the "Advanced tokamak" regime, and this concept is a front-runner for operating future next-generation tokamak reactors. Various methods have been developed to drive the toroidal current non-inductively. The leading candidates are tilted high-power beams of neutral particles and radio frequency waves in various frequency regimes.

1.2.1 *Measuring the current profile*

An important problem for the development of tokamak fusion reactors is confidently specifying and realizing the desired current profile during non-inductive current drive. Various techniques have been developed to measure the current profile. The most successful technique is termed the Motional Stark Effect (MSE) diagnostic, which uses polarized light to determine the local angle of the magnetic field in a manner described in the next chapter.

High-quality measurement of the current profile can then be compared to theory and numerical simulations of current drive. These comparisons challenge the validity of the analytic and numerical models of current drive, and thus aid in the development of improved models. The ultimate goal is to increase confidence that the numerical models can be reliably used to predict and optimize the performance of future tokamak fusion reactors. Using experimental measurements to challenge numerical simulations in regimes of interest on existing devices is a primary strategy for reducing the uncertainties (and thus implementation risks) in designing future experiments or fusion reactors.

1.2.2 *Lower Hybrid current drive*

The most efficient type of non-inductive current drive in modern tokamaks uses waves in the lower hybrid frequency range ($\omega_{LH} \equiv \omega_{pi}/\sqrt{1+(\omega_{pe}/\omega_{ce})^2}$, order GHz on high performance devices) to drive fast electrons in the plasma and is termed lower hybrid current drive (LHCD). Waves of frequency $\omega_0 \sim \omega_{LH}$ are launched in one toroidal direction using a phased array of waveguides and directly deposit their power and momentum by Landau damping on electrons that are traveling roughly in phase with the waves. The fast electrons (with energies from $\sim 3v_{thermal}$ to relativistic) are weakly collisional and have long slowing-down times, making this an efficient mechanism to drive a substantial amount of the plasma current.

The lower hybrid wave is launched into the plasma as a slow wave with an $n_{||}$ ($\equiv ck_{||}/\omega_0$) spectrum set by the launcher and propagates according to its dispersion relation. Once it reaches a location in the plasma where strong Landau damping occurs ($\frac{v_{thermal}}{c} \sim \frac{1}{n_{||}}$) the wave modifies the electron distribution function asymmetrically, driving current. The damping accelerates electrons mostly in the parallel direction, affecting the passing particles instead of trapped particles, enabling this technique to drive current off-axis. The technique can be used to drive tailored current profiles in the plasma by launching waves with different $n_{||}$ that damp at different temperatures—thus providing profile control. The development of continuous-wave trans-

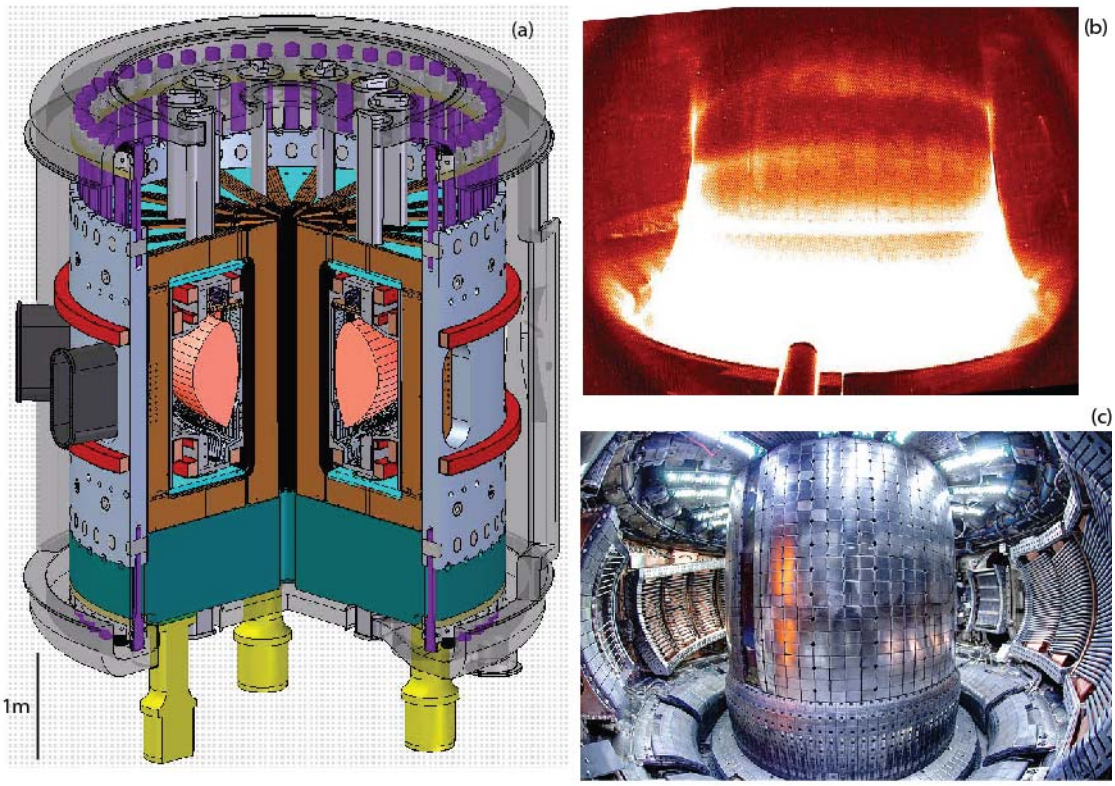

Figure 2: The ALCATOR C-MOD tokamak at MIT. An engineering diagram (a) showing the toroidal field magnets (brown), the poloidal field magnets (red), the supporting superstructure (gray), and the plasma (pink). A photo of the interior of the vessel during a plasma (b). The interior of the tokamak during a maintenance period (c). The LHCD launcher is visible immediately to the right of the central column (c). Photo credit: Robert Mumgaard.

mitters and amplifiers in this frequency regime enables this current drive to be truly steady-state.

The technique has been applied to several existing devices with good results. However, current profiles measurements for comparison to modeling during LHCD at reactor relevant parameters have been fairly sparse. It is therefore important to make extensive measurements of the current profile during LHCD to benchmark predictions from numerical models. It is desirable for this work to be done in as reactor-like an environment as possible.

1.3 ALCATOR C-MOD

The work in this thesis was conducted on the ALCATOR C-MOD tokamak at the Massachusetts Institute of Technology [4]. This tokamak is a compact machine operating at high magnetic field and high density, with metallic walls (molybdenum) and high-power radio frequency heating and lower hybrid current drive. The primary research directions include the study of core transport, radio frequency heating and current drive, and plasma-material interactions at the densities, mag-

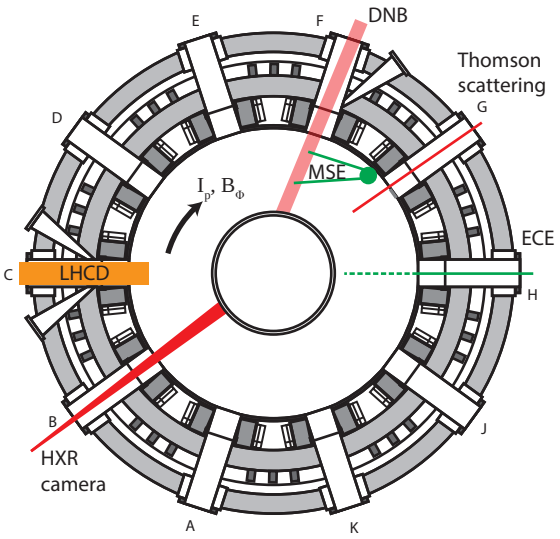

Figure 3: The layout of diagnostic and heating systems on ALCATOR C-MOD utilized in this thesis.

netic fields, shaping, and power densities anticipated in a reactor. The operating parameters of C-MOD are listed in Table 1.

Table 1: Operating parameters of the ALCATOR C-MOD and ITER tokamaks.

	C-MOD	ITER
R_0	0.68m	6.2m
a	0.22m	2.0 m
κ	1.6	1.7
B_0	5.4T	5.3T
I_p	1MA	15MA
$\bar{n}_e$	$3-50\times10^{19}\mathrm{m}^{-3}$	$10\times10^{19}\mathrm{m}^{-3}$
$< T_e >$	$<$ 4keV	9keV
P_{ext}	6MW ICRF	20MW ICRF
	+1MW LHCD	+ 20MW ECCD
	+ 0.2MW NBI	+33MW NBI
P_{fusion}	$<$ 250W	500MW

The work comprised in this thesis involved performing several upgrades to the C-MOD MSE diagnostic, using it to perform systematic studies of the current profile during LHCD and comparing those measurements to numerical simulations. The capability to drive all or most of the current using LHCD and to measure the location of the current drive using the MSE diagnostic is a unique attribute of C-MOD in this parameter range. This work utilized the 1MW of LHCD on C-MOD and several diagnostic systems. In addition to the MSE system observing a diagnostic neutral beam, this work relied upon a Thomson scattering diagnostic for temperature and density profiles, a hard x-ray camera (HXR) for measurements of the fast-electron bremsstrahlung, and an electron cyclotron emission diagnostic (ECE) for measurements of the sawtooth inversion radius and the non-thermal emission from fast-electrons. The location of these systems is identified in Figure 3.

1.3.1 *Next generation devices*

Significant progress has been made in tokamak fusion research over the preceding five decades with performance increasing over five or-

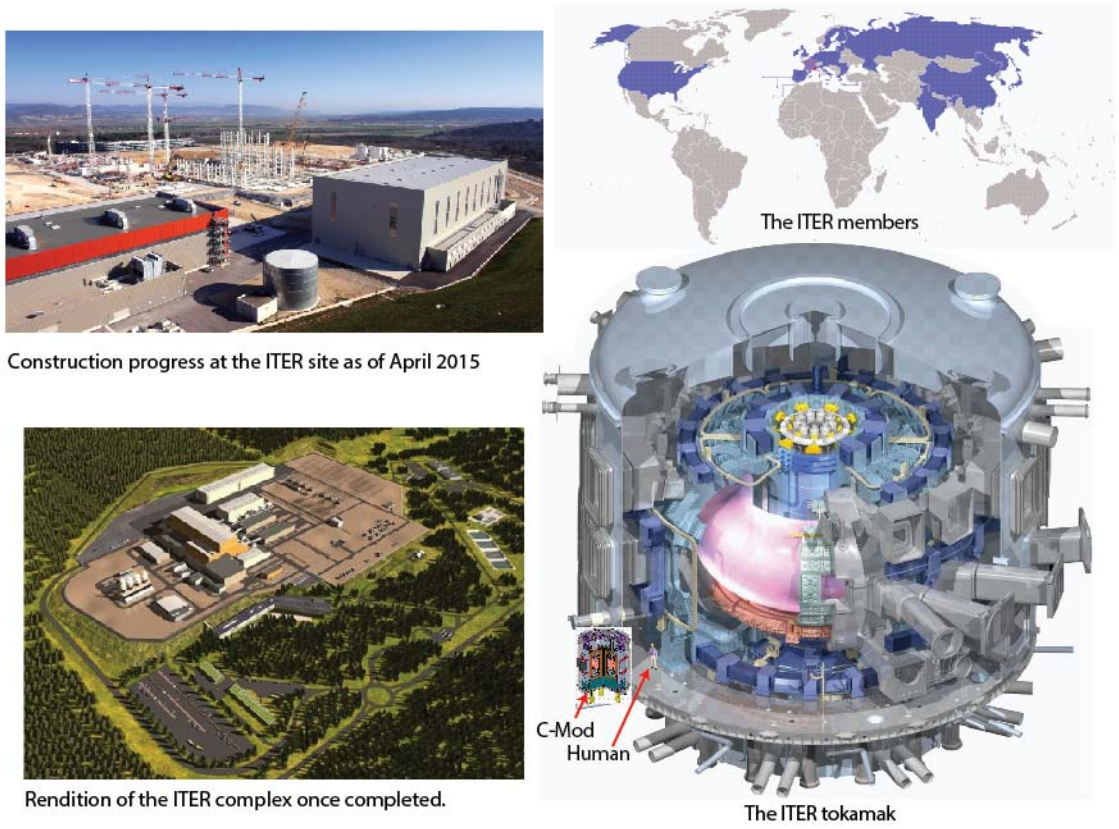

Figure 4: The ITER tokamak under construction in France (top left) will be the first burning plasma experiment. The organization includes member states from much of the industrialized world (top right). The large complex (bottom left) will house and operate the largest tokamak ever constructed (bottom right). A person and C-MOD are super imposed for scale. Images from www.iter.org

ders of magnitude. However, existing devices typically do not make significant fusion power. The next generation of tokamaks are expected to demonstrate significant fusion power, reaching the "burning plasma" regime where new physics may be found. ITER, a large tokamak currently under construction by an international collaboration of most of the world's industrialized nations, will be the first such experiment [5]. The parameters for this machine are listed in Table 1 and the machine is shown in Figure 4, along with a representation of C-MOD superimposed for scale. The C-MOD tokamak operates in a similar parameter range as ITER in terms of field, density, current density, magnetic geometry and material surfaces, but at a much reduced scale, making C-MOD an important devices to test physics at reactor parameters.

ITER and other burning plasma experiments are large expensive nuclear installations that require low-risk solutions to experimental problems. The challenges of fielding MSE diagnostics in such an environment will be explored as part of this thesis. It is anticipated that experience on ALCATOR C-MOD, which faces many similar MSE diag-

nostic issues as burning plasma experiments, will prove to be helpful in reducing implementation risk of MSE in these next-step devices.

1.4 SUMMARY OF NEW RESULTS

There are two questions asked in this thesis:

1. **What advances are necessary to make accurate magnetic pitch angle measurements using MSE in ALCATOR C-MOD and next-step devices, and can these be demonstrated?**

2. **What is the parametric dependence of the current profile during lower hybrid current drive on various parameters, including LHCD power, launched $n_{\parallel}$, plasma density, and plasma current? Can existing numerical simulation models accurately reproduce the measured profiles and observed parametric trends?**

The key contributions of this thesis to the diagnostic and current drive communities are:

1. **A comprehensive study of systematic errors in MSE-LP diagnostics.**
   The origin of polarization errors and interpretation errors unique to MSE-LP diagnostics is derived. These errors, and the susceptibility of the C-MOD MSE implementation to them, were explored experimentally using a novel invessel robotic calibration system. Knowledge of these effects can be used to design more error-resistant MSE diagnostics and inform mitigation and compensation strategies. The operation of the C-MOD diagnostic was found to be near-ideal except for stress-induced birefringence, increasing confidence in the measurements.

2. **First in-situ calibration of an MSE-LP diagnostic.**
   A mechanical system was fielded to accurately calibrate the MSE diagnostic at arbitrary times during operation—the first demonstration a capability long-sought by the diagnostic community. This system was used to characterize stress-induced birefringence in the C-MOD diagnostic and guided the successful development of mitigation strategies.

3. **First study of the origin and impact of polarized background light on MSE-LP diagnostics.**
   The impact of partially-polarized background light on MSE-LP diagnostics is derived. The origin and nature of the partially-polarized background light was determined. Polarization upon reflection is the primary cause of the polarized light, and three important sources have been identified: visible bremsstrahlung, blackbody emission from hot components, and a molecular deuterium component located in the divertor. These sources were

studied to develop improved subtraction techniques and to inform projections of this challenge on next-generation devices.

4. **Development of the MSE multi-spectral line polarization technique.**
   A technique to measure and subtract the background in real time using wavelength-interpolation with a high throughput polarization sensitive polychromator was developed. This technique was shown to properly subtract polarized background, extending the operational range of the diagnostic and retiring background subtraction risk in next-generation devices. This system also allows increased signal collection and error monitoring by simultaneously observing different transitions in the MSE multiplet and has been adopted for use on ITER.

5. **First current profile measurements in plasmas dominated by LHCD across a range of parameters.**
   The upgraded C-MOD MSE system was used to study the current profile under strong LHCD as a function of plasma density, plasma current, launched $n_{\|}$, LHCD power, and magnetic geometry. It was shown that the current profile evolution qualitatively agrees with the expected time scales and reaches a stationary state which allows for the study of fully-relaxed profiles, including those during non-inductive conditions. The current profile is typically broader than the ohmic profile, but with a significant contribution on-axis. The current drive-efficiency and LHCD current and hard x-ray profiles were found to be most sensitive to plasma current, with higher efficiency and with wider LHCD current and HXR profiles at higher current. In experiments performed in this thesis the current and hard x-ray profiles and current drive efficiency are insensitive to changes in $n_{\|}$ or loop voltage when other parameters were held constant. The profile of the LHCD current and HXR emission does not significantly change as the plasma density is raised. Measurements of the current profile at high density showed that effective current drive was recovered in limited plasma geometry, in qualitative agreement with past HXR measurements.

6. **Discrepancies found between simulations and measured profiles across a wide range of parameters.**
   Although simulations using the ray-tracing Fokker-Planck code GENRAY/CQL3D, which is a regularly used in the community, are able to predict the total current drive at non-inductive conditions, the simulations fail to predict the current and HXR profiles. The simulations consistently predict more current drive at the outer half of the plasma and less at the center than was measured and correspondingly much broader HXR profiles than measured. The simulations are unable to predict many of the

profile effects and only some of the general trends versus plasma parameters. The simulations over predict the total plasma current in partially-inductive discharges with high-power LHCD and significant loop voltage, appear to numerically slide-away. The simulations show increased sensitivity to changes in the input temperature and density profiles while the experiments consistently show the same HXR and current profile shapes. Sensitivity studies across reasonable parameters were unable to bring the model into agreement. This work suggests that the simulations may be missing important physics in this operational regime which is typically thought of a relatively simple with good current drive. In this parameter range the rays make a few bounces while parametric decay instabilities and scrape-off layer changes are not typically observed.

The thesis is organized in two parts. First the MSE diagnostic is described along with key advances to the technique to enable better operation on ALCATOR C-MOD and next generation devices. Then the diagnostic is used with other measurements to study the effects of LHCD in C-MOD plasmas, concluding with profile and 0-D comparisons to numerical simulations.

BIBLIOGRAPHY

[1] International Energy Agency. *World Energy Outlook 2014*. 2014.

[2] Jeffrey P. Freidberg. *Plasma physics and fusion energy*. Cambridge : Cambridge University Press, 2007., 2007.

[3] John Wesson and D. J. Campbell. *Tokamaks*. Oxford science publications. Oxford : Clarendon Press ; New York : Oxford University Press, 2004., 2004.

[4] M. Greenwald, A. Bader, S. Baek, M. Bakhtiari, H. Barnard, W. Beck, W. Bergerson, I. Bespamyatnov, P. Bonoli, D. Brower, D. Brunner, W. Burke, J. Candy, M. Churchill, I. Cziegler, A. Diallo, A. Dominguez, B. Duval, E. Edlund, P. Ennever, D. Ernst, I. Faust, C. Fiore, T. Fredian, O. Garcia, C. Gao, J. Goetz, T. Golfinopoulos, R. Granetz, O. Grulke, Z. Hartwig, S. Horne, N. Howard, A. Hubbard, J. Hughes, I. Hutchinson, J. Irby, V. Izzo, C. Kessel, B. LaBombard, C. Lau, C. Li, Y. Lin, B. Lipschultz, A. Loarte, E. Marmar, A. Mazurenko, G. McCracken, R. McDermott, O. Meneghini, D. Mikkelsen, D. Mossessian, R. Mumgaard, J. Myra, E. Nelson-Melby, R. Ochoukov, G. Olynyk, R. Parker, S. Pitcher, Y. Podpaly, M. Porkolab, M. Reinke, J. Rice, W. Rowan, A. Schmidt, S. Scott, S. Shiraiwa, J. Sierchio, N. Smick, J. A. Snipes, P. Snyder, B. Sorbom, J. Stillerman, C. Sung, Y. Takase, V. Tang, J. Terry, D. Terry, C. Theiler, A. Tronchin-James, N. Tsujii, R. Vieira, J. Walk, G. Wallace, A. White, D. Whyte, J. Wilson, S. Wolfe, G. Wright, J. Wright, S. Wukitch, and S. Zweben. 20 years of research on the Alcator C-Mod tokamak a). *Physics of Plasmas (1994-present)*, 21(11):110501, November 2014.

[5] V. Mukhovatov, M. Shimada, A. N. Chudnovskiy, A. E. Costley, Y. Gribov, G. Federici, O. Kardaun, A. S. Kukushkin, A. Polevoi, V. D. Pustovitov, Y. Shimomura, T. Sugie, M. Sugihara, and G. Vayakis. Overview of physics basis for ITER. *Plasma Physics and Controlled Fusion*, 45(12A):A235, December 2003.

2

THE MOTIONAL STARK EFFECT DIAGNOSTIC

Chapter goals:

- Introduce the physics of the Motional Stark Effect (MSE) diagnostic
- Describe the ALCATOR C-MOD MSE diagnostic
- Discuss the challenges of fielding the diagnostic in next-step facilities and how C-MOD's installation can contribute to solutions

Controlling the current profile and the q-profile is a focus of research effort to optimize plasma operation during discharges. easuring them is vital for physics understanding including the validation of first-principles numerical simulations of plasma turbulence, transport, current drive, and stability.

No technique has been devised to directly measure either the q-profile or the current profile in a tokamak. However, these quantities are simply related to the magnetic field which can be measured in a variety of ways.

Modern tokamaks do not have circular cross-sections and are instead highly shaped with large, non-negligible, Shafranov shifts. However, a close relationship between the current density and the magnetic field remains; but instead of solving the relationship analytically, the quantities of interest are typically determined by numerically solving the Grad-Shafranov equation in a magnetic equilibrium reconstruction using a variety of measurements both internal and external to the plasma. This is covered in depth in Appendix B.

One possible measurement is the angle of the magnetic field relative to the toroidal direction in the tokamak, referred to as the magnetic pitch angle $\gamma = \tan^{-1}(\frac{B_{pol}}{B_\phi})$, the measurement of which is the subject of a large portion of this thesis.

2.1 PRINCIPLES OF AN MSE DIAGNOSTIC

Despite efforts across many devices for many years, accurate measurements of the internal safety factor and current profile in tokamaks remained sparse until the development of the Motional Stark Effect (MSE) diagnostic the operation of which is described in the remainder of this chapter. This diagnostic uses atomic physics to determine the properties of the magnetic field inside the plasma.

The atomic physics under-pinning the diagnostic technique is the Stark effect [1] which is discussed in detail in many atomic physics

texts [2–9]. This section presents a short summary of the results related to the MSE diagnostic in the limit of the pure Stark effect. The Stark effect is a perturbation to the atomic energy levels due to the presence of a strong electric field that is analogous to the more familiar Zeeman effect due to the magnetic field. The unperturbed atom in primary energy level n is $2n^2$-way degenerate in the l and m_l quantum numbers. The Stark perturbation leads to a splitting of the line emission. In fusion plasmas, the species of interest is typically hydrogenic neutrals where the Stark effect is large and linear in the strength of the electric field[1]. The effect is present in all the atomic transitions, including the intense Lyman-α series in the ultraviolet ($L_\alpha = 121.6$nm in air). However, the weaker Balmer-α transition, $n = 3$ to $n = 2$, is typically used since it is has significant intensity in the visible range (H_α= 656.281nm and $D_\alpha = 656.103$nm in air [10]), simplifying the optical system required to collect the emission. The work presented in this thesis will deal with the Balmer-α transition in hydrogen, which is split into 15 different lines from a possible 36 transitions due to the Stark effect. The energy of the H_α emission, $\Delta\mathbf{E}_{H\alpha}$, under the Stark effect is:

$$\Delta\mathbf{E}_{H\alpha} = \frac{3}{2} e a_0 \left(0, \pm1, \pm2, \pm3, \pm4, \pm5, \pm6, \pm8\right) E \tag{2}$$

where e is the electron charge, a_0 is the Bohr radius and E is the electric field strength in the atom's frame.

This Stark split emission is net unpolarized (and remains so in the Stark-Zeeman case [9]); however, the emission is comprised of two types of transitions, referred to[2] as σ and π. These types differ depending on the details of the Stark atomic states which leads to differences in the polarization of the emission. The Stark split separates the emission in wavelength, which allows the different types of transitions to be observed separately, each with net polarization. The linear polarization direction is directly related to the direction of the electric field in the atom's frame. The observed polarization along a sightline is then a geometric projection of the electric field onto that sightline. Each transition type also has different intensity patterns depending on the angle Φ between the electric field direction and the observation sightline. The intensity of the individual lines depends on this geometric factor; the population density of the initial state, P_i; and the transition probability between the initial and final states, A_{if}. The

1 There is a contribution in the energy shift which is quadratic in the electric field: $\Delta\mathbf{E}_{H\alpha} = \pm aE - bE^2$ where a and b depend on the specific parabolich states of the transition. At $E = 15$MV/m the contribution to the shift from the quadratic term is $0.4 - 1.4\%$, depending on the transition [9], this increases to $1.2 - 4.5\%$ for a 1MeV beam in a 5.4T machine such as ITER. The work presented here considers only the linear Stark effect.

2 An interesting history of the σ and π spectral naming convention can be found in reference [11].

character of the Stark split Balmer-α hydrogen emission is summarized below:

σ EMISSION: From atomic transitions with $\Delta m_l = \pm 1$. When viewed transverse to the electric field, it is polarized linearly perpendicular to the electric field. When viewed parallel to the electric field, the transition is polarized circularly with the handedness dependent on the sign of Δm_l. However, there are an equal number of atoms transitioning $+\Delta m_l$ as $-\Delta m_l$ producing equal amounts of left and right-handed circular light. Thus, when viewed along the electric field the total emission is net unpolarized. The intensity is:

$$I_\sigma = \frac{1}{2}\left(1 + \cos^2(\Phi)\right) A_{if} P_i \tag{3}$$
$$\lambda_\sigma = 656.281 + (0, \pm 1, \pm 5, \pm 6)\ 0.0277\ E \text{ nm}$$
in atom's frame, E in $^{MV}/_{m}$

π EMISSION: From transitions with $\Delta m_l = 0$. Consists of dipole transitions along the axis of the electric field. When viewed perpendicular to the electric field, the emission is purely linearly polarized parallel to the electric field. The emission is not present when viewed along the electric field. The intensity is:

$$I_\pi = \sin^2(\Phi) A_{if} P_i \tag{4}$$
$$\lambda_\pi = 656.281 + (\pm 2, \pm 3, \pm 4, \pm 8)\ 0.0277\ E \text{ nm}$$
in atom's frame, E in $^{MV}/_{m}$

By convention, each of the lines in the Stark split are referred to by the type and number of their transition (i.e., π_{+2} and σ_{-1}). In fusion plasmas, the upper states are typically populated via collisions with the plasma electrons. When all the upper states are populated in thermodynamic equilibrium, the system is said to be statistically populated. When the neutrals are nearly statistically populated, there are only nine Stark lines with significant emission levels (σ_0, $\sigma_{\pm 1}$, $\pi_{\pm 2}$, $\pi_{\pm 3}$, $\pi_{\pm 4}$). This work deals with situations near statistical equilibrium. The Stark lines are shown schematically with their relative emission from statistical population levels in Figure 5.

There are very few hydrogenic neutrals in the interior of the plasma, and therefore little H_α emission, at high fusion-relevant plasma temperatures. For the neutrals that do exist, the Stark effect is unresolvable since the electric fields are typically small ($\mathcal{O} \sim {}^{kV}/_{m}$) due to the high conductivity of fusion plasmas. The magnetic field is often high ($\mathcal{O} \sim T$) in large tokamaks thus the Zeeman effect dominates the Stark split. However, when neutrals are injected by a high energy neutral beam they can penetrate deep into the plasma before they are ion-

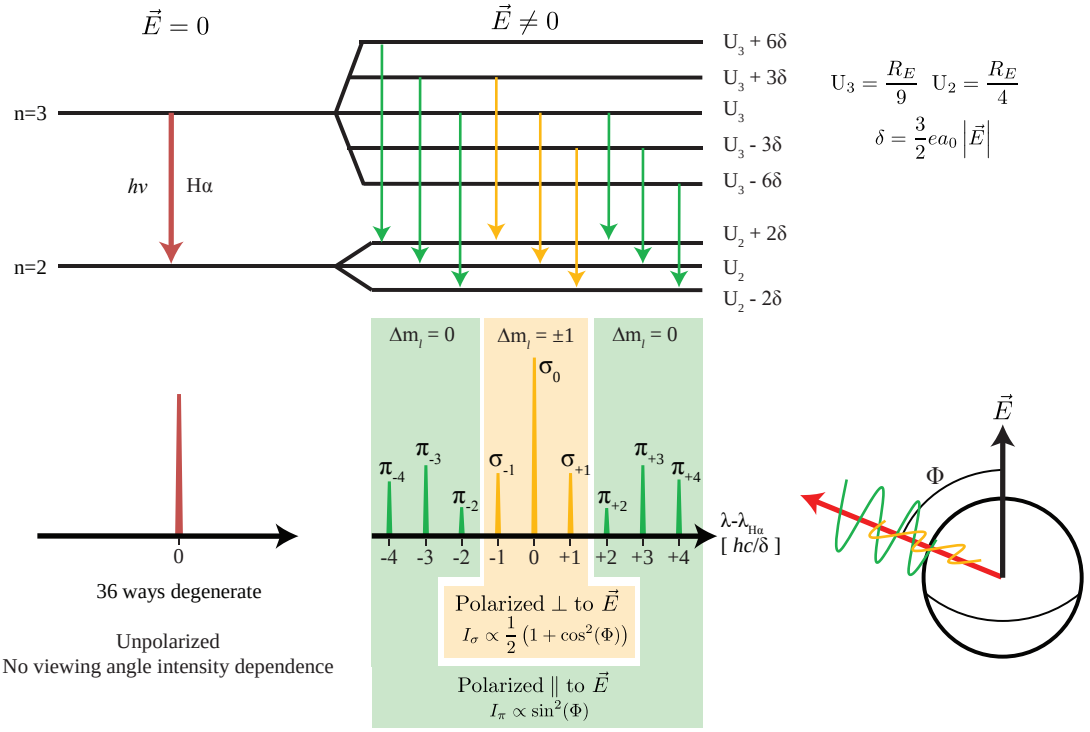

Figure 5: Application of an electric field splits the hydrogen atom's energy level, removing degeneracy resulting in a split of the H_α emission into 15 lines (9 with significant emission). The split in the emission is linear in the electric field and consists of two types of emission, σ and π, depending on the character of the transition. The σ emission is polarized perpendicular to the electric field and the π emission is polarized parallel to the electric field.

ized. These neutrals cross a the strong magnetic field at high velocity, experiencing a large Lorentz electric field in the atom's frame:

$$\vec{E}_{\text{Lorentz}} = \vec{v}_{\text{beam}} \times \vec{B} \tag{5}$$

In ALCATOR C-MOD, the neutrals have energies of 50 keV and cross the $\sim$ 5 T magnetic field nearly perpendicularly, leading to Lorentz electric field of $\sim$ 17 $^{\text{MV}}/_{\text{m}}$ and a Stark split of $\sim$ 0.47 nm. When the Stark split is primarily caused by the Lorentz field via the velocity of the atoms, the effect is referred to as the motional (or translational) Stark effect.

When viewed at an angle other than perpendicular to the beam (ψ_{observe}), the emission is shifted in the lab frame due to the Doppler shift from the high velocity of the neutrals:

$$\lambda_{\text{observe}} = \lambda_{\text{emit}} \left(1 + \frac{v}{c} \cos(\psi_{\text{observe}})\right) \tag{6}$$

The large Doppler shift and modest Stark split separate the polarized emission due to the neutral beam from the unpolarized H_α emission from the much lower velocity edge neutrals. The finite collection volume and aperture of the diagnostic then lead to substantial broadening of the individual lines.

The motional Stark effect emission carries information about the geometry of the Stark electric field in its polarized spectrum. Because the electric field arises from the beam neutrals motion across the magnetic field this information is geometrically related to the magnetic field in the plasma at the point where the light was emitted. In the very simple case where the beam and sightline reside on the plasma mid-plane and there is no background electric field, the polarization angle of the σ emission ($\theta^{\sigma}_{\text{pol}}$) collected by the diagnostic can be related to the magnetic pitch angle $\tan^{-1}(\frac{B_z}{B_\phi})$ as:

$$\tan(\theta^{\sigma}_{\text{pol}}) = \frac{-B_z}{B_\phi} \frac{\cos(\alpha + \Omega)}{\sin \alpha} \tag{7}$$

where α and Ω are the angles of the sightline and beam relative to the local toroidal direction respectively. The geometry is shown in Figure 6.

By collecting and analyzing the polarization, intensity, and/or spectral properties of the light, information about the geometry of the magnetic field can be recovered remotely from the interior of the plasma using only an optical periscope viewing a neutral beam, which is commonly present for heating the plasma. The capability of using the motional Stark effect to diagnose the fields deep inside fusion plasmas was recognized soon after the development of high energy neutral beams capable of penetrating and heating the plasmas [12, 13]. Although the detailed theory of the Stark effect was developed in the

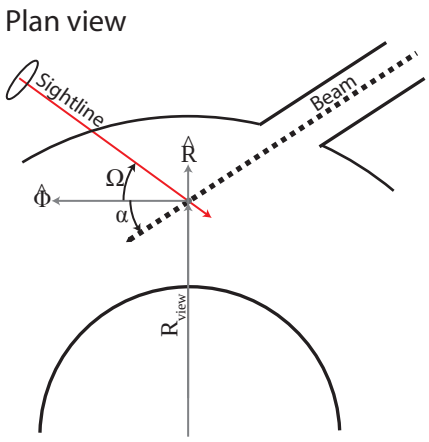

Figure 6: Simplified MSE viewing geometry where both the beam and the sightline reside in the plasma midplane.

1950's [3, 4, 14], the specifics for high temperature plasmas and high energy neutral beams were calculated only in the 1980's [5–7] and remain a topic of intense research by atomic theorists [15–22] and experimentalists [23–27], particularly in cases that are not statistically populated.

2.2 THE MSE LINE POLARIZATION (MSE-LP) APPROACH

By far the most successful and widely implemented MSE technique is based on determining the polarization angle of either the σ or π multiplets of the neutral beam emission. This is done by using a polarimeter consisting of rapidly vibrating crystals. In this technique, the light from the beam is collected by an optical periscope and transmitted via polarization preserving optics out of the tokamak where the polarization is incident on a polarimeter consisting of a pair of photo-elastic modulators (PEMs). The PEMs encode the polarization Stokes vectors into the frequency domain at tens of kHz. The frequency modulated light is then transmitted via optical fibers to a remote diagnostic hall where either the σ or π multiplet is isolated using narrow bandpass filters and the light is detected by the photo-diodes or photomultiplier tubes. The frequency modulation is decoded using lock-in amplifiers or is digitized and demodulated using a numerical phase-locked loop. The ratio between the amplitudes at the PEM's second harmonic then gives the polarization angle incident on the polarimeter. This angle is then used to calculate the angle of the magnetic field in the plasma using the known viewing geometry. The technique is referred to as MSE line-polarization (MSE-LP) and is shown schematically in Figure 7.

The approach was first implemented in 1989 in PBX-M by Levinton [28] and has since been installed on most large tokamaks with varying degrees of success. The last formal review of MSE-LP instruments and their results was conducted in 1999 by Levinton [29]. A more complete and up-to-date account is discussed in Reference [30].

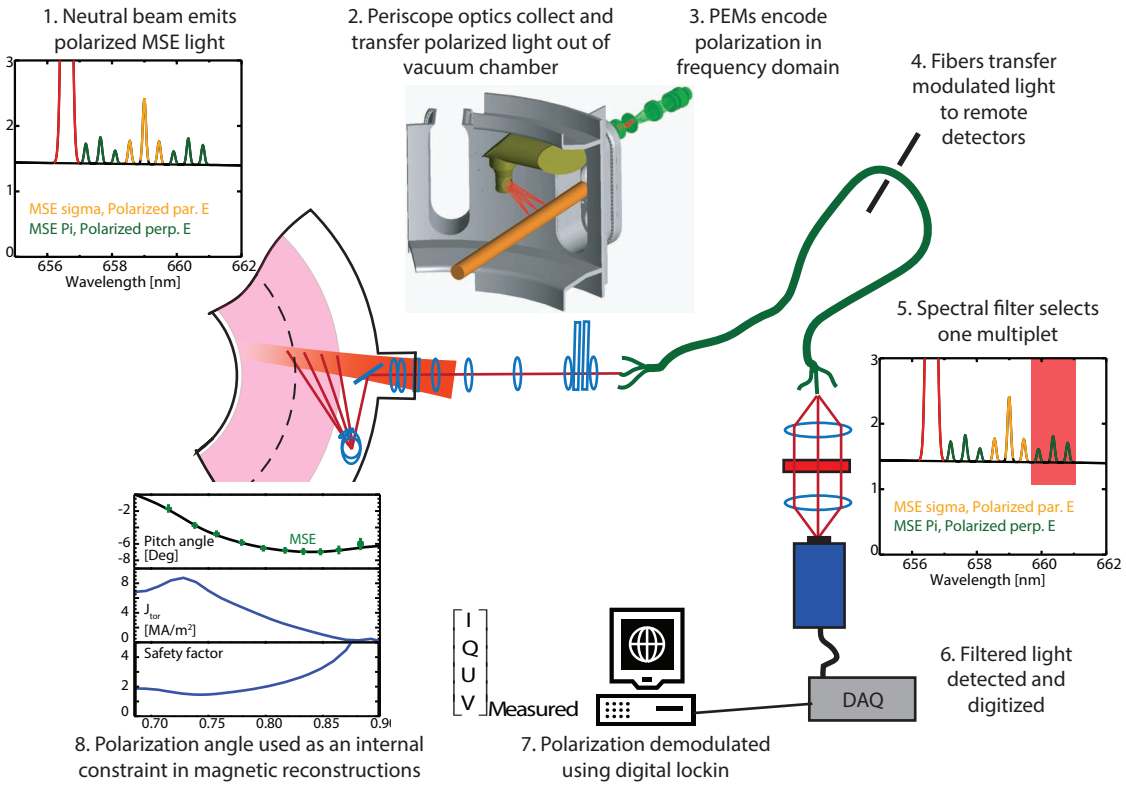

Figure 7: Layout of a MSE-LP system. Starting from the top left and moving clockwise.

Because the polarization properties of the light are transmitted from the tokamak as different intensities in the frequency domain and detected with a single simple detector and amplifier system, the MSE-LP approach can very accurately determine the polarization angle of the light incident on the polarimeter with high noise rejection. However, the approach requires detection of the signal modulated at approximately 40kHz. Therefore, the spectrum is filtered for multiple lines from the same σ or π triplet and absorbed by a high quantum efficiency detector. The decoding of the polarization angle is relatively straightforward and can be done with analog electronics or fast digital processing, making the quantity of interest available in near real-time for plasma control purposes.

The primary draw-backs of the MSE-LP technique are: (1) the transmission of the polarized light to the PEM-based polarimeter requires a polarization-preserving optical periscope which can be challenging to construct, (2) the diagnostic requires substantial light collection and thus large optics, and (3) only emission from part of the multiplet is utilized, discarding more than half of the available emission.

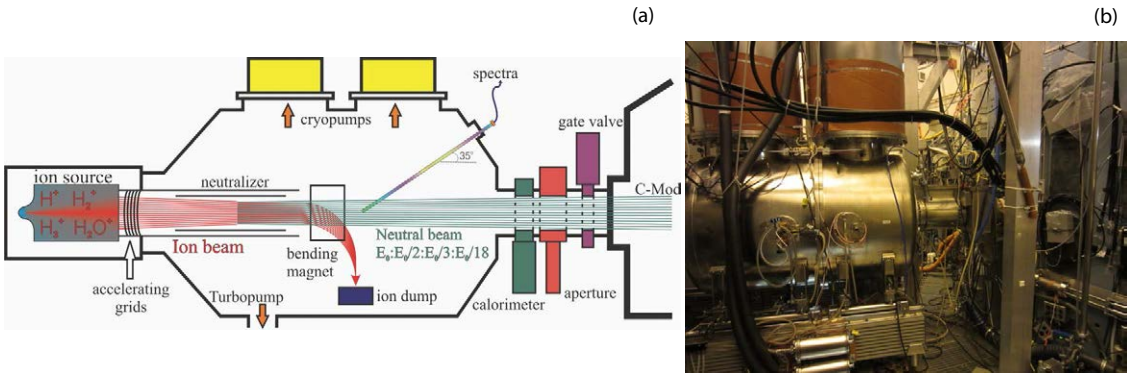

Figure 8: Layout of the C-MOD DNB shown schematically with important subsystems. Adapted from [34] (a). Photograph of the DNB installed on the tokamak (b).

2.3 ALCATOR C-MOD'S MSE DIAGNOSTIC

The MSE-LP system for ALCATOR C-MOD was proposed in 1997 [31] and designed from 1999 to 2002 as part of a collaboration between PPPL and the ALCATOR team [32]. The system was installed and commissioned by Howard Yuh and Steve Scott from 2000-2005 [9]. Necessary upgrades were added prior to the first physics result by Jinseok Ko from 2004-2008 [33]. Since the system's installation it has been almost completely rebuilt several times, both to withstand the unforeseen harsh operational conditions inside ALCATOR C-MOD and to provide the necessary accuracy and confidence for physics studies. This section discusses the main components and operation of the diagnostic system.

2.3.1 *Neutral beam*

The MSE system observes a 50keV diagnostic neutral beam (DNB) developed by the Budker Institute in Novosibirsk, Russia [35]. Unlike all other operating MSE systems, the C-MOD system observes a low power diagnostic beam instead of a high power heating beam. Due to the space constraints in the tokamak, the beam is injected nearly radially[3] through F-port on the tokamak. The DNB consists of an ion source, a set of accelerator optics, a neutralizer cell, a beam tank, and a beam-line coupled to the tokamak.

Depending on the plasma density, a fraction of the beam neutrals will be in excited upper states due to collisions. The spontaneous or collisionally induced radiation from these states leads to the motional Stark-shifted emission. Some of the light from the beam neutrals is then collected by the MSE periscope and transmitted out of the tokamak. The ion creation, extraction, and acceleration process sets the

3 An injection angle of only 6.7° in the horizontal plane is used to reduce the effect from secondary neutral emission during beam-into-gas experiments [36].

Table 2: Typical DNB operating conditions

Parameter		
Acceleration voltage	44-50	keV
Ion current	5-7	A
Neutralization efficiency	0.50-0.56	[-]
Neutral density fractions	$0.45 : 0.08 : 0.29 : 0.18$	H, H_2, H_3, H_{14} [37]
Size at calorimeter	0.08	m FWHM [38]
Size in plasma center	0.16	m FWHM [38]
Beamlet divergence	$\sim 1.6°$	FWHM
Peak neutral density at plasma edge	$1 - 2x10^{14}$	m^{-3} [34]
Voltage fluctuation	± 1	keV
Settle time	10-20	ms
Integrated on time	< 1.5	s per shot

fundamental size and neutral density of the beam. This size and density affects the MSE signal level, spatial resolution and systematic error level. For best diagnostic operation the goal is to provide smallest (i.e., most collimated) beam as possible at the highest reliable current with high full energy fractions, thus producing high full-energy neutral densities.

The beam is operated in a pulsed mode to allow for beam on-off background interpolation, which is covered in detail in Chapter 5. The DNB is typically operated in a $60 - 80$ms beam-on, $40 - 20$ms beam-off pulse train across the entire discharge. Beam modulation is often utilized on other tokamaks with MSE systems, although concerns about modulating the plasma heating and beam-driven current often conflict with the needs of MSE systems viewing heating beams. A primary constraint on the availability of the C-MOD MSE measurement is the beam maintainability and reliability. Recent experience indicates that operating the beam at slightly reduced acceleration voltage, 45keV vs 50keV, and at currents < 7A greatly increases reliability with little sacrifice in performance. Typical beam performance parameters are summarized in Table 2.

2.3.2 *MSE hardware*

The beam emission must be collected in a location near the mid-plane but between two C-MOD vacuum ports for the following reasons: (1) the compact nature of the ALCATOR C-MOD tokamak provides very few ports; (2) the nearly radial DNB constrains viewing angles; and (3) the viewing geometry required to obtain sufficient Doppler shift and polarization sensitivity. Therefore, a complex periscope is used

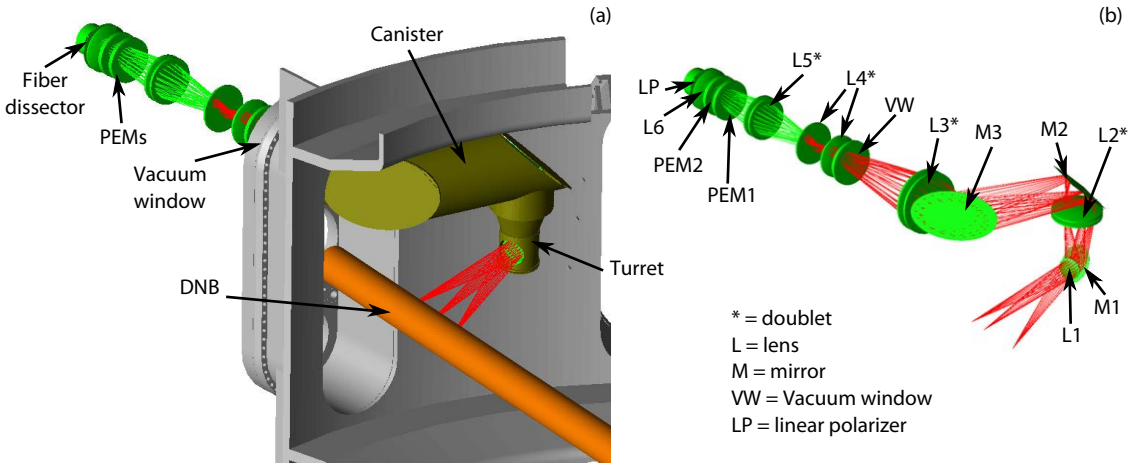

Figure 9: The MSE periscope inside the tokamak viewing DNB (orange) with optical train. The interior periscope consists of two components, the canister and the turret (a) and showing rays within each of three of the ten sightlines with all the optical components labeled (b).

to collect the light from an optimal location. This periscope uses five lenses and three mirrors mounted inside the vessel vacuum to transfer the light to the single vacuum window placed immediately above the DNB duct entrance. Due to the large radial build of the C-MOD support structure and cryostat, the light is further transported radially in air using five lenses. Finally, it is incident on the dual-PEM-based polarimeter. A large étendue is required for adequate signal collection from the relatively weak DNB leading to large optical components for the MSE system. The optical periscope is shown in Figure 9.

The dual-PEM-based polarimeter operating at 20 and 22kHz encodes the polarization of the light into amplitude-modulated frequency components. The unit consists of two separate PEMs with an aperture diameter of 106mm[4] and a removable linear polarizer. The three components are pin-aligned to maintain the correct orientation.Various systematic errors in the operation of the PEMs will be discussed in detail in Chapter 3.

After being encoded by the PEMs, the light is focused by the tenth lens onto a curved image plane. A set of ten ~ 30m fiber bundles, each containing 16 1mm core diameter (numerical aperture = 0.37) fibers, collect the light at the image plane and transmit it out of the tokamak cell to the the diagnostic hall ~ 20m away. The fiber bundles are attached to the optical periscope with a complex fiber dissector that is shaped to align the fibers to the image plane. The geometry of these ten fiber bundles on the image plane defines the MSE viewing sightlines. The image of these fiber bundles at the intersection between the beam and sightline defines the viewing volume. The objective lens (L1) defines the nominal entrance pupil. Extensive tests indicate there is little vignetting in the complicated optical periscope. The fibers are

4 Hinds PEM-90 hindsinstruments.com

under filled at numerical aperture ~ 0.3 by the periscope. Due to the complex geometry and the desire to frequently change the fiber layout to refine the various views (nearly every campaign), the fiber dissector was fabricated using additive manufacturing (i.e., 3D printing) techniques, a first for an operational component on ALCATOR C-MOD and possibly any tokamak.

The ten optical fiber bundles each input the light into a filter oven assembly. Each oven contains lenses that collimate the light through a narrow-bandpass (FWHM $0.4 - 0.8$nm) 50mm diameter optical interference filters and refocuses it onto 10mm diameter avalanche photodiode (APD) detectors. The filter ovens are temperature controlled to tune the bandpass of the filters to only pass the desired part of the beam emission spectrum.

The APDs detect the frequency modulated light with high quantum efficiency (~ 0.9) and internal gain ($M = 30 - 100$). The output current is amplified by a trans-impedance amplifier ($2 \times 10^7 \mathrm{V/A}$) integrated into the APD module before the signal is recorded by a 16 channel, 14-bit, differential analog to digital converter sampling at 1MHz. The square wave drive signals from each of the PEMs are transmitted over a fiber optic link from the PEM drivers in the tokamak cell to the diagnostic lab and are digitized with the same unit. The data, with setup parameters, calibrations, and analysis is stored in the MDSPLUS database system. Photographs of the periscope, control, detection, and digitization hardware are shown in Figure 10.

A GUI program controls the voltage applied to the APDs to vary their internal gain and turns the APDs on before a plasma discharge and then off again afterwards. Additional software controls the temperature of the filter ovens by computing the filter temperature required to place the filter passband at the correct location relative to the Stark emission spectrum, based on the DNB beam energy, the toroidal magnetic field, the MSE viewing geometry, and the filter transmission curve.

2.3.3 *MSE analysis software*

The analysis process is launched automatically after the data is stored from a discharge. The data processing consist of the following general procedures: (1) determining the amplitude in the detected signal at the various PEM harmonics, (2) calculating the polarization angle incident on the objective lens (taking into account background light and calibration), (3) calculating the corresponding plasma pitch angle.

Traditionally, MSE installations use analog lock-ins to determine these components. However, this approach is hardware-intensive, requiring a lock-in amplifier for each desired frequency harmonic. A digital approach offers the advantages of reduced hardware complexity, increased flexibility, decreased noise [39], and the ability to deter-

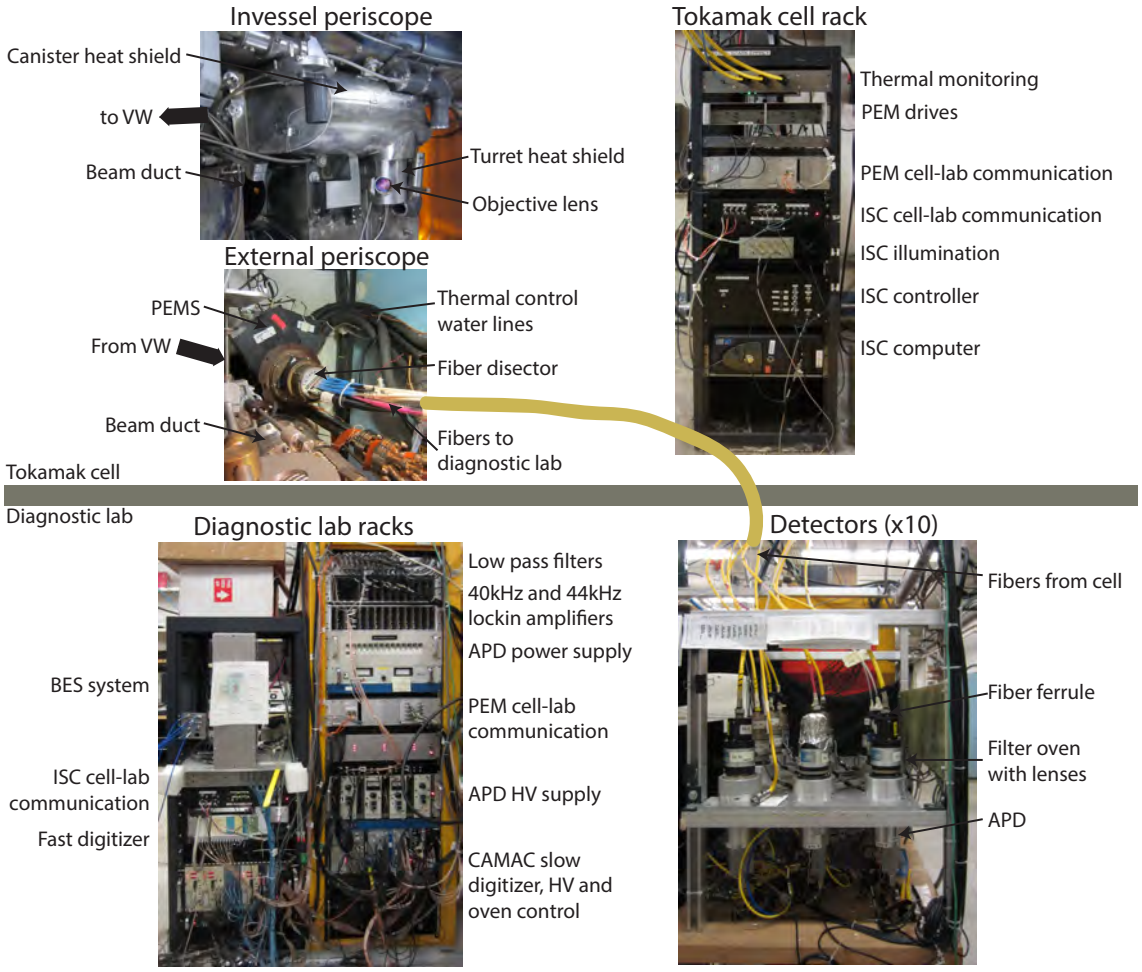

Figure 10: Photographs of the MSE hardware system. Clockwise from upper right, The internal periscope and external periscope relay optics with PEMS, the control rack in the cell, the bandpass filters and APDS, and the control and digitization equipment in the diagnostic lab.

mine the intensity at an arbitrary number of harmonics. A technique based on fast-Fouier transforms (FFTS) was attempted but was unsuccessful due to inaccuracy of determining the peak amplitudes which need to be calculated at a fraction of a percent to achieve the required accuracy in polarization angle. Therefore, a numerical lock-in technique was developed. This was the first such technique used for MSE diagnostics.

Next the background light is estimated and subtracted. This technique is discussed in Chapter 5. The calibration is then used to determine the polarization angle incident upon the diagnostic objective lens. The view geometry is used to compute the magnetic pitch angle from the plasma under simplified assumptions.

With ten spatial channels covering the entire radius of the plasma, this diagnostic should be able to measure the safety factor profile to better than $\Delta q \sim 0.2$ if an accuracy of $\Delta\gamma \sim 0.3^\circ$ in pitch angle is achieved. Due to the geometric projection of the pitch angle into polarization angle this requires a polarization uncertainty of $\Delta\theta_{pol} \sim 0.1^\circ$. The geometric projection is more unfavorable at the edge of the plasma in the C-MOD geometry.

The hardware discussed in this section existed in basic form and function prior to this thesis. Significant hardware upgrades were performed to improve the measurement accuracy and increase the diagnostic availability enabling the diagnostic to be used for physics studies. The upgrades include a robotic calibration system used to calibrate MSE during maintenance periods. An intra-shot calibration system used to calibrate systematic errors immediately after shots. A thermal management and monitoring system to stabilize the diagnostic response. A new multi-spectral detection system.

2.4 CHALLENGES FOR MSE-LP ON NEXT-STEP DEVICES: C-MOD IN CONTEXT

The integration of MSE-LP systems into next generation facilities faces challenges, most of which will need to be addressed on ITER. Many of the problems faced in future devices have severely hampered the utility of the C-MOD diagnostic prior to the work presented in this thesis. The ALCATOR C-MOD MSE-LP system is unique in ways that make it a valuable test bed for developing solutions to these burning-plasma integration challenges. In an effort to make the diagnostic useful for physics studies of current drive, these shortcomings were studied and techniques were developed to overcome them. These topics are covered in the next four chapters.

Next step burning plasma facilities will create high fluxes of high-energy neutrons. To prevent these neutrons from free streaming out of the vessel, plasma-viewing diagnostic must traverse a long optical path with many bends through the blanket, i.e., an optical labyrinth

using polarization preserving mirrors[5]. C-MOD has extensive experience with large optical labyrinths including optimizing their polarization properties fielding robust designs. Because of the optical complexity, the C-MOD periscope has polarization aberrations which are significant enough to warrant study and compensation techniques. Significant work was undertaken to verify that the diagnostic is operating correctly and to catalog sources of systematic errors which are also present on other and future MSE-LP installations. These topics are explored in Chapter 3.

The first mirror for all optical diagnostics in long pulse reactors requires line of sight to the plasma where ion and charge-exchange products will impinge upon it, sputtering and deposited thin coatings on the mirror surface. In addition to decreased reflectivity, the polarization upon-reflection properties will also be significantly modified [40] [41], directly affect the systematic errors of the MSE-LP measurement. Simulations indicate mirror surface modification will occur across a small number of discharges and possibly even significantly within discharges. In addition to changing across time, the polarization properties are likely to change across the surface of the mirror due to spatially non-uniform coatings and erosion [40]. The nature of the degradation will depend on plasma properties, impurity content, and details of the geometry, making ab-inito calculation and online correction difficult. Furthermore, due to availability and operational constraints, plasma and beam-into-gas discharges will not be available to calibrate the MSE-LP systems as is often done on many existing systems. Therefore, an accurate form of in-situ polarization calibration, including an illumination source, will need to be integrated at the front of the diagnostic to allow it to be calibrated at convenient times. The C-MOD installation does not have problems with mirror coatings, but does have significant issues with the lenses introducing analogous, time-dependent, stress-induced retardation into the system as discussed in Chapter 4. This led to the development of the first in-situ calibration system to calibrate the diagnostic after each shot.

As the devices get larger and denser and thus more fusion relevant, the ability of neutral beams to penetrate deep into the core becomes impaired leading to decreased signals and next-generation devices will have substantially brighter background emission from non-MSE sources. This means future MSE systems will operate at low signal to background intensity ratios and will require background subtraction techniques. Fortunately the MSE-LP technique is not directly affected by unpolarized background light—The PEM modulation scheme is a very effective way to isolate only the polarized component of the collected light. However, unpolarized light within the tokamak can become partially polarized upon reflection from internal components,

5 Glasses cannot withstand the neutron fluence in this region

skewing measurements.The background will likely consist of many different sources interacting making estimation and subtraction difficult. Although the C-MOD DNB does not have significant problems penetrating the small, dense, C-MOD plasma, the MSE signal is still weak due to the low power and large size of the DNB leading to the smallest signal to background ratios of any existing MSE diagnostics. The character and subtraction of this light is the subject of Chapter 5 and techniques were developed to subtract the polarized background using wavelength interpolation as discussed in Chapter 6.

Each of these problems for next-step machines can be explored in current devices where solutions can be tried quickly and at relatively low cost. It is therefore prudent to tackle these challenges now so that an experience base can be created prior to deployment on expensive, unforgiving burning plasma experiments and reactors. The requirement to develop solutions to the unique—and burning-plasma relevant—diagnostic challenges in C-MOD to enable physics studies makes the C-MOD MSE installation an important contribution to the field.

Furthermore, although the C-MOD system may not have the most sightlines, or the fastest time resolution, or sharpest spatial resolution, it is the only operable system installed on a tokamak with dominant lower hybrid current drive capable of non-inductive operation. This, combined with solutions to the unique—and burning-plasma relevant—diagnostic challenges makes the C-MOD MSE installation an important contribution to the field.

BIBLIOGRAPHY

[1] J. Stark. Beobachtungen über den Effekt des elektrischen Feldes auf Spektrallinien. I. Quereffekt. *Annalen der Physik*, 348(7):965, January 1914.

[2] P. S. Epstein. Stark effect from the point of view of Schroedinger's quantum theory. *Physical Review.*, 28:695–710, October 1926.

[3] E. U. Condon and G. H. Shortley. *The theory of atomic spectra, by E. U. Condon and G. H. Shortley*. Cambridge [Eng.] University Press, [1951], 1951.

[4] Hans A. Bethe and Edwin E. Salpeter. *Quantum mechanics of one- and two-electron atoms, by Hans A. Bethe and Edwin E. Salpeter*. Berlin, Springer; New York, Academic Press, 1957., 1957.

[5] R. C. Isler. Profiles and polarizations of the Balmer-α line from high-temperature hydrogen atoms in strong magnetic fields. *Physical Review A*, 14(3):1015, 1976.

[6] Brenton, C, De Michelis, C, Finkenthal, M, and Mattioli, M. Hα and Hβ spectral profiles from neutral beams and plasmas in high magnetic fields. *Journal of Applied Physics B: Atomic and Molecular Physics*, 13(8):1703, 1980.

[7] E. K. Souw and J. Uhlenbusch. Calculation of the combined Zeeman and translational Stark effect on the Hα-multiplet. *Physica B+C*, 122(3):353–374, 1983.

[8] B. H. Bransden and C. J. Joachain. *Physics of atoms and molecules / B.H. Bransden and C.J. Joachain*. Harlow, England ; New York : Prentice Hall, c2003., 2003.

[9] H.Y. Yuh. *The Motional Stark Effect diagnostic on Alcator C-Mod*. PhD, Massachusetts Institute of Technology, 2005.

[10] C. W. Allen and Arthur N. Cox. *Allen's astrophysical quantities / Arthur N. Cox, editor*. New York : AIP Press : Springer, c2000., 2000.

[11] Ja Weil. The life of pi and sigma - A tutorial review of the ubiquitous use of these symbols in Zeeman and magnetic-resonance spectroscopy. *Concepts in magnetic resonance part A*, 32A(2):134–142, March 2008.

[12] A. Boileau, M. von Hellerman, W. Mandl, H.P. Summers, H. Weisen, and A. Zinoviev. Observations of motional Stark features in the Balmer spectrum of deuterium in the JET plasma. *Journal of Applied Physics B: Atomic and Molecular Physics*, 22(7):L145–52, 1989.

[13] R.C. Mandl, R.C. Wolf, M. von Hellerman, and H. P. Summers. Beam emission spectroscopy as a comprehensive plasma diagnostic tool. *Plasma Physics and Controlled Fusion*, 35(10):1373, October 1993.

[14] R. J. Damburg and V. V. Kolosov. An asymptotic approach to the Stark effect for the hydrogen atom. *Journal of Physics B: Atomic and Molecular Physics*, 11(11):1921, June 1978.

[15] S. Suzuki, T. Shirai, M. Nemoto, K. Tobita, H. Kubo, T. Sugie, A. Sakasai, and Y. Kusama. Attenuation of high-energy neutral hydrogen beams in high-density plasmas. *Plasma Physics and Controlled Fusion*, 40(12):2097, December 1998.

[16] I. H. Hutchinson. Excited-state populations in neutral beam emission. *Plasma Physics and Controlled Fusion*, 44(1):71, January 2002.

[17] E. L. Foley and F. M. Levinton. A collisional-radiative model including sublevel parameters (CRISP) for Hα radiation. *Journal of Physics B: Atomic, Molecular and Optical Physics*, 39(2):443, January 2006.

[18] M. G. von Hellermann, E. Delabie, R. Jaspers, P. Lotte, and H. P. Summers. Modelling and evaluation of spectra in beam aided spectroscopy. In *AIP Conference Proceedings*, volume 1058, pages 187–194. AIP Publishing, October 2008.

[19] E. Delabie, M. Brix, C. Giroud, R. J. E. Jaspers, O. Marchuk, M. G. O'Mullane, Yu Ralchenko, E. Surrey, M. G. von Hellermann, K. D. Zastrow, and JET-EFDA Contributors. Consistency of atomic data for the interpretation of beam emission spectra. *Plasma Physics and Controlled Fusion*, 52(12):125008, December 2010.

[20] O. Marchuk, Yu Ralchenko, R. K. Janev, W. Biel, E. Delabie, and A. M. Urnov. Collisional excitation and emission of Hα Stark multiplet in fusion plasmas. *Journal of Physics B: Atomic, Molecular and Optical Physics*, 43(1):011002, January 2010.

[21] Yu Ralchenko, O. Marchuk, W. Biel, T. Schlummer, D. R. Schultz, and E. Stambulchik. A non-statistical atomic model for beam emission and motional Stark effect diagnostics in fusion plasmas. *Review of Scientific Instruments*, 83(10):10D504, June 2012.

[22] L. Fernández-Menchero and H. P. Summers. Stark effect in neutral hydrogen by direct integration of the Hamiltonian in parabolic coordinates. *Physical Review A*, 88(2):022509, August 2013.

[23] H. Anderson, M. G. von Hellermann, R. Hoekstra, L. D Horton, A. C. Howman, R. W. T. Konig, R. Martin, R. E Olson, and H. P. Summers. Neutral beam stopping and emission in fusion plasmas I: deuterium beams. *Plasma Physics and Controlled Fusion*, 42(7):781, July 2000.

[24] M. F. Gu, C. T. Holcomb, R. J. Jayakuma, and S. L. Allen. Atomic models for the motional Stark effect diagnostic. *Journal of Physics B: Atomic, Molecular and Optical Physics*, 41(9):095701, May 2008.

[25] A. Iwamae, A. Sakaue, M. Aake, K. Sawada, M. Goto, and S. Morita. Alignment creation and deviation from statistical population distribution in hydrogen $n = 3$ levels observed on MSE spectra of LHD plasma. *Plasma Physics and Controlled Fusion*, 51(11):115004, November 2009.

[26] J. Ko and J. Klabacha. Improved spectral analysis for the motional Stark effect diagnostic. *Review of Scientific Instruments*, 83(10):10D513, July 2012.

[27] I. O. Bespamyatnov, W. L. Rowan, K. T. Liao, O. Marchuk, Yu Ralchenko, and R. S. Granetz. Benchmark of collisional radiative models for ITER beams at the ALCATOR C-MOD tokamak. *Nuclear Fusion*, 53(12):123010, December 2013.

[28] F. M. Levinton, R. J. Fonck, G. M. Gammel, R. Kaita, H. W. Kugel, E. T. Powell, and D. W. Roberts. Magnetic field pitch-angle measurments in the PBX-M tokamak using the motional Stark effect. *Physical Review Letters*, 63(19):2060, November 1989.

[29] F. M. Levinton. The motional Stark effect: Overview and future development (invited). *Review of Scientific Instruments*, 70(1):810–814, January 1999.

[30] R. Mumgaard. Review of Results from MSE Diagnostics. MIT PSFC Research Report PSFC/RR-15-2, MIT PSFC, April 2015.

[31] E. S. Marmar, J. L. Terry, W. L. Rowan, and A. J. Wootton. Diagnostic neutral beam and active spectroscopy requirements for the Alcator C-Mod tokamak (invited). *Review of Scientific Instruments*, 68(1):265, 1997.

[32] N. Bretz, D. Simon, R. Parsells, R. Bravenec, W. Rowan, N. Eisner, M. Sampsell, H. Yuh, E. Marmar, and J. Terry. A motional Stark effect instrument to measure q(R) on the C-Mod tokamak. *Review of Scientific Instruments*, 72(1):1012, 2001.

[33] J. Ko. *Current profile measurements using Motional Stark Effect on Alcator C-Mod*. PhD, Massachusetts Institute of Technology, 2009.

[34] I. O. Bespamyatnov, W. L. Rowan, and K. T. Liao. ALCBEAM - Neutral beam formation and propagation code for beam-based plasma diagnostics. *Computer Physics Communications*, 183(3):669–676, March 2012.

[35] D. Beals, R. Granetz, W. Cochran, W. Byford, W. Rowan, A. Ivanov, P. Deichuli, V. Kolmogorov, and G. Shulzhenko. Installation and operation of new long pulse DNB on Alcator C-Mod. In *21st IEEE/NPS Symposium on Fusion Engineering SOFE 05*, pages 1–4, Knoxville, TN, USA, September 2005.

[36] Howard Y. Yuh, F. M. Levinton, S. D. Scott, and J. Ko. Simulation of the motional Stark effect diagnostic gas-filled torus calibration. *Review of Scientific Instruments*, 79(10):10F523, 2008.

[37] William L. Rowan, M. B. Sampsell, and R. S. Granetz. Interpretation of neutral beam emission spectra as the beam-component density distribution. *Review of Scientific Instruments*, 75(10):3487, 2004.

[38] Igor O. Bespamyatnov, William L. Rowan, and Robert S. Granetz. Compact, accurate description of diagnostic neutral beam propagation and attenuation in a high temperature plasma for charge exchange recombination spectroscopy analysis. *Review of Scientific Instruments*, 79(10):10F315, 2008.

[39] J. D. King, M. A. Makowski, C. T. Holcomb, S. L. Allen, R. Geer, W. H. Meyer, D. N. Hill, D. Pham, and E. C. Morse. A digital lock-in upgrade of the motional Stark effect diagnostic on DIII-D. *Review of Scientific Instruments*, 81(10):10D739, 2010.

[40] M. Kuldkepp, E. Rachlew, N. C. Hawkes, and B. Schunke. First mirror contamination studies for polarimetry motional stark effect measurements for ITER. *Review of Scientific Instruments*, 75(10):3446–3448, October 2004.

[41] J. N. Brooks and J. P. Allain. Particle deposition and optical response of ITER motional stark effect diagnostic first mirrors. *Nuclear Fusion*, 48(4):045003, April 2008.

3

SYSTEMATIC ERRORS IN MSE-LP DIAGNOSTICS

Chapter goals:

- Discuss the importance of systematic errors in the MSE diagnostic response, particularly when they can change over a campaign
- Discuss geometric and spectroscopic effects that can lead to systematic errors
- Discuss polarization aberrations in the optical periscope that can lead to systematic errors
- Discuss non-ideal operation of the PEMs and detectors which can lead to systemic errors
- Summarize the various types of systematic errors, their character, and mitigation strategies

To provide adequate internal constraints to the magnetic reconstruction, the absolute polarization angle measurements must be made to high accuracy and must have accompanying uncertainty estimates. This thesis terms the interpretation of detected signals as an absolute polarization angle emitted from a specified position in the plasma as the "diagnostic response." It is important to quantify the various ways in which the diagnostic response can lead to a misinterpretation of the polarization angle—particularly when this error is not reflected in the reported uncertainty. These errors are usually non-statistical in nature (i.e., time-averaging is unlikely to mitigate them) and are termed "systematic errors" in this work.

Unlike a diagnostic operating only on radiometry (e.g., a visible bremsstrahlung measurement), the MSE-LP diagnostic measures a polarization angle. It is therefore subject to a variety of novel systematic errors not typically encountered in other tokamak diagnostics. The systematic errors in a MSE-LP system can be reduced through design choices. The most remaining systematic errors may be accurately characterized and accounted for in the calibration which relates measured signals to input polarization angle. This approach is likely sufficient if the diagnostic response is stationary in time.

However, the complexity and polarization-based nature of a MSE diagnostic makes it particularly susceptible to changing environmental conditions. The system is usually operated in a harsh environment that can lead to a changing diagnostic response which quickly becomes problematic for interpreting diagnostic results.

Many current devices have fairly simple MSE-LP systems, often only incorporating a single or a few optical elements in the MSE periscope that resides entirely outside the vacuum vessel. These diagnostics operate in the relatively benign environments of present short-pulse tokamaks. The C-MOD installation contains many optics inside the vessel where they are subject to large disruption forces and thermal transients. Other MSE-LP diagnostics with similar complexity have encountered serious operational issues.

Sources of systematic errors novel to MSE-LP diagnostics can be broadly defined into three categories organized roughly into the collection, transportation, and encoding/decoding of the polarized light:

NON-IDEAL SOURCE ERRORS There are various effects due to the fields in the plasma, geometric averaging, and spectral effects that make interpreting the polarization angle more complicated than the ideal-case. This can lead to mis-interpretation of and sensitivities in the measurement if not properly accounted for. These effects influence the net polarization of the light incident on the diagnostic entrance pupil and are independent of the specifics used to transport and analyze the polarized light.

POLARIZATION ABERRATIONS IN THE OPTICAL SYSTEM The complex polarization-preserving optical system transports the light from the diagnostic objective lens to the PEM-based polarimeter where the polarization is encoded into the frequency domain. Various effects due to non-ideal polarization-preserving optics can systematically alter the polarization before it is encoded by the polarimeter. These are referred to as polarization aberrations.

NON-IDEAL POLARIMETER RESPONSE The polarization of the light incident on the PEM-based polarimeter is encoded into time-varying signals and is decoded. The interpretation of the polarization angle from these signals can be systematically changed by errors in the construction and operation of the PEM-based polarimeter and non-ideal behavior in the amplification and analysis processes.

The work presented here was conducted to elucidate these effects, to aid the design of future MSE-LP systems, and to understand what effects could cause a changing diagnostic response in the C-MOD MSE system and to determine viable mitigation strategies. This is the first comprehensive study of the various MSE-LP-specific systematic and interpretation errors to be published.

These systematic errors are derived using Müeller calculus and Stokes vectors, the correct way to account for the light inside the tokamak. The reader unfamiliar with Stokes vectors and the sometimes non-intuitive behavior of polarized light is directed to Appendix A

which contains the definitions of the polarization terms and examples of the behavior of polarized light when combining multiple sources.

3.1 POLARIZATION MEASUREMENT SYSTEMS USED ON C-MOD

Many of these errors were experimentally explored on C-MOD using two types of calibration systems. These are briefly mentioned here; their operation and design are covered elsewhere.

The first system is the invessel robotic calibration system. The design and construction of this system is detailed in Reference [1]. The robotic calibration system illuminates the MSE objective lens with linearly polarized light of known polarization angle from positions corresponding to the intersection of the various MSE sightlines and the beam trajectory. The diagnostic response is determined by fitting the detected signals at the PEM harmonics to the calibration equation:

$$-\frac{1}{2}\tan^{-1}\left(\frac{I_{2\omega_1}}{I_{2\omega_2}}\right) = B_0 + \theta_{pol} + B_2\cos(2\theta_{pol} + B_{2p}) + B_4\cos(4\theta_{pol} + B_{4p}) \quad (8)$$

This fit typically results in residuals of $< 0.03°$. The system can fully illuminate an MSE sightline with uniform Lambertian source or can perform a polarized ray trace through the diagnostic. This system is also used to obtain the geometry of the view. This can only be used during maintenance periods.

The other calibration system is the inter-shot calibration (ISC) system. This system is installed on the MSE periscope and inputs polarized light into the diagnostic lens at any time. The design and construction of this system is described in Reference [1]. The system can input four different polarization angles into the diagnostic very repeatably. The illumination fills the MSE sightlines and is fairly uniform. This system can operated at any point during the campaign including during plasma discharges. The use of this system is detailed in Chapter 4.

3.2 HOW ACCURATELY TO MEASURE?

An important consideration is how accurately the properties of the magnetic field must be measured in order to properly constrain the magnetic equilibrium reconstructions. This is a non-trivial question to answer because the problem is non-linear and depends on the geometry, the other diagnostics used, and the desired accuracy of the q-profile or current density. Thus it is a global optimization, making the contribution from any one measurement more difficult to discern.

Numerical studies have been undertaken for a small number of equilibria to determine how well internal measurements constrain

equilibrium reconstructions. One study [2] used ITER, MAST, and JET geometries included realistic boundary magnetic measurements and monotonic q-profiles with no internal transport barriers. This study concluded that measuring the magnetic pitch angle with uncertainty $\delta\gamma = 0.3°$, 1.5°, and 1.3° on each device respectively at many (~ 20) points spanning the radius effectively eliminated qualitatively macroscopically different equilibrium solutions, though the accuracy of the resulting solution was not quantified. The general problem has been tackled most recently by Zakarov using the theory of variances [3] to develop a methodology to determine how well an internal diagnostic set can constrain equilibrium reconstructions.

Table 3: The measurement uncertainty required to obtain physics-study quality equilibrium reconstructions for modern, fusion relevant, standard aspect ratio tokamaks. Achieving a $\delta\gamma \sim 0.3°$ is a goal for the work presented in this thesis.

Parameter	Value
δq	0.05-0.2
Number of points	10-20
Time resolution	$10 - 20$ms
Penetration	Past magnetic axis
Accuracy	$\delta\gamma = 0.3° - 0.5°$ or $\delta\theta_{pol} = 0.1 - 0.3°$

Foley [4] has applied Zakharov's methodology to determine the efficiency of constraining the equilibrium reconstructions using different internal magnetic field measurements. The study quantified the resulting uncertainty in the safety factor (δq) and pressure profile (δp) using the magnetic field magnitude (δB) and the magnetic pitch angle ($\delta\gamma$) as constraints. The dependence on the number, distribution, and quality of internal measurements was systematically studied. These studies indicate that measurement uncertainty at the level summarized in Table 3 is desirable for physics studies. Measuring the polarization angle to such high accuracy is a difficult proposition, requiring the elimination of or accounting for may error sources.

3.3 NON-IDEAL BEHAVIOR OF MSE-LP EMISSION

The polarization angle from the motional Stark effect is a function of the projection of the viewing sightline onto the electric field in the atom's frame. This electric field is composed of the field from the plasma itself and the Lorentz field due to the neutral traversing the magnetic field at high velocity: $\vec{E} = \vec{E}_{plasma} + \vec{v}_{beam} \times \vec{B}_{plasma}$. The linear polarization angle relative to the toroidal plane of the σ multiplet (θ^{σ}_{pol}) emitted at a location in the plasma is thus a function of the local field components, the beam velocity, and the sightline viewing vector.

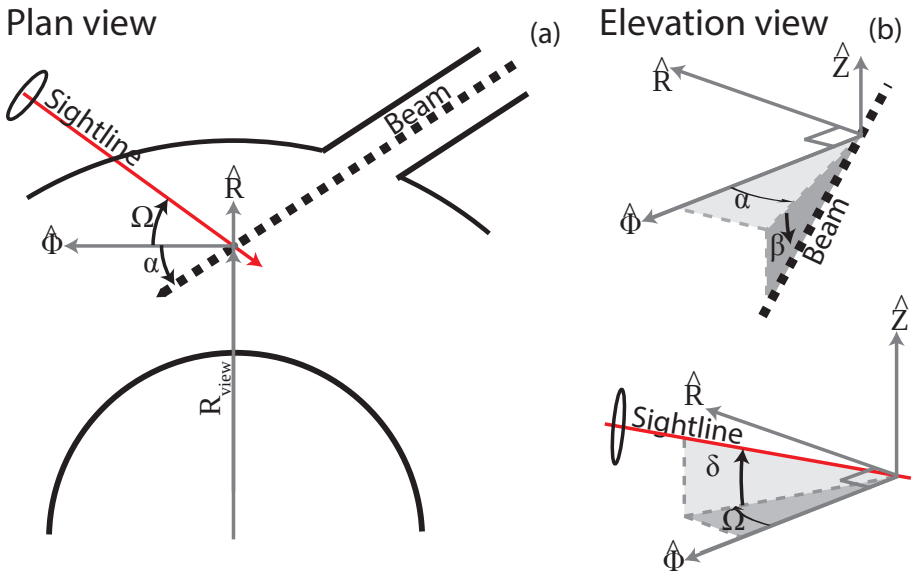

Figure 11: The MSE geometry is can be reduced to the location of the viewing volume in R, Z coordinates and four angles which determine how the fields in the plasma are projected into the polarization angle observed at the diagnostic objective lens. This is shown in plan view (a) and elevation view (b).

The most general form for the polarization angle, published for the first time as part of this thesis work, is:

$$\tan(\theta^{\sigma}_{pol}) = \frac{A_1 B_z + A_9 B_R + A_8 B_\phi + A_5 E_R/v + A_{10} E_\phi/v}{A_2 B_\phi + A_3 B_R + A_4 B_z + A_6 E_z/v + A_7 E_R/v + A_{11} E_\phi/v} \tag{9}$$

$$\begin{aligned}
A_1 &= -\cos(\alpha+\Omega)\cos\beta \\
A_2 &= \sin\alpha\cos\beta\cos\delta + \sin\beta\sin\Omega\sin\delta \\
A_3 &= \cos\alpha\cos\beta\cos\delta - \sin\beta\cos\Omega\sin\delta \\
A_4 &= \sin(\Omega+\alpha)\cos\beta\sin\delta \\
A_5 &= -\cos\Omega \\
A_6 &= -\cos\delta \\
A_7 &= \sin\Omega\sin\delta \\
A_8 &= -\sin\beta\cos\Omega \\
A_9 &= -\sin\beta\sin\Omega \\
A_{10} &= \sin\Omega \\
A_{11} &= \cos\Omega\sin\delta
\end{aligned}$$

where α is the angle between the beam velocity and local toroidal direction, $(\hat{\phi})$ in the horizontal plane; β is the angle between the beam velocity and the horizontal plane; Ω is the angle between the sightline $\vec{k}$ and the local toroidal direction in the horizontal plane; and δ is the angle between the sightline and the horizontal plane. Finally, v is the beam scalar velocity. The geometry is shown in Figure 11. Note that when the beam lies in the toroidal plane ($\beta = 0$) A_1 - A_7 are

equivalent to those presented in Equation 2 in reference [5], the previous most complete form. When the beam and sightline reside on the plasma midplane and the plasma electric field is neglected, the result reduces to the standard simple dependence on the vertical and toroidal magnetic field:

$$\tan(\theta^{\sigma}_{\text{pol}}) = \frac{-B_z}{B_\phi}\frac{\cos(\alpha+\Omega)}{\sin\alpha} \tag{10}$$

The polarization angle of the π emission and σ emission are exactly perpendicular when the Zeeman effect is neglected [6].

The model of a MSE-LP diagnostic discussed in the previous chapter assumes: (a) the emission from the beam is from a ray-like beam; (b) the emission is collected from an infinitely small viewing volume; (c) the sightline consists of a single ray; and (d) only a magnetic field is present in the plasma. In reality, there are many effects that complicate the interpretation of the polarization that is incident on the diagnostic's objective. Spectral and polarization modifications arise from the finite size of the viewing volume, the beam properties, and the finite size of the objective lens. These effects are not present in the single point emission model of MSE previously discussed but are present in real-world implementations. Work was therefore undertaken to elucidate the concepts and determine the impact of these effects on the ALCATOR C-MOD MSE system.

3.3.1 *Er and Stark-Zeeman mixing effects*

The simplified model of MSE-LP assumes a pure Stark shift from a plasma magnetic field only. However, even a point-source viewing volume can have other fields present which impact the polarization angle.

The σ and π emission is typically orthogonally polarized. However, atomic modeling previously performed for ALCATOR C-MOD showed that in strong magnetic fields the Stark and Zeeman energy levels are mixed [6]. The resulting hybrid transitions can result in different emitted Stokes vectors relative to a pure Stark case. The σ_0 line is emitted from two different types of transitions. In the Stark-Zeeman hybridized state the resulting polarization angle of the σ_0 line is altered when the upper energy levels are not statistically populated. However, the effect is only present in devices with significantly non-statistical populations—predominately in beam-into-gas discharges. This effect is likely to be negligible on C-MOD and on future devices that operate at high plasma densities. The effect is not important in devices with high-energy beams where the Motional Stark effect is dominant over the Zeeman effect.

The polarization angle is related to the total electric field in the atom's frame ($\vec{E} = \vec{E}_{plasma} + \vec{v}_{\text{beam}} \times \vec{B}_{\text{plasma}}$). Background electric

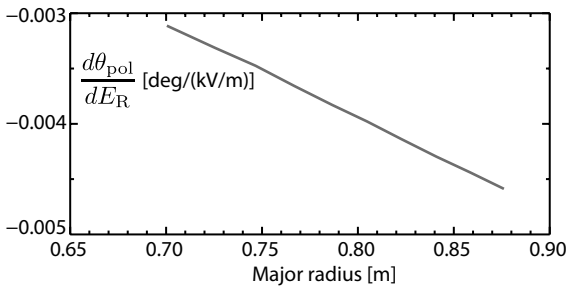

Figure 12: The sensitivity of the polarization angle to changes in E_R.

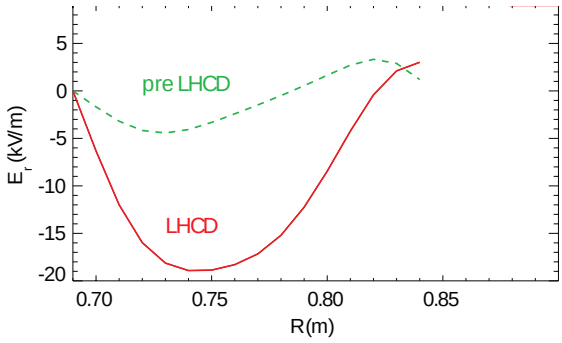

Figure 13: Profile measurements of E_R from the x-ray crystal spectrometer on C-MOD for a typical L-mode discharge with LHCD. Adapted from [12].

fields in the tokamak, which are mostly in the radial direction, thereby influence the detected polarization angle. Although the radial electric field is small in magnitude compared to the Lorentz field (10s of $^{kV}/_{m}$, vs. 10s of $^{MV}/_{m}$) it is in a different, and often orthogonal direction. The background electric field can therefore cause a measurable change in the polarization angle detected by the MSE system. The susceptibility of MSE-LP diagnostics to the radial electric field has been given significant treatment in the MSE literature [5, 7–11].

Starting from Equation 9 the sensitivity of the diagnostic to the radial electric field can be calculated as:

$$\frac{d\theta_{pol}}{dE_R} = \tag{11}$$

$$\frac{\cos^2(\theta^{\sigma}_{pol})}{v} \frac{A_5 - A_7 \tan(\theta^{\sigma}_{pol})}{A_2 B_\phi + A_3 B_R + A_4 B_z + A_6 E_z/v + A_7 E_R/v + A_{11} E_\phi/v} \tag{12}$$

For systems with the beam and the sightline both in the toroidal plane ($\theta = 0$ and $\beta = 0$)—such as C-MOD—the result can be reduced to:

$$\frac{d\theta_{pol}}{dE_R} = -\frac{\cos^2\theta^{\sigma}_{pol}}{vB_\phi}\frac{\cos\Omega}{\sin\alpha} \tag{13}$$

The sensitivity to E_R in a representative C-MOD discharge (I_p = 800kA) is shown in Figure 12. Measurements of the radial electric fields in a typical C-MOD L-mode LHCD plasma are shown in Figure 13. Multiplying the measured E_R by the diagnostic sensitivity to E_R yields the effect of E_R on the polarization angle. It is apparent that

this is a small effect in these discharges, $< 0.1°$. The effect of E_R on the polarization angle is therefore currently ignored during magnetic reconstructions on C-MOD. This decision should be re-evaluated for discharges and measurement locations with strong E_R such as what would occur in a transport barrier or in the pedestal region. In principle, the radial electric field measured with the X-ray crystal spectroscopy diagnostic on C-MOD [13] could be used to correct the MSE data for the contribution from E_R during the plasma equilibrium reconstruction process.

3.3.2 *3D collection effects*

Actual MSE diagnostics do not collect light from a single point and instead have finite viewing viewing volumes which are averaged over. This can lead to systematic dependencies in the measured polarization angle:

UNCERTAINTY IN VIEWING GEOMETRY Unlike most tokamak diagnostics, the interpretation of the measurement depends both on the viewing volume location and several angles. Therefore, determining the six geometric quantities in Equation 9 is important. On C-MOD, these quantities are determined using the robotic calibration system in a procedure detailed in Reference [1]. The uncertainty in the R and Z location of the centroid of the viewing volume at the center of the beam is estimated at 0.002m. The uncertainty in the geometric angles relating to the sightline is estimated at $< 0.5°$ leading to uncertainties in the polarization angle of $< 0.03°$. A method used to verify that the viewing geometry is stable throughout the campaign is discussed in Appendix C. This error source is therefore negligible.

SPATIAL VARIATION OF THE MAGNETIC FIELDS The beam width and MSE sightlines have a finite size in the plasma, thus the intersection of the beam and sightline creates a viewing volume. The extent of this volume in major radius is referred to as spatial resolution of the diagnostic. Different points in this volume have different magnetic field strengths and magnetic field directions. These points have different Stark splits and electric field vectors with systematic relationships between the two quantities. Thus measurement at different wavelengths measures different plasma positions.

FINITE VIEWING VOLUME EFFECTS Each point across the viewing volume has a slightly different angle between the beam and the view ray, leading to a slightly different Doppler shift. This broadens of the spectra. Each emission point also has a slightly different angle between the view ray and torodial direction and between the toroidal field and the beam leading to variations δ,

Ω, and α and thus polarization angle. So measurement at different wavelengths observes a different polarization angle from the same pitch angle.

FINITE APERTURE EFFECTS The diagnostic entrance pupil is not infinitely small, but rather an extended surface. In a similar manner to the viewing volume broadening, each point on the entrance pupil observes each point in the viewing volume with slightly different angles. Therefore the polarization angle will be different due to variations in δ and Ω and the spectrum will have different Doppler shifts.

The interaction of the wavelength and polarization angle can lead to a dependence of the polarization angle on the collected wavelength. If this is not probably accounted for an error in interpreting the measured polarization angle will result.

3.3.3 *Realistic beam effects*

The neutral beams used in most tokamaks are not truly constant energy, mono-energetic, ray-like beams. They have a variety of non-ideal behaviors that can influence the production of the polarized light, even in the case of an infinitely small viewing volume and collection solid angle.

FINITE BEAM DIVERGENCE The beam has angular divergence due to space charge effects in the ion optics —it is not a perfect pencil beam but rather spreads out as it propagates. The divergence leads to a distribution of beam velocity vectors at each point in the plasma. This leads to a distribution of geometric projection angles β and α at each point in the viewing volume. The result is a broadened spectrum and the collection of a variety of polarization angles.

MULTIPLE BEAM COMPONENTS The neutral beam does not produce a single mono-energetic beam of neutrals. Beams commonly have H,H_2, H_3 and H_2O in their source plasma which are extracted and accelerated, creating what is often referred to as full-, half-, third-, and eighteenth-energy components. These components have different velocities and thus different Doppler shifts, Lorentz electric fields, and Stark splits. Typically the half-energy component π emission overlaps the full-energy σ component. In the absence of a radial electric field, the polarizations from the full energy π and half energy σ are orthogonal. Collecting light from both beam components should not result in changes to the net polarization angle, but would reduce the net degree of linear polarization (DOLP). In the presence of a radial electric field, the total electric field direction is slightly different for the different beam components because of the different

Lorentz electric field. This difference was used to measure the radial electric field in TFTR [9]. On ALCATOR C-MOD, the full energy π emission is collected in preference to the full energy σ to avoid contamination from the half energy π. However, modeling with the beam penetration code ALCBEAM [14] shows that the half-energy component is weak and is attenuated after interacting with the neutral gas prior to hitting the plasma edge. This component is then further attenuated as it propagates into the plasma.As previously shown for the full energy component, the C-MOD MSE diagnostic is not susceptible to the radial electric field. The polarization angle from the half-energy component is only $\sqrt{2}\times$ more susceptible. The polarization angle from collecting the small amount of half-energy π along with full-energy σ should not cause deviations in the net polarization angle due to E_R. Negative-ion beams are mono-energetic, thus these effects are likely not important on next-generation devices.

VOLTAGE RIPPLE The accelerator voltage has voltage ripple at the level of 1 to 2 percent. This creates fluctuations in the velocity of the beam at the frequency of the voltage ripple. This in turn creates variation in the Doppler shift and Stark split and thus broadening of the MSE emission. However, the voltage ripple does change the location of the beam spectrum relative to the spectral bandpass filter by changing the Doppler shift (and to some extent the Stark split). This can change the spectral Stokes averaging. The ripple on C-MOD leads to changes in the location of the Stark emission relative to the fixed bandpass filter of $\sim \pm 0.05$nm in the core and $\sim \pm 0.01$nm in the edge.

3.3.4 *Simulation using* MSESIM

The previously discussed non-ideal source effects couple into one another. For example, the beam divergence is present and is different at each point in the viewing volume. A simulation tool must therefore be used to determine polarization angle sensitivity to the various effects—they can be difficult to tackle analytically. One such tool is the spectral-Stokes MSE simulation code MSESIM authored by DeBock [15] and used as part of the design effort for the MSE diagnostic on MAST [16]. This code numerically determines the Stokes spectrum of the emission while accounting for many of the non-ideal situations discussed above. A collaboration between C-MOD and Eindhoven University conducted an investigation of the various effects mentioned above in the C-MOD MSE geometry using MSESIM simulations performed by Paul Geelen [17] under supervision by the author.

Figure 14 shows the result of simulations for a core (left column), central (middle column), and edge (right column) sightline. Only the full energy component of the beam is included for clarity. The in-

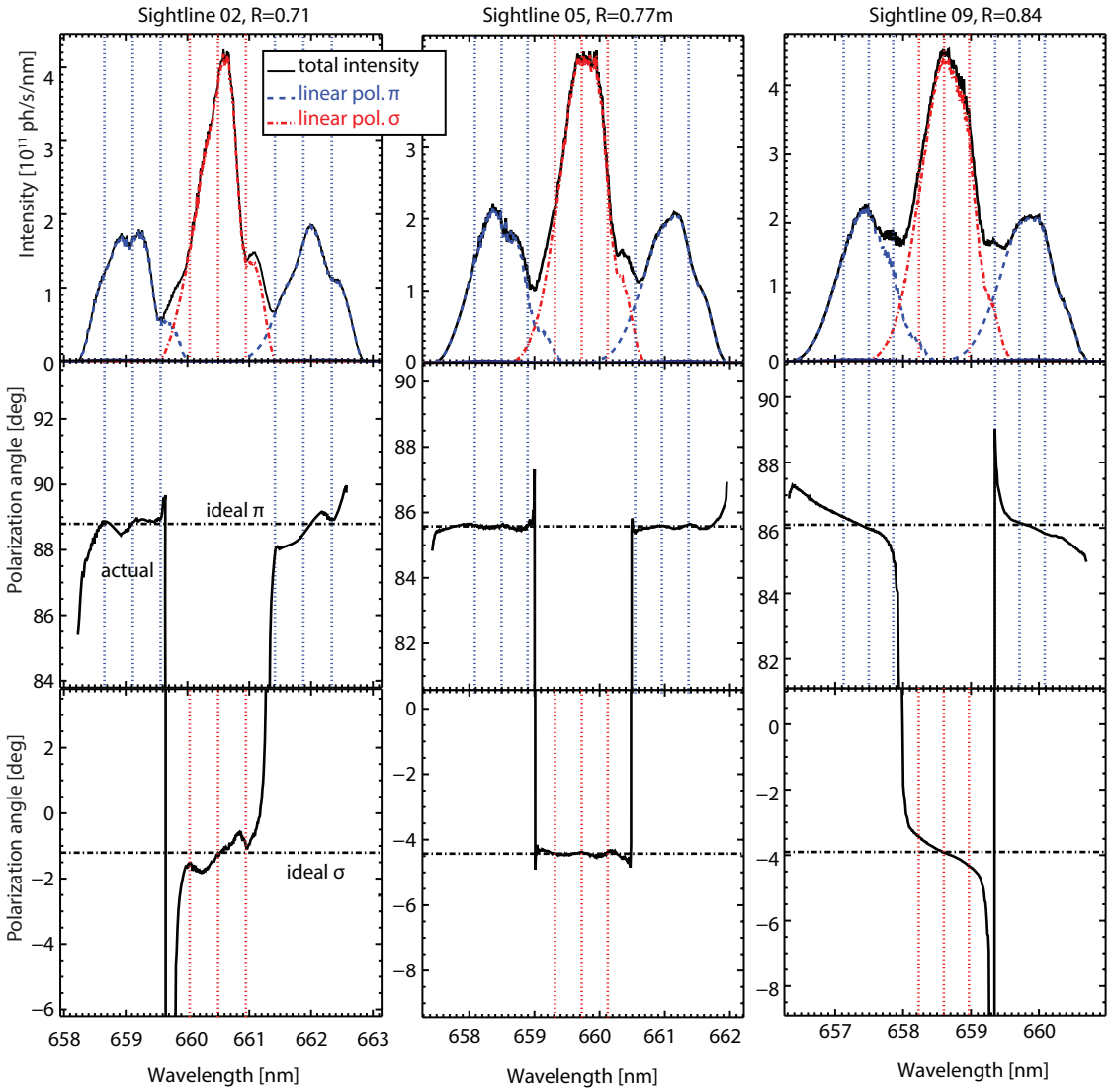

Figure 14: The simulated spectra (top row) and polarization angle of the π (middle row) and σ (bottom row) for a core (left column), mid-radius (middle column) and edge (right column) sightline from MSESIM. Only the full-energy beam component is included. The ideal polarization angles assuming a point viewing volume, pencil beam, and single ray are shown as horizontal dashed lines and the location of the Stark lines under these assumptions is shown as vertical dashed lines. Adapted from [17].

tensity spectra are shown in the top row. The resulting polarization angle incident on the diagnostic objective lens at each wavelength bin is shown for both the σ and π-dominated light (middle row and bottom row, respectively). The "ideal" polarization angle[1] is shown as the horizontal dashed line. This is the ideal polarization angle usually assumed when interpreting MSE diagnostics—it is the angle plasma equilibrium reconstructions assume would be measured. The nominal locations of the nine dominant Stark lines indicated as dashed vertical lines[2]. The polarization angle collected by the diagnostic (bottom) switches from one angle to another (off the bottom of the scale) depending on if MSE π or σ is dominant. The polarization angle shows significant structure as a function of wavelength within both the π or σ dominant regions with variations at the $\pm 1^\circ$ level. This structure in the collected polarization angle as a function of wavelength is due to the interactions between the variation in fields, projections, Doppler shifts, and Stark splits across the actual diagnostic implementation.

It is apparent that the polarization angle incident on the diagnostic entrance pupil depends systematically on which parts of the spectrum are collected due to these realistic-geometry effects. The polarization angle systematically increases as the wavelength increases for the core sightline, is flat as a function of wavelength for the middle sightline, and decreases as a function of wavelength for the edge sightline. The effect is apparent and similar in both the σ and π-dominate emission.

An investigation was carried out to determine the dominant causes of this systematic change in polarization angle as a function of wavelength:

AVERAGING OVER FIELDS The variation in magnetic geometry due to a finite spatial resolution is responsible for most of the polarization angle variation in the core sightline. The magnetic pitch angle is becoming more positive and the Stark shift is getting larger as the sightline crosses flux surfaces further into the core. This leads to $d\theta_{pol}/d\lambda > 0$. The effect is smaller at the edge where the sightline is more tangent to the flux surfaces.

FINITE APERTURE The variation in the polarization angle projections among the rays filling the diagnostic objective lens from a single viewing volume point has a large impact on the polarization angle variability for the edge sightlines because the polarization projection angle Ω is strongly covariant with the angle that determines the Doppler shift.

1 Assuming a point viewing volume located at the center of the beam trajectory and the centroid of the MSE view footprint with a single sightline ray and a monoenergetic pencil beam.

2 The Stark line location are calculated under the same assumptions at the ideal polarization angle.

Table 4: The polarization variability due to realistic geometry calculated by MSESIM. The numbers are given for the ideal MSE π_{+3} location. Adapted from [17].

	Core	Mid-radius	Edge
$d\theta_{pol}/d\lambda$ unfiltered	$2.6^\circ/nm$	$-0.1^\circ/nm$	$-1.1^\circ/nm$
$d\theta_{pol}/d\lambda$ filtered	$1.0^\circ/nm$	$0.0^\circ/nm$	$0.5^\circ/nm$

3.3.5 *Implications and mitigation of source-side effects*

The most important result from this study is the conclusion that the measured polarization angle is a function of wavelength—it is not the ideal polarization angle as is typically assumed. The slope of the dependence from the simulations is given in Table 4 for cases with no filtering and with a Gaussian filter with FWHM of 0.9nm swept over the spectrum.

The variation of polarization angle as a function of wavelength has not been verified on C-MOD in any systematic way. It may be possible to observe the simulated dependence of measured polarization angle on spectral position in discharges where the neutral beam voltage changed significantly due to an equipment failure [3] DIII-D has reported systematic changes in the measured polarization angle as the filter center wavelength is tuned [18]. Magnetic pitch angle dependences of up to $\sim 25^\circ/nm$ were observed using tilt tuning of bandpass (0.3nm FWHM) filters. This may be due to the effects discussed in this section.

The simulation results indicate that it is important to monitor the placement of the bandpass filters relative to the spectrum at the level of $\sim$ 0.1nm at the core and 0.2nm at the edge. Accurate knowledge and control of the filter bandpass and of the diagnostic geometry is therefore important if systematic errors from these effects are to be minimized and monitored. On C-MOD, the filters are carefully measured in-situ to obtain their passbands and to verify the operation of the filter tuning. Sensitive tests have also been developed to determine the placement of the filter bandpasses relative to the beam spectrum using magnetic field sweeps. These techniques, and a method to monitor the position of the viewing volume, are detailed in Appendix C.

The sensitivity of the measured polarization angle to the placement of the filter bandpass relative to the beam spectrum also adds new constraints to the operation of the DNB. The voltage of the neutral

3 Future experiments with the new MSE-MSLP system discussed in Chapter 6 will measure the polarization angle of the σ and π emission simultaneously. It may be possible to systematically vary one filter center wavelength while keeping the other filter fixed to look for systematic differences in polarization angle between the two measurements. This may be a sensitive test for the dependence of polarization angle on wavelength.

beam is important to properly locate the spectrum relative to the filters. On C-MOD, the location of the MSE spectrum shifts due to the Doppler shift with a dependence $d\lambda/dE = 0.047^{nm}/kV$ in the core and $d\lambda/dE = 0.013^{nm}/kV$ in the edgeleading to $d\theta_{pol}/dE = 0.05^{\circ}/kV$ in the core and $d\theta_{pol}/dE = 0.007^{\circ}/kV$. The diagnostic should therefore be operated with constant DNB accelerator voltage to avoid the systematic shifts in the polarization angle, particularly in the core. It is highly likely that one could compensate for the effect of dependence of polarization angle on spectral position as the conditions change using simulated diagnostic responses since the effects can be understood from first-principle theory. In the future, it may be possible to couple MSESIM (or equivalent) calculations into the reconstruction methodology or to develop a look-up table framework. Such a technique would likely enable high-accuracy correction from these view and beam geometry effects.

3.4 POLARIZATION ABERRATIONS IN MSE-LP OPTICS

Once the light from the diagnostic beam is incident on the objective lens it is transported via the complex optical periscope prior to being encoded by the PEM-based polarimeter. There are many ways that the optical elements in a periscope can modify the polarization as it is transmitted. These modifications to the polarization are termed "polarization aberrations." For MSE-LP systems, one is mostly concerned with polarization aberrations that alter the polarization angle of linearly polarized light .In general, the polarization aberrations transform the polarization angle of the light from that collected by the objective lens to a different angle incident on the PEMs. Each optical element can contribute a transformation:

$$\theta_{out} = F(\theta_{in}) \tag{14}$$

where θ_{in} is the polarization angle of the light incident on the optical element and θ_{out} is the polarization angle of the light after the optical element. An ideal optical system would be linear with an offset that depends only on the orientation of the PEM-based polarimeter. In an actual system, the dependence is non-linear.

In principle, detailed polarization calibration of the diagnostic fully characterizes the relationship between θ_{PEMs} and θ_{pol}, including the non-linearities. Experience on C-MOD shows that the previously discussed calibration methodology can account for large polarization aberrations. However, polarization aberrations introduce sensitivities into the diagnostic which may change the response if the state of the diagnostic changes. Such changes include temperature changes, force on components, changes in the illumination pattern on the diagnostic, or mechanical warping of the periscope. It is therefore important to examine the system for polarization aberrations, determine their

character, and determine if they can can change in time due to environmental changes.

As polarized light is transported through an optical train there are five main polarization operations that could change the polarization of a ray of light: rotation, diattenuation, retardation, depolarization, and absorption. The first three of these effects are the most important in MSE-LP diagnostics because they can rotate the linear polarization angle of the light prior to it being encoded with the PEM-based polarimeter. Each of these effects is dependent on the local condition of the optical element and the geometry between the incident polarization and the element. These effects are therefore both ray- and polarization dependent. The cumulative effects from these can be calculated using Müeller calculus by combining various operators.

3.4.1 *Rotation*

As light is transmitted through transparent media its polarization can be rotated. The Müeller matrix for rotating the polarization through angle ψ is:

$$\mathbf{R}(\psi) = \begin{bmatrix} 1 & 0 & 0 & 0 \\ 0 & \cos(2\psi) & -\sin(2\psi) & 0 \\ 0 & \sin(2\psi) & \cos(2\psi) & 0 \\ 0 & 0 & 0 & 1 \end{bmatrix} \tag{15}$$

The rotator operating through angle ψ on an input Stokes vector with elliptical polarization at is $\mathbf{S_{out}} = \mathbf{R}(\psi)\mathbf{S_{in}}$. It is apparent that the new linear polarization angle is then:

$$\theta_{out} - \theta_{in} = \psi. \tag{16}$$

The rotator simply rotates the polarization angle of the light. It does not change the intensity, the degree of linear polarization (DOLP), or the degree of circular polarization (DOCP) of the light. Note that the addition of multiple rotators sequentially acting on the ray of light is a simple addition of the different rotation angles; there are no nonlinear effects.

The concept of rotation is important as a tool to compute the Müeller matrices of rotated polarization components and to rotate the coordinate system of the polarization calculation. When a polarization element ($\mathbf{M}$) is rotated by ψ about the coordinate system, its new Müeller matrix is: $\mathbf{M}' = \mathbf{R}(\psi)\mathbf{M}\mathbf{R}(-\psi)$. Conversely, if the coordinate system is rotated by ψ while the element stays fixed the new Müeller matrix is: $\mathbf{M}' = \mathbf{R}(-\psi)\mathbf{M}\mathbf{R}(\psi)$.

Rotators are often due to optical activity in nature. The most important rotator the MSE application is due to the Faraday Effect which

arises when light is transmitted through materials in a magnetic field. The optical element then acts like a rotator with an angle:

$$\psi_{\text{Faraday}} = B\mathcal{V}d \tag{17}$$

where B is the magnetic field in the direction of the light's propagation, $\mathcal{V}$ is the Verdet constant of the optical medium, and d is the distance of the ray's propagation through the medium. This effect can be very important in tokamaks which operate at high magnetic field where a finite Verdet constant can lead substantial rotation.

The Faraday effect will only occur when the magnets are energized. The magnitude of the rotation depends on the magnetic field at the location of optical elements which will depend on the details of the magnetic geometry—including the plasma contribution. For this reason, materials with very low Verdet constants are often used for the transmissive elements in MSE-LP diagnostics. In C-MOD, SFL6 glass is used for all the transmissive elements except the PEMs. This glass has a Verdet constant of $\sim 0^{\circ}/\text{T m}$ [19] versus $243^{\circ}/\text{T m}$ for a more common glass such as BK7 or $1160^{\circ}/\text{T m}$ for a low-stress birefringence glass such as SF57 [20]. The Verdet constant of the C-MOD optics was confirmed to be low, $2.6^{\circ}/\text{T m}$, during measurements on the bench [6].

Previous work on C-MOD's MSE system calculated the Faraday rotation in the optical periscope to be low [6] and measurements with a fixed invessel polarizer illuminated by plasma confirmed this [21]. The ISC system on C-MOD offers an opportunity to characterize this effect more accurately. The ISC system carries its own illumination source and can therefore be used to measure Faraday rotation with different combinations of fields in the absence of plasma as well as during plasma discharges.

Figure 15 shows an example of Faraday rotation measurements for a discharge with and without plasma. The toroidal magnetic field was pulsed (a), while a plasma was created in only one of the two discharges (b). The measured polarization angle changes with the application of the field from prior to the discharge (c). In the shot with no plasma (red), the polarization angle measured by the diagnostic increases by $\sim 0.03^{\circ}$ when the toroidal field is ramped up. The polarization angle then decreases back to the starting value when the field is ramped down. The addition of poloidal fields due to the plasma and poloidal field coils at $t = 0$s (green) causes the polarization angle to decrease by $\sim 0.1^{\circ}$ relative to the value with the toroidal field only. Note that the rotation from the toroidal field and the poloidal fields are in opposite directions, partially canceling the effect. The magnitude of the changes are $< 0.1^{\circ}$ and have a slight channel dependence (not shown). The magnitude of the changes agrees with first-principle calculations of the effect given the measured Verdet constant. The input polarization angle was changed to one that was $\sim 90^{\circ}$ displaced

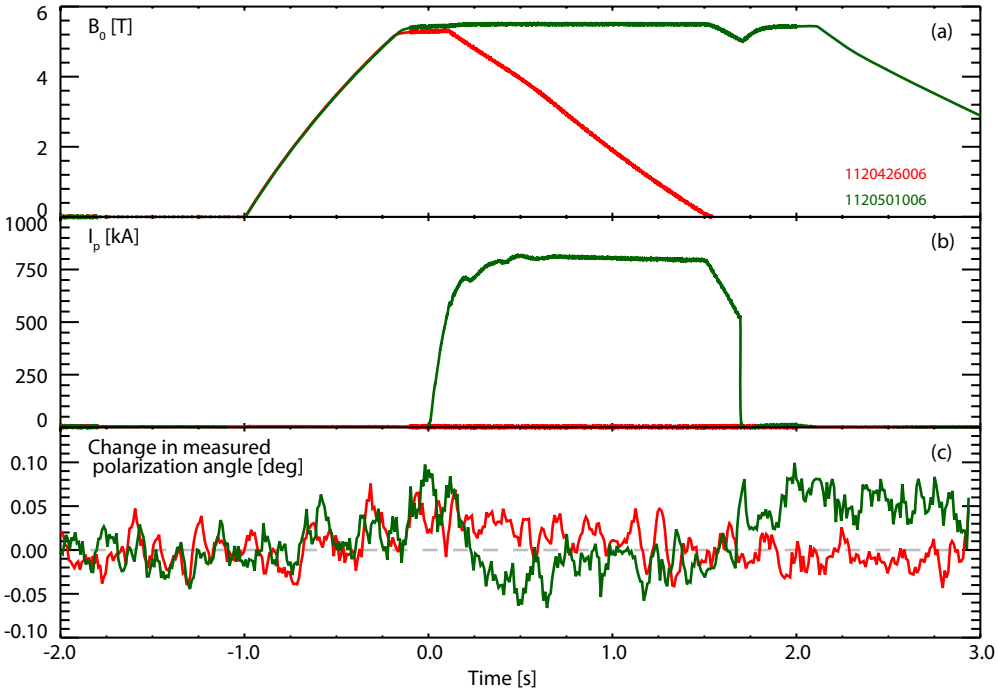

Figure 15: Measurement of the Faraday Effect in the MSE periscope. The magnetic field was pulsed (a) with and without plasma current (b). The change of the polarization angle was measured using the ISC (c). One discharge had only the toroidal field (green) and the other had full poloidal fields and plasma current (red).

and parts of the experiment were repeated, confirming that the aberration is indeed a rotation of the polarization angle.

Fortunately, the Faraday effect is very reproducible and it is therefore possible to compensate for the Faraday effect during plasma equilibrium reconstructions. This could be done by parameterizing the contribution from different field components at key lenses. Since the ISC system allows for precise measurements of Faraday rotation while pulsing different magnetic field configurations the correction would likely be very accurate. The small Faraday rotation on C-MOD is not currently compensated for during plasma equilibrium reconstruction. Future devices are likely to have fewer transmissive elements in the periscope due to neutron damage considerations. The Faraday Effect is therefore unlikely to be a problem and an in-situ calibration source could likely compensate for any residual effect very accurately. There are very few other types of rotators.

3.4.2 *Diattenuation*

Transparent materials can preferentially absorb one linear polarization state while passing the orthogonal state. In a similar manner, reflective materials can reflect one linear polarization state preferentially relative to the orthogonal polarization. These elements are

known as linear diattenuators[4]. A linear diattenator with its diattenuation axis horizontal has a Müeller matrix:

$$\mathbf{M}_{\text{diat}} = \frac{1}{2}\begin{bmatrix} q+r & q-r & 0 & 0 \\ q-r & q+r & 0 & 0 \\ 0 & 0 & 2\sqrt{qr} & 0 \\ 0 & 0 & 0 & 2\sqrt{qr} \end{bmatrix} \tag{18}$$

where q is the transmittance for the horizontal polarization and r is the transmittance for the vertical polarization. Diattenuation underpins the operation of linear polarizers—a perfect linear polarizer aligned to the horizontal axis is a special case where $q = 1$ and $r = 0$. All transparent and reflective optical elements have some amount of diattenuation.

Defining $\Psi = 1 - \frac{q}{r}$, the deviation from unity of the horizontal to vertical polarization transmission ratio—a perfect linear polarizer has $\Psi = \text{inf}$ and perfect optics have $\Psi = 0$. It is assumed that the MSE-LP optics have little diattenuation; $\Psi << 1$, allowing the approximation $\sqrt{1-\Psi} \sim \frac{2-\Psi}{2}$. Inputing light with polarization angle θ_{in} and DOLP_{in} into a horizontal diattenuator leads to light with a different polarization angle, θ_{out}. The magnitude of this effect is calculated using Müeller matrices: $\mathbf{S_{out}} = \mathbf{M}_{\text{diat}}(q, \Psi)\mathbf{S_{in}}$:

$$\mathbf{S_{out}} = \frac{q}{2}\begin{bmatrix} 2-\Psi & \Psi & 0 & 0 \\ \Psi & 2-\Psi & 0 & 0 \\ 0 & 0 & 2-\Psi & 0 \\ 0 & 0 & 0 & 2-\Psi \end{bmatrix} I_{\text{in}} \begin{bmatrix} 1 \\ \text{DOLP}_{\text{in}}\cos(2\theta_{\text{in}}) \\ \text{DOLP}_{\text{in}}\sin(2\theta_{\text{in}}) \\ \text{DOCP}_{\text{in}} \end{bmatrix} \tag{19}$$

The polarization angle after the diattenuator, θ_{out} is then:

$$\tan(2\theta_{\text{out}}) = \frac{\text{DOLP}_{\text{in}}(2-\Psi)\sin(2\theta_{\text{in}})}{\Psi + (2-\Psi)\text{DOLP}_{\text{in}}\cos(2\theta_{\text{in}})}$$

after significant algebra this yields:

$$\sin(2(\theta_{\text{out}} - \theta_{\text{in}})) = \frac{-\Psi}{\text{DOLP}_{\text{in}}(2-\Psi)}\sin(2\theta_{\text{out}})$$

Assuming the diattenuation is small allows the use of the small angle approximation and the replacement of θ_{out} with θ_{in} in the right hand side of the equation, and if the diattenuator is mounted at an angle, ψ_{diat} the change in angle becomes:

$$\theta_{\text{out}} - \theta_{\text{in}} \approx \frac{-\Psi}{2\ \text{DOLP}_{\text{in}}}\sin(2(\theta_{\text{in}} - \psi_{\text{diat}})) \tag{20}$$

4 There are also circular diattenators which preferentially transmit/reflect LHCP or RHCP light.

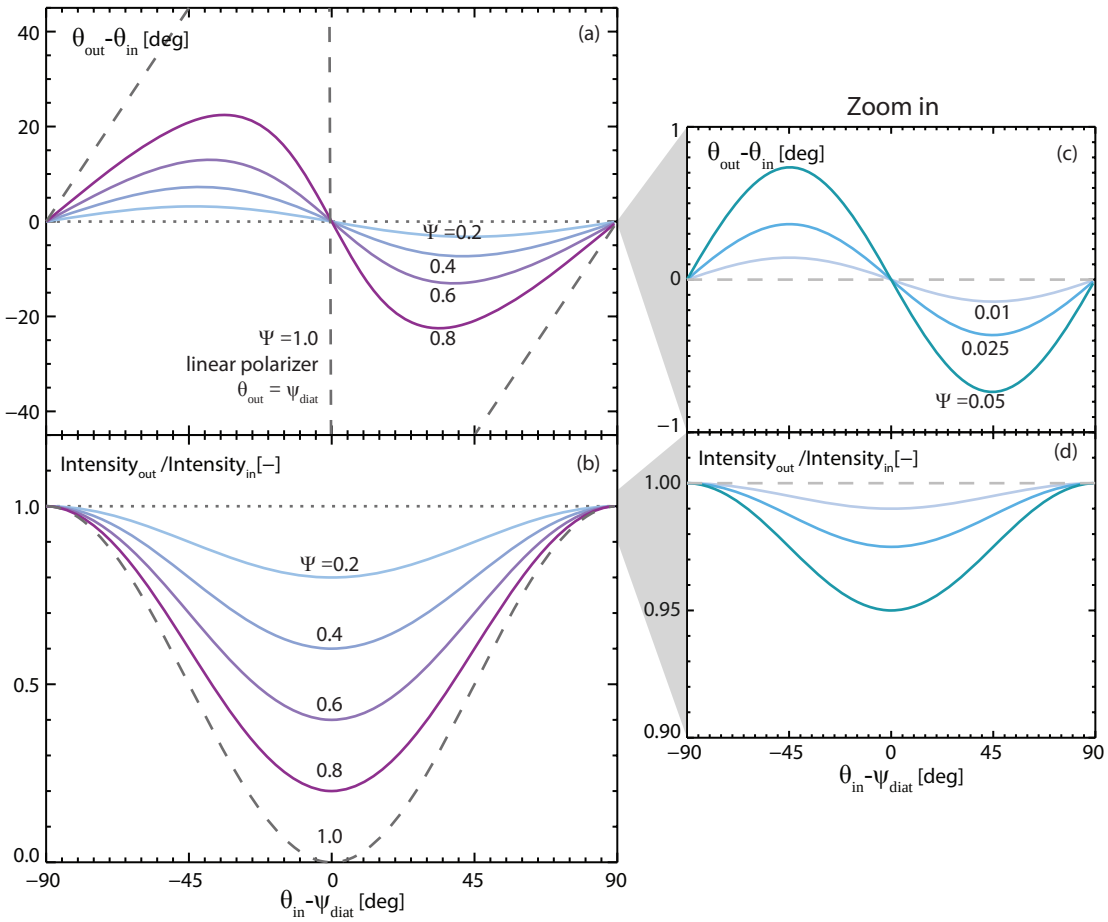

Figure 16: The change in polarization angle (a) and total intensity (b) as a function of the difference between the input polarization angle θ_{in} and the axis of the diattenuator, ψ_{diat}. This assumes $DOLP_{in} = 1$ and $q = 1$. The area near the axis is enlarged to show changes with small amounts of diattenuation.

A diattenuator creates a shift in the polarization angle that depends non-linearly on the polarization angle θ_{in} with modulo π and linearly on the magnitude of the diattenuation. Multiple diattenutors stacked together continue to shift the polarization angle and can almost be treated as the sum of their individual shifts. Note that diattenuators do not create elliptical light from linearly polarized light nor does the change in angle depend on the circular polarization of the incident light. Diattenuation does not decrease the DOLP of linearly polarized light, though it does decrease the intensity.

Figure 16 shows the change in polarization angle (a) and output intensity (b) for different input angles and amounts of diattenuation. Note that as the amount of diattenuation increases, the resulting intensity decreases with a $\sin^2(\theta_{in} - \psi_{diat})$ dependence. The element behaves like a linear polarizer at large diattenuation, producing only polarized light that is nearly aligned with the diattenuation axis independent of the polarization angle of the incident light.

Mirrors are commonly diattenuators and can be an important source of polarization aberration. The diattenuation arises from the difference in the s-p reflection ratio. In real mirrors with the plane of incidence vertical $\Psi = 1 - \frac{R_s}{R_p}$. To induce non-linear dependencies $< 0.1°$, a s-p reflection ratio of $0.986 < \frac{R_s}{R_p} < 1.014$ is required. The s-p reflection ratio is typically dependent on the angle of incidence and wavelength of the incident light. The s-p reflection ratio is also very sensitive to the thin-film coatings on the mirror surface. Plasma exposure will alter the mirror coatings, thereby changing the s-p reflection ratio and resulting polarization aberrations [22]. This resulting polarization angle shifts will have a $\sin(2(\theta_{pol} - \psi_{mirror}))$ functional dependence. Two sources of orthogonally polarized incident light will thus be altered such that the difference in the two polarization angles will increase or decrease. The consequences of this are discussed in detail in Chapter 5.

The C-MOD MSE mirrors have s-p reflection ratios that are very nearly unity; specified at $\frac{R_s}{R_p} > 0.99$ ($\Psi < 0.01$). Each mirror should therefore contribute $\theta_{out} - \theta_{in} < 0.07°$ of non-linear polarization aberrations. With three mirrors this would potentially contribute $\theta_{out} - \theta_{in} < 0.21°$. However, M2 and M3 mirrors are mounted with their planes of incidence orthogonal to one another and thus the s-plane on M2 becomes the p-plane on M3. This leads to some "canceling out" of differences in s-p reflection ratios if the mirrors have identical properties. In practice, it is found that the polarization calibration term that varies as $\sin(2\theta_{in})$ has a magnitude $< 0.1°$ on C-MOD making this error only marginally important on C-MOD. The mirrors are encased inside the periscope and are protected from the plasma—the s-p reflection ratio does not change over the campaign. The diattenuation from the lenses was measured by the University of Arizona Polarization Lab to be < 0.011, thus the transmissive elements do not contribute to this polarization aberration.

Importantly, diattenuators can partially-polarize unpolarized incident light. This is important when trying to make measurements in situations where there is a large background of unpolarized light. The $DOLP_{out}$ of incident light with $DOLP_{in} = 0$ is:

$$DOLP_{out} = \frac{\Psi}{2 - \Psi} \tag{21}$$

Non-unity s-p reflection ratios will also partially polarize incident unpolarized light. A s-p reflection ratio of 0.9 will lead to a $DOLP = 0.053$ from originally unpolarized light. This effect is therefore not important on C-MOD due to high quality mirrors. As will be discussed in Chapter 5, partially-polarized light can interfere with the operation of the diagnostic. The s-p reflection ratio of the mirrors should therefore be kept high to prevent spurious polarization of unpolarized light in addition to preventing changes to the polarization angle of polar-

ized light. The creation of spurious polarized light from unpolarized light by a mirror could be important on a device with plasma-facing mirrors with modest diattenuation.

3.4.3 *Retardance*

The index of refraction in the transmissive optical materials can depend on the incident polarization state. A phase difference between the two orthogonal linear polarization states thus develops as the light propagates—a phenomenon known as retardance. Retardance can transform linearly polarized light into elliptical or circularly polarized light and conversely transform circularly polarized light into elliptical or linearly polarized light. Retarders also change the polarization angle of the incident light. This can be be calculated using Müeller matrices: $\mathbf{S_{out}} = \mathbf{M}_{\text{ret}}(\Delta)\mathbf{S_{in}}$:

$$\mathbf{S_{out}} = \begin{bmatrix} 1 & 0 & 0 & 0 \\ 0 & 1 & 0 & 0 \\ 0 & 0 & \cos(2\pi\Delta) & \sin(2\pi\Delta) \\ 0 & 0 & \sin(2\pi\Delta) & \cos(2\pi\Delta) \end{bmatrix} I_{in} \begin{bmatrix} 1 \\ \text{DOLP}_{in}\cos(2\theta_{in}) \\ \text{DOLP}_{in}\sin(2\theta_{in}) \\ \text{DOCP}_{in} \end{bmatrix} \quad (22)$$

where Δ is the retardance is in units of wavelengths (e.g., a half wave retarder has $\Delta = 0.5$). The polarization angle after the retarder, θ_{out} is then:

$$\tan(2\theta_{out}) = \frac{\text{DOLP}_{in}\sin(2\theta_{in}) + \text{DOCP}_{in}\sin(2\pi\Delta)}{\text{DOLP}_{in}\cos(2\theta_{in})}$$

Assuming that the retardance is small, $\Delta << 1$, the small angle approximation is then substituted:

$$\tan(2\theta_{out}) \approx \frac{(1 - 2\pi^2\Delta^2)\sin(2\theta_{in}) + \frac{\text{DOCP}_{in}}{\text{DOLP}_{in}}2\pi\Delta}{\cos(2\theta_{in})}$$

which after some algebra yields:

$$\sin(2(\theta_{out} - \theta_{in})) \approx -2\pi^2\Delta^2\sin(2\theta_{in})\cos(2\theta_{out}) + \frac{\text{DOCP}_{in}}{\text{DOLP}_{in}}\ 2\pi\Delta\ \cos(2\theta_{out})$$

Assuming small retardance and thus angle changes, $\theta_{out} - \theta_{in} << 1$, allows the small angle approximation on the left-hand side of the equation and θ_{in} to be substituted for θ_{out} in the right-hand side of the equation. Allowing an arbitrary fast axis direction, $\psi_{\text{fast axis}}$ then yields:

$$\theta_{out} - \theta_{in} \approx -\frac{\pi^2\Delta^2}{2}\sin(4(\theta_{in} - \psi_{\text{fast axis}}) + \frac{\text{DOCP}_{in}}{\text{DOLP}_{in}}\ \pi\Delta\ \cos(2(\theta_{in} - \psi_{\text{fast axis}}))$$

(23)

The retarder converts some linearly polarized light to circular polarized light and vise-versa, changing the ellipticity. The output DOCP is then:

$$\mathrm{DOCP}_{\mathrm{out}} = \mathrm{DOLP}_{\mathrm{in}} \sin(2\pi\Delta) \sin(2(\theta_{\mathrm{in}} - \psi_{\mathrm{fast\ axis}}) + \mathrm{DOCP}_{\mathrm{in}} \cos(2\pi\Delta) \tag{24}$$

When linearly polarized light (DOCP $= 0$) is incident on the retarder, the change in polarization angle has a $\sin(4(\theta_{\mathrm{in}} - \psi_{\mathrm{fast\ axis}})$ character and is quadratic in retardance, Δ. The resulting DOCP has a $\sin(2(\theta - \psi_{\mathrm{fast\ axis}})$ character with a magnitude that is nearly linear in the retardance, Δ.

Figure 17 shows the resulting polarization parameters (calcuated using the full Müeller-matrix calculus) when DOCP $= 0$, DOLP $= 1$ light is incident on a retarder with different amounts of retardance. The $\sin(4(\theta_{\mathrm{in}} - \psi_{\mathrm{fast\ axis}})$ character is apparent in the change in polarization angle at small retardances (d). The $\sin(4(\theta_{\mathrm{in}} - \psi_{\mathrm{fast\ axis}})$ character becomes distorted at large retardance values until the quarter-wave retardance (QWP is reached, at which point the light at all input angles is transformed to light with polarization angle aligned with the fast axis of the retarder. At increasing retardance the process is mirrored until a half wave of retardance is reached (HWP) which simply reverses the input polarization angle (a). The $\sin(2(\theta_{\mathrm{in}} - \psi_{\mathrm{fast\ axis}})$ character is clear in the output DOCP (b,e). The DOLP decreases at points 45° away from the $\psi_{\mathrm{fast\ axis}}$ as the retardance is increased (c). The maximum change in angle increases approximately quadratically with increasing retardance while the maximum DOCP increases linearly with increasing retardance (f). Note that $\Delta < 0.02$ waves is required to prevent angle non-linearities greater than 0.1°.

The change in angle is zero when averaged over a 2π of $\theta_{\mathrm{in}} - \psi_{\mathrm{fast\ axis}}$. A retarder with constant Δ but a symmetric distribution of $\psi_{\mathrm{fast\ axis}}$ will therefore not change the polarization angle of linearly polarized light incident onto it. This has been confirmed using Müeller calculus.

It is clear that a relationship exists between the change in polarization angle and the resulting DOCP. Figure 18 shows this relationship. Curves of constant retardance are traversed with changes in $\theta_{\mathrm{in}} - \psi_{\mathrm{fast\ axis}}$. Note that small changes in polarization angle can correspond to rather large |DOCP|. It is therefore difficult to use the output DOCP to determine the change in angle without knowing either the retardance or $\theta_{\mathrm{in}} - \psi_{\mathrm{fast\ axis}}$. However, it is not possible to have a change in angle without some accompanying change in DOCP, particularly at at small retardances.

From Equation 23 it is clear that the change in polarization angle is affected by the DOCP of the input light with a character of

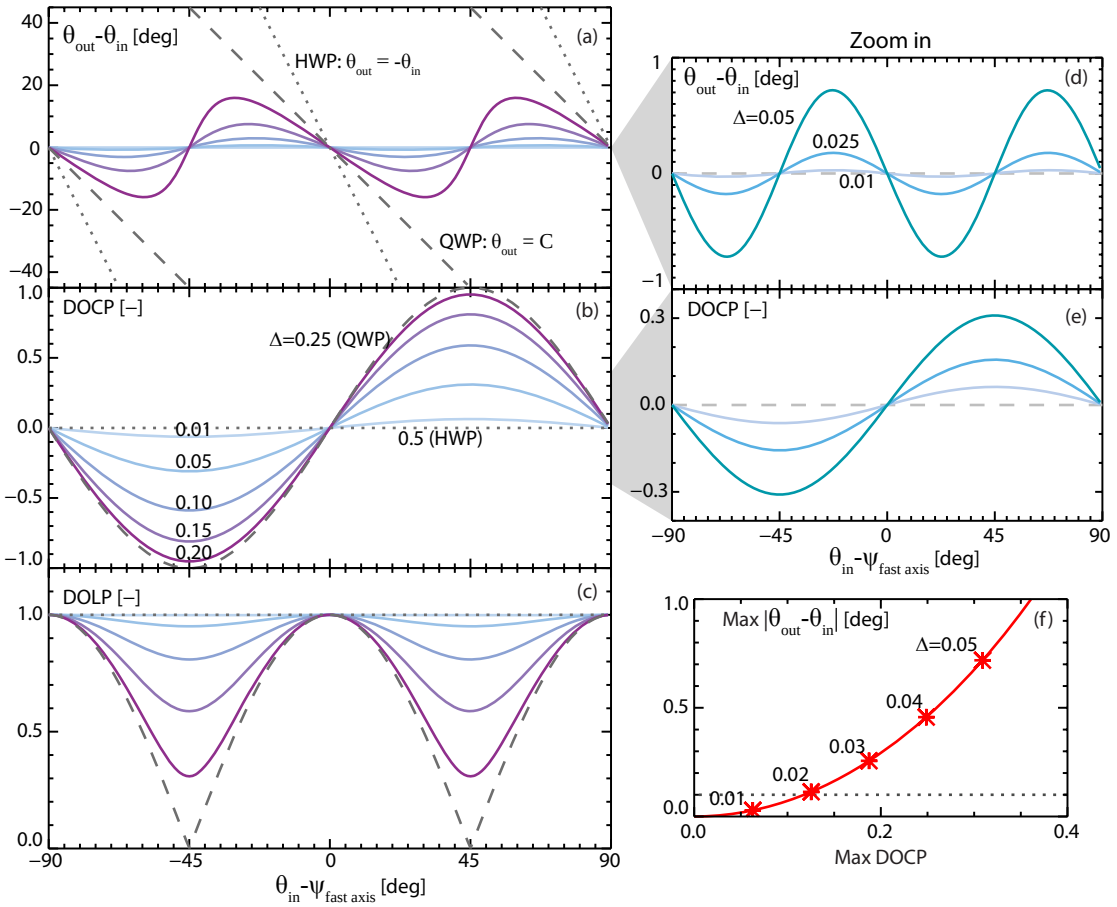

Figure 17: The resulting polarization properties when DOCP = 0, DOLP = 1 light is incident on a retarder with a fast axis angle $\psi_{\text{fast axis}}$ and retardance Δ (units of waves) calculated using Müeller calculus. The change in polarization angle ($\theta_{\text{out}} - \theta_{\text{in}}$) for a large range of retardance (a) and for a small amount of retardance (d). The output DOCP for large (b) and small (e) amounts of retardance and the output DOLP (c). The maximum change in angle as a function of the maximum output DOCP and the amount of retardance (f).

Figure 18: The change in DOCP as a function of change in angle and amount of retardance for light input with DOLP = 1, DOCP = 0.

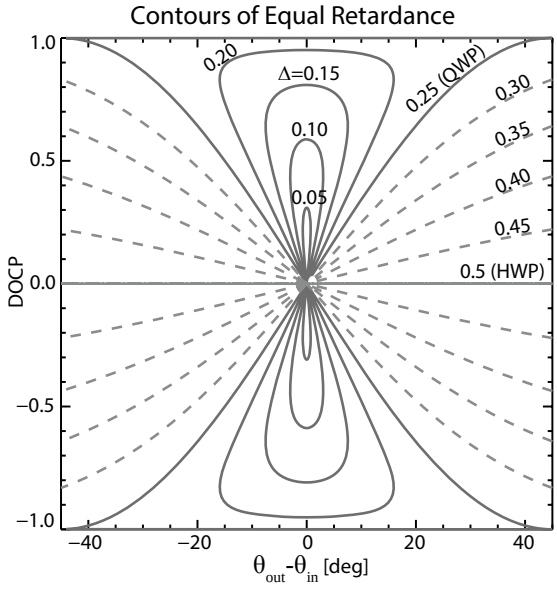

$\sin(2(\theta_{in} - \psi_{fast\ axis}))$ and a linear dependence on both $\frac{DOCP_{in}}{DOLP_{in}}$ and Δ. This has important consequence—multiple retarders can change the polarization angle in a complex manner. Complicated optical systems can therefore be problematic as optical elements early in the optics can introduce retardance, increasing the DOCP which then changes the polarization aberrations of the subsequent elements. Figure 19 shows the change in polarization angle and the output DOCP after light with $DOLP_{in} = 1$ is incident on the first of two sequential retarders, each with small amounts of retardance. It is clear that the change in polarization angle has a complex character in the two-retarder case. Note that when averaging over all orientations of one retarder, $\theta_{in} - \psi_{fast\ axis\ A}$, the change in polarization angle no longer averages to zero.

There are two main sources of retardance in MSE-LP periscopes; phase shifts from reflection, and birefringence in transmissive elements. The s- and p-polarizations can experience different phase shifts when light is reflected from a mirror surface. This introduces retardance with a fast-axis aligned to, or perpendicular to, the plane of incidence. A phase shift of $\Delta = 0$ or $\Delta = \pi$ does not introduce any non-linearities ($\Delta = \pi$ simply reverses the polarization angle). The phase shift depends on the angle of incidence and wavelength of the light; metal coatings in particular can have large phase shifts. The mirrors used in the C-MOD MSE system are dielectric coated with a specified phase shift of $\pm < 2.8°$, i.e., $\Delta\pm < 0.008$ waves, over the range of wavelengths and angles of incidence in the MSE optical train. This would lead to a non-linear polarization aberration of $< 0.02°$ with character $\sin(4(\theta - \psi_{fast\ axis})$ for $DOCP = 0$ incident light. However, it would only require light with $\frac{DOCP_{in}}{DOLP_{in}} > 0.07$ to change the polarization angle by $0.1°$. This is a relatively small amount of DOCP and could make this a problem, therefore the creation of circular light in the periscope should be avoided. The MSE optical train consists of three mirrors, each with similar angles of incidence and identical coatings. Two of the mirrors have nearly orthogonal planes of incidence which leads to some cancellation of the phase shift. Phase shift upon reflection are thus not expected in C-MOD MSE optics. The magnitude of the $\cos(4\theta_{pol})$ term in the calibration fit can be very small, $< 0.02°$, indicating phase shift in the MSE mirrors is not a significant issue. Transmissive elements can also create retardance due to birefringence—where light with one polarization experiences a different index of refraction than light with the orthogonal polarization. Anti-reflective coatings can also be a important source of retardance in transmissive optics, thus care should be taken when using these coatings [23]. The retardance of the lenses mounted in their mounts was measured by the University of Arizona Polarization Lab to be $< 1°$—and often closer to $0.3°$—corresponding to $\Delta < 0.003$.

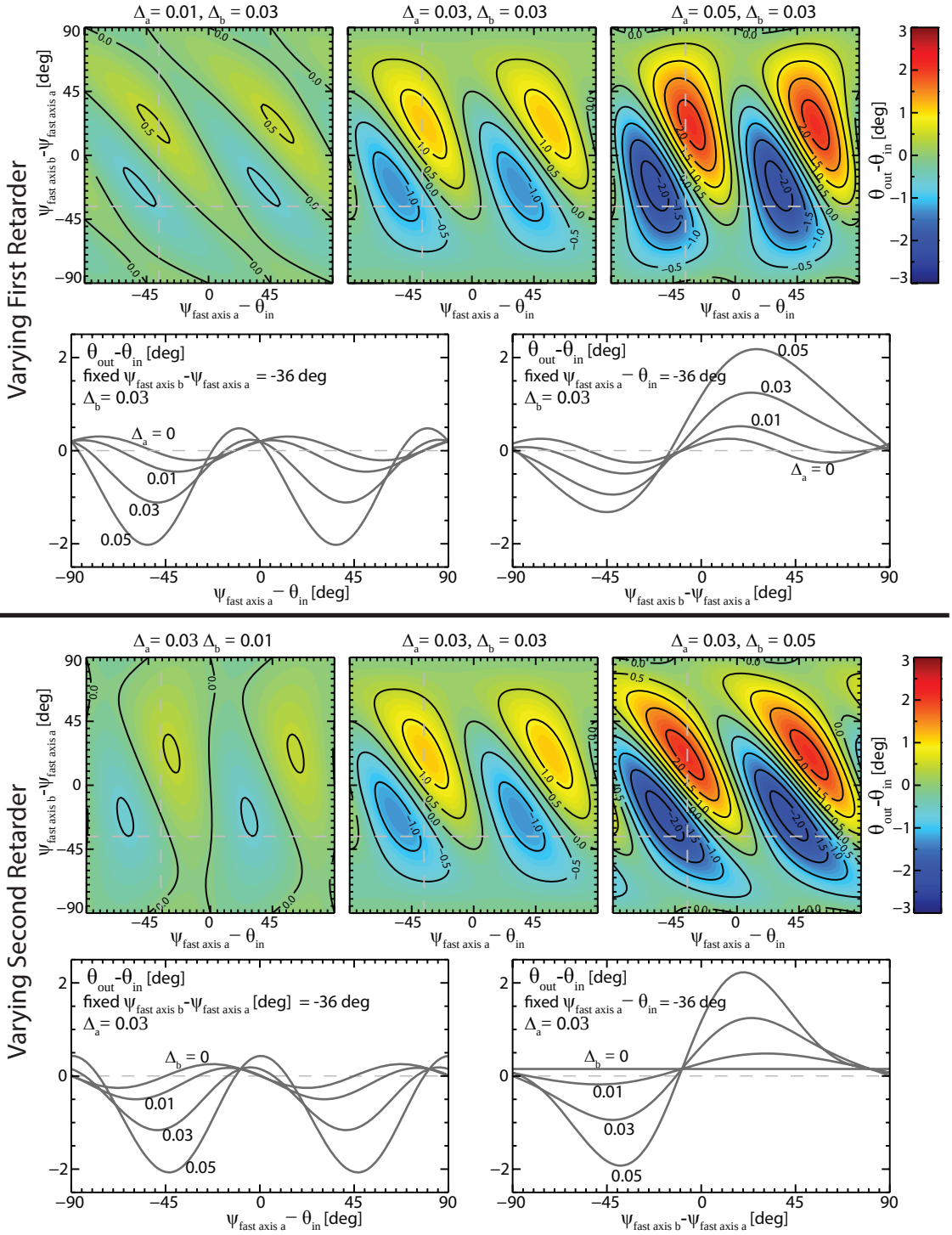

Figure 19: Two retarders create complex polarization behaviors and should be avoided. The pattern of change in polarization angle depends sensitively on the details of the configuration though some symmetries are apparent—polarization aberrations are not arbitrary functions.

If the optical system is constant in time, the polarization aberrations from retardance can be calibrated out very accurately using an invessel calibration system. However, mirrors can be coated or eroded leading to changes in phase-shift upon reflection [24] and stress induced birefringence may arise from changes in temperature or mounting force [21]. It is therefore important to either prevent both these effects from occurring or to provide a means to quantify the change in retardance. The topic of stress-induced birefringence is covered in the next chapter along with the use of the ISC system to monitor changes in the polarization aberration.

Additional checks on the presence of polarization aberrations are discussed in Appendix C. These measurements confirm the nearly ideal behavior of the periscope.

3.5 PEM-BASED POLARIMETER AND DETECTOR EFFECTS

After propagating through the periscope the light is incident on the dual-PEM-based polarimeter which converts the Stokes vectors into amplitudes at various PEM harmonics. The operation of these PEM-based polarimeters is covered in depth in references [25–31]. Reference [30] presents the entire expansion of the intensities at the PEM harmonics. The intensity at the second harmonic of each PEM are primarily of interest in the MSE-LP diagnostic:

$$\begin{aligned} I_{2\omega_1} &= J_2(R_1)\sin(2\alpha)\cos(2\beta)\left(Q\sin(2\alpha) - U\cos(2\alpha)\right) \\ I_{2\omega_2} &= J_2(R_2)\sin(2\alpha)\sin(2\beta)\left(Q\cos(2\alpha) + U\sin(2\alpha)\right) \end{aligned} \tag{25}$$

where $I_{2\omega_1}$ and $I_{2\omega_2}$ are the intensities of the light at the second harmonic of the first and second PEM, respectively. J_2 is the second order Bessel function of the first kind. R_1 and R_2 are the magnitude of the retardance of each PEM at the location of the incident light. α is the angle between the modulation axis of the first PEM and the second PEM, β is the angle between the linear polarizer and the second PEM. Finally, Q and U are the Stokes components of the light incident on the polarimeter.

The angles are chosen to discriminate between the different Stokes components using the choice of $\alpha = \pi/4$ and $\beta = \pi/8$, yielding:

$$\frac{1}{2}\tan^{-1}\left(\frac{J_2(R_1)}{J_2(R_2)}\frac{I_{2\omega_2}}{I_{2\omega_1}}\right) = \theta_{in} \tag{26}$$

where θ_{in} is the polarization angle of the light incident on the PEM-based polarimeter. Both retardances are usually set to be near 3.054 radians, which maximizes the signal intensities at the second harmon-

ics of the PEMs. Typically the retardances of the two PEMs are assumed to be equal, yielding:

$$\frac{1}{2}\tan^{-1}\left(\frac{I_{2\omega_2}}{I_{2\omega_1}}\right) \equiv \theta_{PEMs} \tag{27}$$

where θ_{PEMs} is defined as this ratio between the measured signal harmonics.

When interpreting most MSE-LP measurements, it is assumed that the PEM-based polarimeter is ideal and thus $\theta_{PEMs} = \theta_{in}$. However, if the polarimeter geometry is not identical to what is assumed or if the retardances are not equal or if other errors occur then θ_{PEMs} is not identical to θ_{in}:

$$\theta_{PEMs} = \theta_{in} + F(\theta_{in}) \tag{28}$$

Importantly, these errors are not actually deviations in the polarization angle but problems due to incorrect knowledge of the state of the PEM-based polarimeter. These types of errors can be non-linear and have been investigated in references [32] and [30]. Typically such errors are incorporated into the calibration of the diagnostic with high accuracy. However, these errors can change when the operation of the PEMs changes during the campaign.

3.5.1 *Geometric errors in PEM alignment*

Incorrectly setting the angle between the second PEM and the linear polarizer, β, can induce errors. Setting $\alpha = \pi/4$ and equal retardances ($R_1 = R_2$) in Equation 25 yields:

$$\frac{I_{2\omega_2}}{I_{2\omega_1}} = \frac{\sin(2\beta)U}{\cos(2\beta)Q} \tag{29}$$

Setting $\beta = \pi/8 + \delta\beta$, where $\delta\beta$ is the alignment error from the desired angle yields:

$$\frac{\sin(2\theta_{PEMs})}{\cos(2\theta_{PEMs})} = \tan(\pi/4 + 2\delta\beta)\frac{\sin(2\theta_{in})}{\cos(2\theta_{in})} \tag{30}$$

assuming that $2\delta\beta << 1$ allows the tangent term to be approximated as:

$$\tan(\pi/4 + 2\delta\beta) = \frac{\tan(\pi/4) + \tan(2\delta\beta)}{1 - \tan(\pi/4)\tan(2\delta\beta)} \approx (1 + 2\tan(2\delta\beta)) \tag{31}$$

Substituting into the previous equation yields:

$$\sin(2(\theta_{PEMs} - \theta_{in}) \approx 2\tan(2\delta\beta)\sin(2\theta_{in})\cos(2\theta_{PEMs}) \tag{32}$$

Using the small angle approximation for $\tan(2\delta\beta)$ and substituting θ_{in} for θ_{PEMs} in the right hand side yields:

$$\theta_{PEMs} - \theta_{in} \approx \delta\beta \sin(4\theta_{in}) \tag{33}$$

Misaligning the linear polarizer relative to the PEMs therefore creates an error term that is modulo $\pi/2$. This was tested on C-MOD by removing the linear polarizer, rotating it $\pi/2$, and re-inserting it into PEM-based polarizer. The diagnostic was calibrated using the robotic calibration system in each configuration. The only coefficients that changed were the offset term, which changed by almost exactly 90°, and the term with character $\cos(4\theta_{pol})$ which changed by 0.2°, confirming the character of this error.

It is also possible to have an error in the alignment between the two PEMs, i.e., $\alpha \neq \pi/4$. Setting $\beta = \pi/8$ and assuming equal retardances in Equation 25 yields:

$$\frac{I_{2\omega_2}}{I_{2\omega_1}} = \frac{Q\cos(2\alpha) + U\sin(2\alpha)}{Q\sin(2\alpha) - U\cos(2\alpha)} \tag{34}$$

Setting $\alpha = \pi/4 + \delta\alpha$ where $\delta\alpha$ is the deviation from ideal, yields:

$$\frac{\sin(2\theta_{PEMs})}{\cos(2\theta_{PEMs})} = \frac{-Q\sin(2\delta\alpha) + U\cos(2\delta\alpha)}{Q\sin(2\delta\alpha) - U\cos(2\delta\alpha)}$$

Assuming $\delta\alpha$ is small allows the small angle approximation to be applied which, after some algebra yields:

$$\sin(2(\theta_{PEMs} - \theta_{in})) \approx -2\delta\alpha\cos(2(\theta_{PEMs} - \theta_{in}))$$

An additional small angle approximation results in:

$$\theta_{PEMs} - \theta_{in} \approx -\delta\alpha \tag{35}$$

Thus a misalignment of the first PEM relative to the second PEM acts as a simple rotation of the interpreted polarization angle.

This analysis shows that it is important to obtain the proper alignment of the PEMs relative to one another and relative to the linear polarizer. Errors in linear polarizer alignment lead to non-linear errors with modulo $\pi/2$ while errors in aligning the first PEM relative to the second PEM lead to offset errors. These alignment errors are fully accounted for in the calibration procedure. However, this analysis shows that it is important that the PEMs and linear polarizer be kept in alignment during the campaign with an accuracy on the same order as required to make the MSE measurement.

3.5.2 *Non-equal* PEM *retardance*

Equation 25 has a dependence on the retardances of the two PEMs, R_1 and R_2. These are assumed to be equal when interpreting the polarization angle. However, obtaining equal retardances is difficult in practice, and the retardance has been shown to drift as a function of time. This section explores the consequences of not having equal PEM retardances.

$$\frac{I_{2\omega_2}}{I_{2\omega_1}} = \frac{J_2(R_2)Q}{J_2(R_1)U}$$

supposing that the retardance of the second PEM differs from the retardance of the first PEM causing the Bessel functions to differ i.e., $\Delta J_2 = J_2(R_2) - J_2(R_1)$, the preceding expression then becomes:

$$\frac{\sin(2\theta_{\text{PEMs}})}{\cos(2\theta_{\text{PEMs}})} = \left(1 + \frac{\Delta J_2}{J_2(R_1)}\right) \frac{\sin(2\theta_{\text{in}})}{\cos(2\theta_{\text{in}})}$$

which can be simplified as :

$$\sin(2(\theta_{\text{PEMs}} - \theta_{\text{in}})) = \frac{\Delta J_2}{J_2(R_1)} \cos(2\theta_{\text{PEMs}}) \sin(2\theta_{\text{in}}) \tag{36}$$

assuming $|\frac{\Delta J_2}{J_2(R_1)}| << 1$ allows the small angle approximation to be applied to the left side of the equation and θ_{in} to be substituted into the cosine in the right side of the equation yielding:

$$\theta_{\text{PEMs}} - \theta_{\text{in}} \approx \frac{\Delta J}{4J_2(R_1)} \sin(4\theta_{\text{in}}) \tag{37}$$

The retardance of both PEMs is typically set to maximize J_2, which occurs at $R = 3.054$. Near the maximum, the value of the Bessel function varies quadratically with changes in its argument. This can be evaluated numerically as:

$$\begin{aligned} J_2(R_2) &= J_2(3.054 + \Delta R) \approx 0.485 - 0.139(\Delta R)^2 \\ J_2(R_1) &= J_2(3.054) = 0.485 \end{aligned}$$

substituting this into Equation 37 yields:

$$\begin{aligned} \theta_{\text{PEMs}} - \theta_{\text{in}} &\approx -0.0716(R_2 - 3.054)^2 \sin(4\theta_{\text{in}}),\ R_1 = 3.054 \\ \theta_{\text{PEMs}} - \theta_{\text{in}} &\approx +0.0716(R_1 - 3.054)^2 \sin(4\theta_{\text{in}}),\ R_2 = 3.054 \end{aligned} \tag{38}$$

Thus it would require $\Delta R = 0.16$ radians to change the angle by 0.1°. Away from operation at $R = 3.054$ the value of the J_2 varies linearly in its argument in which case the angular deviation will become linear in the deviation in retardance.

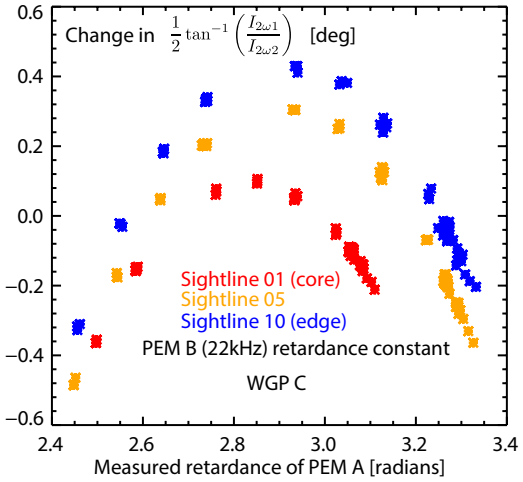

Figure 20: The ISC was used to input light with constant polarization angle into the diagnostic while varying the retardance of the first PEM. The measured angle from the intensity ratio (θ_{PEMs}) varies as a function of the retardance. The optimal retardance is dependent on MSE sightline.

The PEMs' retardance varies across the PEM aperture. The retardance variation was measured in reference [33] for a type of PEM very similar to that used in the C-MOD MSE diagnostic. This variation was also measured in one direction on the bench for the C-MOD PEMs.The laser ray-tracing capability of the robotic calibration system also allows the retardances of the PEMs to be explored in depth. Unfortunately, the large étendue of MSE systems makes it difficult to impose equal and optimum retardances for both of the two PEMs. Each MSE sightline strikes the PEM at a different mean location on the PEM surface. The PEM retardances are therefore set so that all the sightlines receive $R_1 = R_2 = 3.054$ radians as close as possible. Furthermore, each ray strikes the PEM at a different position, thus it experiences a different retardance. The rays that make up the sightlines are spread across a relatively large portion of the PEM surface in the C-MOD diagnostic (~ 0.5 of the PEM diameter), thus many different retardances are averaged together[5].

The measured polarization angle's dependence on the PEM retardances was observed on C-MOD using the ISC system to input light with a fixed polarization angle while one of the PEM retardances was changed. The results are shown in Figure 20 which shows the change in θ_{PEMs} as the retardance of the first PEM was varied. The quadratic dependence of the angle on the change in retardance from optimum is apparent in the data for three sightlines. The point with no change in angle is the nominal operating point. In addition to directly measuring the retardance, the magnitude of the $\cos(4\theta)$ term from polarization calibrations can be used to tune the PEM retardance by adjusting the relative retardances until this term is minimized. This effect

5 This method of using PEMs is significantly different from the typical laboratory-bench methods used in other fields of science. The manufacturer recommends that only a small (order centimeter) portion of the PEM surface at the center be used under normal incidence. However, MSE-LP diagnostics require much larger étendue than typical laboratory-bench experiments.

was tested by changing the retardance of the first PEM while performing polarization calibrations. It was found that only the calibration fit term that is modulo $\pi/2$ varied during the experiment and that it varied roughly quadratically with the change in the magnitude of the retardance, confirming these calculations.

The sensitivity of the measured angle to the ratio of PEM retardances can cause uncompensated systematic errors if the retardance is allowed to change during a campaign. To prevent errors with $|\theta_{PEMs} - \theta_{in}| > 0.1^\circ$ the retardance must be kept stable to ± 0.15 radians throughout the campaign. The inter-shot calibration system provides a means to monitor the retardance of the PEMs while simultaneously measuring θ_{PEMs} by inputing polarized light into the diagnostic at any point during the campaign. It is found that the retardance is usually stable on long and short timescales with an occasional large change. The details of this behavior are presented in Appendix C. Furthermore, the ISC system discussed in the next chapter compensates for any change in the measured angle due to changes in the PEM retardance.

3.5.3 *Frequency-dependent detector gain*

The interpretation of the measured signals as a polarization angle depends on the detector responses being identical at the second harmonics of the PEM frequencies $2\omega_1$ and $2\omega_2$. If there is a frequency dependence to the detection and amplification circuits it would lead to a misinterpretation of the measured angle:

$$\frac{I_{2\omega_2}}{I_{2\omega_1}} = \frac{G_2 U}{G_1 Q}$$

where G_1 is the gain of the detection system at $2\omega_1$ and G_2 is the gain of the detection system at $2\omega_2$. Setting $\frac{G_2}{G_1} = 1 + \delta G$ yields:

$$\sin(2(\theta_{PEMs} - \theta_{in}) = \delta G \cos(2\theta_{PEMs}) \sin(2\theta_{in})$$

Assuming the perturbation is small allows the small angle approximation to be applied to the left side of the equation and the replacement of θ_{PEMs} with θ_{in} in the right side of the equation:

$$\theta_{PEMs} - \theta_{in} \approx \frac{\delta G}{4} \sin(4\theta_{in}) \tag{39}$$

Thus a non-unity gain at the two harmonic frequencies will produce an error with modulo $\pi/2$. For the magnitude of this error to be $> 0.1^\circ$, the ratio of the gains at the two frequencies would have to be $\frac{G_2}{G_1} > 1.007$ or $\frac{G_2}{G_1} < 0.993$. In C-MOD, where the $2\omega_1 = 20.0$kHz and $2\omega_2 = 22.2$kHz, this would correspond to a non-linear frequency dependent gain of $0.0035^{-}/_{\text{kHz}}$. Previous measurements done by Ko on the MSE APD detectors showed that the ratio of gains at $2\omega_1$ and $2\omega_2$

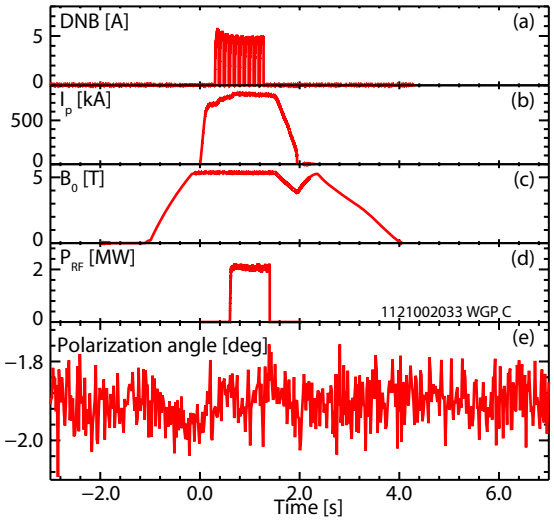

Figure 21: The MSE diagnostic observed the ISC during a plasma discharge to determine if operation of the tokamak systems changes the diagnostic response. The polarization angle (e) does not show large changes due to the DNB (a), the plasma current (b), the magnetic field (c), and ICRF heating.

did not statistically differ from 1 with a measurement uncertainty of ~ 0.001 [21]. This represents a deviation of the angle by $< 0.014°$. Thus this effect is not significant for C-MOD. Furthermore, the ratio of the gains at such closely spaced frequencies should be very insensitive to drifts and would be correct for using the ISC system.

Incorrectly detecting the amplitudes at the PEM harmonics due to phase-shift errors can also produce errors with modulo $\pi/2$ for the same reason that an incorrect gain will produce these errors.

3.5.4 *Electrical interference from tokamak systems*

It is conceivable that the tokamak systems could interfere with the operation of the PEMs which are installed on the tokamak, an environment with many sources of electrical noise. If the PEMs were affected by the tokamak it could skew the polarization angle measured by the diagnostic.

One potential source of noise is the operation of the DNB which has noisy high-voltage power supplies mounted near the PEM optical and electronic heads. Interference from this source was evaluated using the ISC system to input a constant polarization angle into the diagnostic while the DNB was fired into the tokamak. The polarization angle during the periods when the beam was on was compared to the polarization angle measured during the times the DNB was off. The polarization angle during beam operation does not differ significantly from the polarization angle without beam operation, indicating the beam does not interfere with the operation of the diagnostic.

The high power ICRF and LHCD heating, tokamak magnets, and inductive current drive could conceivably interfere with the operation of the PEMs. This was tested in a similar manner; using the ISC to input a constant polarization angle into the diagnostic during a discharge. The results are shown in Figure 21. The polarization angle (e)

does not show systematic changes due to any of the major tokamak subsystems beyond that from the previously discussed Faraday Effect which is most apparent from $t = -1s$ to $t = 0s$.

These PEM-based polarimeter errors are all small on C-MOD. The error due to unequal retardance is the largest error. This can be minimized for a single MSE sightline but cannot be eliminated for all sightlines due to how the sightlines fill the PEMs. This is also the only error that conceivably changes during the campaign. Any change would be sensed by the diagnostic and automatically corrected for by the ISC methodology. Additional checks on possible sensitivities in the polarimeter and detection systems are discussed in Appendix C. These measurements confirm that the system behaves very nearly ideally.

3.6 RAY-DEPENDENT EFFECTS

All the systematic error sources discussed in the sections about polarization aberrations and non-ideal polarimeters operate on a ray of polarized light. A sightline is composed of many rays filling the entrance pupil, each with different trajectory and each experiencing essentially a different diagnostic. Each ray is incident on the optics at specific locations with specific angles of incidence and therefore experiences a specific set of polarization aberrations and PEM-based polarimeter retardance. The resulting signals at the detectors are then a sum over all the individual contributions. This has important consequences for the operation of the diagnostic; although it may be conceptually simple to treat the calibration for a single sightline as a unified quantity, the actual diagnostic response will depend on the details of the subset of rays contributing to the sum. Because the C-MOD MSE diagnostic collects a large étendue, ray-dependent effects can be important—there are many different rays.

Experiments were conducted using the invessel calibration robot to determine the magnitude of ray-dependent effects. The objective lens of the diagnostic (i.e., the entrance pupil) was masked, blocking part of the lens. This was done with masks that block the top half of the lens, the bottom half of lens, the side of the lens, and with no mask. Calibrations were then performed and the fits to Equation 8 were compared.

The results are shown in Figure 22. It was found that the calibration fit coefficients depend on which part of the diagnostic lens is illuminated. The offset term is the most sensitive to this (a). There is a smooth sightline dependence in this term and the value depends on the illumination at the $\pm 1^\circ$ level at the field edges. Note that changing which side of the lens is illuminated (green) does not differ much from illuminating the entire lens (grey) whereas illuminating the top (red) or bottom (blue) of the lens has a large effect. It is clear that the no-mask case represents the average between the top-masked and

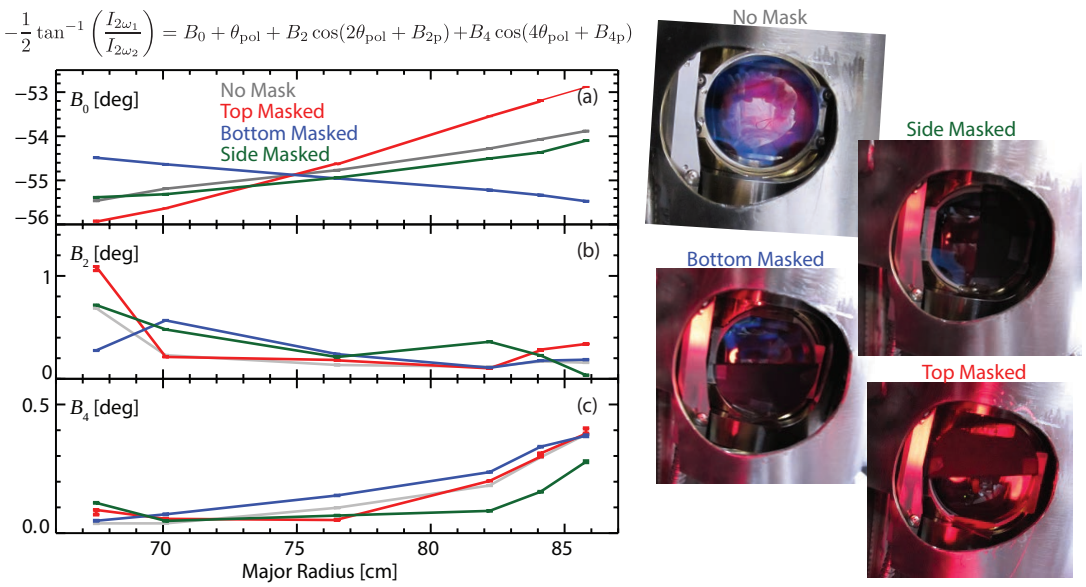

Figure 22: The robotic calibration system was used to perform repeated calibrations of the diagnostic with different portions of the objective lens illuminated (right). The resulting data was fitted to the standard calibration equation. The resulting fit parameters for the linear term (a), term with character $\cos(2\theta_{\rm pol})$ (b), and character $\cos(4\theta)$ are shown to be dependent on which part of the objective lens the rays pass through.

bottom-masked cases for all sightlines. The masking dependence is linear across the sightlines with all the curves crossing near the optical axis. This hints at angle of incidence effects on the various mirrors being important since the angle of incidence is semi-symmetric about the optical axis. The first mirror in particular has a large difference in angle of incidence between illuminating the upper and lower portions of the entrance pupil. The non-linear terms show less dependence on which part of the lens is masked with a less discernible sightline structure. A similar experiment was conducted by masking the calibration source at the beam position with similar, but smaller variation within a sightline.

The robotic calibration system enables polarized ray tracing to be performed through the diagnostic. The laser source is used to shine a $\sim$ 1mm diameter polarized ray from a location at the viewing volume, to the objective lens, through the periscope and PEMs, into the fibers, and finally into the detector. The process is discussed in Appendix C. This enables the calibration fit coefficients (Equation 8) to be obtained as a function of which ray is traversing the system. The striking results of this test are shown in Figure 23. The difference between the angle measured using a ray trace and using the fully illuminated source is shown in panel A for three rays. Note that there is $\cos 2\theta_{\rm pol}$ and $\cos(4\theta_{\rm pol})$ structure evident in addition to an offset. The effect is smallest at the center of the lens but is largest at the quarter-radius of the lens for this particular position. The fit coefficients are shown in panel B for two sightlines as a function of the radius of the laser strike

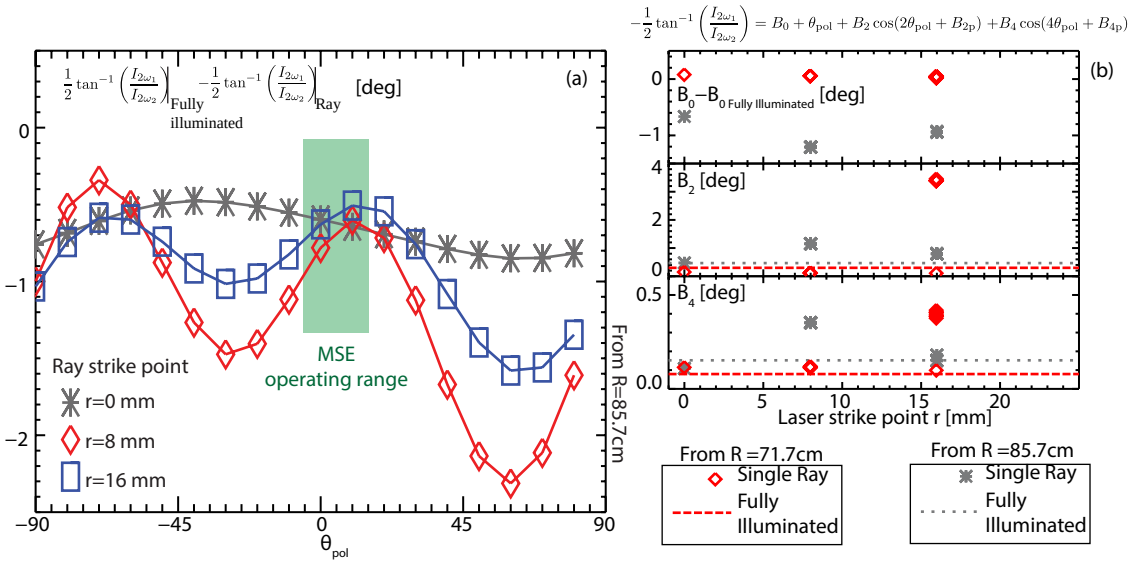

Figure 23: The robotic calibration system was used to perform a polarized ray trace through the diagnostic. Calibration cycles were performed while the ray was incident at different points on the 25mm radius objective lens. The polarization angles measured for each ray were then compared to the angles measured under full illumination. A subset of the data for three such rays is shown as function input polarization angle (a). The range of angles typically observed by the MSE diagnostic is shown as the green shaded region. Calibration fits were then performed for the rays and compared to the calibration under full illumination. Four different positions at each lens radius were examined from two different sightline viewing volumes.

point. There are large differences but they are not generally very well ordered as a function of laser strike point radius or sightline.

All of these studies were done in with the diagnostic in its static configuration and the resulting measurements are well outside of the uncertainties in the calibration system. These investigations have shown that there are order 1° difference in the diagnostic response depending on how the diagnostic is illuminated, presumably due to ray-dependent effects at the mirrors and PEMs. It is therefore important to calibrate the diagnostic with an illumination source that is representative of what is observed from the plasma. Fortunately, the emission from the neutral beam is fairly Lambertian—uniform across the viewing volume and across the collection solid angle. From these experiments, it is clear that a uniformity of $\sim \pm 10$ percent across the entrance pupil is required, especially for sightlines near the edges of the field of view. The illumination sources used in the invessel calibration robot and the ISC are therefore both designed to be as uniform as possible.

These experiments also indicate how important ray-dependent effects could be if the diagnostic response changes. The diagnostic response can change in a way that can does not affect all rays equally. Mirrors could be deposited on or eroded non-uniformly across their surface, changing their phase shift and s-p reflection ratios for rays that strike different portions of the mirror. Or stress-induced birefringence could be non-uniform in the lenses, changing the retardance

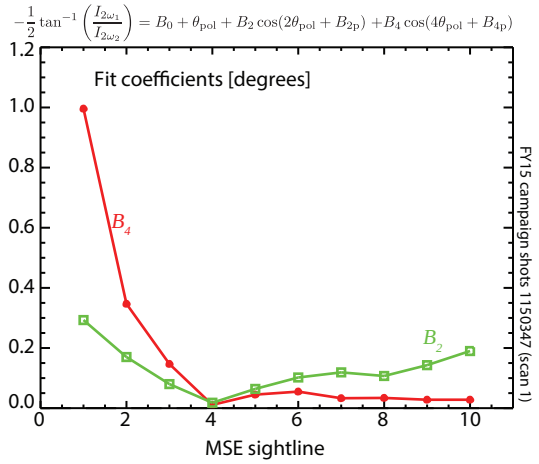

Figure 24: The non-linear calibration fit coefficients from a recent calibration using the invessel calibration robot. The rms residual in the fits were $< 0.05°$.

applied to individual rays. It is important to properly average across the changes using a uniform calibration source.

3.7 SUMMARY: SYSTEMATIC ERRORS IN MSE-LP DIAGNOSTICS

A comprehensive exploration of the various types of systematic errors that may affect MSE-LP diagnostics has been undertaken to better understand the operation of these diagnostics. The various types of systematic errors, their character, and mitigation strategies are shown in Table 5. Knowledge of the errors can be used optimize MSE diagnostics. For example, depending on the exact implementation it might be advantageous to use a low stress-coefficient glass to minimize retardance and tolerate Faraday rotation than to use a low Verdet glass and tolerate retardance. This table can also be used to help identify what physic effect may be causing problems in MSE diagnostics using the character of the error (i.e., modulo $\pi/2$ vs π).

The C-MOD MSE diagnostic is calibrated using Equation 8 which was developed using the concept of a Fourier decomposition of the input polarization angle and experience with data. Typical values of the calibration coefficients are shown in Figure 24. This approach and fitting procedure has been empirically proven to accurately describe the diagnostic operation. In the light of the derivation of different systematic errors the fitting terms are shown to carry physical significance. Previous work on C-MOD used a Müeller matrix model to fit the calibration response assuming the non-linearities were all due to mirrors [6]. This is not an accurate description since it ignored the non-ideal polarimeter operation which has recently been shown to be important for many of the MSE sightlines and which contributes most of the term with character $\cos(4\theta_{pol})$. The complexity of the diagnostic operation and the knowledge that the variations in angle arise with only offset, $\sin(2\theta_{pol})$, and $\sin(4\theta_{pol})$ character indicates that the

Table 5: Sources of systematic errors in MSE-LP diagnostics, their character, and mitigation strategies.

Error source	Character	Mitigation
View movement	Shifts in viewing volume, projection angles	System to monitor alignment, sturdy mounts
Radial electric field	$\frac{d\theta_{pol}}{dE_R} \approx -\frac{\cos^2\theta^{\sigma}_{pol}}{vB_\phi}\frac{\cos\Omega}{\sin\alpha}$	Choice of viewing geometry, complementary views, E_R measurements from other diagnostics
Polarized background subtraction	$\Delta\theta_{beam} \approx \frac{-f}{2SB}\sin\left(2\left(\theta_{beam}-\theta_{bgkd}\right)\right) + \frac{-\Delta\theta_{bkgd}}{SB}\cos\left(2\left(\theta_{beam}-\theta_{bgkd}\right)\right)$	Multi-spectral MSE (see Chapter 5)
3D geometry	$d\theta_{pol}/d\lambda \neq 0$	Simulation, careful filter placement and control of filter bandpasses
Realistic beam	Interacts with 3D geometry effects	Monitor beam voltage
Faraday Rotation	$\theta_{out}-\theta_{in} = BVd$	Low Verdet constant glass, compensation with in-situ measurements
Diattenuation	$\theta_{out}-\theta_{in} \approx \frac{-\Psi}{2\,DOLP_{in}(2-\Psi)}\sin(2(\theta_{in}-\psi_{diat}))$	Low diattenuation mirrors and components, in-situ monitoring if mirrors are plasma-facing
Retardance	$\theta_{out}-\theta_{in} \approx -\frac{\pi^2\Delta^2}{2}\sin(4(\theta_{in}-\psi_{fast\ axis}) + \frac{DOCP_{in}}{DOLP_{in}}\pi\Delta\cos(2(\theta_{in}-\psi_{fast\ axis}))$ $DOCP_{out} \approx DOLP_{in}2\pi\Delta\sin(2(\theta_{in}-\psi_{fast\ axis})) + DOCP_{in}$	Mirrors with low phase-shift-upon-reflection, low stress-coefficient lenses, in-situ monitoring if mirrors are plasma-facing and/or if lenses are subject to temperature changes
PEM-polarizer misalignment	$\theta_{PEMs}-\theta_{in} \approx \delta\beta\sin(4\theta_{in})$	Proper setup, sturdy mounting, in-situ calibration
PEM-PEM misalignment	$\theta_{PEMs}-\theta_{in} \approx -\delta\alpha$	Proper setup, sturdy mounting, in-situ calibration
Unequal PEM retardance	$\theta_{PEMs}-\theta_{in} \approx \frac{\Delta J}{4J_2(R_1)}\sin(4\theta_{in})$	Proper setup, on-line PEM retardance monitoring, in-situ calibration
Frequency dependent gain	$\theta_{PEMs}-\theta_{in} \approx \frac{\delta G}{4}\sin(4\theta_{in})$	Proper detector design, in-situ calibration
Phase-lock errors	$\theta_{PEMs}-\theta_{in} \propto \sin(4\theta_{in})$	Digitial locking with phase-sensing, in-situ calibration
Tokamak-PEM interference	unknown	Shielding if necessary
Ray-dependence	Most of the above	Matching calibration illumination pattern to that observed during use

Fourier decomposition method of calibration is likely to be sufficient and very accurate.

The C-MOD MSE diagnostic is shown to operate very nearly ideally with few significant source-side effects, polarization aberration, and PEM-based polarimeter effects. Furthermore, the ISC system can track most of these sources of error very accurately. The various types of non-ideal operation are:

RETARDANCE DUE TO THERMAL STRESS-INDUCED BIREFRINGENCE is covered in the Chapter 4. This previously led to time varying changes in the diagnostic response of $\sim 1°$. This has been reduced to $< 0.2°$. This is compensated for with the ISC system.

POLARIZED BACKGROUND SUBTRACTION is covered in Chapter 5 and can be mitigated using the multi-spectral MSE system. This changes during a discharge.

3D SOURCE EFFECTS cause a dependence of the measured polarization angle on the wavelength of $|d\theta_{pol}/d\lambda| < 1.0°/nm$. This is worst at the sightlines viewing the core due to poor radial resolution, important at the sightlines viewing the edge, and negligible at the mid-radius. This is mitigated using filter position scans, careful measurement of the filter bandpass, and magnetic field sweeps. The location of the filter bandpass relative to the spectrum can be located and controlled with < 0.1nm accuracy, mitigating this error and changes in this error.

RAY-DEPENDENT EFFECTS cause the diagnostic response to vary over the ensemble of rays used during diagnostic operation. Illumination uniformity is thus required for the ISC and invessel calibration system. This effect doesn't change unless the spatial properties of the optical elements change, which is the case for stress-induced birefringence.

NON-EQUAL PEM RETARDANCE is responsible for non-linear errors of $\sim 1.0°$ for some sightlines but is typically $< 0.2°$. This effect is accurately captured in the calibration and PEM retardance is monitored for every plasma discharge and at regular intervals across the campaign. If the PEM retardance changed, the error would be compensated for using the ISC system.

All other sources of systematic error are shown to be small and/or unchanging. In addition to the work presented here, Appendix C presents work performed to measure other properties of the MSE diagnostic. It was found that the periscope is stable across the experimental runday and campaign, and that the filters are well-controlled and have the appropriate bandpasses. The periscope optics have little depolarization, vignetting, scattering, polarization-dependent transmission, or spurious polarization, and the diagnostic response is independent of wavelength. The detectors all behave identically and

produce polarization measurements that are independent of gain or intensity.

The only significant sources of time-varying systematic error found in this study are due to thermal stress-induced birefringence, a topic covered in depth in Chapter 4 and polarized background subtraction, covered in Chapter 5. The ISC system can account for polarization aberration error and efforts have been made to minimize it. Better background subtraction was developed to minimize this effect. In total, it is estimated that the total systematic error that is not compensated for during operation of the diagnostic is $< 0.2°$. This means the diagnostic should be able to measure the absolute polarization angle from the beam at this level.

BIBLIOGRAPHY

[1] R. Mumgaard. Engineering Upgrads to the Motional Stark Effect Diagnostic on Alcator C-Mod. MIT PSFC Research Report PSFC/RR-15-5, MIT PSFC, April 2015.

[2] F. S. Zaitsev, D. P. Kostomarov, E. P. Suchkov, V. V. Drozdov, E. R. Solano, A. Murari, S. Matejcik, N. C. Hawkes, and Jet-Efda Contributors. Analyses of substantially different plasma current densities and safety factors reconstructed from magnetic diagnostics data. *Nuclear Fusion*, 51(10):103044, October 2011.

[3] Leonid E. Zakharov, Jerome Lewandowski, Elizabeth L. Foley, Fred M. Levinton, Howard Y. Yuh, Vladimir Drozdov, and D. C. McDonald. The theory of variances in equilibrium reconstruction. *Physics of Plasmas (1994-present)*, 15(9):092503, September 2008.

[4] E.L. Foley, F.M. Levinton, H.Y. Yuh, and L.E. Zakharov. Comparison of motional Stark effect diagnostic approaches for equilibrium reconstruction. *Nuclear Fusion*, 48(8):085004, August 2008.

[5] B. W. Rice, D. G. Nilson, K. H. Burrell, and L. L. Lao. Simultaneous measurement of q and E_R profiles using the motional Stark effect in high-performance DIII-D plasmas (invited). *Review of Scientific Instruments*, 70(1):815, 1999.

[6] H.Y. Yuh. *The Motional Stark Effect diagnostic on Alcator C-Mod*. PhD, Massachusetts Institute of Technology, 2005.

[7] M. C. Zarnstorff, F. M. Levinton, S. H. Batha, and E. J. Synakowski. The effect of E_R on motional-Stark effect measurements of q, a new technique for measuring E_R, and a test of the neoclassical E_R. *Physics of Plasmas*, 4(4):1097, 1997.

[8] B. W. Rice, K. H. Burrell, L. L. Lao, and Y. R. Lin-Liu. Direct measurement of the radial electric field in tokamak plasmas using the Stark effect. *Physical Review Letters*, 79(14):2694, October 1997.

[9] F. M. Levinton, R. E. Bell, S. H. Batha, E. J. Synakowski, and M. C. Zarnstorff. Radial electric field measurements in reversed shear plasmas. *Physical Review Letters*, 80(22):4887–4890, June 1998.

[10] K. Kamiya, H. Kimura, K. Hoshino, N. Isei, H. Kawashima, H. Ogawa, T. Ogawa, K. Tsuzuki, K. Uehara, and JFT-2M Group.

Multichannel motional Stark effect diagnostic discriminating radial electric field in the JFT-2M tokamak. *Review of Scientific Instruments*, 72(7):2931, 2001.

[11] C. T. Holcomb, M. A. Makowski, R. J. Jayakumar, S. A. Allen, R. M. Ellis, R. Geer, D. Behne, K. L. Morris, L. G. Seppala, and J. M. Moller. Motional Stark effect diagnostic expansion on DIII-D for enhanced current and E_R profile measurements. *Review of Scientific Instruments*, 77(10):10E506, 2006.

[12] J.E. Rice, A.C. Ince-Cushman, P.T. Bonoli, M.J. Greenwald, J.W. Hughes, R.R. Parker, M.L. Reinke, G.M. Wallace, C.L. Fiore, R.S. Granetz, A.E. Hubbard, J.H. Irby, E.S. Marmar, S. Shiraiwa, S.M. Wolfe, S.J. Wukitch, M. Bitter, K. Hill, and J.R. Wilson. Observations of counter-current toroidal rotation in Alcator C-Mod LHCD plasmas. *Nuclear Fusion*, 49(2):025004, February 2009.

[13] A. Ince-Cushman, J. E. Rice, M. Bitter, M. L. Reinke, K. W. Hill, M. F. Gu, E. Eikenberry, Ch Broennimann, S. Scott, Y. Podpaly, S. G. Lee, and E. S. Marmar. Spatially resolved high resolution x-ray spectroscopy for magnetically confined fusion plasmas (invited)a). *Review of Scientific Instruments*, 79(10):10E302, October 2008.

[14] I. O. Bespamyatnov, W. L. Rowan, and K. T. Liao. ALCBEAM - Neutral beam formation and propagation code for beam-based plasma diagnostics. *Computer Physics Communications*, 183(3):669–676, March 2012.

[15] M. F. M. De Bock, N. J. Conway, M. J. Walsh, P. G. Carolan, and N. C. Hawkes. Ab initio modeling of the motional stark effect on MAST. *Review of Scientific Instruments*, 79(10):10F524, 2008. Printed.

[16] N. J. Conway, M. F. M. De Bock, C. A. Michael, M. J. Walsh, P. G. Carolan, N. C. Hawkes, E. Rachlew, J. F. G. McCone, S. Shibaev, and G. Wearing. The MAST motional Stark effect diagnostic. *Review of Scientific Instruments*, 81(10):10D738–10D738–6, October 2010.

[17] Paul Geelen. *Simulation of the Motional Stark Eeffect on C-MOD using MSESIM and PERF*. Internship report, Eindhoven University of Technology, 2013.

[18] M. J. Lanctot, C. T. Holcomb, S. L. Allen, M. E. Fenstermacher, and T. C. Luce. Pedestal magnetic field measurements using a motional Stark effect polarimeter. *Review of Scientific Instruments*, 83(10):10E319–10E319–3, July 2012.

[19] Faraday effect in optical glasses. The wavelength dependence of the Verdet constant. *Schott Glaswerke*, (No. 17), 1985.

[20] Gerhard Westenberger, Hans J. Hoffmann, Werner W. Jochs, and Gudrun Przybilla. Verdet constant and its dispersion in optical glasses. volume 1535, pages 113–120, 1991.

[21] J. Ko. *Current profile measurements using Motional Stark Effect on Alcator C-Mod*. PhD, Massachusetts Institute of Technology, 2009.

[22] J. N. Brooks and J. P. Allain. Particle deposition and optical response of ITER motional stark effect diagnostic first mirrors. *Nuclear Fusion*, 48(4):045003, April 2008.

[23] Lan Sun and Samad Edlou. Low-birefringence lens design for polarization sensitive optical systems. volume 6289, pages 62890H–62890H–9, 2006.

[24] M. Kuldkepp, E. Rachlew, N. C. Hawkes, and B. Schunke. First mirror contamination studies for polarimetry motional stark effect measurements for ITER. *Review of Scientific Instruments*, 75(10):3446–3448, October 2004.

[25] G. R. Boyer, B. F. Lamouroux, and B. S. Prade. Automatic measurement of the Stokes vector of light. *Applied Optics*, 18(8):1217–1219, April 1979.

[26] J. Badoz, M. P. Silverman, and J. C. Canit. Wave propagation through a medium with static and dynamic birefringence: theory of the photoelastic modulator. *Journal of the Optical Society of America A*, 7(4):672–682, April 1990.

[27] Baoliang B. Wang. Stokes polarimeter using two photoelastic modulators. In *Proceedings of SPIE*, pages 1–8, Seattle, WA, USA, 2002.

[28] Baoliang Wang. A polarimeter using two photoelastic modulators. In *Proceedings of SPIE*, pages 367–374, Denver, CO, USA, 2004.

[29] Mattias Kuldkepp, Nick C. Hawkes, Elisabeth Rachlew, and Beatrix Schunke. Accurate polarization measurements with a dual photoelastic modulator. *Applied Optics*, 44(28):5899–5904, October 2005.

[30] Wei Guan, Grenville A. Jones, Yanwei Liu, and Tiehan H. Shen. The measurement of the Stokes parameters: A generalized methodology using a dual photoelastic modulator system. *Journal of Applied Physics*, 103(4):043104, 2008.

[31] Wei Guan, Paul J. Cook, Grenville A. Jones, and Tiehan H. Shen. Experimental determination of the Stokes parameters using a dual photoelastic modulator system. *Applied Optics*, 49(14):2644–2652, May 2010.

[32] F. A. Modine, Jr. Jellison, and G. R. Gruzalski. Errors in ellipsometry measurements made with a photoelastic modulator. *Journal of the Optical Society of America*, 73(7):892–900, July 1983.

[33] Baoliang Wang. Basic optical properties of the photoelastic modulator: Part I. Useful aperture and acceptance angle. In *Proceedings of SPIE*, pages 58881I–58881I–8, San Diego, CA, USA, 2005.

4

IN-SITU CALIBRATION OF THE DIAGNOSTIC

Chapter goals:

- Investigate stress-induced birefringence—a significant source of changing systematic error found in the C-MOD MSE system—and the role of ray-dependent effects
- Discuss the implementation of an in-situ calibration system that can calibrate the diagnostic response throughout the campaign
- Discuss the thermal stabilization applied to the diagnostic to stabilize the diagnostic response

The previous chapter explored the different sources of systematic error—many of which are unique to polarization—that can occur in an MSE-LP diagnostic. Investigations on C-MOD showed that most of these errors are small in magnitude and can be accurately accounted for during calibration of the diagnostic.

However, some of these errors can change if the diagnostic condition changes. Previous work on C-MOD showed that the diagnostic response drifts substantially between plasma discharges with changes of up to 2° in polarization angle [1]. After significant investigation, this change was attributed to thermal stress-induced birefringence in the internal periscope. In addition to this time-dependent diagnostic response change, recent studies have highlighted the diagnostic response changes due to erosion and deposition on plasma-facing mirrors in future devices [2]. The revelation that the MSE-LP diagnostic response can and does change as a function of time in C-MOD and that future devices will also have a changing diagnostic response led to the development of calibration strategies that can account for these changes.

4.1 CALIBRATION STRATEGY

There are currently two main approaches used to calibrate the diagnostic response, but these have problems accounting for a changing diagnostic response.

4.1.1 *Use the beam to calibrate the diagnostic*

In many tokamaks, the MSE calibration is determined by using a beam-into-gas technique in which the neutral beam is fired into a gas-filled torus with the tokamak magnet system energized [3]. The

calibration, relating measured PEM signals to the applied vacuum magnetic fields, is developed using different fields in successive discharges or magnetic field ramps within a discharge. The main advantage of this technique is that the diagnostic is calibrated in a situation very similar to the operational conditions during plasma experiments, although the beam spectra has been shown to differ significantly [4].

Unfortunately, the prompt polarized emission from the beam is partially polluted by emission from secondary beam neutrals. These neutrals ionize, then gyrate about the local magnetic field—changing their local velocity direction—and then charge exchange and emit a photon before leaving the viewing volume [5]. This emission systematically biases the net collected polarization during a beam-into-gas discharge. The effect is strongest in tokamaks with near radial beam injection, such as ALCATOR C-MOD, and increases as the torus gas pressure is increased.

Other neutral beam-based techniques have been developed in which the magnetic pitch angle at the edge of the plasma is used to calibrate the MSE sightlines. This is done for sightlines near the edge of the plasma using the known plasma current and data from external magnetic diagnostics. The input polarization angle is scanned at multiple sightlines either through plasma position jogs [6–8] or by ramping the plasma current at various plasma sizes [1].

These beam-based calibration techniques capture the full diagnostic response—often providing a mapping directly from magnetic pitch angle to measured signals. If the diagnostic response was stationary in time, then only a a handful of calibration discharges may be required. A diagnostic with a slowly drifting diagnostic response would require these calibration discharges to occur multiple times during the actual campaign with the frequency dependent on the timescale of the diagnostic changes. If the diagnostic response changes on the between shot timescale, the calibration must be within the discharge itself, placing severe constraints on discharge planning and operations. This has been the case on C-MOD for the last several campaigns [9].

Unfortunately, beam-based techniques require significant dedicated tokamak plasma operation time to establish a calibration database. Even then, the result is a very limited set of calibration data, perhaps only a few polarization angles, usually with larger uncertainties than desired for verifying diagnostic operation or to characterize systematic errors and sensitivities in the diagnostic.

4.1.2 *Invessel robotic calibration system*

To overcome some of these limitations some tokamaks have augmented beam-based calibrations with invessel calibrations. In this strategy, a linear polarizer is placed in front of the objective lens or at the view-

ing volume location to illuminate the diagnostic objective lens with light with a known polarization angle during maintenance periods. Different angles are produced to determine the relationship between the measured signals and the input polarization. This can be done with fixed polarizers or with calibration sources with rotating polarizers. Historically, such a calibration technique has been used as the primary calibration for the C-MOD MSE diagnostic since beam-into-gas calibration is not viable. Similar techniques have been implemented on the DIII-D [10] and JET [11, 12] tokamaks.

Once it was determined that there were many potential systematic errors in MSE-LP diagnostics and that the diagnostic response could change from invessel calibration conditions to operational conditions it became important to understand the nature of these changes in order to eliminate them. An invessel robotic calibration system was designed and constructed to explore these potential systematic errors on C-MOD in addition to obtaining high-quality calibrations of the diagnostic response. The details of this instrument's construction and operation can be found in Reference [13]. This instrument can calibrate the diagnostic response to 0.05° using a uniform illumination source or a laser ray trace mounted at the beam line. The system is automated to provide rapid calibration of the diagnostic and controls various other diagnostic subsystems.

In theory, the polarization can be accounted for using the Mueller matrix formulation for polarized light. Results have been discussed for a single non-ideal mirror [10, 11]. However, the inclusion of three mirrors, many lenses, and a non-ideal polarimeter (e.g. slightly misaligned PEM or linear polarizer, or unequal PEM retardances) presents a highly non-linear system with a large number of required parameters. It is unlikely the accuracy required for the calibration can be reliably achieved using a Mueller formalism with a-priori optical properties and geometry for a system this complex and with significant ray-dependence. Therefore an empirical technique is used to fit the calibration coefficients as discussed in Reference [13].

Using the invessel robotic calibration system, it has been shown that the MSE diagnostic polarization response drifts by $< 0.05^\circ$ over 48 hrs during tokamak maintenance periods when the tokamak is at atmospheric pressure and temperature. The high accuracy and flexibility of the system enabled a large study of the details of MSE-LP diagnostic operation. This included tests for various types of systematic errors in the diagnostic and the evaluation of methods to minimize potential impacts from these errors. The major problem with the invessel calibration strategy is the fact that the diagnostic must be calibrated in air, without fields, at room temperature, without plasma, but is then operated under vacuum, with fields, exposed to plasma, and at operational temperature. Any change in the diagnostic

Table 6: Comparison of calibration sources.

Properties	invessel robot	inter-shot calibration (ISC)	beam-into-plasma
Operates in air	only	yes	no
Operates in vacuum	no	yes	only
Operates with fields	no	yes	only
Operates with plasma	no	yes	only
Number of angles	many	4	limited
Accuracy of angles	$< 0.05°$	$< 0.05°$	$\sim 0.3°$
Range of angles	360°	100°	$1 - 10°$
Illumination	full field or ray	full field	full field
Angle uniformity	$\pm 0.05°$	$\pm < 1°$	NA

response between these conditions goes uncharacterized—becoming a systematic error that will skew magnetic reconstruction results.

4.1.3 *3 techniques: A complementary calibration strategy*

An approach was devised to bridge the gap between highly accurate and flexible invessel robotic calibration during maintenance periods and sparse calibration using beam-into-gas or beam-into-plasma discharges during normal operation. This approach involved installing an in-situ calibration system to calibrate the diagnostic during and between discharges. This system is able to fill the diagnostic objective lens with linearly polarized light at any desired time, from operation in air to operation with plasma. The system can then be used to monitor changes to the diagnostic response with greater flexibility and accuracy than using plasma discharges.

This strategy thus provides three calibration techniques to determine and monitor the diagnostic response. These are shown schematically in Figure 25: the very accurate invessel robotic calibration system; the very flexible in-situ calibration system; and observing the beam directly in sparse beam-into-plasma calibration discharges. Table 6 compares the capabilities of the three different sources. Using the in-situ system, the diagnostic response can be continuously determined between the time of the invessel robotic calibration, to the actual operation of the diagnostic during physics experiments, to the next invessel robotic calibration.

4.2 THE INTER-SHOT CALIBRATION (ISC) SYSTEM

The system consists of a calibration carousel containing four different wire grid polarizers (WGPS) which rotates around the turret portion of the MSE periscope on precision bushings. The system accurately me-

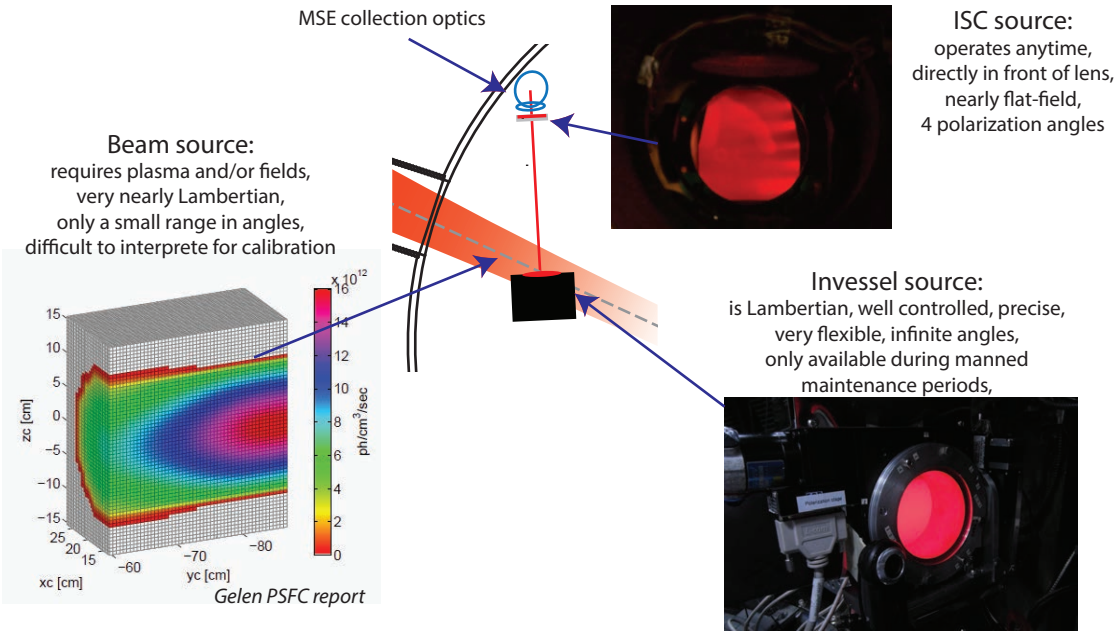

Figure 25: An in-situ calibration system was installed to bridge the gap between the very flexible and high-accuracy invessel robotic calibration robot and actual tokamak operation observing the neutral beam. The in-situ system has the flexibility to operate at any time under any condition and has adequate accuracy and polarization granularity to provide a comprehensive snapshot of the diagnostic response.

chanically aligns the different polarizers in front of the objective lens. Each polarizer is nearly the size of the objective lens and is illuminated using a backlight scatterer technique similar to a LCD monitor. Light from remote LEDs is transmitted to the backlight scatterer via a fiber optic system and a ferrule affixed to the turret. The carousel is rotated via a cable-in-conduit system using linear motors acting on linear vacuum push-pull feedthrus. A computer controls the actuation using an optical feedback system on the ferrule. The entire system can be operated within 2s of the plasma discharge and can input the four different polarization angles within 10s of the plasma discharge. The detailed construction and operation of the system is described in Reference [13]. Figure 26 shows a schematic of the ISC and photographs of the system in the open position viewing the plasma, and in a calibration position.

The system is actuated immediately after every discharge. It cycles through the four different calibration positions, pausing $\sim$ 0.5s at each position to make the measurement before moving to the next position. The signals from the MSE detectors, $-\frac{1}{2}\tan^{-1}\left(\frac{I_{2\omega 1}}{I_{2\omega 2}}\right)$, are averaged across this time period, producing statistical uncertainties due to photon statistics of $< 0.05°$. The four angles are measured over a period of ten seconds at the end of the plasma discharge. This provides the calibration of all ten MSE sightlines simultaneously. The data acquisition cycles allows these measurements to be repeated every two minutes. Alternatively, the ISC system can remain in a fixed

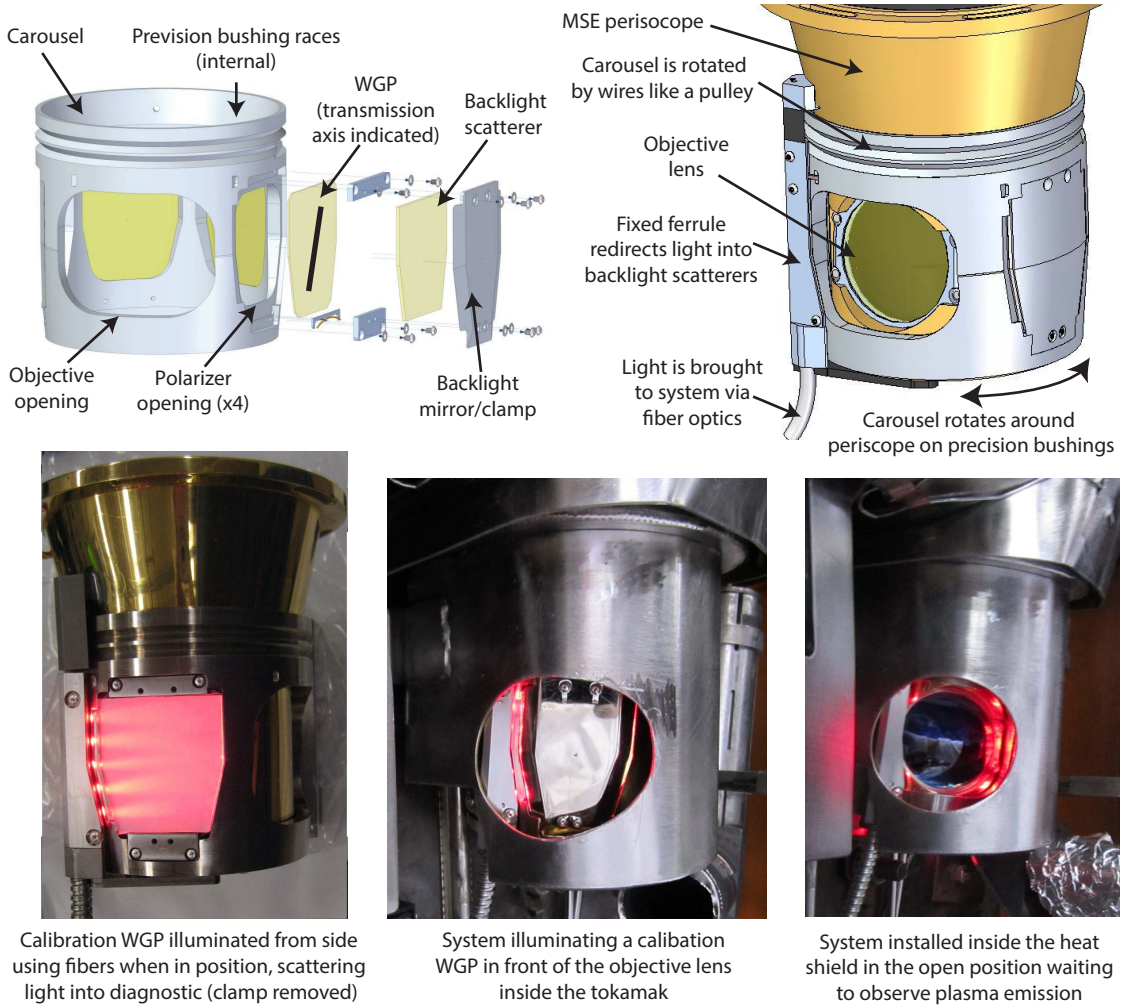

Figure 26: An overview of carousel-based ISC system. A carousel and a fiber-optic based illumination system are mounted on the MSE turret portion of the invessel periscope. Four different wire grid polarizers (WGP) are accurately mounted in the carousel with specific polarization axes. Each WGP is backed by a backlight scatterer. The carousel rotates about the MSE periscope on precision bushings, actuated by a cable-in-conduit system. Each WGP is illuminated by a fiber-optic and prism system when it is in front of the objective lens (bottom left, note the backlight scatterer clamp has been removed to show the effect of the scattering). The system installed in the vessel in one of the four calibration positions with the illumination system activated (bottom middle). The system in the open position, allowing the objective lens to view the plasma (lower right).

calibration position and repeated digitizer cycles can be taken approximately once a minute. The ISC is used to monitor the diagnostic throughout the campaign by obtaining data once every half an hour.

The diagnostic response is determined from three ISC of the calibration angles which span the range of polarization angles usually observed by the plasma. The angle calculated from amplitude of the detected PEM second harmonics, $-\frac{1}{2}\tan^{-1}\left(\frac{I_{2\omega 1}}{I_{2\omega 2}}\right)$, when observing the ISC and the known calibration polarization angles from the ISC, $\theta_{pol}^{WGP\,X}$ are used to interpolate the value of $-\frac{1}{2}\tan^{-1}\left(\frac{I_{2\omega 1}}{I_{2\omega 2}}\right)$ from plasma observation into a polarization angle. Likewise, the change in $-\frac{1}{2}\tan^{-1}\left(\frac{I_{2\omega 1}}{I_{2\omega 2}}\right)$ can also be monitored relative to its starting value at the beginning of the campaign to determine changes in diagnostic response; this is referred to as a change in angle throughout the rest of this chapter. The fourth polarization angle, nearly orthogonal to the other three, allows the character of the diagnostic response change to be determined as discussed in Reference [13] by utilizing the fact that polarization aberrations are π and $\pi/2$ modulo in input angle and retardance creates changes in DOCP that are modulo π.

The repeatability of the ISC system is very important to the calibration strategy. The entire technique relies on the ISC system's ability to repeatedly input the same polarization into the diagnostic despite changes to the diagnostic environment. To test its repeatability, the ISC system is cycled repeatedly during quiescent environmental conditions when nothing is expected to be changing. The standard deviation of these measured angles are $< 0.05^\circ$ for all sightlines for all four WGP positions when actuated over $20-50$ cycles. The variability in the measured ISC angles is not significantly greater than the error in an individual measurement from photon statistics. The reproducibility is found to be better than the requirement irrespective of whether the tokamak is under vacuum or at atmospheric pressure. The ISC system has been cycled > 8000 cycles to date and shows no degradation of its reproducibility. This data indicates that the ISC system is extremely reproducible, always inputting the same polarization into the diagnostic.

This system, combined with the very flexible invessel robotic calibration system, allows a variety of systematic errors to be studied both during maintenance periods and during experimental rundays. This is the first system fielded on a tokamak to calibrate an MSE-LP diagnostic in-situ. It is projected that future tokamaks will require in-situ calibration because the harsh environment precludes traditional invessel calibration, because operational constraints restrict the use of calibration discharges, and because the time-varying diagnostic response will require characterization. Though the exact architecture of the system used on C-MOD cannot be applied to burning plasmas, it

is expected that lessons learned from this system will inform future designs.

The ISC system was installed for the FY12 experimental campaign. It was routinely operated during this campaign, though it was determined that illumination source was far from uniform due to errors during installation. The ISC was then upgraded for the FY14 campaign with uniform illumination sources.

4.3 THERMAL STRESS-INDUCED BIREFRINGENCE ON C-MOD

The only significant changing systematic error found in the C-MOD MSE diagnostic is due to birefringence in the various lenses and the vacuum window. The importance of birefringence was identified in previous work by Ko [1] as the cause of diagnostic response changes on the order of several degrees throughout experimental run day, though this work concluded the problem was significant only in a single lens.

Stress in glass creates birefringence, introducing retardance into the system:

$$\Delta = \mathcal{K}(\sigma_1 - \sigma_2)\frac{d}{\lambda} \tag{40}$$

where $\mathcal{K}$ is the stress-optic coefficient (also known as the photoelastic constant) of the glass, σ_1 and σ_2 are the principle stresses in the material, d is the path length through the material, and λ is the wavelength of the light. The fast axis of the birefringent material is along the σ_1 direction for materials with a positive stress-optic coefficient and along the σ_2 direction for materials with a negative stress-optic coefficient. On C-MOD, the lenses and vacuum window are composed of SFL6 which has a stress-optic coefficient of $\sim 0.7\text{x}10^{-6}\text{MPa}^{-1}$ (taken as SF6 a similar glass) compared to $\sim 2.8\text{x}10^{-6}\text{MPa}^{-1}$ for BK7 and ~ 0 for low-stress-coefficient glass SF57 [14].

Stress in the lenses can increase greatly due to thermal gradients in the materials. These gradients create differential thermal expansion within the lens itself, creating stress at various points in the element. This can even occur in an unmounted lens. The temperature gradients can arise from external steady-state gradients imposed on the optical element via conduction or from a spatially uniform, but time-varying temperature environment in which the temperature gradients occur due to the finite thermal capacitance and thermal conduction in the element.

4.3.1 *Tests for stress-induced birefringence*

Extensive thermal tests were conducted both invessel and on the bench during previous work on the MSE system. These tests con-

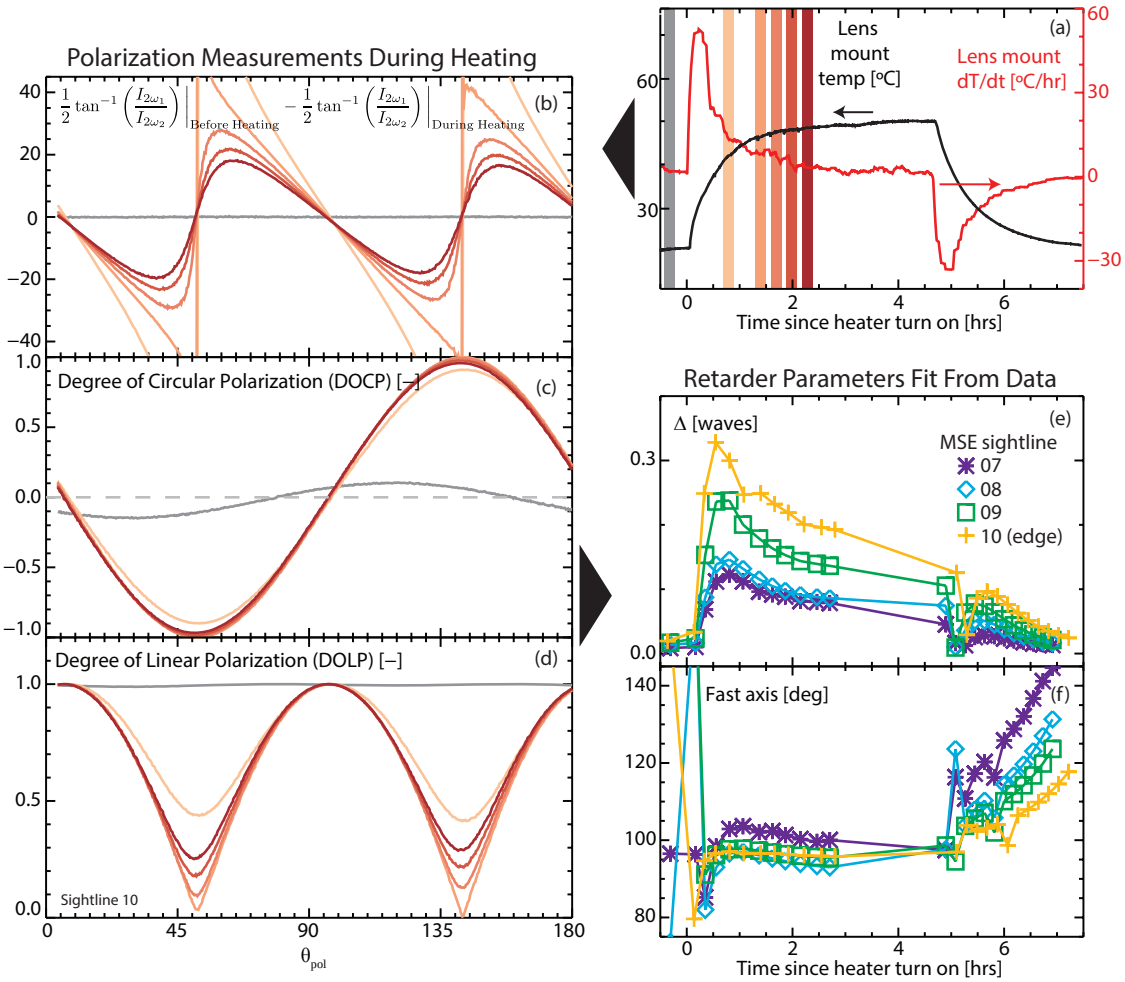

Figure 27: The L2 lens doublet was strongly heated (a) while the polarization aberrations in the periscope were monitored using the invessel robotic calibration system. The change in polarization angle (b), DOCP (c), and DOLP (d) are indicative of rapidly changing retardance in the system. The measured change in angle and DOCP can be used to constrain a fit of the amount of retardance (e) and the fast axis of the retarder (f) as a function of time and sightline.

cluded that the L2 lens doublet was the main element susceptible to thermal stress-induced birefringence. The tests parameterized the observed changes in polarization angle as a function of temperature gradient and temperature slew rates at that lens position [1].

The topic was revisited after it was determined that thermal-stress induced birefringence was the primary systematic error in the MSE diagnostic and after previous efforts to stabilize the thermal environment of the suspected problematic lens failed to eliminate the time-varying birefringence. Various parts of the optical system were repeatedly heated and cooled using hot air blowers while the system performance was monitored with the the robotic calibration and the ISC systems.

Figure 27 shows the results of an experiment in which the L2 lens doublet was strongly heated and then allowed to cool while the in-

vessel system completes a full cycle of polarization angles every ~ 12 minutes. The change in the measured polarization angle (a) follows the pattern calculated in the analytic calculation (Figure 17) as does the DOCP (b) and DOLP (c). It is very clear that substantial amounts of retardance occurs in the lens—it becomes a quarter-waveplate at one point early in the heating when the temperature slew rate of the lens peaks (a, red). The change in polarization has a strong dependence on the sightline, with sightlines at the edge of the field of view experiencing the largest retardance while sightlines near the optical axis experience much less retardance.

The change in polarization angle and DOCP can be fit to determine the amount of retardance (e) and the fast axis of the retarder (f) as a function of time for the four sightlines monitored with the invessel calibration robot. It is clear the amount of retardance correlates with the temperature slew rate of the lens. The fast axis reaches a new orientation when the heating starts and then rotates to a different angle when the heating ceases. The amount of retardance is different at each sightline but the fast axis orientation is similar for all four sightlines. The ISC is also used to monitor changes in DOCP as shown in Reference [13].

It was generally found across many tests that the birefringence in the optics was not repeatable under similar heating conditions. This is likely due to changes in the stress state of the lens leading to changes in the amount of birefringence and the orientation of its fast axis. All heated optics showed changes due to birefringence. This experiment had a ~ 30× larger slew rate and a ~ 10× larger temperature difference across the lens than is typically observed during plasma operation with the upgraded thermal management system (to be discussed in a later section). Thus thermal-stress induced birefringence in this lens doublet is not believed to be a significant contribution to a changing diagnostic response during operation.

Fortunately, because it is due to thermal conduction in the lenses, birefringence changes on a relatively slow timescale compared to the length of plasma discharges. Figure 28 shows birefringence changes due to heating of the vacuum window, creating substantial thermal gradients. The maximum rate of change of the polarization angle is only $0.003^{\circ}/s$. Birefringence therefore cannot cause significant changes within a plasma discharge or in the ten seconds between the plasma discharge and the ISC calibration.

In practice, the ISC data is used to determine the diagnostic response using interpolation. However, if retardance is the only changing systematic error it may be possible to use a model fit to the the ISC measurements. There are eight measurements; four measurements each of change in angle and DOCP, and only two free parameters in the model, Δ and $\psi_{\text{fast axis}}$. This may provide a better parameterization

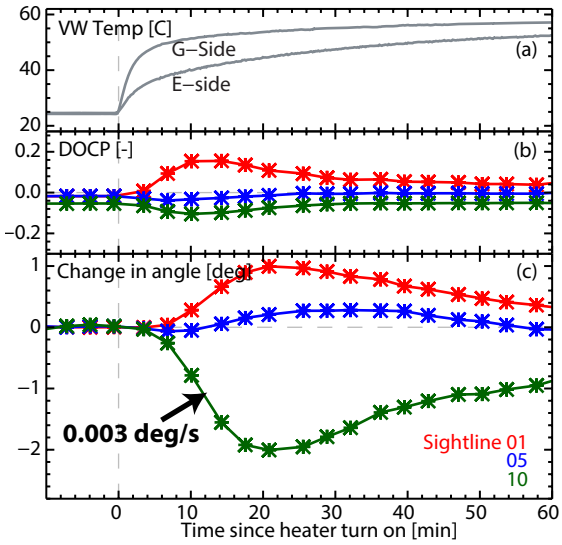

Figure 28: The timescale for changes due to birefringence. The vacuum window was strongly heated (a) leading to changes in DOCP and polarization angle (c). The fastest angle change observed in bench tests occurred at a rate of only $0.003^{\circ}/s$.

of the diagnostic response than simple angle interpolation. However, this would only be important in cases with significant birefringence.

4.3.2 *Ray-dependent effects*

The C-MOD MSE optical system has ten transmissive elements placed prior to the PEMS, each of which can cause polarization changes due to thermal stress-induced birefringence. The configuration of the optics, their composition and representative ray-tracing through them are shown in Figure 29. The optical path through the diagnostic is such that each element is illuminated with a different pattern.At some elements (i.e., L2 and L4) these rays strike the lens all at the same place but with different angles, i.e., the rays are focused. At other elements the rays strike the elements at many points, the rays are defocused (i.e., L1, M3, L3, and L5).

Because each sightline has a different path through the optical system, the character of the polarization change can vary as a function of MSE sightline. The L2 lens doublet was heated as in the previous experiments while the invessel robotic calibration system was quickly translated from one MSE sightline to another to quantify this effect. At each sightline position, the Lambertian light source illuminated the MSE diagnostic with linearly polarized light having a single, known polarization angle close to that observed during plasma operation. An analogous experiment was conducted by blowing heated air on the flange containing the vacuum window, causing temperature variation across the vacuum window in the same manner as across the L2 lens.

One reason the vacuum window and L2 lens doublet were specifically chosen for these heating experiments is the spatial character of the rays incident on them. As shown in the center of Figure 30,

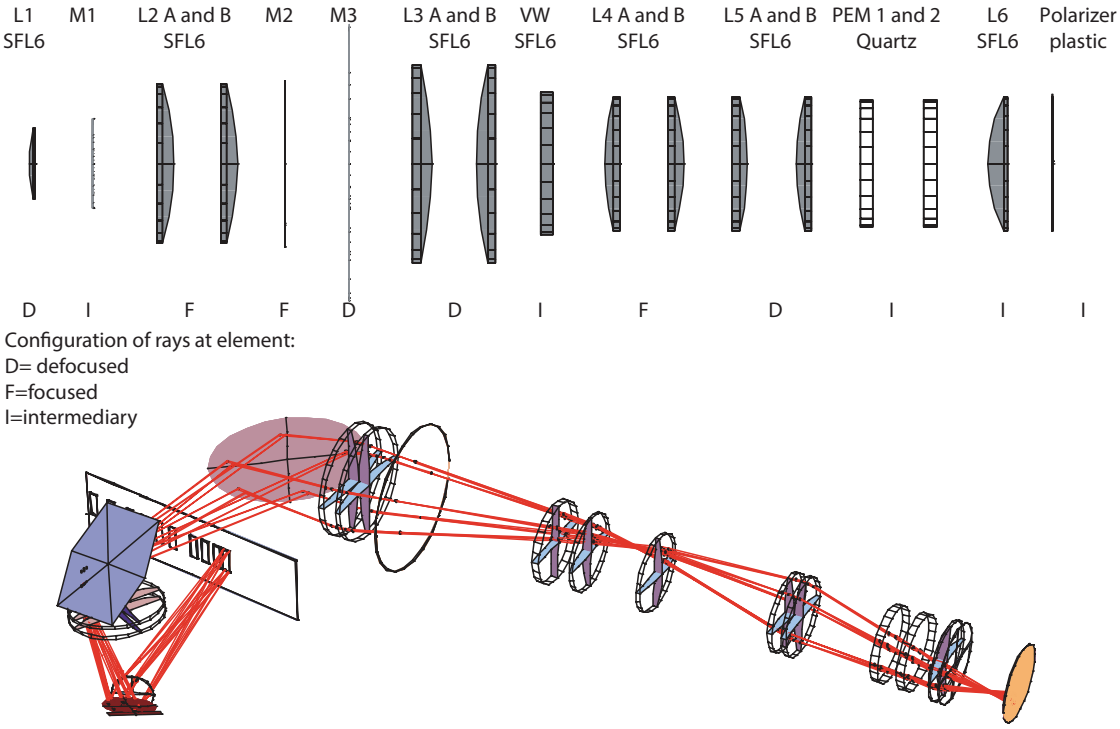

Figure 29: The configuration of the optics inside the MSE periscope along with their material composition (top). The configuration of the rays within a sightline is noted as either focused (F), defocused (D), or intermediary (I). The rays from a single, edge-viewing, sightline traced through the optical system (bottom). Figure credit: Jinseok Ko.

rays for a given MSE sightline are nearly focused at L2, i.e. they all pass through the lens at nearly the same location. Each sightline thus densely samples a different part of the birefringent stress pattern on the L2 lens doublet. Conversely, the rays that make up a given MSE sightline are defocused at the vacuum window and sample a larger portion of the vacuum window surface. Rays from different sightlines are thus intermixed, i.e., they pass through largely overlapping parts of the vacuum window surface. These heating tests thus examined the sightline dependence while perturbing an optical element where the sightlines are focused versus an optical element where the sightlines are defocused.

The results of the experiment are shown in Figure 30 with heating the vacuum window shown on the left and heating the L2 lens doublet shown on the right. Note that the time-history of the changes in polarization angle and circular polarization fraction are similar to the time-history of temperature slew rate, consistent with the previously discussed experiment. The change in polarization angle and circular polarization fraction is larger when heating the vacuum window than when heating L2, possibly due to the larger temperature slew rate and larger overall temperature excursion. More importantly, there is a clear difference in character within the set of sightlines between the two experiments. When heating the vacuum window, all the sightlines show nearly the same qualitative and similar quantitative behavior. The angles increase $1° - 1.4°$ after the heater turns on, then slowly return to the starting angle. Conversely, when L2 is heated there is a significant variation in the behavior among the sightlines. Rather than all sightlines experiencing a similar change in angle, the angle changes range from $-0.5°$ to $+0.3°$. The edge-viewing sightlines (09 and 10, pink and brown) decrease in angle early in time and then abruptly increase, while the core-viewing sightlines (01 and 02, red and blue) are always more negative, and the sightline near the optical axis (05, green) shows very little change. The change in DOCP also shows variation among the sightlines when heating L2—some of the sightlines have a DOCP that is oppositely directed to the other sightlines early in the heating. However, the DOCP in all sightlines behave similarly when heating the vacuum window.

To further explore the effect of stress-birefringence on measured polarization angles, another heating experiment was conducted in which the laser light source on the polarization generation head was used to simulate multiple individual rays within a single MSE sightline. The experiment was conducted at sightline 03 using linearly polarized light with fixed polarization angle. The robotic calibration system positioned the laser at a fixed MSE viewing volume along the beam trajectory and simulated eight optical rays by pointing the laser at different points on the MSE objective lense while the periscope near

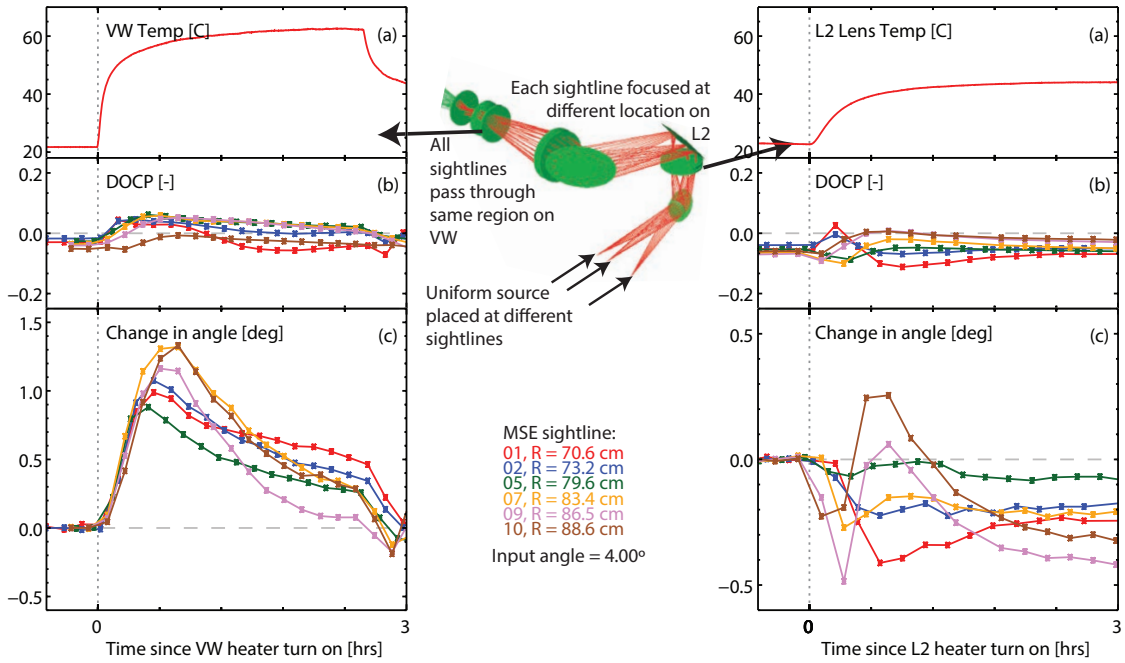

Figure 30: The sightline dependence of the birefringence when heating the vacuum window (VW, left) and when heating the L2 lens doublet (right). The temperature of the element (a), the DOCP (b), and the change in polarization angle referenced from prior to heating (c). Data from different sightlines are shown.

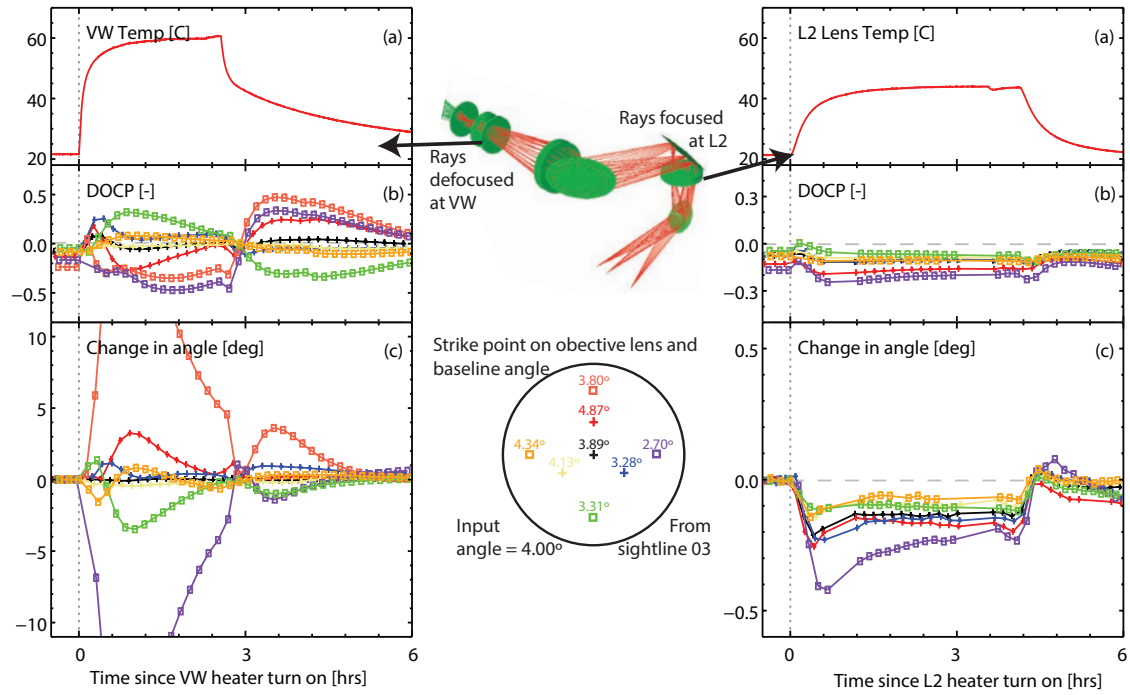

Figure 31: The ray dependence of the birefringence when heating the vacuum window (VW, left) and the L2 lens doublet (right). The temperature of the element (a), the DOCP of the individual rays (b), and the change in polarization angle from prior to the heating (c). Note the difference in scales between the VW and L2 change in angle. The strike-point of the laser on the objective lens is shown in the lower middle along with the starting polarization angle at each strikepoint location.

L2 was heated. A similar experiment was conducted while the flange containing the vacuum window was heated.

In these tests, the rays from a given sightline all sample nearly the same region of L2, but each ray samples different regions of the vacuum window. The results of the experiment are shown in Figure 31 with heating the vacuum window shown on the left and heating the L2 lens doublet shown on the right. The location of the ray when striking the objective lens is shown in the lower center with its measured polarization angle prior to heating.

The results show a very significant difference between heating the L2 doublet and the vacuum window for the group of rays. When the L2 doublet is heated all the rays experience a qualitatively similar change in angle and circular polarization fraction. The polarization angle becomes more negative after the heater turn on, stabilizes at a new value, and then experiences an abrupt change after the heater turn off. The magnitude of the change is $< 0.5°$. The previous experiment caused a polarization angle change of $-0.3°$ on this sightline due to nearly identical heating of L2 when calibrating with the Lambertian source. The results are very different when the vacuum window is heated; there is substantial qualitative and quantitative variation among the rays. Some rays experience a polarization angle change up to $\pm 15°$ while the central ray (black pluses) experiences a change of $< 0.5°$. In this experiment, rays that strike the outer portion of the aperture (square symbols) experience a larger change in polarization angle than rays that strike near the center of the aperture. Rays that strike the lower portion of the lens experience a negative change in polarization angle while rays that strike the high portion of the aperture experience a positive change. There is likewise a very large variation in the DOCP among the rays at the vacuum window, ranging from -0.4 to $+0.4$.

When heating the vacuum window, the variation within the set of rays is very large—$150\times$ larger than the desired measurement accuracy. The previous experiment using the uniform light source measured a polarization angle change of only $+1.0°$ on this sightline under nearly identical heating of the vacuum window. It is apparent that the rays at the vacuum window experience a significantly different polarization aberration depending on where they strike the vacuum window, and that the average polarization aberration for the entire sightline is a weighted average of all the individual rays. Due to the Stokes vector nature of the average, the large variations can average to fairly small changes in angle and DOCP of there are symmetries in the polarization changes.

The principle stresses in the lens are dependent not only on the local temperature gradient but on the temperature distribution across the entire lens as it deforms as a free body. Furthermore, the lens temperature distribution has a complex dependence on the temperature

time history of the lens environment. Once the lens is birefringent, the associated change in the polarization angle is dependent on both the magnitude of the stress and the orientation of stress relative to the incident polarization angle. In the experiments described above, the temperature distribution in the lens and vacuum window are likely very complex and thus the resulting stress magnitude and orientation is also complex. The birefringence then changes the polarization angle of the light with a dependence not only on the magnitude of the stress but also on the relative difference between the principle stress direction and the polarization angle.

These polarized ray-tracing experiments show that individual rays experience a wide range of birefringence as they transit through the optical periscope. Where the rays within a sightline are nearly focused as they transit the optical element they all sample nearly the same stress magnitude and orientation and thus the rays have similar polarization aberration due to stress. The MSE sightlines are incident at different points on that optical element, sampling a different local stress orientation and magnitude. Each sightline therefore has a significantly different net polarization aberration due to the birefringence.

At optical elements at which the rays within a sightline are near an image of the aperture, the ensemble of rays strikes the element over a significant fraction of its surface. Each ray in the ensemble samples a different stress state and therefore has a different polarization aberration. However, the various *sightlines* have a very similar ray patterns on the element and therefore the polarization aberrations, when averaged over the ensemble of rays that comprise each sightline, will show little variation amongst the sightlines. The customary calibration procedures that illuminate the entire objective lens and viewing volume conceals the magnitude of this ray-dependent variation because they average the effect out.

There are some differences between this work and the prior work done by Ko [1] where the L2 lens doublet and L3 lens doublet were heated. The results from heating L2 are in agreement between this and the prior work. However, the results while heating the vacuum window here show changes of $\sim 1-3^\circ$ in polarization angle. The prior work showed only very modest polarization angle changes ($< 0.5^\circ$) from heating the L3 doublet which is defocused similar to the vacuum window. The argument put forward for the lack of a dependence on heating was that the polarization aberrations from birefringence "average out" due to a symmetric stress and illumination pattern. While polarization aberrations from birefringence can average out, it requires very symmetric patterns of illumination and stress. The prior work used a heating tape to heat the L3 lens uniformly around its periphery, likely creating a symmetric stress pattern. The current work used hot air blowers to heat the vacuum window, likely

imposing a non-symmetric stress pattern which is more likely to occur during actual operation. This difference in heating, and the fact that the light is more defocused at L3 compared to the vacuum window, may explain the apparent discrepancies. In operation, the stress pattern is unlikely to be symmetric, thus polarization angle changes averaging to zero is unlikely.

4.3.3 *Importance of* ISC *uniformity*

The ray-to-ray and sightline-sightline dependence of thermal stress-induced birefringence place stringent requirements on designs of systems that attempt to calibrate the effects of birefringence during operation. **For a calibration system to properly capture the diagnostic response for all sightlines and all the possible stress states, it must fill the diagnostic with light that is nearly identical to the illumination pattern from the beam—uniform in area and solid angle.** This is true for calibration sources placed at the viewing volume as well as calibration sources placed at the entrance pupil. Spatial non-uniformities in a calibration source placed across the field (i.e. at the viewing volume) will incorrectly average the complex birefringence in optical elements near focal points. Spatial non-uniformities in a calibration source placed at the pupil (i.e. the objective lens) will incorrectly average the complex birefringence in optical elements near defocused points. It is unlikely that a calibration strategy which only monitors a few rays or places calibration sources at the edge of the field of view will capture the correct weighted average over all the rays normally collected from the neutral beam.

Information from the ray-tracing experiments led to important upgrades to the ISC system. The first implementation of the ISC system was tested to determine how well it could track the changes in the diagnostic response. The optical periscope was heated to create stress-induced birefringence while the diagnostic observed the invessel robotic calibration robot and then the ISC system. Both of these systems illuminated the objective lens with approximately the same input polarization angles, allowing the diagnostic response inferred from each system to be compared as a function of time.

The tests showed that the ISC could track changes due to birefringence at the L2 lens doublet. However, the tests were repeated while heating the vacuum window. An example test is shown in Figure 32 which shows the temperature at the vacuum window (a). The ISC system did not properly track the changing DOCP (b) or change in polarization angle (c). Instead, the polarization angle measured by the ISC system showed opposite changes in polarization angle. The ISC system did not properly track any of the four polarization angles at any of the sightlines when the vacuum window is heated—The ISC system measured the wrong diagnostic response.

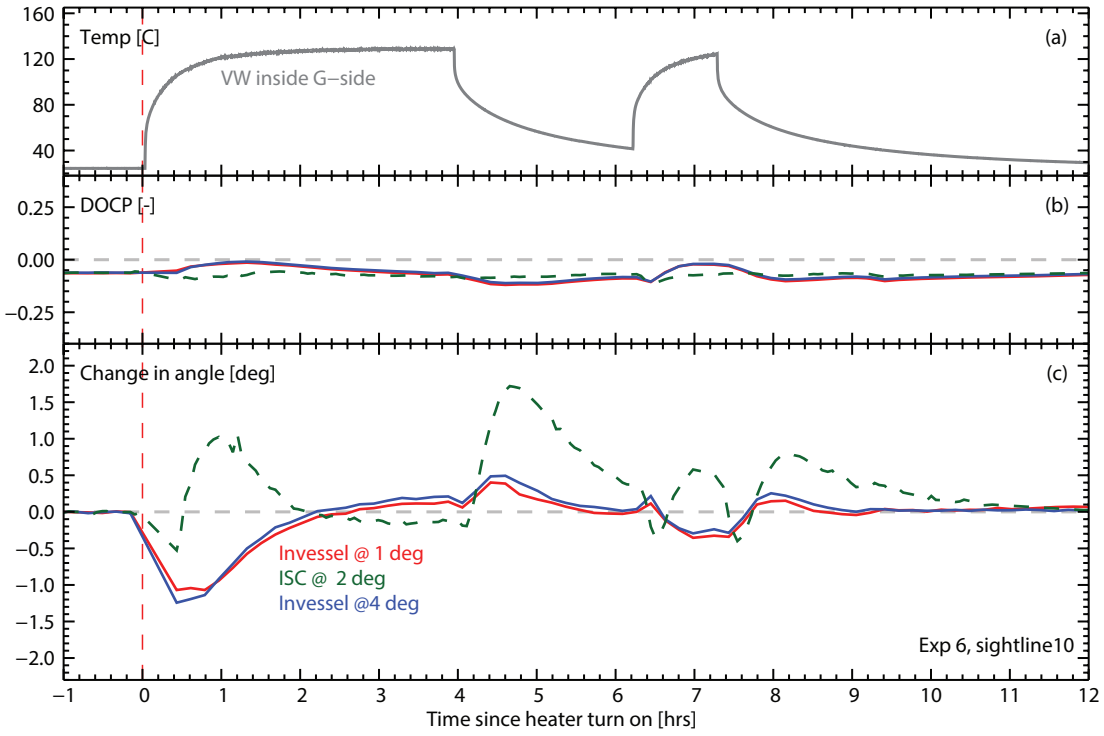

Figure 32: The ISC and invessel robotic calibration systems were used to simultaneously tracking changes in the diagnostic response due to heating of the vacuum window (a). The DOCP (b) and change in polarization angle (c) measured with the ISC and invessel robotic calibration system do not agree.

The original ISC illumination system was not uniform, the illumination pattern for each WGP is shown in Figure 33 (top). Note that each ISC position had areas of very bright illumination near where the fibers shine into the side of the backlight scatterers. The ISC system was therefore launching a different set of rays into the diagnostic than the invessel robotic calibration system which uses a uniform source. Because the ISC system inputs the light at objective lens, spatial non-uniformity leads to a non-uniformity in sampling the optical elements which are at defocused points in the optical train, such as the vacuum window. In effect, the ISC system was performing a different averaging across all the input rays.

The ISC illumination system was rebuilt prior to the FY14 campaign to eliminate this problem. Each of the ISC backlight scatterers was custom-tuned to achieve as uniform illumination as possible. The illumination pattern of the rebuilt illumination system is shown in Figure 33 (bottom). Table 7 lists the maximum brightness divided by the mean brightness and the standard deviation in the brightness divided by the mean brightness for each of the WGP positions prior to and after the rebuilding of the ISC illumination—the uniformity was improved by a factor of two to three.

The tests were repeated with the rebuilt, more uniform, ISC illumination system. The heating of the L2 lens mount is shown in Figure

Table 7: The uniformity of the ISC illumination prior to and after rebuilding the ISC illumination system.

Property	WGP A	WGP B	WGP C	WGP D
max/ave prior to rebuild	3.2	2.2	3.1	2.1
stdev/ave prior to rebuild	0.43	0.31	0.52	0.26
max/ave after rebuild	1.3	1.3	1.6	1.5
stdev/ave after rebuild	0.12	0.10	0.15	0.13

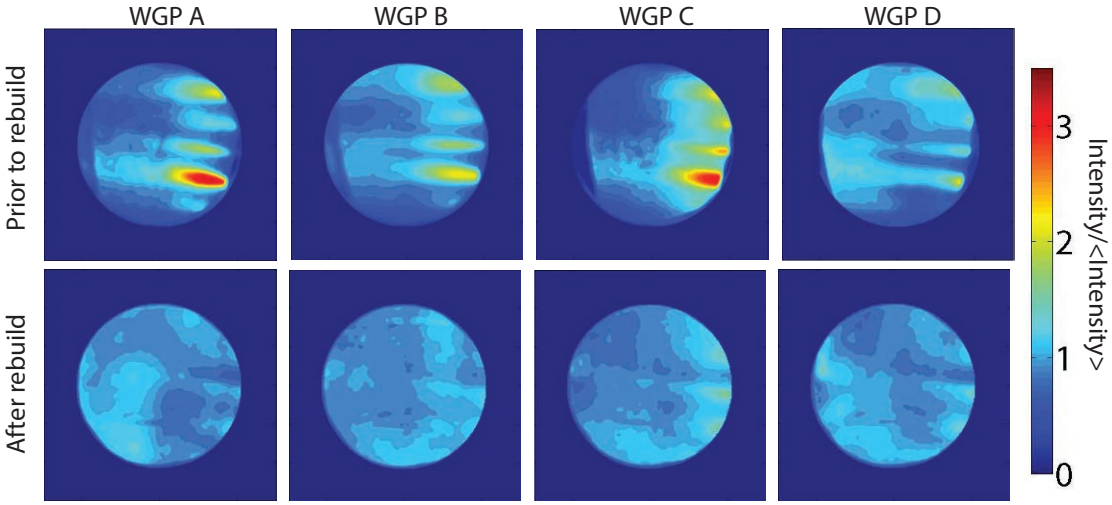

Figure 33: The ISC illumination pattern prior to (top) and after (bottom) the rebuilding of the ISC illumination system. The intensity is normalized to the mean intensity within the objective lens aperture for each case.

34. Again the ISC system tracks the proper response during the heating of this element. The heating of the vacuum window is shown in Figure 35. In this case the rebuilt ISC system tracks the DOCP and change in angle during the different heating phases. This agreement is at the $\sim 0.05°$ level. The ISC tracks the changes in all four polarization angles for all sightlines within $\sim 0.2°$.

These tests indicate that with the rebuilt, uniform illumination source, the ISC system properly captures changes in the diagnostic response due to birefringence at both elements in the optical system where a sightline is focused and defocused. It should be noted that these heating tests were much more severe than what is typically observed during diagnostic operation, particularly for the heating of the L2 lens mount. Therefore, one should expect the rebuilt ISC system to properly track changes in the diagnostic response at changes in polarization angle up to a few degrees.

4.3.4 *Observations of birefringence during operation*

The ISC system was used to observe changes in the diagnostic response during tokamak operation, confirming the presence of time-varying birefringence in the optics. An example from a single MSE sightline is shown in Figure 36. The ISC system was used to input three polarization angles (the fourth angle was not operating correctly) allowing the DOCP (d) and change in polarization angle (e) to be measured. All three ISC polarization measurements show similar changes in polarization angle as a function of time, with a magnitude of $< 1°$ change over the experimental run day. The two orthogonal angles (blue solid and dashed) show opposite changes in DOCP indicating that the changes in diagnostic response are due to birefringence. The changes in DOCP most closely follow the temperature difference across the vacuum window, indicating this element is a likely cause of the changes.

The ISC system can also be used to track large changes in the diagnostic response over long periods of time. Figure 37 shows an example where the the ISC system is used to measure the diagnostic response over the course of 36 hours. The invessel components experience relatively minor temperature changes (except for the heat shield) during the runday (a). However, the external components, particularly the vacuum window, experience large changes, decreasing in temperature by 75°C (b), and developing large temperature differences (c). The DOCP (d) and change in polarization angle (e) are large and variable during the runday with significant sightline dependence. The DOCP reaches almost 0.5 at some periods, indicating that the optics developed $\Delta > 0.07$ waves of retardance. During the overnight periods, when the machine is not being operated, the polarization an-

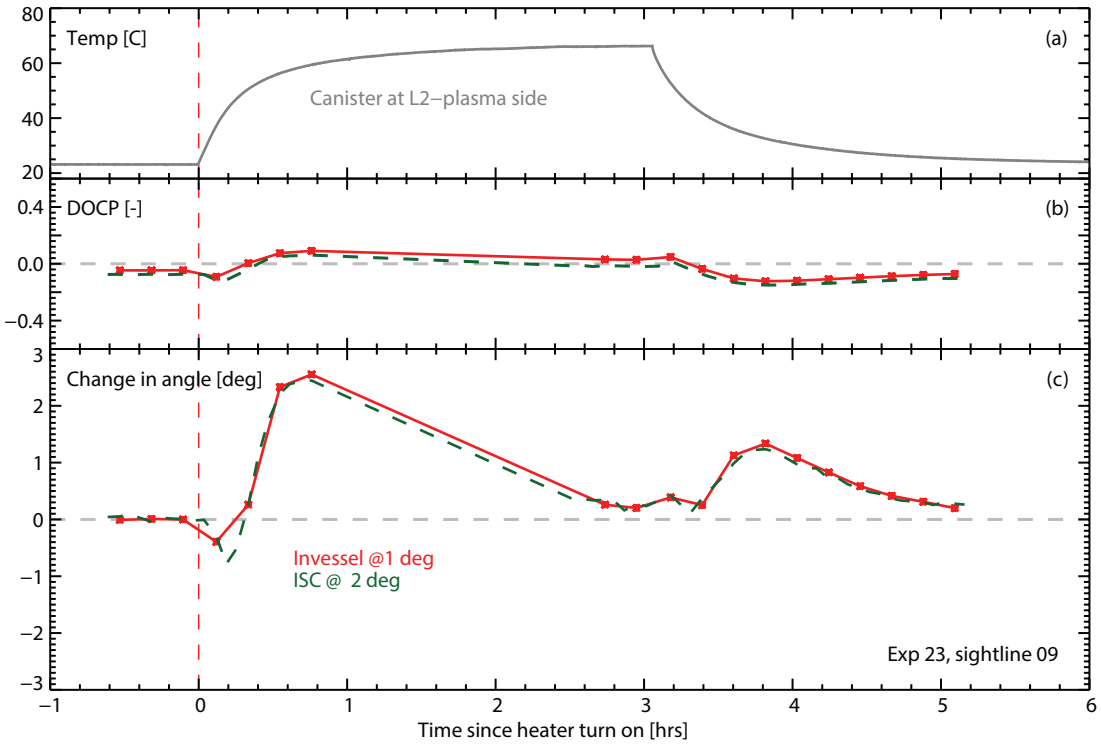

Figure 34: The ISC and invessel robotic calibration systems were used to simultaneously track changes in the diagnostic response due to heating of the L2 lens doublet (a) after the ISC illumination uniformity was corrected. The DOCP (b) and change in polarization angle (c) measured both systems agree.

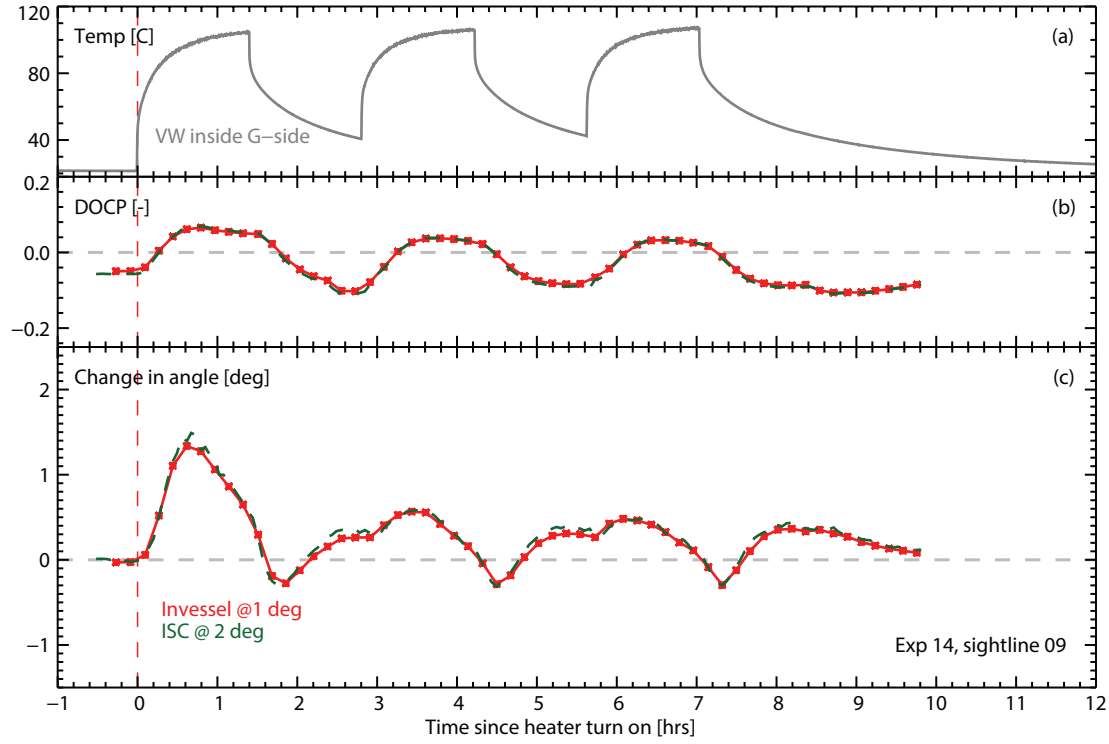

Figure 35: The ISC and invessel robotic calibration systems were used to simultaneously track changes in the diagnostic response due to heating of the vacuum window (a) after the ISC illumination uniformity was corrected. The DOCP (b) and change in polarization angle (c) measured with both systems agree.

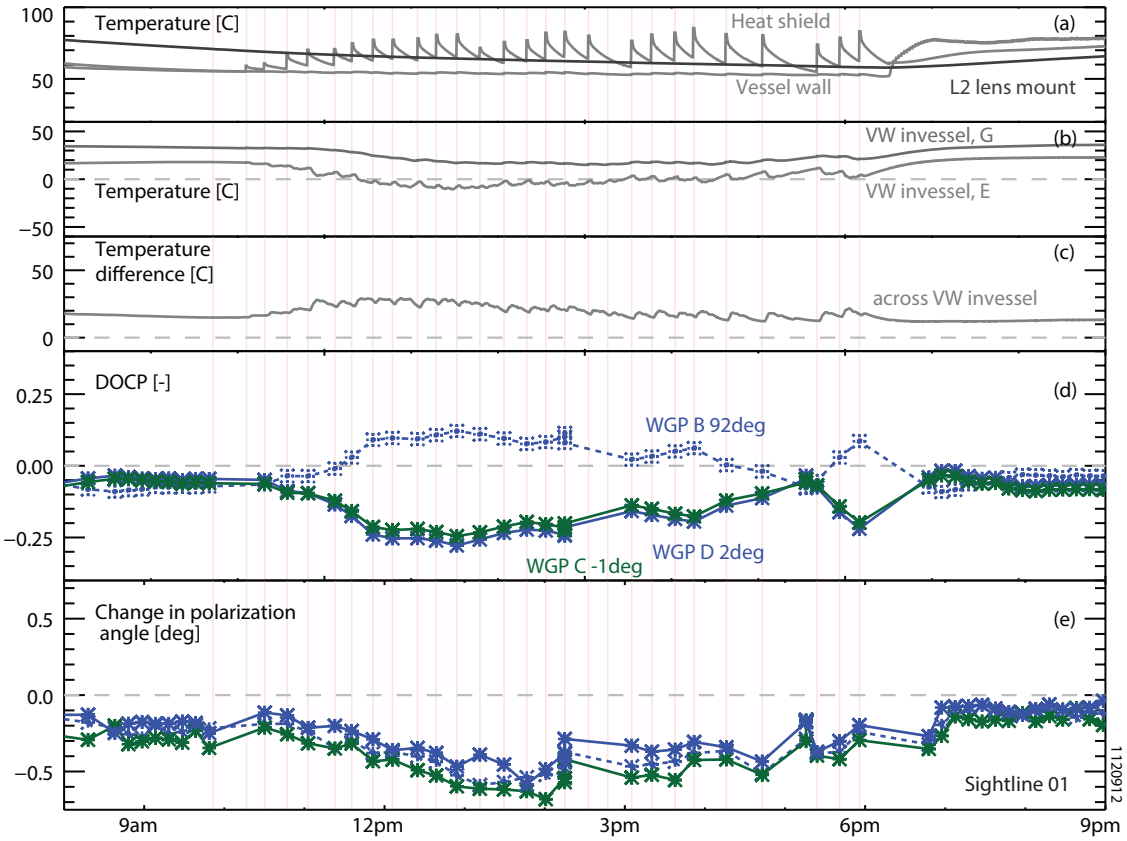

Figure 36: The ISC system is used to input three polarization angles into the diagnostic during a typical experimental runday. The temperature of the internal components (a) and vacuum window (b) change during the day, leading to large temperature differences, particularly across the vacuum window (c). The DOCP (d) and change in polarization angle (e) change across the day. The time of plasma discharges is indicated with vertical lines.

gle and DOCP are fairly constant (except for a period at midnight where vessel wall cools, changing the DOCP).

The ISC system can also be used to track the diagnostic response on the fast timescale. Figure 38 shows the diagnostic response change from a period within the runday shown in Figure 37. Each plasma discharge heats the MSE heat shield but does not affect the temperature of the internal optics (a). However, the cryogenic cooling of the tokamak magnets after the discharges has a large effect on the temperature of the vacuum window and external optics (b), decreasing their temperature by $\sim 10°C$. The temperature then increases before the next discharge but generally ratchets down in temperature across the runday. A large and variable temperature difference develops across the vacuum window (c). The DOCP (d) and change in polarization angle (e) are smoothly varying on the measurement timescale, consistent with the timescale of thermal birefringence shown in Figure 28. The changes in DOCP and polarization angle are clearly related—they show the same "cusp" time trajectories between the discharges. This trajectory is similar to the temperature and temperature difference of the vacuum window. The timescale of the changes to the diagnostic response validates the ISC calibration strategy of calibrating within seconds of every discharge. Note that one plasma discharge cannot be used to obtain the diagnostic response for a different discharge 15 minutes later in the presence of this amount of birefringence.

The time dependence of the change in DOCP and polarization angle suggest that the vacuum window is the cause of birefringence in the MSE optics (note: the internal periscope was thermally isolated during this campaign). Further database studies showed that the amount of DOCP was well correlated with the temperature difference across the vacuum window.

4.4 THERMAL CONTROL OF THE DIAGNOSTIC

The identification of stress-induced birefringence in the L2 lens assembly during previous work [1] led to the development of a thermal isolation system to stabilize the temperature of the invessel periscope. This system was installed as part of this work for the FY09 campaign and all of the work completed in this thesis was done with this system completed. However, as the observations discussed in the previous section indicate, this was not successful in stabilizing the diagnostic response. The system met its thermal isolation goals but only marginally decreased the birefringence in the diagnostic.

The understanding that stress-induced birefringence can occur in any of the ten transparent optical elements, and can significantly affect the polarization, led to the development of thermal control schemes for the entire MSE periscope, particularly the vacuum win-

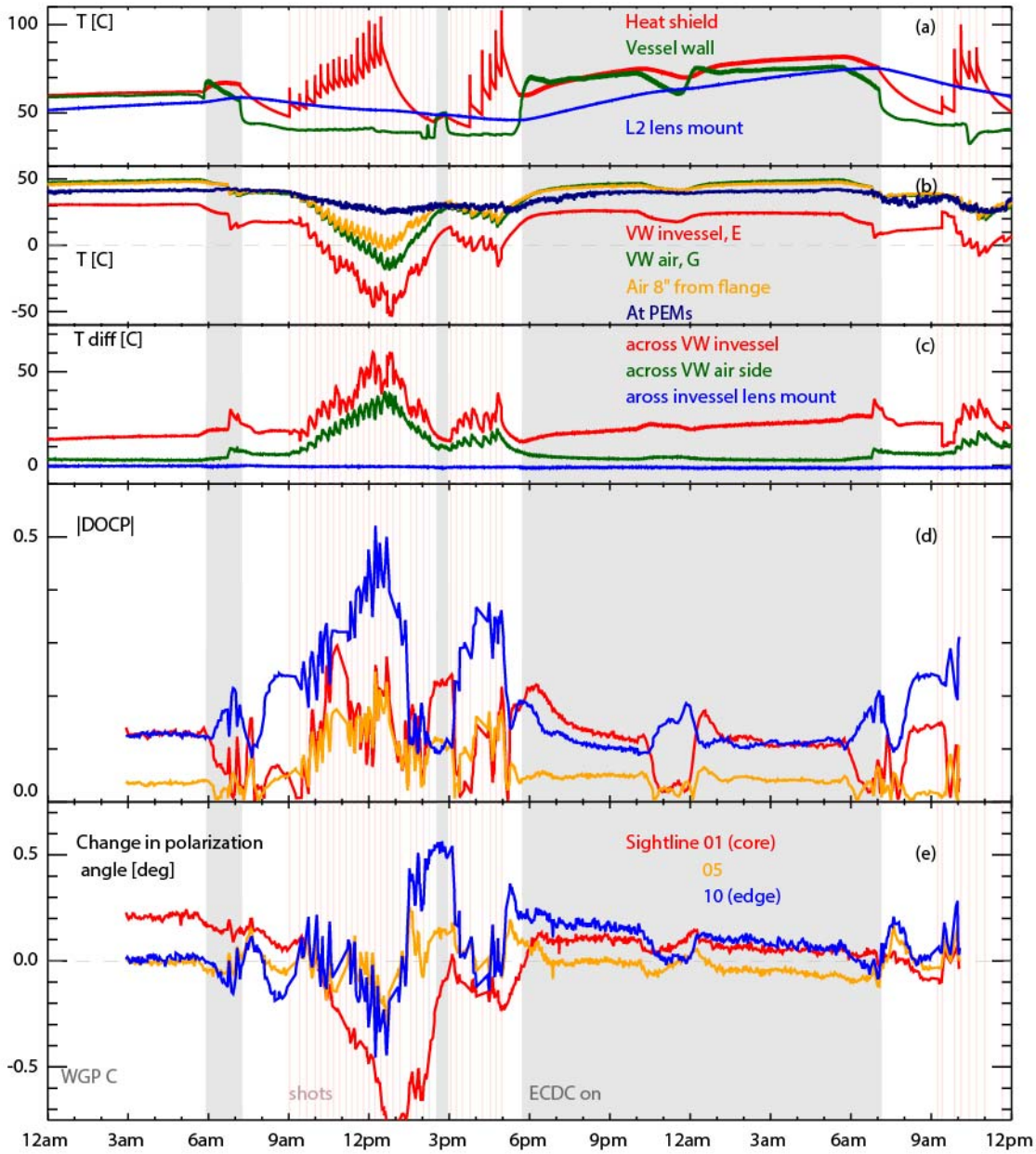

Figure 37: The ISC is used to track the diagnostic response across a 36 hour period. The temperature of the invessel components (a) and the external components (b) which change significantly and develop ~ 50°C across the vacuum window (c). The DOCP (d) and change in polarization angle (referenced to the values during invessel calibration) are shown (e).

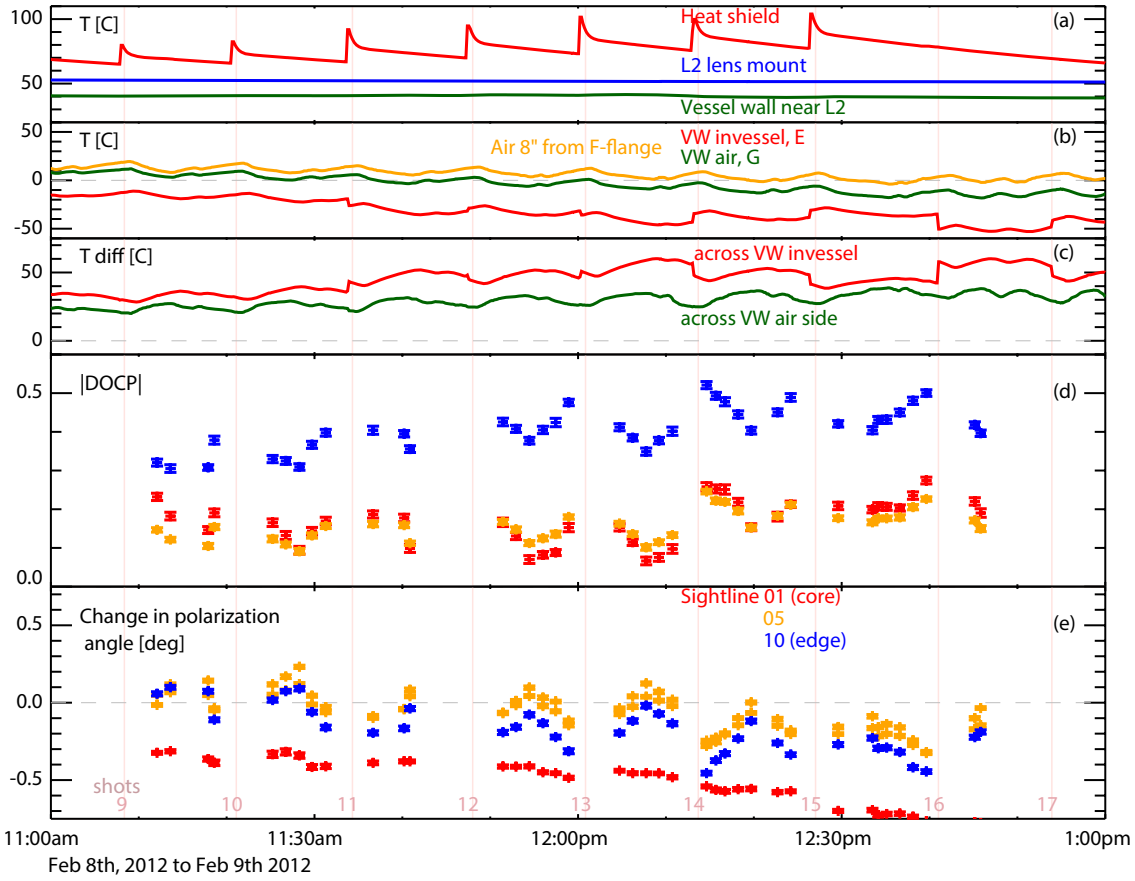

Figure 38: The ISC was used to evaluate the stability of the diagnostic response approximately every two minutes. The temperature of the invessel components (a) and external components (b) changes on the fast time scale, with the vacuum window developing a large temperature difference (c). The DOCP (d) and change in polarization angle (e) measured on three MSE sightlines for a single ISC angle.

dow. The development of the passive thermal isolation system for the internal periscope and the active thermal control system for the external periscope is described in Reference [13]. The goal being to not only in-situ calibrate the diagnostic, but also eliminate or substantially reduce the diagnostic response changes.

The thermal isolation of the internal components limits the temperature slew rate of the internal optics to $< 2°C$ per hour with temperature differences across the internal periscope of $< 1°C$, an improvement of an order of magnitude in both quantities. The external, active thermal control system maintains the external optics and vacuum window at a constant temperature. This system limits the temperature change of the external optics to $< 1°C$ and the temperature change of the vacuum window to $< 10°C$ with temperature differences across the vacuum window of $\sim 5°C$. This represents an improvement in the thermal environment of $\sim 5-10$ compared to the conditions without thermal stabilization.

The impact of the active thermal control scheme on the diagnostic response was tested using the ISC system. The results of these tests are shown in Figure 39. The active thermal control system on the external optics was disabled (left)[1] and the resulting diagnostic response changes were compared to a similar runday with the system enabled (right). The active thermal control system stabilizing the temperature of the vacuum window (a) in addition to all the external optics. The resulting DOCP (b) and change in polarization angle (c) as measured by the ISC system are much more stable and smaller (note the change in scale) with the active thermal control system enabled. The active thermal control system limits the change in polarization angle measured with the ISC system to $< 0.2°$.

4.5 VERIFICATION OF THE DIAGNOSTIC OPERATION

In addition to tracking the diagnostic response using the ISC system, the diagnostic response can also be tracked using light from the beam. These tests are performed during experiments where the target plasma is repeated as some parameter other than the magnetic geometry is varied discharge-to-discharge. Typically, only the first portion of the discharge is used to infer the diagnostic response since conditions change later in the discharge as different amounts of LHCD or ICRF power is applied or some other condition is varied. The tests allow changes to the diagnostic response to be determined under illumination conditions that are identical to those experienced in normal operation of the diagnostic.

The results of one such scan during a runday in FY12 (prior to the rebuilding of the ISC illumination system) is shown in Figure 40. The polarization angle measured from the beam changes discharge-

1 The internal system is passive and thus always remains in place.

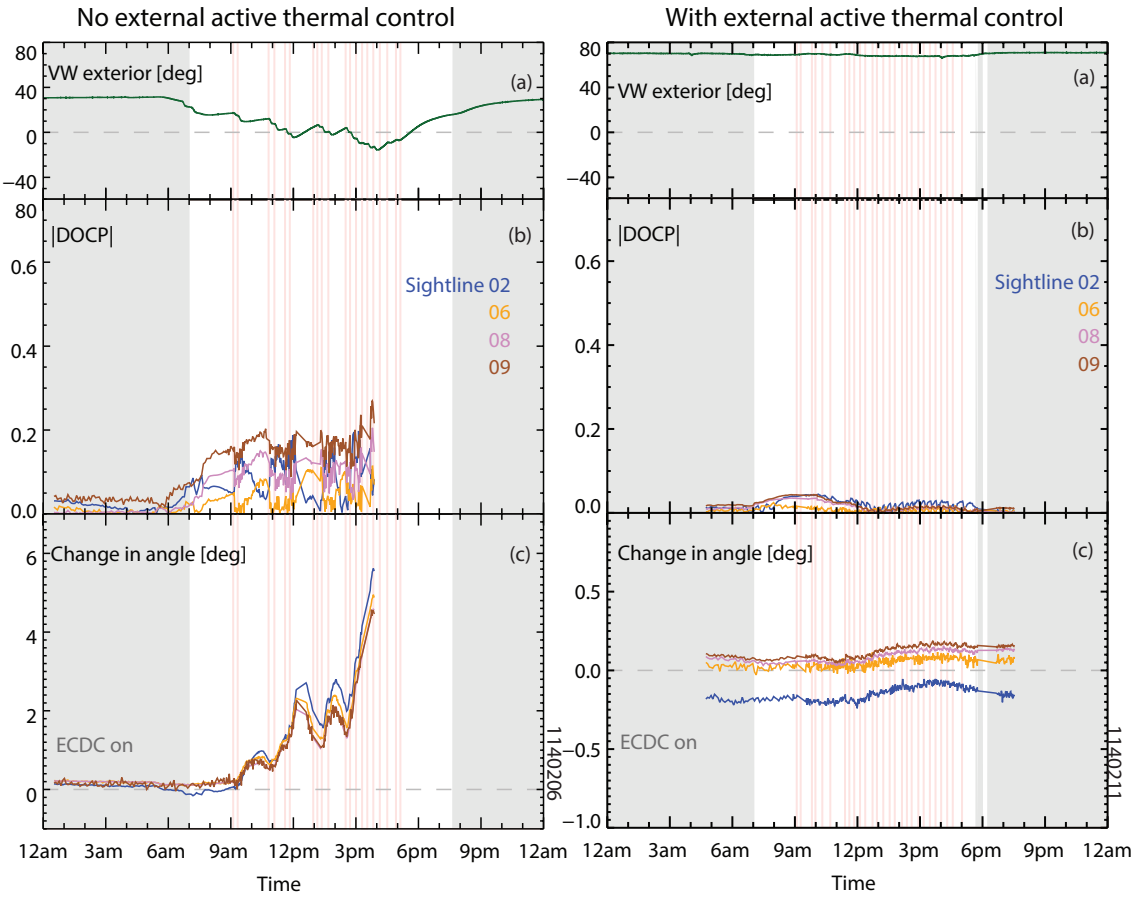

Figure 39: The impact of the active thermal control of the external optics on the changes in the diagnostic response. The diagnostic response was measured using the ISC on a day with the active thermal control system enabled (right) and disabled (left). The thermal control system stably maintains the temperature of the vacuum window (a). The resulting DOCP (b) and change in polarization angle (c) are much smaller and less variable with the thermal control system active. The vertical lines indicate the times of plasma discharges.

to-discharge for all sightlines, indicating the diagnostic response was changing. This behavior is similar to that discussed in reference [1] despite the installation of the passive thermal control system proposed in that work. The change in the polarization angle is $\sim 1°$, with the largest changes occurring at the edges of the field of view in a similar manner to that observed during the invessel heating tests. The DOCP measured using the beam was also changing in these discharges, consistent with stress-induced birefringence.

The ISC system did not measure the same changes in the diagnostic response as measured using the beam in this test—this was before the ISC illumination was rebuilt. The ISC system showed changes that were at times oppositely directed to those inferred from the beam during this test similar to that shown in the heating tests previously discussed. These observations prompted the rebuilding of the ISC illumination system after the FY12 campaign.

The beam was again used to determine the diagnostic response changes after the installation of the ISC and thermal-isolation upgrades. The results of the tests are shown in Figure 41. The diagnostic response is evidently stable throughout the run day, indicating that the active control system successfully stabilizes the diagnostic. The discharge-to-discharge variability of the diagnostic response was only marginally (~ 30 percent) larger than the uncertainty estimate of the individual beam pulse measurements compared to much larger, systematic changes prior to the installation of the active thermal control system. The ISC also indicated that the diagnostic response was constant during the run day, demonstrating agreement between the two methods to measure the diagnostic response under vacuum.

Tests were attempted with the active thermal control system disabled to compare changes in the diagnostic response measured with the ISC system to those measured with the neutral beam when the diagnostic response was *drifting*. However, this led to technical difficulties—disabling the thermal control system caused a small vacuum leak—and thus these tests were abandoned. This experiment will be revisited in the future to demonstrate that the ISC system can accurately track a time-varying diagnostic response when compared to the diagnostic response measured from the beam.

4.6 SUMMARY: ACCOUNTING FOR A CHANGING DIAGNOSTIC RESPONSE

A comprehensive calibration strategy was developed to understand errors from birefringence, to account for it during operation, and to enable the development and qualification of mitigation techniques.

An invessel robotic calibration system that can accurately calibrate the diagnostic to $< 0.03°$ was fielded. This system, the first of its kind, was used to determine the diagnostic's susceptibility to the

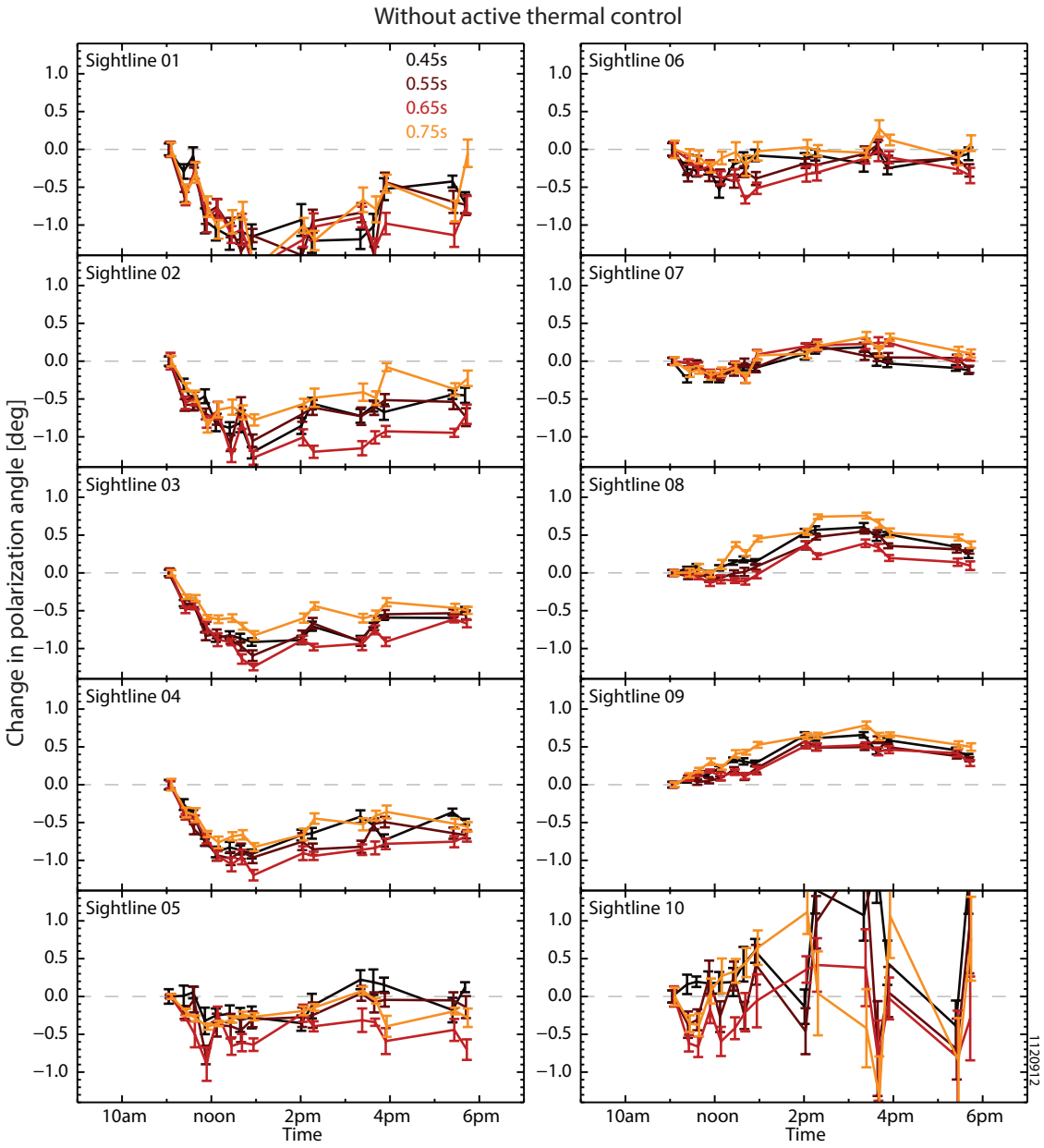

Figure 40: The change in polarization angle measured by observing the neutral beam in identical plasmas without the external active thermal control system enabled. The polarization angles are referenced to the value at the first shot of interest. Data taken from four different times in the plasma pulse are shown.

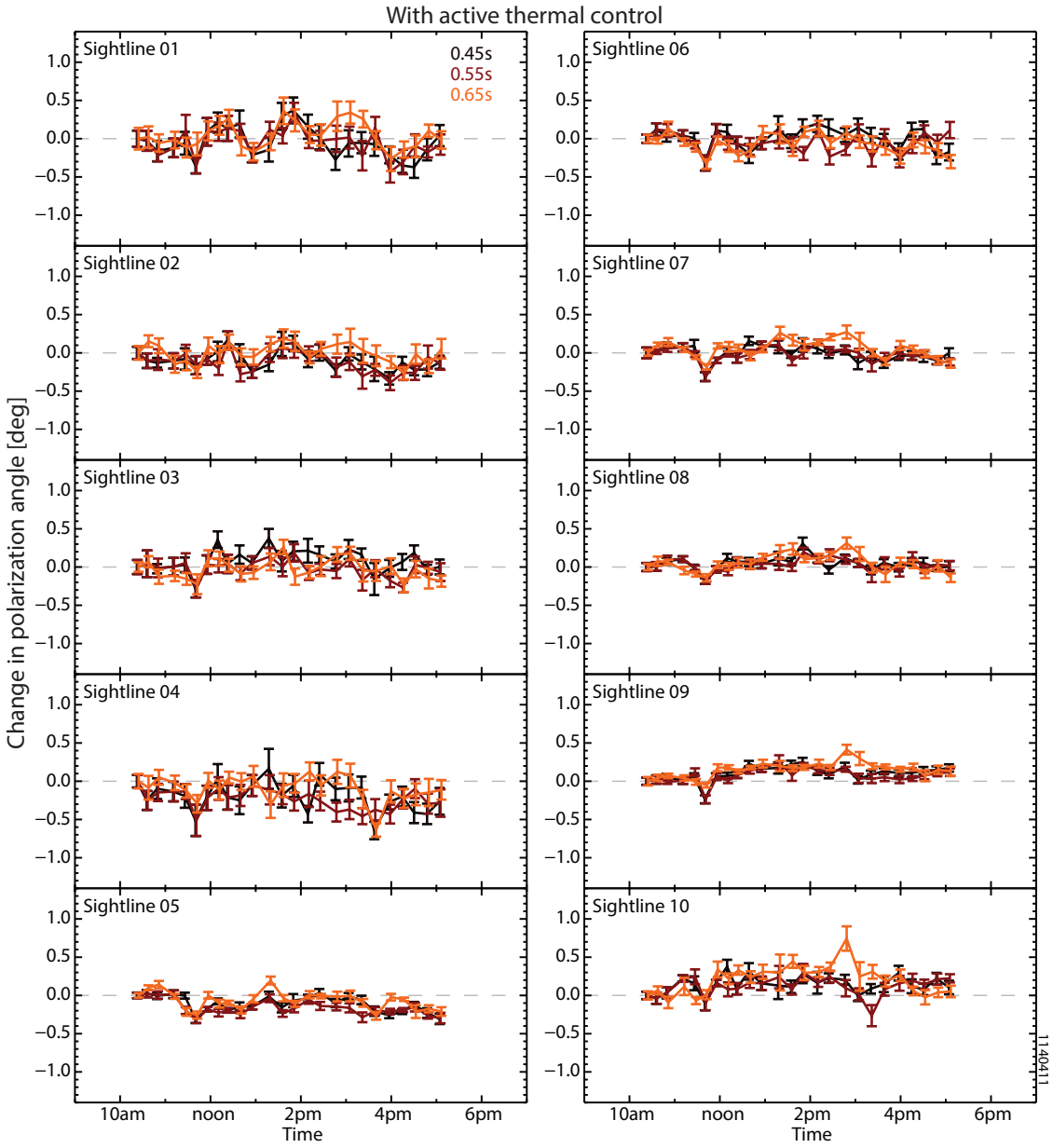

Figure 41: The change in polarization angle measured by observing the neutral beam in identical plasmas with the external active thermal control system enabled. The polarization angles are referenced to the value at the first shot of interest. Data taken from three different times in the plasma pulse are shown.

different systematic errors and to investigate the character of these errors. Thermal stress-induced birefringence was found to be important in many of the transparent diagnostic elements, contradicting previous analysis [1]. Tests indicated that thermal stress-induced birefringence creates a non-linear polarization aberration with characteristics very close to the theoretical predictions of retardance discussed in Chapter 3. The polarization aberration was found to be highly ray-dependent. Optical elements placed near intermediate focal points create minimal ray-to-ray variation within a sightline but significant sightline-to-sightline variation. Optical elements placed near images of the aperture create significant ray-to-ray variation within a sightline but much less sightline-to-sightline variation. The final sightline aberration is the weighted average across a disparate collection of polarization aberrations. This is the first known discussion or experimental result highlighting the importance of ray-dependent effects in MSE-LP diagnostics.

Knowledge of the specific type of polarization aberration in the diagnostic informed the development of a in-situ calibration system to calibrate the diagnostic at any time during operation. This system, termed the inter-shot calibration system (ISC), inputs linearly polarized light into the diagnostic lens. This system has four different calibration sources, each with a different polarization angle chosen to capture the character of the diagnostic response. The ISC system produces high quality polarized light that fills the diagnostic objective lens, is repeatable to better than 0.05°, and has proven to be very reliable. It was determined that the ISC system could only capture the actual diagnostic response when it illuminated the objective lens with uniform polarized light intensity. A comparison between the ISC and the robotic calibration system demonstrated that the ISC can properly track changes in systematic errors in the diagnostic with a uniform source.

The ISC was used to monitor the diagnostic response changes during plasma operation. It was found that the changes in polarization angle are accompanied by changes in DOCP—indicating that the culprit is indeed birefringence. The ISC system showed that the birefringence can cause very large changes on a between-discharge timescale. The data indicated that the temperature changes of the external optics were likely responsible for the birefringence, particularly from the vacuum window.

This data led to the development and deployment of an active thermal control system for the external optics to complement the passive thermal isolation system installed for the internal optics. Tests using the ISC system showed that this eliminated the drift in the diagnostic response. The diagnostic response was also monitored by firing the neutral beam into identical plasma discharges. This technique showed changes in the diagnostic response at the level of 1° prior

to the installation of thermal isolation. After the installation of the active thermal control system and the rebuilding of the ISC illumination system this test was repeated. The results showed that the diagnostic response was constant in time, which was confirmed by the ISC.

The specifics of the C-MOD ISC system do not transfer to a burning plasma (though are applicable on future and current non-burning plasma experiments) due to the choice of materials. The WGP, backlight scatterer, and fiber optics are all acting in transmission and would not survive the neutron fluence at the front of the diagnostic optical train. However, the concept of using a small number of mechanically-operating calibration sources is applicable. Future device will have shutters and mirror-cleaning systems that will need to move in vacuum and the light could be delivered via mirrors to neutron-resisting polarizers acting in reflection. Furthermore, knowledge of the expected types of polarization aberrations can be used to inform the choice of optimal calibration angles.

The impact of spatial and temporal variation can have general consequences outside transmissive optics. The uncontrolled deposition of thin films on mirrors during plasma operation in next-generation devices is likely to have many of the same consequences as thermal-stress induced birefringence. These films create spatially non-uniform diattenuation and retardance across the surface of the mirror. Plasma-facing mirrors could therefore create time- and ray-dependent aberrations that differ from the stationary aberrations arising from imperfect mirror properties at the time of installation. To properly capture this effect would require a full-field illumination calibration system. A calibration strategy which relies on using only a small portion of the field, (or a few rays) is unlikely to properly capture the aberrations which occur in a fully illuminated sightline. Fortunately the changes in diattenuation and retardance from mirror modification have a well-defined and fixed diattenuation and fast axis set by the mirror orientation.

BIBLIOGRAPHY

[1] J. Ko. *Current profile measurements using Motional Stark Effect on Alcator C-Mod*. PhD, Massachusetts Institute of Technology, 2009.

[2] M. Kuldkepp, E. Rachlew, N. C. Hawkes, and B. Schunke. First mirror contamination studies for polarimetry motional stark effect measurements for ITER. *Review of Scientific Instruments*, 75(10):3446–3448, October 2004.

[3] F. M. Levinton, G. M. Gammel, R. Kaita, H. W. Kugel, and D. W. Roberts. Magnetic field pitch angle diagnostic using the motional Stark effect (invited). *Review of Scientific Instruments*, 61(10):2914, 1990.

[4] M. F. Gu, C. T. Holcomb, R. J. Jayakuma, and S. L. Allen. Atomic models for the motional Stark effect diagnostic. *Journal of Physics B: Atomic, Molecular and Optical Physics*, 41(9):095701, May 2008.

[5] Howard Y. Yuh, F. M. Levinton, S. D. Scott, and J. Ko. Simulation of the motional Stark effect diagnostic gas-filled torus calibration. *Review of Scientific Instruments*, 79(10):10F523, 2008.

[6] F. M. Levinton, S. H. Batha, M. Yamada, and M. C. Zarnstorff. q-profile measurements in the Tokamak Fusion Test Reactor. *Physics of Fluids B: Plasma Physics (1989-1993)*, 5(7):2554–2561, July 1993.

[7] F. M. Levinton, S. H. Batha, and M. C. Zarnstorff. Calibration of the upgraded motional Stark effect diagnostic on TFTR. *Review of Scientific Instruments*, 68(1):926, 1997.

[8] T. Fujita, H. Kuko, T. Sugie, N. Isei, and K. Ushigusa. Current profile measurements with motional Stark effect polarimeter in the JT-60U tokamak. *Fusion Engineering and Design*, 34-35:289–292, March 1997.

[9] J. Ko, S. Scott, S. Shiraiwa, M. Greenwald, R. Parker, and G. Wallace. Intrashot motional Stark effect calibration technique for lower hybrid current drive experiments. *Review of Scientific Instruments*, 81(3):033505, 2010.

[10] M A Makowski, M. Brix, and N C Hawkes. Semi-Empirical Calibration Technique for the MSE Diagnostic on the JET and DIII-D Tokamaks. Heronsissos, Greece, June 2008.

[11] Yuejiang Shi. Improved signal analysis for the calibration of the motional Stark effect diagnostic. *Review of Scientific Instruments*, 77(2):023503, 2006.

[12] N. C. Hawkes, M. Brix, and JET EFDA Contributors. Calibration and operational experience with the JET motional Stark effect diagnostic. *Review of Scientific Instruments*, 77(10):10E509, 2006.

[13] R. Mumgaard. Engineering Upgrads to the Motional Stark Effect Diagnostic on Alcator C-Mod. MIT PSFC Research Report PSFC/RR-15-5, MIT PSFC, April 2015.

[14] Lan Sun and Samad Edlou. Low-birefringence lens design for polarization sensitive optical systems. volume 6289, pages 62890H–62890H–9, 2006.

5

IMPACT OF POLARIZED BACKGROUND ON MSE-LP MEASUREMENTS

Chapter goals:

- Discuss how partially-polarized background subtraction affects MSE measurements
- Determine the mechanism that polarizes the background light
- Identify the sources of the light that becomes polarized
- Discuss the impact of these sources on C-MOD and future devices

5.1 POLARIZED BACKGROUND

The MSE diagnostic collects not only emission from the neutral beam: The narrow bandpass spectral filters also collect emission from several other sources in the plasma that produce light in the MSE wavelengths. Figure 42 illustrates the various sources of light that can exist "underneath" the MSE emission. These sources of light comprise the "MSE background" and are described in Section 5.3.

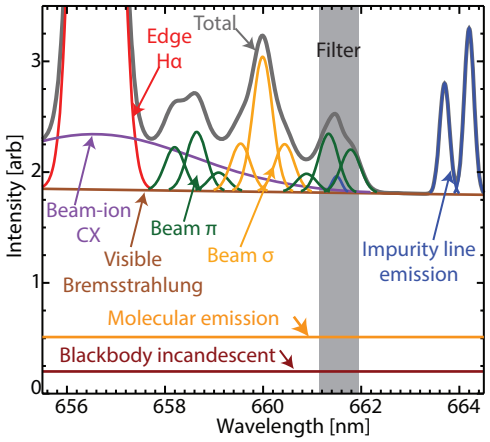

Figure 42: Various sources of light exist in the spectral region in addition to the MSE σ (yellow) and π (green) light. Some of these sources are collected by the MSE narrow bandpass filters (gray) and are thus MSE background.

The MSE diagnostic is not sensitive to this background light if the light is unpolarized. However, C-MOD's experience with MSE indicates that the background light is actually partially-polarized. An example discharge is shown in Figure 43. The DNB is modulated on and off (a), which modulates the total light collected by the diagnostic. The beam contribution to the total light collection is small compared to the total background light (b). Between beam pulses, the polarized light collected by the diagnostic (c) does not disappear, indicating that the background has a polarized component. The ratio of the beam enhancement in the polarized light to the background polarized light is plotted as a function of the ratio of the beam enhancement in total light to the total background light for two sightlines (d). Note that there is a strong correlation between these two ratios, though with significant scatter. This shows that, in C-MOD, the background emission is always partially-polarized and the polarized intensity can vary over

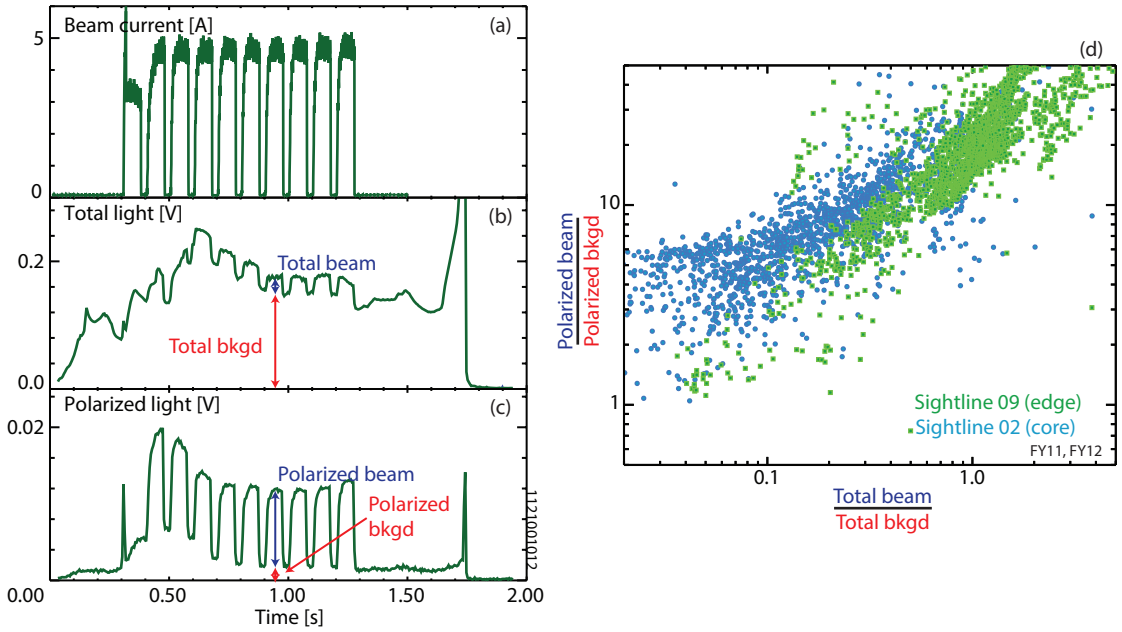

Figure 43: The DNB is modulated on and off (a) while the MSE observes a small increase in the total light (b) and a large increase in the linearly polarized light (c). The ratio of the polarized beam contribution to the polarized background contribution is plotted vs. the ratio of the total beam contribution to the total background contribution for two representative MSE sightlines (d).

several orders of magnitude. As will be discussed throughout this chapter, the fact that there is always a partially-polarized background has significant consequences for the MSE diagnostic—unlike most diagnostics, a signal to background ratio of 10 is typically insufficient for useful MSE measurements.

5.1.1 *The impact of background subtraction on the MSE measurement*

The MSE diagnostic collects the polarized MSE light from the beam and the polarized background light simultaneously and fundamentally cannot distinguish between the two sources:

$$\begin{bmatrix} I \\ Q \\ U \\ V \end{bmatrix}_{meas} = \begin{bmatrix} I \\ Q \\ U \\ V \end{bmatrix}_{beam} + \begin{bmatrix} I \\ Q \\ U \\ V \end{bmatrix}_{bkgd} \tag{41}$$

Therefore, the polarized background must be estimated and subtracted from the measurement to obtain the contribution from the beam. However, since the background cannot be measured directly, this estimate is imperfect. The misestimation will lead to a misestimate in the component from the beam. Recall that the measured Stokes compo-

nent is comprised of the actual background and actual beam emission yielding:

$$\begin{bmatrix} I \\ Q \\ U \\ V \end{bmatrix}^{\text{est}}_{\text{beam}} = \begin{bmatrix} I \\ Q \\ U \\ V \end{bmatrix}_{\text{beam}} + \begin{bmatrix} I \\ Q \\ U \\ V \end{bmatrix}_{\text{bkgd}} - \begin{bmatrix} I \\ Q \\ U \\ V \end{bmatrix}^{\text{est}}_{\text{bkgd}} \tag{42}$$

An important question is then: How does an imperfect background estimate lead to an error in the estimated polarization angle from the beam? It is often more intuitive to describe polarization in terms of linear polarization intensity and polarization angle than with the Stokes vectors themselves.[1] Therefore, the calculation is transformed into these quantities using the relations $L = \sqrt{Q^2 + U^2}$, $Q = L\cos(2\theta)$, and $U = L\sin(2\theta)$. The background polarization is parameterized in terms of the background polarization angle θ_{bkgd}, the background linear polarization intensity L_{bkgd}, while the beam has polarized intensity L_{beam}, and the beam polarization angle θ_{beam}. This transformation gives the two estimated linear Stokes vectors Q:

$$\begin{aligned} &L^{\text{est}}_{\text{beam}}\cos(2\theta^{\text{est}}_{\text{beam}}) = \\ &\qquad L_{\text{beam}}\cos(2\theta_{\text{beam}}) + L_{\text{bkgd}}\cos(2\theta_{\text{bkgd}}) - L^{\text{est}}_{\text{bkgd}}\cos(2\theta^{\text{est}}_{\text{beam}}) \end{aligned}$$

and U:

$$\begin{aligned} &L^{\text{est}}_{\text{beam}}\sin(2\theta^{\text{est}}_{\text{beam}}) = \\ &\qquad L_{\text{beam}}\sin(2\theta_{\text{beam}}) + L_{\text{bkgd}}\sin(2\theta_{\text{bkgd}}) - L^{\text{est}}_{\text{bkgd}}\sin(2\theta^{\text{est}}_{\text{beam}}) \end{aligned}$$

With improper background estimates, the estimated beam angle will differ from the actual beam angle: $\theta^{\text{est}}_{\text{beam}} = \theta_{\text{beam}} + \Delta\theta_{\text{beam}}$. The two equations can be combined into a single equation to describe the background's effect on the estimated beam polarization angle:

$$\begin{aligned} &\tan(2(\theta_{\text{beam}} + \Delta\theta_{\text{beam}})) = \\ &\frac{L_{\text{beam}}\sin(2\theta_{\text{beam}}) + L_{\text{bkgd}}\sin(2\theta_{\text{bkgd}}) - L^{\text{est}}_{\text{bkgd}}\sin(2\theta^{\text{est}}_{\text{beam}})}{L_{\text{beam}}\cos(2\theta_{\text{beam}}) + L_{\text{bkgd}}\cos(2\theta_{\text{bkgd}}) - L^{\text{est}}_{\text{bkgd}}\cos(2\theta^{\text{est}}_{\text{beam}})} \end{aligned} \tag{43}$$

Equation 43 is exact, though not very tractable. To make progress, it is therefore assumed that the estimate in the background polarization angle is perfect: $\theta^{\text{est}}_{\text{bkgd}} = \theta_{\text{bkgd}}$, but the intensity of the background is

1 The actual background compensation computations are done Stokes component-wise.

misestimated by a relative amount f: $L^{est}_{bkgd} = (1-f)L_{bkgd}$. Under these assumptions the preceding equation becomes:

$$\tan(2(\theta_{beam}+\Delta\theta_{beam})) = \frac{L_{beam}\sin(2\theta_{beam}) + fL_{bkgd}\sin(2\theta_{bkgd})}{L_{beam}\cos(2\theta_{beam}) + fL_{bkgd}\cos(2\theta_{bkgd})} \quad (44)$$

The ratio of the beam linear polarized light to the background linear polarized light can be parameterized with a polarized signal to background ratio $SB = L_{beam}/L_{bkgd}$ yielding:

$$\tan(2(\theta_{beam}+\Delta\theta_{beam})) = \frac{\sin(2\theta_{beam}) + \frac{f}{SB}\sin(2\theta_{bkgd})}{\cos(2\theta_{beam}) + \frac{f}{SB}\cos(2\theta_{bkgd})} \quad (45)$$

This problem lends itself to complex analysis. Which after some algebra reduces to:

$$\sin(2\Delta\theta_{beam}) = -\frac{f}{SB}\sin\left(2\left(\theta_{beam}-\theta_{bgkd}-\Delta\theta_{beam}\right)\right) \quad (46)$$

It is assumed that f is small and SB is large, leading to a small $\Delta\theta_{beam}$ that allows the small angle approximation:

$$\Delta\theta_{beam} \approx -\frac{f}{2\,SB}\sin\left(2\left(\theta_{beam}-\theta_{bgkd}\right)\right) \quad (47)$$

And for $\Delta\theta_{beam}$ in degrees this becomes:

$$\Delta\theta_{beam} \approx -28.67\frac{f}{SB}\sin\left(2\left(\theta_{beam}-\theta_{bgkd}\right)\right) \quad [deg] \quad (48)$$

The effect of misestimating background polarization angle can be approached in a similar manner. Instead of assuming a perfect estimate in background polarization angle and an imperfect estimate in intensity, one instead assumes a perfect estimate in intensity and an imperfect estimate in polarization angle: $L^{est}_{bkgd} = L_{bkgd}$ and $\theta^{est}_{bkgd} = \theta_{bkgd} + \Delta\theta_{bkgd}$. Substituting these relations into Equation 43 yields:

$$\tan(2(\theta_{beam}+\Delta\theta_{beam})) = \frac{\sin(2\theta_{beam}) + \frac{1}{SB}\sin(2\theta_{bkgd}) - \frac{1}{SB}\sin(2\theta_{bkgd}+2\Delta\theta_{bkgd})}{\cos(2\theta_{beam}) + \frac{1}{SB}\cos(2\theta_{bkgd}) - \frac{1}{SB}\cos(2\theta_{bkgd}+2\Delta\theta_{bkgd})} \quad (49)$$

Again, this can be approached with complex analysis. After significant algebra the result is:

$$\sin(2\Delta\theta_{beam}) = \frac{1}{SB}\sin(2(\theta_{beam}-\theta_{bgkd}+\Delta\theta_{beam}-\Delta\theta_{bkgd})) - \frac{1}{SB}\sin(2(\theta_{beam}-\theta_{bkgd}+\Delta\theta_{beam})) \quad (50)$$

By substituting $K_1 = 2\left(\theta_{beam} - \theta_{bkgd} + \Delta\theta_{beam}\right)$ and $K_2 = -2\Delta\theta_{bkgd}$ and using trigonometric identities, this can be recast as:

$$\sin(2\Delta\theta_{beam}) = \frac{1}{SB}\left(\sin K_1\left(\cos K_2 - 1\right) + \cos K_1 \sin K_2\right)$$

Assuming K_2 is small (i.e., there is not a large uncertainty in the background angle) allows the use of the small angle approximation:

$$\sin(2\Delta\theta_{beam}) \approx \frac{K_2}{SB}\left(\cos K_1 - \frac{K_2}{2}\sin K_1\right)$$

A further assumption that $\left|\frac{K_2}{SB}\right| << 1$ allows the use of the small angle approximation for $\Delta\theta_{beam}$:

$$\Delta\theta_{beam} \approx \frac{-\Delta\theta_{bkgd}}{SB}\left(\cos\left(2\left(\theta_{beam} - \theta_{bgkd}\right)\right) + \Delta\theta_{bkgd}\sin\left(2\left(\theta_{beam} - \theta_{bgkd}\right)\right)\right)$$

Which to first order in $\Delta\theta_{bkgd}$ is then:

$$\Delta\theta_{beam} \approx \frac{-\Delta\theta_{bkgd}}{SB}\cos\left(2\left(\theta_{beam} - \theta_{bgkd}\right)\right) \tag{51}$$

Equations 48 and 51 parameterize the consequences of polarized background for MSE-LP diagnostics. It is important to realize that the effect of misestimating the background is not to input additional statistical scatter, but to systematically skew the derived beam polarization angle. The systematic error is nearly linear in the uncertain parameter and inversely related to the polarized-signal-to-polarized-background ratio, SB. In an actual implementation, both the background intensity and polarization angle are uncertain, and both contribute to systematically altering the polarization angle from the beam.

Figure 44 illustrates the effect of background estimation uncertainty on the operational space of a MSE diagnostic. The y axis is the uncertainty in the polarization angle from the beam due to misestimation of the background polarization in degrees. The x axis is the polarized-signal-to-polarized-background ratio. Lines of constant misestimates of the relative intensity f (gray) and constant misestimates of the background polarization angle $\Delta\theta_{bkgd}$ (red) are shown. It is assumed for each case that the background polarization angle is in the least favorable orientation. The target measurement uncertainty for measurements from the beam, $\Delta\theta_{beam} = 0.1°$, is shown as a horizontal dashed line. Recall that the uncertainty in the polarization angle translates to a larger uncertainty in the magnetic pitch angle due to the geometric projection.

Completely neglecting to subtract the background ($f = 1$) can lead to errors above the target when the polarized signal-to-polarized back-

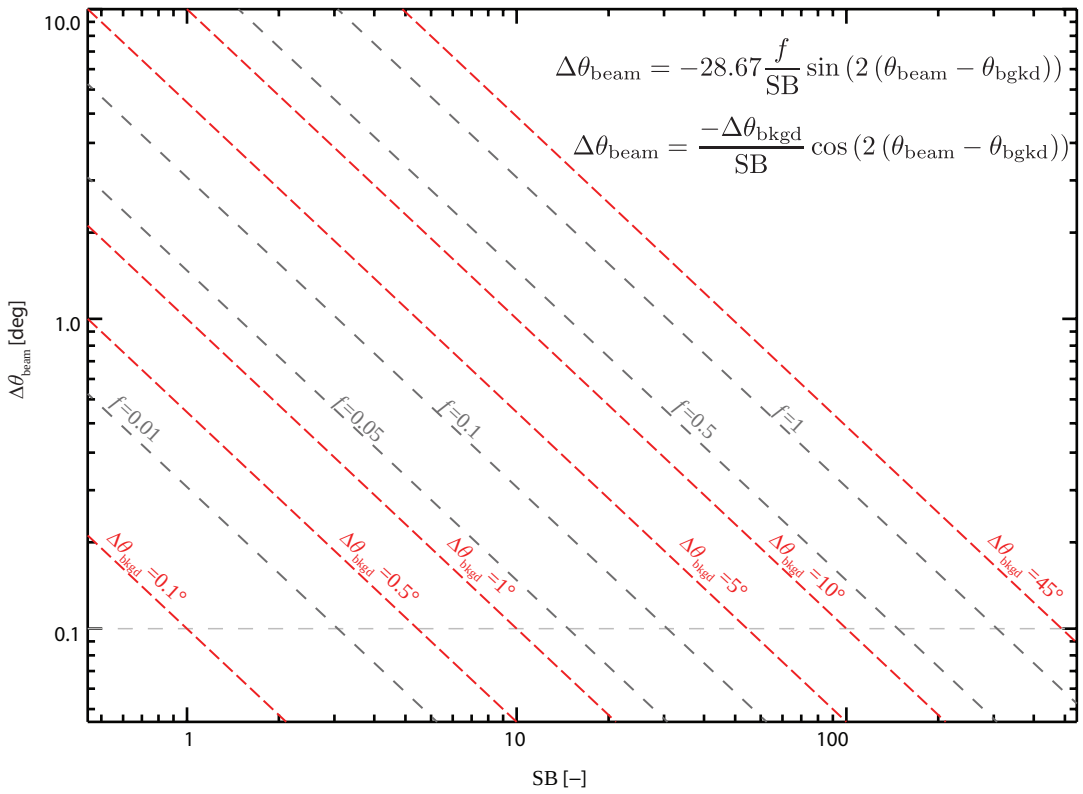

Figure 44: The uncertainty in the polarization angle from the beam $\Delta\theta_{beam}$ due to imperfect polarized background subtraction vs. the polarized signal to polarized background ratio SB. Lines of constant relative uncertainty in the background polarization intensity f (gray) and constant uncertainty in the background polarization angle $\Delta\theta_{bkgd}$ (red) are shown. The target beam polarization angle measurement uncertainty for MSE measurements is indicated (dashed).

ground ratio is below 300. For MSE systems operating at SB < 100, the uncertainty due to background subtraction can be the dominant uncertainty in the measurement, requiring very accurate estimates of the background polarization properties. Achieving the desired measurement uncertainty with SB < 10 is very challenging, requiring the background intensity to be estimated to better than 4% and the angle to be estimated to better than 1°. Table 8 gives some examples of the required background estimate at different polarized-signal-to-polarized-background ratios.

Fortunately, with a more intense polarized background it is easier to measure the background polarization angle and polarized intensity since more background photons are available. Therefore, if the low SB is primarily caused by an intense background polarization, then the ability to estimate the background likely increases as SB decreases. Minimizing the spectral width of the bandpass filters that select the MSE emission is also important to avoid collecting excess background light, and thus lowering SB.

Table 8: How well the background polarization must be estimated in order to achieve an uncertainty in beam polarization angle of less than 0.1°.

SB	f	$\Delta\theta_{bkgd}$
1	< 0.003	$< 0.1°$
5	< 0.02	$< 0.5°$
10	< 0.04	$< 1°$
50	< 0.17	$< 5°$
100	< 0.4	$< 10°$

Many existing MSE systems operate at high SB, meaning they may not need to subtract the background at all. This is the case for MAST, DIII-D, and NSTX. However, other experiments have reported problems due to background subtraction. JET reports observing polarized light from ELMs [1, 2]. JT60-U also observes ELMs in their MSE polarization angles [3, 4]. TORE SUPRA reports angle changes up to 2° due to reflections from glowing components [5]. The DIII-D "radial" array observes a current and field dependent "drift" of up to 8° in the pitch angle derived from this array [6]. Many, or most, of these problems are likely due to errors in background subtraction. The MSE diagnostic is unusual in that it requires such a high signal-to-background ratio, much greater than that typically accepted by other tokamak diagnostics. This is due to the very high polarization angle accuracy required to make meaningful measurements. The diagnostic has been successful to date because of the high polarized-signal-to-polarized-background ratio environments it has been operated in—there is not a large amount of polarized light inside the many existing tokamaks. Though this is not the case for C-MOD and likely other future devices, as will be discussed in the rest of this chapter.

5.1.2 *Scaling of the polarized-signal-to-polarized-background ratio*

The proceeding analysis shows that the scaling of the polarized signal to the polarized background ratio in different plasmas will set the operating limits of an MSE diagnostic when background subtraction is important. This will be the case even if sufficient photons are collected from the beam to make a high quality polarization angle

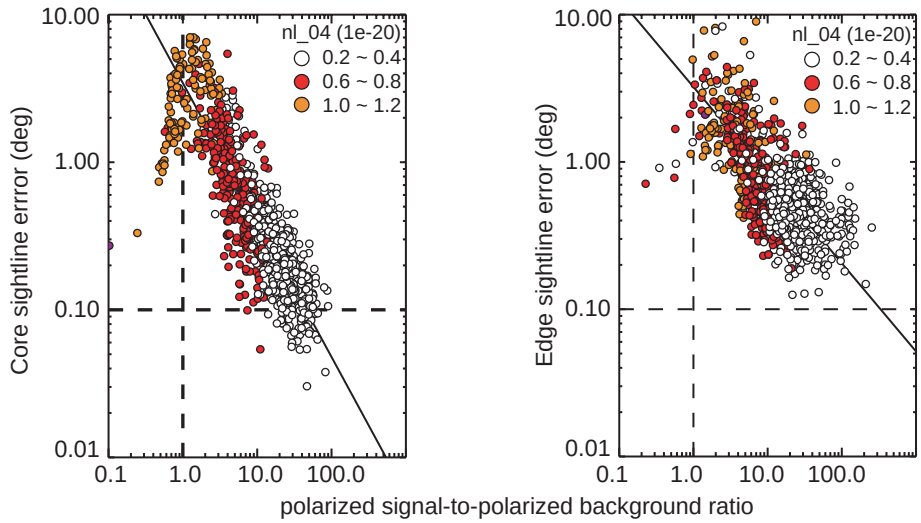

Figure 45: The statistical variability in the calculated pitch angle for two sightlines as a function of the polarized-signal-to-polarized-background ratio and the line-integrated density. Adapted from [7].

Figure 46: The measured polarized-signal-to-polarized-background ratio, SB, for three MSE sightlines during the 2014 experimental campaign plotted as a function of line-averaged plasma density.

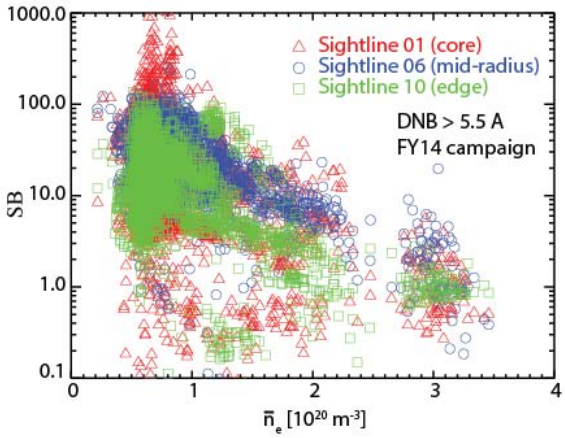

measurement in the absence of polarized background. Previous work by Ko [7], reproduced in Figure 45, showed that the statistical scatter in the measured pitch angle had a strong scaling with the polarized-signal-to-polarized-background ratio while the second strongest scaling was with the the line-integrated density.

Database studies were performed on data from the C-MOD MSE system to determine how the SB scales with important plasma parameters. Figure 46 shows that the measured polarized signal-to-polarized background ratio, SB, has a strong inverse scaling with density. This was the strongest scaling found, though there is much scatter in the plots indicating there must be other hidden parameters. Above line averaged densities of $2 \times 10^{20} \mathrm{m}^{-3}$ on C-MOD, the SB is rarely greater than 10, potentially leading to significant errors due to background subtraction.

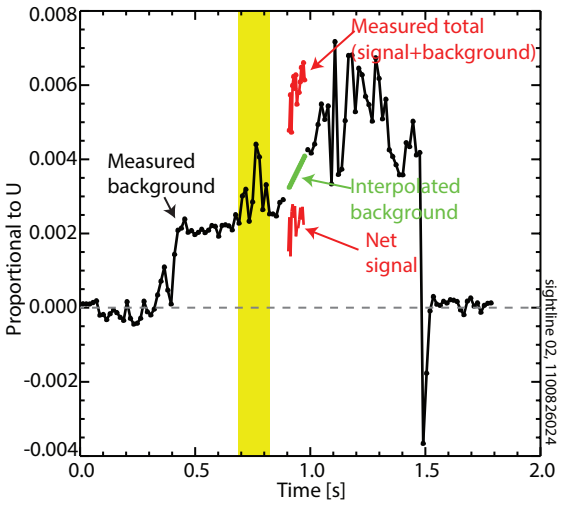

Figure 47: An example of beam modulation time-interpolation for the quantity proportional to U (Amplitude at 44kHz). During the single beam pulse, the background and beam emission are simultaneously collected (top red). For the remainder of the discharge, the background is collected alone (black). During the beam pulse, the background is straight-line time-interpolated (green) using the measurements just before and after the beam pulse. This estimate is subtracted from the measurement to yield the net signal (lower red). Note that there are times when this type of straight-line time-interpolation would not properly account for the background (yellow highlight).

5.1.3 *Time-interpolation is often insufficient*

A common method to estimate the background in beam-based diagnostics is to time-interpolate the background using beam-off periods, a scheme commonly used for MSE on C-MOD and other devices. This the method was used for all the physics data presented in the later chapters of this thesis.

To use time-interpolation, the beam is intentionally turned off occasionally, allowing the background Stokes vector to be measured. Then, during the beam-on phase, the Stokes vector of the combined background and beam is measured. The background Stokes vector components are then straight-line time-interpolated each of across the beam pulse using the measured background before and after each beam pulse. The time-interpolated Stokes vector is subtracted from the measured Stokes vector on the microbin (every $2-5$ms) timebase to yield the Stokes vector solely from the beam. The polarization angle from the beam is then calculated on the microbin timebase from the Stokes components and averaged for $20-60$ms to reduce the statical uncertainty in the beam polarization angle. The magnetic pitch angle is calculated on the microbin timebase using the geometry projection factor and averaged in the same manner and then used in reconstructions[2]. The process for a single Stokes component is shown in Figure 47.

This time-interpolation method for estimating and subtracting the background is problematic for several reasons:

1. Changes in either the background polarized intensity or polarization angle (or equivalently U and Q) are not captured using a straight-line trajectory. For example, placing the beam pulse at

2 In practice these calculations are performed using the APD output voltages measured at the two PEM's second harmonics, which are proportional to the Stokes vector components U and Q.

the shaded position in Figure 47 and time-interpolating across the pulse would miss the peak in the emission. After background subtraction, the signal attributed to the beam would then be too high for this Stokes component.

2. No MSE measurement is available when the beam is off.

3. The short background measurements are noisy, leading to errors in interpolation.

4. Though not a problem on C-MOD due to the weak neutral beam, modulating the heating beams on other tokamaks changes the heating power and heating mix. It is unclear if future devices will be able to modulate their heating beams on the required timescale.

5. The use of time-interpolation is incompatible with using the MSE measurement for real-time control applications—the next beam-off measurement is not known.

Experience with MSE signal levels, desired time resolution, measurement timing, and background variability is used to select appropriate beam-on and beam-off intervals. In practice this usually results in $10-20$ms beam-off periods. The beam-on periods are then made to be $50-80$ms to allow sufficient signal collection for a MSE measurement and to give the beam voltage and current time to settle. Significant effort is expended planning the beam timing in order to minimize the problems due to background subtraction. Changes in the heating power, plasma confinement mode, and impurity content are known to cause changes in the background that can cause an undiagnosed change in the background.

If the magnetic geometry is stationary and if the beam voltage is constant the beam should produce a constant polarization fraction and polarization angle over the length of the beam pulse. Incorrect estimation and subtraction of polarized background can often be identified by examining individual beam pulses for deviation from these characteristics at times when the background is expected to change such as due to heating faults. Examples of a discharges with correct and incorrect background subtraction are shown in Figure 48. These two discharges differed only in density (lower density on the left) and that in one of them had faults in the LHCD power (right). The inferred polarization fraction and polarization angle from the beam emission differ significantly during the LHCD faults relative to their values in the companion, non-faulting, discharge. The speed and extent of the change in polarization angle is too fast and large to represent changes in the magnetic geometry.

In practice, estimating the background using time-interpolation limits the achievable accuracy of the estimated intensity, f, to $0.1-0.5$

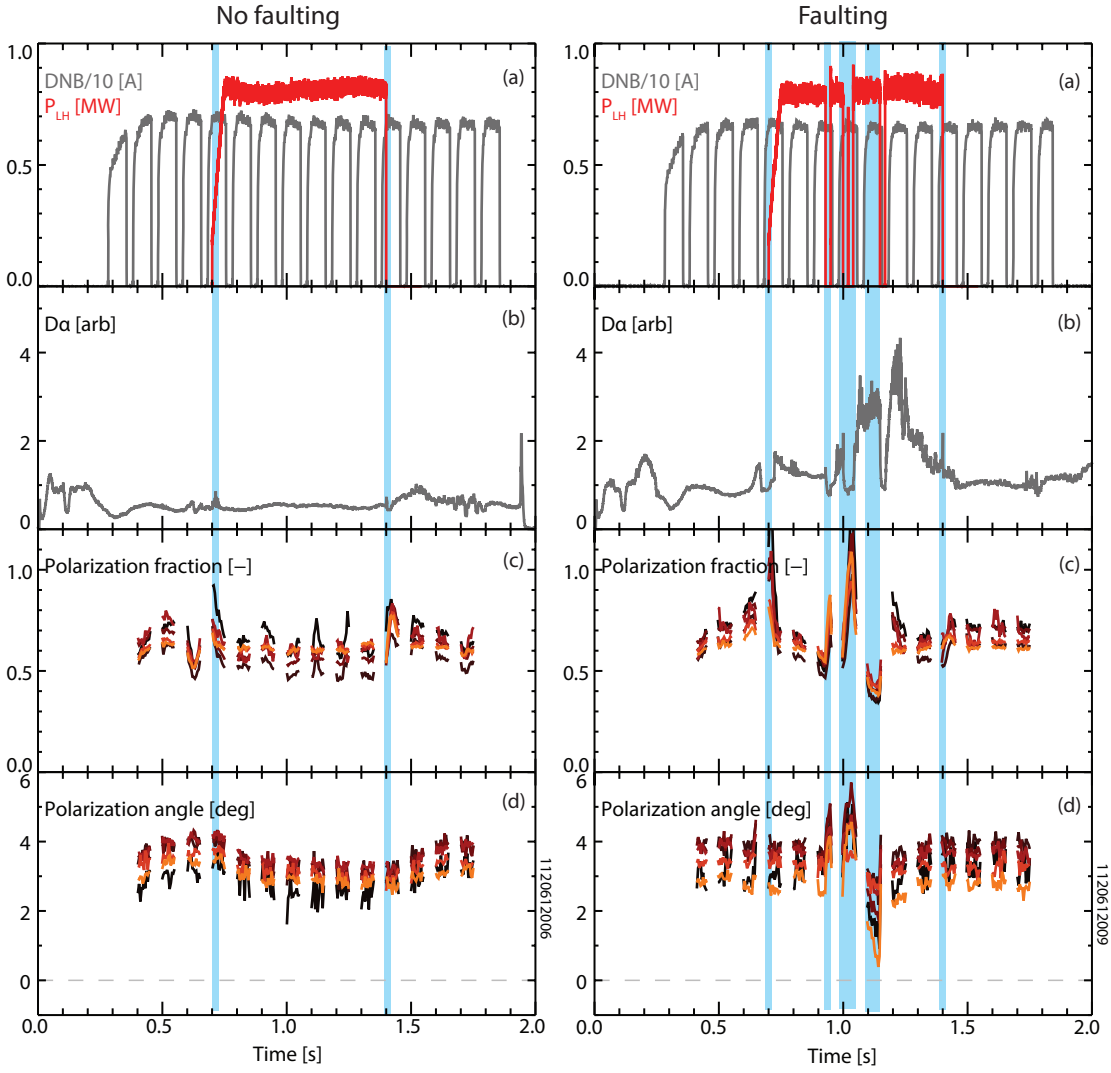

Figure 48: An example of incorrect background subtraction due to the failure of straight-line time-interpolation. Two nearly identical discharges with LHCD applied are compared, one without any LHCD faults (left) and one with faults around 1s (right). The DNB ion current and LHCD power were nearly identical (a) in each discharge. The D_α was brighter and more transient in the faulting discharge (b). The background is estimated using time-interpolation across each beam pulse and subtracted from the total polarized signal to yield the polarization fraction (c) and the polarization angle (d). The periods where the LHCD started, stopped, or faulted which led to large, spurious changes in the inferred polarization properties from the DNB are highlighted in blue. Note that most beam pulses show constant polarization fraction and angle throughout the pulse as one would expect.

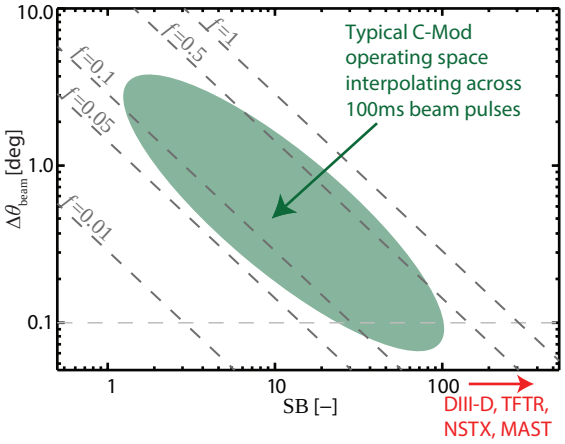

Figure 49: The uncertainty in the in the polarization angle from the beam $\Delta\theta_{beam}$ vs the polarized signal to polarized background ratio SB. The operating regime of the C-MOD MSE diagnostic using beam modulation with time-interpolation is shown. Many other MSE systems operate at high SBs, and do not require extensive background subtraction.

and the achievable accuracy of the estimated background polarization angle to $\Delta\theta_{bkgd}$ to $1° - 10°$ for many of the discharges of physics interest on C-MOD. This makes background subtraction a dominant uncertainty for the ALCATOR C-MOD MSE diagnostic except at the lowest densities and powers as shown in Figure 49. Many modes of operation with varied heating powers or the likelihood of heating systems tripping off during beam pulses are precluded due to background subtraction issues. The discharges used for physics study to date, including in this thesis, have predominately been at low densities and only data when the plasma was quiescent during the beam-on period and the preceding and following beam-off periods is used for reconstructions. Even in these cases the analysis output for each beam pulse is examined to ensure there are no problems due to using time-interpolation to estimate the background that would skew the measurement past what would be incorporated into the estimated uncertainty.

Therefore, a better understanding of the polarized background—and a better method to estimate it—is required to extend the MSE measurement on C-MOD into more interesting operating regimes.

5.2 POLARIZATION UPON REFLECTION

Very few sources of light inside the vessel emit grossly linearly polarized light[3]. However, there are many sources of unpolarized light in the tokamak. Therefore, to produce a large polarized background, a mechanism is required to transform unpolarized light into polarized light. The most obvious mechanism is reflection from a surface which partially polarizes the light.The exact details of the polarization after reflection depend sensitively on both the optical properties of the surface and the angle of incidence.

3 Examples include: Zeeman split atomic lines which are split too narrowly to be a problem for MSE, and synchrotron emission covered in Appendix D

The interior of the a tokamak is composed of many complicated surface geometries. This is particularly true inside C-MOD due to the numerous components mounted on the vessel wall and the lack of a close-fitting first wall near the plasma. Unlike the interior of many existing tokamaks, which are covered in poorly reflecting carbon tiles, C-MOD's internal components are made of reflective metals as shown in Figure 50.

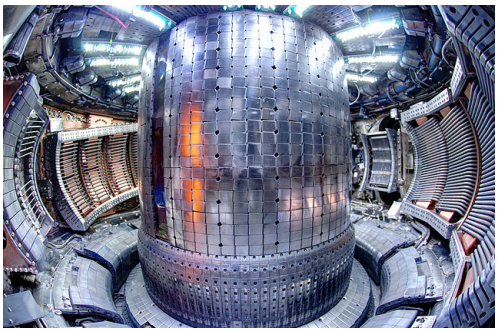

Figure 50: C-MOD's interior is composed of highly reflective metals, surface films, and complex component geometries. Photo credit: Robert Mumgaard

Due to spatial constraints inside the vessel, the C-MOD MSE diagnostic does not have a dedicated view dump as is common in other tokamaks. Instead, the sightlines, which come to a focus in the plasma, expand and terminate on the ICRF antennas on the opposite wall. Figure 51 shows the MSE views backlit onto the the antenna. Note the expanded views from neighboring MSE sightlines largely overlap and cover much of the antenna surface.

An experiment was conducted during a maintenance period to test whether reflection from the antenna contributes to the partially polarized background. Nominally unpolarized light from a bright source was shined onto the antenna, and moved around the poloidal plane manually while the MSE diagnostic observed the light reflected off the antenna. This experiment shows the linear polarization fraction of the reflected light is fairly high, $0.4 - 0.6$, while the circular polarization fraction is low, < 0.05. This indicates the reflected light is partially linearly polarized with little ellipticity, consistent with a sub-unity s-p reflection ratio and little phase shift from the antenna surfaces.

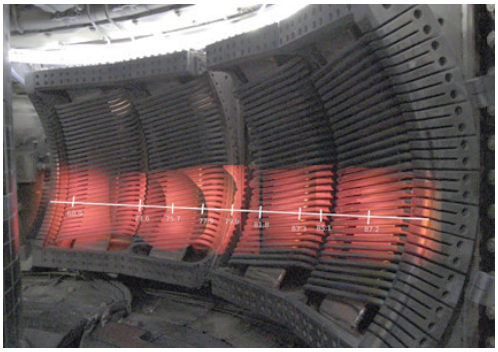

Figure 51: MSE sightlines backlit to show the viewing volume projection onto the D and E-port ICRF antennas. The image is composed of multiple photos.

These results prompted a comprehensive survey of the reflection properties of the antenna. A novel polarization-sensitive camera was constructed that can measure the total intensity, linear polarization fraction, and polarization angle (or equivalently I, Q, and U) of an image. The development and testing of this camera is discussed in Reference [8]. The camera was placed at the approximate location of the MSE objective lens and pointed at the antenna. Unpolarized red light was shined onto the antenna from outside of the camera's field of view while polarization exposures were taken. The results are shown in Figure 52.

It is immediately apparent that the antenna creates complex polarization with the polarized intensity, angle, and fraction that vary significantly as a function of source angle. So although the MSE sight-

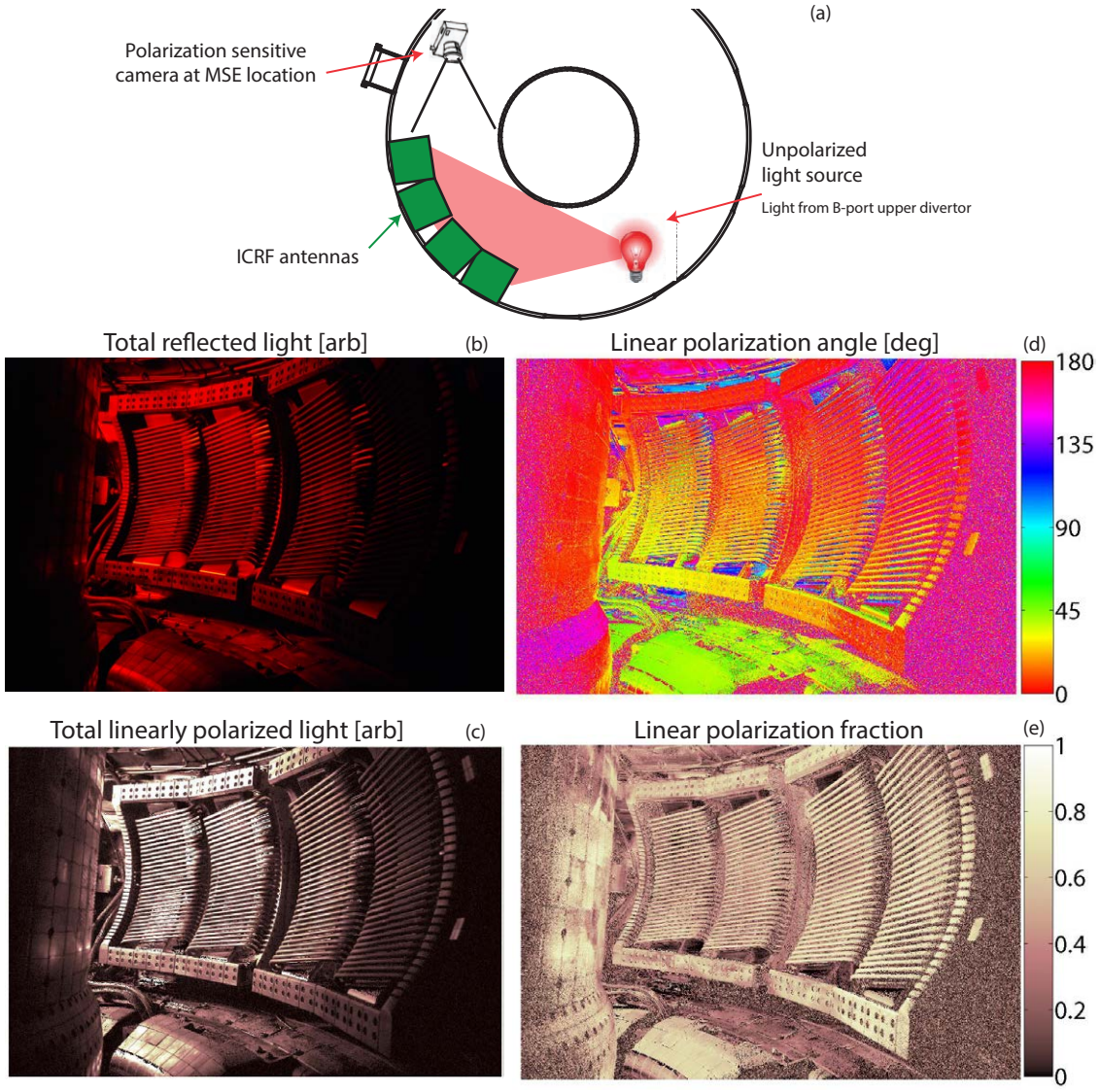

Figure 52: Unpolarized light was shined onto the antenna from near B-port. A linear polarization camera was placed at the location of the MSE objective to image the reflected light (a). The total (red) light reflected from the antenna (b). The total linearly polarized light reflected from the antenna (c). The polarization angle of the reflected light with 0° corresponding to roughly vertical (d) and the linear polarization fraction of the reflected light (e).

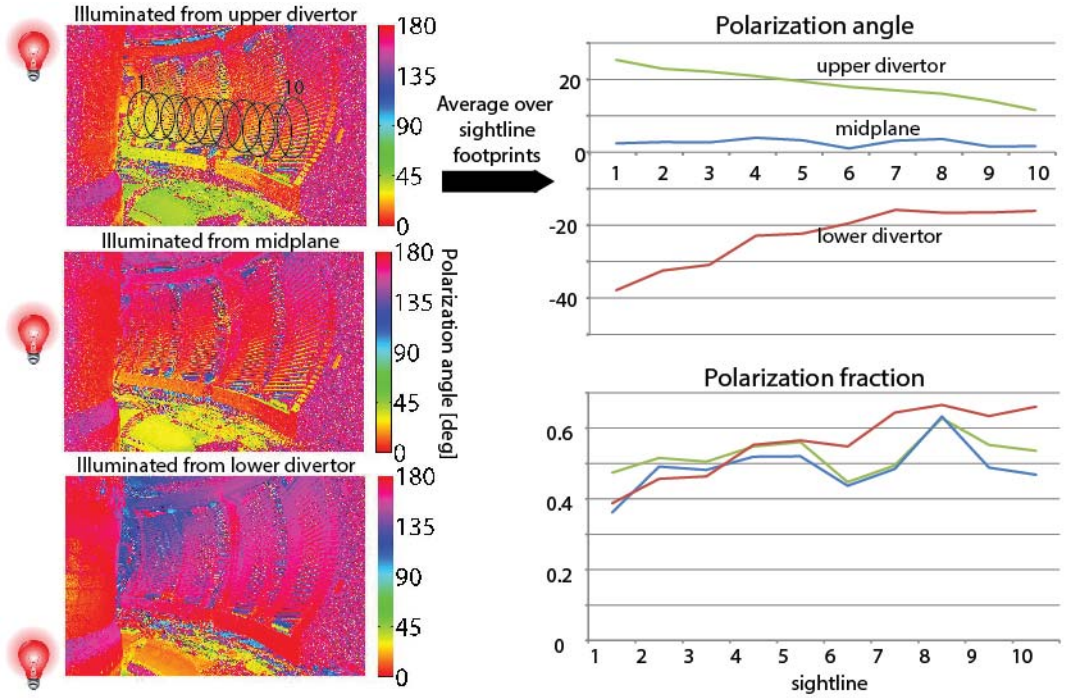

Figure 53: Images of the linear polarization angle of light reflected from the ICRF antennas from sources at different locations: from a source at the upper divertor (top left), midplane (middle left) and lower divertor (lower left). The polarization properties are Stokes component-averaged over the footprint of the MSE sightlines to obtain the polarization angle (upper right) and the polarization fraction (lower right) for each sightline from each source location.

lines each cover a large area of the antenna surface, they are actually integrating a complex spatial field (integrating in Stokes vectors).

The location of the unpolarized light source was moved in the poloidal plane to determine what effect the source location had on the polarization properties of the antenna. The results of this experiment are shown in Figure 53. There is a significant change in the polarization angle as the location of the source is changed, likely due to the change in angle of incidence. The complexity of the antenna (and its many curved surfaces) guarantees that wherever the light originates, some of it is reflected toward the MSE diagnostic. To estimate what the individual MSE sightlines would measure for the different source locations, the pixels inside each of the MSE sightline viewing footprints were summed Stokes vector-wise. As the source moves up and down, the resulting polarization angle also moves up and down. The light at the midplane produces nearly vertical polarization angles. The polarization angles are smoothly varying across the sightlines. This source-position-dependent effect can be used to locate the source of the emission in a plasma discharge via the detected light's polarization angle. All of the source positions produce reflected light with nearly the same polarization fraction. Interestingly, sightlines six and seven fall into the space between the antennas, resulting in slightly lower polarization fractions.

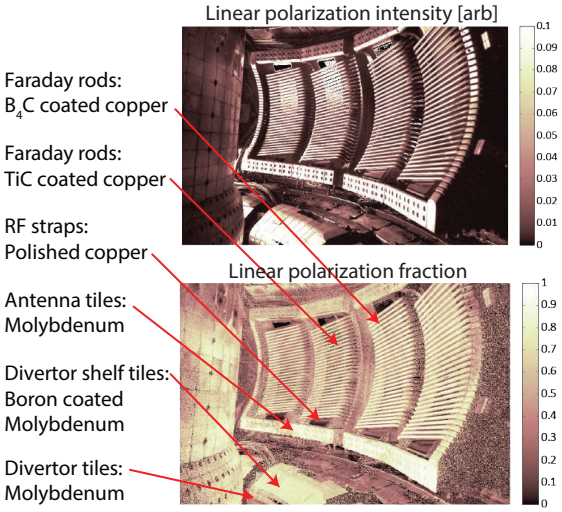

Figure 54: The total polarized intensity (top) and linear polarization fraction (bottom) of light reflected from the ICRF antennas. The different antenna components and materials are called out. It can be assumed that most of the materials have a thin layer of boron deposited on them due to wall conditioning. The pixelated black spots on the top of the antenna straps are due to saturation in the polarization camera.

Figure 54 shows the polarization intensity (top panel) and linear polarization fraction (bottom panel) from the various material surfaces on the antennas. Most of the surfaces produce significant polarized light. The dielectric coated Faraday rods create particularly bright polarized light at very high polarization fractions. The copper straps behind the rods are highly reflective (see Figure 52 panel B) but produce low polarization fractions and moderate polarization intensities. The tiles surrounding the antenna produce high polarization fraction and intensity. The boron-coated molybdenum tiles on the outer divertor "shelf" produce high polarization fractions while the stainless steel cable trays between these tiles and the antenna produce low polarization fractions. Interestingly, the light reflected from the inner wall must be a secondary reflection since these tiles do not have a direct line of sight to the unpolarized source (the only source of light in the vessel).

Essentially, the ICRF antenna view dump acts as a large polarizing reflector for any light in the tokamak. The complex geometry makes the antenna act as if it composed of many reflectors, each with a different normal direction. Thus, light from inside the vessel can enter the MSE sightline if it reflects from the proper point in the vessel from a piece of the antenna. Some of the materials are Lambertian reflectors (the Faraday rods) and some are specular reflectors (the copper straps) but most are in-between. The sources of light that can be reflected into the MSE diagnostic can be either volumetric or highly localized. Importantly, any one part of the antenna, if it reflects a bright source located just right, can dominate reflections from other parts of the antenna. **Any source of light in the MSE wavelengths inside the tokamak can dominate the MSE background.** As will be discussed in the next sections, the partially-polarized reflection from the antenna combined with a knowledge of the various sources of

light can provide a comprehensive explanation for the MSE partially-polarized background.

5.3 SOURCES CONTRIBUTING TO POLARIZED BACKGROUND

The light must originate somewhere inside the tokamak and the source must be bright in the MSE wavelengths ($658 - 662$nm). Correlations between the background polarization and other plasma parameters are used to determine the source of polarized background light. Fortunately, unlike most diagnostics, the MSE system is sensitive to the entire Stokes vector instead of only the total intensity. In practice, the time history of the background polarization expressed in terms of polarized intensity, linear polarization fraction, and polarization angle is examined and compared to other visible diagnostic signals. If a source is spatially stationary in the plasma and is polarized upon reflection, the background polarization angle is expected to also be stationary. If only one source is contributing to the background polarization, the background polarization fraction is expected to remain constant even if the polarized intensity of the background is changing. Furthermore, the polarization angle of the light can be used to determine the location of the source.

However, examining correlations has only been partly successful; most of the correlations are only partial and are only valid over short time periods. This is because the polarized background is usually composed of multiple sources, each with their own time history. The different sources are incoherent, independent, and often come from different parts of the tokamak, leading to different polarizations upon reflection. The fact that sources are differently polarized upon reflection can be used to separate and identify the sources. Recall, as the relative intensity of two orthogonally polarized sources is varied, the resulting polarized light does not change in angle until one source becomes brighter than the other, at which point the polarization abruptly changes.During this process the polarization fraction decreases and then increases again. Therefore, to identify contributions from mixed sources we look for changes in angle and polarization fraction when one source suddenly becomes dominate over another.

There is one additional complication in determining background sources: the various MSE sightlines have a different viewing chord and a different narrow bandpass spectral filter with a covariance between the two. This can be overcome using repeated discharges while moving filters between sightlines. Using these methods, targeted experiments and a database study were undertaken to identify and characterize the sources of light that contribute to the MSE background and determine when multiple sources are present. The results are summarized in the following sections in roughly the order of the

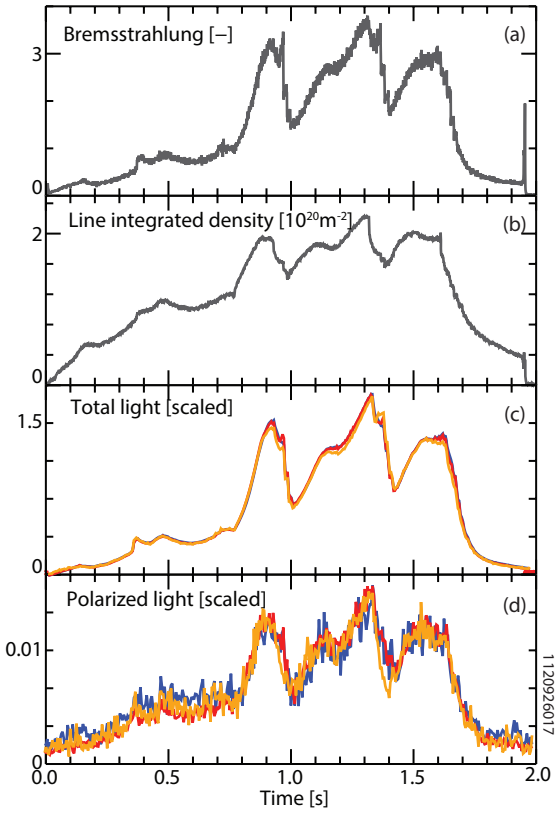

Figure 55: The contribution of visible bremsstrahlung to the MSE partially-polarized background. The signal from the Z_{eff} diagnostic measuring the bremstrahlung emission intensity (a) shows peaks due to the changes in plasma density as the plasma goes in and out of H-mode (b). The total light (c) and polarized light (d) from three MSE sightline. The MSE sightlines have been normalized to agree early in the shot.

complexity of the source and its impact on the MSE background. Details on the behavior of the various sources, further examples, other types of sources, and the methodology used to determine sources can be found in Appendix D.

5.3.1 *Visible bremsstrahlung*

The most obvious and unavoidable source of background light is visible bremsstrahlung (VB), which creates quasi-broadband light throughout the visible spectrum and is always present in the plasma. At times, the partially-polarized MSE background light appears to correlate well with the visible bremsstrahlung measurement from the Z_{eff}-monitoring diagnostic, which measures the light in an impurity-line contamination-free region in the green wavelengths. Figure 55 shows an example of a plasma with large changes in density as it transitions in and out of H-mode. It is apparent that the total light detected by the MSE diagnostic is dominated by visible bremsstrahlung. The polarized component of the light also appears to track the visible bremsstrahlung. In this case, the different sightlines have been normalized to be the same intensity early in the discharge to show relative changes. It is clear that all three sightlines, center, middle, and edge, observe nearly the same time history of total light and polarized light. The visible bremsstrahlung is seen both upon first pass

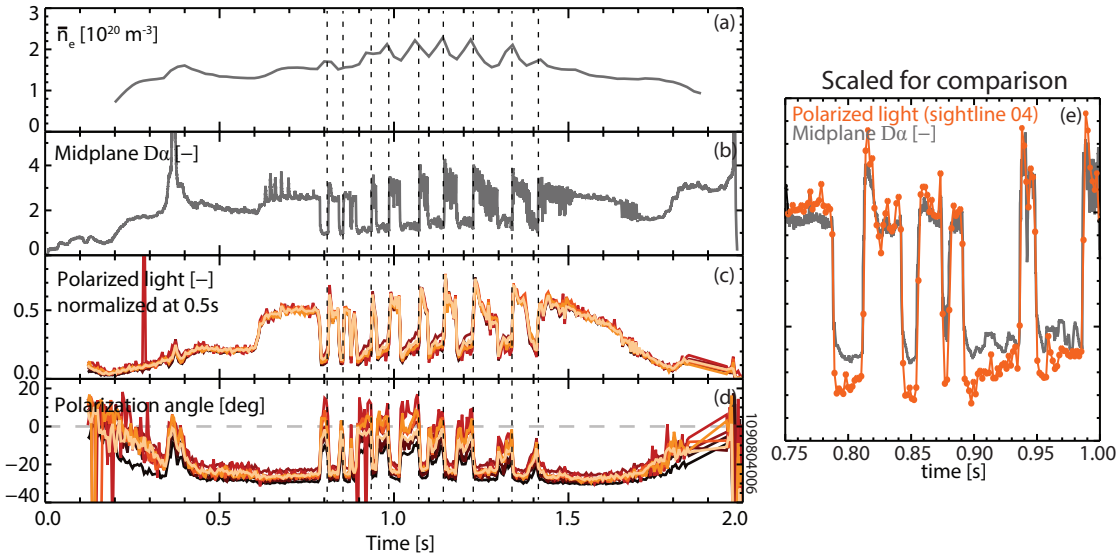

Figure 56: A lower-diverted discharge with many L to H-mode and H to L-mode transitions as indicated by the line average density (a) and midplane D_α (b) traces. The H to L-mode transitions are indicated with vertical dashed lines. The polarized light detected by the MSE system (c) and the polarization angle (d). Note the intensity is scaled to match at 0.5s. A comparison bewteen the midplane D_α (grey) and the polarized intensity from sightline 04 (orange) on the microbin timescale is shown in (e).

and upon reflection leading to a spatially-varying polarization fraction from 0.005 to 0.1 with a polarization angle consist with a source located in the middle of the poloidal plane. This is rarely the only source present.

5.3.2 *Divertor quasi-continuum*

Most times it is apparent that there is an additional source of light present that appears to be closely related to the D_α emission from the cold edge and divertor plasma. This partially polarized source has been previously noted on C-MOD [7, 9].

An example of this "D_α-correlated" source is shown in Figure 56. This plasma undergoes many transitions between L and H-mode with step changes in the midplane D_α (b). The polarized light intensity detected by MSE (c), which has been normalized at 0.5s to better show changes, has the same temporal behavior as the D_α. Note that all of the sightlines have the same behavior and nearly the same relative changes in polarized intensity at the transitions. Focusing on the time 0.75s to 1.00s (e) shows the D_α (grey) and the polarized intensity from sightline 4. It is very clear that the background follows the D_α trace during the L-mode phases when D_α is bright. The timing of the transitions is nearly identical with little to no phase lag; even bumps in wiggles in the D_α show up in the polarized intensity, particularly when the D_α is bright. Whenever the D_α and polarized intensity are high, the polarization angle is $< 20°$. When the D_α and polarized

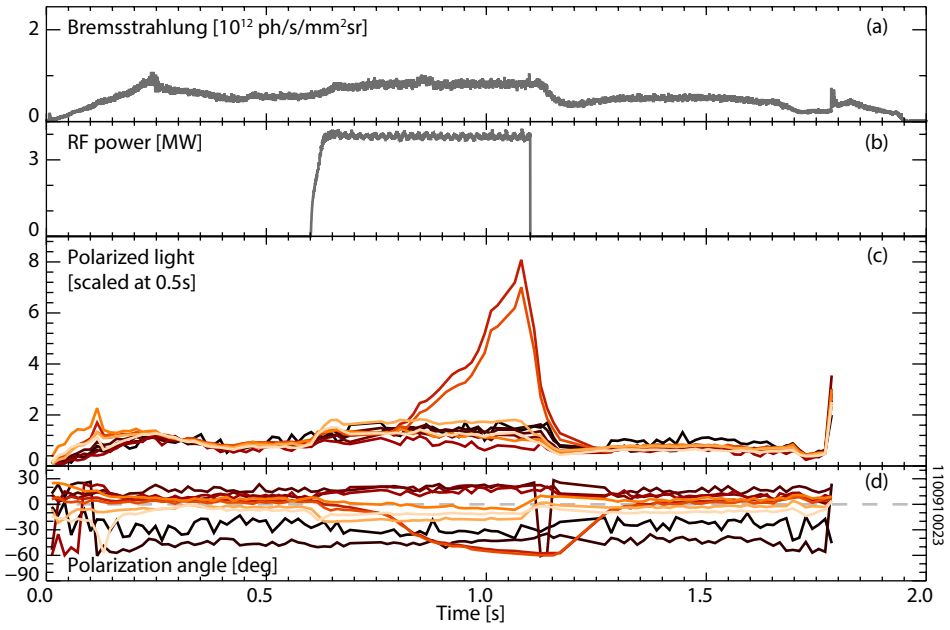

Figure 57: An example of a hot glowing surface contributing to the MSE partially-polarized background. ICRF power is applied to the plasma (b) without raising the visible bremsstrahlung appreciably (a). The polarized light detected by the MSE sightlines (c) (normalized at 0.5s to show changes). The polarization angle of the light (d).

intensity decrease, the background moves toward 0°. This behavior is very indicative of two competing sources of polarized light. This weaker source appears to be near the midplane and is likely visible bremsstrahlung.

Further studies have identified the bright source as only being present in deuterium plasmas, being located in the active divertor and MARFEs, being broadband across all the MSE wavelengths, seen mostly upon reflection. Examples of the localization and spectra of this source can be found in Appendix D. The conclusion is that this source is from molecular deuterium emission.

5.3.3 *Blackbody radiation from glowing surfaces*

Blackbody emission from hot glowing surfaces inside the tokamak can dominate the partially-polarized MSE background. This light is seen only upon reflection and can have fast time dynamics. The surfaces can become hot due to heating from plasma, heating from RF, and heating from disruptions. The highly localized nature of this light means that light from small glowing surfaces can reflect off a very small portion of the view dump, creating problems in a single MSE sightline, but not adjacent sightlines.

Figure 57 shows a discharge with significant ICRF heating where such a situation occurs. The visible bremsstrahlung stays relatively constant (a) while 4MW of ICRF power is applied (b). The polarized

light detected by two adjacent MSE sightlines suddenly increases at 0.8s (c). Note the polarized intensities have been normalized at 0.5s to show sightline-to-sightline changes. Presumably this rapid increase is caused by some plasma-facing component receiving a significant power flux making it glow. During this time, the polarization angle of these two sightlines changes significantly while the other sightlines stay fairly constant (d). After the turn-off of the ICRF, system the polarized light in these two sightlines decays exponentially, presumably because the heat flux to the component is removed and the surface starts to radiatively and conductively cool. During this cooling phase the two sightlines are no longer dominated by the reflection from the glowing surface and their polarization intensity and polarization angle return to the level prior to the heating event. The polarization angle change to more negative values during the event indicates the glowing source is likely located in the lower divertor.

5.3.4 *Other sources*

Other sources of light that can become partially polarized upon reflection have been identified. Atomic line emission from species with lines within the MSE bandpass filters can become polarized upon reflection. The most problematic species on C-MOD are neon, and to a lesser extent nitrogen. Synchrotron emission from runaway electrons can become extremely bright. It is emitted polarized and can blind the MSE diagnostic when the electrons are traveling toward the diagnostic objective lens. Fortunately, it is a rare occurrence. Other sources were considered, such as divertor bremsstrahlung, beam self-reflection, charge-exchange with impurities and fast ions, and radiation-induced fluorescence, but no evidence was found for these sources inside C-MOD.

5.4 POLARIZED BACKGROUND ON FUTURE DEVICES

On C-MOD, the problems due to background subtraction are a direct result of the relatively low density beam, the high density plasmas, the high power fluxes to the internal components, the high density divertor, and the complicated reflective view dump. C-MOD is the only machine with these characteristics with an operating MSE diagnostic[4]. As a result of these characteristics, the C-MOD diagnostic is the only system operating at such low signal-to-total-background and polarized-signal-to-polarized-background ratios (SB).

Most current devices do not have background subtraction problems because they view very bright beams and have carbon-walls that are less susceptible to reflections. However, it can be shown that future

4 TORE SUPRA was similar but that MSE diagnostic was permanently hampered by background reflections.

burning plasma devices are also likely to operate at a low polarized-signal-to-polarized-background ratio. This is because, compared to most current devices, future devices:

- Will be larger and denser and thus have lower beam penetration, even with higher energy beams.
- Will have higher energy beams and thus have lower neutral density and thus lower MSE brightness for the same beam power density.
- Will have larger Stark shifts due to higher energy beams and higher field, thus requiring wider and/or more filters to collect the MSE emission. These wider filters will also collect more background emission, lowering the SB.
- Will have higher core density and therefore significantly brighter visible bremsstrahlung emissivity from the main plasma, though the higher temperatures will counteract this to some extent.
- Will be larger, thus having longer path lengths through the plasma and thus higher visible bremsstrahlung brightness.
- Will have higher density in the divertor, leading to a divertor visible bremsstrahlung source.
- Will have higher density divertors and thus more emission from the deuterium component.
- Will have higher power densities to the divertor and other plasma-facing components and thus create more blackbody emission.
- May operate with hot walls routinely.
- Will have metallic walls and thus higher polarized reflections.
- Will not have dedicated MSE view dumps.

A comparison between measurements obtained from the DIII-D $\vec{B}$-stark system and simulations for the ITER MSE system is shown in Figure 58. The DIII-D measurement shows the beam is much brighter than the quasi-continuum background, which is likely from visible bremsstrahlung. The ITER simulation from Reference [11] shows the much stronger visible bremsstrahlung and the large Stark and Doppler shifts. On DIII-D, the π_{-3} emission is $\sim 20\times$ as bright as the continuum. On ITER, the same line is $\sim 0.5\times$ as bright as the visible bremsstrahlung simulation; a ratio similar to that observed in C-MOD. This simulation includes only the first-pass bremsstrahlung and does not include any polarization information.

A key consideration for estimating the MSE performance on future devices is the polarized-signal-to-the-polarized-background ratio, SB. On C-MOD, the SB is primarily set by the sources becoming partially-polarized upon reflection. Therefore, the reflection of sources is very important. Modeling the details of reflections is difficult, and has not

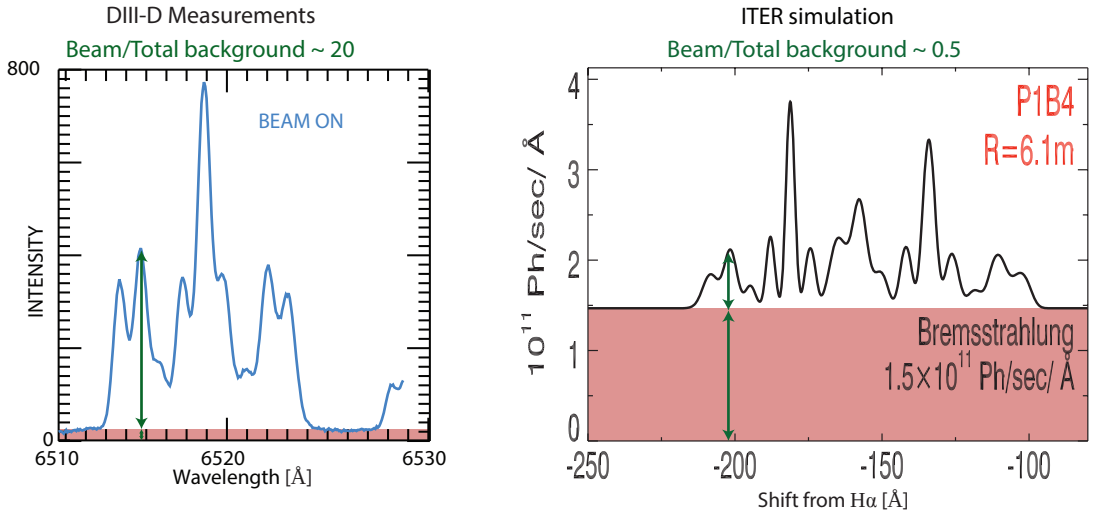

Figure 58: Measured MSE spectrum on DIII-D (left) showing the relatively high MSE to total background. Adapted from [10]. A simulated spectrum from an ITER sightline (right) showing the much lower MSE to total MSE background. Adapted from [11].

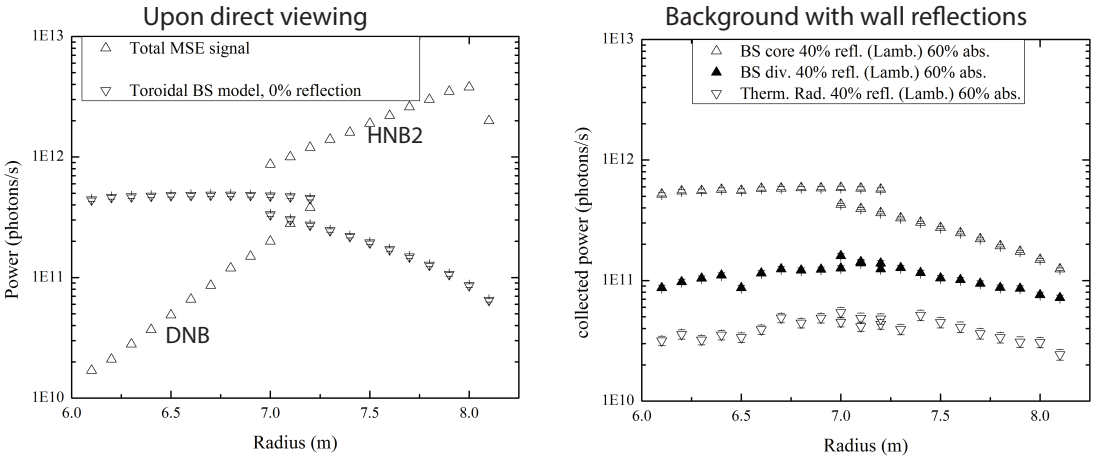

Figure 59: Simulation results for the effect of reflections on the ITER MSE viewing geometry. Adapted from [12]. The left plot shows the first pass light collection for entire MSE multiplet and the core visible bremsstrahlung (Toroidal BS model, 0% reflection) integrated over a bandpass of 0.5nm for the DNB (DNB) and heating beam (HNB). The right plot shows the intensity of background light, including wall reflections from the core visible bremsstrahlung (BS core, seen on first-pass and reflection), divertor visible bremsstrahlung (BS div., seen only reflection), and the nominal heated divertor (Therm. Rad., seen only on reflection). It is assumed that the light is 40% diffusely reflected and 60% absorbed on each reflection and the divertor emissivity is 0.2.

yet been done in a predictive manner for any existing device, partly because existing devices operate in a regime where polarized-signal-to-polarized-background is not important.

The only study to examine the reflections in a device for MSE was undertaken by von Ren who analyzed MSE for ITER [12]. This study used the numerical software LIGHTTOOLS to simulate how emission inside the tokamak reflects many times and eventually reflects into the MSE sightline. The results of the study are shown in Figure 59. The left plot shows the light collected from the beams and from the first-pass core visible bremsstrahlung. The MSE light includes the entire MSE multiplet, while the bremsstrahlung is within a 0.5nm bandpass[5]. The heating beam is more than an order of magnitude brighter than the visible bremsstrahlung at the edge of the plasma, and the total MSE emission is similar to the first-pass bremsstrahlung at the plasma mid-radius. Note that the DNB is substantially dimmer by several orders of magnitude than the visible bremsstrahlung.

The right plot shows the total background light when factoring in reflections, assuming the walls are 40 percent Lambertian reflective and 60 percent absorbing. Three different sources were examined: core visible bremsstrahlung that is approximately 10-50 percent from reflection, divertor visible bremsstrahlung that is only seen upon reflection, and thermal radiation from a 1650°C divertor that is only seen upon reflection; For all three cases, the reflected light is a similar order of magnitude as the DNB light and is approximately an order of magnitude less than the heating beam emission. Factoring in viewing only the brightest MSE σ_0 line within the 0.5nm bandpass, the system would observe $\frac{\text{signal}}{\text{reflections}} \sim 0.05$ for the core-most DNB sightlines, $\frac{\text{signal}}{\text{reflections}} \sim 0.25$ for the DNB at mid-radius, $\frac{\text{signal}}{\text{reflections}} \sim 2$ for the heating beam at mid-radius, and $\frac{\text{signal}}{\text{reflections}} \sim 10$ for the heating beam at the edge. These numbers are likely sensitive to the reflectivity of the surfaces, but can be used to obtain an order of magnitude estimate.

This study did not include any polarization effects from reflections. However, experience on C-MOD indicates that the last reflection of the light prior to its collection sets the important polarization. If the last reflection creates polarization fractions of 0.1 to 0.5, similar to that seen on C-MOD, this would create SB of $\sim 0.1 - 0.5$ for the core-most DNB sightlines, $\sim 0.5 - 2.5$ for the DNB at mid-radius, and $\sim 4 - 20$ for the heating beam at mid radius, $\sim 20 - 100$ for the heating beam at the edge. This extension of von Rens's analysis indicates that the SB is likely to require accurate estimates of the background polarization, and that measurements from the DNB may be unfeasible due to

5 In actuality, the entire MSE emission cannot be collected, instead <0.5 of it can be collected without collecting orthogonal polarizations. Furthermore, collecting an entire σ or π multiplet would not be possible within a 0.5nm bandpass. Instead, the brightest line (σ_0) could be collected, which would capture ~ 0.25 of the total MSE emission while collecting the second brightest line ($\pi_{\pm 3}$) would capture ~ 0.12 of the total MSE emission [13].

Table 9: The characteristics of the sources of partially-polarized background light that have been identified on C-MOD

Source of emission	Evidence	Spectral character	Temporal character	Spatial character	Direct or reflected
Visible Bremsstrahlung	-Correlation w/ VB diagnostics	Continuum	Slow	All sightlines	Reflected and direct
Edge and divertor deuterium emission	-He vs D plasmas -Geometry sweeps -Divertor spectroscopy	Quasi-continuum	Very fast, recycling time	All sightlines	Mostly reflected
Blackbody emission from glowing surfaces	-Light post disruption -Correlation w/ video hot spots -Exponential growth/decay	Continuum	Slow, except at peaks	Very localized	Reflected
Impurity lines (Ne I, N II, Ar II)	-Impurity puffing -Impurity spectroscopy	Broadened lines	Impurity time scale	Sightlines w/ filter overlap	Either dominant
Synchrotron emission from relativistic e^-	-Runaway e^- experiments -Startup slideaways -LHCD experiments	Continuum	Fast	All sightlines	Emitted polarized

very low SB. Even when viewing the heating beam, the measurement will be challenging due to low SB and will require estimates of the background at the level of $f < 0.1$ and $\Delta\theta_{bkgd} < 5°$.

5.5 CONSTRAINTS ON SUBTRACTION TECHNIQUES

Table 9 summarizes the character of the different sources of background light that have been identified, each of which can become dominant. The characteristics of the sources is important in constraining the technique used to estimate the partially-polarized background.

Impurity emission is avoided on C-MOD by the judicious selection of filter wavelengths and seeding gases. Runaway electron synchrotron emission is much too bright to accurately subtract. Fortunately, this source is very rare and results from unwanted, off-normal conditions that do not require an operating MSE diagnostic. Therefore, only the remaining three problematic sources: visible bremsstrahlung; a deuterium component; and blackbody emission from hot surfaces, will considered moving forward.

As apparent in Equation 48 and 51, the systematic errors due to background subtraction can be decreased by either increasing the polarized signal-to-polarized background ratio, SB, or by decreasing the error in the estimated intensity, f, and estimated angle, $\Delta\theta_{bkgd}$.

5.5.1 *Option #1: Increase SB*

Increasing the signal is extremely difficult in most devices since it is tied to the beam performance. Unfortunately, increasing the power of the beam by increasing the beam energy at fixed beam current is counterproductive, actually decreasing the beam's neutral density and resulting brightness. Furthermore, as the beam energy is increased, the Stark shift increases, spreading the same beam emission across a larger wavelength range, requiring broader spectral filters that collect proportionally more background light[6].

Decreasing the background sources is also very difficult. Visible bremsstrahlung is intrinsic, always present, and tightly coupled to the plasma scenario. The deuterium component is tied to the divertor conditions and likely scales with the divertor density. The blackbody emission is tied to the surface temperatures, which will be hot.Many future devices plan to use metals such as beryllium, tungsten, and molybdenum as plasma facing components; all these materials have significant reflectivity. On C-MOD, changes are impractical as the "view dump" is actually an important heating subsystem. In all devices, the geometry required for the MSE diagnostic likely yields a large footprint on the far wall making view dumps unlikely.

5.5.2 *Option # 2: Decrease* f *and* $\Delta\theta_{bkgd}$.

Therefore, the solution to background subtraction errors in MSE diagnostics must be to decrease the uncertainty in the estimate of the background itself, f and $\Delta\theta_{bkgd}$. Since there is almost always more than one component of the light present, no other single diagnostic can be used as a proxy. Even if there was such a diagnostic, the fact that the background must be subtracted Stokes component-wise would require that diagnostic to be polarization sensitive at the accuracy level of the MSE diagnostic.

The fastest changing source of the background light is the source that limits the applicability of time-interpolation across beam pulses. In C-MOD, this is the deuterium component that changes on an edge recycling time ($<$ 5ms), particularly during plasma transitions. **The fast temporal character of these sources requires a measurement of the background polarization in near-real time.** The fact that the polarization arises upon reflection from a very non-uniform antenna structure makes the background observation spatially-dependent. The problem is enhanced by a spatially localized source, such as small hot glowing elements, which can be reflected off of a small piece of this reflector and dominate the view. The spatial non-uniformity of the background means using offsetting views for background subtraction like is often done on CXRS systems, is likely insufficient—there is

6 Increasing the magnetic field can lead to lower SB for the same reason

no view in the tokamak that captures the same background as that seen by a MSE sightline. Therefore, **a background subtraction scheme should make the background measurement on the same sightline as the mse measurement.**

Fortunately, all three problematic sources of background polarized light have one characteristic in common: all three are quasi-continuum over the short range of wavelengths near MSE. Visible bremsstrahlung is a continuum in the visible. Blackbody emission from hot surfaces is quasi-continuum. The component related to divertor deuterium is also quasi-continuum, as evidenced by its appearance in all the MSE sightlines (though the spectral extent of the emission is unknown). Therefore, a background estimation technique based on measuring the polarization of the background on the same sightline at different spectral wavelengths may be successful.

5.6 SUMMARY: POLARIZED BACKGROUND

This chapter has explored the impact of a partially-polarized background on the MSE measurement and has described the Stokes vector method to subtract the MSE background. A key finding is that the systematic errors due to background subtraction depend on a few key parameters: the polarized-signal-to-polarized-background ratio, SB; the relative error in estimating the background polarized intensity, f; and the error in estimating the polarization angle of the background, $\Delta\theta_{bkgd}$. In MSE-LP systems with SB < 300, the background must be accurately estimated and subtracted to avoid errors at the desired measurement accuracy. At SB < 50, the background intensity and polarization angle must be estimated with an accuracy that is hard to achieve using background time-interpolation across beam modulations. MSE measurements on C-MOD are often at SB low enough that partially-polarized background subtraction becomes the dominant source of error in the measurement, particularly in situations of interest for many physics studies.

It was found that the surfaces that comprise the MSE view dump partially-polarize the light that is reflected from them. Thus, any unpolarized light emitted inside the tokamak can become partially-polarized MSE background light once reflected into the MSE sightlines. The polarization-inducing properties of the spatially complex view dump were explored. All of the materials present in the view dump are partially-polarizing at some level, and the polarization fraction and polarization angle of the reflected light depends on the angle of incidence of light incident on the view dump.

The various sources of light that contribute to the partially-polarized MSE background were determined by examining instances when one source dominates the other sources as indicated by the properties of the light's partial-polarization. Several important sources were iden-

tified including visible bremsstrahlung, molecular emission from the divertor, hot glowing components, and atomic line emission. These sources place constraints on the methods used to estimate the background. The background must be measured on the same sightline in real-time with the MSE measurement.

C-MOD is relatively unique among current devices due to its low SB ratio. However, future devices are likely to have low SB and therefore better methods to estimate the background are desired.

BIBLIOGRAPHY

[1] R. De Angelis, F. Orsitto, M. Baruzzo, P. Buratti, B. Alper, L. Barrera, A. Botrugno, M. Brix, K. Crombe, L. Figini, et al. Determination of q profiles in JET by consistency of Motional Stark Effect and MHD mode localization. *EXS*, 2:03.

[2] R. Coelho, D. Alves, N. Hawkes, M. Brix, and JET EFDA Contributors. Real-time data processing and magnetic field pitch angle estimation of the JET motional Stark effect diagnostic based on Kalman filtering. *Review of Scientific Instruments*, 80(6):063504, 2009.

[3] T. Fujita, H. Kuko, T. Sugie, N. Isei, and K. Ushigusa. Current profile measurements with motional Stark effect polarimeter in the JT-60U tokamak. *Fusion Engineering and Design*, 34-35:289–292, March 1997.

[4] T. Suzuki and T. Fujita. Impact of edge localized mode on photoelastic-modulator based motional stark effect polarimetry. *Fusion Engineering and Design*, 87(2):188–194, February 2012.

[5] Ph. Lotte, M. H. Aumeunier, P. Devynck, C. Fenzi, V. Martin, and J. M. Travére. Wall reflection issues for optical diagnostics in fusion devices. *Review of Scientific Instruments*, 81(10):10E120, 2010.

[6] C. T. Holcomb, M. A. Makowski, S. L. Allen, W. H. Meyer, and M. A. Van Zeeland. Overview of equilibrium reconstruction on DIII-D using new measurements from an expanded motional Stark effect diagnostic. *Review of Scientific Instruments*, 79(10):10F518, 2008.

[7] J. Ko. *Current profile measurements using Motional Stark Effect on Alcator C-Mod*. PhD, Massachusetts Institute of Technology, 2009.

[8] R. Mumgaard. Development of a Polarization Camera. Technical Report PSFC/RR-15-8, MIT PSFC, May 2015.

[9] H.Y. Yuh. *The Motional Stark Effect diagnostic on Alcator C-Mod*. PhD, Massachusetts Institute of Technology, 2005.

[10] N. A. Pablant, Beam-on MSE spectrum in DIII-D without beam-off subtraction. Private communication, 2014.

[11] E. L. Foley, F. M. Levinton, H. Y. Yuh, and L. E. Zakharov. The motional Stark effect diagnostic for ITER using a line-shift approach. *Review of Scientific Instruments*, 79(10):10F521, 2008.

[12] FM van Rens Jasper. *LightTools simulations on the effect of reflections of bremstrahlung and thermal radiation on the ITER MSE signal*. Masters, Eindhoven University of Technology, 2013.

[13] Hans A. Bethe and Edwin E. Salpeter. *Quantum mechanics of one- and two-electron atoms, by Hans A. Bethe and Edwin E. Salpeter*. Berlin, Springer; New York, Academic Press, 1957., 1957.

6

MULTI-SPECTRAL LINE POLARIZATION (MSE-MSLP)

- Describe wavelength-interpolation background subtraction and its associated hardware
- Demonstrate the advantages of this background subtraction technique
- Describe how system can be expanded by measuring other lines within the MSE multiplet
- Discuss how this approach applies to future devices

The previous discussion of polarized background inside the tokamak motivates better techniques to estimate the polarization properties of the background. Due to the complexity of the polarized light inside the tokamak this estimation must be done on the same sightline and at the same time as the polarization measurement. However, the sources that contribute to the background light were identified as being quasi-broadband in the MSE wavelengths.

6.1 WAVELENGTH-INTERPOLATION BACKGROUND ESTIMATION

Figure 60 shows a schematic of the different sources of light in the MSE spectral region. A new technique is proposed to measure the polarization of the light at multiple wavelengths on the same MSE sightline simultaneously; the typical MSE measurement and measurements at "proxy" wavelengths adjacent to the MSE emission. When the beam is firing, the background under the MSE emission can be estimated in real time using measurements at these "proxy" wavelengths just to the red and blue of the beam emission. In fact, these proxy measurements could be wavelength-interpolated to determine the MSE background. The estimate in the background then becomes:

$$\begin{bmatrix} I \\ Q \\ U \\ V \end{bmatrix}^{\text{estimate}}_{\text{bkgd}} = C_{\text{red}} \begin{bmatrix} I \\ Q \\ U \\ V \end{bmatrix}_{\text{red proxy}} + C_{\text{blue}} \begin{bmatrix} I \\ Q \\ U \\ V \end{bmatrix}_{\text{blue proxy}} \tag{52}$$

where the coefficients C_{red} and C_{blue} are constant in time while the Stokes vectors themselves change significantly. In this formulation, the Stokes vectors for the blue and red proxy have already had the

gains of the detectors and any relative transmissions of the different optical paths accounted for—coefficients C_{red} and C_{blue} represent the correlation between different wavelengths.

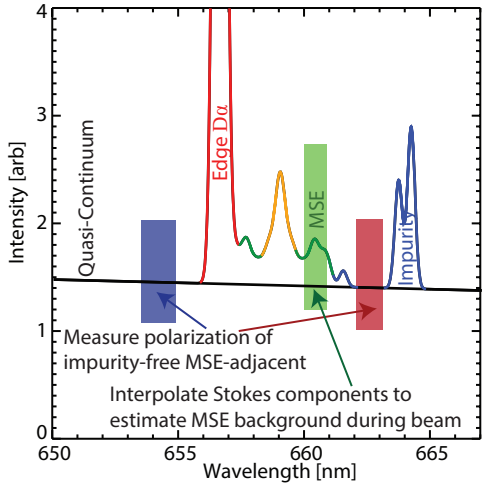

Figure 60: In a multi-wavelength scheme, the background is measured at wavelengths free of impurity emission to the red and blue of the beam emission and is used to estimate the background under the MSE emission in real-time using wavelength-interpolation.

The advantage of this technique over time-interpolation is that the multi-spectral technique only assumes the spectral shape of the emission changes slowly instead of assuming that the absolute intensity of the emission and its polarization changes slowly. This assumption is well satisfied for most sources (aside from atomic lines). **A multi-spectral approach could be executed in real-time and on the exactly same sightline as the mse measurement by spectrally splitting the light from the sightline.** Such a system does not require a different front-end optical system, instead it reuses the optical periscope, PEMS, and fibers which are the primary cost drivers for an MSE-LP system. The multi-spectral technique only requires changing the detector to a new system capable of recovering the polarization of the light in the same manner as the MSE measurement at different wavelengths simultaneously. A similar concept was carried out on JT60-U, where a half-slivered mirror was used to examine the polarization at 649nm to subtract the background from the beam [1] for a few isolated sightlines.

The key assumptions for this technique are that the polarizing mechanism for the background emission is wavelength-independent and that the background sources can be treated as quasi-continuum over the narrow wavelength range covered by the MSE and proxy filters. Polarization by reflection satisfies the first criterion across small wavelength ranges. The second criterion implies the spectral shape of the emission is important—the coefficients C_{red} or C_{blue} capture the spectral slope in this region. The simplest multi-spectral estimation technique uses only one proxy measurement. This requires an assumption that the background spectral shape is constant in time.

A more robust technique uses a proxy measurement on each side of the MSE wavelengths for that sightline, requiring only that the background spectrum be linear in the narrow wavelength range of interest. In this case, the weight coefficients C_{red} and C_{blue} may be equal or inversely proportional to the spectral distance between the MSE channel and each proxy. In principle, the same weighting can be applied to the entire Stokes vector or the weighting could be component-dependent. A constant weighting would be ideal, but it also may be possible to update the weightings during a discharge using comparisons to the actual MSE background during beam-off periods. The rest of this sec-

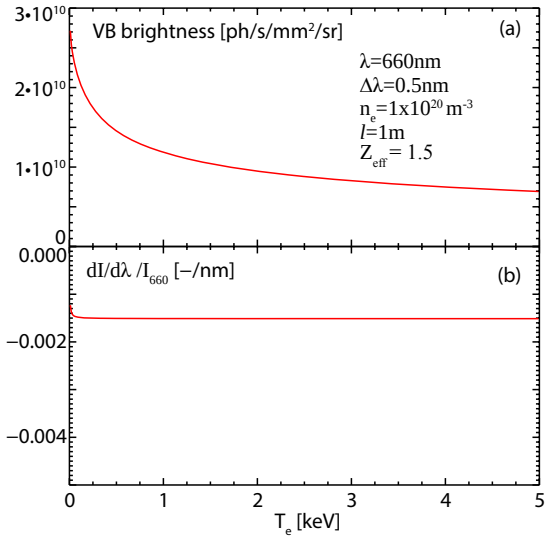

Figure 61: The brightness of visible bremsstrahlung at 660nm as a function of electron temperature for a plasma density of $1e20m^{-3}$ and a 1m chord length (a). The normalized slope of the spectrum at 660nm as a function of electron temperature.

tion will focus on how well the intensity at a given wavelength can be approximated by the intensity at adjacent wavelengths.

The spectral shape can be calculated analytically for two of the important sources: visible bremsstrahlung and blackbody emission. The quantity of interest is the derivative of the intensity with respect to wavelength at 660nm normalized by the intensity at 660nm, $\frac{dI}{d\lambda}/I_{660}$. A zero derivative would mean a measurement at an adjacent wavelength perfectly matches a measurement at 660nm. If this derivative is independent of plasma conditions and source combinations, then only one proxy measurement is required. If this derivative changes with plasma conditions, then it is important to know by how much. It is therefore important to know how this normalized derivative varies between the sources, as this will impact how different combinations of sources change the spectral shape.

The visible bremsstrahlung emission spectrum is [2]:

$$\epsilon_{VB} = 2.39x10^{-22} g \frac{n_e^2 Z_{eff}}{\lambda_{nm} T_{e\,keV}^{1/2}} \exp\left(\frac{-1.24}{\lambda_{nm} T_{e\,keV}}\right) \tag{53}$$

Where ϵ_{VB} is the emissivity of the plasma in $^{photons}/_{s\ sr\ m^3\ nm}$, n_e is the plasma electron density in m^{-3}, λ_{nm} is the wavelength of interest in nm, $T_{e\,keV}$ is the electron temperature in keV, and g is the Gaunt factor, usually between 3 and 4 for most fusion plasmas. The emissivity is line-integrated through the plasma along the sightline to obtain a brightness:

$$B_{VB} = \int_{sightline} \epsilon_{VB} dl \tag{54}$$

Figure 61 shows brightness of visible bremsstrahlung at 660nm for a constant density of $1e20m^{-3}$ with a chord length of 1m (a) and the

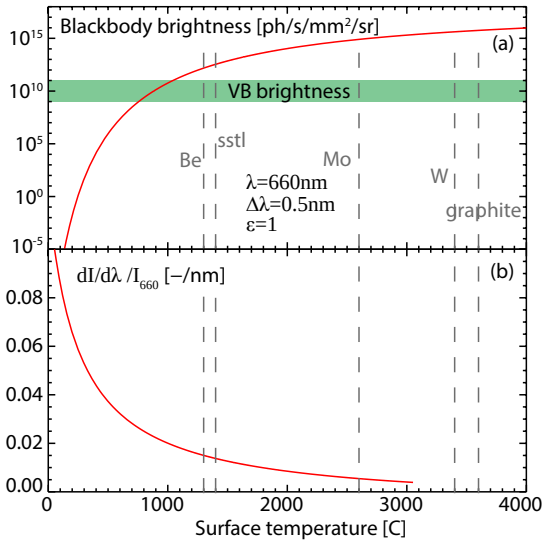

Figure 62: The brightness of blackbody emission at 660nm as a function of surface temperature (a). The visible bremsstrahlung brightness for a 1keV, $1 \times 10^{20} m^{-3}$, 1m chord length plasma is shown as the shaded box for comparison. The normalized slope of the spectrum at 660nm as a function of surface temperature (b). The melting temperatures of several common plasma-facing materials are indicated by vertical dashed lines.

normalized slope of the visible bremsstrahlung spectrum at 660nm ($\frac{dI}{d\lambda}/I_{660}$) (b) as a function of electron temperature. This calculation ignores the recombination edges, which are far enough from the MSE emission to be neglected (Balmer at 365nm and Paschen at 891nm). The assumption of constant spectral shape across plasma parameters is well satisfied by the visible bremsstrahlung emission, which has a normalized spectral slope near zero and is independent of plasma conditions in the regime of interest. Therefore, measuring the visible bremsstrahlung at even a single proxy wavelength within 10nm of the MSE light is likely sufficient to estimate the visible bremsstrahlung contribution at the MSE wavelengths to high accuracy.

The assumption of a weak spectral shape is less well satisfied for blackbody emission. Planck's law shows that the blackbody emission brightness is:

$$B_{BB} = \frac{5.97x10^{35}}{\lambda_{nm}^4} \frac{1}{\exp\left(\frac{1.439x10^7}{\lambda_{nm} T}\right) - 1} \tag{55}$$

Where B_{BB} is the brightness of the hot surface in $^{photons}/_{s\ sr\ m^2\ nm}$, λ_{nm} is the wavelength of interest in nm, and T is the surface temperature in K. For a gray body the brightness is multiplied by the emissivity.

Figure 62 shows the brightness of a blackbody at 660nm (a) and the normalized slope of the blackbody spectrum at 660nm ($\frac{dI}{d\lambda}/I_{660}$) as a function of surface temperature (b). The brightness of the visible bremsstrahlung from the previous example is shown as a horizontal shaded region, and the melting temperatures of various plasma facing materials are indicated. Note that there is significant variation in the normalized spectral slope since the blackbody spectrum shape and peak depends strongly on temperature. However, the brightness of the source is very weak and does not compete with the first pass

bremsstrahlung until ~ 700C. In reality, a small glowing element is likely to dominate the view, which would require the source to be several orders of magnitude brighter than bremsstrahlung. This would require temperatures in excess of 1500C, at which point the normalized slope is closer to zero. The many indications of surface melting on the stainless steel LHCD launcher, and molybdenum divertor and limiter tiles in C-MOD indicate that very high temperatures do occur in the vessel. Note that the slope becomes zero when the peak in blackbody emission coincides with the MSE wavelengths, which occurs at 4120C—higher than the melting point of any material.

The spectral shape is fairly weak for both of these sources, so a single nearby proxy wavelength can be used to estimate the MSE background to within $< 10\%$ if that proxy is within ~ 5nm of the MSE measurement. However, problems arise if higher accuracy is required and the mix of visible bremsstrahlung and blackbody emission is varied. Since the spectral derivatives are different for the two sources, changing the mix would modify the effective slope of the spectrum. For example, the slope would change from $\frac{dI}{d\lambda}/I_{660} = -0.001^{-}/_{nm}$ to $\frac{dI}{d\lambda}/I_{660} = +0.02^{-}/_{nm}$ as a 2000C surface emitter became dominant over visible bremsstrahlung. If a single proxy measurement 5nm away is used, this would lead to $f = 0.095$, which would limit the measurement to $SB > 25$. To compensate, the estimates for C_{Red} or C_{Blue} could be updated by normalizing during beam-off periods, though this is not as desirable. A better approach is to field proxy measurements at wavelengths on each side of the MSE emission. Two proxy measurements can then be used to obtain the spectral slope of the emission directly, thus mitigating simple changes in the shape of the background spectrum. The two proxy measurement technique should be able to estimate the contribution from these two sources very accurately.

Unfortunately, the source of the background emission that scales like D_α is not definitely known, so its spectral shape over the wavelength range that might use as a proxy measurement is uncertain. However, this source appears nearly equally-strongly in all the MSE wavelengths, indicating that the source is quasi-continuum, an observation confirmed using divertor spectroscopy. The spectrally monotonic assumptions used with two proxies needs to be tested for this source component. This test was performed using a proof-of-principle experiment and a prototype system. The key indicator is how well the MSE background can be estimated using proxy wavelengths over plasma transitions when the source that correlates with D_α is changing rapidly.

6.1.1 *Proof of principle experiment*

To test how well the proxy wavelengths follow the MSE wavelength a simple proof-of-principle multi-spectral experiment was conducted.

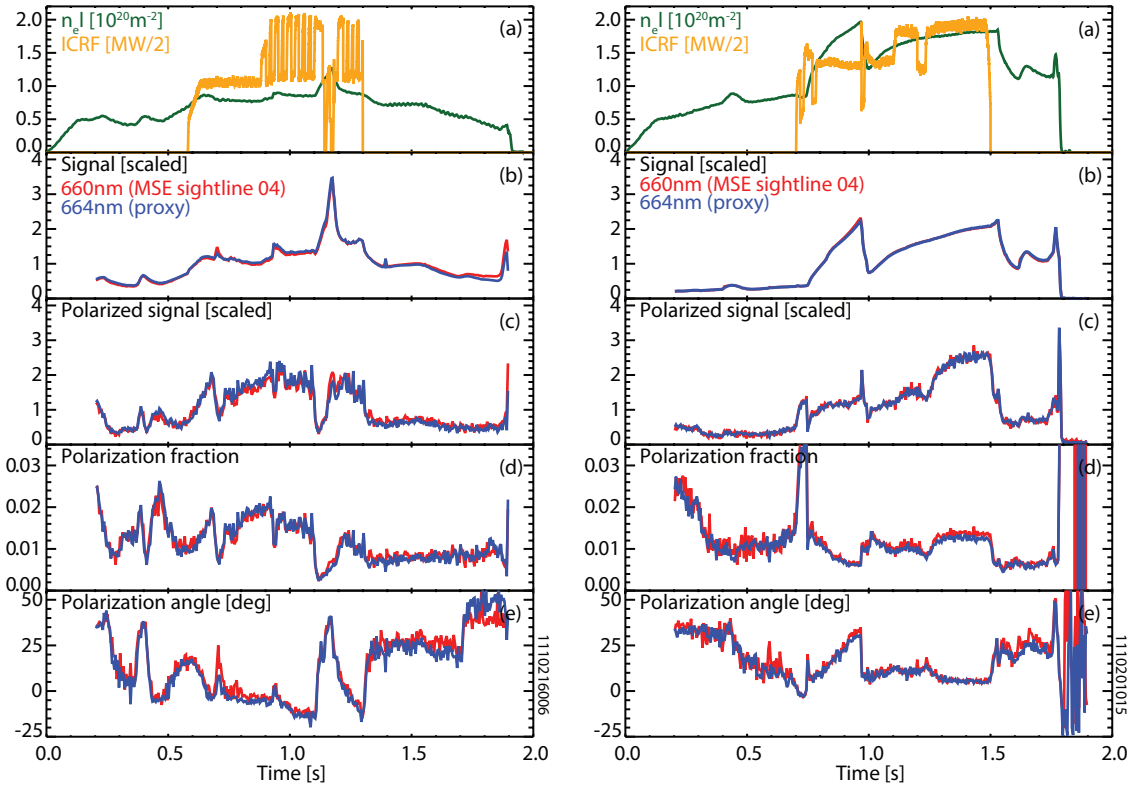

Figure 63: Two proof-of-principle tests to determine how well the polarization correlates at adjacent wavelengths. The discharges have varying densities (a, green, line-integrated) and faulty ICRF power (a, orange). The polarization measurements are shown for a sighline with a fiber bundle split into two different filter and APD assemblies. One filter observes the actual MSE background (red) while another observes a proxy at 664nm (blue). The total light (b) and polarized light (c) have been scaled to obtain system gains using a period early in the discharge. The polarization fraction (d) and polarization angle (e) are unscaled.

A 16-fiber bundle for a single MSE sightline was split into two bundles of eight randomly selected fibers. One bundle was input into a filter and APD assembly containing the typical MSE filter for that sightline. The other bundle was input into another detector assembly with a filter heated so that the center wavelength was at 664nm (the furthest redshift achievable with the given filter set) to act as a proxy measurement. The tests were done without puffing argon to avoid the strong impurity line under this filter. In this way the polarization could be simultaneously measured on *nearly* the same sightline at two spectral locations 4nm apart. The goal was to determine how well the polarization correlates across wavelengths, especially across large transients in the background, on nearly the same sightline.

The results are shown in Figure 63 for two representative discharges with high heating power, multiple ICRF faults, and multiple plasma mode transitions. It is apparent that the proxy measurement (blue) follows the MSE (red) measurement very well despite large changes in line-integrated density (a, green) and faults in the ICRF power (a,

orange). The total light (b) and polarized light (c) have each been normalized so the proxy and MSE match at times early in the shot to obtain A_{red}. The polarization fraction (d) and polarization angle are not altered and show that the proxy has the same polarization properties as the MSE measurement for these two discharges.

6.2 POLYCHROMATOR FOR MULTI-WAVELENGTH POLARIZATION DETECTION

The preceding sections have described the concept of wavelength-interpolation and have shown that the background polarization agrees across part of the wavelength range in a proof-of-principle experiment. The next step is to build an instrument capable of replacing the current MSE detector system with one that can measure the polarization at multiple wavelengths on the same sightline simultaneously. The requirements for such a multi-spectral MSE detector system are:

1. The system should be able to detect three or more different wavelengths on the same sightline, two for proxy measurements, and one or more for MSE measurements.
2. The system should have good spectral selectivity (i.e., it should be able to select a bandpass of $\sim$ 0.5nm FWHM with transmission $>$ 50 percent).
3. The system should discriminate between very closely spaced, and possibly overlapping, spectral regions and the wavelength should be tunable.
4. The detection system should be compatible with the existing MSE analysis workflow, which uses the PEM harmonics to determine the Stokes vectors.
5. The system should be optically fast, allowing the full étendue of the MSE sightline ($\sim$ 9mm^2 sr) to be passed to each detector and should be non-vignetting.
6. The system will be located in the diagnostic lab, replacing the existing MSE detectors and not require changes to upstream optics.
7. The system should be easy to construct and maintain and should low cost since each sightline requires its own multi-spectral detector.

Various instrument concepts for spectrally splitting the light were considered. Dispersion-based systems were ruled out due to the need for a such a large étendue, the need to use APD detectors, and the flexibility required to tune the spectral positions. Half-silvered mirrors which were ruled out because of their in-efficient use of photons—they lose a substantial amount of light with each additional

spectral bin. Dichroic mirror or beamsplitter-based geometries were ruled out due to their inability to split closely spaced spectral regions. Collecting the light reflected by the filter and using fibers to transfer it to other filters was ruled out because this would have significant vignetting.

The chosen instrument is an interference filter-based "polychromator." This concept uses matched relay lenses and field mirrors to sequentially re-image light from fiber optics placed at an input port through narrow-bandpass interference filters placed within a slightly skewed ($< 5°$) optical cavity. Light within each interference filter passband passes through the filter and is imaged onto a plane at an output port where the APD detector is placed. Light outside each filter passband is reflected from the filter and is re-imaged onto the next interference filter. This is repeated for as many interference filters/detectors as desired by extending the skewed cavity. In this manner, the optical system efficiently transfers the image of the fiber onto each APD with carefully controlled spectral filtering.

6.2.1 *Polychromator design*

Though similar in concept, this polychromator is substantially differs in important ways from typical polychromators used for Thomson scattering. It passes an order of magnitude higher étendue, has a smaller skew angle which enables better filter performance, is imaging, and incorporates ovens to tune the filters. The polychromator designed for MSE is discussed in depth in Reference [3] and is summarized here. The polychromator layout is shown in Figure 64. The cavity has a 3° skew angle. Light from the fiber ferrule is collected by an objective lens that creates a real image at high magnification at the first field mirror. The field mirror re-converges the light toward the first interference filter, which has a relay lens directly in front of it. The field mirror focal length is such that the objective lens is imaged onto the first relay lens. The relay lens collimates the light, which is then incident on the interference filter directly behind the lens. The light that is rejected by the interference filter, which is still collimated, is re-imaged on the next field mirror by the same relay lens acting in double pass. Thus, the second field mirror has an image on it just like the first field mirror, but with a spectral region "missing." The process then repeats for each leg of the polychromator cavity. Light that is transmitted through the filter is then focused onto an image plane by a condensing lens. Therefore, a filtered image of the fiber ferrule is created at each detector surface. This image is at a magnification of ~ 0.5 allowing a relatively small APD surface area to decrease costs.

The small skew of the cavity and the small angle of incidence on the filters are very important because they allow the instrument to achieve the desired interference filter bandpass narrowness and trans-

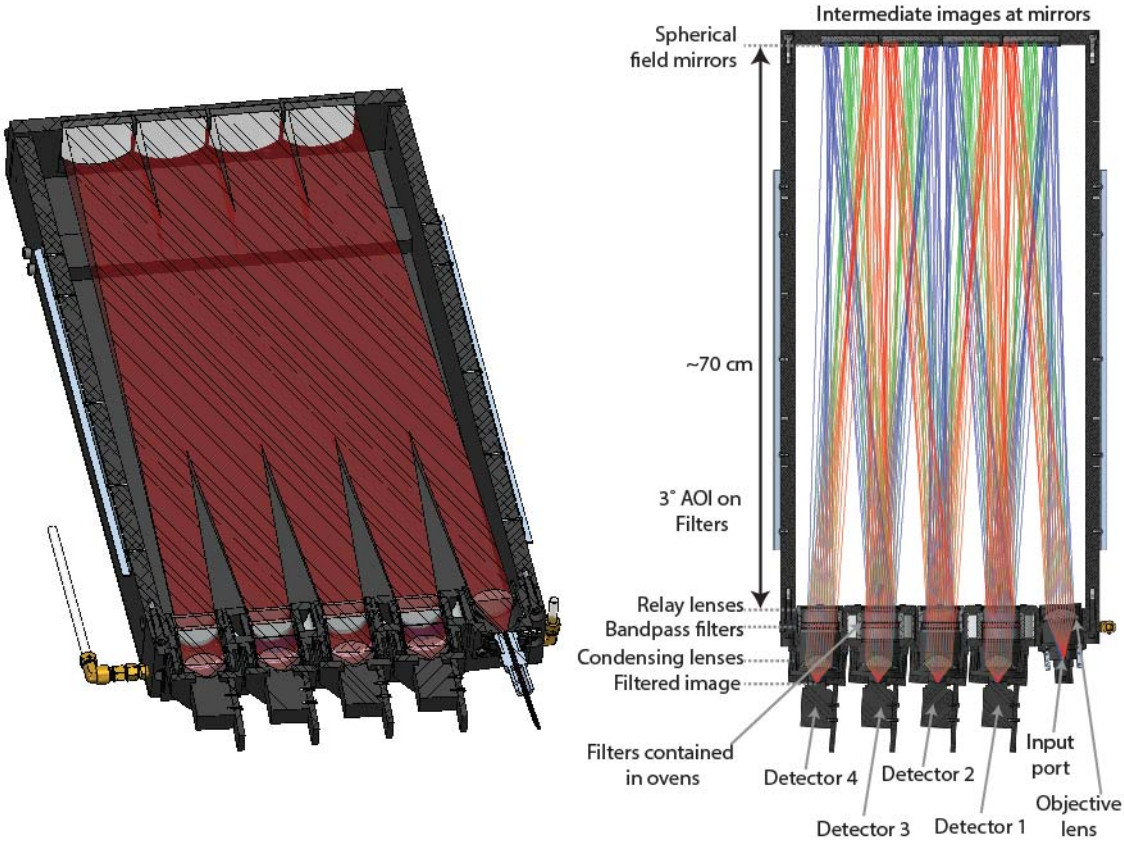

Figure 64: The mechanical model for the polychromator (left). The light path (red) fills the space, traversing back and forth between the mirrors and filters. The optical layout with components labeled (left). The different colored rays correspond to different locations on the fiber ferrule face at the input port and are overplotted from a ray-tracing code.

Figure 65: A photograph of the completed polychromator with the top cover of the cavity removed. The four spherical curved field mirrors are apparent at the far end of the cavity. The input port with a fiber bundle attached is at the lower left and three APDs are attached to the first three of the four output ports.

mission. The use of the filters sequentially allows the filters to be placed spectrally very close to one another, or even overlapping in wavelength as opposed to using branching dichroic mirrors. The filter design also incorporates adequate blocking of the D_α line. The filters are contained in custom ovens that are used to tune the filter bandpass wavelength by changing the filter temperature. APD detectors are used for each wavelength and are digitized and analyzed in the same manner as the traditional MSE detection system. The use of large optics (50mm diameter) allows a large étendue to be passed through the polychromator (~ 15mm² sr). The relay lens and field mirror layout are non-vignetting; only reflection and transmission losses are present, which are managed with high quality mirror coatings and non-reflective coatings for the lenses. The system replaces the existing detectors in the lab and accepts the MSE fiber ferrule. By taking only a small portion of the spectrum and passing the rest to the next detector, the system is very photon efficient—better utilizing the front-end optics. Careful consideration was given during the opto-mechanical design to make the system easy to manufacture, install, align, and maintain.

6.2.2 *Implementation*

To evaluate the multi-spectral polarization technique, a single sight-line, four wavelength, prototype polychromator was constructed and various filters were collected from other laboratories to examine the polarization in the MSE spectral region. A photograph of the prototype system is shown in Figure 65. Aligning the system was straightforward, and it was verified that the system does not vignette. The measured port-to-port transmission loss of 4% is consistent with the number of optical surfaces involved. New APDs were purchased and compared with existing APDs showing similar performance.

As will be discussed in Section 6.4, the polychromator has filters for two simultaneous measurements within the MSE spectrum in addition to the two proxy measurements. This enables measurement of the

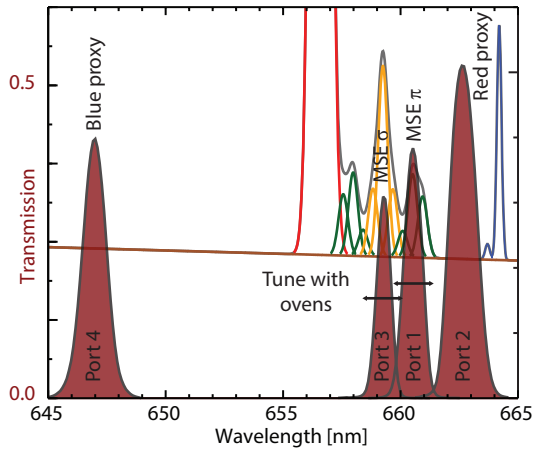

Figure 66: The polychromator filters transmission were measured in-situ in the skewed cavity (red shaded). They are overplotted on a simulated spectrum of the MSE emission and background. The filters dedicated to measuring MSE σ and MSE π can have their wavelengths temperature-tuned ±0.9nm using the custom filter ovens installed in the polychromator.

MSE π and MSE σ simultaneously for increased signal as well as for a check on the systematic polarization errors. The filter passbands were measured in-situ and are shown in Figure 66 along with a schematic of the MSE emission.

6.3 PERFORMANCE EVALUATION

The prototype polychromator was operated for several experimental run days at the end of the FY12 C-MOD experimental campaign. Due to digitizer limitations and analysis code inflexibilty, the polychromator replaced four sightlines of traditional MSE. Thus, it was not used for the MSE pitch angle measurement directly but was instead used to evaluate how well the wavelength-interpolation scheme estimates the MSE partially-polarized background. During this experiment, various filters were swapped in and out and heated to observe different portions of the spectrum.

Figure 67 shows the polychromator operating in a plasma with several H-modes (left) and several I-modes (right). Panel A illustrates the wavelengths observed by the different detectors with the traces colors corresponding to the shaded regions. Panel B displays the total light, panel C shows the polarized light, panel D and E show the stokes components Q and U, panel F shows the polarization fraction and panel G shows the polarization angle. In each case, the coefficients C_{red} and C_{blue} are determined for the entire Stokes vector using the linearly polarized intensity from time 0.9s to 1.1s. From these traces it is apparent that the polarization of the four different wavelengths agree very well. The spectral region with the least agreement is furthest to the blue, $>$ 15nm from the other measurement wavelengths. Even in this case, the polarization tracks very well across all the spectral regions.

The polarization correlation across the spectral region was examined by swapping various filters into the polychromator and observing discharges with different gases puffed into the plasma. The re-

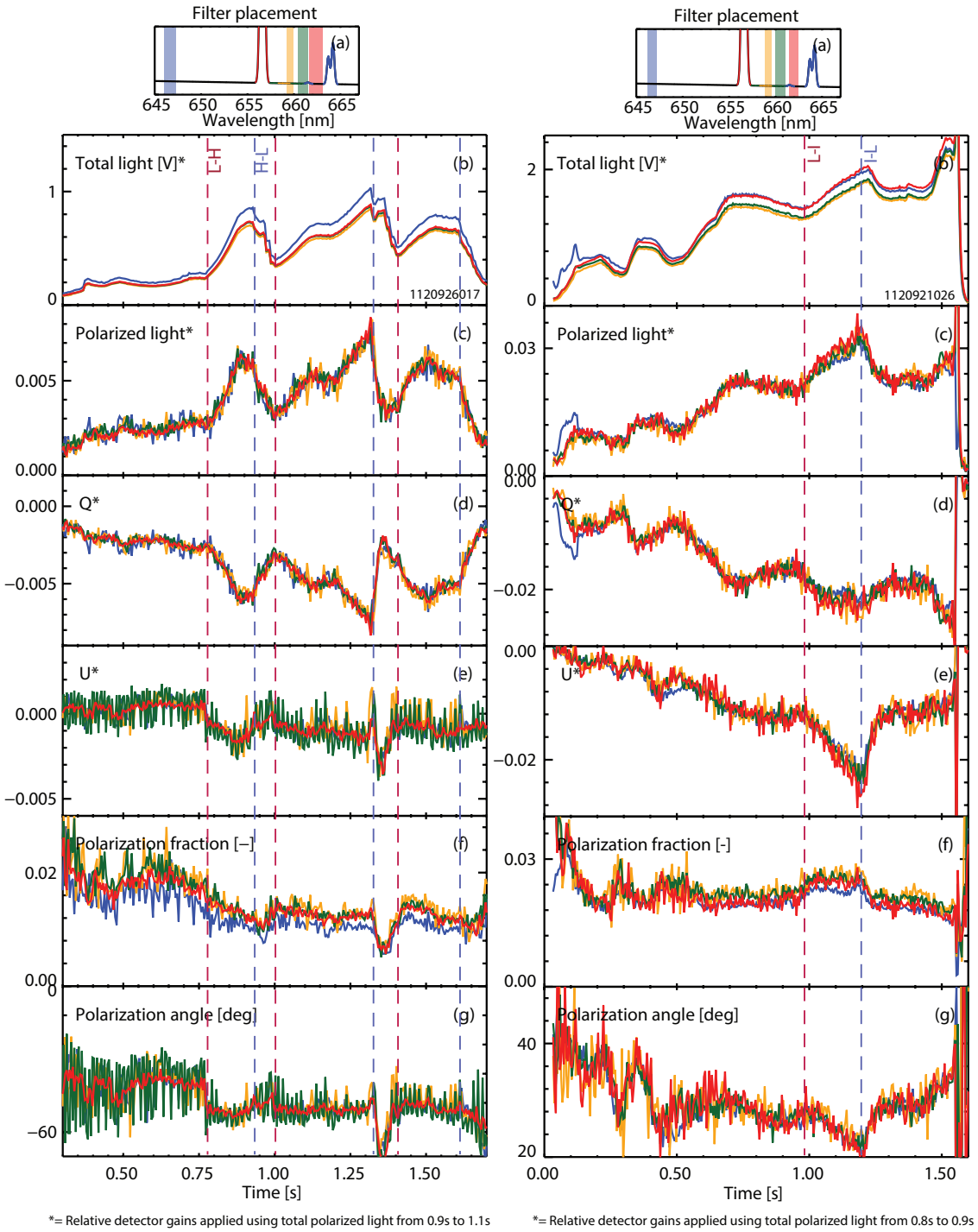

Figure 67: Example traces from the polychromator for shots with multiple transitions between L-, I-, and H-modes. Panel A shows the filter placement with the trace colors corresponding to the shaded regions. Panel B shows the total light, panel C shows the polarized light, while panels D and E show the Q and U Stokes components of the polarized light, respectively. These components have been normalized at the noted times to obtain the detector-to-detector gains. Panels F and G show the polarization fraction and polarization angle of the different wavelength bins, respectively. The transitions between different confinement modes are indicated as the vertical dashed lines.

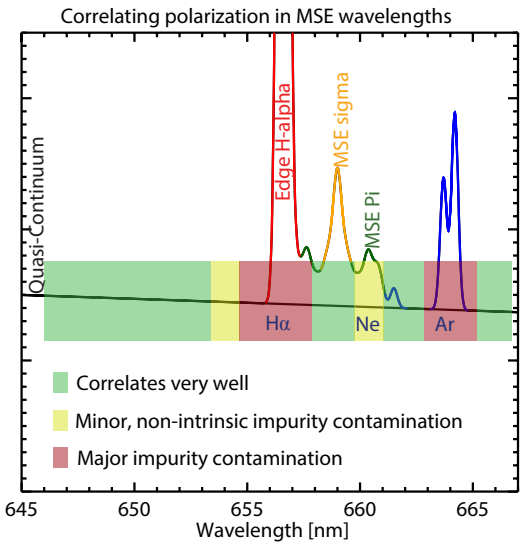

Figure 68: The polarization in different spectral regions as measured by swapping various filters into the polychromator. Regions that correlate well with eachother are shown in green, regions to be avoided are shown in red and regions that have some minor impurity contamination are shown in yellow. A simulated MSE spectrum and quasi-continuum background are shown for reference.

sults are shown in Figure 68 with a simulated MSE spectrum overplotted. There are several spectral regions to the red and blue of the MSE emission that are free of impurities and correlate well, though care must be taken to avoid strong impurity emission, particularly due to argon at 664nm. There is also some weak neon emission under the MSE wavelengths that may cause problems during seeding experiments.

To determine how well the background can be estimated an algorithm was developed that calculates the relative misestimate of the background intensity, f, and angle, $\Delta\theta_{bkgd}$, for both the time-interpolation scheme and the multi-wavelength scheme for direct comparison. This technique is applied to discharges without beam pulses where the actual MSE background can be measured. Instead of an actual beam pulse where the background would be unknown, ersatz beam pulses are used. The process is shown in Figure 69.

The background intensity and polarization angle is straight-line time-interpolated across each ersatz beam pulse to estimate how well time-interpolation estimates the background. The time-interpolated background is subtracted from the actual MSE background measurement, yielding a residual. The misestimate in angle, $\Delta\theta_{bkgd}$, is simply the residual. The relative misestimate of the intensity, f, is calculated by dividing the residual by the actual value of the background at each time point within the beam pulse. Each result is averaged over the ersatz beam pulse to yield a mean value of f and $\Delta\theta_{bkgd}$ for the time point at which that ersatz beam pulse is centered. The standard error in f and $\Delta\theta_{blgd}$ is also calculated for the ersatz beam pulse. This is repeated for each microbin time-point throughput the discharge for a total of ~ 200 different values.

A background estimate using wavelength-interpolation is also constructed for each ersatz beam pulse. For this test the the coefficients

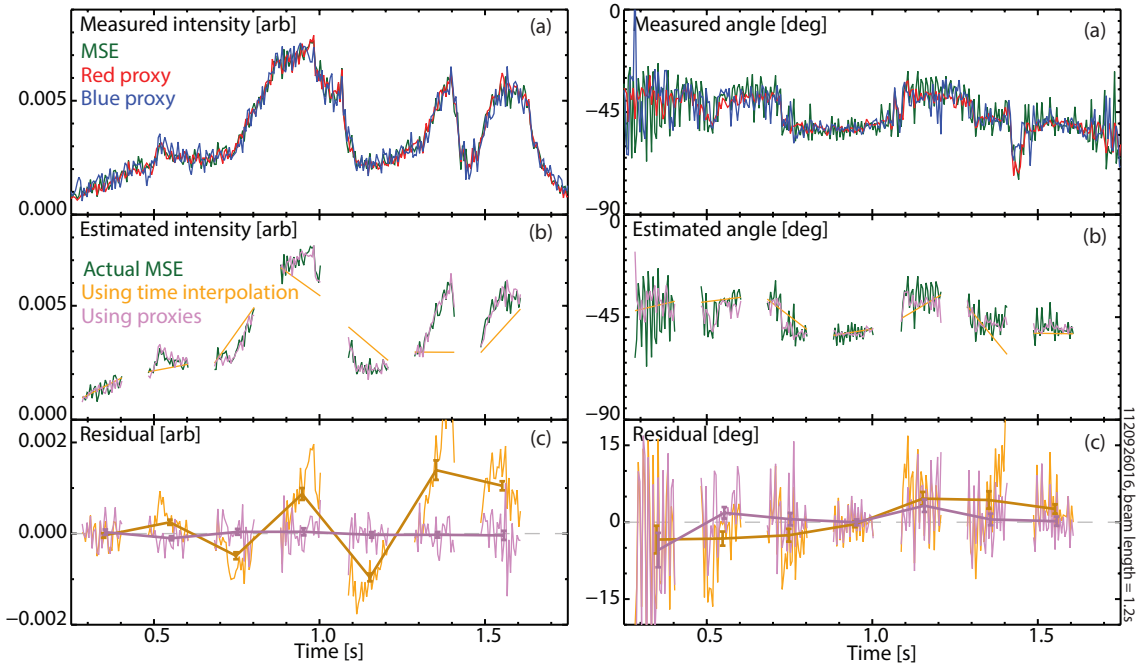

Figure 69: Example of the methodology used to determine the accuracy of the wavelength-interpolation background estimate. The polarized intensity (left) and polarization angle (right) measured at the MSE and two proxy wavelengths (a). Ersatz beam periods are used to estimate the accuracy of the two different background estimation techniques. The intensity and angle during the beam pulse are estimated using time and wavelength-interpolation and compared to the actual background (b). The residuals from the two techniques are calculated (c).

C_{red} and C_{blue} are chosen to be equal. The relative detector gains are calculated by normalizing to a period within the discharge; this normalization is found to not vary discharge-to-discharge. The reconstructed background intensity and angle using the proxy measurements is subtracted from the actual MSE background measurement to yield a residual. The relative misestimate in polarization intensity, f, and polarization angle, $\Delta\theta_{bkgd}$, and their standard errors are calculated during each ersatz beam pulse in the same manner as in the time-interpolation case.

The process and result for an example discharge is shown in Figure 69, which shows seven of the ~ 200 possible ersatz beam pulses. The polarized intensity and polarization angle of the MSE and proxy wavelengths match very well across the entire discharge (a). The estimated background intensity using time-interpolation does not agree for most of the shown ersatz beam pulses (b). The intensity estimated using wavelength-interpolation matches the background very well for each beam pulse, following fast changes in the background. This agreement is apparent in the small residuals (c). The time-interpolated residual is much larger than the wavelength-interpolation residual. The wavelength-interpolation residual is centered at zero within the standard error of each beam pulse, indicating this misestimate is not statistically different than zero. The time-interpolated residual usually differs from zero by several standard errors. The difference in performance between the time-interpolation and wavelength-interpolation for the polarization angle is smaller than for the intensity, probably because the polarization angle varies less in magnitude and more slowly than in time than the intensity.

Figure 70 shows the calculated f and $\Delta\theta_{bkgd}$ using both the time-interpolation and wavelength-interpolation estimation technique. Each data point represents a single ersatz 0.1s long beam pulse throughout this sample discharge. The relative misestimate in the intensity (b) and misestimate in the polarization angle (c) are shown. The time-interpolation technique has large and systematically varying misestimates (orange). Whenever the background intensity changes its time derivative, f—as calculated from time-interpolation—increases substantially. The discharge-averaged absolute value of the relative misestimate is $< |f| >= 0.14$, though there are excursions that are up to $f > 0.5$. The average absolute value of the angle misestimate is $< |\Delta\theta_{bkgd}| >= 2.7°$, though this value can be $> 10°$ for some ersatz beam periods. The standard error of f and $\Delta\theta_{bkgd}$ during each beam pulse are shown as shaded regions, which represents roughly the photon statistical level. The background estimate is usually systematically wrong; the standard error does not capture the magnitude of the misestimate.

The wavelength-interpolation technique has systematically low misestimates of the background (violet); f is very close to zero. The vari-

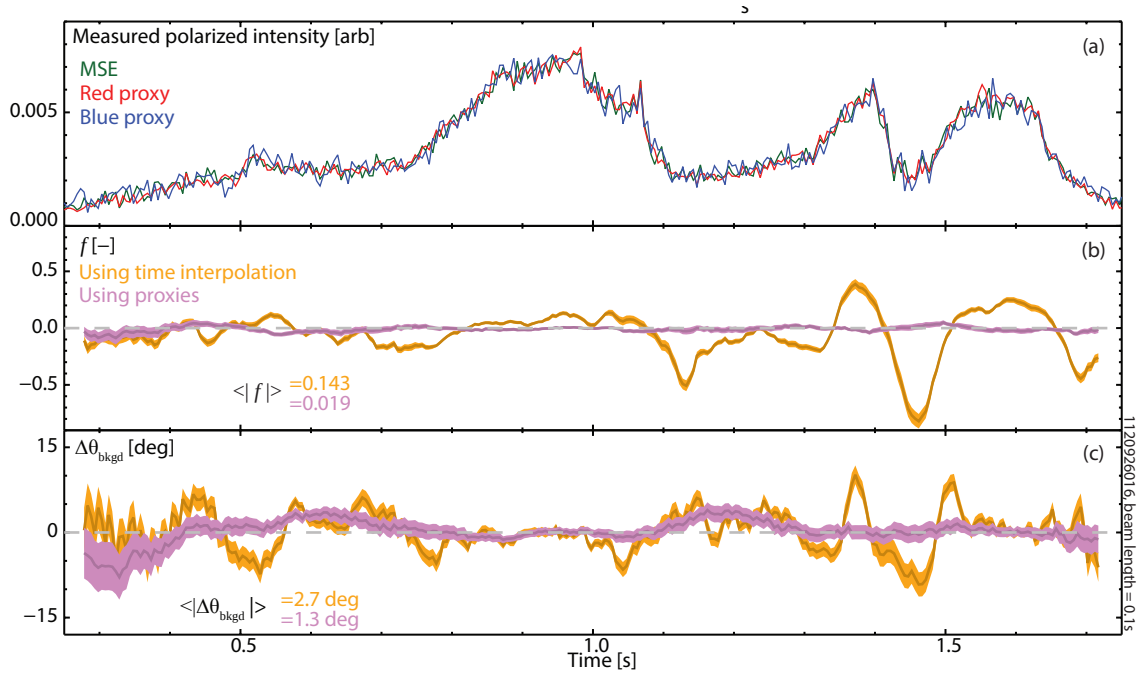

Figure 70: The measured polarized intensity of the MSE background and proxy wavelengths (a). The relative misestimate in the polarized intensity, f, from time-interpolation and wavelength-interpolation (b). The misestimate in polarization angle $\Delta\theta_{bkgd}$ (c). Ersatz beam pulses lasting 0.1s are used in this calculation. The shaded regions are the ± 1 standard error for the quantity within a each single ersatz beam pulse.

ability time-point-to-time-point in f is similar to the standard error of f within a beam pulse, indicating that f is not statistically different than zero. The same is true for the misestimate of the background angle. The discharge-averaged magnitude of the relative misestimate of the intensity is $< |f| >= 0.02$, and the magnitude of the misestimate of the angle is $< |\Delta\theta_{bkgd}| >= 1.3°$. This represents a factor of 7 and 2 improvement in the background estimate relative to time-interpolation on this discharge. With this performance, a polarized-signal-to-polarized-background ratio of SB = 10 could be tolerated and still produce polarization angles with uncertainties less than 0.1°.

Figure 71 shows the relative misestimate of the background intensity and the misestimate of the polarization angle for time-interpolation and wavelength interpolation as a function of the polarized background level for this discharge. Because the wavelength-interpolation technique is photon limited, it becomes more accurate at higher polarized background levels. This feature is very important, allowing for more accurate background estimates—and more accurate background subtraction—as the polarized-signal-to-polarized-background ratio decreases. The wavelength-interpolation estimate is least accurate at the lowest signal levels, but even then is almost within a standard error of zero.

The polychromator was operated for several run days during the campaign to evaluate its performance across a variety of plasmas.

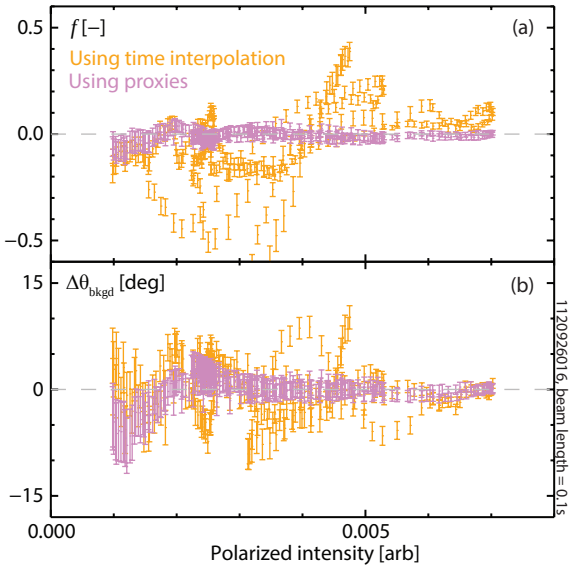

Figure 71: The relative misestimate in background intensity (a) and misestimate in the polarization angle (b) for time-interpolation and wavelength-interpolation with a 0.1s ersatz beam length for the same discharge shown in Figures 69 and 70.

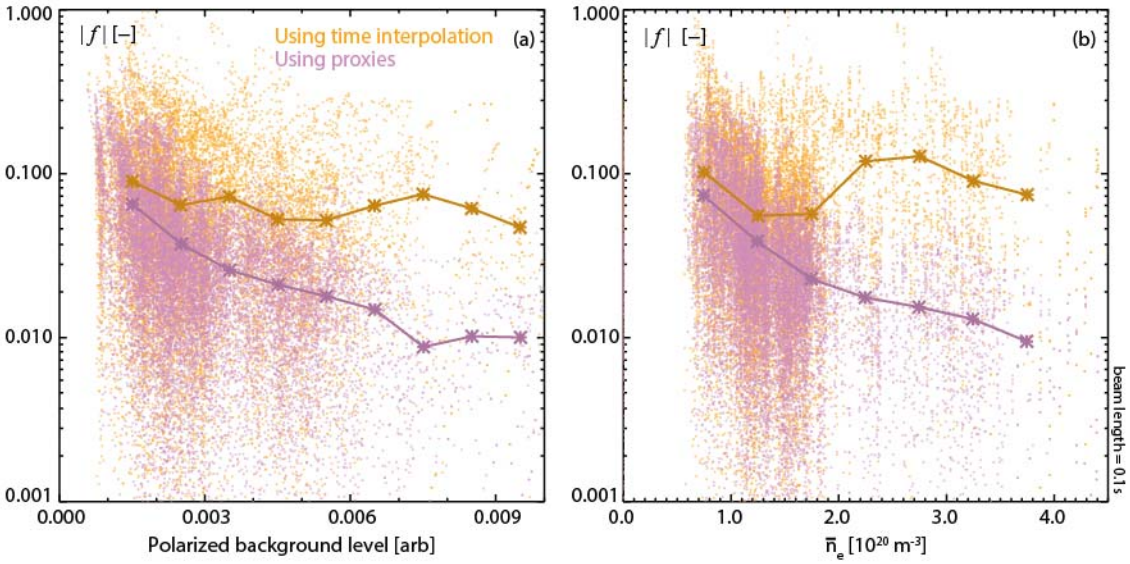

Figure 72: The magnitude of the relative error in estimating the polarization intensity vs. polarized background polarized (left) and plasma line averaged density (right) using both the time-interpolation estimate of the background and the wavelength-interpolation technique.

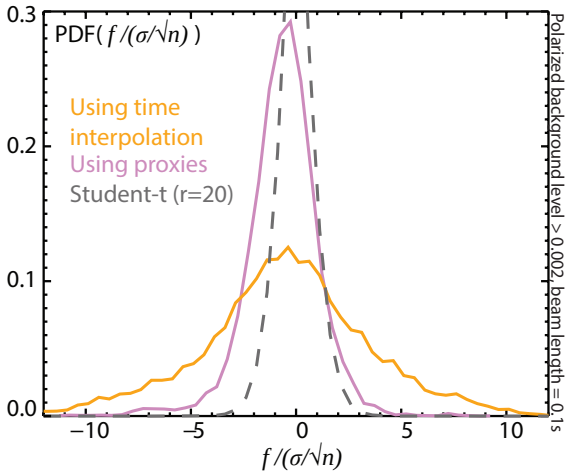

Figure 73: The probability distribution of $\frac{f}{\sigma/\sqrt{n}}$ for the two methods to estimate the background. The student-t expectation for 20 degrees of freedom is overplotted.

The results for each possible ersatz beam pulse in ~ 40 discharges are shown in Figure 72. The results are plotted to show the polarized background intensity (left) and a related quantity, the plasma line averaged density (right). The results are binned by background level and density, and the averages for the bins are overplotted. The time-interpolation technique produces nearly the same misestimate of the background, independent of background level or density. This is because the error in time-interpolation depends mostly on how variable the background is and not on how bright the background becomes. Note that there are some points where the background intensity is misestimated by nearly 100 percent. The wavelength-interpolation scheme performs substantially better for nearly all conditions. The wavelength-interpolation technique reduces the misestimate by a factor of ~ 10 decrease in the misestimate at both high background levels and high line-averaged densities. Significantly, the wavelength-interpolation scheme performs best at the highest background levels, exactly where high quality background subtraction is needed.

Not only does wavelength-interpolation perform better at estimating the background intensity and angle, it also performs much better at estimating the uncertainty in this estimate. As previously shown, the time-interpolation technique often misestimates the background well outside of the standard error derived within a beam pulse. In contrast, the wavelength-interpolation scheme rarely reports f or $\Delta\theta_{bkgd}$ outside of the standard error of the data used to calculate the mean value. Figure 73 shows the probability distribution function of f divided by the standard error in f for both types of background estimates. The student-t distribution function for 20 degrees of freedom is also shown.

It is apparent that the wavelength-interpolation technique produces a narrower probability distribution than the time-interpolation technique. The fact that the wavelength-interpolation technique's probability distribution function is nearly the same width as the student-

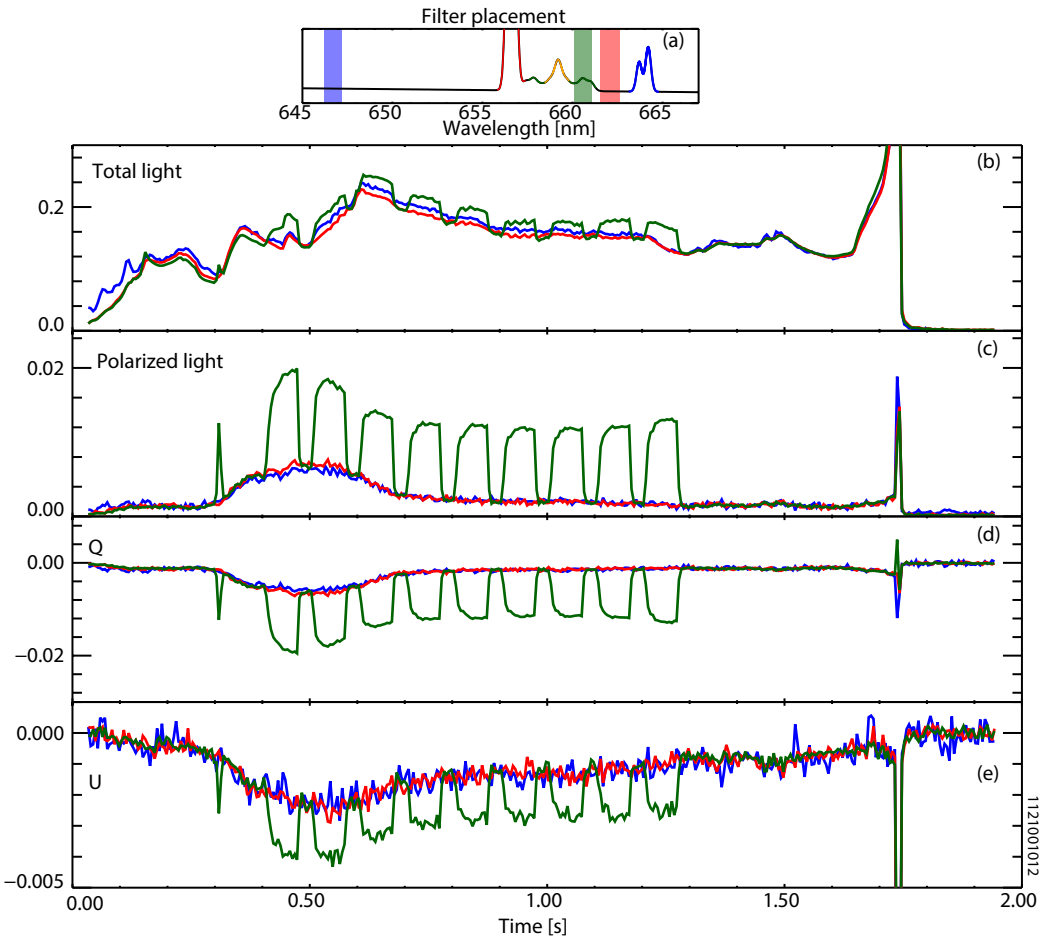

Figure 74: An example of firing the beam into the plasma while using proxy wavelengths to measure the background. The filter placement is shown in panel A, note the green trace is observing the MSE π emission for this sightline. Panels B, C, D, and E show the total light, polarized light, Q, and U respectively.

t distribution indicates that the variability in the mean f is nearly within the standard error of the data used to calculate each mean f. Thus any error in estimating the background will have the proper uncertainties propagated to the measured beam polarization angle when the mean error of that signal is calculated. The time-interpolation technique has a much wider distribution function with a large fraction of the mean f falling more than five standard errors away from zero. In this case, errors from estimating the background will not be properly propagated to the uncertainty in the polarization angle using statistical means. Note that both estimates are nearly centered at zero, indicating it is almost equally likely to overestimate the background as it is to underestimate it. The fact that the wavelength-interpolation scheme is statistically well-behaved likely indicates that the technique is operating near the photon-limit; the estimate of the background is limited by the random fluctuations in the proxy and background measurements. This would also explain why this method performs better as the light level is increased, as shown in Figure 72.

To fully illustrate the multi-spectral MSE technique, the beam was fired into plasma for a few discharges with the polychromator observing both the beam emission and the two proxy wavelengths. An example is shown in Figure 74. Note that when the beam is not firing, the polarization at the MSE wavelengths agrees with the polarization measured at the proxy wavelengths. When the beam fires, these proxy measurements provide the background Stokes components throughout the pulse. In this case, the individual Stokes components were normalized at the end of the shot to obtain the detector-to-detector gains.

6.3.1 *Beam-modulation is no longer required*

The MSE-MSLP technique provides an estimate of the MSE background in real-time. Therefore, a real-time MSE measurement including accurate background subtraction is possible. This could have implications for future experiments where the MSE diagnostic will be used to provide information for real-time magnetic reconstruction in environments with low SB. If the gains of the detectors in the polychromators are stable and two proxies are used then the background can be estimated accurately from the proxy wavelengths without comparing to the actual MSE background during beam-off periods. This condition is satisfied within the previously discussed database study of wavelength-interpolation. If the background itself does not need to be measured during beam-off periods the beam can be operated in a continuous mode.

The methodology used to estimate f and $\Delta\theta_{bkgd}$ across the database of C-MOD discharges is used to examine how long the beam pulses could be extended and still provide accurate background estimates. The length of the ersatz beam pulses within the discharge is increased from 0.05s to 0.95s and the shot-averaged magnitude of f and $\Delta\theta_{bkgd}$ are calculated using both the wavelength-interpolation and the time-interpolation techniques. The results are shown in Figure 75 for eight representative discharges that went in and out of H-mode. It is immediately apparent that the wavelength-interpolation technique is nearly independent of beam length and even benefits from longer beam lengths (likely due to increased photon counting in each beam pulse). This indicates the polarization between different wavelengths is highly correlated in the same way throughout the discharge. As would be expected, the time-interpolation technique provides progressively worse background estimates as the beam pulse is lengthened, becoming useless for beam lengths longer than $\sim$ 0.1s. In no case does the time-interpolation technique out-perform the wavelength-interpolation technique, even at the shortest beam pulses.

The usefulness of avoiding modulating the beams is limited on C-MOD since the low power DNB does not affect the plasma and other

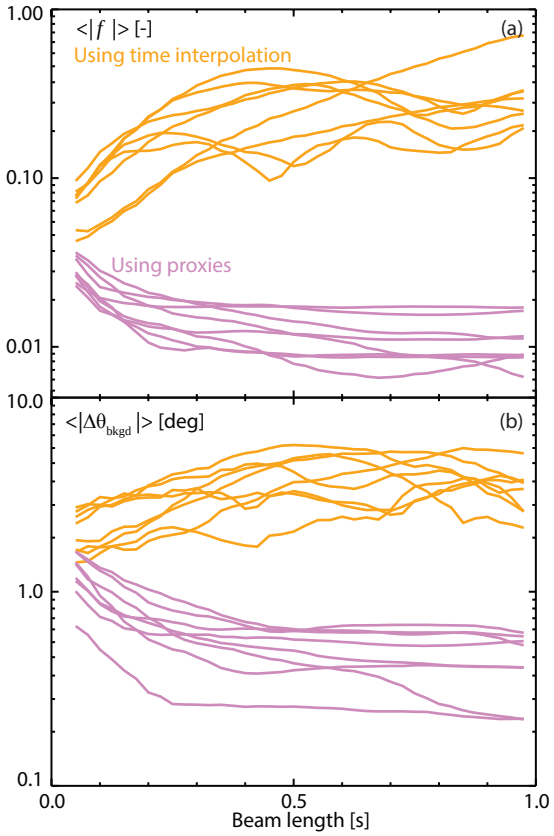

Figure 75: The shot averaged magnitude of f (a) and $\Delta\theta_{bkgd}$ (b) as a function of the length of the ersatz beam pulses for 8 H-mode discharges.

diagnostics require it to be modulated for their background subtraction schemes. Additionally, the DNB operates best when modulated; the beam current decreases as the beam length is extended. However, the ability of MSE to operate without beam modulation is important for systems which observe a heating beam, which is the case for most existing and planned future devices.

6.4 SIMULTANEOUS MEASUREMENT OF σ AND π

One key advantage of the multi-spectral MSE technique is the ability to measure both the MSE σ and π emission simultaneously on the same sightline using the same front-end optics and fiber links. The obvious advantage is an increase in signal collection; two MSE channels with almost no up-stream changes to the system. When the upper states are statistically populated, the MSE σ is approximately twice as intense as each MSE π triplet to each side of it (averaged over all observation angles). In reality, the $\frac{\sigma}{\pi}$ ratio can be as low 1.2 on some fusion devices and is closer to 1.8 even at C-MOD densities [4]. The ratio is also dependent on the viewing geometry. Thus, simultaneous collection offers an increase of $\sim 50-80$ percent in signal collection for systems already measuring the MSE σ and an increase of $\sim 120-180$ percent for systems, such as C-MOD, that currently observe the MSE π.

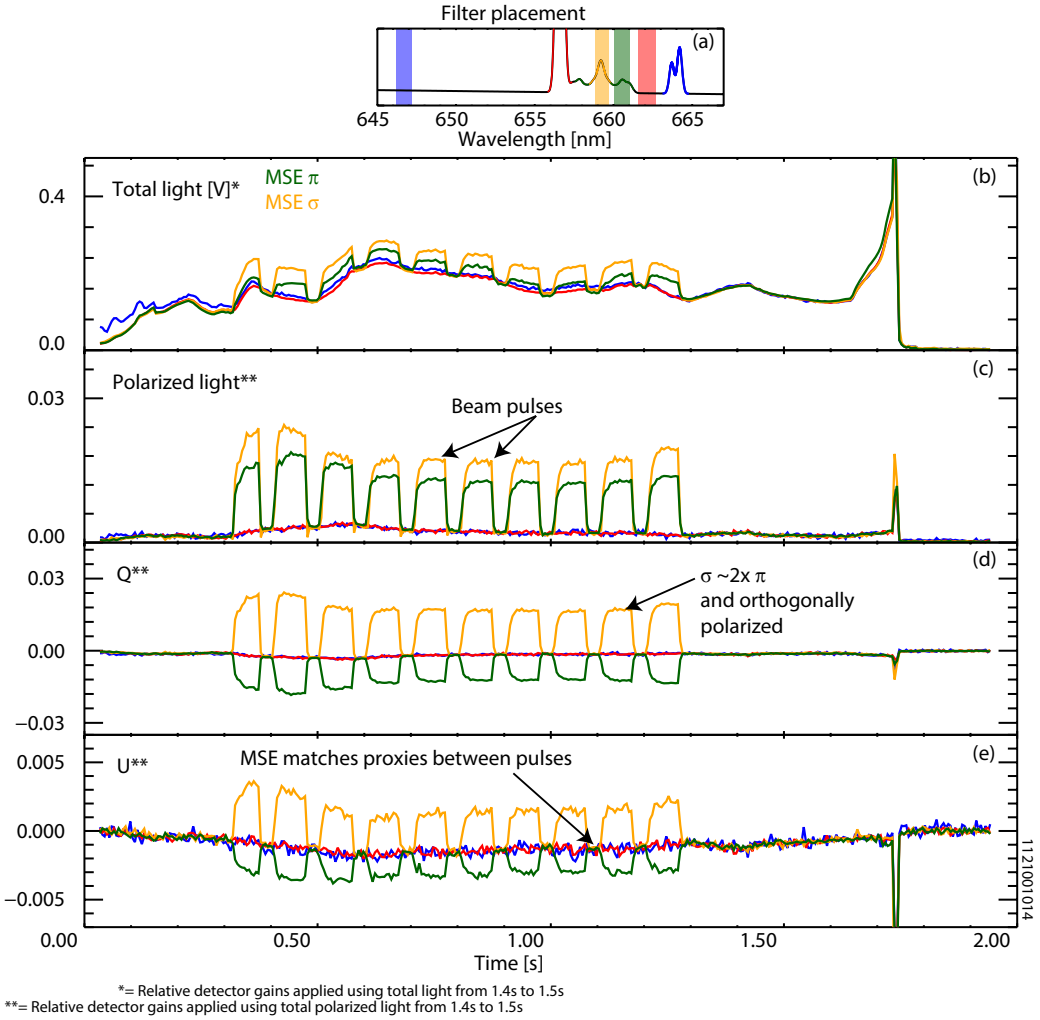

Figure 76: An example of firing the beam into the plasma while using proxy wavelengths to measure the background along with simultaneous measurement of the MSE σ and π emission. The filter placement is shown in panel A, note the green trace is observing the MSE π emission and the yellow trace is observing the MSE σ emission for this sightline. Panels B, C, D, and E show the total light, polarized light, Q, and U respectively.

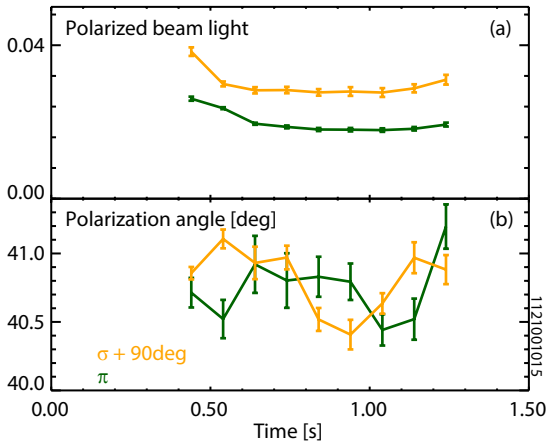

Figure 77: The polarized intensity (a) and polarization angle (b) of the MSE σ and π emission using time-interpolation for a discharge with a reduced-performance DNB.

An example of measuring the MSE σ and MSE π emission simultaneously is shown in Figure 76. The filter placement is indicated with measurement of the red and blue proxy spectral regions simultaneously with the MSE σ and π. The total light (b) collected from the σ is approximately twice that from the π. The change in sign between the σ and π Q (d) and U (e) shows the light is orthogonally polarized[1].

An example showing the different beam components for a similar, low SB discharge is shown in Figure 77. In this case the background is estimated using time-interpolation instead of wavelength-interpolation. Note the polarization intensity of MSE σ is about 1.5× the MSE π polarized intensity. The polarization angles are nearly orthogonal, though there is structure as function of time. This is likely due to the use of time-interpolation to subtract the background, as will be discussed next. This discharge had a beam with significantly reduced performance, making further investigation difficult.

An additional advantage to the simultaneous collection of the MSE σ and π emission is the ability to precisely tune the overlap of the filter functions onto each spectral component from the beam. Because the two sources of emission come from the same collection of beam atoms, the ratio of their intensities is fixed despite changes in beam neutral density or plasma density. Therefore, the ratio of collected σ and π is a function only of the location and bandwidth of the interference filters relative to the Stark spectrum. This means plasma discharges can be used to precisely tune the filter location to the center of the spectral lines without having to keep identical plasma conditions.[2] This is done by changing the center wavelength of the filters shot-to-shot by changing the temperature of the ovens.

1 Note the expected $\frac{\sigma}{\pi}$ ratio is not evident in total polarized light (c) because of the relative alignment between the polarized background and the polarized light from each beam component.

2 This analysis assumes that the relative population levels of the upper states which populate the lines stays the same, which is probably a good assumption in plasmas that would be used for this type of tuning (i.e., avoid large density ramps). The beam energy and plasma magnetic field also need to be kept constant to keep the same

6.4.1 *Using simultaneous σ and π collection to monitor the diagnostic performance*

The fact that the MSE σ and π emission are emitted with orthogonal linear polarization angles can be used to monitor the MSE system performance directly[3]. Recall that one of the most important polarization aberrations in a MSE optical system is diattenuation from non-equal s-p ratios from mirrors which could change throughout a campaign or within a shot, altering the polarization response of the MSE diagnostic. For mirrors with non-unity s-p ratio, the diattenuation can be formulated in terms of the s-orientation reflectivity, R_s, and the p-orientation reflectivity, R_p. In this case $\Psi \equiv 1 - \frac{R_p}{R_s}$. The change in polarization angle from Equation 20 due to diattenuation from non-unity s-p ratio then becomes:

$$\theta^{out} \approx \theta^{in} + \frac{R_p/R_s - 1}{2\,DOLP^{in}} \sin\left(2(\theta^{in} - \psi_{mirror\,s})\right) \tag{56}$$

where $\psi_{mirror\,s}$ is the axis of the mirror's angle of incidence.

With simultaneous collection of the σ and π emission, it may be possible to monitor and compensate for the effects of a changing first mirror diattenuation by monitoring the polarization angle between the two different signals:

$$\theta_\sigma^{out} - \theta_\pi^{out} \approx \frac{\pi}{2} + \frac{R_p/R_s - 1}{DOLP^{in}} \sin\left(2(\theta_\sigma^{out} - \psi_{mirror\,s})\right) \tag{57}$$

where θ_σ^{out} has replaced θ^{in}. Therefore, the departure from orthogonality of the measured MSE σ and π emission, combined with knowledge of the mirror orientation, can provide information about R_p/R_s: the term required for calibrating the mirror diattenuation.

Retardance from the first mirror (i.e., mirror phase shift) produces changes in the polarization angle that are modulo $\frac{\pi}{2}$ instead of the modulo π from diattenuation. Therefore, changes in first mirror retardance will not change the measured angle between two sources of orthogonally polarized light. However, the retardance modifies the circular polarization with modulo π in the input polarization angle. Thus, changes in the relative DOCP of the measured MSE σ and π light could be a sign that the optical system retardance has changed. This could be from a changing retardance from plasma-facing mirrors in future devices or from stress-induced birefringence in C-MOD.

The fact that the MSE σ and π emission is orthogonally polarized may also be used to determine the quality of the background estimate in the background subtraction scheme. Recall from Equations 47 and

Doppler and Stark shifts. The background needs to be subtracted prior to taking the ratios.

3 In configurations where both are un-contaminated by other beam components.

51 that the error from background subtraction is module $\pi/2$. The background estimate for the σ and π wavelengths is likely to be estimated through the same methodology, leading to correlated errors in the background intensity estimate for each component: $f_\sigma = f_\pi \equiv f$. The polarized-signal-to-polarized-background for each channel can also be related, $SB_\pi = \frac{1}{R} SB_\sigma$, where usually $1 < R < 2$. R is predominately a function of the spectrum and filter placement and does not depend on the background intensity. Finally, the two sources of light are emitted orthogonally, $\theta_\sigma - \theta_\pi = \pi/2$. Putting these assumptions into the equations yields:

$$\theta_\sigma^{est} - \theta_\pi^{est} \approx \frac{\pi}{2} + \frac{f}{SB_\sigma}(R-1)\sin\left(2(\theta_\sigma - \theta_{bkgd})\right) \tag{58}$$

A similar methodology can be applied to misestimates of the background polarization angle, assuming the misestimate in background angle, $\Delta\theta_{bkgd}$, is correlated for the two channels.

So a change from orthogonality of the estimated beam σ and π polarization angles could be due to poor estimation of the background properties. Importantly, polarization changes due to misestimation of the background are modulated by the intensity of background through SB. Therefore, a misestimate of the background intensity will cause the angle between the estimated MSE σ and π to be correlated with changes in the magnitude and angle of the background light. A near perfect background estimate should result in measured angles that change no faster than the current diffusion timescale and are orthogonal to one-another (or at least separated by a constant angle). A changing polarization calibration due to first-mirror erosion or deposition is likely to occur over a much longer timescale than the effects from misestimates of the background. So long term changes in the angle between MSE σ and π light are indicative of changing diattenuation while faster, background-correlated changes are indicative of misestimates of the background polarization intensity or angle. This time-scale separation may allow the two effects to be separated.

These ideas will be tried using the new full-implementation of the MSE-MSLP approach on C-MOD in the next campaign[4]. If successful this could offer a low-cost method to monitor calibrations in burning plasmas without any calibration sources inside the vacuum vessel.

6.5 EXTRAPOLATION TO OTHER DEVICES

An example of applying the MSE-MSLP approach to the ITER heating beams is shown in Figure 78. The geometry of the ITER MSE system is shown on the left of the Figure. The MSE spectrum is simulated with a representative quasi-continuum background on the right. Example

4 Unfortunately, the effects from diattenuation cannot be tested on C-MOD since the mirrors are not exposed to plasma.

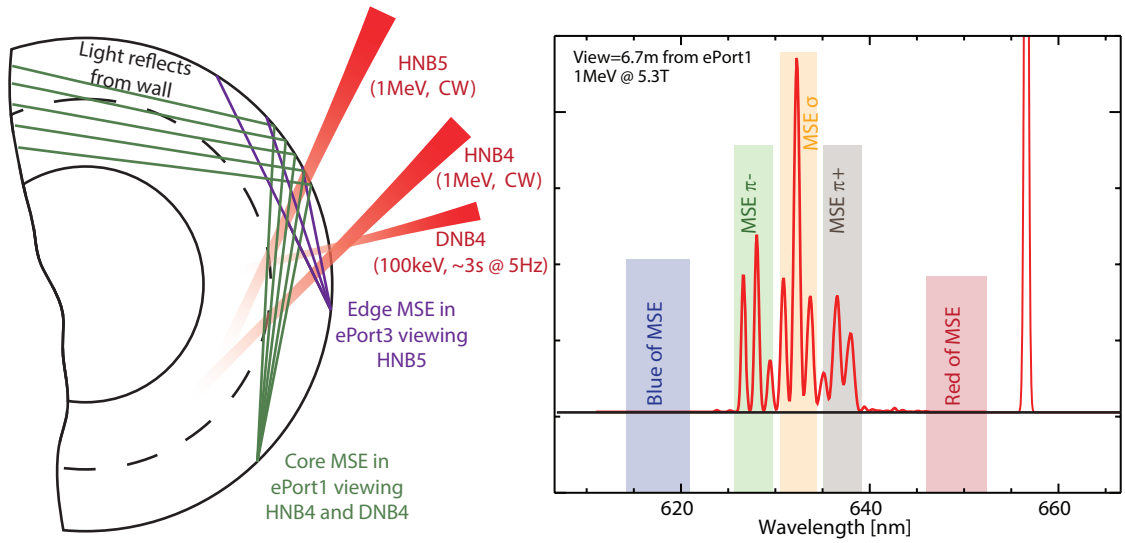

Figure 78: An example of the application of MSE-MSLP to the ITER MSE system. The system has two arrays viewing three different neutral beams (left). A simulated spectrum of one of the sightlines viewing the high energy heating beam is shown (right). The large Stark and Doppler shifts allow the three regions of the MSE σ and π to be measured along with proxy wavelengths.

filters for collecting the MSE σ emission (orange) and both strong triplets of the MSEπ emission (green, gray) are shown as shaded regions. This schematic uses filter full-widths of ~ 4nm for each component, though individual lines within the multiplet, likely the brightest, could be collected with narrower filters (i.e., 1nm) to increase the SB at the expense of absolute signal. Spectral regions for the proxy measurements are also shown to the red (red) and blue (blue) of the MSE emission. With high energy negative-ion beams, the emission is well-separated from the cold edge H_α, and there are no intermediate energy beam components. Therefore, it may be possible to place a proxy spectral region between the MSE emission and the cold H_α, though this may not be difficult due to spectral contamination from other beams. As in C-MOD, a database and spectral study of the anticipated impurity line emission should be conducted prior to selecting proxy wavelength regions.

The modification from MSE-LP to MSE-MSLP could be completed with only a change in detector design—the up-stream optics and transfer fibers would remain unchanged. By collecting multiple polarizations within the multiplet, the polarization calibration could be monitored. For these reasons, the development of MSE-MSLP and experience on C-MOD is important for MSE on next-step facilities.

6.6 SUMMARY: MSE-MSLP

Using a polarization polychromator it was found that the polarization at various spectral regions correlated very well, even across typically problematic plasma transitions and the system could properly track

the three dominant sources of polarized background. The wavelength-interpolation technique outperformed the time-interpolation technique by a factor of $2-10$, particularly at high background levels and plasma densities, where accurate estimates of the background are most required. **The technique can estimate the background with** $f < 0.01$ **and** $\Delta\theta_{bkgd} < 1^\circ$ **at high background levels, extending the mse measurement to** $SB < 10$, operating near the photon-noise level. Additionally, it was shown that the wavelength-interpolation technique does not rely on periodic modulation of the beam, providing a background estimate in real-time.

The ability to measure the polarization at multiple wavelengths on the exact same sightline opens additional diagnostic capabilities beyond wavelength-interpolation background subtraction. The C-MOD polarization polychromator was used to measure the MSE σ and MSE π emission simultaneously along with two proxy regions. Due to the nature of polarization aberrations, monitoring the difference in polarization angle between σ and π on an identical sightline can be used to monitor changes in diattenuation from deposition and erosion of the first mirror, or errors due to improper background subtraction. Monitoring the changing DOCP of these two components can also be used to monitor for changing retardance or phase shift in the diagnostic optical train.

The wavelength-interpolation and simultaneous measurement of different parts of the Stark multiplet lead to a qualitatively different diagnostic than a typical MSE-LP system. This is termed the multi-spectral line-polarization MSE (MSE-MSLP) approach. The technique has the following elements:

1. Polarization measurement at multiple wavelengths on an identical sightline.
2. Real-time measurement of the polarized background using polarization measurements at proxy wavelengths.
3. Simultaneous polarization measurement of both MSE σ and π on the same sightline.
4. Use of the different MSE component measurements to identify and correct for systematic errors.

Therefore, this approach can be used to help solve two pressing issues for MSE diagnostics on next-step devices: 1) proper background estimation and subtraction, and 2) in-situ, real-time monitoring of the diagnostic calibration. Experience on C-MOD can be informative for the planning of future MSE systems where the MSE-MSLP approach could easily be deployed.

BIBLIOGRAPHY

[1] T. Fujita, H. Kuko, T. Sugie, N. Isei, and K. Ushigusa. Current profile measurements with motional Stark effect polarimeter in the JT-60U tokamak. *Fusion Engineering and Design*, 34-35:289–292, March 1997.

[2] M A Van Zeeland, J H Yu, N H Brooks, W W Heidbrink, K H Burrell, R J Groebner, A W Hyatt, T C Luce, N Pablant, W M Solomon, and M R Wade. Active and passive spectroscopic imaging in the DIII-d tokamak. *Plasma Physics and Controlled Fusion*, 52(4):045006, April 2010.

[3] R. Mumgaard. Engineering Upgrads to the Motional Stark Effect Diagnostic on Alcator C-Mod. MIT PSFC Research Report PSFC/RR-15-5, MIT PSFC, April 2015.

[4] E. Delabie, M. Brix, C. Giroud, R. J. E. Jaspers, O. Marchuk, M. G. O'Mullane, Yu Ralchenko, E. Surrey, M. G. von Hellermann, K. D. Zastrow, and JET-EFDA Contributors. Consistency of atomic data for the interpretation of beam emission spectra. *Plasma Physics and Controlled Fusion*, 52(12):125008, December 2010.

7

MEASUREMENTS OF THE CURRENT PROFILE DURING LHCD

Chapter goals:

- Systematically measure the current and hard x-ray profile in scans of various plasma and LHCD parameters including:
  - At non-inductive conditions
  - Plasma current
  - LHCD power
  - Launched $n_{\|}$
  - Plasma density
  - Diverted and limited
- Quantify the results of these studies in preparation for comparison to numerical modeling

Sustaining a tokamak in steady-state and controlling the radial profile of toroidal current and plasma safety factor has been a long-standing goal of the fusion community. Injecting lower hybrid waves into a plasma was recognized early [1, 2] as a potential mechanism to drive plasma current efficiently, particularly off-axis. Over the last three decades LHCD has been studied extensively on several tokamaks [3]. A 20 MW LHCD system is also under consideration [4, 5] to sustain long pulses (3000 seconds) in the "steady-state" scenario of the ITER tokamak now under construction. Looking forward, LHCD is also commonly considered for use in fusion reactors, including the ARIES-AT [6] and the ARIES-RS [7] designs.

The design of LHCD systems for future devices and the utilization of LHCD in present devices relies heavily on numerical simulations. Vigorous tests of these models are required to gain confidence in their predictive capabilities and to identify possible areas for improvement. In particular, it is important to benchmark model predictions of current drive across a range of parameters in regimes of interest for reactors.

The comparison of the simulated current profile driven by LHCD to the experimentally measured current profile can provide a sensitive test of the model. Comparisons made over a range of parameters can be used to determine the sensitivities in the experiment and in the model to gain insight into the applicability and uncertainties in the simulation results. This chapter reports measurements of the current profile using the C-MOD MSE diagnostic during LHCD across a range of

Table 10: Tokamaks with LHCD systems indicating the current profile measurement capabilities

Tokamak	Geometry	MSE	Polarimetry	Status
C-MOD	diverted	yes	yes	operating
JT60-U	diverted	yes	no	decommissioned
JET	diverted	yes	yes	LHCD mothballed
TORE SUPRA	circular	attempted*	yes	decommissioned
FTU	circular	attempted*	yes	?
KSTAR	diverted	planned	no	operating
EAST	diverted	planned	no	operating
PBX-M	bean	yes	no	decommissioned
ASDEX	diverted	no	no	decommissioned
ALCATOR C	circular	no	no	decommissioned
PLT	circular	no	no	decommissioned

* A MSE system was installed but detailed measurements were not published and the system has since been removed.

parameters. The systematic changes in current profiles are explored in the low-density operating range on C-MOD[1] where the LHCD system has been observed to drive significant current with global efficiencies roughly in agreement with that predicted by theory [3, 8]. The results will be compared to numerical simulations by the GENRAY/CQL3D and LHEAF codes in the next chapter.

7.1 PREVIOUS LHCD CURRENT PROFILE MEASUREMENTS

Table 10 lists some of the tokamaks that have fielded LHCD systems and indicates their current profile measurement capabilities.

The overlap between diverted tokamaks with significant LHCD programs and operating MSE diagnostics consists only of JT60-U, JET, and C-MOD. The JT60-U tokamak operated with both an LHCD system and a high-quality MSE system, enabling the most detailed study of the current profile during LHCD to date. Scenarios were studied with off-axis peaked current drive using LHCD and neutral beams [9]. Non-inductive discharges predominately driven by LHCD and bootstrap current were created with reverse magnetic shear using two launchers operating simultaneously ($B_0 = 2T$, $P_{LH} = 2.5MW$, $\bar{n}_e \sim 1 \times 10^{19} m^{-3}$, $T_{e0} = 3.5keV$) [10]. MSE measurements were also used to control q_0 in real-time using the LHCD power as an actuator [11]. Measurements of the current profile from LHCD were compared to simulation [12] and showed a on-axis peaked current profile with good agreement to ray-

1 The density range in these experiments is on the low end of the typical ALCATOR C-MOD operating range, but is high for most tokamaks and comparable to that envisioned in ITER and fusion reactors.

tracing simulations. The device has been since been decommissioned and LHCD is not planned on the replacement tokamak.

The JET tokamak also operated with an LHCD system and an MSE system. LHCD was used along with beams to create non-inductive discharges [13] and "current holes" that were measured with MSE [14]. Current profile measurements were compared to simulations with LHCD operation along with significant neutral beam heating [15]. LHCD was used to create a variety of q-profile [16] and current profile control using LHCD and MSE was successfully accomplished [17]. However, the LHCD system on JET has recently been decommissioned. The circular/limited TORE SUPRA and FTU tokamaks operated at densities and magnetic fields nearest to that of C-MOD and reactors but were limited to only polarimetry for current profile measurements and did not produce significant studies of the current profile under strong LHCD.

C-MOD offers an important platform for performing tests of the LHCD current profile because it operates at the proper field, density, and LHCD frequency for testing reactor physics. Both JT60-U and JET operate at low field and low density compared to C-MOD or a reactor. Unlike JT60-U and JET which often use neutral beam current drive, in C-MOD the plasma current is driven only by the transformer (Ohmic) or by the LHCD providing relatively "simple" target discharges in which the plasma can be dominated by the effects of LHCD[2]. Additionally, the small size of the C-MOD tokamak leads to short current relaxation times relative to the pulse length. The current profile can therefore be modified by LHCD, allowed to reach an equilibrium, and then the stationary state can be measured, providing straight-forward comparison to simulations.

The non-inductive current profile was measured during this work as reported in [18, 19] and a preliminary scan in launched $n_{\|}$ was conducted [20]. Preliminary comparisons to theory were performed [21]. However, the diagnostic calibration response changed by many degrees shot-to-shot, the data was sporadically compromised by background subtraction issues, and the view of the diagnostic sometimes shifted.

Work during this thesis quantified the calibration and possible systematic errors, stabilized the diagnostic response, identified sources of background light allowing better avoidance, developed new background subtraction techniques, refined analysis techniques, and developed in-situ calibration (not used for this data). This increased confidence in and availability of the diagnostic, and enabled operation across a wider range of parameters during the FY12 and FY14 experimental campaigns. Additionally, equilibrium reconstruction methodologies were refined to capture more detail in the profiles and to en-

2 The experiments conducted in this work are performed in L-mode plasmas where the bootstrap current is small.

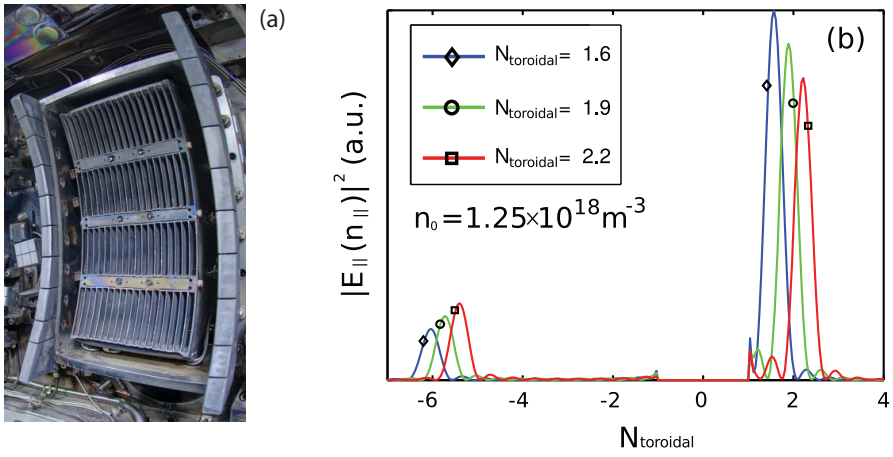

Figure 79: The C-MOD LHCD launcher as seen from the plasma location (a) and the launched toroidal mode number (related to $n_{||}$) for different phasings (b, adapted from [22]).

able more reconstructions—over 600 time slices were reconstructed as part of this work.

7.2 EXPERIMENTAL SETUP

The C-MOD LHCD system operates at 4.6GHz using 12 klystron amplifiers each capable of producing 250kW. The power system can operate for up to five seconds [23]. Up to 1MW of power is coupled to the plasma via a novel launcher structure which consists of 16 columns with four poloidal rows [18, 24]. The launcher can vary the launched $n_{||}$ from 1.6 to 3.8 in real time allowing the physics of LHCD to be explored as a function of the launched wavenumber—an important quantity in the wave physics[3]. The launched $n_{||}$ spectrum and a photograph of the plasma-facing end of the LHCD launcher is shown in Figure 79. This launcher is the second LHCD launcher installed on C-MOD, replacing the launcher used for the first current profile measurements [25]. The system has recently been upgraded to couple power to the plasma for up to 1 second [26].

Each discharge in this study follows the same basic structure. First, an Ohmic target plasma is established prior to the application of LHCD which starts between 0.1 to 0.3 seconds after the beginning of the current flattop. This allows the DC electric field to fully penetrate the plasma and provides an Ohmic reference period for the intra-shot calibration technique. Next, the LHCD is ramped (usually quickly) to the target power and is kept steady for 0.5 to 1 second. During this time the plasma control system maintains a constant total plasma current by decreasing the loop voltage and thus decreasing the Ohmic

3 Physically, the phase difference between the different columns of the launcher is changed, leading to a different spectrum of launched toroidal modes. The location of the peak in these modes is referred to here as the $n_{||}$.

current drive. Finally, after the cessation of LHCD, the plasma control system resumes driving Ohmic current by raising the loop voltage until the end of the pre-programmed current flattop at which point the plasma current is ramped down.

The DNB is pulsed into the plasma, typically with a period of 0.1 seconds and a duty cycle of 60 to 75 percent and is shown to be non-perturbing to the density and temperature profiles. The DNB typically starts pulsing just prior to the current flattop and stops when the plasma ramp-down begins. In the plasmas studied in this work, the MSE measurement is averaged over 50-60 milliseconds during the steady portion of each DNB pulse. This results in an MSE measurement every 0.1 seconds throughout the discharge. The measurement uncertainty is taken as the standard error of the MSE data over the bin length, resulting in typical errors of 0.1° to 0.5° in magnetic pitch angle, depending on the MSE sightline. The ten MSE sightlines at each measurement time point are inspected for problems from improper background subtraction as discussed in Chapter 5. Typically the beam pulses overlapping the beginning and the end of LHCD produce spurious polarization measurements due to background changes and are omitted from reconstructions.

The pitch angle profiles obtained from the MSE diagnostic and the pressure profiles derived from the Thomson scattering diagnostic are used to constrain the magnetic reconstruction at each time point where MSE data is available. An Ohmic portion of the discharge is used to intra-shot calibrate the MSE diagnostic using the methodology discussed in Appendix B for all the data discussed in this work. Most discharges use two adjacent time-slices to obtain the calibration offset for the MSE data. The reconstructions during LHCD use spline basis functions with four knot locations (which are allowed to vary time slice-to-time slice and discharge-to-discharge). The plasma parameters are kept constant (i.e. constant density, current, power, etc) throughout the LHCD pulse. The effect from LHCD is then measured by scanning the parameter of interest discharge-to-discharge. The resulting pitch angle, safety factor, and current density profiles are extracted from the equilibrium reconstruction for comparison as the parameter of interest is scanned. .

7.2.1 *HXR camera*

The LHCD-driven electrons produce Bremsstrahlung emission due to collisions with the plasma bulk ions and electrons. A mono-energetic electron beam produces a range of photons in the hard x-ray range, primarily in the direction of motion, that can then be detected with spatial localization using a hard x-ray camera (HXR) camera installed on C-MOD [27]. The 32-sightline cadmium zinc telluride pinhole camera views the plasma in the poloidal plane as shown in Figure 80.

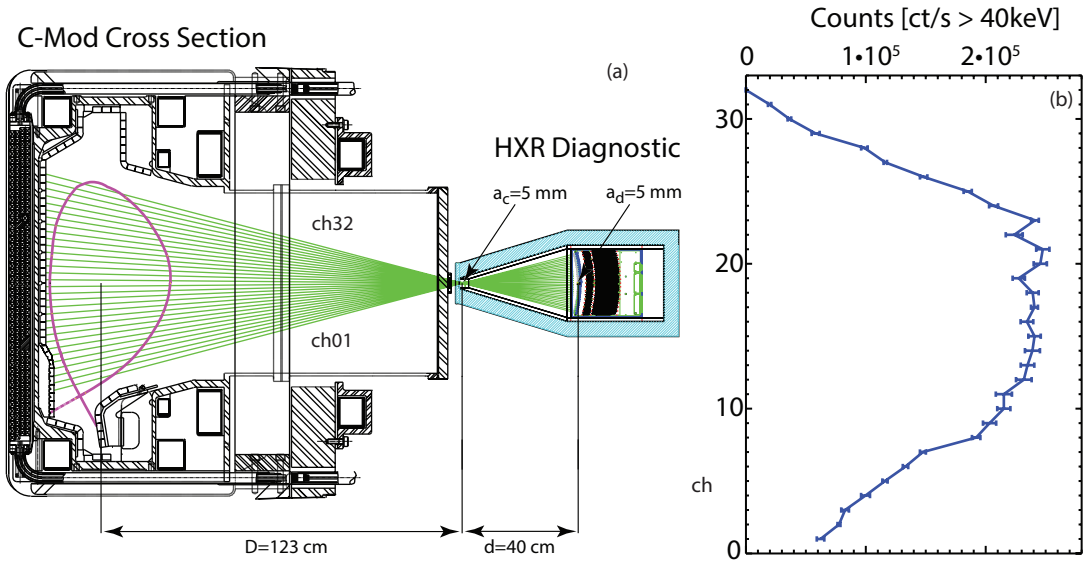

Figure 80: The hard x-ray (HXR) camera on C-MOD views the plasma mostly poloidaly with a fan of 32 sightlines (left, adapted from [27]). The energy-resolved count rate from each sightline is reported, giving information about the spatial profile of the fast-electron Bremsstrahlung (right).

The camera has 1μs time resolution and is sensitive to photons from 20keV to 200keV with 1keV energy resolution. The pulse-height data is analyzed, binned, and stored in the MDSPLUS database. Background counts due to neutron detection are subtracted, although this the errors associated with this process precludes measurements at high plasma temperatures.

The camera sightlines span most of the cross-section of the confined plasma and are inherently line-integrated measurements of brightness. The poloidally-viewing camera is more sensitive to the electrons that have been pitch-angle scattered compared to the electrons that are carrying the toroidal current. This limitation and the lack of a one-to-one relation between photon energy and electron energy makes interpreting the signals from the HXR camera as a spatially-dependent electron distribution function challenging. The details on the construction, operation, and analysis for the HXR camera can be found in references [27, 28]. Efforts have been undertaken to invert the HXR data [29], however this approach is not taken in this work. The photon energy distribution of the HXR emission is observed to be independent of the parameters that were scanned. All the photons greater than 40keV are therefore binned for each sightline for the work presented here.

The HXR camera provides basic information about the spatial extent of the fast electron population even without inversion—there must be fast electrons outside of a given sightline for hard x-rays to be detected by that sightline. The un-inverted camera data is particularly useful to track *changes* in the magnitude and spatial extent of the fast electron population, as well as its evolution in time. The HXR profiles,

combined with the spatially-resolved measurements of the plasma current profile from MSE-constrained reconstructions, provides two separate and complementary measures of the effects of LHCD on the core plasma. These profiles can then be compared to synthetic diagnostics in numerical simulations.

Non-thermal electron-cyclotron-emission (ECE) is an additional indicator of fast electrons in the plasma and is detected by two grating polychromator systems and a Michelson interferometer [30]. The fast-electrons produce radiation that is relativistically down-shifted into the detection range of the ECE systems, particularly those usually observing the edge, and is termed "non-thermal ECE emission." This contamination makes these systems inadequate for measurements of the bulk electron temperature[4] but the ECE detectors do provide information about the fast electrons [31]. However, interpreting these signals in terms of fast electron energy and spatial position is difficult, thus these system are used to identify qualitative changes (or lack there of) as different parameters are scanned in this work.

7.3 PROFILE TIME EVOLUTION

Figure 81 shows time traces and profiles from a typical LHCD experiment at moderate current (530kA). The traces of important plasma parameters are shown on the left. At 0.7 seconds LHCD power is applied, generating fast electrons which produce hard x-rays. The plasma control system responds to the current carried by the LHCD-driven fast electrons by decreasing the loop voltage by nearly 80 percent. Significant non-thermal ECE is observed during this period. The profiles of the pitch angle, safety factor, and current density from the shaded regions are shown on the right. The profiles from the Ohmic period prior to LHCD are extracted from the dark gray shaded region and are shown as a dashed gray lines.

The top collection of panels shows the time evolution of the plasma shortly after the start of LHCD. The MSE pitch angle profile responds quickly to the application of LHCD, with the largest changes occurring at mid-radius while the pitch angle at larger radius changes slightly. An edge feature outside of $R_{mid} \sim 0.8$m appears in the current profile almost immediately after the start of LHCD whereas the central current density takes several hundred milliseconds to reach a stationary state. Note that the edge feature in the current density profile carries significant total current since the plasma has a much larger area at the larger minor radius. The central current density, although it draws attention to the eye due to the large changes and peaked nature, does not represent much total current due to the small area at the center of the plasma. q_0 rises above unity by 120 milliseconds

4 Thomson scattering measurements are thus used for temperature profiles during LHCD for the results presented in this work.

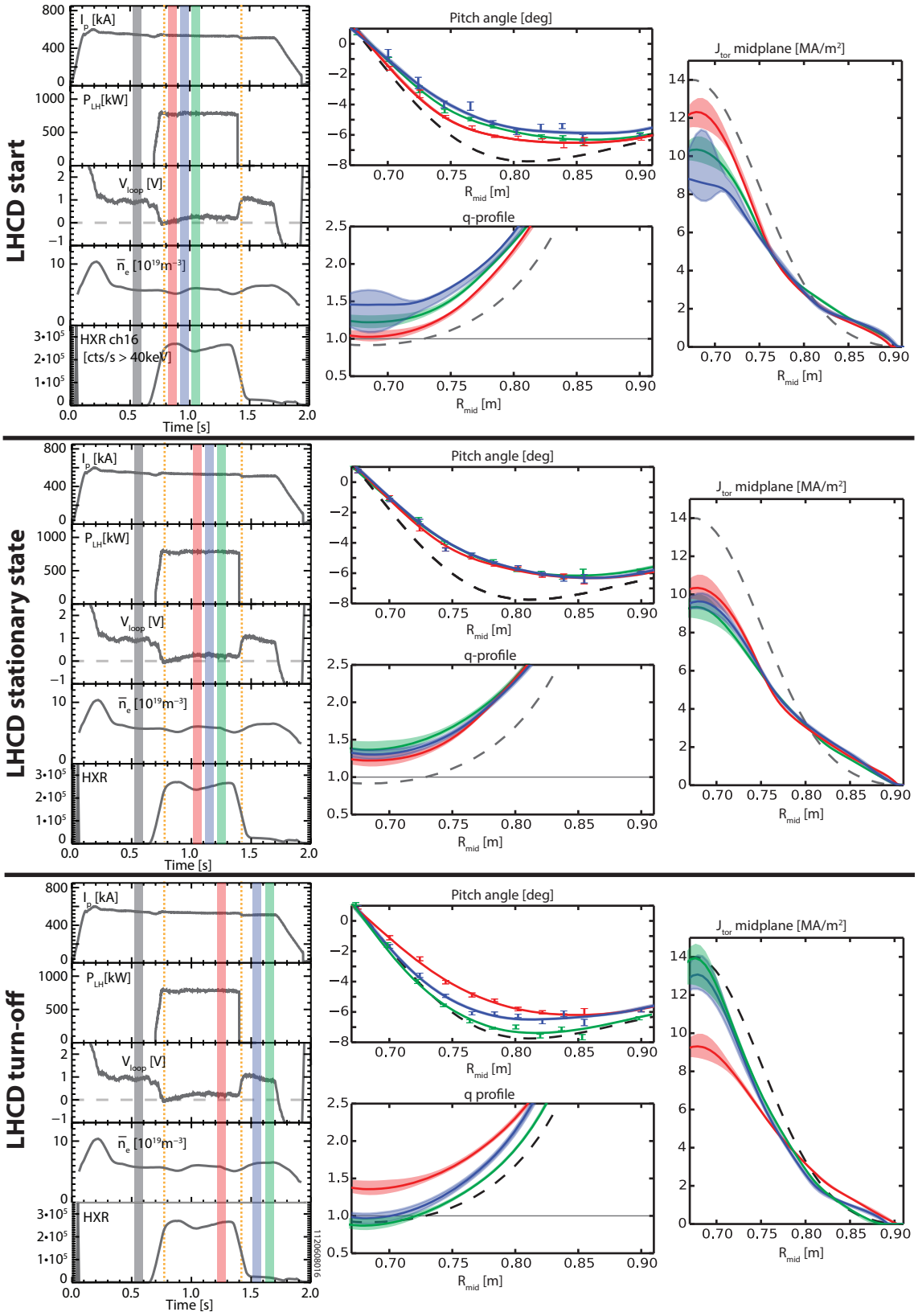

Figure 81: Time traces (left) from a typical LHCD experiment showing the (from top to bottom) plasma current, net LHCD power, surface loop voltage, line-averaged density, and hard x-ray count rate (> 40keV from a central HXR camera chord). The period where sawteeth are suppressed is indicated by the two vertical orange dashed lines. The profiles from the reconstructions show the magnetic pitch angle with MSE data (top middle), the q-profile (bottom middle) and the midplane current density (right). Traces are selected from different time periods in each of the three horizontal panels.

after the start of LHCD (red) which coincides with the suppression of sawteeth indicated as the vertical dashed orange line on the time traces. The current profile continues to evolve (blue, green) for the next 200 milliseconds as changes in the parallel electric field penetrate the plasma—eventually the plasma reaches a new equilibrium.

The middle collection of panels shows that the pitch angle, safety factor, and current profiles reach a stationary state by 320 milliseconds after the start of the LHCD (red) and remain stationary for the remaining 300 milliseconds of the LHCD pulse. The loop voltage stabilizes at ~ 20 percent of its value prior to the start of LHCD, indicating that the majority of the current is being driven non-inductively. q_0 rises to ~ 1.3 and the current profile is broader than the Ohmic profile but still centrally peaked.

The bottom collection of panels shows the plasma evolution after the end of LHCD. The last time point during LHCD is indicated in red. The pitch angle profiles evolve back to the Ohmic profile (blue) and nearly reach it (green) prior to the ramp-down of the plasma current. q_0 decreases to one near the time that sawteeth resume and the q-profile continues to evolve back toward the Ohmic profile. The edge feature in the current profile disappears and the central current density peaks upward although it does not reach its Ohmic profile prior to the plasma ramp down. (Note: there are cases where there is sufficient time after LHCD for the profiles to evolve to match the profiles prior to LHCD.)

Uncertainty analysis of the equilibrium reconstruction was not performed for every discharge and every time slice. However, collating the reconstruction variability using Monte-Carlo analysis on single time-slices, repeated discharges, and variability during stationary states has been used to estimate typical uncertainties in the current density at different locations in the radial profile. These uncertainties are identified in the figures that follow. Note that the details of the MSE measurement lead to much larger current density uncertainties in the core region than in the edge region. On C-MOD the uncertainty in the pitch angle is a minimum of ~ 0.1° at the mid-radius and ~ 0.25° at the core and edge[5] while the absolute pitch angle changes significantly across the profile—the relative measurement uncertainty is thus largest at smallest major radius and smaller at the edge and smallest at the mid-radius. Furthermore, the total plasma current is constrained using the Rogowski coil measurement and changes in current density at the outer part of the plasma produce much larger changes in total current due to the larger area than at inner radii.

The HXR profile (a) and the flux surface-averaged current profile (c) for the times from the beginning of LHCD to the end of LHCD are shown in Figure 82. The HXR emission is averaged over the same time

5 The polarization angle uncertainty is greatest in the core due to photon statistics while the pitch angle sensitivity is worst at the edge, thus the two effects act in opposite directions leading to a minimum uncertainty in pitch angle at mid-radius.

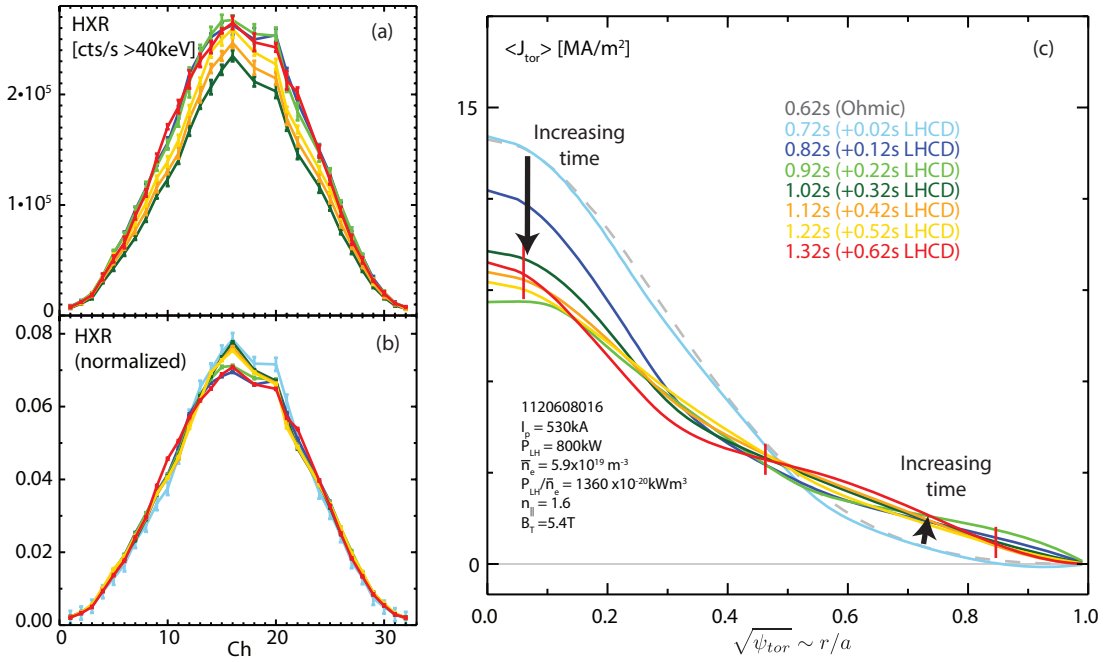

Figure 82: The-time dependent profiles of HXR emission (a) and flux-surface averaged J_{tor} (c) for a low current discharge. The HXR profiles are normalized to the total count rate (b) to show changes in profile shape.

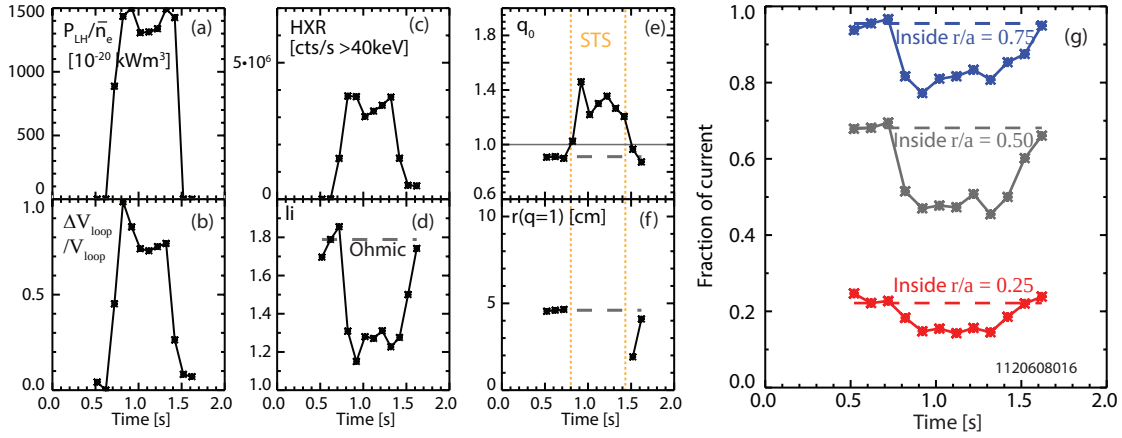

Figure 83: The time-dependence of o-D equilibrium quantities from a low-current, high-power LHCD discharge. The LHCD power divided by the density—a measure of the strength of the LHCD drive (a), the fractional change in loop voltage from prior to the start of LHCD (b), the total HXR count rate summed over all channels (d), the plasma ℓ_i—indicating the broadness of the current profile (c), the central safety factor (e), and location of the q = 1 flux surface (f). The vertical dashed orange lines indicate the time of the stop and start of sawteeth. The fraction of the current inside of different minor radius locations—a means to quantify changes in the current profile (g). The horizontal dashed lines indicate the ohmic values.

period as the MSE measurement and the variability is indicated as the error bars in the figure. Both the HXR and current profiles are centrally peaked during application of LHCD. The current profile takes 200-300 milliseconds to evolve to its final profile shape while the HXR profile is established immediately after the start of LHCD as are the non-thermal ECE features.

The HXR profile shape remains self-similar throughout the discharge (b). This self-similarity is apparent even in the very earliest time slices (light blue), similar to that observed on TORE SUPRA [32]. In a similar manner, the non-thermal ECE emission profiles rise promptly and maintain constant shape throughout the application of LHCD (not shown). This implies that the LHCD drives the fast electrons in a constant profile independent of the details of the plasma equilibrium, which is a function of time due to the penetration of the parallel electric field. (Although, as these results show, the equilibrium changes only mildly even with substantial amounts of LHCD.) Past studies on C-MOD have shown that there is little fast-electron diffusion or convection —the LHCD-driven electrons stay on the flux surface where they are born [33] in the absence of MHD which is consistent with these results.

In addition to the current and HXR profiles, there are several zero-dimensional measures of the current drive that can be used to quantify the effects of LHCD. These are shown in Figure 83. The drive term ($P_{LH}/\bar{n}_e$) is high and relatively constant (a). The fractional change in loop voltage (b) shows that the majority of the plasma current is being driven non-inductively. The HXR count rate follows a trajectory similar to $P_{LH}/\bar{n}_e$ (c). The plasma ℓ_i decreases from 1.8 during the Ohmic target plasma to 1.2 during the LHCD phase, reflecting that the current profile has broadened (d). q_0 increases from ~ 0.9 to ~ 1.3 (e) causing the $q = 1$ surface to disappear and then reappear after the end of LHCD (f), the timing of which coincides with the period when the sawteeth are suppressed (STS) as indicated by the vertical dashed orange lines.

The current profile can be parameterized simply in terms of the fraction of current located inside different minor radii (g). The application of LHCD broadens the current profile, decreasing the fraction of current inside $r/a = 0.25$, $r/a = 0.5$, and especially inside $r/a = 0.75$. In this discharge nearly 20 percent of the current is located in the outer quarter of the plasma radius during LHCD compared to only 5 percent during the Ohmic-driven periods of the discharge. Significantly, there is still a considerable amount of current, ($\sim$ 45 percent), inside the mid-radius even though this is a strongly LHCD-driven plasma. The current fraction locations, ℓ_i, q_0, and $r(q = 1)$ all return to their pre-LHCD values after the end of LHCD.

Another example of time-dependent MSE measurements of LHCD is shown in Figure 84 for a high current (800kA) discharge with mod-

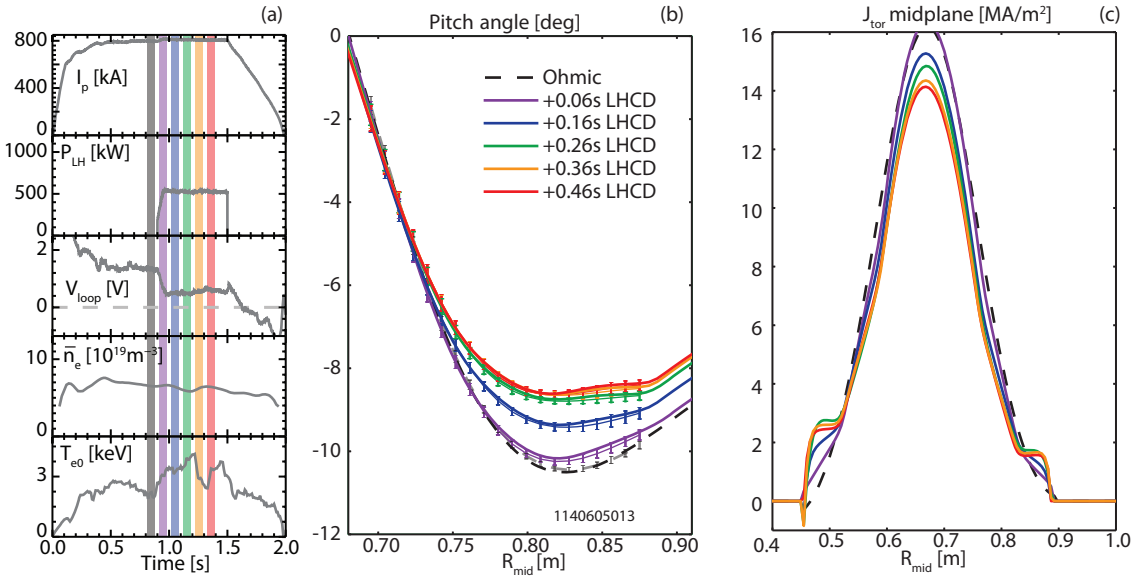

Figure 84: The time dependence of the pitch angle (b) and current density (c) profiles at high current in a moderate LHCD power discharge that did not suppress sawteeth but did substantially reduce the loop voltage.

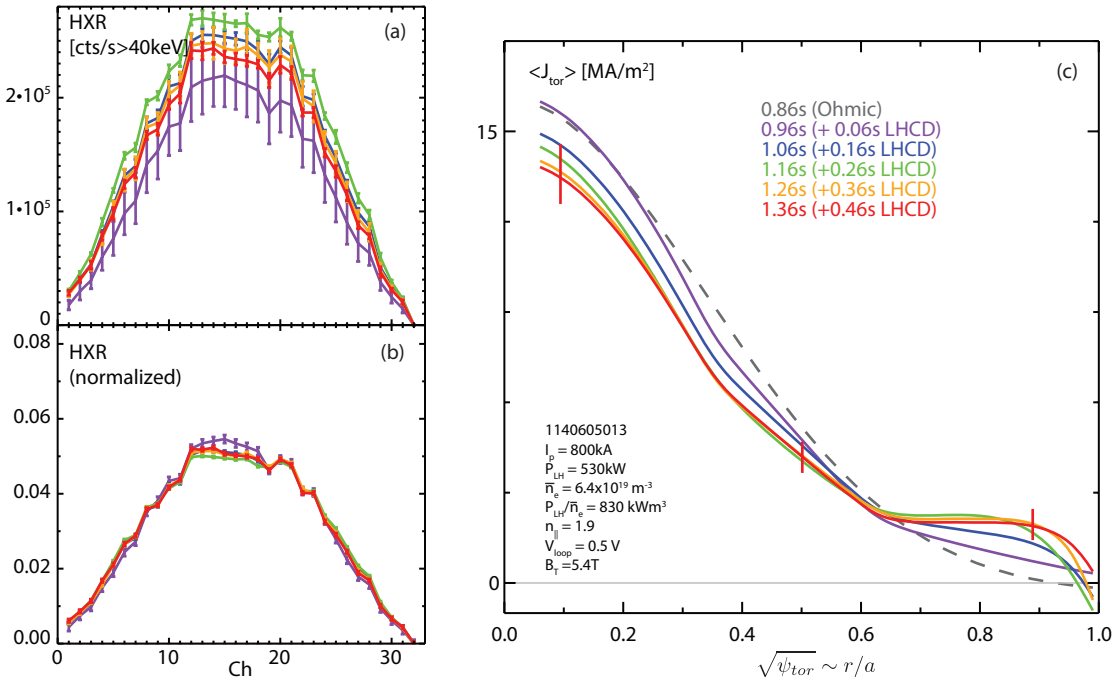

Figure 85: The HXR and $< J_{tor} >$ evolution during the LHCD turn-on and plasma equilibrium evolution of a high current discharge.

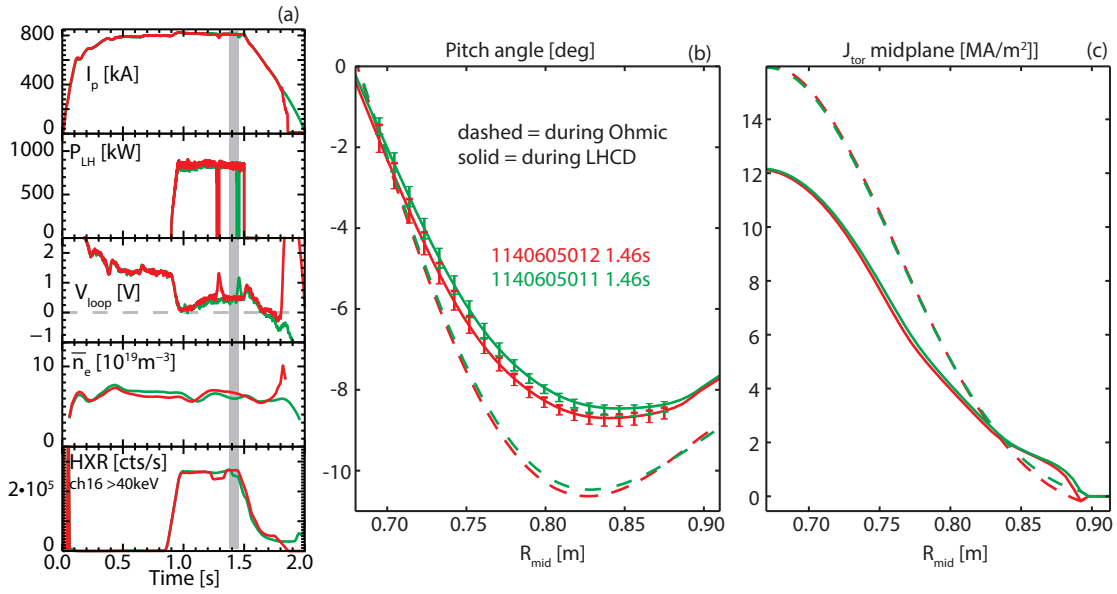

Figure 86: The reproducibility of the current profile measurement. Two nearly identical discharges were created, both reaching similar loop voltages and HXR count rates. The measurement time of interest is indicated with a shaded region. The pitch angles measured by MSE (after Guassian process regression) are similar between the discharges (middle) leading to similar current profiles (right).

est amounts of LHCD power (500kW). The modest amount of LHCD ($P_{LH}/\bar{n}_e = 850 \times 10^{-20}$kW m²) is sufficient to reduce the surface loop voltage by ~ 55 percent and generate an increase in the central temperature.

The pitch angle evolution and resulting current profile are shown for the periods from the start of LHCD throughout the LHCD pulse. Note that the MSE pitch angles and thus the resulting equilibrium stabilizes approximately 260 milliseconds after the start of LHCD. The resulting current profile shows "shoulders" at the edges of the plasma due to the application of LHCD. The largest changes in the MSE pitch angle are in the outer portion of the plasma—further out than the previously discussed case at low current. The shoulder features appear from $0.8 < R_{mid} < 0.9$, and are driven by the pitch angle changes in the outer two to three MSE sightlines. These features smoothly appear as a function of time while the central current density is only mildly affected. (Note that this plasma remains sawtoothing throughout while the sawtooth inversion radius decreases.) Figure 85 shows the HXR profiles and $< J_{tor} >$ for the time slices. The HXR profiles are broader than the low-current discharge. The current profile shows a large relative change off-axis ($r/a > 0.6$) with a new equilibrium reached approximately 260 milliseconds after the start of LHCD. Again the HXR profile evolution is relatively prompt while the current profile takes time to equilibrate. The HXR profile shape remains self-similar at all the time points during the application of LHCD.

The measurement of the current profile is very reproducible in similarly prepared plasmas. Figure 86 shows two repeated discharges (800kA) with the same LHCD power and plasma density, generating the same HXR count rate and loop voltage. The pitch angles measured by MSE are very similar between the two discharges, yielding very similar MSE-constrained reconstructed current profiles. The HXR and non-thermal ECE profiles are also very similar between the discharges. Other examples at different current and power levels show similar levels of reproducibility.

The time evolution of these discharges agrees well with expectations. The current penetration time can be approximated as:

$$\tau_{CR} = \frac{1.4\ a^2 \kappa\ T_e^{\frac{3}{2}}}{Z_{eff}} \tag{59}$$

where a is the device minor radius in meters, κ is the elongation, T_e is the electron temperature, and Z_{eff} is the effective charge [8]. This yields current relaxation times for C-MOD from 0.2s (at 2keV) to 1.4s (at 7kev). The discharges considered in this work are on the lower end of this range due to their low temperature, thus the current should be diffused by ~ 0.3 seconds after the start of LHCD—consistent with the profile evolution shown here. Early work with the MSE system showed that the loop voltage had equilibrated throughout the plasma cross-section during this time frame [25]. For the work presented in the remainder of this chapter, the data will be taken as late in the LHCD pulse as possible to allow the current to fully penetrate, typically more than 0.3 seconds after the start of LHCD. This enables a comparison of current profile shapes under fully-equilibrated conditions across a range of parameters, as well as comparisons of the measured current profile shapes to steady-state simulations.

7.4 FULLY NON-INDUCTIVE DISCHARGES

The LHCD system on C-MOD has sufficient power to drive and maintain the plasma fully non-inductively across a small range of plasma parameters (low current and low density at high power). Data from a non-inductive discharge ($I_p = 530$kA, $\bar{n}_e = 5.2 \times 10^{19} m^{-3}$, and $P_{LH}/\bar{n}_e = 1600 \times 10^{20}$kW m^3) is shown in Figure 87. Note that the application of LHCD leads to a significantly reduced loop voltage (even going negative shortly after the start of LHCD and recharging the transformer in some discharges) and then becomes stationary at zero during the LHCD pulse. There is central heating of the electrons (as measured by Thomson scattering) and a high hard x-ray count rate. The pitch angle, q profile, midplane J_{tor} and HXR profiles are shown for time points 0.35 and 0.45 seconds after the start of LHCD. The profiles—including the MSE measurements—are stationary between the

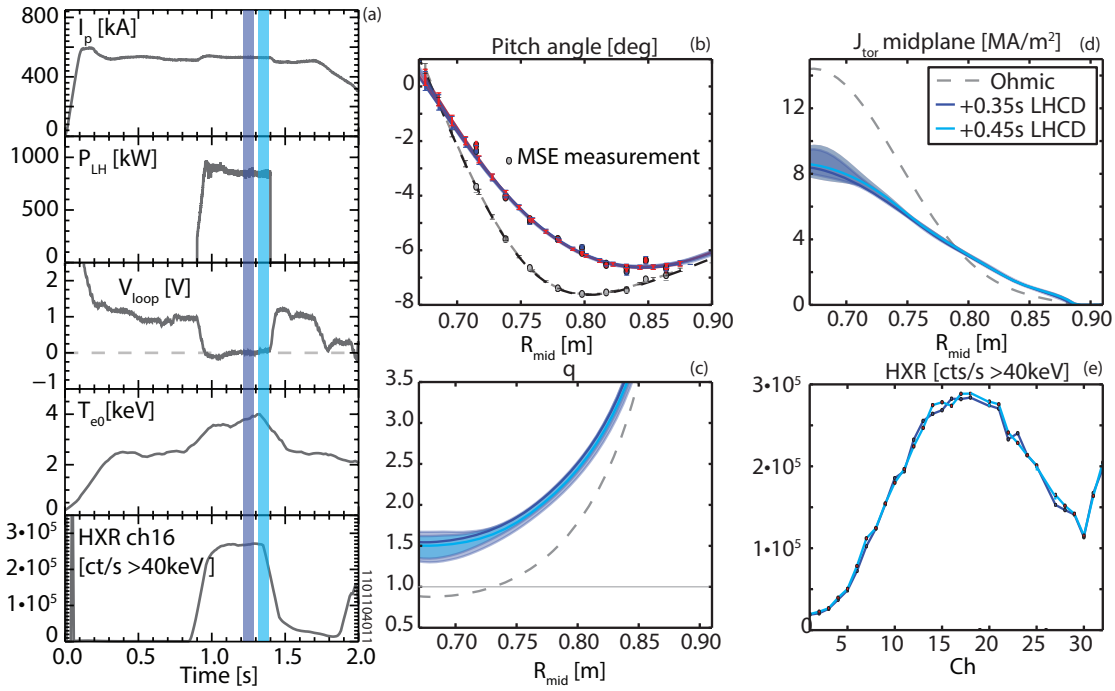

Figure 87: A discharge driven 100% non-inductively using LHCD. The plasma loop voltage is driven to zero at constant total current (left). The pitch angle, q-profile, midplane J_{tor}, and HXR profiles are shown for the two time periods late in the LHCD pulse indicated by the vertical shaded regions.

two time points. The current profile is broad but still centrally peaked with q_0 of ~ 1.5.

In this plasma, the vast majority of the current is being driven by the RF system which allows straight forward comparison of the measured current density profile to numerical simulations and measurements on other tokamaks. The peaked LHCD current profile is very similar to the profile observed in JT60-U [12]. However, the centrally peaked HXR profile, which agrees qualitatively with the current profile, is different from that observed on TORE SUPRA which observes off-axis peaks in HXR emission [32], implying off-axis peaked current profiles.

The centrally peaked current profile measured by MSE and the strong centrally peaked HXR profile is consistent with other measurements on C-MOD. Significant MHD activity is not observed in this discharge as might be expected if the current profile was peaked off-axis creating a non-monotonic q-profile. The temperature profile of the plasma remains peaked on-axis and the central temperature rises from 2.5keV to 3.5keV during LHCD as the ~ 500kW of Ohmic power is completely replaced with ~ 800kW of LHCD power.

The current drive efficiency is usually expressed as:

$$\eta = \frac{\bar{n}_e \; R \; I_{LH}}{P_{LH}} \tag{60}$$

where $\bar{n}_e$ is the line-averaged plasma density, R is the tokamak major radius, I_{LH} is the current driven by the LHCD system, and P_{LH} is the power supplied to the plasma by the LHCD system. Theoretically, η is expected to scale as $1/{n_\parallel}^2$, where $n_\parallel$ is the parallel refractive index of the lower hybrid wave at absorption, with weak a dependence on the plasma Z_{eff} ($\eta \propto 1/Z_{eff} + 5$) [1]), and a positive correlation with electron temperature (roughly doubling in efficiency between $T_e = 5$ and 20 kev [34] due to lower $n_\parallel$ at absorption). The theoretically expected LHCD efficiency $\eta \sim 2.0 - 2.5 \times 10^{19} A/Wm^2$ has been observed in a number of tokamaks at low density ($\bar{n}_e < 3 \times 10^{19} m^{-3}$) but a wide variety of phenomenon can decrease the current drive efficiency at high density as discussed elsewhere [3]. For non-inductive conditions the current drive efficiency is unambiguous since all the quantities are well known. For the cases presented above the current drive efficiency is $\eta = 1.6 \times 10^{19} A/Wm^2$.

7.5 DETERMINING THE LHCD PERFORMANCE AWAY FROM NON-INDUCTIVE CONDITIONS

The traditional current drive efficiency is difficult to study across a range of parameters due to the need to determine I_{LH} and the limited range of non-inductive conditions achievable on C-MOD. Therefore, to study systematic dependences of LHCD efficiency, an approximate current drive efficiency is estimated by subtracting an estimated residual Ohmic drive in a method similar to that presented in reference [35]. The current can be approximated as being composed of several components:

$$I_{total}(t) \approx I_{OH}(t) + I_{LH}(t) + I_{hot}(t) + I_{BS}(t) \tag{61}$$

where $I_{OH}(t)$ is the current driven by the parallel electric field from the transformer acting on the bulk electrons, $I_{LH}(t)$ is the current carried by the fast electrons driven by the RF electric fields in the absence of any parallel electric field, $I_{hot}(t)$ is the current driven by the parallel electric field on the fast electrons [36], and $I_{BS}(t)$ is the bootstrap current, which is small in the low-pressure L-mode plasmas studied here.

An estimate of the residual Ohmic current is made using $I_{OH} = \sigma_{neo} E_{||}$ in partially-inductive conditions. The neoclassical conductivity can be scaled to first order in bulk plasma parameters as:

$$\sigma_{neo} \approx \sigma_0 \frac{T_e^{1.5}}{Z_{eff}} \tag{62}$$

The constant, σ_0, can then be determined by scaling current and parallel electric field from prior to the application of LHCD at time t_0 to

during the LHCD pulse at time t. The amount of current driven by the transformer during the LHCD pulse is then estimated as:

$$I_{OH}(t) \approx I_p(t_0)\frac{V_{loop}(t)}{V_{loop}(t_0)}\left(\frac{T_e(t)^{1.5}}{T_e(t_0)^{1.5}}\right) \tag{63}$$

where the volume-averaged $T_e^{1.5}$ from the Thomson scattering diagnostic is used while averaging across ~ 60ms and thus many sawteeth. The plasma Z_{eff} is assumed to be constant. This analysis assumes the parallel electric field is penetrated throughout the cross-section and thus is only valid once the plasma has reached a stationary state. The current driven by the LHCD system is then approximated as:

$$I_{LH}(t) + I_{hot}(t) = I_p(t) - I_p(t_0)\frac{V_{loop}(t)}{V_{loop}(t_0)}\left(\frac{T_e(t)^{1.5}}{T_e(t_0)^{1.5}}\right) s \tag{64}$$

allowing an approximate current drive efficiency to be calculated for partially-inductive conditions:

$$\eta^\star \equiv (I_p(t) - I_p(t_0))\ \frac{V_{loop}(t)}{V_{loop}(t_0)}\left(\frac{T_e(t)^{1.5}}{T_e(t_0)^{1.5}}\right)\frac{n_e R}{P_{LH}} \tag{65}$$

$\eta^\star$ is equal to η when the parallel electric field is zero and is a good approximation when the hot conductivity term is negligible.

The approximations made in this analysis are most valid in conditions where the LHCD is dominant and the plasma profiles have not changed drastically between the application of LHCD and the reference time t_0. Studies indicate that the Z_{eff} magnitude is fairly constant across LHCD in the discharges used in this study, though quantifying this effect remains to be done. Note that contamination from hard x-rays make the bremsstrahlung based Z_{eff} measurement unusable. Changes in Z_{eff} profiles during the discharge are not accounted for nor are changes in the temperature profile except through the volume-averaged temperature. The hot conductivity term can be calculated as using the methodology in Reference [37] or (I_{hot}) can be deduced from the dataset using scans of parallel electric field during LHCD experiments as done in Reference [36]. Early experiments with LHCD on C-MOD using this method showed that the effect of hot electron conductivity was not significantly different from zero [8] as evidenced by the fractional change in loop voltage being linearly dependent on $\frac{P_{LH}}{\bar{n}_e I_p R_0}$.

Database studies were performed by Steve Scott to identify trends in $\eta^\star$ as a function of different plasma parameters across the entire collection of LHCD discharges on C-MOD (~ 2000 time slices). This work was not motivated by an expectation that the observed zero-D trends would be necessarily useful as benchmarks to numerical simulations but rather to identify trends for follow-up studies in dedicated ex-

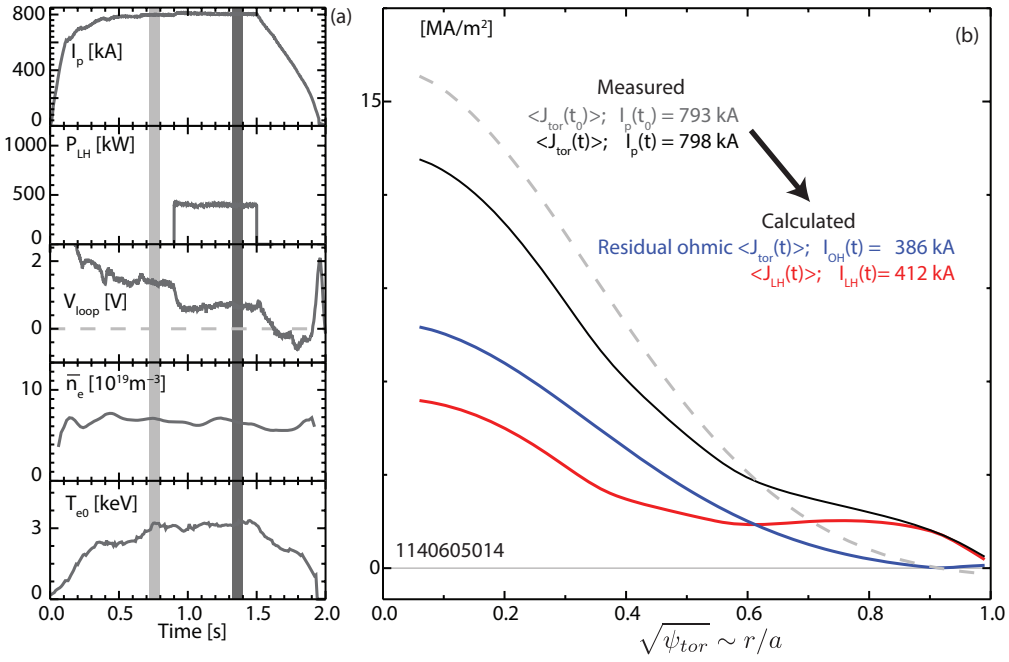

Figure 88: The current profile during LHCD is decomposed into two constituents using Equation 66. The measured current profile prior to LHCD (light gray) is scaled and used to subtract the estimated residual Ohmic current (blue) from the measured current profile during LHCD (dark grey) to yield the contribution from LHCD (red).

periments in which the current profile could be measured with the upgraded MSE system. In these experiments both the current and HXR profiles were measured as a single plasma parameter (density, power, $n_{\|}$, I_p) was scanned, holding fixed the other parameters. The current and HXR profiles are then compared across parameter scans where other variables are held fixed.

7.5.1 *Decomposing the current density*

The previous analysis for the total current driven by LHCD in partially-inductive conditions can be extended to decompose the current density profile from the equilibrium reconstructions into components due to LHCD and due to the residual parallel electric field by replacing the total current with the current density:

$$< J_{LH}(t) > \approx < J_{tor}(t) > - < J_{tor}(t_0) > \frac{I_p(t)}{I_p(t_0)} \frac{V_{loop}(t)}{V_{loop}(t_0)} \left(\frac{T_e(t)^{1.5}}{T_e(t_0)^{1.5}} \right) \tag{66}$$

where the calculation is done with the flux-surface averaged current densities[6]. $< J_{LH} >$ includes any contribution from the residual elec-

6 The average temperature is used thus the temperature profiles effects are not accounted for in this analysis.

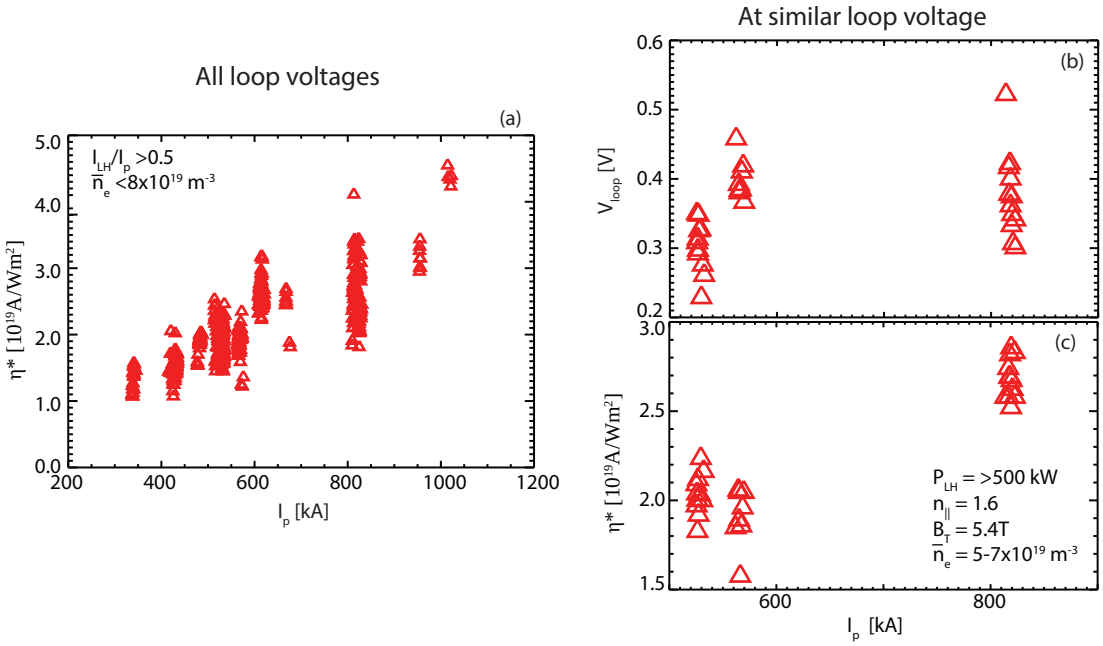

Figure 89: Database studies show that η* increases as the plasma current is increased (a) in plasmas with a large contribution of the LHCD to the plasma current. The trend is also apparent when comparing plasmas with similar loop voltages at different currents and LHCD powers (b,c).

tric field acting on the fast-electrons. Figure 88 shows this decomposition technique for a partially-inductive plasma. The current profile during the Ohmic period (gray) is scaled (blue) and subtracted from the current profile measured during LHCD (black) to yield the estimated current profile due to the LHCD (red).

7.6 PLASMA IP SCAN

The strongest dependency identified in the η* database is an increased current drive efficiency at increased plasma current. This trend is a robust observation in the entire database, apparent in all the operational years of the LHCD system from both generations of LHCD launchers. An example database plot is shown in Figure 89. Examining discharges with a significant fraction of the current driven by LHCD shows an increasing η* (a). Confining the database to discharges with similar loop voltages shows the effect is still present (b,c). Further investigation using similar shots show increased HXR emission and larger relative changes in loop voltage at higher current with other parameters fixed. This trend is also apparent in the control-room during LHCD experiments—many of the best-performing (i.e., largest absolute change in loop voltage) plasmas during current drive experiments have been at higher current.

This trend is also observed in TORE SUPRA where the current drive efficiency during fully non-inductive discharges nearly doubles by

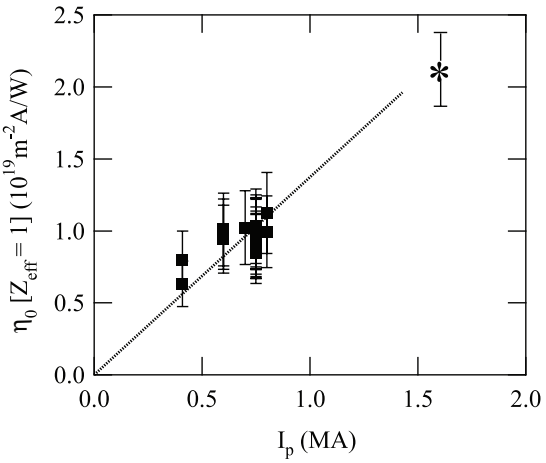

Figure 90: TORE SUPRA also observes an increased current drive efficiency at increased plasma current during fully non-inductive operation. From [32].

doubling the plasma current as shown in Figure 90 [32]. Similar increases of current drive efficiency were also observed on JT60-U [38] and FTU [39] during non-inductive discharges.

The lower hybrid wave propagation $n_{||}$ upshift is affected by the poloidal field, thus a plasma current dependence could be expected due to changes in the poloidal field structure. The lower hybrid absorption is dependent on the local plasma temperature and thus an apparent dependence on plasma current could also be an artifact of the temperature profile changing—it typically broadens as the current is increased in a given device. Regression studies on FTU show an explicit plasma current effect [39]. The result is less clear in C-MOD as the database has a covariance in temperature and plasma current, though the data has less scatter when organized by plasma current. The effect could also be due to changes in the scrape-off layer (SOL) in which the lower hybrid wave propagates—SOL profiles are dependent on plasma current.

The previously discussed time-dependent profiles hinted at a profile plasma current dependence— the high current discharge showed "shoulders" that were not apparent in the low current discharge and also produced broader hard x-ray profiles. Dedicated experiments were then conducted to determine the effect of plasma current on the current profile during LHCD. Figure 91 shows the change in pitch angle at different plasma currents and the resulting change in current density profile. The profile broadens significantly at increased plasma current, even in the Ohmic period (dashed lines) but change in current profile during LHCD also shows more broadening at increased plasma current. Figure 92 shows several zero dimensional measures of the effect of LHCD during the plasma scan. The drive term, $P_{LH}/\bar{n}_e$, was fairly stationary across the scan (a) leading to a similar relative change in loop voltage (d) and increased current drive (b) and current drive efficiency (c). The total HXR count rate also increases (e) and the plasma ℓ_i decreases in both the Ohmic stage of the target plasma

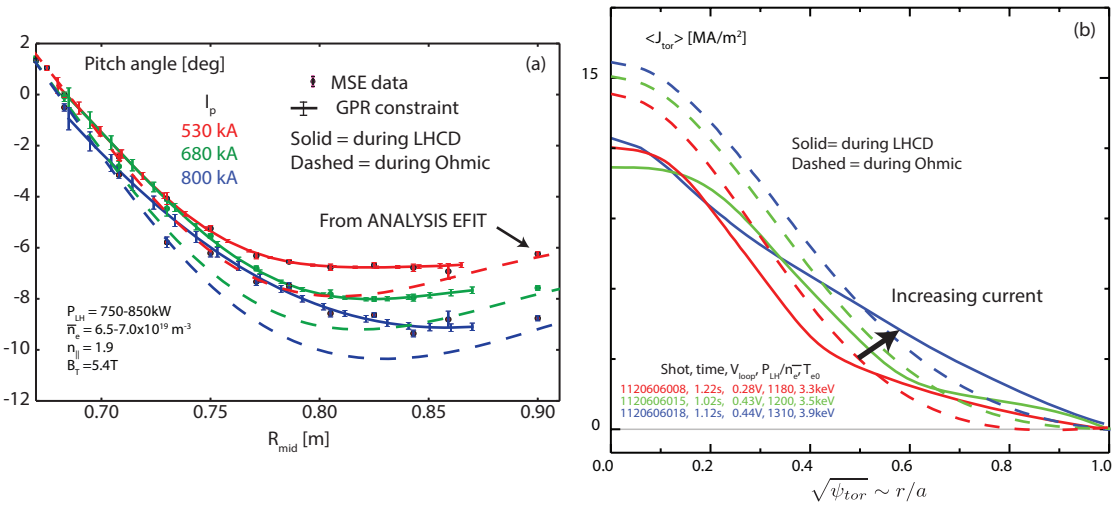

Figure 91: The pitch angle (a) and resulting current profile (b) dependence on plasma current.

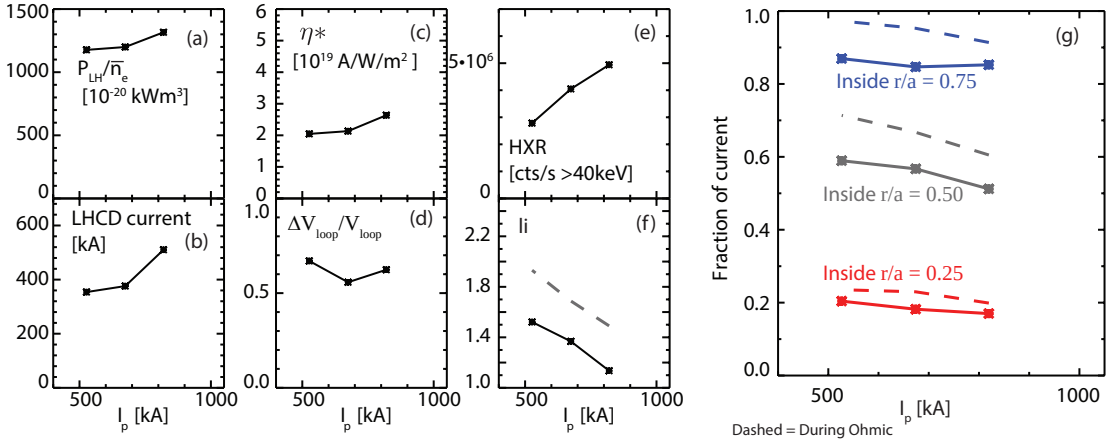

Figure 92: Zero-D quantities as a function of plasma current.

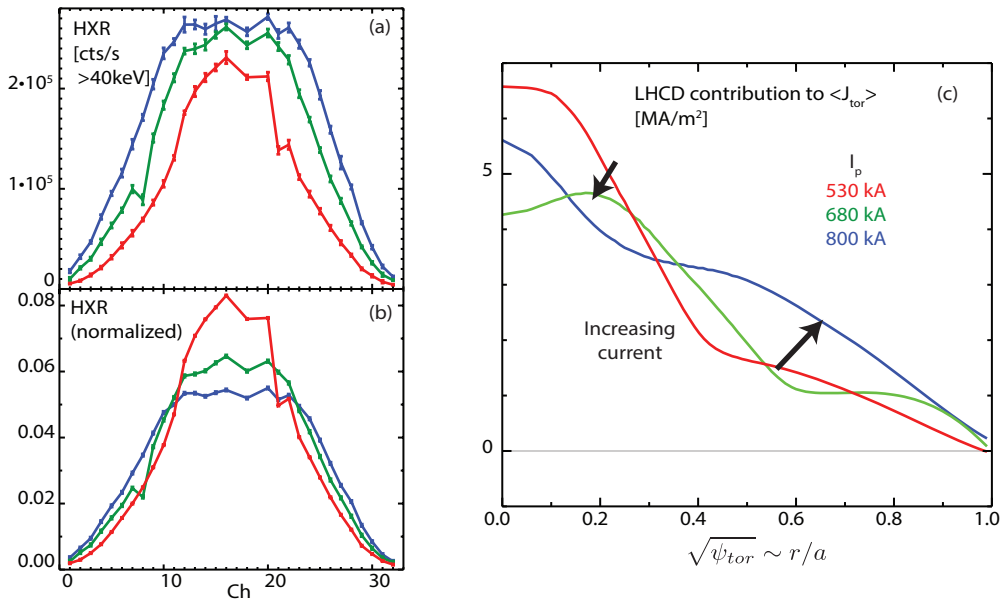

Figure 93: The HXR profile (a,normalized to total b) and LHCD contribution to the current profile as a function of plasma current.

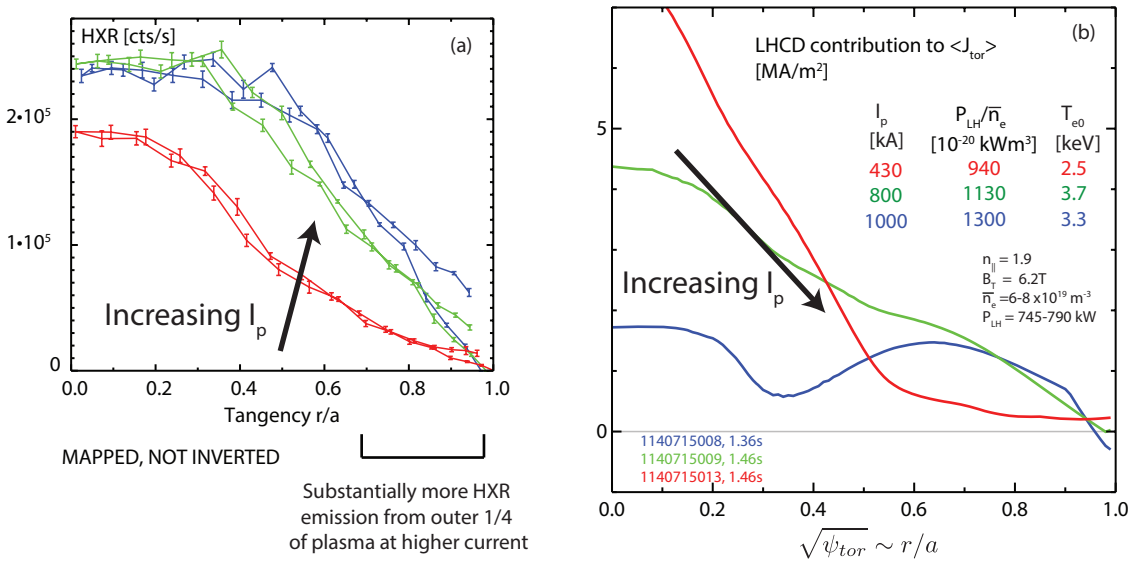

Figure 94: The HXR profile (mapped to sightline tangency radius but not inverted) and estimated LHCD contribution to the total current as a function of plasma current for a large scan of plasma current but not at fixed LHCD drive.

and during LHCD (f). The effect of broadening the current profile is apparent in the metrics of the current profile (g).

The HXR profile and contribution from LHCD to the total current profile are shown in Figure 93. The HXR count rate increases and the profile becomes broader at higher current. This effect is also present in plasmas with lower LHCD power and lower HXR count rates. The contribution from LHCD to the total current also appears to become broader at higher plasma current.

An additional scan of plasma current over a larger range (400 – 1000kA) was conducted but with a poorer match in density. The results are shown in Figure 94 where the HXR emission has been mapped into r/a but not inverted. It is apparent that there is significantly increased HXR emission coming from $r/a > 0.7$ at the higher currents. Note that due to the line integrated nature of the HXR camera, the increased emissivity at the outer portion of the plasma also contributes to brightness on chords passing through the middle of the plasma, thus the emissivity might be becoming peaked off-axis in the discharges at high current. This effect is also apparent in previous work on C-MOD ($n_{||} = 3.1$, $\bar{n}_e = 9 \times 10^{19} m^{-3}$) using inverted HXR data [33]. The contribution from LHCD to the total current shifts from being peaked on axis in the low current discharges to being very broad at the high current with substantial current being driven outside $r/a \sim 0.7$, consistent with the HXR data and the previously discussed shoulders in the current profile.

Broadening of the current profile and the HXR emission during higher current operation was also observed on TORE SUPRA [32] and

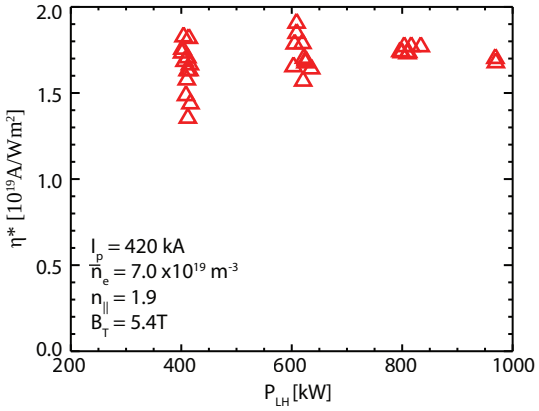

Figure 95: $\eta^\star$ scaling as a function of P_{LH} in a dedicated power scan.

JT60-U [38] and linked to broader temperature profiles, which may also be important in the C-MOD results.

7.7 LOWER HYBRID POWER SCAN

One possible explanation for the observed current dependence could be the influence of the residual parallel electric field which is largely covariant with I_p in the previously discussed scans. The residual parallel electric field could in principle skew the various 0-D measures of current drive and could also affect the HXR profiles by preferentially accelerating electrons in the low density region (i.e., outer part of the radial profile). Any effect would also be included in the current profile attributed to the LHCD using the current profile decomposition.

The dependence of $\eta^\star$ on the residual parallel electric field was determined using a scan of LHCD power into identical low current target plasmas ($\bar{n}_e = 7.0 \times 10^{19} m^{-3}$, $I_p = 420$kA, $B_T = 5.4$T, $T_{e0} = 2.0$keV, launched $n_{||} = 1.9$) resulting in a variation in current drive from < 10 percent non-inductive to fully non-inductive. The $\eta^\star$ as a function of LHCD power for various time points in the study are shown in Figure 95. The current drive efficiency is relatively independent of LHCD power—as expected. Since the loop voltage varied during this scan (0.7V to 0.06V), this places an upper limit on the residual parallel electric field's effect on the fast electrons. This indicates that the effect is not important in determining the current drive efficiency in this parameter range, consistent with prior work on C-MOD [8, 21], and FTU [35].

The measured pitch angle profiles and the resulting total current profiles are shown in Figure 96. The pitch angle changes most significantly at the mid to inner radius in these low current discharges. As expected, the largest change in pitch angle are observed with the highest LHCD power, though there is still a significant change in pitch angle even at the lowest power. The resulting current profile has an off-axis contribution at $r/a \sim 0.6$ that increases as the power increases

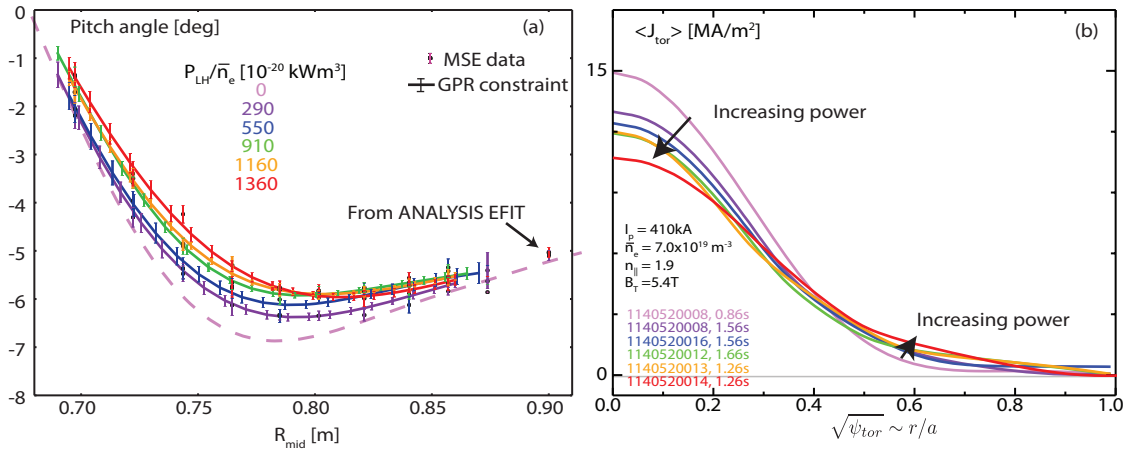

Figure 96: The dependence of the pitch angle as measured by MSE and the resulting J_{tor} profile on P_{LH}.

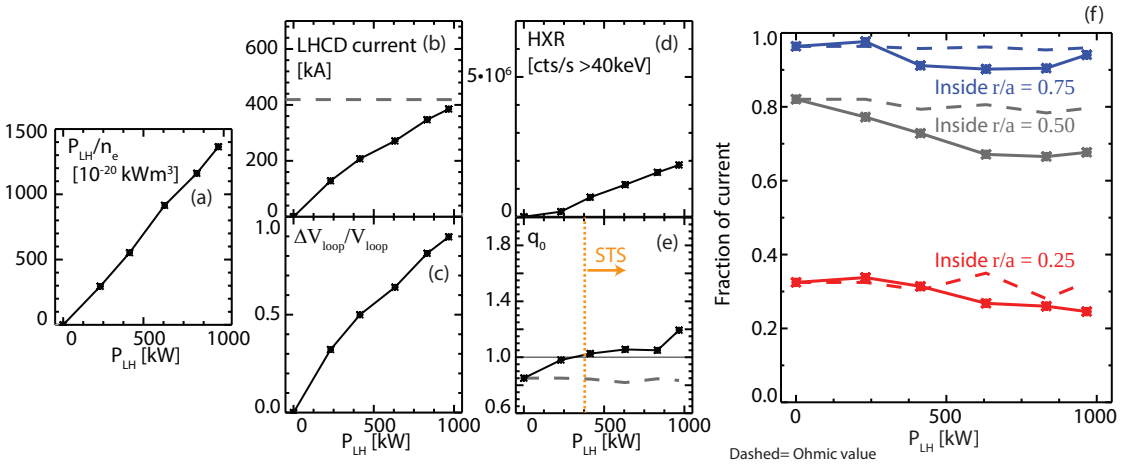

Figure 97: The dependence of zero-D quantities on P_{LH}. STS indicates periods of sawtooth stabilization.

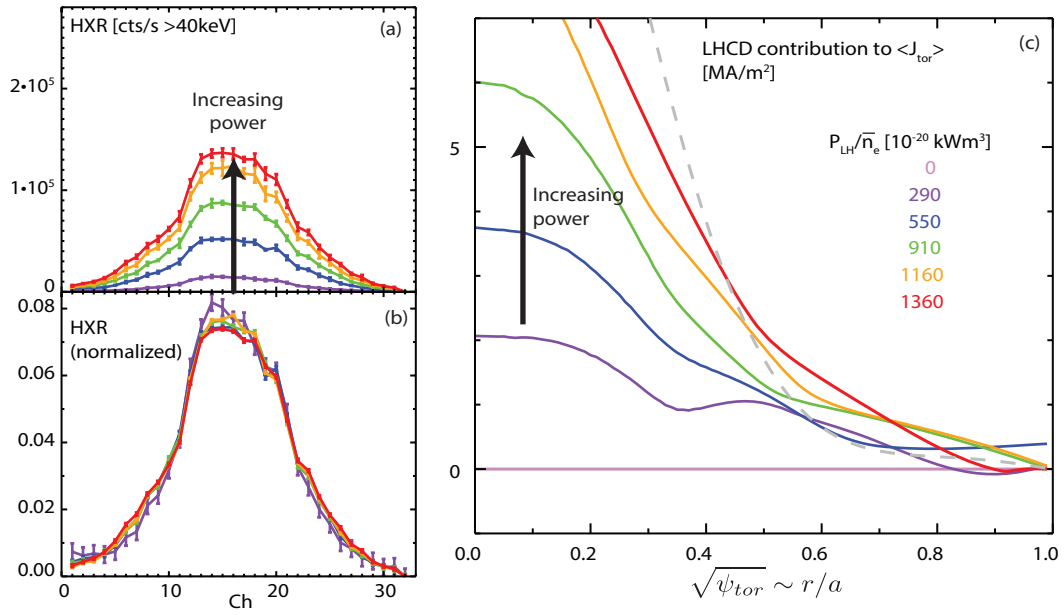

Figure 98: The HXR profiles and the contribution of LHCD to the current profile as function of P_{LH} as calculated from Equation 66.

while the central current density decreases as the power increases, though the effects are not drastic at any location in the profile.

Zero-dimensional indicators of current drive are shown in Figure 97. The LHCD drive term (a) was kept linear (i.e. the density was constant) across this scan leading to a large scan in the normalized change in loop voltage (c). The inferred LHCD driven current (b), and total HXR count rate (d) are all fairly linearly dependent on the lower hybrid power similar to that observed in TORE SUPRA [32]. Sawteeth are suppressed in discharges with power above 400kW ($P_{LH}/\bar{n}_e \sim 500 \times 10^{-20}$kWm^{-3}) consistent with q_0 rising above 1 in the reconstructions (e). The current profile broadens somewhat until $P_{LH} \sim$ 500kW after which the profile changes very little (f). Even at high power, where the plasma is nearly non-inductive, there is still a significant fraction of current inside the half radius.

The HXR profiles and the inferred contribution of LHCD to the total current are shown in Figure 98. The HXR emission intensity increases with increasing power as expected (a) while the profile shape remains self-similar at all powers (b). $< J_{LH} >$ is centrally peaked at all LHCD powers and is also fairly self-similar. These results indicate that the LHCD driven current is fairly independent of changes in the magnetic equilibrium or the amount of current already driven by the LHCD system.

7.8 LAUNCHED $n_{||}$ SCAN

The C-MOD LHCD system can vary the launched $n_{||}$ spectrum, thus changing the wave propagation trajectories. Database studies indicated that there is little dependence of the current drive efficiency as a function of launched $n_{||}$. Database studies from the FY10, FY11, FY12, and FY14 campaigns showed consistent results across multiple parameters with the indicators of current drive (change in loop voltage, non-thermal ECE, and HXR emission) showing little to no dependence on launched $n_{||}$ at fixed $\frac{P_{LH}}{\bar{n}_e}$.

A dedicated experiment was conducted where the $n_{||}$ was varied shot-to-shot into identical target plasmas ($\bar{n}_e = 6.0 \times 10^{19}$m^3, $I_p =$ 615kA, $B_T = 5.4$T, $T_{e0} = 2.4$keV, $P_{LH} = 630$kW), resulting in non-inductive fractions of $\sim 0.5 - 0.6$. The time traces from the discharges are shown in Figure 99. Note that the discharges achieved nearly the same loop voltage and similar central electron temperatures at similar LHCD powers despite a large variation in launched $n_{||}$. The reflection coefficient from the launcher increased with increasing $n_{||}$ from 0.35 to 0.55 qualitatively consistent with expected coupling of different $n_{||}$ [22], confirming that the launched $n_{||}$ was indeed varying as reported by the system.

The measured pitch angle profiles and resulting current profiles from late in the LHCD pulse are shown in Figure 100. The pitch angle

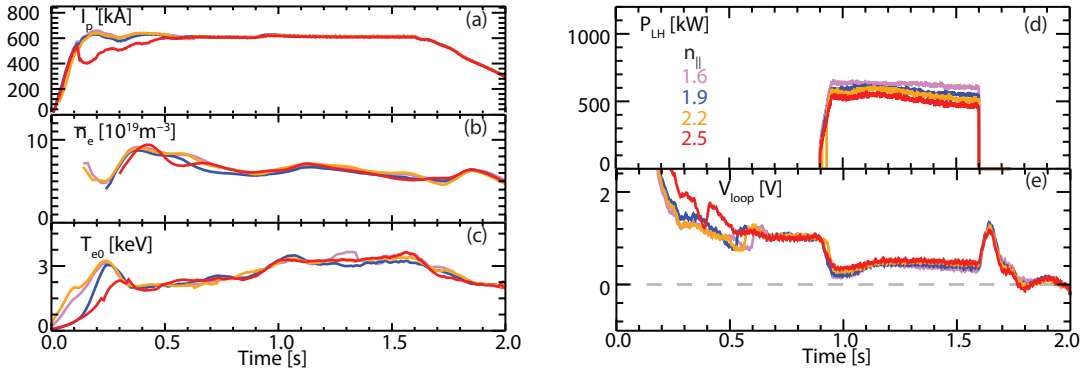

Figure 99: Time traces from varying the launched $n_{||}$ in matched discharges.

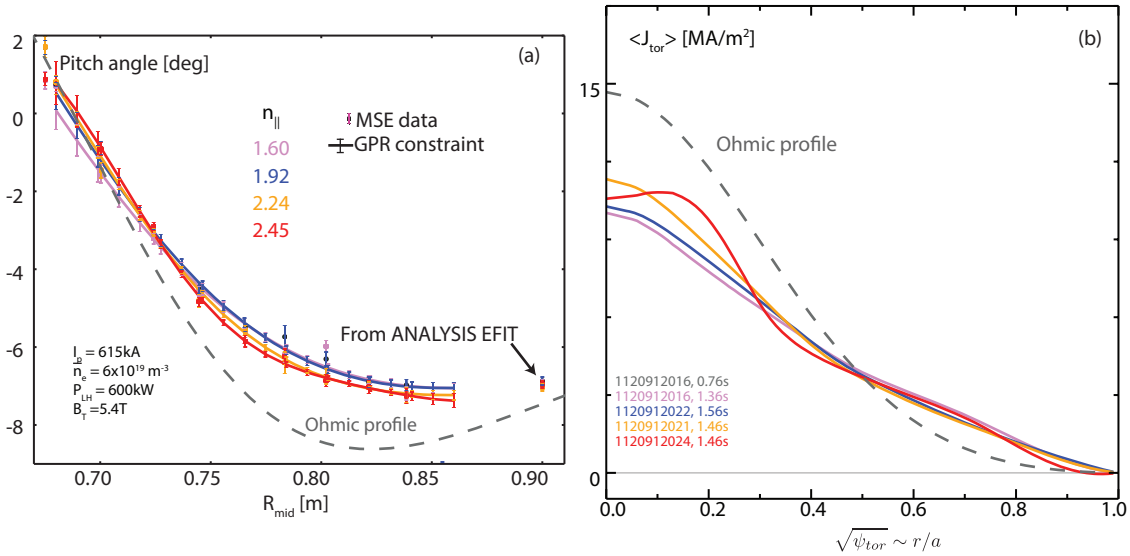

Figure 100: The pitch angle (a) and J_{tor} (b) dependence on the launched $n_{||}$.

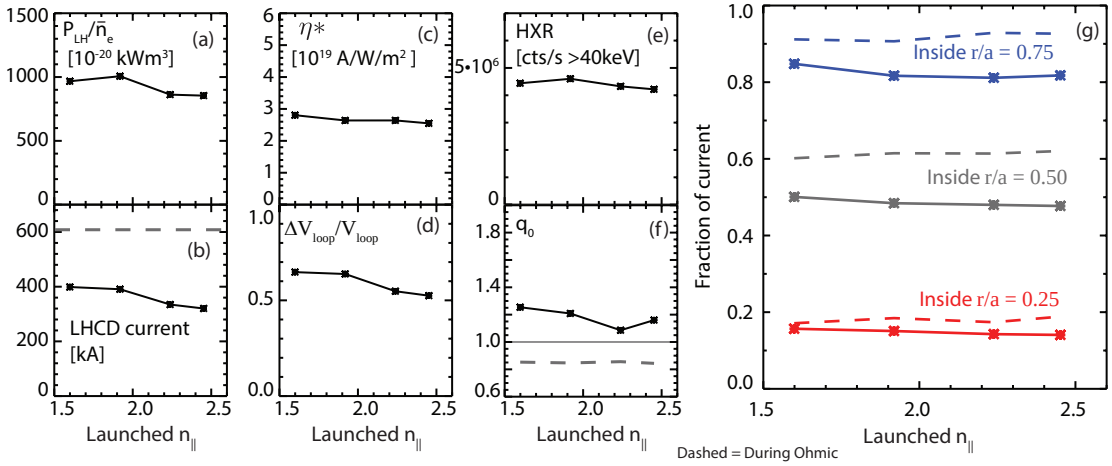

Figure 101: Zero-D quantities as a function of launched $n_{||}$.

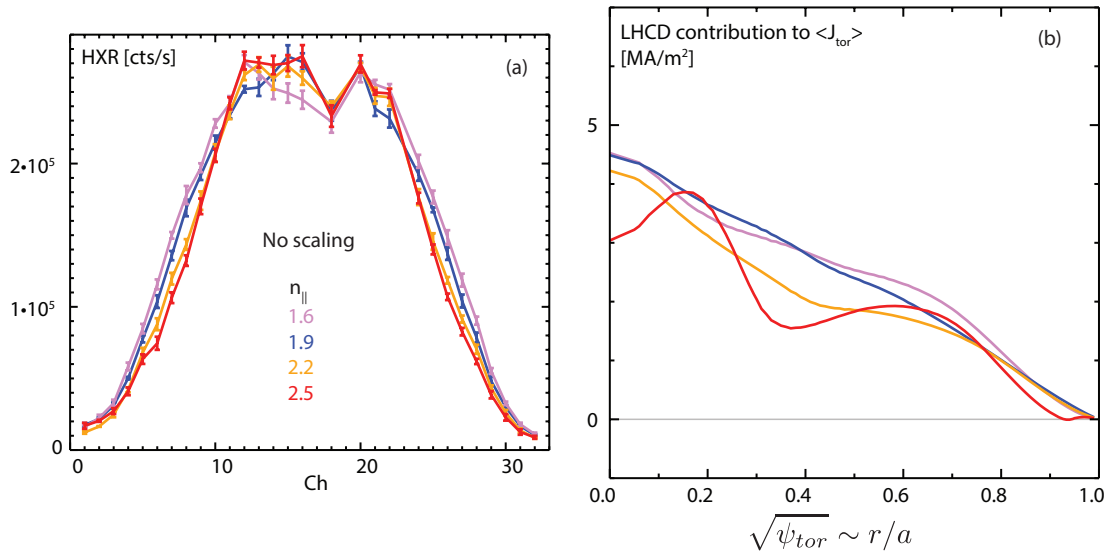

Figure 102: The HXR profiles (a) and the contribution from LHCD to J_{tor} (b) as a function of launched $n_{||}$

profiles are nearly identical across the variation in launched $n_{||}$ (a). This results in very similar current profiles across launched $n_{||}$ (b) with a contribution to the plasma current density outside of $r/a \sim 0.6$ above the Ohmic current profile and a decrease in the core. The profiles of the non-thermal ECE are also nearly identical among the different launched $n_{||}$.

The zero-dimensional quantities extracted from the measurements are shown in Figure 101. This scan had a well matched LHCD drive (a, $P_{LH}/\bar{n}_e$) resulting in a fairly constant non-inductive current fraction (~ 0.5). The current drive efficiency (c) and hard x-ray total count rate (e) are both constant. All discharges were sawtooth suppressed consistent with $q_0 > 1$ (f). The plasma ℓ_i (not shown) increases slightly at higher $n_{||}$, indicating the current profile is slightly narrower at higher launched $n_{||}$. As expected from the current profiles, the fractions of current at different minor radii are fairly independent of launched $n_{||}$ (g).

The HXR profiles and the LHCD contribution to the total plasma current is shown in Figure 102. The HXR profiles are very self-similar in shape and magnitude at each phasing and the LHCD-driven component of the current profile is also is nearly the same for all launched $n_{||}$. This behavior is consistent with all the zero dimensional parameters. A similar scan was conducted at $I_p = 800$kA but was not as well-controlled in density. However, the result was very similar—the current profile, HXR profiles, and current drive indicators did not depend on launched $n_{||}$. This differs significantly from observations on TORE SUPRA where the location of off-axis peaks in HXR emission are sensitive to launched $n_{||}$ at the $\Delta n_{||} \sim 0.05$ level [40].

Interestingly, the observed insensitivity of current drive to launched $n_{\parallel}$ in these experiments and database studies differs qualitatively from earlier (~ FY08) experiments discussed in references [21, 25]. The current drive efficiency was shown to be strongly dependent on $n_{\parallel}$ in these experiments which were conducted at modestly higher current (800kA vs. 600kA), higher magnetic field (6.2T vs. 5.4T), nearly the same density. In the earlier experiments a strong dependence of current profile and current drive efficiency was observed. In addition, standard 0-D measures of current drive such as non-thermal ECE, HXR emission (note the core chords were saturated) and delta ℓ_i also showed a positive correlation with launched $n_{\parallel}$[7]. It is hard to challenge the validity of the earlier high-level conclusions that the launched $n_{\parallel}$ affected the current drive efficiency in the 2008 experiments: Both the HXR and MSE profiles and several 0-D metrics between the two eras, although this issue has not been addressed quantitatively. However, the more recent experiments are equally compelling: both the HXR and MSE profile diagnostics and several 0-D indicators of current drive show no dependence on launched $n_{\parallel}$—even the loop voltage was the same. This conundrum seems unlikely to be attributable to the relatively minor differences in plasma condition.

There was however a qualitative change in technology between the 2008 experiments and the 2010+ experiments: the 2008 experiments were conducted with an earlier LHCD launcher (LH1) that was a traditional grill-based launcher with each row and column individually powered [41]. The 2010+ experiments use a novel four-way splitter design that couples the rows together (LH2). The launched $n_{\parallel}$ spectra are slightly different between the two launchers and the 2010+ experiments had a larger reflection coefficient than the 2008 experiments.

7.9 PLASMA DENSITY SCAN

Various tokamaks have observed a decrease in current drive efficiency as the density is raised above $3-6\times10^{19}\mathrm{m}^{-3}$. A good review is presented in references [3, 42]. The various mechanisms that impair performance of LHCD at high density in ALCATOR C-MOD are reviewed in reference [19]; a short summary is provided here. Early on in the program significant melting of the lower-hybrid launcher was observed at the same regions where video cameras observed bright spots during LHCD injection. In addition, parallel current densities of order 500 $\mathrm{kA/m^2}$ were observed on divertor Langmuir probes just outside the separatrix during high power LHCD when $\bar{n}_e$ exceeded about $10\times10^{19}\mathrm{m}^{-3}$, and the plasma density in the outer SOL was observed

7 Some of the plasmas in the earlier experiment experienced deleterious MHD which may have reduced the current drive efficiency at higher $n_{\parallel}$, although this behavior was recognized during data analysis and the selected time slices were chosen to minimize the effect

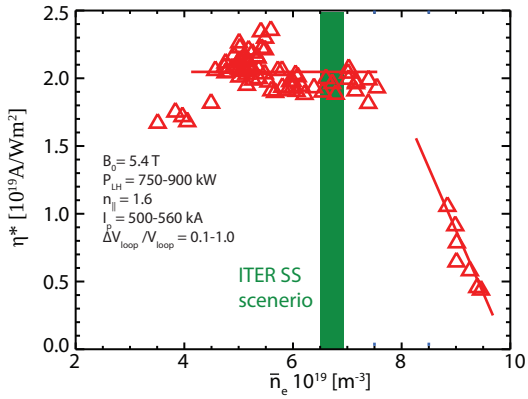

Figure 103: $\eta^\star$ as a function of plasma density across a large range of densities. The density of the ITER steady-state scenario is indicated by the green shaded region.

to promptly increase at the application of lower hybrid power, presumably due to ionization in the scrape-off layer [43]. All this evidence suggested that lower hybrid power is partially absorbed in the SOL, particularly at high density. Fast electron Bremsstrahlung emission was observed to drop suddenly above $\bar{n}_e = 10 \times 10^{19} m^{-3}$, (corresponding to $\omega/\omega_{LH} \approx 4$), below the density limit previously observed on other experiments ($\omega/\omega_{LH} \approx 2$) [44]. The density dependence of the hard x-ray emission was found to be poorly represented by conventional modeling, but models which included collisional absorption in the SOL were in better agreement with the observed behavior [45]. Parametric decay instabilities have also been proposed as a mechanism to decrease the current drive efficiency at high density [46].

Figure 103 shows the results of a $\eta^\star$ database study showing that the current drive efficiency is independent of density at densities below $\sim 8 \times 10^{19} m^{-3}$ above which the current drive efficiency inferred rapidly decreases [8] (note that at high density the accuracy of estimating the current drive efficiency is degraded since the LHCD current drive is no longer dominant over the Ohmic current drive and becomes the result from subtracting two similar numbers).

Dedicated experiments were conducted to measure the current profile dependence on the plasma density. The plasma parameters were specifically chosen to correspond to the discharges used in previous studies of the anomalous loss of current-drive efficiency utilizing the HXR camera. The magnetic configuration was the same for all discharges: diverted, lower single null, ($B_0 = 5.43$ T, $I_p = 0.56$ MA, $q_{95} = 6.5$). On individual shots the C-MOD density feedback system was commanded to maintain nominally constant electron density throughout the current flattop including the period of LHCD, spanning a range $\bar{n}_e = 5.8$ to $10.9 \times 10^{19} m^{-3}$ over the shot ensemble. The lower hybrid power was sustained for 700 ms to allow the discharge to reach equilibrium.

8 The experiments in previous sections were conducted at lower densities where current drive is shown to be efficient and robust.

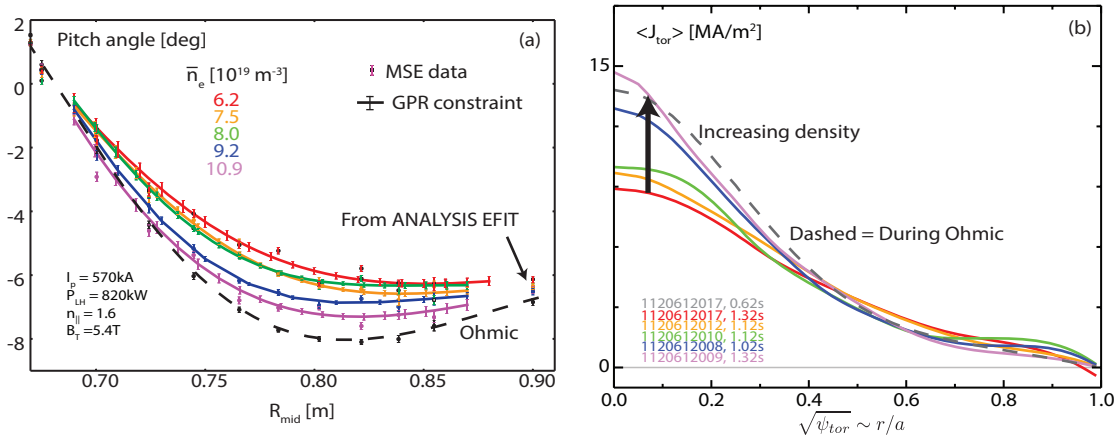

Figure 104: Pitch angle measurements (a) and reconstructed J_{tor} (b) from a scan of plasma density.

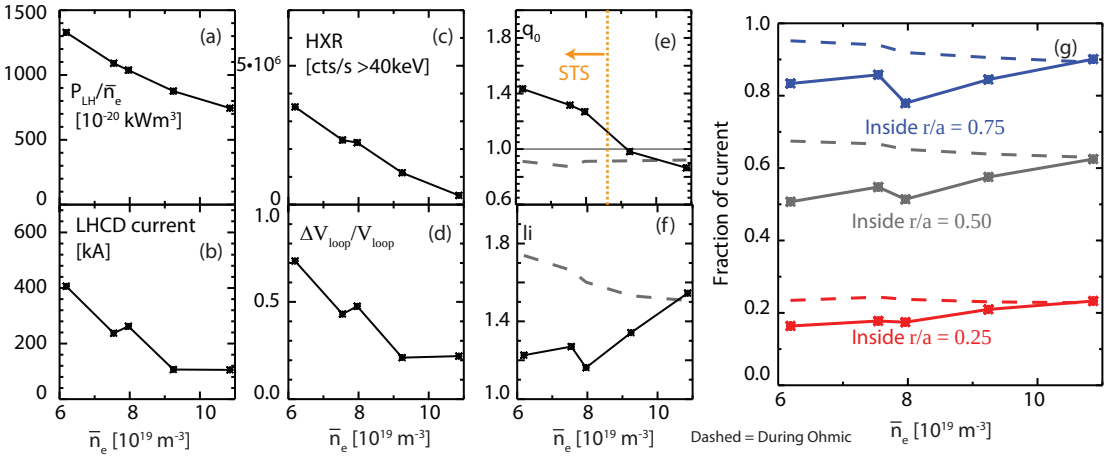

Figure 105: Zero dimensional measures of current drive as a function of plasma density.

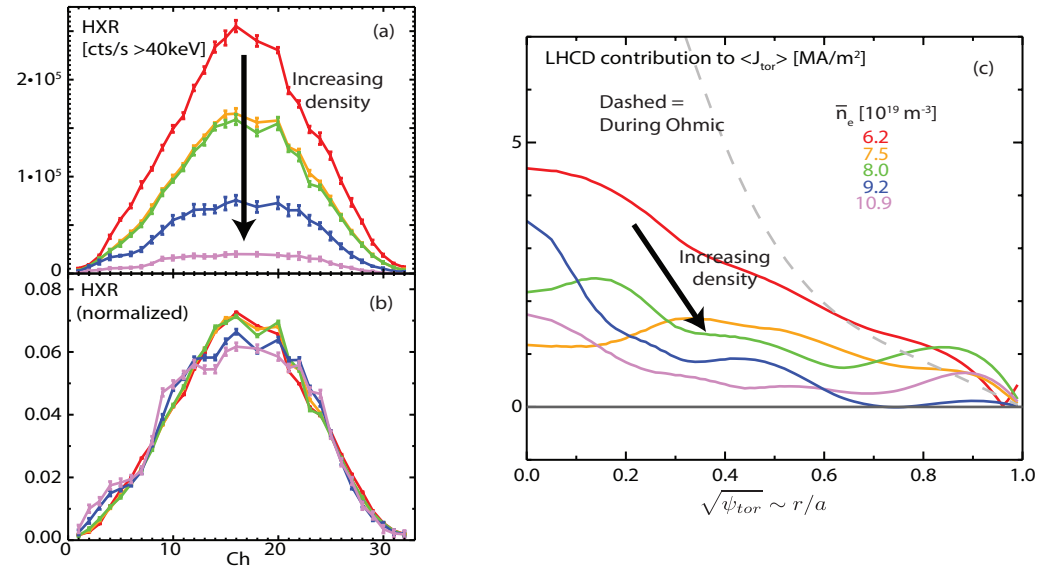

Figure 106: HXR profiles (a,b) and the estimated LHCD contribution to the current profile (c) as a function of plasma density.

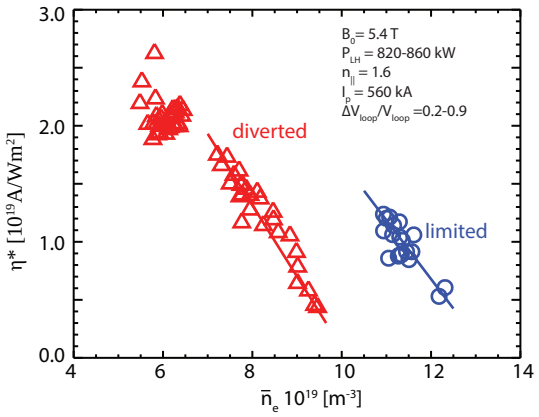

Figure 107: The estimated current drive efficiency as a function of plasma density for diverted (red) and limited (shots).

Figure 104 shows the measured pitch angles as a function of plasma density. As the plasma density is increased the change in pitch angle decreases and the resulting current profile increasingly resembles the Ohmic current profile. The zero dimensional measures of the current drive are shown in Figure 105. The HXR emission (c), relative change in loop voltage (d) and inferred current drive (b) all decrease as the density is increased while q_0 (e) decreases and ℓ_i (f) increases back to the Ohmic value. The parameterization of the current profile returns to the Ohmic values at high density.

The HXR profile and inferred contribution to the current drive are shown in Figure 106. The HXR profile shape is nearly self-similar at all densities—perhaps slightly broader at higher density. The contribution of LHCD to the total current drive decreases to nearly zero and perhaps moves outward at higher density, though the uncertainty is large. Generally there is not a significant effect on either of these profiles due to density changes. The lack of a strong density dependence of the HXR profile on density is also observed in TORE SUPRA where the HXR emission become slightly narrower as the density increases from $1.5 - 5.5 \times 10^{19} \mathrm{m}^{-3}$ [47].

The estimated current drive efficiency for time periods within this density scan is shown in Figure 107.

7.10 LIMITED VS DIVERTED

Previous experiments showed that the expected density dependence of current drive efficiency is recovered for inner-wall-limited plasmas up to $\bar{n}_e = 1.5 \times 10^{20} \mathrm{m}^{-3}$ [48]. Further observations showed that the population of LHCD-driven fast electrons at high density ($\bar{n}_e > 10^{20}$ m^{-3}) could be increased by operating with an inner gap of less than 5 mm or by a change in topology from single- to double-null [49].

The density dependence experiment discussed in the previous section was extended to include discharges that were inner-wall limited

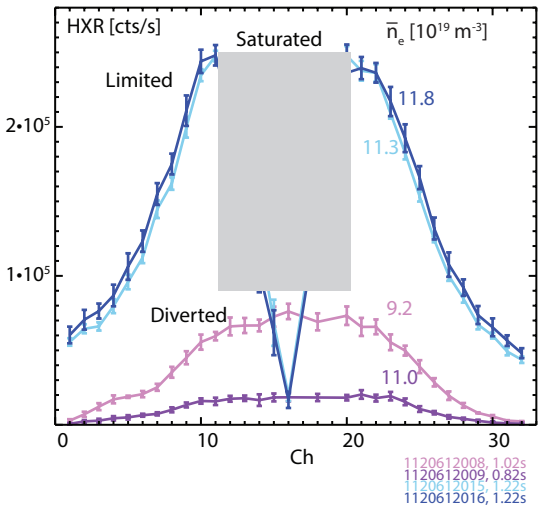

Figure 108: Comparison of the HXR profiles in limited and diverted discharges at high density. Note that the central chords are saturated in the limited discharges (gray shaded region), presumably due to thick-target bremsstrahlung from fast electrons striking the inner wall within the view of the chords.

at $\bar{n}_e > 1 \times 10^{20} m^{-3}$ where significant current drive is no longer observed in diverted discharges[9]. The $\eta^\star$ inferred from these discharges is shown in Figure 107 where changes in the loop voltage in the limited discharges indicate current drive efficiencies that are higher than those in diverted discharges at lower densities.

The HXR profiles in limited and diverted discharges are compared in Figure 108. The limited discharges produce dramatically higher HXR emission than the diverted discharges. A few caveats should be noted. The central hard x-ray camera chords are saturated during the limited discharges presumably due to fast electrons striking the inner wall within the view of the central chords. Also, the edge-most HXR chords observe emission from outside of the confined plasma, thus the entire HXR profile likely observes some of this emission. However, the increased production of HXR emission remains a robust feature of limited discharges.

A comparison between the pitch angle profiles and resulting current profile measurements in limited and diverted discharges is shown in Figure 109. The limited discharge shows a significantly larger change in pitch angle between the ohmic and the LHCD period than the diverted discharge despite being at a 20 percent higher density and correspondingly lower LHCD drive. The current profiles in the limited discharges show small changes in the outer parts of the profile and less central current. These experiments indicate that current drive is indeed recovered in inner-wall limited discharges with current drive off-axis.

9 Lower density limited discharges are difficult to obtain due to fueling from the limited surface.

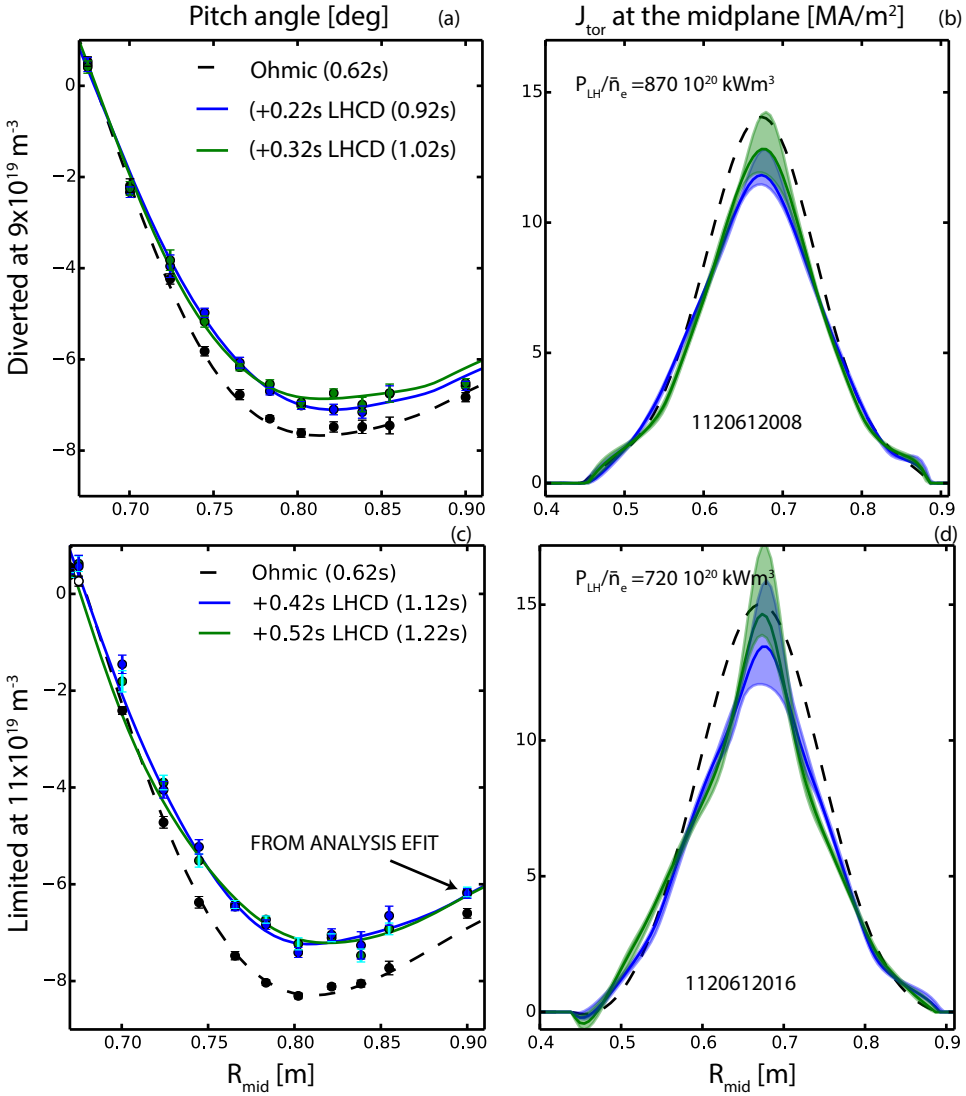

Figure 109: Comparison of pitch angle profiles (left) and resulting current profiles (right) in diverted (top) and limited (bottom) discharges at high density.

7.11 SUMMARY: PARAMETRIC DEPENDENCE OF LHCD PROFILES

The first systematic measurements of the current profile were performed on ALCATOR C-MOD using the upgraded MSE system and the HXR camera. This study is the first published study across many different parameter ranges at the field, frequency, and density envisioned for a reactor in a diverted geometry. The measured current profile has the expected time dynamics, settling into an equilibrium within 0.3 seconds while the HXR profile is prompt and self-similar.

Database studies indicated parameter ranges of interest for detailed studies in parameter scans. The strongest dependence identified was due to plasma current with broader LHCD-driven current and HXR profiles and more efficient current drive occurring at higher plasma current in a manner also observed on other tokamaks at lower density and field. There is current drive across the entire plasma minor-radius at all plasma currents including near the edge of the plasma. The current drive in the outer $r/a \sim 0.3$ increases at increased plasma current and is apparent even at modest (< 500kW) LHCD power.

However, at nominal low current operating conditions (< 900kA) the LHCD-driven current remains centrally peaked. The current profile broadens from that observed during Ohmic drive but does not typically create an off-axis peak (except in plasmas with an internal transport barrier, not discussed here). q_0 is raised in these plasmas but does not typically reach values as high as 2. These results are consistent with temperature profiles remaining peaked on-axis, MHD observations, and the appearance and cessation of sawteeth. Additional comparisons to the polarimetry system installed on C-MOD using a MK-EFIT-driven synthetic diagnostic show consistent results in all three chords [50] adding confidence that the current profile is correctly represented by the reconstructions.

The driven current profile and HXR profiles are self-similar across large ranges of LHCD power with a linear dependence of HXR emission on power. The LHCD current profiles and current drive efficiency are independent of the residual parallel electric field, consistent with previous results on C-MOD and results on other tokamaks operating at high density.

Database studies were conducted on global indicators of current drive efficiency as a function of the launched $n_{\|}$. It was found that the current drive efficiency is generally a weak function of this parameter in the last several campaigns. A very well controlled dedicated experiment was conducted which indicated that the current drive efficiency was independent of launched $n_{\|}$ as were the current and HXR profiles. Other experimental scans confirm this in the operating range of interest on C-MOD. However, a previous experiment conducted seven years ago with a previous lower hybrid launcher in a similar regime on C-MOD showed a strong dependence which could not be reproduced.

Resolving this apparent contradiction may provide insight into some aspects of LHCD that could be important for future experiments.

Experiments were conducted to determine the dependence of the current drive profiles on plasma density in the regime where the current drive efficiency rapidly degrades with increasing density. The driven current profile may become slightly broader as the density is raised but generally does not show significant dependence on the plasma density—there is no major shift in any of the profiles, the current drive just goes away. When the plasma becomes inner wall limited the current drive is recovered, consistent with previous observations, and the current profile is indeed significantly modified.

Generally it is observed that the LHCD acts mostly to replace the Ohmic driven current with a similar current profile. The large changes in MSE pitch angle and current profile with the accompanying MHD activity seen in other tokamaks with current profiles peaked off-axis are not typically observed on C-MOD. The central electron temperature also typically peaks or stays the same in these discharges despite replacing the Ohmic heating with LHCD heating. The shape of the LHCD current profile is also robust, aways producing self-similar HXR and LHCD contributions to the current profile—except as a function of plasma current.

It is as if the lower hybrid waves simply find the hottest part of the plasma—the core in these plasmas—and mostly damp there. At higher current this hotter part of the plasma is broader, possibly explaining differences as a function of current. The upgraded multi-spectral MSE system will enable profile measurements in plasmas with extensive ICRF heating, a regime where the MSE diagnostic was blinded by background light and the HXR diagnostic has contamination from fusion neutrons. Previous experiments have indicated that increasing the temperature may increase the current drive efficiency and these will be revisited with this enhanced measurement capability to determine profiles. It may be interesting to determine if the LHCD driven current profile can be broadened in low current discharges using auxiliary heating or if the current profile can be made off axis using off-axis heating.

Previous work has highlighted the role of the SOL and edge parameters on the lower hybrid current drive at high densities when the device operates in the multi-pass regime. However, the work reported here was conducted at lower densities where good current drive efficiencies, in agreement with theory, are typically achieved. However, these discharges are still in the multi-pass regime. The lack of a LHCD current profile and HXR profile dependence on parameters such as launched $n_{\|}$ and density, which are important in the wave propagation and damping, could hint that something besides traditional lower hybrid wave physics is influencing the current drive even at these low densities similar to what has been studied at higher

densities. Thus selected scans will be compared to simulation in the next chapter. One could speculate that the role of the SOL and reflections is important even in this density regime. Perhaps the edge modifies the wave power or $n_{||}$ prior to absorption or the wave makes many passes, filing the tokamak until it damps in the hottest region, leading to peaked profiles and the lack of any strong dependency besides the current dependence—an important parameter for the SOL profiles. Future experiments such as $n_{||}$ scans into limited discharges (where the SOL profiles are significantly different than diverted discharges) would be illuminating, particularly if dependencies could be observed that are not observed in limited discharges.

BIBLIOGRAPHY

[1] N. J. Fisch and A. H. Boozer. Creating an Asymmetric Plasma Resistivity with Waves. *Physical Review Letters*, 45(9):720–722, September 1980.

[2] N.j. Fisch. Theory of current drive in plasmas. *Rev. Mod. Phys.; (United States)*, page 175, 1987.

[3] Paul T. Bonoli. Review of recent experimental and modeling progress in the lower hybrid range of frequencies at ITER relevant parameters. *Physics of Plasmas (1994-present)*, 21(6):061508, June 2014.

[4] C. Gormezano, A. C. C. Sips, T. C. Luce, S. Ide, A. Becoulet, X. Litaudon, A. Isayama, J. Hobirk, M. R. Wade, T. Oikawa, R. Prater, A. Zvonkov, B. Lloyd, T. Suzuki, E. Barbato, P. Bonoli, C. K. Phillips, V. Vdovin, E. Joffrin, T. Casper, J. Ferron, D. Mazon, D. Moreau, R. Bundy, C. Kessel, A. Fukuyama, N. Hayashi, F. Imbeaux, M. Murakami, A. R. Polevoi, and H. E. St John. Chapter 6: Steady state operation. *Nuclear Fusion*, 47(6):S285, June 2007.

[5] C. E. Kessel, G. Giruzzi, A. C. C. Sips, R. V. Budny, J. F. Artaud, V. Basiuk, F. Imbeaux, E. Joffrin, M. Schneider, M. Murakami, T. Luce, Holger St John, T. Oikawa, N. Hayashi, T. Takizuka, T. Ozeki, Y.-S. Na, J. M. Park, J. Garcia, and A. A. Tucillo. Simulation of the hybrid and steady state advanced operating modes in ITER. *Nuclear Fusion*, 47(9):1274, September 2007.

[6] Farrokh Najmabadi, A. Abdou, L. Bromberg, T. Brown, V. C. Chan, M. C. Chu, F. Dahlgren, L. El-Guebaly, P. Heitzenroeder, D. Henderson, H. E. St. John, C. E. Kessel, L. L. Lao, G. R. Longhurst, S. Malang, T. K. Mau, B. J. Merrill, R. L. Miller, E. Mogahed, R. L. Moore, T. Petrie, D. A. Petti, P. Politzer, A. R. Raffray, D. Steiner, I. Sviatoslavsky, P. Synder, G. M. Syaebler, A. D. Turnbull, M. S. Tillack, L. M. Waganer, X. Wang, P. West, and P. Wilson. The ARIES-AT advanced tokamak, Advanced technology fusion power plant. *Fusion Engineering and Design*, 80(1-4):3–23, January 2006.

[7] S. C. Jardin, C. E. Kessel, C. G. Bathke, D. A. Ehst, T. K. Mau, F. Najmabadi, and T. W. Petrie. Physics basis for a reversed shear tokamak power plant. *Fusion Engineering and Design*, 38(1-2):27–57, December 1997.

[8] P. T. Bonoli, J. Ko, R. Parker, A. E. Schmidt, G. Wallace, J. C. Wright, C. L. Fiore, A. E. Hubbard, J. Irby, E. Marmar, M. Porkolab, D. Terry, S. M. Wolfe, S. J. Wukitch, the Alcator C.-Mod Team, J. R. Wilson, S. Scott, E. Valeo, C. K. Phillips, and R. W. Harvey. Lower hybrid current drive experiments on Alcator C-Mod: Comparison with theory and simulationa). *Physics of Plasmas (1994-present)*, 15(5):056117, May 2008.

[9] S. Ide, T. Fujita, O. Naito, and M. Seki. Sustainment and modification of reversed magnetic shear by LHCD on JT-60u. *Plasma Physics and Controlled Fusion*, 38(10):1645, October 1996.

[10] S. Ide, O. Naito, T. Oikawa, T. Fujita, T. Kondoh, M. Seki, K. Ushigusa, and Jt-60 Team. LHCD current profile control experiments towards steady state improved confinement on JT-60u. *Nuclear Fusion*, 40(3Y):445, March 2000.

[11] T. Suzuki, S. Ide, T. Oikawa, T. Fujita, M. Ishikawa, M. Seki, G. Matsunaga, T. Hatae, O. Naito, K. Hamamatsu, M. Sueoka, H. Hosoyama, M. Nakazato, and the JT-60 Team. Off-axis current drive and real-time control of current profile in JT-60U. *Nuclear Fusion*, 48(4):045002, April 2008.

[12] O. Naito, Z. Cui, S. Ide, T. Suzuki, T. Oikawa, M. Seki, T. Hatae, T. Fujita, T. Kondoh, H. Shirai, Y. Ikeda, and K. Ushigusa. Evolution of lower-hybrid-driven current during the formation of an internal transport barrier. *Physical Review Letters*, 89(6):065001, July 2002.

[13] A Ekedahl, Yu.F Baranov, J.A Dobbing, B Fischer, C Gormezano, T.T.C Jones, M Lennholm, V.V Parail, F.G Rimini, J.A Romero, P Schild, A.C.C Sips, F.X SÃ¶ldner, and B.J.D Tubbing. Profile control experiments in JET using off-axis lower hybrid current drive. *Nuclear Fusion*, 38(9):1397–1407, September 1998.

[14] N. C. Hawkes, B. C. Stratton, T. Tala, C. D. Challis, G. Conway, R. DeAngelis, C. Giroud, J. Hobirk, E. Joffrin, P. Lomas, P. Lotte, J. Mailloux, D. Mazon, E. Rachlew, S. Reyes-Cortes, E. Solano, and K-D. Zastrow. Observation of zero current density in the core of JET discharges with lower hybrid heating and current drive. *Physical Review Letters*, 87(11):115001, August 2001.

[15] R. C. Cesario, C. Castaldo, A. Fonseca, R. De Angelis, V. Parail, P. Smeulders, M. Beurskens, M. Brix, G. Calabro, P. De Vries, J. Mailloux, V. Pericoli, G. Ravera, and R. Zagorski. Lower hybrid current drive in experiments for transport barriers at high βN of JET (Joint European Torus). *AIP Conference Proceedings*, 933(1):265–268, September 2007.

[16] E. Joffrin, G. Gorini, C. D. Challis, N. C. Hawkes, T. C. Hender, D. F. Howell, P. Maget, P. Mantica, D. Mazon, S. E. Sharapov, G. Tresset, Workprogramme, and contributors to the EFDA-JET. Triggering of internal transport barrier in JET. *Plasma Physics and Controlled Fusion*, 44(8):1739, August 2002.

[17] E. Joffrin, F. Crisanti, R. Felton, X. Litaudon, D. Mazon, D. Moreau, L. Zabeo, R. Albanese, M. Ariola, D. Alves, O. Barana, V. Basiuk, A. BÃ©coulet, M. BÃ©coulet, J. Blum, T. Bolzonnella, K. Bosak, J. M. Chareau, M. de Baar, E. de la Luna, P. de Vries, P. Dumortier, D. Elbeze, J. Farthing, H. Fernandes, C. Fenzi, R. Giannella, K. Guenther, J. Harling, N. Hawkes, T. C. Hender, D. F. Howell, P. Heesterman, F. Imbeaux, P. Innocente, L. Laborde, G. Lloyd, P. J. Lomas, D. C. McDonald, J. Mailloux, M. Mantsinen, A. Messiaen, A. Murari, J. Ongena, F. Orsitto, V. Pericoli-Ridolfini, M. Riva, J. Sanchez, F. Sartori, O. Sauter, A. C. C. Sips, T. Tala, A. Tuccillo, D. Van Ester, K.-D. Zastrow, M. Zerbini, and contributors to the JET EFDA Programme. Integrated scenario in JET using real-time profile control. *Plasma Physics and Controlled Fusion*, 45(12A):A367, December 2003.

[18] S. Shiraiwa, O. Meneghini, R. R. Parker, G. Wallace, J. Wilson, I. Faust, C. Lau, R. Mumgaard, S. Scott, S. Wukitch, W. Beck, J. Doody, J. Irby, P. MacGibbon, D. Johnson, A. Kanojia, P. Koert, D. Terry, R. Vieira, and the Alcator C.-Mod Team. Design, and initial experiment results of a novel LH launcher on Alcator C-Mod. *Nuclear Fusion*, 51(10):103024, October 2011.

[19] S. Shiraiwa, G. Baek, P. T. Bonoli, I. C. Faust, A. E. Hubbard, O. Meneghini, R. R. Parker, G. M. Wallace, J. R. Wilson, R. W. Harvey, A. P. Smirnov, D. Brunner, B. LaBombard, C. Lau, R. Mumgaard, S. Scott, N. Tsujii, S. Wolfe, and the Alcator C.-Mod Team. Progress towards steady-state regimes in Alcator C-Mod. *Nuclear Fusion*, 53(11):113028, November 2013.

[20] J. Ko, S. Scott, S. Shiraiwa, M. Greenwald, R. Parker, and G. Wallace. Intrashot motional Stark effect calibration technique for lower hybrid current drive experiments. *Review of Scientific Instruments*, 81(3):033505, 2010.

[21] J. R. Wilson, R. Parker, M. Bitter, P. T. Bonoli, C. Fiore, R. W. Harvey, K. Hill, A. E. Hubbard, J. W. Hughes, A. Ince-Cushman, C. Kessel, J. S. Ko, O. Meneghini, C. K. Phillips, M. Porkolab, J. Rice, A. E. Schmidt, S. Scott, S. Shiraiwa, E. Valeo, G. Wallace, J. C. Wright, and the Alcator C.-Mod Team. Lower hybrid heating and current drive on the Alcator C-Mod tokamak. *Nuclear Fusion*, 49(11):115015, November 2009.

[22] Orso (Orso-Maria Cornelio) Meneghini. *Full-wave modeling of lower hybrid waves on Alcator C-Mod*. Thesis, Massachusetts Institute of Technology, 2012.

[23] M. Grimes, D. Terry, R. Parker, D. Beals, J. Irby, R. Vieira, D. Gwinn, J. Zaks, J. Hosea, N. Greenough, and J.r. Wilson. The Alcator C-Mod lower hybrid current drive experiment transmitter. *Fusion Engineering and Design*, 74(1):495–499, November 2005.

[24] O. Meneghini, S. Shiraiwa, W. Beck, J. Irby, P. Koert, R.r. Parker, R. Viera, J. Wilson, and S. Wukitch. Integrated numerical design of an innovative lower hybrid launcher for Alcator C-Mod. In *AIP Conference Proceedings*, volume 1187, pages 423–426. American Institute of Physics, January 2009. 1187.

[25] J. Ko. *Current profile measurements using Motional Stark Effect on Alcator C-Mod*. PhD, Massachusetts Institute of Technology, 2009.

[26] G. M. Wallace, S. Shiraiwa, J. Hillairet, M. Preynas, W. Beck, J. A. Casey, J. Doody, I. C. Faust, E. Fitzgerald, D. K. Johnson, A. D. Kanojia, P. Koert, C. Lau, Y. Lin, R. Leccacorvi, P. MacGibbon, O. Meneghini, R. Murray, R. R. Parker, D. R. Terry, R. Vieira, J. R. Wilson, S. Wukitch, and L. Zhou. Advances in lower hybrid current drive technology on Alcator C-Mod. *Nuclear Fusion*, 53(7):073012, July 2013.

[27] J. Liptac, R. Parker, V. Tang, Y. Peysson, and J. Decker. Hard x-ray diagnostic for lower hybrid experiments on alcator C-mod. *Review of Scientific Instruments*, 77(10):103504–1–7, October 2006.

[28] John E. Liptac. *Lower hybrid modeling and expiments [sic] on Alcator C-Mod*. PhD, Massachusetts Institute of Technology, 2006.

[29] Andrea E. W. Schmidt. *Measurements and modeling of Lower Hybrid Driven fast electrons on Alcator C-Mod*. PhD, 2011.

[30] N. P. Basse, A. Dominguez, E. M. Edlund, C. L. Fiore, R. S. Granetz, A. E. Hubbard, J. W. Hughes, I. H. Hutchinson, J. H. Irby, B. LaBombard, L. Lin, Y. Lin, B. Lipschultz, J. E. Liptac, E. S. Marmar, D. A. Mossessian, R. R. Parker, M. Porkolab, J. E. Rice, J. A. Snipes, V. Tang, J. L. Terry, S. M. Wolfe, S. J. Wukitch, K. Zhurovich, R. V. Bravenec, P. E. Phillips, W. L. Rowan, G. J. Kramer, G. Schilling, S. D. Scott, and S. J. Zweben. Diagnostic Systems on Alcator C-Mod. *Fusion Science and Technology*, 51(3):476–507, April 2007.

[31] M. Brusati, D. V. Bartlett, A. Ekedahl, P. Froissard, A. Airoldi, G. Ramponi, R. P. da Silva, and Y. Peysson. Determination of the suprathermal electron distribution function during lower hybrid current drive in JET. *Nuclear Fusion*, 34(1):23, January 1994.

[32] Y. Peysson, the TORE SUPRA Team, and Y. Peysson. Progress towards high-power lower hybrid current drive in TORE SUPRA. *Plasma Physics and Controlled Fusion*, 42(12B):B87, December 2000.

[33] A. Schmidt, P. T. Bonoli, O. Meneghini, R. R. Parker, M. Porkolab, S. Shiraiwa, G. Wallace, J. C. Wright, R. W. Harvey, and J. R. Wilson. Investigation of lower hybrid physics through power modulation experiments on Alcator C-Moda). *Physics of Plasmas (1994-present)*, 18(5):056122, May 2011.

[34] Charles F. F. Karney and Nathaniel J. Fisch. Efficiency of current drive by fast waves. *Physics of Fluids (00319171)*, 28(1):116, January 1985.

[35] V. Pericoli-Ridolfini, E. Barbato, S. Cirant, H. Kroegler, L. Panaccione, S. Podda, F. Alladio, B. Angelini, M. L. Apicella, G. Apruzzese, L. Bertalot, A. Bertocchi, M. Borra, G. Bracco, A. Bruschi, G. Buceti, P. Buratti, A. Cardinali, C. Centioli, R. Cesario, S. Ciattaglia, V. Cocilovo, F. Crisanti, R. De Angelis, F. De Marco, B. Esposito, D. Frigione, L. Gabellieri, G. Gatti, E. Giovannozzi, C. Gourlan, G. Granucci, F. Gravanti, M. Grolli, A. Imparato, M. Leigheb, L. Lovisetto, G. Maffia, G. Maddaluno, M. Marinucci, G. Mazzitelli, P. Micozzi, F. Mirizzi, S. Nowak, F. P. Orsitto, D. Pacella, M. Panella, L. Pieroni, G. B. Righetti, F. Romanelli, F. Santini, M. Sassi, S. E. Segre, A. Simonetto, C. Sozzi, E. Sternini, O. Tudisco, V. Vitale, G. Vlad, N. Tartoni, B. Tilia, A. A. Tuccillo, V. Zanza, M. Zerbini, and F. Zonca. High Plasma Density Lower-Hybrid Current Drive in the FTU Tokamak. *Physical Review Letters*, 82(1):93–96, January 1999.

[36] G. Giruzzi, E. Barbato, S. Bernabei, and A. Cardinali. Measurement of the hot electrical conductivity in the PBX-M tokamak. *Nuclear Fusion*, 37(5):673, May 1997.

[37] Nathaniel J. Fisch. Conductivity of rf-heated plasma. *Physics of Fluids (1958-1988)*, 28(1):245–247, January 1985.

[38] Ikeda, Y., Naito, O, Kondoh, M, Seki, M., Ide, S, and et al. High Power Lower Hybrid Current Drive Experiments in JT-60u. In *PROCEEDINGS OF THE FIFTEENTH INTERNATIONAL CONFERENCE ON PLASMA PHYSICS AND CONTROLLED NUCLEAR FUSION RESEARCH*, volume 1, pages 415–422, Seville, Spain, 1994. IAEA.

[39] V. Pericoli Ridolfini, G. Calabro, L. Panaccione, F. T. U. Team, and E. C. H. Team. Study of lower hybrid current drive efficiency over a wide range of FTU plasma parameters. *Nuclear Fusion*, 45(11):1386, November 2005.

[40] Y. Peysson and Tore Supra Team. High power lower hybrid current drive experiments in the Tore Supra tokamak. *Nuclear Fusion*, 41(11):1703, November 2001.

[41] S. Bernabei, J.c. Hosea, C.c. Kung, G.d. Loesser, J. Rushinski, and J.r. Wilson. Design of a compact lower hybrid coupler for Alcator C-Mod. *Fusion Science and Technology*, 43(2):145–152, March 2003.

[42] M. Goniche, L. Amicucci, Y. Baranov, V. Basiuk, G. Calabro, A. Cardinali, C. Castaldo, R. Cesario, J. Decker, D. Dodt, A. Ekedahl, L. Figini, J. Garcia, G. Giruzzi, J. Hillairet, G. T. Hoang, A. Hubbard, E. Joffrin, K. Kirov, X. Litaudon, J. Mailloux, T. Oosako, R. Parker, V. Pericoli Ridolfini, Y. Peysson, P. Platania, F. Rimini, P. K. Sharma, C. Sozzi, and G. Wallace. Lower hybrid current drive for the steady-state scenario. *Plasma Physics and Controlled Fusion*, 52(12):124031, December 2010.

[43] Gregory M. Wallace. *Behavior of lower hybrid waves in the scrape off layer of a diverted tokamak*. Thesis, Massachusetts Institute of Technology, 2010.

[44] Y. Takase, M. Porkolab, J. J. Schuss, R. L. Watterson, C. L. Fiore, R. E. Slusher, and C. M. Surko. Observation of parametric instabilities in the lower-hybrid range of frequencies in the high-density tokamak. *Physics of Fluids (1958-1988)*, 28(3):983–994, March 1985.

[45] G. M. Wallace, R. R. Parker, P. T. Bonoli, A. E. Hubbard, J. W. Hughes, B. L. LaBombard, O. Meneghini, A. E. Schmidt, S. Shiraiwa, D. G. Whyte, J. C. Wright, S. J. Wukitch, R. W. Harvey, A. P. Smirnov, and J. R. Wilson. Absorption of lower hybrid waves in the scrape off layer of a diverted tokamak. *Physics of Plasmas*, 17(8):082508, August 2010.

[46] S. G. Baek, R. R. Parker, P. T. Bonoli, S. Shiraiwa, G. M. Wallace, B. LaBombard, I. C. Faust, M. Porkolab, and D. G. Whyte. High density LHRF experiments in Alcator C-Mod and implications for reactor scale devices. *Nuclear Fusion*, 55(4):043009, April 2015.

[47] M. Goniche, V. Basiuk, J. Decker, P. K. Sharma, G. Antar, G. Berger-By, F. Clairet, L. Delpech, A. Ekedahl, J. Gunn, J. Hillairet, X. Litaudon, D. Mazon, E. Nilsson, T. Oosako, Y. Peysson, M. Preynas, M. Prou, and J. L. SÃ©gui. Lower hybrid current drive at high density on Tore Supra. *Nuclear Fusion*, 53(3):033010, March 2013.

[48] G.M. Wallace, A.E. Hubbard, S. Shiraiwa, P.T. Bonoli, I.C. Faust, R.W. Harvey, J.W. Hughes, B.L. LaBombard, C. Lau, O. Meneghini, R.R. Parker, M.L. Reinke, A.e. Schmidt, A.P. Smirnov, J.L. Terry, D.G. Whyte, J.R. Wilson, J.C. Wright, and S.J. Wukitch.

Lower hybrid current drive in a high density diverted tokamak. In *AIP Conference Proceedings*, volume 1406, pages 419–422. American Institute of Physics, January 2011. 1406.

[49] G. M. Wallace, A. E. Hubbard, P. T. Bonoli, I. C. Faust, R. W. Harvey, J. W. Hughes, B. L. LaBombard, O. Meneghini, R. R. Parker, A. E. Schmidt, S. Shiraiwa, A. P. Smirnov, D. G. Whyte, J. R. Wilson, J. C. Wright, S. J. Wukitch, and the Alcator C.-Mod Team. Lower hybrid current drive at high density in Alcator C-Mod. *Nuclear Fusion*, 51(8):083032, August 2011.

[50] Peng Xu. *Polarimetry measurements of current density profile and fluctuation changes during lower hybrid experiments on Alcator C-Mod*. Thesis, Massachusetts Institute of Technology, 2013.

8

COMPARISON OF LHCD CURRENT PROFILES TO SIMULATION

Chapter goals:

- Compare the current and HXR profile measurement to numerical simulations performed by GENRAY/CQL3D
- Determine whether the simulation accurately predicts the general 0-D measures of current drive
- Determine whether the simulation accurately predicts the measured profiles
- Determine whether the simulation accurately predicts trends in the data
- Discuss what can be learned from any disagreements/agreements

Significant progress has been made in developing numerical models of the LHCD current profile that are capable of utilizing experimental profiles. These simulations are approaching the completeness required to be used as predictive as well as interpretive tools. The outputs of the equilibrium reconstructions and the HXR profile from experiment can be compared to these simulations to quantitatively benchmark them. The aspects of agreement and disagreement between the simulations and the experiment can then be used to determine which parts of the model are properly capturing the physics in the experiment and where improvements can be made.

Most of the previous experimental and simulation work on C-MOD LHCD was conducted in the higher density regime ($> 9 \times 10^{19} \mathrm{m}^{-3}$) where anomalous loss of current drive is found. The work presented here is confined to the low-density range where LHCD is shown to work well, (except for the density scan), achieving the theoretical current drive efficiencies and creating measurable macroscopic changes on the plasma equilibrium. This chapter presents comparisons between simulation and experimental results for several of the conditions presented in the previous chapter. This is the first systematic comparison between experiment and simulation across a wide range of parameters using both the HXR and current profile in any tokamak operating in this density and field regime.

8.1 GENRAY/CQL3D

GENRAY/CQL3D was chosen to start the benchmarking process because its work flow is well established at ALCATOR C-MOD. It has been used to simulate LHCD profiles on existing devices [1–4] and to predict LHCD profiles in proposed devices [5, 6]. The code treats the LHCD current drive as an initial value problem. This section discusses the principles underlying these codes and previously derived results. The workflow is managed by the πSCOPE software [7], which assembles input data files from the C-MOD experimental data, submits jobs to the local computation cluster, and aggregates the results.

GENRAY [8][1] is a ray-tracing code that solves the ray equations using geometric optics and the WKB approximation[2]. Rays are launched from the edge of the plasma with an initial $n_{||}$ and power. The wavenumber at each position along each independent ray is evolved using the local dispersion relation. The rays are followed until their wave power is reduced below a user-set threshold. Modification by Wallace [9] enabled the ray-trajectories to propagate outside the confined plasma until one of the following events happens: the rays hit a reflecting surface; the local plasma density decreases below the cutoff density; or the ray power is damped below the threshold.

Inside the confined plasma, the wavenumber and RF electric field of the collection of rays at each flux surface is used by a Fokker-Planck solver to calculate the ray-absorption and the perturbed distribution function. The new distribution function in turn changes how much power is absorbed from the rays at each flux surface, leading to a different RF electric field at each point (note this process does not change the ray trajectory, which is therefore only calculated once). This leads to a different absorption at each point and so the cycle is iterated until convergence is obtained.

GENRAY is coupled to the code CQL3D [10][3], which solves the Fokker-Planck equation to determine the electron distribution function in the presence of the LHCD electric field. CQL3D is bounce-averaged, includes trapping effects, and uses flux-surface averaged, toroidally-symmetric 3-D ($v_\perp$, $v_{||}$, r) distribution functions. The code is actually a time-dependent calculation that determined the electron distribution function by balancing the time derivative of the electron distribution function with the RF sources, toroidal electric field, collisional slowing-down, and pitch-angle scattering. The distribution function is evolved until the power removed from the collection of rays passing through each flux surface is equal to the power absorbed by the

1 Available from http://www.compxco.com/genray.html.
2 Which requires that the spatial scale over which the changes be much longer than the wavelength.
3 Available from http://www.compxco.com/cql3d.html.

distribution function each the flux surface[4]. The system starts with a Maxwellian distribution function and advances in time-steps until a stationary-state is reached (although this is not guaranteed to be the case in either the simulation or the plasma; an example would be a runaway discharge). A key element of the Fokker-Planck code is its inclusion of the effect from any residual DC electric field in the plasma self-consistently in addition to the RF electric fields.

The ray power can be observed by collisional damping in the low-temperature, high-density SOL plasma. Previous work [11] (Section 5.2.1) showed that at the densities presented in this work, the ray-trajectories themselves do not change when the rays are allowed to propagate through the SOL (with collisional absorption disabled), i.e., they remain similar to the case of a reflecting plasma boundary. The collisional absorption outside the plasma is determined by the specifics of the ray-trajectories and the SOL profiles since the absorption is strongest in locations with low temperatures (< 10eV) and high densities (i.e., the divertor), affecting the rays that enter this region. This creates sensitivities in the model that have recently been pointed out by Shiraiwa [12].

GENRAY/CQL3D has been successfully benchmarked against other 3-D Fokker-Planck ray-tracing LHCD codes using a standard ITER discharge [5] in a single-pass regime. GENRAY/CQL3D with the SOL model was used to simulate LHCD discharges on the EAST tokamak in the multi-pass regime ($\bar{n}_e = 1 \times 10^{19} m^{-3}$, $T_e = 1 - 3$keV, $I_p = 250$kW) and predicted a current profile strongly peaked off-axis around $r/a \sim 0.4$ [3], after a significant number of reflections.

The code has been used extensively at C-MOD to design and interpret experiments. Previous simulation studies in the experimental regime of this work on C-MOD show that the waves are only weakly damped on the first-pass, requiring several passes to damp completely.

8.1.1 *Simulation inputs*

The GENRAY/CQL3D code uses the MK-EFIT equilibrium, but symmetrizes the equilibrium about the plasma midplane. Thus the ray-trajectories calculated from GENRAY include the actual poloidal field in the experiment[5]. The experimental loop voltage is included in the simulation and the loop voltage is assumed to be constant as a function of radius in these plasmas, which have reached a stationary state. The simulation uses the net LHCD power (i.e., the reflected component is subtracted from the total launched power). The simulation launches rays from four positions, corresponding to the poloidal cen-

4 In effect, in the absence of fast-electron diffusion, the ray-trajectories are the only link between the different flux surfaces.

5 Note, self-consistency between the input current profile/equilibrium and the calculated current profile/equilibrium is not enforced

ter of each LHCD launcher row. In this work, 100 rays are launched to represent the launched $n_{\|}$ spectra, including the reversed component with proper weighting to account for the coupler's directivity. The 25 rays launched from each launcher row have a $n_{\|}$ spectrum that represents the spectrum calculated from LHCD coupling codes (the rays are equally distributed within a $sinc$ function).

The same electron temperature and density data used during the equilibrium reconstruction is used for the temperature and density profiles in GENRAY/CQL3D within the confined plasma The ion temperature profile is assumed to be 0.66 of the electron temperature profile (note that the ions do not play a significant role in the wave propagation or absorption). The Thomson scattering measurements are averaged over 50-80 milliseconds and are processed using Gaussian process regression to produce smooth profiles.

The SOL profiles for the plasma density and temperature consist of exponentially decaying profiles based on the distance from the separatrix to the SOL—the same profile shapes are used in reference [9]. The SOL density profile is two-dimensional with an e-folding length defined as a function of poloidal angle: 0.1m at the divertor and 0.02m at the midplane. The temperature profile is poloidally uniform (1-D) with an e-folding length of 0.005m until the temperature reaches 5eV. The plasma temperature at the separatrix is adjusted in the core profile fits to be 70eV, and the density is adjusted to be $\sim 0.6 \times \bar{n}_e$ to provide consistent SOL profiles across all the simulations. This value was determined using a database study of the edge Thomson scattering system in similar low-density L-mode discharges.

8.1.2 *Specifying* Z_{eff}

The Z_{eff} in the experiment is poorly measured by the dedicated visible bremsstrahlung diagnostic, which reports anomalously high values of Z_{eff} at these low densities, possibly due to errors in interpretation. This diagnostic is further contaminated during LHCD by hard x-rays. Therefore the Z_{eff} is calculated using CQL3D in a self-consistent manner using the Ohmic period prior to the LHCD pulse. CQL3D has been successfully benchmarked to resistivity models—it is able to model the Ohmic resistivity (and thus current profile) in the absence of LHCD [13]. The experimental temperature and density profiles, the experimental loop voltage, and an estimate of Z_{eff} (flat across the profile) from the Ohmic period are loaded into CQL3D and a simulation is performed with $P_{LH} = 0$, which yields a calculated total plasma current. The Z_{eff} is then adjusted until the calculated total current predicted by the simulation is the same as that measured in the Ohmic phase of the discharge. The computed Z_{eff} values are typically 1.4 to 2.0 using the technique.

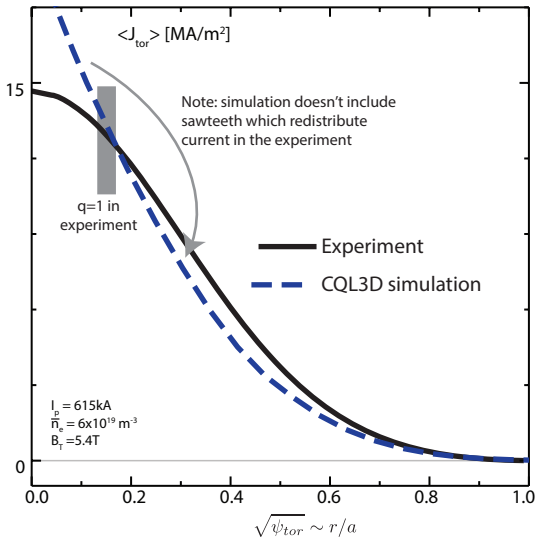

Figure 110: CQL3D is run during the Ohmic period prior to LHCD to determine the Z_{eff} by matching total current. The resulting CQL3D current profile matches the experimental Ohmic current profile except for details around the sawtooth inversion radius.

In this way, the simulation during the Ohmic period is self-consistent, producing the measured plasma current with the measured loop voltage and the measured temperature and density profiles. The current profile during this Ohmic time period from GENRAY/CQL3D is compared to the reconstructed current profile from the experiment in Figure 110. Note that the profiles are similar except in the central region where the current in the experiment is modified by the sawtooth instability that clamps the current density on-axis, redistributing current outside of the $q = 1$ radius. The CQL3D simulation does not incorporate this MHD and therefore over-predicts the central current density during sawtoothing periods.

The value of Z_{eff} measured during the Ohmic phase of the plasma is assumed to remain constant throughout the simulated LHCD period. In support of this assumption, it is observed that the measured Bremsstrahlung emission is similar immediately before and after the LHCD pulse. In most discharges used in this study, the radiated power and soft x-ray emission does increase by $\sim$ 30 to 50 percent, respectively, during LHCD. Thus the constant-Z_{eff} assumption could underpredict the actual Z_{eff} during LHCD (though interpretation is difficult since the temperature typically increases and typically the LHCD injects more power than the Ohmic heating it replaces). Improvements to Z_{eff} measurement and analysis are planned to better determine Z_{eff} during the LHCD pulse. Discharges where large changes in impurity content as indicated from impurity spectroscopy between the Ohmic period and the LHCD period have been omitted from the modeling effort due to problems estimating Z_{eff}.

Note that this use of GENRAY/CQL3D differs from that presented in by Schmidt [14], which adjusts either the Z_{eff}, the parallel electric field, or the fast-electron diffusion coefficient to force a match on the total plasma current. The approach taken in this work assumes that

all three of these quantities are reasonably well-known and thus the predicted plasma current is a metric on which to compare the simulation to the experiment.

Considerable attention was placed on data-preparation and simulation practices to limit observer bias in the comparison between simulation and experiment. Automated routines were used whenever possible and simulations were run blindly without observing results until all scans were completed. Most of the measurements were collated and synthesized prior to simulation efforts—comparison between experiment and simulation output was reserved until late in the process. The simulation numerical parameters were not modified discharge-to-discharge. The simulation outputs were compared to previous outputs and work done by others to ensure that the best-practice simulation parameters were followed in this work[6].

8.1.3 *Extracting quantities for comparisons to measurements*

The predicted total plasma current is compared to the measurement from the Rogowski coil and the current density profile predicted by GENRAY/CQL3D is compared to the current profile from the MK-EFIT reconstruction. Additionally, the simulation uses a synthetic diagnostic to predict the count rate on each chord of the HXR camera using the known sightline geometry [15]. This allows for the quantitative comparison of counting rates on each chord. The simulations also include a synthetic diagnostic for non-thermal ECE emission, but this is not used in this study.

8.2 NON-INDUCTIVE COMPARISON

The GENRAY/CQL3D simulation outputs are compared to the measured profile during a non-inductive discharge in Figure 111. The nominal simulation (blue) under-predicts the total current by 13 percent and nearly matches the total HXR production. The electron density profile was scaled and the simulation was performed again to determine the sensitivity of the simulated current, current profile, and HXR profiles to plasma density. Increasing the density by 10 percent results in the simulation predicting 72 percent of the experimental current (a 17 percent change). Decreasing the density 10 percent results in the simulation predicting 101 percent of the experimental current. Thus this simulation predicts fairly accurately the 0-D quantities under current drive —matching the loop voltage, P_{LH}, and I_p simultaneously. (Thus $\eta_{sim} = \eta_{exp} = \eta^{\star}{}_{sim} = \eta^{\star}{}_{exp}$ in this non-inductive case.)

6 The Author wishes to thank P. Bonoli, S. Shiraiwa and G. Wallace for assistance and guidance in defining values of simulation settings and spot-checking simulation results to identify numerical problems.

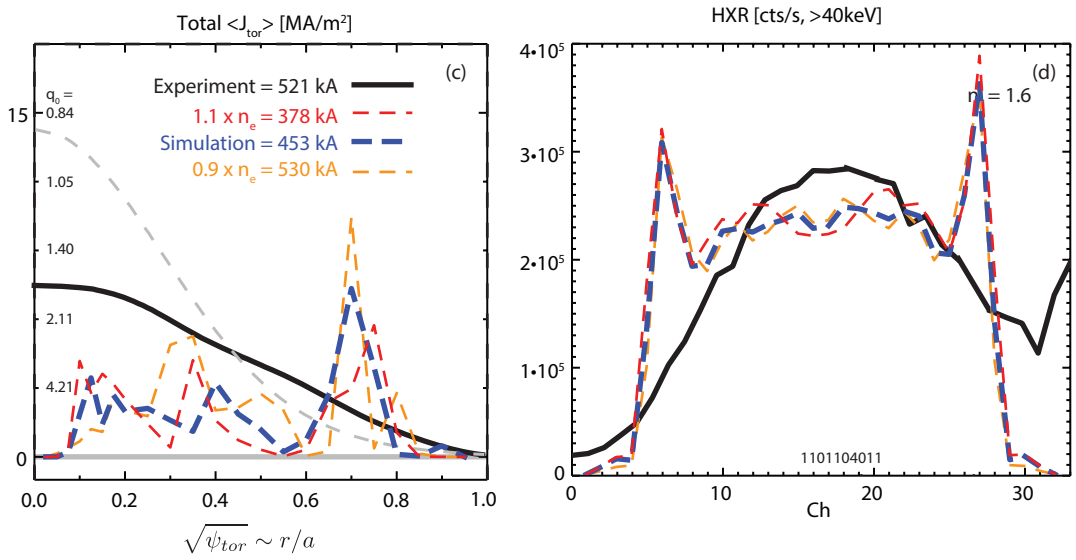

Figure 111: The simulated (dashed) and experimental profiles (solid) for a non-inductive discharge. The density profile is scaled by ±10 percent and the simulation is re-run to judge the sensitivity to this parameter. The measured ohmic current density profile is overplotted (gray dashed) to show the magnitude of changes due to LHCD.

However, the predicted current density and HXR profiles are very poorly matched to the measured profiles. The simulated current density profile has a large spike at $r/a \sim 0.7$ that is not observed in the experiment. This spike contains nearly 50 percent of the total current due to its location at large minor radius, and it has two to three times the local measured current density. The simulation also has very little current on axis—leading to $q_0 \sim 4$ if actualized. Such high q_0 is inconsistent with experimental measurements. The power density (not shown) is also peaked far off-axis, which is inconsistent with the observed temperature profiles. Note that the simulated current profile exhibits local sensitivity to scaling the density profile with the myriad spikes moving around in radius by $r/a \sim 0.1$.

This large spike in the simulated current density outside of mid-radius also results in large "ears" in the simulated HXR count rates, leading to a shallow hollowing of the profile due to the line-integrated nature of the diagnostic. This profile shape—although it nearly matches the total experimental HXR count rate—does not qualitatively match the experimental HXR profile[7].

The disagreement between the simulated and experimental current density profile is statistically significant. Figure 112 shows a synthetic diagnostic of the pitch angle calculated by integrating the current density from the simulation. The simulated current profile would produce a pitch angle profile closer to zero across the entire plasma since

7 Note that the experimental HXR profile has a non-symmetric feature at ch 31 and 32 in this discharge. This is emission originates from the active x-point which is commonly observed on C-MOD and is poorly understood.

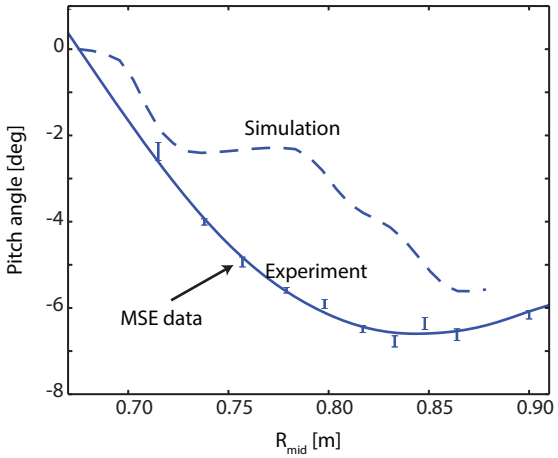

Figure 112: Comparison between a synthetic pitch angle diagnostic in GENRAY/CQL3D and the actual MSE measurements during a non-inductive discharge. The simulated current profile has been scaled to match the total current from the experiment prior to calculating the pitch angle profile. Figure credit: S. Shiraiwa.

the computed current is located so far off-axis. This discrepancy is approximately two sigma in the core and greater than five sigma across most of the plasma.

The simulated profiles help to show how the experimental MSE and HXR profiles are related and how they form a complementary set of diagnostics. In the simulation, there are fast-electrons carrying current far off-axis, leading to a square-top or even hollow HXR profile. In the experiment, there are fast electrons on-axis carrying current and creating a centrally-peaked HXR profile.

This discharge was also simulated by Y. Peysson from the CEA group using the ray-tracing/Fokker-Planck code suite LUKE/C3PO [16, 17]. This suite was developed independently of GENRAY/CQL3D and uses different numerics but the same underlying physics constructs. This analysis, which used independent fitting of the input profiles, yielded a total current drive of $\sim$ 388kA with similar large spikes in the current density profile at $r/a \sim 0.7$ and large ears on an even hollower HXR profile. The fact that this independent simulation yields qualitatively similar profiles and quantitatively similar 0-D results to the GENRAY/CQL3D simulations increases confidence in the work-flow utilized in this study.

The large discrepancy in profile shapes, but small discrepancy in total predicted current, warranted further investigation. The original sensitivity study, which multiplied the entire density profile by a single scaling factor, was expanded to determine whether the various peaks and valleys in the simulated profiles could be caused by subtle changes in the input density and temperature profiles. The experimental temperature and density were fitted in different ways and the simulations were re-run (This work was done by S. Shiraiwa). The results are shown in Figure 113. One simulation has the nominal smooth density fit and follows more closely small changes in the temperature profile, while the other simulation has a nominally smooth temperature profile but a bumpier density profile fit. This results in

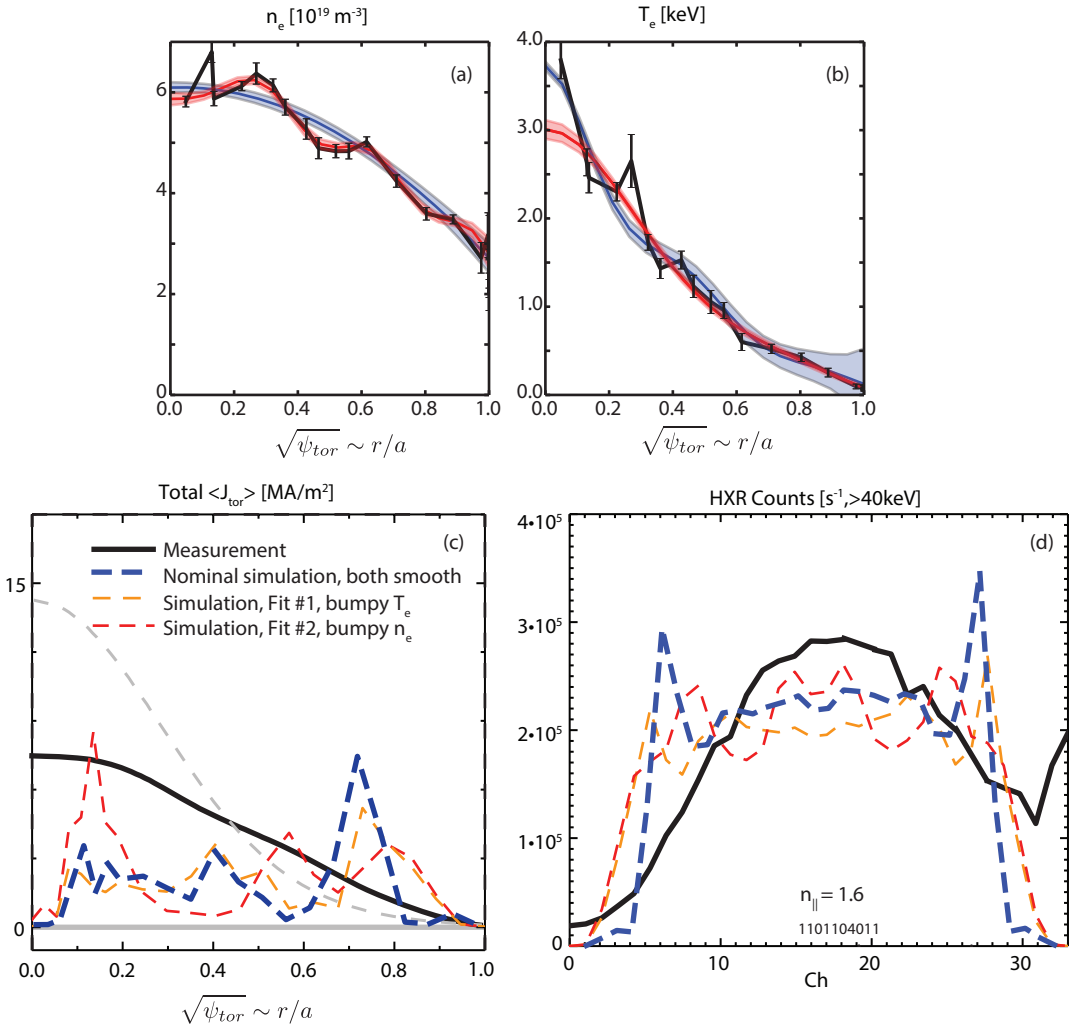

Figure 113: The fitting of the temperature and density profiles was varied to determine how sensitive the resulting simulation outputs were to the details of the input profiles. Two different density (a) and temperature (b) fits were performed with one profile including significant variation in gradient in addition to the nominal fit where both profiles are smooth. The different fits change the location of the peaks and valley in the simulated current density and HXR profiles, but do not change their basic character.

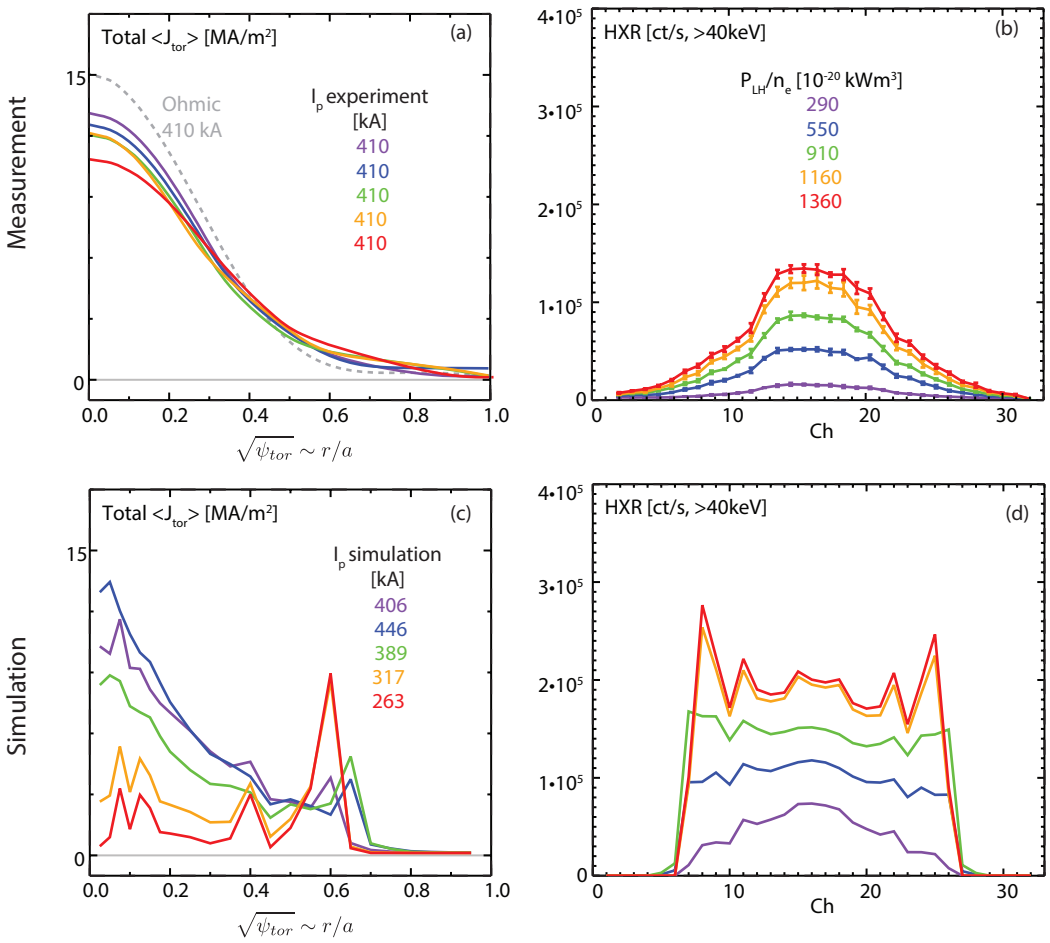

Figure 114: LHCD power and loop voltage scan at low current. The experimental total current density profile (a) and HXR profile (b) compared to the GENRAY/CQL3D simulated total current density profile (c) and HXR profile (d) as a function of LHCD power and loop voltage, which are covariant.

$\Delta r/a \sim 0.1$ changes in the location of the off-axis peak in the current density profile, with the later case developing a spike of current closer to the axis. The HXR profile retains ears, but the location moves inward and outward. Significantly, none of the simulations produce a bell-shaped HXR profile. Overall, the local details in the simulation can change dramatically (e.g., the current density at $r/a \sim 0.6$). This test indicates that there is significant sensitivity in the simulations to the details of the underlying input profiles, particularly the density, but the basic profile shapes do not change significantly. The fast electrons are always predicted to be located far off-axis leading to a flat or hollow HXR emission profile. While the experiment shows fast-electrons on-axis with a Gaussian HXR emission profile.

8.3 LHCD POWER SCAN COMPARISON

GENRAY/CQL3D was used to simulate an LHCD power scan at constant B_T, I_p, $\bar{n}_e$, and $n_{\|}$. This experiment simultaneously varies the applied loop voltage, as the total current is held fixed, thus making this experiment also a scan of non-inductive fraction. The power scan was conducted at $I_p = 410$kA (a relatively low current on C-MOD) at $\bar{n}_e = 7 \times^{10^{19}}$ m^{-3} with powers from $0 < P_{LH} < 1$MW leading to loop voltages of $0.09 < V_{loop} < 0.91$V and $0 < \Delta V_{loop} < 0.9$. The desire to isolate the effects of power and loop voltage means changes from the sensitivity to details in the density profile should be avoided. Therefore the same temperature and density profiles (from the discharge with the middle power) were used for all the simulations, while the loop voltage and LHCD power were set equal to the experimental values. The resulting total current density and simulated HXR profiles are shown in Figure 114.

At high LHCD power the simulated current density profile shows the same off-axis spike in current as the non-inductive discharge, though this time it is located at $r/a \sim 0.5$. The simulated current density approaches the Ohmic current density as the power is decreased and the loop voltage is increased, necessarily resulting in a very large change in on-axis current density. This would correspond to very large changes in the q-profile. In all cases, the simulated current spike at $r/a \sim 0.6$ is apparent along with several smaller spikes at smaller minor radius. The measured current profile remains centrally peaked at all values of LHCD power, and the maximum change in central current density is ~ 30 percent. The predicted HXR profile (Figure 114 (d)) transitions from being peaked on axis at low power to peaked at the edges at high power perhaps hinting at a non-linear feedback effect in the simulation. By contrast, the measured HXR profile shape (Figure 98) remains self-similar at all LHCD power levels.

8.3.1 *Decomposing contributions to the current density*

The simulated contributions to the total current, the current density, and the HXR profile can be roughly decomposed from into components from the LHCD, the residual parallel electric field, and the parallel electric field acting on the fast electrons similar to that presented in Section 7.5. This is accomplished by running the simulation in different configurations:

1. The total predicted value uses both the experimental E_{DC} and experimental the P_{LH}.

2. The component originating directly from the LHCD waves is calculated by setting $E_{DC} = 0$ and using the experimental P_{LH}.

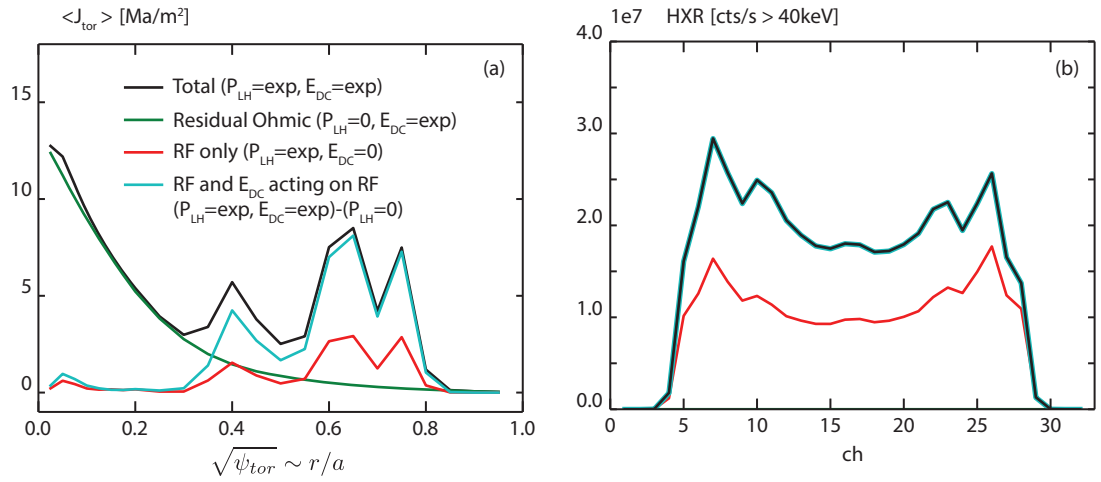

Figure 115: Decomposing the GENRAY/CQL3D output profiles in components due to different physical drive mechanisms. The code is run with the experimental loop voltage and P_{LH}, resulting in a total current density and HXR profile (black). The code is also run under identical conditions except with $P_{LH} = 0$ to obtain the current driven by the residual loop voltage in the absence of the fast-electrons (green) and is then run with the experimental P_{LH}, but no loop voltage, to obtain the current driven by the LHCD in the absence of the residual loop voltage (red). The remainder therefore must be due to the residual loop voltage acting on the fast-electrons (blue). Note this specific example is not part of the LHCD $n_{\parallel}$ scan.

3. The component driven by the residual loop voltage acting only on the bulk plasma is calculated by setting $P_{LH} = 0$ and using the experimentally measured E_{DC}.

4. The component driven by the residual loop voltage acting on the fast-electrons (i.e., the "cross-term"), is calculated by subtracting the component directly due to Ohmic and the component directly due to the LHCD waves from the full simulation (e.g., $1 - 2 - 3$).

5. The "LHCD contribution to J_{tor}" discussed in the previous chapter is best represented by $1 - 2$.

This provides a means to determine the physics that is important in the simulation during partially-inductive situations like the power scan just discussed. An example current profile broken down into various components is shown in Figure 115.

This technique was applied to the P_{LH} scan and the results are shown in Figure 116. The total current driven directly by the LHCD increases linearly with power while the component from the residual Ohmic decreases linearly with power (actually with loop voltage). The sum of the two decreases slightly over the scan—the simulation under predicts the total plasma current at nearly non-inductive conditions by 35 percent. The cross-term is responsible for approximately 20 percent of the total current at the middle powers (500kW and 0.35V) but decreases to zero at the fully inductive and fully-non-inductive conditions.

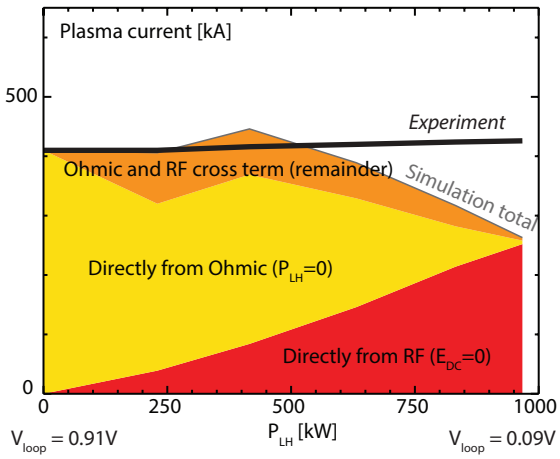

Figure 116: Contributions to the total plasma current during a LHCD power scan at low current by running the code with different combinations of the parallel electric field and the LHCD power. The experimental current is indicated.

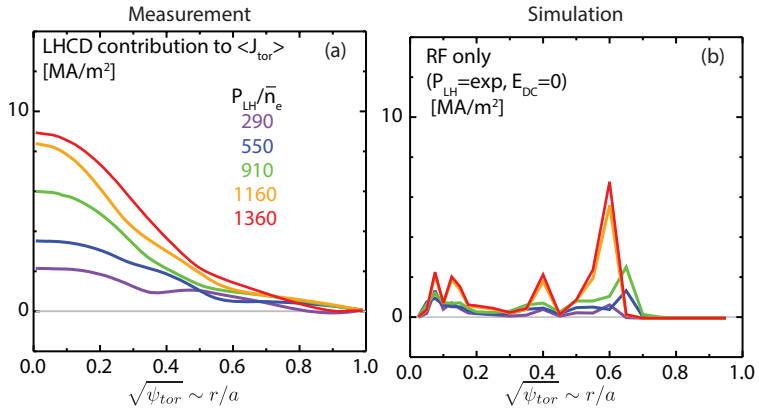

Figure 117: The components contributing to the current profile during a scan in P_{LH} and loop voltage. The component from LHCD deduced from the experiment (a). The GENRAY/CQL3D component only from the RF drive (b).

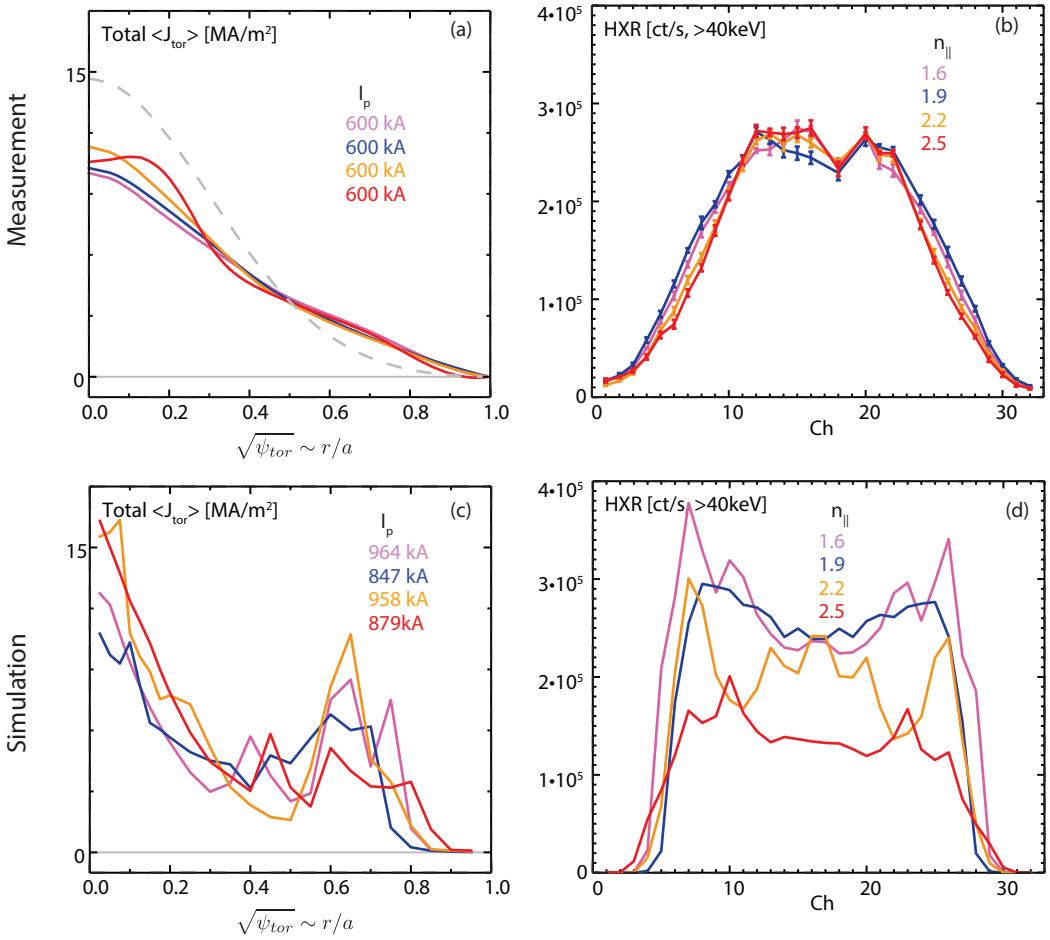

Figure 118: $n_{||}$ scan comparison. The experimental total current density profile (a) and HXR profile (b) compared to the GENRAY/CQL3D simulated total current density profile (c) and HXR profile (d) as a function of launched $n_{||}$.

Figure 117 shows the current profile due to LHCD deduced from the experimental measurements and calculated by the simulation. Note that, as in the non-inductive case, the spatial profile of the LHCD-driven fast electrons in the simulations differs significantly from the measurements. The simulations perhaps indicate that the spike location moves slightly further inward at higher powers, though the typical variability from small perturbations in the density profile likely make this statistically insignificant. Both the simulation and the measurement indicate very little current drive past $r/a \sim 0.7$.

8.4 LAUNCHED $n_{||}$ SCAN COMPARISON

Standard GENRAY/CQL3D simulations were also performed for plasmas in the $n_{||}$ scan discussed in the previous chapter. The simulated profiles are compared to the measurements in Figure 118. The simulated total current was 40-60 percent greater than the experimental

plasma current in these partially-inductive discharges ($V_{loop} = 0.4V$). Note that the experimental current density (a) and HXR (b) profile do not show sensitivity to the launched $n_{\|}$. The simulated current density (c) and particularly the HXR (d) profile show some sensitivity to $n_{\|}$. As observed in previous scans, the simulated current profile has a large feature around $r/a \sim 0.7$. Changing the launched $n_{\|}$ changes the details of the feature, with the highest launched $n_{\|}$ having the smallest edge feature. The simulated total HXR count rate is also dependent on the launched $n_{\|}$, with the highest count rate occurring at the lowest $n_{\|}$ and the lowest count rate occurring at the highest $n_{\|}$. The edge feature is apparent in all of the HXR profiles—they are flat-top or even hollow with the profile shape depending on launched $n_{\|}$.

8.4.1 *Temperature and density sensitivity*

The sensitivity of the simulated HXR and current density profiles to the electron temperature and density input profiles was explored, and the results for one discharge in the $n_{\|}$ scan are shown in Figure 119. Scaling the density profile by $+10, -10$ percent scales the predicted total current by $+21, -17$ percent and moves the spike in the edge of the current profile outward and inward by $\Delta r/a \sim 0.1$, respectively. This also moves the ears on the HXR further outward and further inward and modifies the total count rate. Scaling the temperature profile by ± 10 percent does not have a significant effect on the current density profile except by increasing and decreasing the current on axis and changing the total current drive by ± 5 percent but has very little effect on the HXR profiles.

This sensitivity study shows that the density is the most important factor in determining the current density and HXR profiles and the total predicted current. Relatively small changes in input profiles create large changes in the predicted profiles, particularly in the details of the HXR profile. However, as noted in the non-inductive case, this does not qualitatively change the shape of either the simulated profile.

8.4.2 *Contributions to the total current*

The total current predicted by the simulation when run under different assumptions is shown in Figure 120. The simulations consistently over predict the total measured plasma current. However, they do predict that the total plasma current should be independent of the launched $n_{\|}$ (The contribution from the LHCD is decreasing while the contribution from the Ohmic increases.) The large cross-term in the simulation shows that non-zero electric field acting on the fast-electrons is important in the simulation—its component is larger than either the LHCD or Ohmic only current.

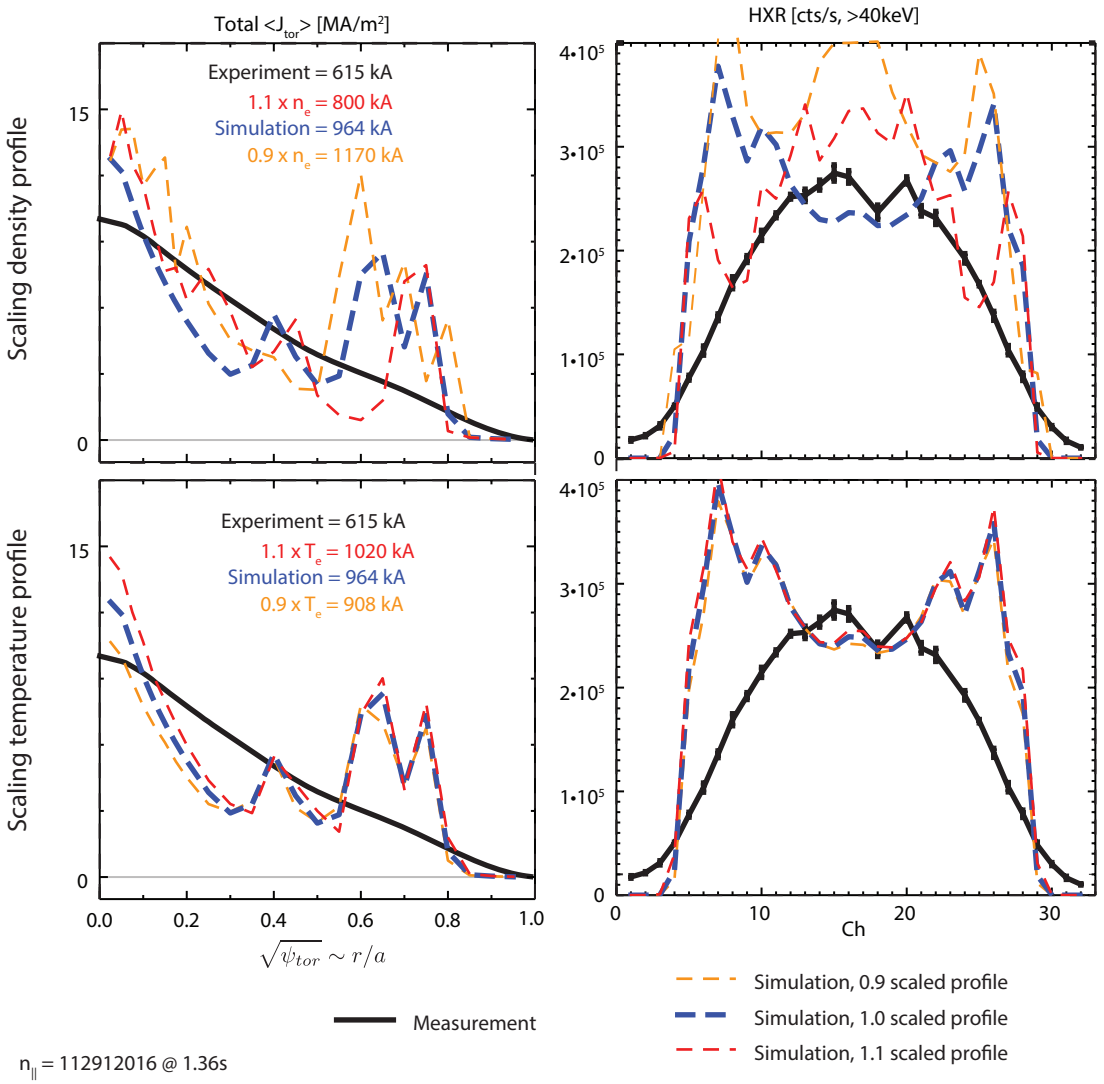

Figure 119: Sensitivity to the temperature and density in the GENRAY/CQL3D simulation. The density is scaled ±10 percent (top) and the temperature profile is scaled ±10 percent (bottom) yielding simulated total current density profiles (left) and HXR profiles (right).

Figure 120: Contributions to the total current prediction by GENRAY/CQL3D during an $n_{||}$ scan determined by running the code multiple times with different P_{LH} and E_{DC} settings. The experimental current is indicated.

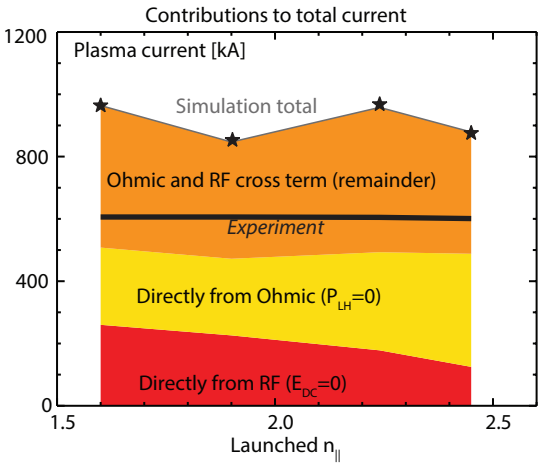

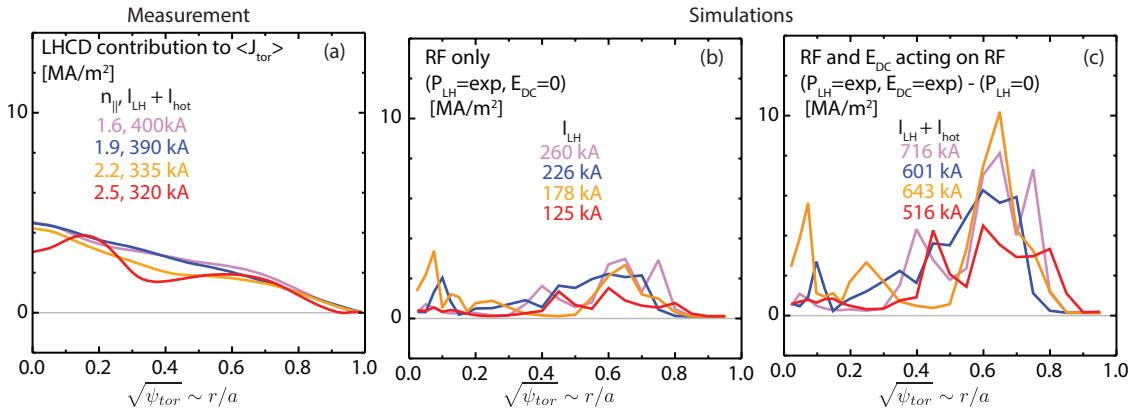

Figure 121: The components contributing to the current profile. The component from LHCD deduced from the experiment (a). The GENRAY/CQL3D component only from the RF drive (b). The GENRAY/CQL3D prediction minus the residual Ohmic acting on only the thermal distribution function (c).

The current profile components are shown in Figure 121. The experimental contribution is broad but peaked on axis (a). The components from the simulations with only LHCD and no electric field (b) produces peaks at $r/a \sim 0.7$ with the typical variability in the profile details. The action of the residual electric field greatly enhances the peaks (c). Note that the combination of lower hybrid fast-electrons and the parallel electric field acting on the fast electrons leads to overestimating the total measured plasma current.

8.4.3 *Slide-aways*

This large synergy effect is due to the residual electric field accelerating the fast electrons to very high velocities within the simulation as discovered by Shiraiwa. Recall that GENRAY/CQL3D is a time-dependent solver. In these simulations, the plasma never reaches a true steady-state—the fastest electrons slide away. Cuts through the distribution function are shown in Figure 122 for both a flux surface near the axis ($r/a = 0.15$) and off-axis ($r/a = 0.6$) where each curve is at a different pitch angle $v_{||}/v_{\perp}$. In both cases, the plateau and long tail are apparent in the parallel direction. However, the electrons slide away at the larger radius, even leaving the velocity-space domain (> 2.5MeV) with the distribution function a factor of 10^{-4} down from the plateau. The flux-surface current density for each location is plotted at the bottom of the figure. The current density near the axis is asymptoting to a constant value while the current density off-axis is continually increasing.

The simulation parameters were varied to determine how sensitive this feature is to the details of how the simulation was executed. Overall there appears to be no "silver-bullet" to eliminate these slide-aways, they seem to be a robust prediction of the code when oper-

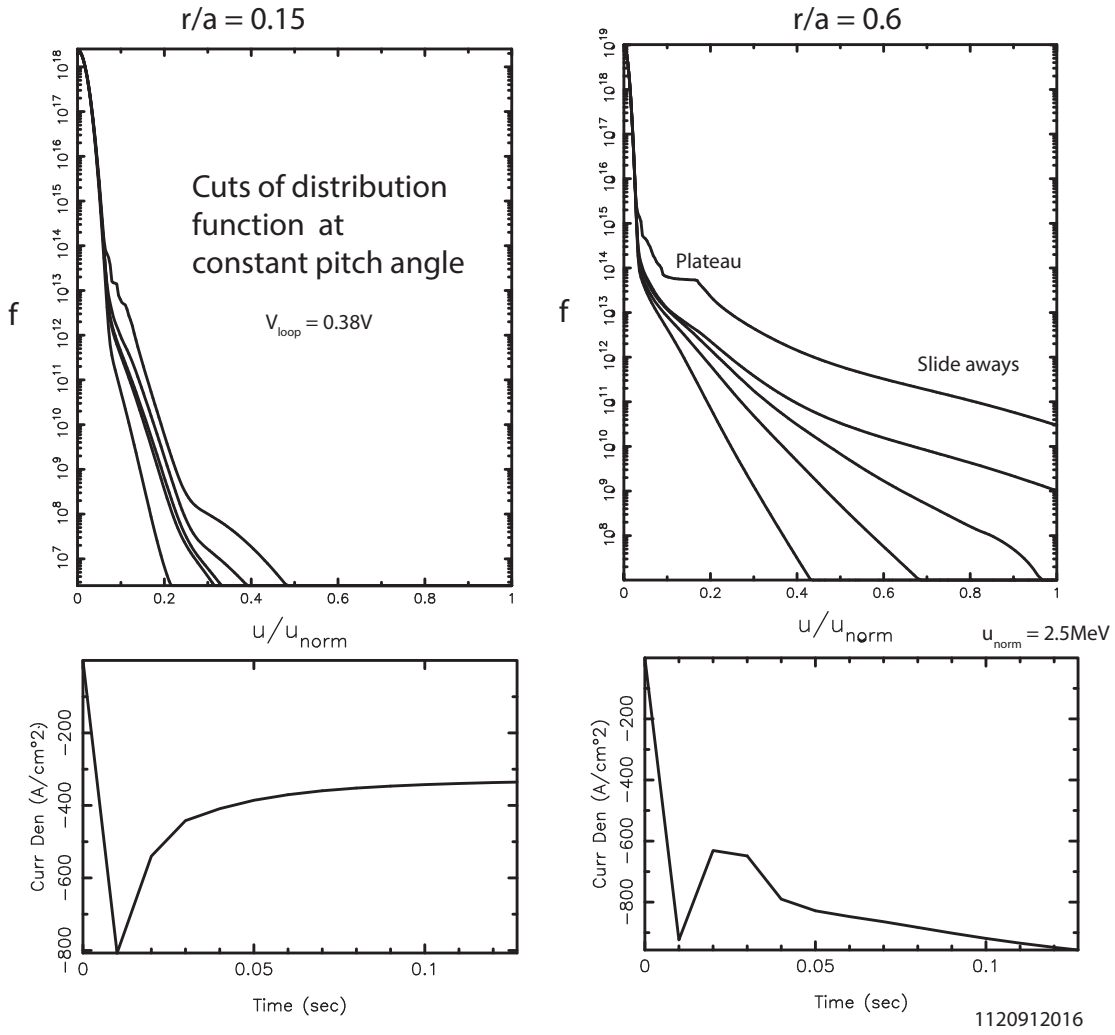

Figure 122: Cuts through the simulated distribution function (top) at small (left) and large (right) minor radius. The current density on the flux surface as a function of time (bottom).

ating with high-power LHCD (> 500kW), high loop voltage (> 0.3V), and low density ($< 7 \times 10^{19} m^{-3}$).

It is doubtful that this effect is observed in the experiment. This effect should be investigated further numerically to determine if it is an artifact of numerics or the particulars of how the code is setup. Simulation results where a large synergy term is predicted should be examined carefully for evidence of this slide-away effect. Note that this effect only amplifies the existing LHCD current and HXR profiles, as apparent in Figure 115, and does not create profile changes.

8.4.4 *Adding radial diffusion*

The over-prediction of the total current, the poor profile agreement, and the presence of slide-aways in the simulation results led to the conjecture that radial diffusion of the fast electrons might bring both the profiles and 0-D parameters into agreement with the simulation. Various levels of fast-electron diffusion were included in the simulations to test this hypothesis. The diffusion coefficient used in the model is of a form consistent with a magnetic turbulence model [18]:

$$D(v_{||}) = D_0 \frac{v_{||}/v_t}{\gamma^3} \tag{67}$$

where D_0 is a user specified diffusion coefficient, $v_{||}$ is the parallel velocity of the electron, v_t is the background plasma thermal velocity, and γ is the relativistic factor.

The results of scanning the diffusion coefficient are shown in Figure 123. Adding radial diffusion leads to a decrease in the off-axis peaks—these electrons diffuse out of the plasma. A diffusion coefficient of $D_0 = 0.08 m^2/s$ is required to match the measured total plasma current in this case. The current density feature at $r/a \sim 0.7$ is retained, leading to the same flat-top character in the HXR emission. Diffusion does not substantially change the character of the central current density.

Previous studies on C-MOD showed that the radial diffusion of fast-electrons is small—measured as $D_0 < 0.02 m^2/s$ [1]. Thus the level of diffusion required to reach zero-degree agreement between experiment and simulation requires four times the empirically measured diffusion rate and still does not agree with the measured profiles. Adding fast-electron diffusion in the models is problematic because it decreases the current drive in this $n_{||}$ scan but the same level of diffusion would decrease the current in the non-inductive simulations which already under-predict the total current.

Note that the velocity-dependence in the diffusion operator (Equation 67) leads to better confinement of the fastest electrons which is the opposite direction as that required to eliminate slide-aways from

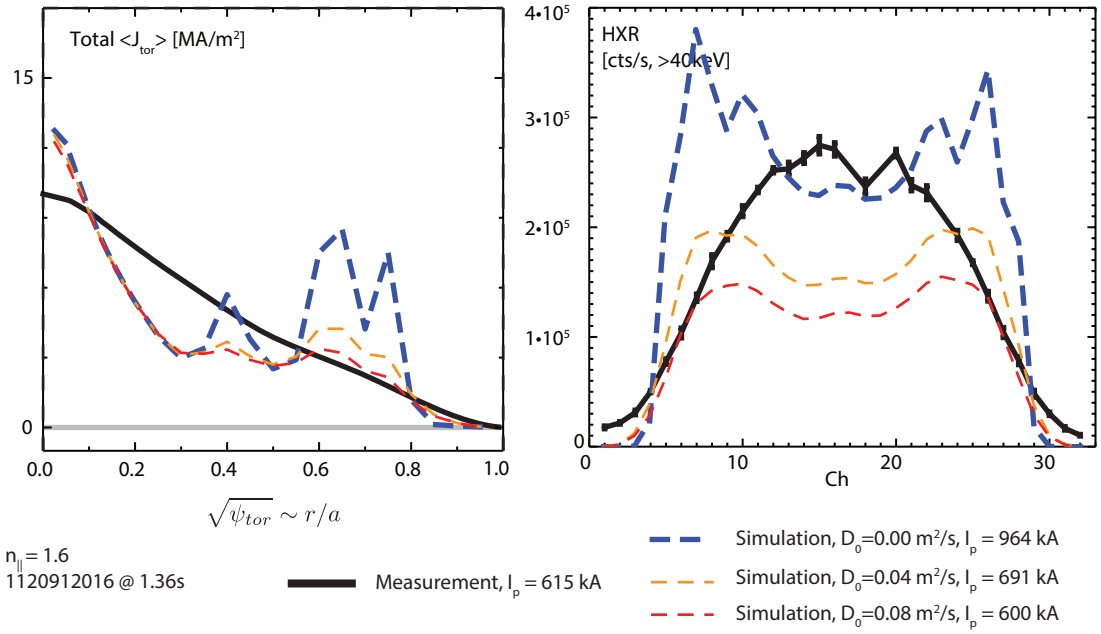

Figure 123: Different levels of radial fast-electron diffusion were included in the model with the resulting current density and HXR profiles compared to experiment.

the simulations. Ideas have been proposed to try to eliminate this long tail in the simulations by inserting an ad-hoc loss-term at high energy, but this approach was not pursued in this work.

8.5 PLASMA CURRENT DEPENDENCE COMPARISON

The strongest dependence observed in the experimental data was a dependence on plasma current, with higher plasma currents having more efficient current drive, independent of the residual loop voltage. At higher plasma current the measured HXR and LHCD-driven current profiles became broader. These plasmas were simulated using GENRAY/CQL3D and the results are shown in Figure 124.

Note that the spikes in the simulated current density profile continues to be present and moves outward, from $r/a \sim 0.4$ to $r/a \sim 0.75$, as the plasma current is increased from 530kA to 800kA. Running the simulation with no electric field also clearly shows this effect. The simulated HXR profile also becomes broader at higher current, the same trend observed experimentally, but total count rate is not as dependent on plasma current. As observed in all previous scans, the predicted spike in off-axis current drive is absent in the measurements, and the measured HXR profile is peaked while the simulations are hollow. This simulation used the experimental T_e profiles, so observed trends in the simulated profiles do not distinguish between "intrinsic" effects of plasma current and effects due to electron tem-

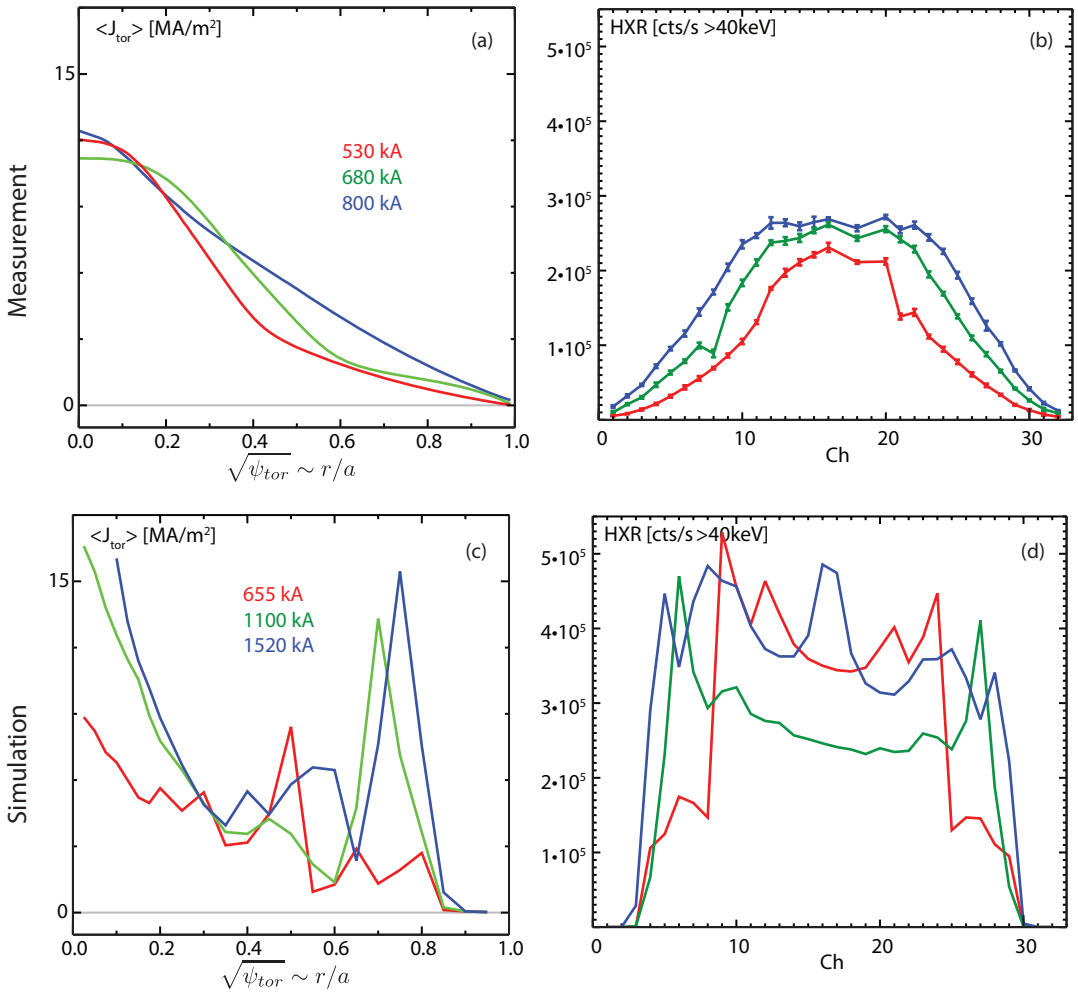

Figure 124: Comparison between measurement and simulation in a plasma current scan.

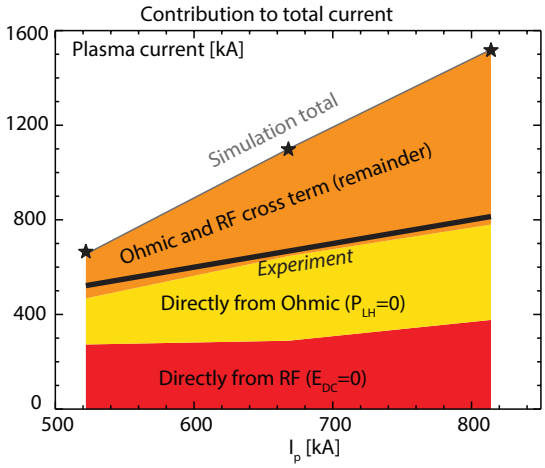

Figure 125: Contributions to the total current predicted by GENRAY/CQL3D during a plasma current scan determined by running the code multiple times with different P_{LH} and E_{DC} settings. The experimental current is indicated.

perature in the simulations. Future work could address this issue by running the simulations with a fixed electron temperature profile.

The contributions from different components are shown in Figure 125. Note that the main prediction of the code in this regime is a very large synergy term (orange) due to the slide-aways previously discussed; these are significantly larger at high current (and high loop voltage) than at low current (and low loop voltage). The predicted current driven directly from LHCD has a slight increase at higher current. The experimental plasma current is most similar to the combination of current driven when setting $P_{LH} = 0$ and then $E_{DC} = 0$, i.e. by neglecting the cross-term.

8.6 DENSITY DEPENDENCE COMPARISON

The previously-discussed simulations highlight how sensitive the current drive and HXR profiles are to changes in plasma density. The measured and simulated profiles from a density scan experiment are shown in Figure 126 where the non-inductive fraction varies from $\sim$ 70 percent to $\sim$ 10 percent. The measurements show self-similar HXR at all densities up to the point where the LHCD does not drive significant current while the measured current current density increases smoothly but modestly with increasing plasma density (i.e., as the profile shape returns to a nearly Ohmic-like profile). The simulations show that the spike in the current density shifts significantly as the density is scanned. The location of this spike is not monotonically dependent on the density, first it moves outward then inward and then outward again. This leads to stark changes in the HXR profiles, with the ears changing relative height and a central contribution appearing and then disappearing again.

Figure 127 shows the various contributions to the total plasma current deduced from executing the code different ways. The component directly due to LHCD decreases at increasing plasma density while

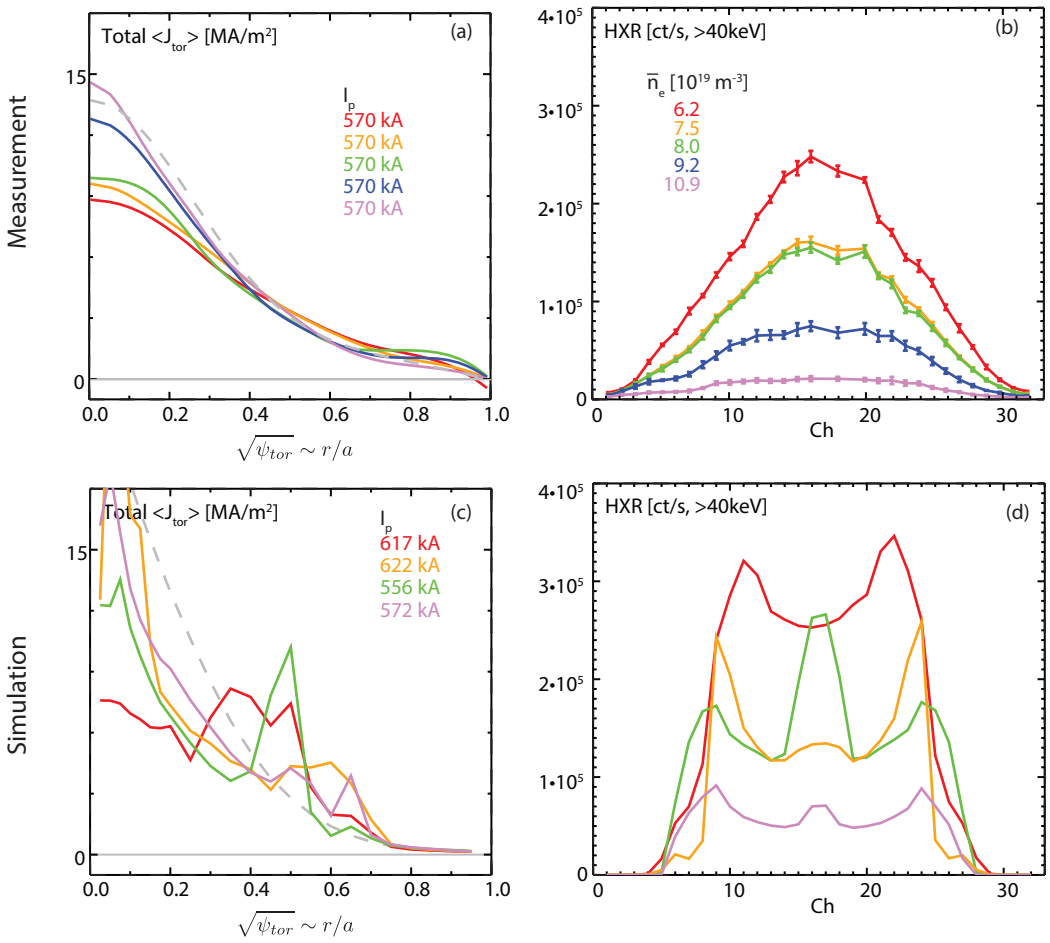

Figure 126: The measured current and HXR profiles are compared to the simulations during a plasma density scan.

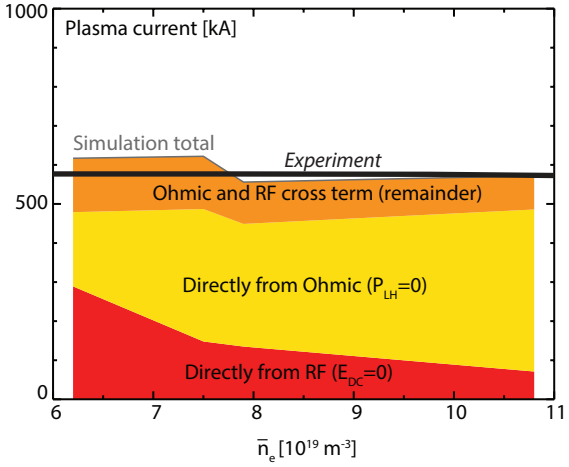

Figure 127: The contribution to the total plasma current from different effects in a density scan.

the component from the ohmic drive increases. There is a small cross-term in these plasmas. The overall predicted plasma current is in fairly good agreement with the experimental value. Note that collisional absorption in the scrape-off layer was included in these simulations and the power lost to this effect increase from ~ 70kW to ~ 150kW (out of a launched 800kW) across this density range.

8.7 SUMMARY OF OBSERVATIONS

The experimental and simulation observations are summarized in Table 11. Overall the experimental results are very robust and insensitive to the details of the experimental setup. The fast electrons appear to be on-axis leading to bell-shaped HXR profiles and central current drive. The only significant profile shape change is due to changes in total plasma current.

The GENRAY/CQL3D simulated current and HXR profiles show considerable variability in their fine structure (e.g., the radial location and magnitude of off-axis current spikes) even when input profiles are changed only modestly, but always drive most of the current far off-axis leading to flat-top HXR profiles. This general behavior is observed in other ray-tracing Fokker-Planck codes applied to C-MOD data and is apparent in previous simulations by other code users [14]. The observed lack of dependency on launched $n_{||}$ is reproduced by the simulations as are the shifts at higher plasma current. Changes in density cause large shape changes. The total current is generally well predicted except at high loop voltage and high LHCD power, where slide-aways are present in the simulation leading to an over-prediction.

8.8 DISCUSSION AND IMPLICATIONS

The simulation/experiment comparison described in this work raises important questions about the validity of using GENRAY/CQL3D (and likely other similar codes) for C-MOD tokamak plasmas even in conditions where efficient current drive is observed. While the simulation predicts reasonable total currents and HXR count rates, it fails to correctly predict any of the important details of the LHCD profiles. The simulation is much more sensitive to perturbations than the experiment and misses important 0-D trends in parameters. Something important appears to be missing.

At a hight level, these results suggest a robust physics mechanism that leads to damping of the waves in the center of the plasma is required to explain the simulation results. It appears that this mechanism must lead to upshifts in $n_{||} \sim 3-4$ to damp waves at the $2-3$keV core plasma. This is often referred to as the spectral gap problem [19]. This upshift must occur without a concomitant large losses in power.

Table 11: Summary of the comparison between measurements and GENRAY/CQL3D.

Character	Experimental observation	GENRAY/CQL3D simulation result
0D current	NA	Usually predicted within 30 percent except in cases with a large synergy term (high power, high loop voltage, low density)
LHCD current profile shape	Broadened from Ohmic but always peaked on-axis.	Large spike at $0.4 < r/a < 0.8$, rarely significant LHCD current on-axis.
HXR profile shape	Always bell-shaped, rarely flat-top and never with significant "ears" (except the active divertor emission). Self-similar at all points in the discharge.	Usually has "ears", rarely peaked on axis.
Sensitivity on $\bar{n}_e$ and T_e profiles	Both current density and HXR profiles are very reproducible, robust, and stationary.	Both profiles are sensitive to small changes in the inputs, particularly in density profile shape and magnitude. Spikes in current profile move around $\Delta r/a \sim 0.1$ and HXR ears appear and disappear. Less dependence on temperature profile. 0D current prediction sensitive at ± 20 percent level.
LHCD power dependence	Small changes in current profile—decreasing central current density by 30 percent between fully-inductive and non-inductive. HXR profile shape very self-similar and count rate linear in power.	Current profile shifts from on-axis peak to far off-axis peak with 80 percent changes in on-axis current density. HXR profile shifts from centrally peaked to having ears. 0D current sometimes under predicted as fully non-inductive current drive is approached.
Launched $n_{\parallel}$ dependence	Very little $n_{\parallel}$ dependence in the current drive, current profile, HXR profile shape, or HXR count rates.	Some dependence in LHCD current location, significant variability in the HXR profile shape and count rates. Total current prediction independent of $n_{\parallel}$ but is too high with a large synergy component.
I_p dependence	Current profile and HXR profile broadens with increasing current. Current drive efficiency increases at higher current.	Spike in off-axis current moves outward and HXR profile broadens at higher current. Total count rate not well ordered. Total current prediction too high with a large synergy term at high current and high power. Current drive efficiency (due to LHCD acting alone) is fairly constant.
Density dependence	Smoothly decreasing LHCD profiles as density is increased. Self-similar HXR profiles at all densities (perhaps slightly broader at higher densities), rapidly decreasing current drive efficiency and HXR count rates at increased density.	Profile details very sensitive to details in density, shifting spike location and changing profile shapes with little correlation. Significant shape changes in HXR profiles and over prediction of count rates at highest density. Total current drive prediction fairly accurate across density range.

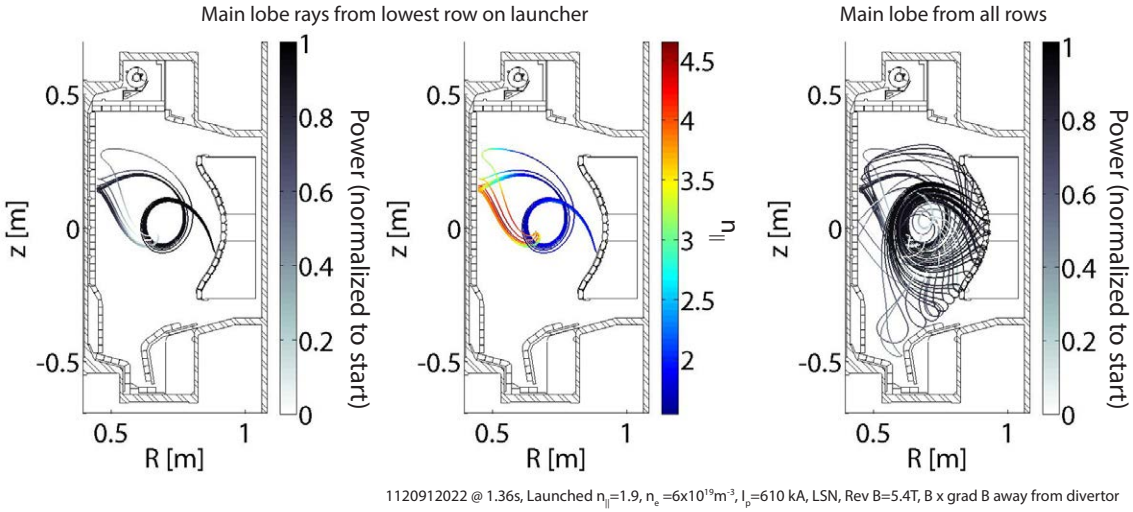

Figure 128: The trajectory of a bundle of rays traversing the plasma prior to damping indicating the normalized power left in the ray (left). The $n_{||}$ of these rays (center). All the main-$n_{||}$-lobe rays from the launcher making many bounces (right). This is from a discharge analyzed as part of the $n_{||}$ scan.

The upshift must occur but not be so large as to damp the waves in the colder regions as indicated by the large spike in the edge observed in the GENRAY/CQL3D simulations. Potential mechanisms that could generate a sufficient $n_{||}$ upshift without unacceptable power loss, and other mechanisms that might reconcile the simulations to the experimental measurements are discussed in the speculative sections below.

8.8.1 *Multi-pass, collisional absorption*

Unlike much of the previous LHCD work on C-MOD, this work was conducted in the low-density regime where the current drive efficiency is high and the plasma responds well to current drive. Unlike what occurs at higher density, the simulated rays make just a few bounces in the plasma prior to damping, but still traverse the central part of the plasma. An example of the ray-trajectories is shown in Figure 128. The left figure shows the power in a single main $n_{||}$-lobe ray from the lowest launcher row as it propagates into and out of the plasma, making a reflection on the inner wall prior to damping at mid-radius. The $n_{||}$ upshift in this bundle of rays occurs near the reflection on the inner wall (center). All of the main-lobe rays make similar bounces around the boundary of the tokamak prior to damping (right).

Since the change of trajectory of the rays results in the upshift which leads to damping, the model is sensitive to the details of the ray trajectories, likely creating the sensitivity to the details of the density and density profile (and to an extent the launched $n_{||}$) as this affects the trajectories and where the rays eventually bounce. Reference [11] Figure 5-26 shows that at these low densities (5×10^{-19}), the rays only make a few bounces prior to damping. Cutting the ray off

after 1 reflection significantly changes the HXR production from the fully damped case (2 orders of magnitude) whereas cutting the ray off after 2 reflections only degrades the HXR production by a small amount (this work was done with a separatrix that is perfectly reflecting). These low density plasmas have little collisional absorption ($<$ 100kW) predicted by the simulations.

8.8.2 *Diffusion and advection*

Radial diffusion was invoked to try to smooth the profiles. However, this also leads to significant fast-electron loss from the plasma, lowering the predicted total current. Thus different levels of fast-electron diffusion would be required in different plasma conditions to match the total current. Diffusion also has a difficult time creating centrally peaked profiles from a source of fast electrons off-axis. Inward advection would help this. Small levels of inward advection $0.05^{m}/_{s}$ was also used in the simulation to reconcile the profile discrepancies and was found to not significantly change the profiles. Previous experiments bounded the advection in C-MOD to $< |0.5|^{m}/_{s}$ [1].

8.8.3 *Full-wave codes*

Full-wave codes have been developed to explore the multi-pass regime where diffraction and interference of the LHCD wave could potentially be important. A full-wave code named LHEAF was used previously to simulate C-MOD plasmas including a low-density plasma similar to that studied in this work. The results can be found in [20] with the relevant portions shown in Figure 129.

The simulated current profile remains peaked very far off-axis in this simulation which is at 800kA with $V_{loop} = 0.2(V)$[8]. The HXR profiles show the same ears as the GENRAY/CQL3D simulations and only under significant fast electron diffusion ($\sim 5\times$ that observed in experiments) does the HXR profile begin to match that observed in the experiment. This result hints that the full-wave approach is not significantly different from GENRAY/CQL3D in this low-density few-pass regime.

8.8.4 *Scattering off density fluctuations*

An alternate hypothesis is that the launched wave is affected due to interactions immediately in the front of the launcher. This could spread the launched $n_{\|}$, allowing the spectral gap to be bridged on the first pass into the plasma. This conjecture was explored computationally by the group from CEA [21]. In addition to launching a main

8 The experiment had a $V_{loop} = 0.4V$ and no MSE making quantitative comparison between experiment and simulation difficult for this result.

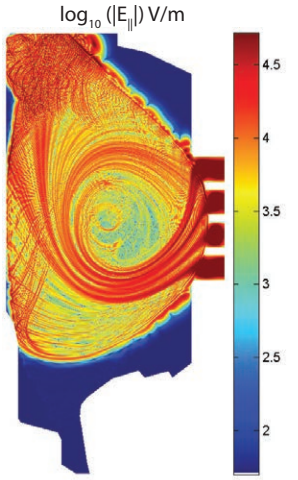

Fig 7-5 in Meneghini thesis

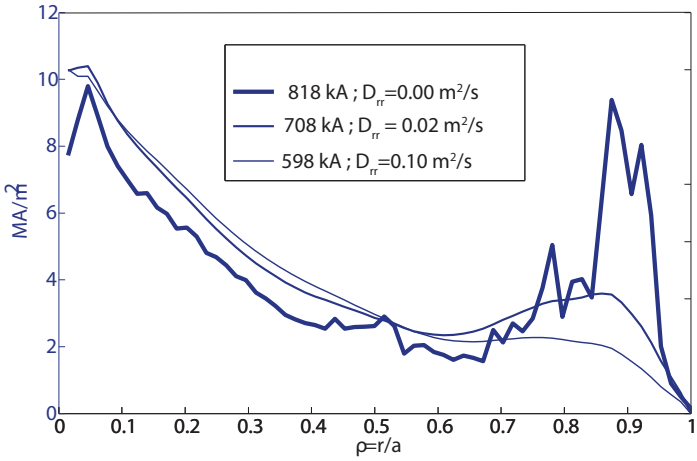

Fig 7-6 in Meneghini thesis

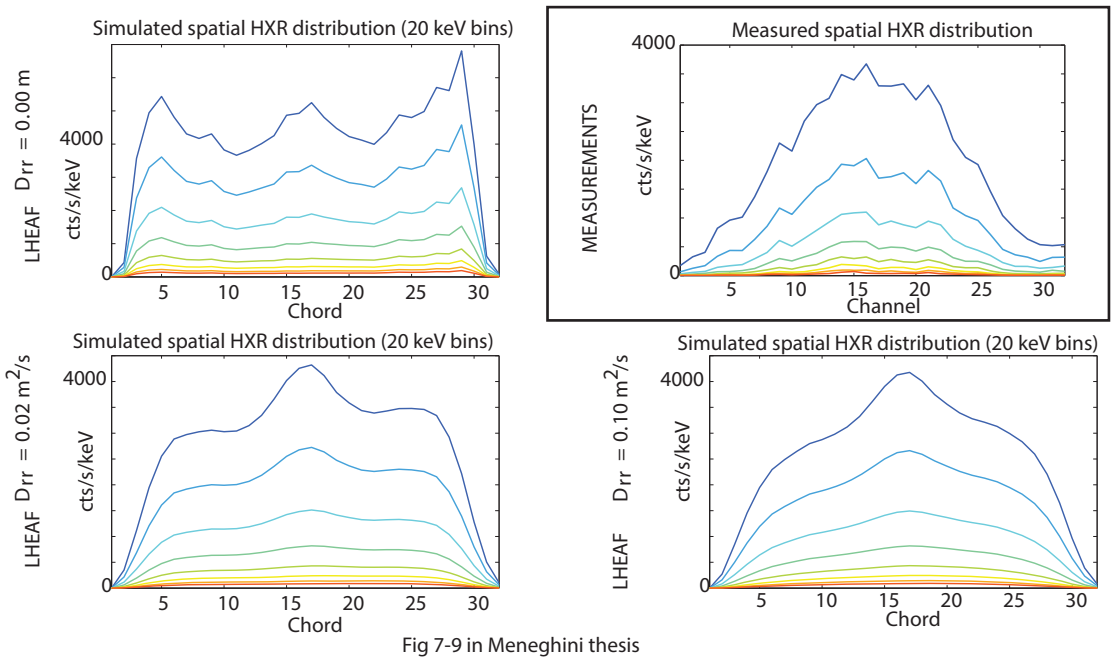

Fig 7-9 in Meneghini thesis

1080429007 @ 0.84s, n_e=7x10^{19}m^{-3} P_{LH}=560kW, P_{SOL}=6kW, $n_{||}$=1.9, Z_{eff}=2.0, V_{loop} (sim) = 0.2V, V_{loop} (exp) = 0.4V, I_p= 800kA

Figure 129: Full-wave simulations of a plasma similar to that used in this study. The wave fields and current profile are shown along with the HXR profile under various assumptions of fast-electron diffusion. Adapted from [20]

$n_{\|}$ lobe, many lower-power lobes were launched at higher $n_{\|}$. These lobes contained approximately half the power and are conjectured to arise from an as-yet unobserved edge fluctuation. The initial results of this model are promising as the the simulations better matched the measured HXR profiles on TORE SUPRA during LHCD, and the sensitivity of the ray-tracing models to input profiles was significantly decreased.

GENRAY/CQL3D was adapted to explore the effects from wave scattering from density fluctuations in the edge of the plasma on ALCATOR C-MOD in the density range of $6 \times 10^{19} m^{-3}$ [22]. The results showed that scattering alters the deposited LHCD power with the power deposition profile still being strongly peaked off-axis at $r/a \sim 0.4 - 0.7$ (implying it also didn't change the current profile). However, the results did show a broader peak with scattering than the case with no scattering.

BIBLIOGRAPHY

[1] A. Schmidt, P. T. Bonoli, O. Meneghini, R. R. Parker, M. Porkolab, S. Shiraiwa, G. Wallace, J. C. Wright, R. W. Harvey, and J. R. Wilson. Investigation of lower hybrid physics through power modulation experiments on Alcator C-Moda). *Physics of Plasmas (1994-present)*, 18(5):056122, May 2011.

[2] Li Miaohui, Ding Bojiang, Li Wenke, Kong Erhua, Shan Jiafang, Liu Fukun, Wang Mao, and Xu Handong. Investigation of LHCD Efficiency and Transformer Recharging in the EAST Tokamak. *Plasma Science and Technology*, 14(3):201, March 2012.

[3] C. Yang, P. T. Bonoli, J. C. Wright, B. J. Ding, R. Parker, S. Shiraiwa, and M. H. Li. Modelling of the EAST lower-hybrid current drive experiment using GENRAY/CQL3d and TORLH/CQL3d. *Plasma Physics and Controlled Fusion*, 56(12):125003, December 2014.

[4] S. Shiraiwa, G. Baek, P. T. Bonoli, I. C. Faust, A. E. Hubbard, O. Meneghini, R. R. Parker, G. M. Wallace, J. R. Wilson, R. W. Harvey, A. P. Smirnov, D. Brunner, B. LaBombard, C. Lau, R. Mumgaard, S. Scott, N. Tsujii, S. Wolfe, and the Alcator C.-Mod Team. Progress towards steady-state regimes in Alcator C-Mod. *Nuclear Fusion*, 53(11):113028, November 2013.

[5] P. T. Bonoli. Benchmarking of lower hybrid current drive codes with application to ITER-relevant regimes. 2006.

[6] B. LaBombard, E. Marmar, J. Irby, J. L. Terry, R. Vieira, G. Wallace, D. G. Whyte, S. Wolfe, S. Wukitch, S. Baek, W. Beck, P. Bonoli, D. Brunner, J. Doody, R. Ellis, D. Ernst, C. Fiore, J. P. Freidberg, T. Golfinopoulos, R. Granetz, M. Greenwald, Z. S. Hartwig, A. Hubbard, J. W. Hughes, I. H. Hutchinson, C. Kessel, M. Kotschenreuther, R. Leccacorvi, Y. Lin, B. Lipschultz, S. Mahajan, J. Minervini, R. Mumgaard, R. Nygren, R. Parker, F. Poli, M. Porkolab, M. L. Reinke, J. Rice, T. Rognlien, W. Rowan, S. Shiraiwa, D. Terry, C. Theiler, P. Titus, M. Umansky, P. Valanju, J. Walk, A. White, J. R. Wilson, G. Wright, and S. J. Zweben. ADX: a high field, high power density, advanced divertor and RF tokamak. *Nuclear Fusion*, 55(5):053020, May 2015.

[7] S Shiraiwa. πScope : a python-based scientific work bench with MDSplus data visualization tool. *Fusion Engineering and Design*, To be submitted.

[8] A. P. Smirnov and R. W. Harvey. Calculations of the Current Drive in DIII-D with the GENRAY Ray Tracing Code. *Bulletin of the American Physical Society*, 40(11), 1995.

[9] G. M. Wallace, R. R. Parker, P. T. Bonoli, A. E. Hubbard, J. W. Hughes, B. L. LaBombard, O. Meneghini, A. E. Schmidt, S. Shiraiwa, D. G. Whyte, J. C. Wright, S. J. Wukitch, R. W. Harvey, A. P. Smirnov, and J. R. Wilson. Absorption of lower hybrid waves in the scrape off layer of a diverted tokamak. *Physics of Plasmas*, 17(8):082508, August 2010.

[10] R. W. Harvey and M. McCoy. The CQL3d Fokker-Planck Code. *Proceedinngs of the IAEA Technical Committee Meeting on Simulation and Modeling of Thermonuclear Plasmas*, pages 489–526, 1992.

[11] Gregory M. Wallace. *Behavior of lower hybrid waves in the scrape off layer of a diverted tokamak*. Thesis, Massachusetts Institute of Technology, 2010.

[12] S Shiraiwa. Impact of edge plasmas on Lower Hybrid Current Drive: Experimental evidence, mitigation and modeling approaches. to be submitted. Lake Arrowhead, California, April 2015. AIP Publishing.

[13] R. W. Harvey and M.g. McCoy. The CQL3d Fokker-Plack Code Manual. Technical report.

[14] Andrea E. W. Schmidt. *Measurements and modeling of Lower Hybrid Driven fast electrons on Alcator C-Mod*. PhD, 2011.

[15] R. W. Harvey. X-Ray Energy Spectra Calculated from CQL3d Fokker-Planck Electron Distributions. CompX technical report CompX-2000-2, CompX, CompX, P.O. Box 2672, Del Mar, CA 92014-5672, February 2001.

[16] Y. Peysson, J. Decker, and L. Morini. A versatile ray-tracing code for studying rf wave propagation in toroidal magnetized plasmas. *Plasma Physics and Controlled Fusion*, 54(4):045003, April 2012.

[17] J. Decker and Y. Peysson. DKE: A fast numerical solver for the 3d drift kinetic equation. Technical Report EUR-CEA-FC-1736, 2004.

[18] H. E. Mynick and J. D. Strachan. Transport of runaway and thermal electrons due to magnetic microturbulence. *Physics of Fluids (1958-1988)*, 24(4):695–702, April 1981.

[19] Paul T. Bonoli and Ronald C. Englade. Simulation model for lower hybrid current drive. *Physics of Fluids (1958-1988)*, 29(9):2937–2950, September 1986.

[20] Orso (Orso-Maria Cornelio) Meneghini. *Full-wave modeling of lower hybrid waves on Alcator C-Mod*. Thesis, Massachusetts Institute of Technology, 2012.

[21] J. Decker, Y. Peysson, J.-F. Artaud, E. Nilsson, A. Ekedahl, M. Goniche, J. Hillairet, and D. Mazon. Damping of lower hybrid waves in large spectral gap configurationsa). *Physics of Plasmas (1994-present)*, 21(9):092504, September 2014.

[22] N. Bertelli, G. Wallace, P. T. Bonoli, R. W. Harvey, A. P. Smirnov, S. G. Baek, R. R. Parker, C. K. Phillips, E. J. Valeo, J. R. Wilson, and J. C. Wright. The effects of the scattering by edge plasma density fluctuations on lower hybrid wave propagation. *Plasma Physics and Controlled Fusion*, 55(7):074003, July 2013.

A

OVERVIEW OF POLARIZED LIGHT

This appendix reviews the basics of the polarization of light, its measurement, and its manipulation. These concepts will be central to the discussions to follow in this and the next two chapters of this thesis.

Note that the light from the beam is emitted by a volume of non-interacting atoms and is therefore incoherent—the electromagnetic waves from each atom are out of phase. The proper way to represent the polarization of incoherent light is with Stokes vectors (as opposed to Jones vectors used to represent coherent polarized light). Stokes vectors are convenient since they are complete (they can represent any type of incoherent light) and they are linear. The method in which Stokes vectors are manipulated is termed Müeller calculus. Excellent reviews of the theory of polarization and pertinent examples can be found in references [1–4]. In particular, chapter 22 in reference [1] contains a good overview of polarization and polarimeters.

The stokes vector is composed of four components:

$$\begin{bmatrix} I \\ Q \\ U \\ V \end{bmatrix} \tag{68}$$

The first component, I, relates to the total (polarized and unpolarized) intensity. The second and third components, Q and U respectively, relate to the linear polarized component of the light. The last component, V, relates to the circular polarized component of the light. Note that $I > 0$ and Q, U, and V can range from $-I$ to $+I$ with the condition $\sqrt{Q^2 + U^2 + V^2} \leqslant I$.

Most MSE-LP systems employ a dual photo-elastic modulator (PEM)-based polarimeter [5] which encodes the polarization of the light incident on it into a time-varying signal by passing the light through a pair of vibrating birefringent crystals and a linear polarizer. This signal is then detected and the amplitude of the signal at harmonics of the PEMs' vibration frequencies is then demodulated using a lock-in amplifier or a numerical phased-locked loop [6]. This yields the Stokes vector of the radiation incident on the polarimeter. The PEM-based polarimeters used in MSE-LP diagnostics are complete—all four Stokes components of the radiation incident on the PEMs can be recovered with high precision and good temporal resolution.

Though the calculations are performed with Stokes vectors, the input and output of the MSE-LP diagnostic is primarily concerned with

polarization angle and not the actual Stokes components. When properly aligned, the particular PEM-based polarimeter configuration employed in MSE-LP diagnostics can very accurately determine this angle. Therefore, for the remainder of this thesis, the polarization angle of the light, θ, will be the focus of the discussion. This angle is related to the Stokes components through:

$$\begin{aligned} Q &= L\cos(2\theta) \\ U &= L\sin(2\theta) \\ \theta &= \frac{1}{2}\tan^{-1}\left(\frac{U}{Q}\right) \end{aligned} \tag{69}$$

where L is the linear polarized intensity:

$$L = \sqrt{Q^2 + U^2} \tag{70}$$

Other useful relations between Stokes vectors and commonly used polarization terms are described here for reference. The degree of polarization of the light:

$$DOP = \frac{\sqrt{Q^2 + U^2 + V^2}}{I} \tag{71}$$

sometimes referred to as the polarization fraction or total polarization fraction. The degree of linear polarization of the light:

$$DOLP = \frac{L}{I} = \frac{\sqrt{Q^2 + U^2}}{I} \tag{72}$$

The degree of circular polarization fraction:

$$DOCP = \frac{V}{I} \tag{73}$$

which is positive for right-handed elliptical light and and negative for left handed elliptical light.

It conceptually important to realize that partially-polarized light ($I > \sqrt{Q^2 + U^2 + V^2}$) can be decomposed into a the sum of two stokes vectors, one with $DOP = 1$ (i.e., fully polarized) and one with $DOP = 0$ (i.e, fully unpolarized). This fact is used throughout this thesis to refer to the polarized component of some source of partially-polarized light, often ignoring the unpolarized component. The circular component of the light can also be decomposed in a similar manner. Much of the work dealing with MSE-LP diagnostics deals only with the linear polarized component, represented by Q and U.

A.1 COMBINING MULTIPLE SOURCES OF LIGHT

When multiple sources of polarized light are physically combined the resulting polarization is the sum of their Stokes vectors, which has different polarization properties than either constituent. Note from Equation 69, that combining equal amounts of linearly polarized light with orthogonal polarization angles ($\theta_2 = \theta_1 + 90°$, $L_2 = L_1$) will create completely unpolarized light, effectively "canceling out" each other. In the same manner, equal amounts of right-handed and left-handed circular light ($V_2 = -V_1$) will create unpolarized light. This is particularly important when considering the combination of sources of nearly orthogonal light or nearly aligned light.

Before proceeding, it is important to understand how combining different sources of polarized light together leads to a resulting polarization angle. This is analyzed by combining two DOLP = 1 Stokes vectors, one with linear polarization intensity L_a and polarization angle[1] $\theta_{pol\,a} = +\Delta/2$ and the other with linear polarization intensity L_b and polarization angle $\theta_{pol\,b} = -\Delta/2$. Combining these two sources together yields:

$$\begin{aligned} Q =& L_a \cos(\Delta) + L_b \cos(-\Delta) \\ U =& L_a \sin(\Delta) + L_b \sin(-\Delta) \end{aligned} \tag{74}$$

Setting $\frac{L_a}{L_b} = R$ and and dividing yields the total polarization angle:

$$\tan(2\theta_{pol}) = \frac{R-1}{R+1}\tan(\Delta) \tag{75}$$

The change in polarization angle with respect to the illumination ratio is then:

$$\frac{d\theta_{pol}}{dR} = \frac{\tan(\Delta)}{(R+1)^2 + (R-1)^2\tan^2(\Delta)} \tag{76}$$

which near $R = 1$ is:

$$\frac{d\theta_{pol}}{dR}|_{R=1} = \frac{\tan(\Delta)}{4} \tag{77}$$

The DOLP can also be calculated :

$$\begin{aligned} DOLP =& \frac{\sqrt{Q^2 + U^2}}{L_a + L_b} \\ =& \frac{L_b}{L_a + L_b}\sqrt{(R-1)^2\sin^2\Delta + (R+1)^2\cos^2\Delta} \\ =& \frac{1}{R+1}\sqrt{R^2 + 1 + 2R(2\cos^2\Delta - 1)} \end{aligned} \tag{78}$$

1 The reference coordinate of the Stokes calculation is chosen to bisect the two angles, simplifying the calculation. There is no preferred reference frame.

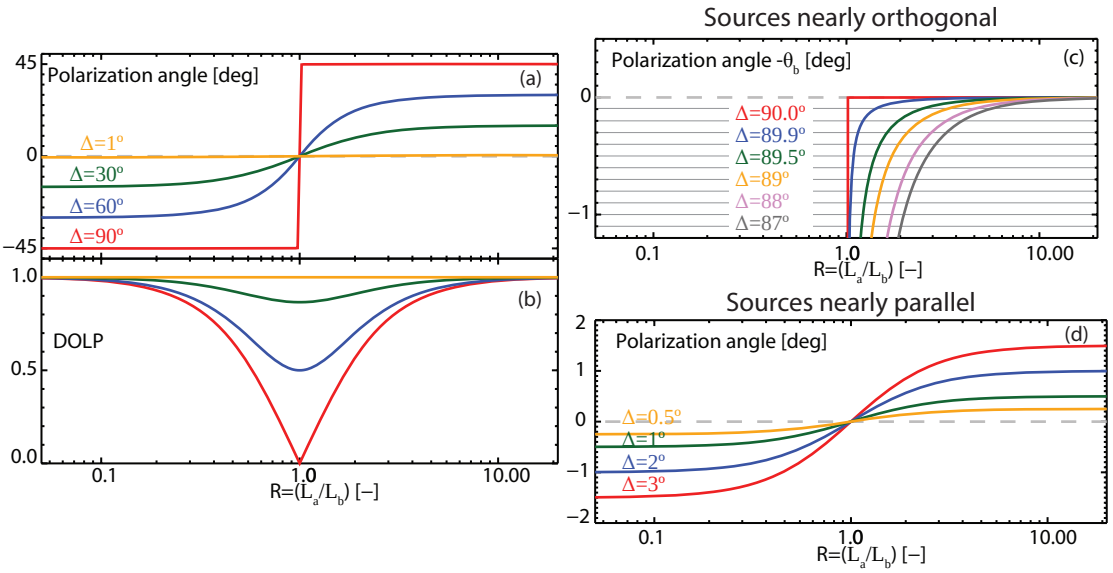

Figure 130: Two DOLP = 1 sources of light with different polarization angles are combined to yield a new polarization angle (a) and DOLP (b). Combining nearly orthogonal (c) and nearly parallel (d) light also influence the resulting polarization angle.

Figure 130 shows the resulting polarization angle (a) and DOLP (b) when two sources of DOLP = 1 light are combined together. The resulting polarization angle switches between the different source angles as the intensity ratio is varied. The DOLP of the combined light decreases when neither source is dominant. The previously discussed effects often result in the MSE-LP diagnostic collecting light with slightly non-parallel or slightly non-orthogonal polarization angles, thus the limits of $\Delta \sim 0$ and $\Delta \sim \pi/4$ are important. Adding two nearly orthogonal sources together slightly rotates the resulting polarization angle (c). Adding two nearly aligned sources shows similar behavior in polarization angle (d).

BIBLIOGRAPHY

[1] Optical Society Of America. *Handbook of Optics, Vol. 2: Devices, Measurements, and Properties, Second Edition*. McGraw-Hill Professional, New York, 2 edition edition, September 1994.

[2] Edward Collett and Society of Photo-optical Instrumentation Engineers. *Field guide to polarization*. SPIE, Bellingham, Wash., 2005.

[3] Harland G. Thompkins and Irene, Eugene A. *Handbook of Ellipsometry*. 2005.

[4] Enric Garcia-Caurel, Razvigor Ossikovski, Martin Foldyna, Angelo Pierangelo, Bernard DrÃ©villon, and Antonello De Martino. Advanced Mueller Ellipsometry Instrumentation and Data Analysis. In Maria Losurdo and Kurt Hingerl, editors, *Ellipsometry at the Nanoscale*, pages 31–143. Springer Berlin Heidelberg, 2013.

[5] G. R. Boyer, B. F. Lamouroux, and B. S. Prade. Automatic measurement of the Stokes vector of light. *Applied Optics*, 18(8):1217–1219, April 1979.

[6] Yuejiang Shi. Digital lock-in technique for the motional Stark effect diagnostic. *Review of Scientific Instruments*, 77(3):036111, 2006.

B

CONSTRAINING MAGNETIC RECONSTRUCTIONS USING MSE

The primary purpose of the MSE measurement is to provide internal constraints for plasma equilibrium reconstructions. The plasma equilibrium, described by the Grad-Shafranov equation, is solved on C-MOD using the EFIT reconstruction code [1] which is used on many magnetic fusion experiments. This code numerically solves the equilibrium for a given time-slice on a R, Z grid in the tokamak with a free-boundary. The code uses basis functions for $FF'(\psi)$ and $P'(\psi)$ in terms of poloidal flux (ψ). The basis functions can either be a polynomial expansion with a user-specified order or can be spline functions with a user-specified number and position of knots (i.e., at $\psi = 0$, $\psi = 1$, and at $\psi = 0.4$). The polynomial expansion does not provide much flexibility for describing the profiles, particularly near the center of the plasma. The spline basis functions allow a more diverse set of profiles but are more difficult to constrain, requiring more internal measurements.

The toroidal current density is calculated from the $FF'(\psi)$ and $P'(\psi)$ as:

$$J_{tor}(R, Z) = R\, P'(\psi) + \frac{FF'(\psi)}{R} \tag{79}$$

where R being the major radius. This is a 2-dimensional quantity across the plasma. The current profile at the plasma midplane or the flux-surface average is reported in the rest of this work.

EFIT uses various measurements to constrain the solution in a χ^2 minimization procedure. Each measurement is provided to the code with an uncertainty estimate and the coefficients in the $FF'(\psi)$ and $P'(\psi)$ basis functions are varied to solve the Grad-Shafranov equation. The chosen solution is the one that minimizes the χ^2 between the measured quantity and the calculated quantity summed over all measurements[1]. The total current in the plasma is constrained with a strong weighting to force the reconstruction to obtain close to the measured plasma current.

The interior of the C-MOD tokamak has many magnetic sensors which detect the magnetic flux and the change in the magnetic fields at specific locations within the tokamak [2]. Together with the measured currents in the tokamak magnet coils, these measurements can adequately constrain the boundary shape of the plasma, though there

1 The various constraints can also be unequally weighted in the fitting, though this is not done in the work presented here except where noted.

is uncertainties in the shape and position of the boundary. However, the plasma is good at "shielding" internal information from external measurement. The problem of equilibrium reconstructions using external magnetics alone is ill-posed [3] with many possible solutions possible within the same plasma boundary shape [4]. Therefore, constraints in the interior of the plasma are required to infer changes in the current profile. The addition of MSE measurements can substantially constrain various possible magnetic equilibrium as shown in numerical studies [5–8]. The MSE data is particularly adept at constraining the current profile since it is gives information about the poloidal magnetic field profile.

An equilibrium calculation using external magnetic measurements and coil currents is automatically performed immediately after every plasma discharge for time slices every 20 milliseconds[2] This reconstruction does not use MSE, instead it uses a q-constraint at the magnetic axis. The on-axis safety factor is set to be $q_0 = 0.95$ and polynomials of order 2 are used for $FF'(\psi)$ and $P'(\psi)$. This analysis is termed the "ANALYSIS EFIT."

B.1 MSE-KINETIC-EFIT

However, the ANALYSIS EFIT is not useful during experiments where the current profile is varied—the q_0 constraint is no longer applicable. Additionally, because it uses low order polynomials as basis functions, the ANALYSIS EFIT reconstruction does not have the flexibility to represent complex internal profiles. Pressure and magnetic pitch angle constraints are added in what is termed MSE-kinetic-EFIT (MK-EFIT) and the q_0 constraint is omitted. These additional constraints are input to the same EFIT numerical solver as used in the ANALYSIS EFIT along with the identical magnetics and coil current data. The use of the internal constraints in the MK-EFIT allow the use of spline basis functions for $FF'(\psi)$ and $P'(\psi)$ which allows a wider range of equilibrium profiles to be calculated [9].

The MK-EFIT process is done using an interactive GUI and work flow manager named πSCOPE developed by Syun'ichi Shiraiwa [10]. This program reads the relevant profile data from the MDSPLUS tree, creates the input file for EFIT, and then executes EFIT. It allows the user to vary knot locations and to visualize the calculated equilibrium to determine the consistency between the solution and the measurements. The GUI also performs the intra-shot calibration technique on the MSE data as discussed in the next section.

The magnetic pitch angle ($\tan^{-1}\left(\frac{B_Z}{B_\phi}\right)$) is calculated from MSE measurement of the polarization angle at each sightline using the polar-

2 This is also done on the Thomson Scattering time basis and on faster time basis when desired

ization projection factor. The ten MSE constraints are input in real-space at the location of the beam-sightline intersection. The magnetic pitch angle is calculated on the microbin time basis ($\sim$ 5ms) and then averaged together for $50-70$ms with the uncertainty taken as the standard error of the ensemble ($\frac{\sigma}{\sqrt{n}}$). The MK-EFIT is performed on a time basis that is the nearest 20 milliseconds to the time point of this macro-binned MSE data. The MK-EFIT is performed on each of the MSE measurement times—typically 10-20 points per discharge spaced $\sim$ 100ms apart. Prior to be included in the reconstruction, the MSE data is manually examined and data points with spurious angle changes due to poor background subtraction are eliminated, therefore some time-slices have fewer than ten measurement points. Poor background subtraction typically precludes using MSE at time points that overlap the start and end of LHCD or ICRF heating, during heating faults, and during impurity injections.

The total plasma pressure is used as an internal constraint in the reconstruction (hence kinetic). The electron pressure is determined from Thomson scattering measurements [11] in the interior of the plasma by averaging the data over $\sim$ 70 milliseconds centered on the time-point of interest. The uncertainty in the measurement points is calculated from the standard error of the different measurements. The Thomson scattering points are used as constraints in real-space at the $z = 0$ plane after being mapped from the actual $R =$ constant measurement locations using the ANALYSIS EFIT. The ion pressure is estimated by scaling the electron temperature and densities profiles to match the neutron production with some assumed spatially-constant Z_{eff} and impurity components (typically $Z_{eff} = 2$, $Z_{imp} = 5$, $A_{imp} = 12$). The ion pressure is typically $\sim$ 25 percent of the total pressure in the analysis for LHCD discharges used in this thesis. The fast-ion contribution to the total pressure is neglected in these discharges, which lack ICRF or strong beam heating. The pressure was varied by $\pm$20 percent and was found to not substantially affect the reconstructed current profile.

The pressure measurements and the ten MSE measurements are interpolated onto a denser grid (typically 25 points) using Gaussian process regression. This process accurately represents the uncertainty in the interpolation of the measurements onto the finer grid assuming the underlying profiles are smooth[3]. It was found prior to the implementation of this feature that the resulting equilibrium was "twitchy" if a knot location was placed near a measurement location. The recon-

3 The MSE data is extrapolated past the center-most measurement point ($\sim$ 0.70cm) to the magnetic axis ($\sim$ 0.68cm) utilizing the fact that the pitch angle must be zero at the magnetic axis, this is done with large uncertainties to prevent this from skewing the results. The pitch angle at the limiter location from ANALYSIS EFIT is also used to inform the Gaussian processing though with less weighting. The interpolated data does not extend past the outer-most MSE sightline and this limiter pitch angle helps constrain the derivative in the interpolation.

struction would qualitatively change depending on which side of the measurement point the knot location was placed, with one result having a much smaller total χ^2. This behavior required a time-intensive χ^2 minimization by manually varying the knot locations. The use of a finer spatially-interpolated measurement set, particularly for the MSE measurement, makes the equilibrium reconstruction much less twitchy—the solution becomes less dependent on the details of the knot locations.

Constraints on the q-profile can also be imposed with both a constraint at the magnetic axis (e.g. $q_0 = 0.9$) or by constraining the location of a rational q-surface (e.g. $q(\psi) = 1$ at $\psi = 0.16$). The boundary location from the ANALYSIS EFIT can also be used as a constraint on the boundary location in MK-EFIT with some a user-specified uncertainty. However, this is not typically done in the work presented here since the boundary shape is expected to change with additional internal constraints, particularly when the ANALYSIS EFIT assumptions force a non-realistic current profile. The edge current density can also be constrained using the experimental loop voltage, estimates of the edge temperature, and Spitzer resistivity[4]. This is occasionally done to prevent large unphysical spikes and/or dips in the edge current due to the lack of a constraint in the outer 2 centimeters of the plasma. These dips and spikes usually accompany large changes in the boundary shape from that produced from ANALYSIS EFIT and yield a larger χ^2 and are thus deemed to be unphysical.

Typically four knot locations are used for both $P'(\psi)$ and $FF'(\psi)$ (e.g., at $\psi = 0$, $\psi = 0.2$, $\psi = 0.6$, and $\psi = 1$), though the interior knot locations are not the same for both $P'(\psi)$ and $FF'(\psi)$. The locations of the spline knots are automatically varied to determine the optimal locations, with a EFIT run at each of $\sim 5^4$ possible knot location combinations. The combination of knot locations that produces the lowest total χ^2 is then selected from the outputs. The knot locations are allowed to move time-slice to time-slice to allow flexibility in the reconstruction, though this is usually inspected to make sure the movement is smooth in time.

An example of a MK-EFIT reconstructed time-slice is shown in Figure 131. The MK-EFIT reproduces the plasma shape, current, and safety-factor profile from the ANALYSIS EFIT but is constrained by pressure and MSE measurements with no ad-hoc q-profile constraints. The simulation uses spline basis functions for $FF'(\psi)$ and $P'(\psi)$. (Note, the MSE data has been intra-shot calibrated as described below.)

A Monte Carlo technique is used to estimate the uncertainty in the reconstruction at time periods of physics interest. The input constraint measurements are randomly varied within each measurement uncertainty and approximately 200 EFIT calculations are run for each time slice of interest. The results are compiled and results with total

4 Bootstrap current is neglected in this calculation.

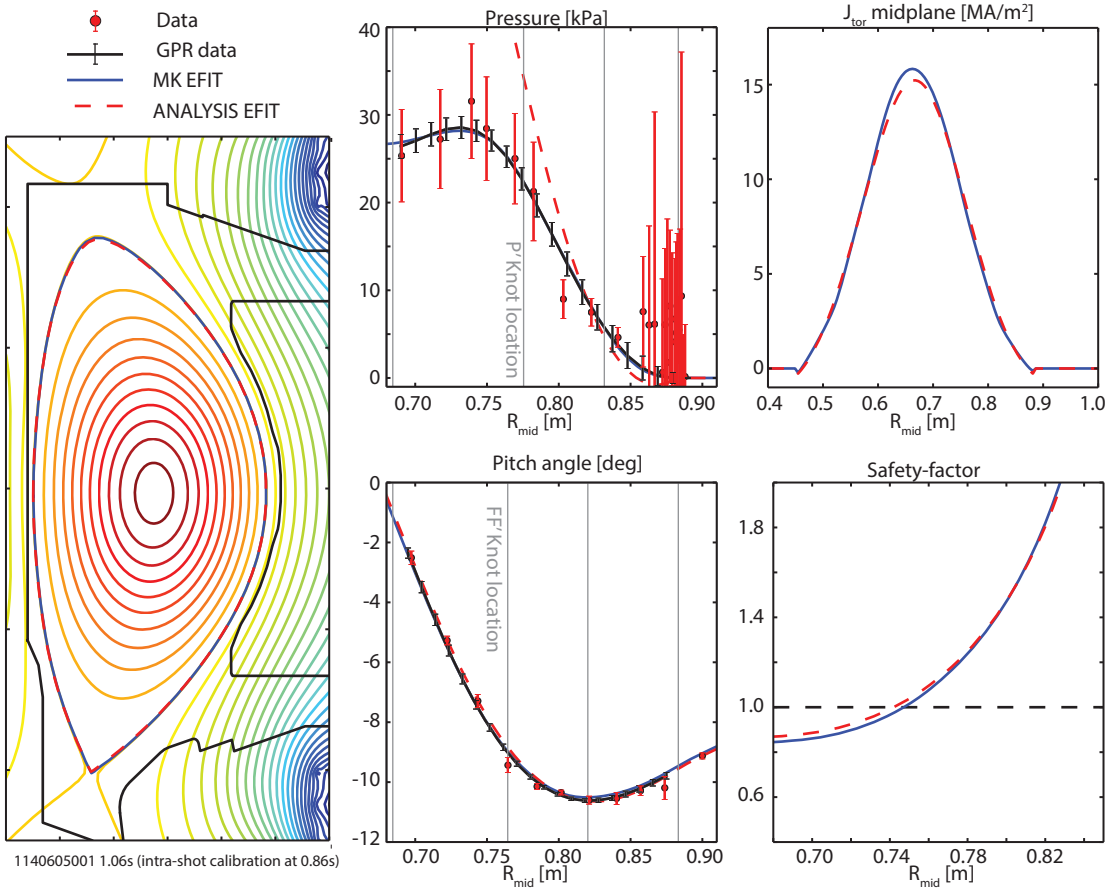

Figure 131: A reconstructed time-slice during an Ohmic disharge. The shape of the plasma is shown (left) with the seperatrix from both the MK-EFIT (blue) and ANALYSIS EFIT (red dashed). The discharge is constrained by pressure and pitch angle measurements from Thomson scattering and MSE, respectively (middle). The raw data (red dots) is interpolated to a finer grid using Gaussian Process regression (black error bars) and used to constrain the reconstruction which uses spline basis functions with the indicated knot locations. The resulting toroidal current density and safety-factor (right).

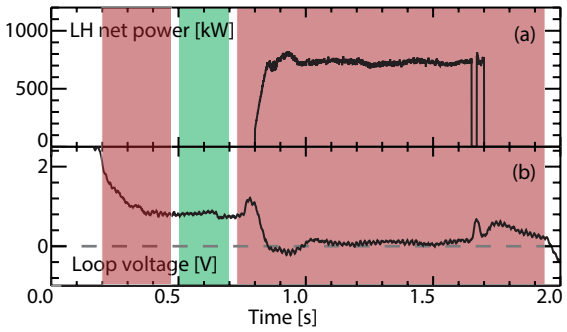

Figure 132: For experiments prior to the commissioning of the ISC system an intra-shot calibration technique was used. Time periods are chosen in each discharge to intra-shot calibrate the MSE diagnostic. Kinetic EFIT reconstructions are obtained using pressure and q constraints for Ohmic periods (green shaded region). The pitch angle from these equilibriums are used to obtain a calibration offset for the MSE data. The MSE is then used as a internal constraint for later time periods where the current profile may be evolving, such as during the application of LHCD (red shaded regions).

$\chi^2 > 10\times$ the minimum are omitted as being spurious. The pressure, pitch angle, q, and current profiles are then collected from the runs and the uncertainty at each point in the profile is taken as the standard deviation of the collection of the runs.

B.2 INTRA-SHOT CALIBRATION OF MSE

The majority of the data obtained for LHCD physics data in this work was obtained when thermal stress-induced birefringence was still still causing the diagnostic response to change on the minute time-scale. An intra-shot technique is therefore used to obtain a MSE calibration in the manner described in Reference [12] and detailed here.

In this procedure, an Ohmic time period is included within the discharge, usually prior to the application of LHCD but several hundred milliseconds after the current flattop is established. The MSE system measures the pitch angles at this period, including the effects of birefringence on the polarization response. Equilibrium reconstructions are then performed at these time periods using kinetic and q-profile constraints but no pitch angle constraints. The calculated pitch angle from the reconstruction is then compared to the pitch angle measured with MSE. An offset for each MSE sightline is calculated such that the MSE agrees with the kinetic EFIT equilibrium reconstruction. This offset differs from discharge-to-discharge due to the changing birefringence. Then, at other time points in the discharge, the intra-shot calibrated MSE data is used as internal constraint and the q-profile constraints are removed. An example is shown in Figure 132.

This is a reasonable approach since the cause of the MSE diagnostic response is well known and characterized. The thermal stress-induced birefringence does not significantly affect the linearity of the diagnostic, but does affect the absolute polarization angle[5]. The thermal-stress-induced birefringence also changes on a slow timescale therefore the offset can be assumed to be stationary throughout the

5 The linearly it slightly affected due to birefringence as apparent in Equation 23. However, taking the derivative shows that > 0.07 waves of retardance would be required to change the slope by ten percent. This is more than typically observed.

discharge. In essence, the intra-shot calibration technique relies on the MSE system being a good measurement of the *change* in the current profile.

The intra-shot calibration technique requires an assumption about the Ohmic equilibrium that is used as the calibration reference for MSE. Constraints on the q-profile are used during these time periods similar to those used in an ANALYSIS EFIT. For most cases these constraints are $q_0 = 0.95$ and $q = 1$ at the saw-tooth inversion radius (as identified using the electron cyclotron diagnostic). Previous experiments in other tokamaks in Ohmic plasmas using absolutely calibrated MSE diagnostics and comparison to MHD mode localization show that q_0 is $\approx 0.9 - 0.95$ prior to the sawtooth crash and rises to $q_0 = 1$ after the crash [13–18]. The lack of a MSE constraint during these Ohmic calibration time periods does not allow the use of spline basis functions on C-MOD. Therefore second or third order polynomials are used, limiting the ability to flatten the central q-profile (and likewise flatten the central current density) precluding both of the q-constraints to be simultaneously achieved. They are given equal weighting which usually results in $0.8 < q_0 < 0.9$ and the $q = 1$ surface being inside of the measured sawtooth inversion radius[6]. This effect is dependent on the plasma current since this affects the location of the sawtooth inversion radius.

This technique leads to uncertainties due to the choice of the Ohmic time period—assumptions are "imprinted" on the MSE data. The value of q_0 and $q = 1$ location are under predicted by order 0.1 and $\frac{r}{a} \approx 0.05$, respectively due to the previously described effects. Due to the use of polynomials the q-profile during the Ohmic reference period is therefore not as flat in the core as would be expected. Thus the evolution of this profile using the MSE constraint will continue to have more positive magnetic shear than is likely in the physical situation. (Note: these errors are still significantly smaller than the use of ANALYSIS EFIT for all discharges without MSE where the internal q-profile and current density essentially go unmeasured.)

The use of an Ohmic time period to perform calibrations places severe constraints on discharge planning. The discharge must include several hundred milliseconds where the plasma kinetic profiles, shape and current is stationary. Time must be given to allow the current profile to diffuse throughout the radius, and the voltage "cross-over" in the magnet power supplies must be avoided. Typically physics scans are done with the same target plasma to avoid systematic errors in the the assumptions about the ohmic equilibrium. For these reasons the in-situ calibration system was developed to enable calibrations immediately before or after a discharge rather than within the discharge.

6 The ANALYSIS EFIT also usually results in the $q = 1$ surface being inside of the sawtooth inversion radius for the same reason.

B.3 VERIFICATION OF THE METHODOLOGY

The Ohmic reference time periods are designed into the discharge to provide approximately 100 to 200 milliseconds of quiescent plasma operation where the current profile is expected to be stationary. Two MSE time-points are typically used to obtain the offset. The offset is calculated separately for each time-point and is then averaged for each sightline, providing a check on the variability in the data. The offset is found to be stable within a discharge as expected. One approach to validating the diagnostic performance is to use MSE data to reconstruct equilibria at other Ohmic time points in a simple, quiescent plasma (i.e., constant magnetic field, current, shape, temperature, and density and no ICRF or LHCD). The measured equilibria should resemble the Ohmic-like profiles if the diagnostic and reconstruction processes are accurate. The addition of the MSE and pressure constraints should not "fight" the magnetics data—the total χ^2 from the magnetics should not increase significantly.

An example of using the technique to measure a stationary Ohmic plasma is shown in Figure 133. The MK-EFIT result matches the ANALYSIS EFIT result for the plasma current, volume, secondary seperatrix, and gaps. Inclusion of the pressure and MSE data only marginally increases the total χ^2 from the magnetic sensors, consistent with the addition of more constraints. This indicates that the inclusion of these extra internal constraints does not conflict with the information from the magnetic diagnostics. The resulting current profile for eight time slices is shownto be stationary across this discharge (right), as would be expected from the stationary pitch angle profiles measured by MSE. This, and other examples show that MK-EFIT does not have difficulty reconstructing Ohmic plasmas. The technique should therefore be able to accurately reconstruct the equilibrium in plasmas where the current profile is changing due to the application of LHCD.

The ability to measure changes in pitch angle once the calibration offset is applied is confirmed using plasma size scans and current scans. A MSE calibration plasma discharge is created (several times per campaign) where the size of the plasma is scanned from full size to very small while simultaneously scanning the current, in a manner similar to that developed on TFTR [19]. This scans the outer midplane of the plasma past the various MSE sightlines, creating a range of magnetic pitch angles. The pitch angle at the edge of the plasma is well known from magnetic sensors and can be used to judge the repeatability and linearity of the diagnostic.

An example of three such discharges is shown in Figure 134. The pitch angle from the MSE diagnostic is calibrated using the intra-shot technique to determine the offset for each sightline in each discharge. The three different discharges time histories (solid) agree with each

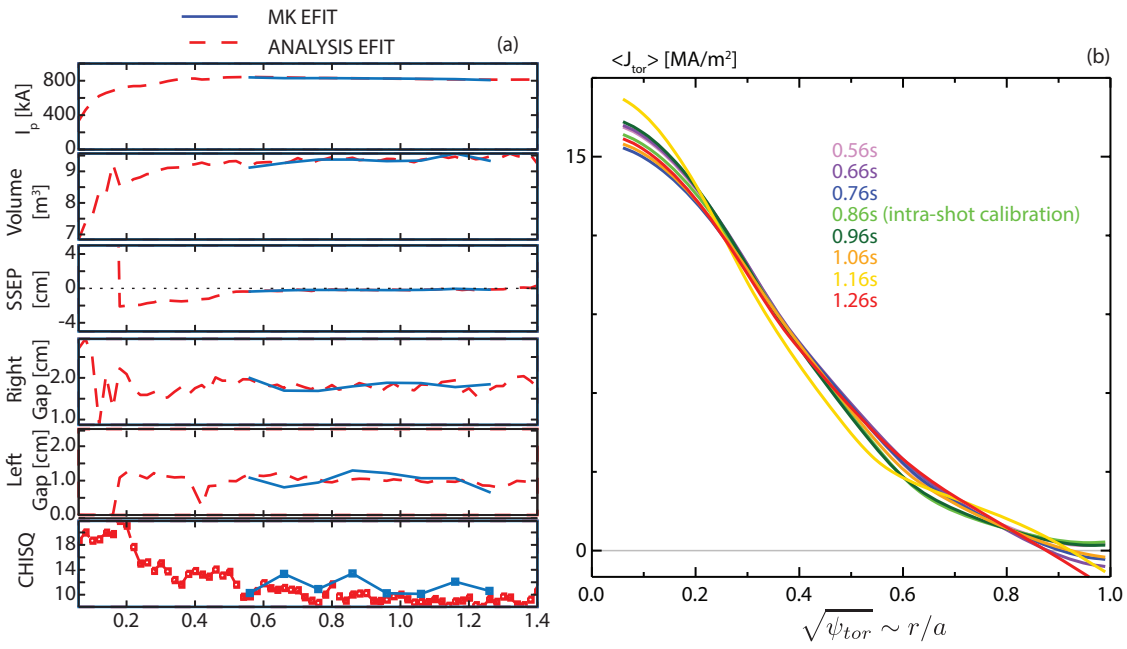

Figure 133: A stationary Ohmic discharge is reconstructed using MK-EFIT with intra-shot calibration of the MSE diagnostic (at 0.86s). The resulting equilibrium has the same macroscopic shape and current as that obtained from ANALYSIS EFIT with only slightly higher total χ^2 from the magnetics sensors (left). The current profile is stationary across all the time points as expected (right).

other and with the pitch angles from ANALYSIS EFIT (dashed) showing the diagnostic measures the proper dynamics and is repeatable.

A similar diagnostic check is performed using a current scan at fixed size. An example is shown in Figure 135. The pitch angle measured by MSE (solid) is compared to the pitch angle calculated from a kinetic EFIT (dashed) as a function of time, showing good agreement. The change in pitch angle measured by MSE can also be compared to the change in pitch angle calculated in the kinetic EFIT as shown in Figure 136. The fits show that the change in MSE pitch angle is nearly linear relative to the change in pitch angle from the kinetic EFIT, except near the core of the plasma where the pitch angle does not change significantly. (Note that kinetic EFIT have significant uncertainty, particularly deep into the plasma thus the deviation from linearity might not be significant). These checks give confidence that the reconstruction process using the intra-shot calibrated data can properly measure the current profile dynamics.

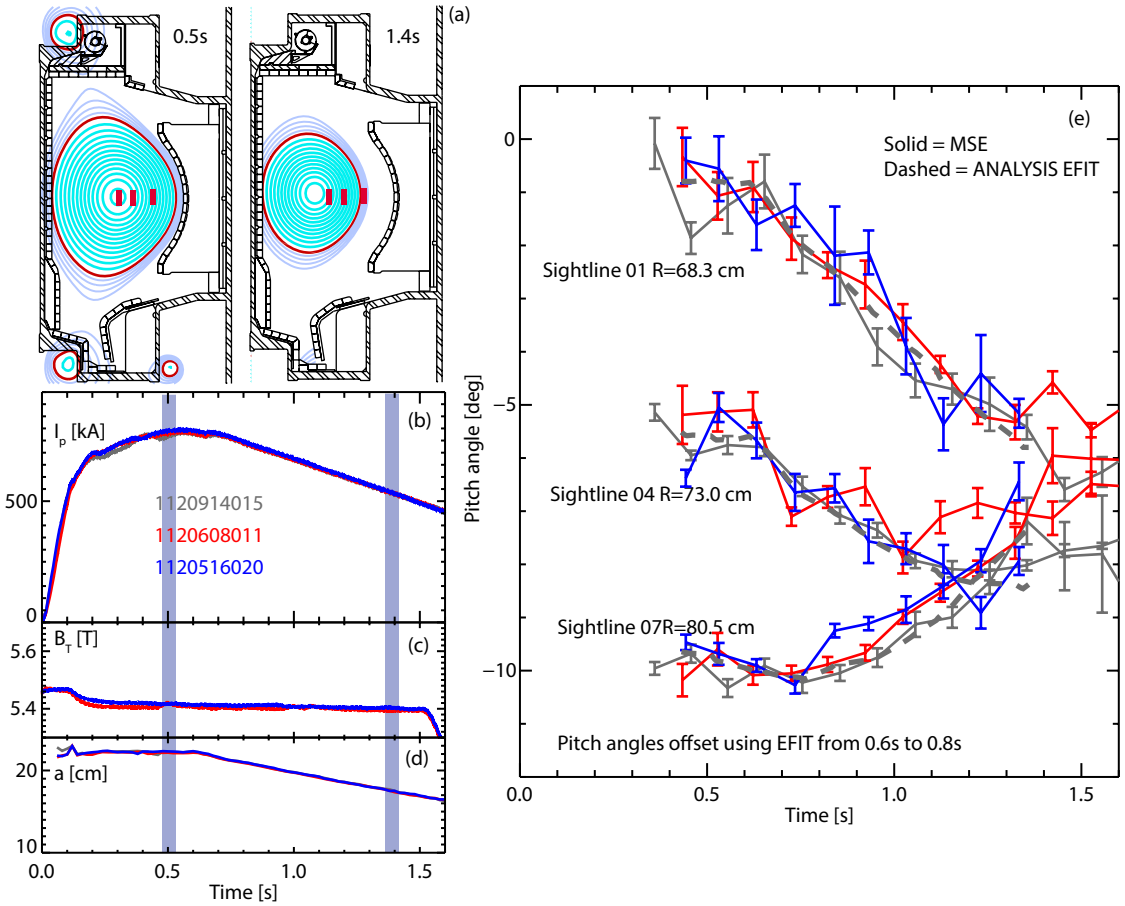

Figure 134: The plasma size is scanned (a), (d) at fixed field (c) and decreasing current (b) scanning the pitch angle at each MSE sightline viewing volume (e). The pitch angles inferred from MSE (solid) are intrashot calibrated and compared to pitch angles at that location in the plasma from ANALYSIS EFIT (dashed).

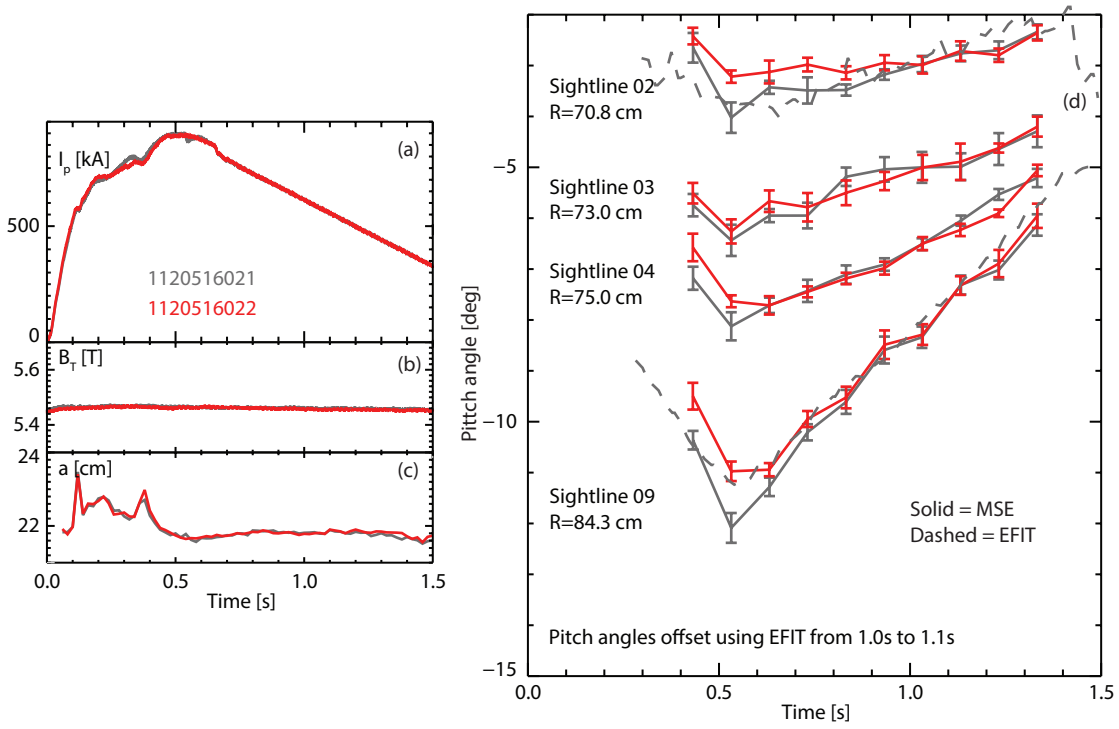

Figure 135: Plasma current scans are used to judge the reproducibility and linearity of the MSE system. The current (a) is scanned at fixed field (b) and size (c). The pitch angles measured by MSE (solid, intra-shot calibrated) are compared to the pitch angles calculated from kinetic EFIT (dashed) at each viewing volume location.

Figure 136: The change in pitch angle measured by MSE is compared to that computed from a kinetic EFIT during a current scan.

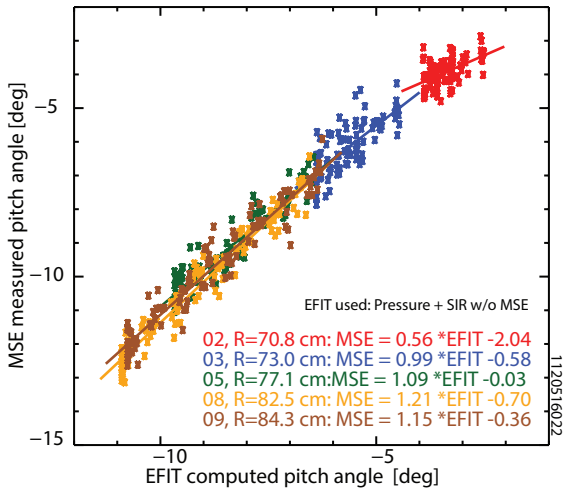

BIBLIOGRAPHY

[1] L. L. Lao, H. St John, R. D. Stambaugh, A. G. Kellman, and W. Pfeiffer. Reconstruction of current profile parameters and plasma shapes in tokamaks. *Nuclear Fusion*, 25(11):1611, November 1985.

[2] R. S. Granetz, I. H. Hutchinson, J. Gerolamo, W. Pina, and C. Tsui. Magnetic diagnostics in Alcator C-MOD. *Review of Scientific Instruments*, 61(10):2967–2969, October 1990.

[3] V. D. Pustovitov. Magnetic diagnostics: General principles and the problem of reconstruction of plasma current and pressure profiles in toroidal systems. *Nuclear Fusion*, 41(6):721, June 2001.

[4] Leonid E. Zakharov, Jerome Lewandowski, Elizabeth L. Foley, Fred M. Levinton, Howard Y. Yuh, Vladimir Drozdov, and D. C. McDonald. The theory of variances in equilibrium reconstruction. *Physics of Plasmas (1994-present)*, 15(9):092503, September 2008.

[5] F. S. Zaitsev, D. P. Kostomarov, E. P. Suchkov, V. V. Drozdov, E. R. Solano, A. Murari, S. Matejcik, N. C. Hawkes, and Jet-Efda Contributors. Analyses of substantially different plasma current densities and safety factors reconstructed from magnetic diagnostics data. *Nuclear Fusion*, 51(10):103044, October 2011.

[6] S.H Batha, F.M Levinton, S.P Hirshman, M.G Bell, and R.M Wieland. Sensitivity of equilibrium profile reconstruction to motional Stark effect measurements. *Nuclear Fusion*, 36(9):1133–1143, September 1996.

[7] M. Brix, N. C. Hawkes, A. Boboc, V. Drozdov, S. E. Sharapov, and JET-EFDA Contributors. Accuracy of EFIT equilibrium reconstruction with internal diagnostic information at JET. *Review of Scientific Instruments*, 79(10):10F325, 2008.

[8] M. Gelfusa, A. Murari, I. Lupelli, N. Hawkes, P. Gaudio, M. Baruzzo, M. Brix, T. Craciunescu, V. Drozdov, A. Meigs, E. Peluso, M. Romanelli, S. Schmuck, B. Sieglin, and Jet-Efda Contributors. Influence of plasma diagnostics and constraints on the quality of equilibrium reconstructions on Joint European Torus. *Review of Scientific Instruments*, 84(10):103508, October 2013.

[9] S. Shiraiwa, J. Ko, O. Meneghini, R. Parker, A. E. Schmidt, S. Scott, M. Greenwald, A. E. Hubbard, J. Hughes, Y. Ma, Y. Podpaly, J. E. Rice, G. Wallace, J. R. Wilson, S. M. Wolfe, and Alcator

C.-Mod Group. Full wave effects on the lower hybrid wave spectrum and driven current profile in tokamak plasmas. *Physics of Plasmas (1994-present)*, 18(8):080705, August 2011.

[10] S Shiraiwa. πScope : a python-based scientific work bench with MDSplus data visualization tool. *Fusion Engineering and Design*, To be submitted.

[11] J. W. Hughes, D. Mossessian, K. Zhurovich, M. DeMaria, K. Jensen, and A. Hubbard. Thomson scattering upgrades on Alcator C-Mod. *Review of Scientific Instruments*, 74(3):1667–1670, March 2003.

[12] J. Ko, S. Scott, S. Shiraiwa, M. Greenwald, R. Parker, and G. Wallace. Intrashot motional Stark effect calibration technique for lower hybrid current drive experiments. *Review of Scientific Instruments*, 81(3):033505, 2010.

[13] D. Wróblewski and R. T. Snider. Evidence of the complete magnetic reconnection during a sawtooth collapse in a tokamak. *Physical Review Letters*, 71(6):859–862, August 1993.

[14] B. W. Rice, D. G. Nilson, K. H. Burrell, and L. L. Lao. Simultaneous measurement of q and E_R profiles using the motional Stark effect in high-performance DIII-D plasmas (invited). *Review of Scientific Instruments*, 70(1):815, 1999.

[15] M. C. Zarnstorff, F. M. Levinton, S. H. Batha, and E. J. Synakowski. The effect of E_R on motional-Stark effect measurements of q, a new technique for measuring E_R, and a test of the neoclassical E_R. *Physics of Plasmas*, 4(4):1097, 1997.

[16] G. J. Kramer, T. Oikawa, T. Fujita, Y. Kamada, Y. Kusama, K. Tobita, T. Ozeki, C. Z. Cheng, and R. Nazikian. The determination of the q-profile in the plasma core from AlfvÃ©n eigenmodes. *Plasma Physics and Controlled Fusion*, 40(6):863, June 1998.

[17] E. A. Lazarus, T. C. Luce, M. E. Austin, D. P. Brennan, K. H. Burrell, M. S. Chu, J. R. Ferron, A. W. Hyatt, R. J. Jayakumar, L. L. Lao, J. Lohr, M. A. Makowski, T. H. Osborne, C. C. Petty, P. A. Politzer, R. Prater, T. L. Rhodes, J. T. Scoville, W. M. Solomon, E. J. Strait, A. D. Turnbull, F. L. Waelbroeck, and C. Zhang. Sawtooth oscillations in shaped plasmas. *Physics of Plasmas*, 14(5):055701, March 2007.

[18] R. De Angelis, F. Orsitto, M. Baruzzo, P. Buratti, B. Alper, L. Barrera, A. Botrugno, M. Brix, K. Crombe, L. Figini, et al. Determination of q profiles in JET by consistency of Motional Stark Effect and MHD mode localization. *EXS*, 2:03.

[19] F. M. Levinton, S. H. Batha, and M. C. Zarnstorff. Calibration of the upgraded motional Stark effect diagnostic on TFTR. *Review of Scientific Instruments*, 68(1):926, 1997.

C

ADDITIONAL CHECKS FOR SYSTEMATIC ERROR IN THE C-MOD MSE DIAGNOSTIC

A variety of physical phenomena and non-ideal component behavior can generate systematic errors in MSE diagnostics. Most—but not all—sources of imperfect behavior that remain constant in time (i.e., remain unchanged from the time the instrument is calibrated to the time it is actually used to measure the pitch angle profile in plasmas) and thus cause little net systematic error because the effects are fully captured by the calibration. More troublesome are behaviors that vary in time, e.g. due to environmental changes of temperature, because these cannot be compensated by a static calibration. The number of phenomena and non-ideal component behaviors that can compromise the measurement at that level is rather large.

Due to the observation of multiple-degree "drift" in the calibration of the C-MOD MSE diagnostic over a time scale of minutes, the issue of which of many potential sources of systematic error actually contribute to uncertainties in the measurement has received considerable attention over the past 12 years [1, 2]. A detailed study of the most credible concerns, including: non-ideal emission of the MSE spectrum; polarization aberrations in the optical system; and a non-ideal polarimeter response is presented in Chapter 3. The conclusion of that study is that the major cause of the observed C-MOD MSE time-varying diagnostic response is thermal stress birefringence in the lenses. This problem was largely resolved by calibrating the instrument within seconds of a plasma discharge and by stabilizing its thermal environment.

In addition to several important systematic error topics covered in the main text of the thesis, additional checks were performed on the MSE diagnostic operation and stability. These effects, the tests to investigate them, and the results are detailed in this appendix. These effects are all shown to be inconsequential to the diagnostic measurement.[1]

C.1 PERISCOPE MOVEMENT

The C-MOD MSE periscope is a large complex optical system—the optical path is over two meters long. This periscope is supported in three locations by the tokamak vacuum vessel: internally at the mid

1 Note that this work was carried out across multiple maintenance periods with corresponding changes in the periscope configuration, thus the polarization calibration coefficients may vary test-to-test.

point of the canister, internally, and externally at the F-port vacuum flange, and externally by the DNB duct near the PEMs. The periscope consists of many individual components that are bolted together—with shims—that can become misaligned due to disruption forces. The long path length means that any mis-alignment of the periscope components due to differential heating, stresses in the vacuum vessel, or mechanical slippage could change the location of the view. For instance, even a small change in angle of an internal mirror could move the view location by several centimeters or vignette the MSE sightlines. Previous comparisons of spatial calibrations taken prior to and after an experimental campaign showed that the MSE optical system shifted over the campaign. This creates three problems for performing reconstructions using MSE data. First, the radial location of the sightline-beam intersection may move, changing the viewing volume from that assumed in the reconstruction. Second, the mapping from polarization angle to magnetic pitch angle depends on the viewing geometry, and therefore may change. And third, the in-situ calibration system (ISC), which is supported by the periscope, relies on its mechanical orientation in absolute space being constant for proper interpretation—the mechanical movement of the periscope itself is one of the diagnostic changes that the ISC cannot detect.

The mounting mechanisms for the periscope were strengthened to alleviate these problems prior to the FY11 campaign. However, a technique that can accurately track changes in the periscope alignment throughout an experimental campaign, including between—or even within—plasma discharges was sought to determine if the problem remains. This technique should be capable of detecting small changes in the periscope alignment that would shift the viewing volume a few millimeters. Previous experiments on DIII-D used plasma edge sweeps to track the viewing geometry of beam-viewing diagnostics [3]. However, this is not a viable solution for C-MOD's MSE system for those viewing volumes well away from the plasma edge. Furthermore, this requires dedicated tokamak operation. Previous experiments on C-MOD used lasers attached to the PEMs and pointed at external structures to monitor the PEM orientation relative to gravity [2]. However, this method is not sensitive to changes in the view location caused by periscope displacement. A new system was therefore devised and implemented.

A new MSE fiber dissector was fabricated during the FY11 maintenance period using stereolithography (i.e., 3D printing). This fabrication technique led to lower cost, increased flexibility in the positioning of the MSE and BES fibers, and a more secure fiber holding mechanism. At this time two commercially available 5mm diameter laser diodes were incorporated into the dissector. These laser diodes are secured in the fiber dissector and shine red laser light through the MSE optical system and into the tokamak. A photo of the lasers

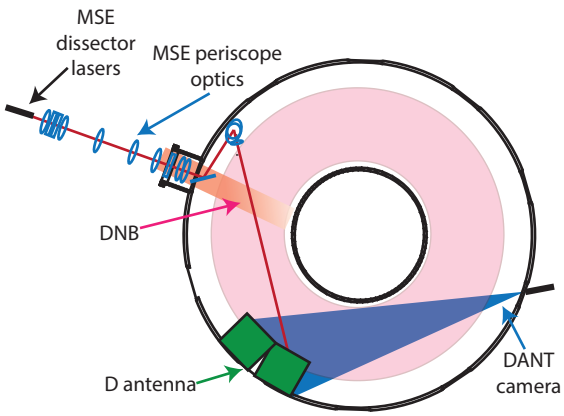

Figure 138: Schematic of the view-tracking laser. The laser, mounted in the MSE fiber dissector, shines through the MSE periscope and strikes the D-port ICRF antenna. The DANT camera is used to image the resulting spots.

mounted in the dissector is shown Figure 137. The two lasers shine through the entire MSE periscope and terminate on the ICRF antenna at D-port, opposite the MSE periscope. One laser strikes the antenna on the top limiting tiles and the other laser strikes the antenna on the lower limiting tiles. The location of the lasers was adjusted campaign-to-campaign by fabricating new fiber dissectors so that they would strike identifiable portions of the D antenna. A photo taken during a maintenance opening shows the lasers striking near the D antenna in Figure 139. Because the lasers and fibers are rigidly mounted in the dissector, any movement of the optical system which moves the view at the beamline would also change the laser trajectory, changing where the lasers strike the—presumably fixed—ICRF antenna. The path length from the MSE objective lens to the the D antenna is 3.2× longer than from the objective lens to the beamline. Therefore, any movement of the viewing volume at the beam would be magnified at the antenna by this factor. The plan view of the setup is shown in Figure 138.

Comparing where the lasers strike the antenna during sequential manned access periods can therefore very accurately monitor changes in the periscope orientation from the beginning to the end of the campaign—tracking changes in the viewing volume location to ~ 1mm. An example showing the laser strike point prior to and after the FY14 campaign is shown in Figure 139. Careful examination of the location of the laser strike points relative to the bolt holes (lower spot) and the Faraday rods (top spot) shows that the periscope did not move between the time these two photos were taken.

A method was also developed to track any view displacements during the campaign. A machine protection camera which views the D antenna is housed in a reentrant tube opposite the vessel from MSE periscope. This camera, known as DANT, is operational during every plasma discharge and can be triggered remotely between discharges. Unfortunately, the camera has a strong neutral density filter installed, and the lasers are much dimmer than the bright plasma, preventing the camera from detecting the laser spots during a discharge. How-

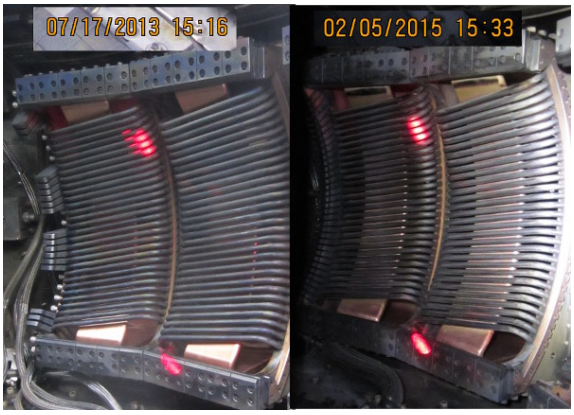

Figure 139: The laser-tracking system used to monitor if the MSE optics have changed alignment across a campaign. The lasers striking D antenna prior to (left) and after (right) the FY14 experimental campaign.

ever, the exposure length and camera sensitivity can be increased, enabling the camera to photograph the antenna between discharges (when supplied with some light such as ECDC or backlighting MSE). The lasers' strike points on the antenna can then be imaged—albeit with large noise—and changes in the strike point can then be determined between discharges.

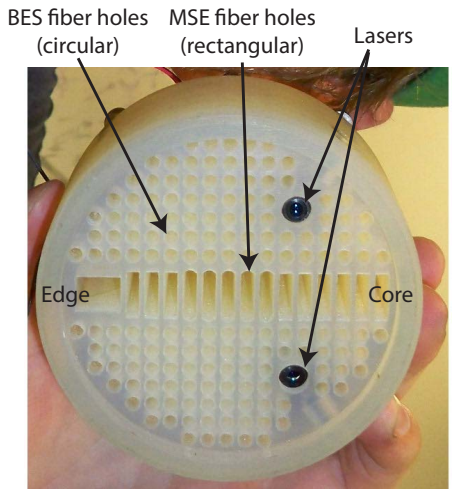

Figure 137: The 3D printed MSE fiber dissector with holes for the MSE and BES fibers and two view-tracking lasers.

The DANT camera is thereby used to monitor the strike points of the lasers on the D antenna (particularly the top laser, as the lower laser misses the antenna during the campaign of interest), detecting changes in the laser strike point across the campaign. Two images are taken to identify the laser spot on the antenna, one with the laser on and one with the laser off. The MSE sightline is backlit to illuminate the antenna structures. The two images are subtracted, enhancing the contribution from the laser. This process can include multiple images taken in succession and averaged to minimize detector noise. An example is shown in Figure 140, which also shows a photo taken using a standard camera from the location of the DANT camera during a maintenance period.

An algorithm was developed to track the location of the MSE view using these DANT images. First, it is determined whether the field of view of the DANT camera has shifted since the last test. This is done using the laser-off image and a spatially frequency-based image co-registration algorithm which compares a recent image to a reference image. The co-registration algorithm is accurate and insensitive of noise since the antenna is a very regular structure with many straight lines. Only image translation is considered. The co-registration algorithm was tested by shifting an image by a known number of pixels, cropping it and comparing it to the original. It was found the algorithm could determine the shifts at the

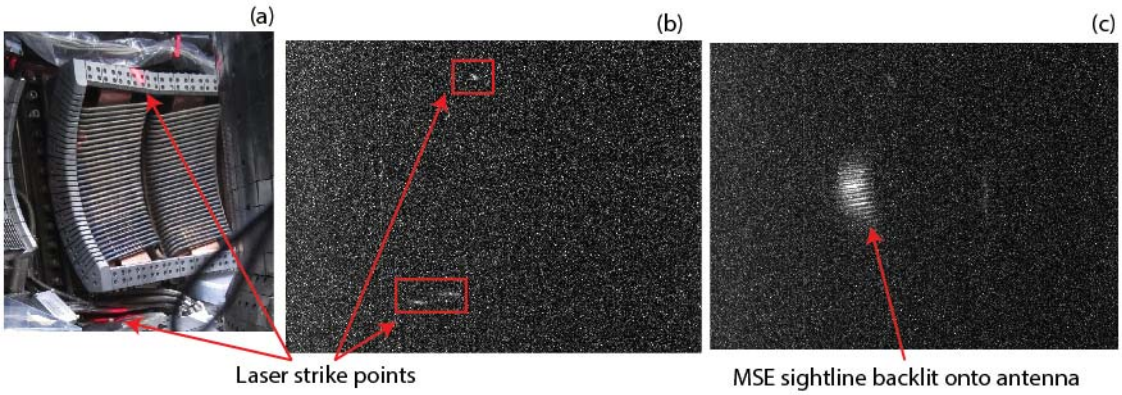

Figure 140: The laser strike points on the D antenna as viewed from the DANT location. Photo using a standard digital camera placed at the DANT periscope location (a). A photo from DANT during the campaign with the lasers on (b). A similar photo during the campaign with the lasers off and the core-most MSE sightline backlit onto the antenna (c).

sub-pixel level. A shift of the subtracted image is applied if it is found that the camera's field of view has moved since the start of the campaign, though that is rarely the case. The laser strike point center is determined by taking a centroid of an area of interest around the expected laser strike point, with a resulting uncertainty of $\sim \pm 1$ pixel. The pixel location of the laser centroid is then compared to the laser centroid at the beginning of the campaign. Any motion in pixel space is then translated to motion on the antenna in real space using the geometry of the antenna and the oblique viewing angle of the DANT camera. This motion on the antenna face is then transformed into angular motion of the sightline, assuming the MSE objective is fixed and misalignments only contribute angular errors. The translation of the viewing volume at the beamline is then calculated. The accuracy of the system is estimated at $\sim 0.5°$ in the sightline viewing direction.

The laser-tracking system was activated on five separate occasions during the FY12 experimental campaign to examine the stability of the MSE view during the campaign,[2]. It was determined that the field of view of the DANT camera did not shift across the campaign, eliminating this complication. The final results of the change in laser strike point location on the antenna are shown in Figure 141. It is apparent that the view did not move within uncertainty estimates across the campaign. This is consistent with measurements made at the beginning and end of the campaign, indicating the strengthened periscope mounts were effective.

In order to determine if the MSE periscope moves shot-to-shot, the laser-tracking system was activated during an experimental runday and images were taken between discharges. Images were also taken prior to the start of the experimental runday, after the end of the runday, and into the evening. The results are shown in Figure 142.

2 1120131, 1120206, (followed by a short manned access), 1120620, 1120913, 1121010

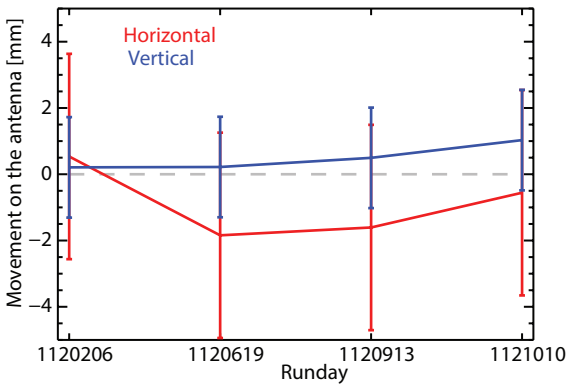

Figure 141: The movement of the laser strike points on the antenna measured by the laser-tracking system across a campaign.

The data shows that the view did not move within the uncertainty of this measurement, even though some of the discharges disrupted. Determining if the view moved within a shot is desirable, however, the lasers are much too dim to be viewed over plasma emission.

The laser-tracking system has been operational since the FY12 experimental campaign. All indications are that the MSE periscope does not move within the vessel despite its large size and complicated optics. This is certainly the case from the beginning of the campaign to the end of the campaign, during the campaign, and during a runday. Unfortunately, the technique cannot track view movements during a discharge, but the robust construction of the periscope and the results on the longer time-scales indicate the periscope is likely stationary.

Future experiments and other diagnostics may benefit from similar laser-tracking techniques to track and identify their viewing sightlines. The lasers can also aid in alignment since the relation between the laser and MSE sightlines is fixed by the dissector geometry. It may therefore be possible to quantify the MSE performance on a test stand and then transplant the entire diagnostic into the tokamak and use the lasers to determine its orientation in the vessel, in addition to tracking any changes over time. Such a technique may be useful for large next-generation tokamaks such as ITER, which will require diagnostic validation and calibration prior to installation. These machines will also have limited access to monitor the diagnostic performance, but will have comprehensive machine-protection camera coverage.

C.2 SPECTRAL CALIBRATION

The location of the filter bandpass relative to the motional Stark spectrum is important to maximize signal and to avoid systematic errors from 3D emission effects discussed in Chapter 3. Careful measurement of the filter bandpasses and verification of the view geometry is therefore required. The ISC cannot capture these errors.

The spectral passbands of the optical filters for the MSE diagnostic on C-MOD were chosen to view the $\pi+$ multiplet from the full-energy beam component. This is because the full-energy σ multiplet is con-

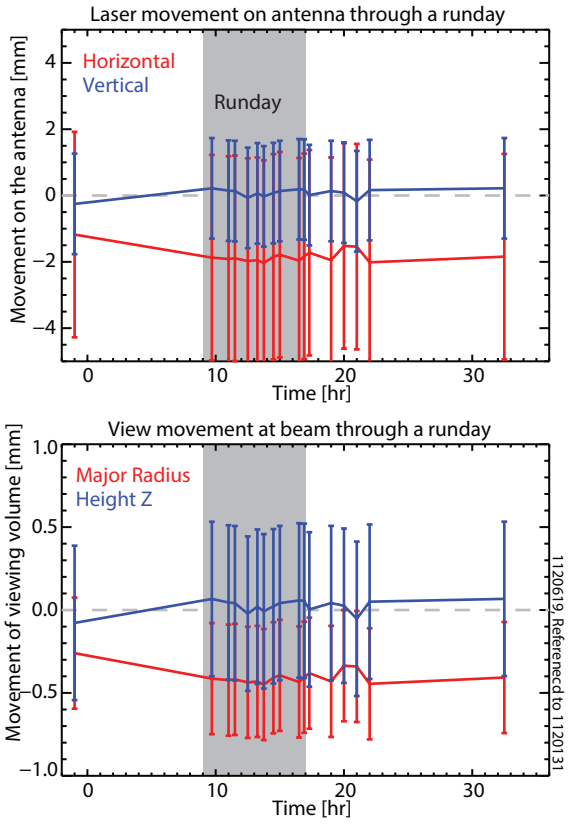

Figure 142: The change in laser spot location across a runday (top). The corresponding change in the MSE viewing volume location (b). The runday is indicated by the gray shaded region.

taminated by emission from half-energy and third-energy π components for some sightlines. The optimal spectral location of the narrow bandpass filters therefore depends on both the beam energy and the magnetic field strength at the location of the MSE viewing volume via the Doppler shift and Stark split, respectively. Proper positioning of the filter bandpass over the π emission is important, and the optimum passband wavelength changes when the strength of the toroidal magnetic field is changed. To accommodate this requirement, the filters are held in thermal ovens that collimate the light from a MSE sightline fiber bundle and allow the filter passband to be temperature tuned from room temperature to 60 °C.

Due to the large étendue of each C-MOD MSE sightline, the ovens are designed so that the the 50mm diameter filter is almost fully illuminated. Even so, the light from the fiber bundle is still incident on the filter with a cone angle of $\sim 5°$. This range of incident angles slightly widens the filter passband, shifts the center to the blue, and decreases the maximum transmission relative to the manufacturer measurements, which were performed only on the center of the filter with highly collimated light. The filter passbands were therefore measured in-situ to determine the extent of these effects, to obtain an effective passband for tuning purposes, and to determine the temperature tuning coefficients.

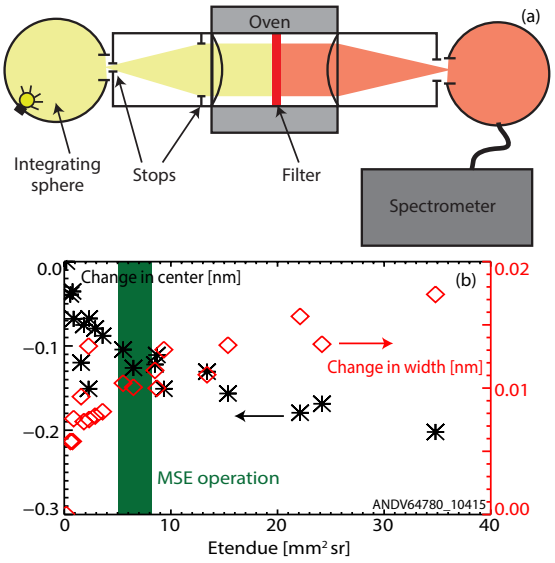

Figure 143: Measurement of filter spectral response. The filters were illuminated with variable étendue using a field and aperture stop on the collimating optics (a). The bandpass was measured using a high resolution spectrometer after collecting the light with an integrating sphere (b). As the étendue is increased, the filter center (*) and filter width (◇) experience a systematic shift to the blue and a widening of the passband respectively.

The filter in the oven was illuminated using variable-sized field and aperture stops. The light that passed through the filter that was collected by an integrating sphere which was connected by a fiber to a high resolution spectrometer [4]. As expected, the filter bandpass has a slight dependence on the illumination configuration, as shown in Figure 143. When illuminated with the same illumination pattern as the MSE system, the filter bandpass centers varied by as much as 0.2nm from those reported by the manufacturer. All the filters were then measured under illumination conditions identical to that from the MSE system.

The oven was commanded to an elevated temperature and the filter bandpass was measured over a period of hours while the heat diffused into the filter to determine the effect of filter heating. In steady-state, the filter passbands shifted to the red when heated with a coefficient of 0.018 ± 0.001 nm/°C. A dynamic heating test was then used to determine that a delay of four minutes is required for the filter to equilibrate to the measured oven temperature, providing confidence that MSE can change filter settings between C-MOD plasma discharges (~ 15 min). The results are shown in Figure 144.

The measured filter responses are integrated into software that controls the filter ovens to account for the Stark split and Doppler shift using the geometric calibration, the local toroidal magnetic field, and the applied beam acceleration voltage. The beam voltage is confirmed using Doppler spectroscopy inside the neutral beam tank. The entire spectral system has been verified by performing beam-into-gas experiments with no field (and thus no Stark split) in which the filter temperature is changed on successive shots to move the passband across the Doppler shifted beam emission. The peak in the measured emission was in good agreement with calculations.

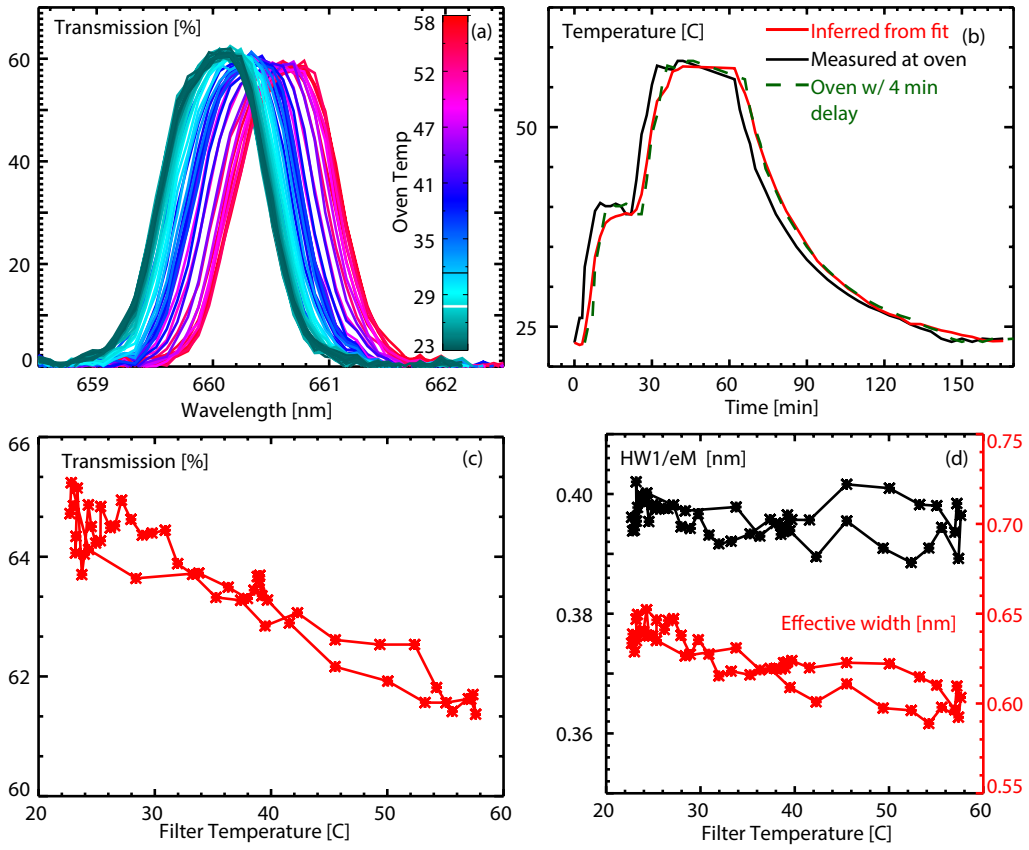

Figure 144: Measurement of the temperature response of the filters. The MSE filters were heated dynamically in their ovens while their bandpass was measured with a spectrometer (a). The filter temperature was inferred by Gaussian fitting the measurement of the bandpass and previously determined temperature tuning coefficients (solid). The filter temperature lags the oven temperature (dotted) by four minutes (dashed) (b). In addition to shifting the filter bandpass to the red, heating also slightly decreases the maximum transmission (c) and the total integrated transmission (i.e., effective width) but does not change the full width half max (d).

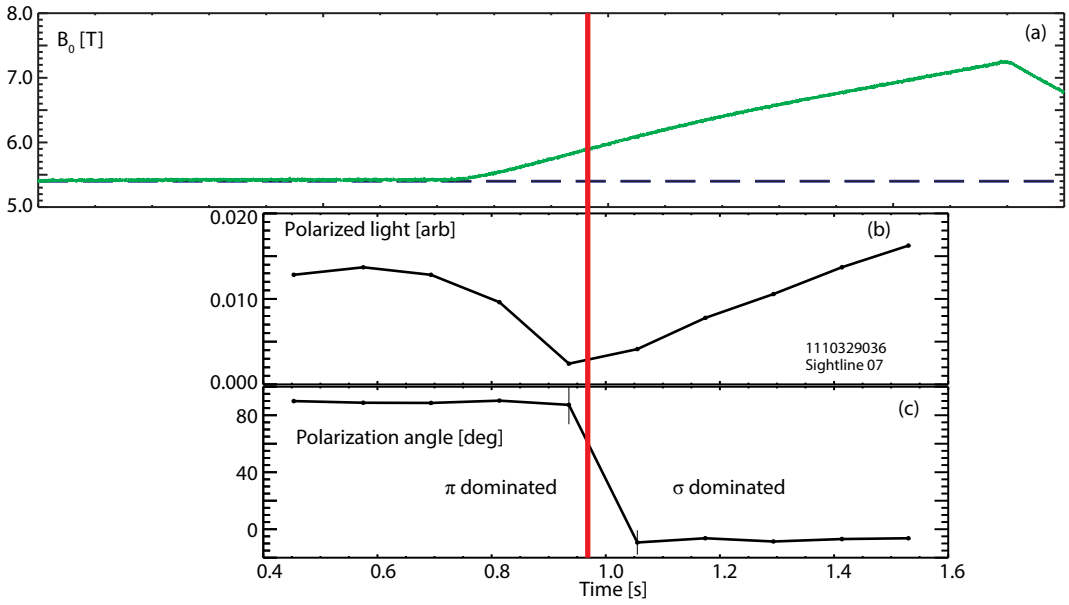

Figure 145: The tokamak magnetic field is scanned by several Tesla (a). Filters are selected to be in the spectral region between MSE σ and MSE π for each MSE sightline. During the B field scan, the changing Stark split moves the beam spectrum relative to the filter passband. The net collected signal transitions from π dominated at low field to σ dominated at high field. This results in the collected net polarized intensity reaching a minimum (b) and the polarization angle changing by 90° (c) as the transition is made. The field magnitude at the minimum in polarized light and the switch in polarization angle is a very sensitive marker of the position of the filter passband relative to the beam spectrum.

The filter overlap with the beam emission was further checked using magnetic field sweeps during plasma discharges. Modifying the Stark shift by changing the field strength changes the ratio of the MSE σ and π emission collected from a fixed filter bandpass positioned between these two components. The magnitude of the magnetic field where equal amounts of σ and π are collected produces a net polarization of approximately zero. The polarization angle switches by 90° on each side of this point as one component dominates the other orthogonal component. This behavior acts as a very precise marker of the filter and beam spectral overlap since the minimum polarized intensity and the change in angle can be identified easily. Filters were selected and installed with bandpasses in the area of the spectrum where σ and π emission overlap. The tokamak magnetic field was then scanned within a discharge while firing the beam into the plasma at fixed beam energy. The results for a MSE sightline are shown in Figure 145.

It is estimated that this approach can locate the spectrum of the beam relative to the filter passband to an accuracy of ~ 0.05nm. These tests found that small < 0.4nm shifts in the manufacturer-specified filter center wavelengths were needed to obtain agreement with simulated diagnostic data. It is unknown if this shift is due to the same filter shifts that were found when comparing the filter passbands measured in-situ to the passbands measured by the manufacturer, due to

an error in the assumed viewing geometry, or due to a difference in the ratio of σ to π emission from the statistical assumption.

These filter tests confirm the proper operation of the filters and give high confidence that the MSE system is both filtering the correct spectral components from the beam and viewing the beam with the correct geometry, minimizing the potential for errors.

C.3 PERISCOPE VIGNETTING

The ALCATOR C-MOD MSE system is designed so that the objective lens (L1) acts as the aperture stop, although other downstream components are almost fully filled. Any misalignment in the large optical periscope could lead to significant vignetting of the MSE sightlines. Previous experiments indicated that this might have occurred in previous campaigns [2]. In addition to investigating the alignment of the MSE optical periscope, the vignetting data can be input into MSE simulation models of the polarized light collection [5], where the extent of the pupil is important because it influences the calculated aperture broadening of the Stark multiplet.

The laser source on the robotic calibration's polarization generation head allows the throughput of the complicated optical system to be tested extensively. The methodology is shown in Figure 146. The positioning system shines a polarized laser through the periscope from a fixed point in space. The laser is aimed at different parts of the objective lens, simulating different rays through the optical system. The rays traverse the optical periscope and are detected by a photodiode positioned at the fiber dissector plane in place of the optical fibers. The highly accurate positioning system allows the collection solid angle to be densely sampled with a transmission measurement at each point. This can then be repeated at different viewing volume locations. Using this system, slight vignetting ($\sim$ 15%) is observed on one side of the aperture across all field points, presumably due to a misalignment in the optical components. The ability to measure the vignetting of the periscope is enabled by the same methodology used to perform polarized ray tracing through the periscope, as discussed in Chapter 3.

The transmission of the entire optical system can also be measured from the viewing volume, through the periscope, through the fiber optics, through the filter ovens, and to the MSE APDs in the same way. In this case, the test ray follows the entire path of a ray from the DNB during tokamak operation. This measurement results in a system transmission factor of $\sim$ 0.45 (note that the PEM-based polarimeter's linear polarizer was removed for this test), a value that is consistent with multiplying the individually-measured transmission and reflection coefficients of the 19 optical elements in the optical system [2].

This entire system ray trace confirms that the fibers used for transport to the diagnostic hall are under-filled by the optical periscope

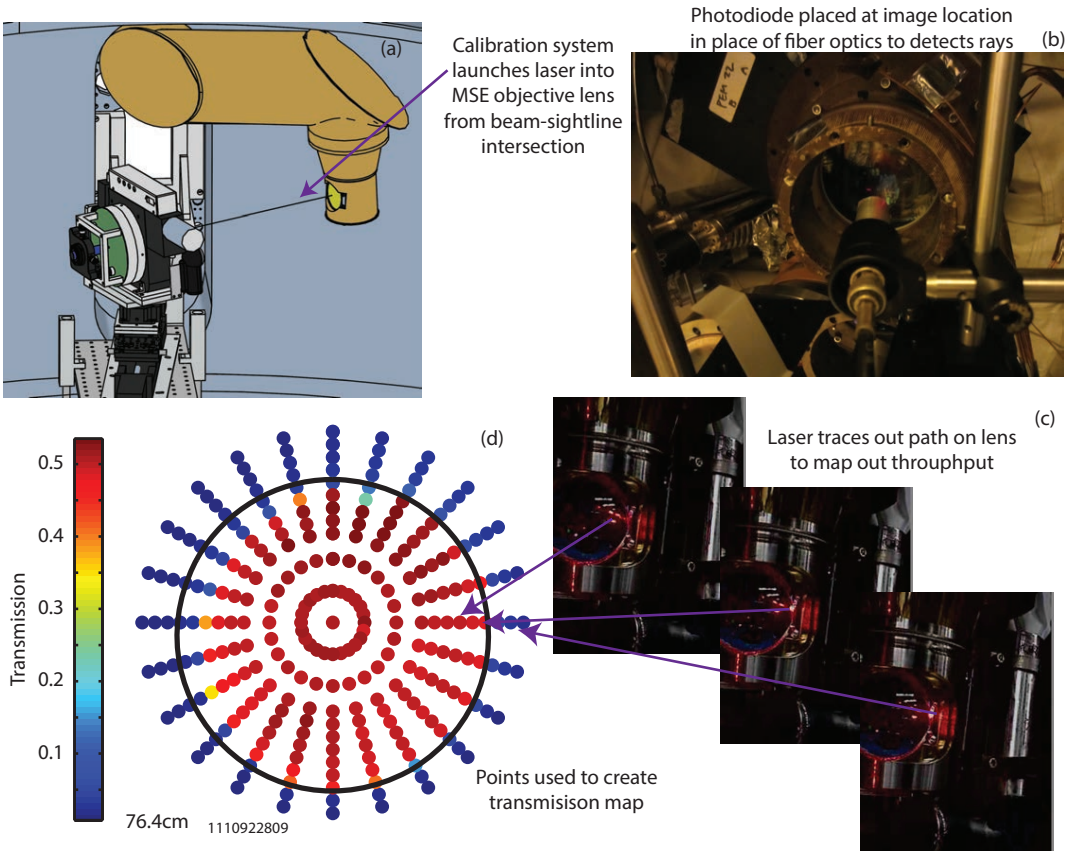

Figure 146: The ray-tracing methodology to test for periscope vignetting. The robotic calibration system shines the laser source from the viewing volume at the beam line through the MSE objective lens (a). The laser is then detected at the image point where a photodiode is placed, replacing the fiber dissector (b). The laser then traces out various points on the lens very precisely (c), making a map of the transmission through the optical system (d). This can be repeated with the photodiode positioned at the fiber exit or at the exit of the filter ovens or polychromator exit ports.

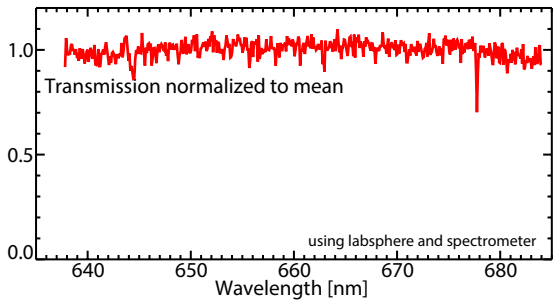

Figure 147: The spectral transmission of the MSE periscope was measured using an integrating sphere with a tungsten lamp and high resolution spectrometer.

and are not acting as the limiting aperture stop. Further tests show that the fiber transmission has not be significantly deteriorated due to neutron or x-ray damage. These tests confirm that the optical system properly collects and transports the light from inside the tokamak to the remote detectors.

C.4 MSE THROUGHPUT

In addition to using the laser source on the polarization generation head to measure the vignetting of the MSE optical periscope, Lambertian sources were mounted on the robotic calibration positioning system and placed at the viewing volumes of the MSE sightlines. The most reliable method involves using a high-power bright red LED (centered at 660nm with 20nm FWHM) mounted onto an integrating sphere to produce a Lambertian output. This source has a sufficiently narrow spectrum to fit entirely within the bandpass of the MSE optics. The brightness of the source is calibrated using a photodiode with a set of apertures (and thus a known étendue). The source is then placed at the beamline, and the light intensity at the APD end of the fibers is measured with the same photodiode. The ratio of the two photodiode measurements and the geometry of the two calibration apertures then gives the total throughout (étendue $\times$ transmission) of the MSE sightline. This test allows the MSE system to be absolutely calibrated for use in measurements of visible bremsstrahlung and runaway electrons.

C.5 PERISCOPE SPECTRAL TRANSMISSION

In addition to measuring the throughput of the MSE optical system at the MSE wavelengths, the transmission of the optical periscope was measured in a wider wavelength range. An integrating sphere with a white tungsten lamp was placed at the MSE viewing volume and a high resolution spectrometer was coupled to the output of the MSE fibers. The results of this experiment are shown in Figure 147. This data confirms that the MSE mirrors perform correctly. The mirrors can

pass light in a sufficiently broad spectral range so that measurements at off-MSE wavelengths are feasible within 20nm of the MSE emission.

C.6 CREATION OF SPURIOUS POLARIZED LIGHT IN THE PERISCOPE

The creation of spurious polarized light from unpolarized light via internal scattering could contaminate the beam-generated signal. This would be especially problematic in situations where even a small fraction of the intense unpolarized light is converted to polarized light. To test for this effect, an integrating sphere is placed in front of the objective lens with the MSE PEMs operating and the linear polarizer in place on the polarimeter. High-quality integrating spheres produce light that is > 99.5 percent unpolarized [6]. Non-zero measured polarization fractions above this level would indicate that either the periscope creates polarized light from unpolarized light or that the PEM-based encoding and decoding technique incorrectly assigns polarization to unpolarized light. The ISC would not account for creation of polarized light inside the periscope from unpolarized plasma emission.

In this configuration, the MSE PEM-based polarimeter measures polarization fractions < 0.2 percent for sightlines on the optical axis and < 1 percent for sightlines at the edges of the field. This indicates that unpolarized light entering the diagnostic is not significantly polarized upon transiting the optical periscope and polarimeter system. However, operation at total unpolarized plasma emission to polarized beam emission ratios higher than ~ 50 may be problematic since it could lead to polarized-signal-to-polarized-background rations (SB) below ten. The unpolarized light would become polarized inside the diagnostic at a sufficiently large enough level to hamper diagnostic operation. This light would be compensated for, to an extent, by the wavelength-interpolation background subtraction technique.

C.7 PERISCOPE POLARIZATION TRANSMISSION

One way unpolarized light can become polarized is due to non-equal s-p reflection ratios in the mirrors (i.e., diattenuation). The MSE mirrors are highly optimized, but not ideal[3], and therefore a small difference in polarization transmission should be expected with mirrors preferentially reflecting specific input polarizations.

The MSE optics are shared with the beam emission spectroscopy (BES) diagnostic system which uses APDs and spectrometers to measure the intensity of the Stark components as part of the development of the $\vec{B}$-stark and MSE-LR techniques. Because the different Stark multiplets are polarized orthogonally, it is necessary to know the transmission dependence of the periscope as a function of polarization

3 The specified performance is a s-p reflection ratio of 1.00 ± 0.01 with reflectivity > 0.99 in the operating range of $658 - 664$nm and over an angle of incidence $30 - 60^{\circ}$.

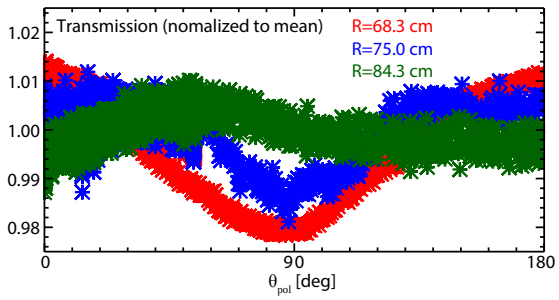

Figure 148: The transmission of the MSE optical system as a function of input polarization angle for three different MSE sightlines.

angle to accurately interpret the spectral measurements. This is not an important effect for the MSE-LP system.

To quantify the transmission as a function of input polarization, the Lambertian LED-based polarized light source is kept at a fixed position while the linear polarizer is free to rotate on the polarization generation head. This configuration eliminates any change in intensity due to the light source rotating. The assembly is positioned at the location of the MSE viewing volume, the PEMs are disabled, and the polarimeter linear polarizer is removed (often the PEMs are turned off and the polarimeter linear polarizer is removed to enable a higher photon throughput during the $\vec{B}$-stark and MSE-LR measurements). The polarizer is then rotated to different angles and the light detected by the MSE APDs is recorded at each input polarization angle.

The results are shown in Figure 148, which plots the measured transmission at different input polarization angles. There is a slight $\cos(2\theta_{pol})$ dependence apparent in the transmission. These tests show there is a ~ 1 percent transmission dependence on the incident polarization angle, with the edges of the field of view having the largest effect. This is consistent with diattenuation causing the previously discussed < 1 percent spurious polarization from unpolarized light. This transmission effect has been integrated into the spectral fitting codes used for interpreting the $\vec{B}$-stark and MSE-LR measurements.

C.8 DEPOLARIZATION BY THE PERISCOPE

The optical periscope can also depolarize the light and therefore decrease signal levels and lead to improper measurement of the polarization fraction from the beam, but this effect would not likely affect the measured polarization angle.

The depolarization imposed by the MSE optical system is measured by illuminating it with constant-intensity, 99 percent linearly polarized light from the Lambertian source on the calibration generation head while the PEMs are turned off and the polarimeter's linear polarizer remains installed. The light intensity at the detectors is measured as the polarization generation head's linear polarizer is rotated.

If the optical system converts polarized light from the polarization source to unpolarized light or circular polarized light, the detected

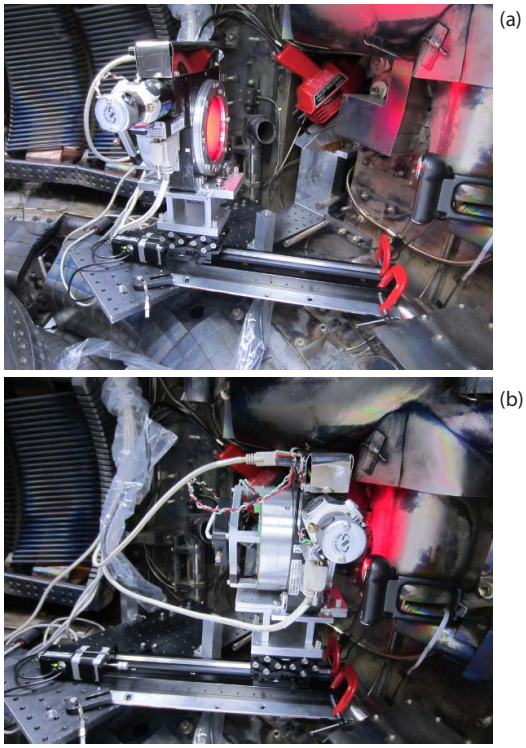

Figure 149: The solid angle filled by the calibration source was varied to test for effects from scattered light inside the optical system. Calibrations were taken with the polarization generation head in its nominal position at the beamline viewing volume (a) and successively closer to the objective lens (b), changing the solid angle filled by the calibration source.

light should have a $\cos^2(\theta_{pol})$ with a DC offset dependence. The magnitude of the DC offset will directly reflect the depolarization in the system. We measure this offset to be at the calibration resolution of ~ 1 percent indicating that the optical train does not depolarize linearly polarized light or convert it to circularly polarized light in its nominal operating configuration beyond this level, despite having many optical elements.

These and the preceding tests of the optical system indicate it is operating very close to ideally and that the mirrors are likely within the specified tolerances on the s-p reflection ratio.

C.9 LIGHT SCATTERING INSIDE THE PERISCOPE

Light can scatter from inside the periscope, change its polarization, and contaminate the light seen directly. The inside of the periscope is blackened, the lenses are anti-reflection coated, and the mounts for the optics are designed to prevent scattering and minimize this effect. This effect would be captured by the ISC since it illuminates the diagnostic with a large solid angle.

Problems due to scattered light inside the periscope were evaluated by varying the solid angle of the calibration source as viewed from the objective lens. The system performance was evaluated by illuminating the MSE diagnostic objective lens in three different configurations. In the first configuration, the calibration light source was positioned at the intersection of an MSE sightline and the beam tra-

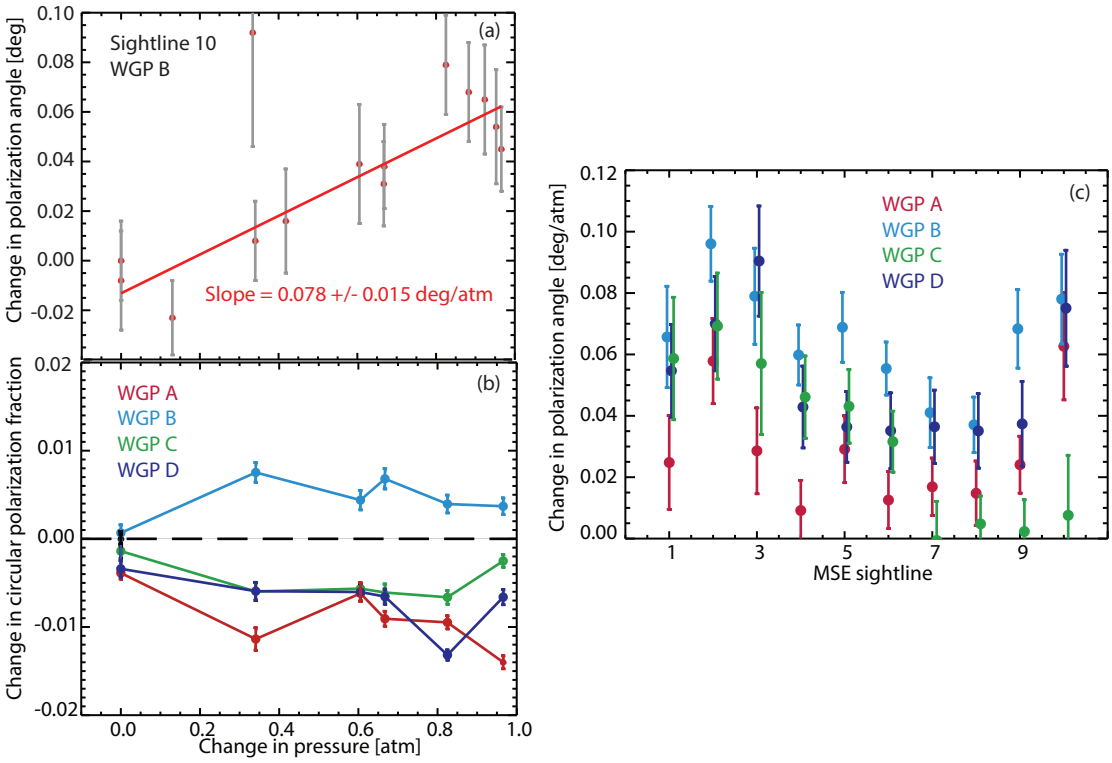

Figure 150: The change in polarization angle from the ISC is measured during a vacuum vessel pump down (a). The measurement also shows an increase in the circular polarization fraction with a dependence that is indicative of birefringence. A linear fit is performed on the change in angle vs. change in vacuum pressure and shown as a function of ISC input angle and MSE sightline (c).

jectory. In the second configuration the light source was positioned immediately in front of the objective lens, which fills the lens with a much larger solid angle of light that can potentially be scattered into the detection system. The third configuration placed the light source at an intermediary position. The test is illustrated in Figure 149. If scattering was important, it would manifest itself in a change in the polarization calibration between these configurations. It was found that there was not a significant effect.

C.10 VACUUM WINDOW STRESS FROM PUMP-DOWN

The differential vacuum causes stress in the vacuum window. To test for this effect, the ISC system was used to illuminate the MSE diagnostic with linearly polarized light of known polarization angle while the vessel was slowly pumped down to operational vacuum. All four angles on the ISC system were used to look for changes that might indicate stress-induced birefringence.

Figure 150 shows the results of the test. The polarization angle measured from the ISC changes as the vacuum vessel is pumped down (a). There is also a small increase in magnitude of the measured circular polarization fraction with a dependence on ISC angle that is consistent

with an increase in stress-induced birefringence (b). A linear dependence on the change in angle versus the change in pressure is then fit to each MSE sightline and ISC angle (c). There is a systematic dependence of the change in polarization angle as a function of vacuum window pressure with the central sightlines having a smaller dependence. This effect is at the level of $< 0.1°$ and can be compensated for by the ISC.

C.11 THERMAL STRESS IN THE PLASMA-FACING LENS

The MSE periscope is thermally controlled using an active system on the external periscope and passive systems on the internal periscope. However, the objective lens (L1) is exposed to the bright plasma emission (to collect it). This lens is thereby subject to significant radiative heat flux of $> 100^{kW/m^2}$ for $\sim$ 1.5s every 15 minutes. This flash heating could create thermal-stresses in the lens and subsequent thermal stress birefringence. However, this is not a large concern since the thermal timescale of the lens is long compared to the duration of the plasma.

An experiment was conducted to observe very plasmas with high radiated power to test for this effect. The ISC system was quickly moved in front of the objective lens immediately after the end of the discharge, coming to rest by $t = 2s$. The evolution of the polarization response was then tracked for the next 9.5s to monitor any changes. This was repeated in plasmas with different radiated energies, as measured by the 2π bolometer, and therefore presumably different flashing heating of the objective lens.

The results of the experiment are shown in Figure 151. The polarization angle does not change due to plasma heating of the first lens—there is no difference in polarization angle between high radiated energy shots and fizzles with no radiated energy (a). However, the circular polarization fraction DOCP changes over the digitization time window and changes at a higher rate with a higher radiated energy (b). The change in the DOCP immediately following the discharge to the end of the time window is found to have a linear dependence on the radiated energy during the discharge (c), and the slope of this dependence is shown to be a smooth function of the MSE sightline (d).

The thermal stress-induced birefringence in the plasma-facing lens thus does not affect the C-MOD MSE diagnostic except for slowly changing circular polarization fractions at the level of a few percent. If the polarization angle was found to change slowly after the discharge, the ISC calibration period could be moved into position prior to the discharge to eliminate this effect. The importance of this effect depends on the thermal time constant of the objective element relative to the length of the discharge and the radiated energy flux. Thus long pulse machines with high power density may encounter this prob-

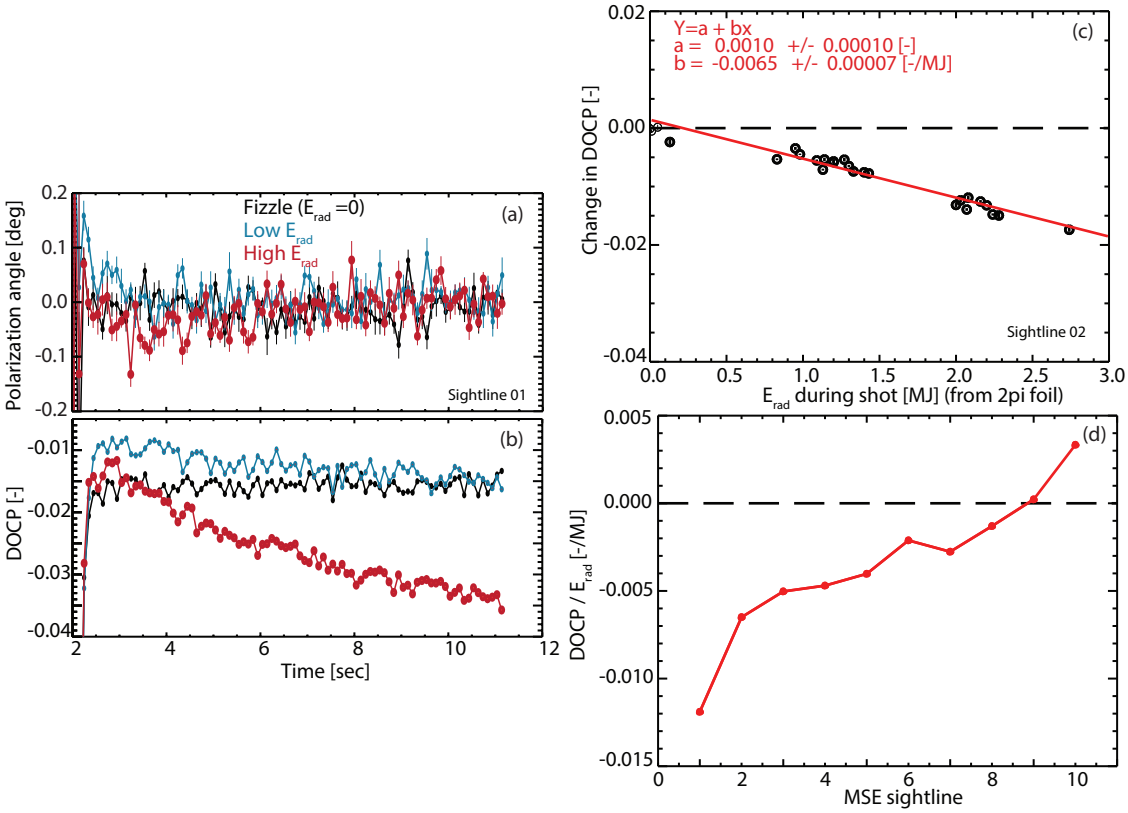

Figure 151: The ISC system is quickly moved in front of the diagnostic objective lens immediately after a discharge to measure changes in polarization angle (a) and circular polarization fraction, CPF, (b). There are either no changes or small changes in discharges with little radiated energy, E_{rad} (black and blue), and larger changes with higher radiated energy (red). The change in CPF is a function of E_{rad} (c). The slope of this effect has a smooth dependence on MSE sightline (d).

Table 12: Calibrating a sightline with different narrow bandpass filters shows the calibration is wavelength independent across the range of wavelengths typically observed by the MSE system.

Wavelength nm	Bandpass nm	B_0 deg	B_4 deg	B_{4p} deg	B_2 deg	B_{2p} deg
657.99	0.85	-62.67	0.41	217	0.04	30
660.25	0.94	-62.68	0.43	217	0.04	31
662.76	1.19	-62.68	0.45	216	0.04	30

lem in the future. To compensate for this problem, the ISC could be quickly actuated the ISC at regular intervals during the plasma discharge to update the calibration. Mirrors do not have thermal birefringence problems. However, they do have erosion and deposition problems as discussed previously.

C.12 POLARIZATION RESPONSE WAVELENGTH DEPENDENCE

The dielectric-coated mirrors in the MSE optical periscope are highly optimized for polarization preservation in the narrow spectral region observed by the diagnostic. However, the phase shifts and s-p reflection ratio are wavelength dependent due to the use of thin films for the coatings. As discussed previously, during routine operation of the C-MOD diagnostic, the bandpass of the spectral filters is varied by adjusting the filter-oven temperature to account for changes in beam energy and/or the tokamak magnetic field. The filter bandpass can also be adjusted to allow the diagnostic to look at the σ multiplet instead of the π multiplet. Furthermore, the MSE-MSLP technique requires multiplexing polarization measurements at different wavelengths.

It is therefore necessary to account for any calibration variations as a function of wavelength for each sightline. Calibrations were repeated on the same sightline using different narrow bandpass filters spanning the entire observed spectral range to determine the calibration sensitivity to wavelength. The result was fit to the standard calibration form. As shown in Table 12, the calibration is wavelength independent across the tested range at the level of 0.02°.

C.13 POLARIZATION RESPONSE INTENSITY DEPENDENCE

The intensity of the linearly polarized light was varied by changing the current supplied to the LED-based Lambertian polarized source. Calibration cycles were then conducted at different intensities and the result was fit to the standard calibration form. As shown in Table 13, the calibration varies $< 0.02°$ as the intensity is varied across a factor of 30. This encompasses the range of intensities observed from the beam and plasma. When the light intensity was reduced yet an-

Table 13: The intensity was varied over a of factor of 30 without any impact on the measured calibration coefficients. *Lowest intensity excluded from statistical calculations.

	Polarization calibration fit coefficients					
Intensity	B_0	B_4	B_{4p}	B_2	B_{2p}	residual
ph/s	deg	deg	deg	deg	deg	deg
9.8×10^9	27.356	0.241	229	0.054	236	0.027
6.8×10^9	27.364	0.243	229	0.064	232	0.022
3.1×10^9	27.361	0.239	231	0.063	236	0.024
1.8×10^9	27.361	0.235	232	0.065	225	0.022
6.8×10^8	27.360	0.247	234	0.043	243	0.043
2.9×10^8	27.366	0.208	237	0.056	250	0.056
$5.1 \times 10^{7*}$	27.260	0.264	209	0.183	375	0.194
STDEV	0.003	0.014	3	0.008	9	
MAX-MIN	0.009	0.056	8	0.140	25	

other factor of three (i.e., a factor of three below that typically realized during routine diagnostic operation), the calibration does not deviate more than the fit residual, which is representative of the statistical error in the measurement points.

C.14 POLARIZATION RESPONSE APD DEPENDENCE

The APDs used as light detectors in the system amplify the signals at the harmonics of the PEMs. As previously discussed, non-equal amplification of the signals at the second harmonics of the two PEMs would lead to a calibration term that varied as $\cos\left(4\theta_{pol}\right)$. Previous tests on an APD and amplifier used for the ALCATOR C-MOD MSE system measured amplification at $I_{2\omega_1}$ to be 1.003 ± 0.001 times the amplification at $I_2\omega_2$ [2], which contributes to a $\cos\left(4\theta_{pol}\right)$ term with a magnitude of $\sim 0.04°$.

This amplification difference at the two components depends on both the APD and the trans-impedance amplifier. The same MSE sightline was calibrated repeatedly using different APD units as detectors to judge the variability arising from this effect. The effect is found to be $\sim 0.05°$, predominately in the B_4 term. Therefore, it is marginally important to use a dedicated APD for each sightline throughout the campaign and during calibration. This effect is absent in the new APDs used for the MSE-MSLP system—each APD is found to be functionally identical in terms of frequency response. This effect would be compensated for by the ISC system.

The gain of the APD is changed throughout an experimental campaign to optimize the detection system signal-to-noise and to prevent digitizer saturation. It is conceivable that the frequency-dependent

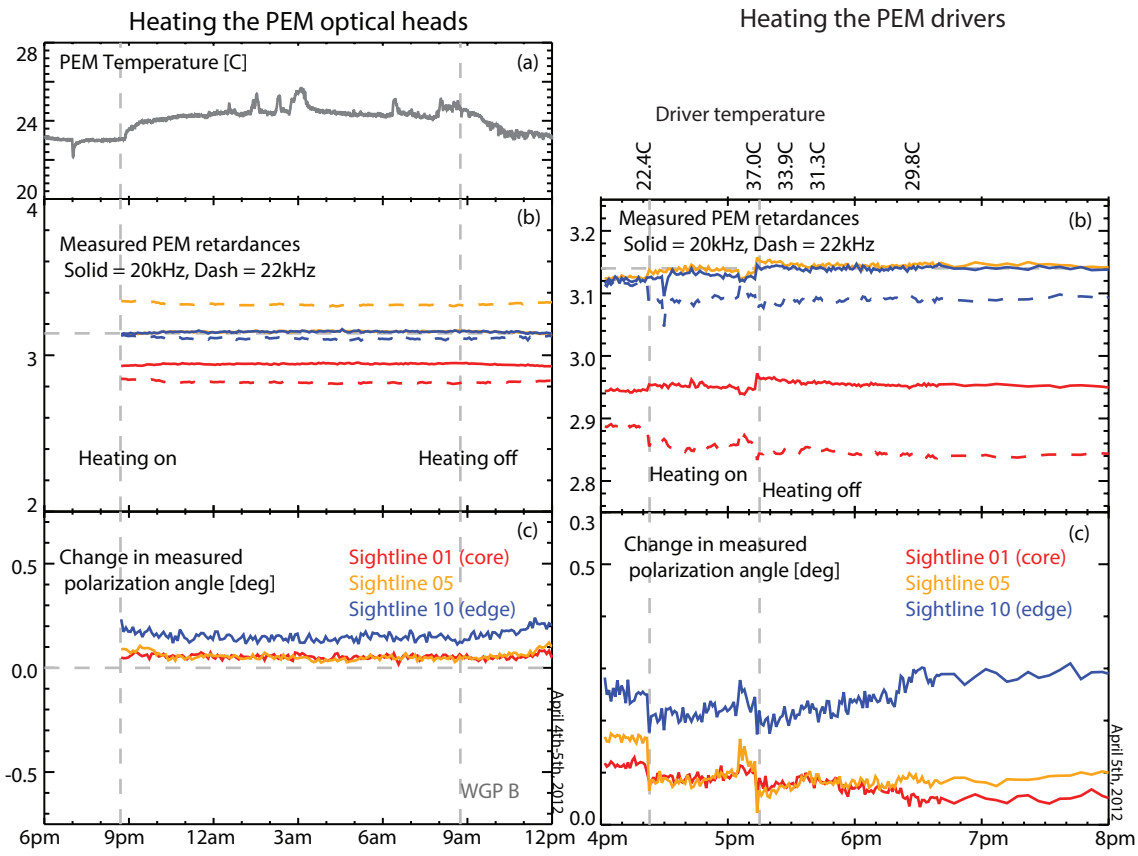

Figure 152: The PEM optical units (left) and drivers (right) were heated using hot air blowers while the ISC input constant polarization angle light. The PEM retardance was extracted from the data for representative sightlines (b) and the change in polarization angle was monitored (c).

amplification at the PEM second harmonic frequency is gain dependent. Repeated calibrations were performed while varying the APD bias voltage. The calibration coefficients were found to be constant to $< 0.02°$ as the APD gain was varied across the typical operating range from 10 to 100. Therefore, no systematic error due to changes in gain during a campaign are expected. This effect is also absent in the new APDs used in the MSE-MSLP system. This effect would be properly compensated for with the ISC system.

C.15 PEM TEMPERATURE

The thermal effects on the PEMs has not been fully explored prior to this thesis. Changing the temperature of either the optical head (the part of the resonant system mounted on the periscope) or the driver (the part of the resonant system mounted in the rack) could change the operational retardance of the PEM and also the measured polarization angle.

To test this, the ISC was used to input a constant polarization angle into the periscope and the PEM optical head was heated while data

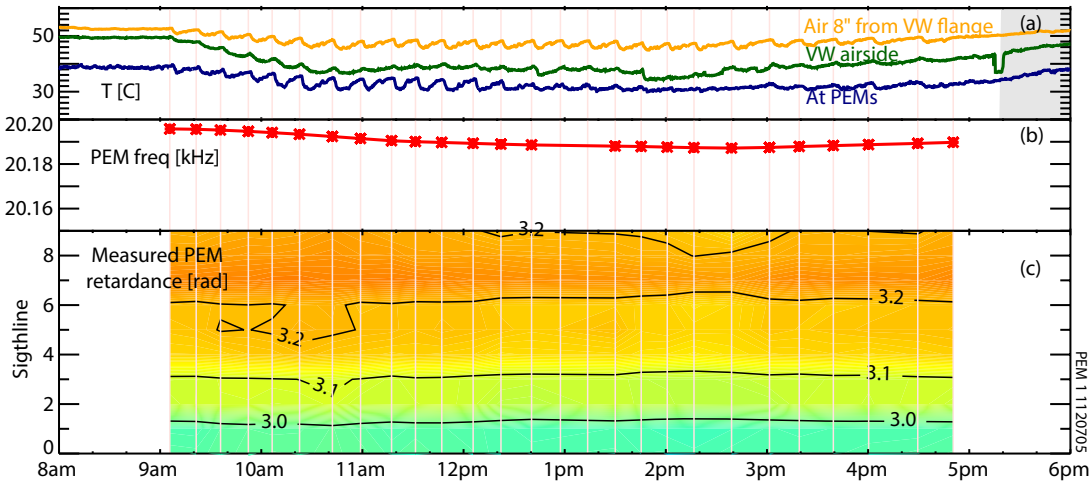

Figure 153: The ISC system is used to measure the retardance of the two PEMs at each sightline during the runday. The retardance is shown to be very stable across the day (c) despite small changes in PEM frequency (b) and the ambient temperature of the PEMs (a).

was taken. A similar test was repeated while heating the PEM driver. Figure 152 shows the results for the heating of the PEM optical heads (left) and the PEM drivers (right). The small temperature increase of the optical heads (a) has negligible effect on the measured PEM retardance (b) and no change in the linear polarization angle beyond what was previously present (c). The more rigorous heating of the PEM drivers has a large impact on the measured PEM retardance (b) and results in a $\sim 1^\circ$ change to the measured polarization angle (c).

Fortunately, the PEM drivers are installed in an electronics rack that has a fairly constant temperature environment. Additionally, the ISC system would correct for any drift in the PEM retardance if it were to occur. On-line monitoring of the PEM retardance would also indicate potential problems which could be investigated.

C.16 PEM RETARDANCE CHANGE

The dependence of the polarization angle on the PEM retardance was previously discussed. Experimentally using the ISC it is found that the retardance is usually stable. Figure 153 shows the retardance measured by the ISC system across all MSE sightlines during a typical experimental runday. The temperature of the area around the PEMs fluctuates during the experiment (a) causing the PEM frequency to drift slightly (b). The PEM retardance is fairly constant across all the sightlines throughout the day, varying by < 0.05 radians. The PEM retardance can also be tracked across a large time span by using the ISC and it is typically found to be stable to ± 0.02 radians.

Figure 154 shows the retardance of the two PEMs averaged over all of the sightlines and over all of the discharges from that runday. Note

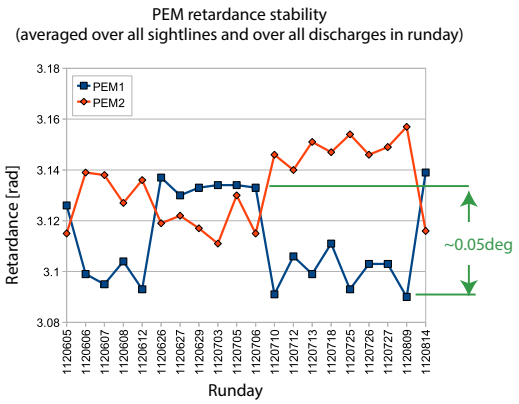

Figure 154: The ISC is used to monitor the stability of the PEM retardance across the entire campaign. The retardance averaged across all sightlines and across all shots during the day is plotted for rundays spanning two months.

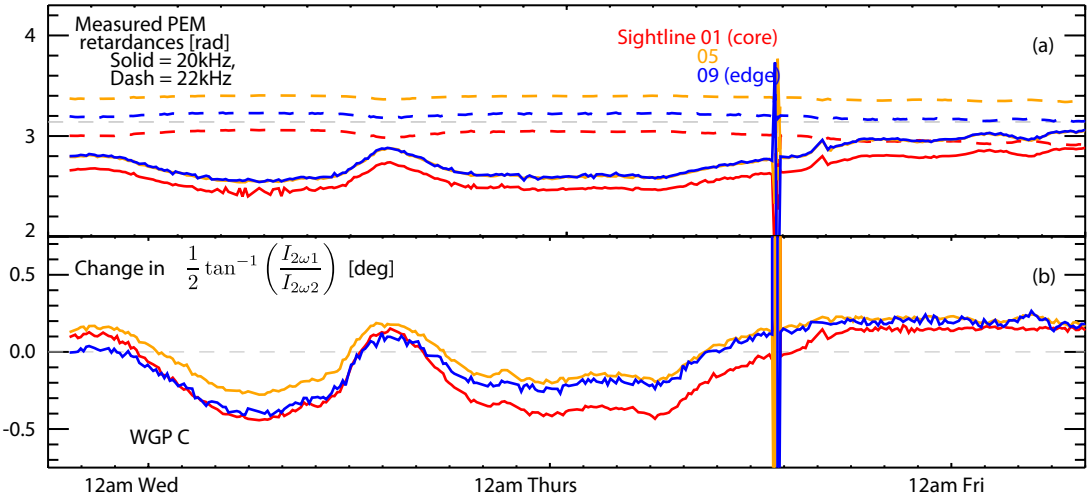

Figure 155: The PEM retardance, measured using the ISC drifted significantly across several days when the tokamak was up to atmosphere (a). This led to a change in the measured angle when the input angle was constant (b) with similar behavior in all sightlines. The reason this drift occurred was never identified.

that the retardance is stable except for two jumps which would cause a change in angle of $\sim 0.05°$ during this two month period.

There are occasions when the PEM retardance drifts significantly. Such an instance is shown in Figure 155 where the measured retardance (a) changed across several days. The ISC was used to input light with constant polarization angle yet the measured angle (θ_{PEMs}) (b) changed significantly. The cause for the retardance changes was never identified. The PEMs were subsequently sent for refurbishment after which the retardance stability was greatly improved.

C.17 PHASE-LOCK-LOOP ERRORS

Most MSE systems use a phase-locked loop to detect the intensities at $2\omega_1$ and $2\omega_2$. The drive signal from the PEMs is transmitted to the diagnostic lab and used as the reference signal in this loop. The proper phase difference between this drive signal and the de-

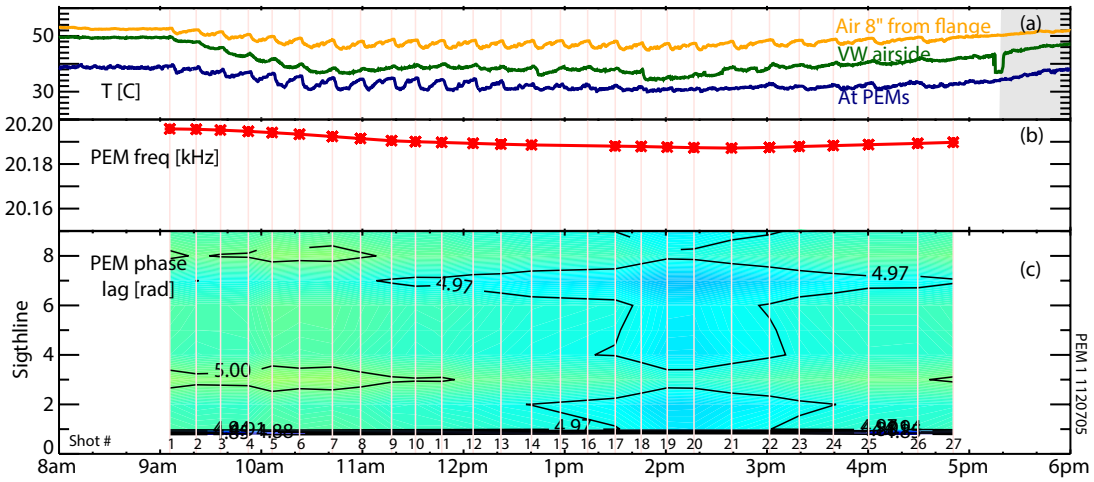

Figure 156: The ISC system is used to measure the phase lag between each sightline and the PEM drive signal for both PEMs during the runday. The phase is shown to be very stable across the day (c) despite small changes in PEM frequency (b) and the ambient temperature of the PEMs (a).

tected signal is determined during calibration by setting the phase to maximize the detected amplitude at $2\omega_1$ and $2\omega_2$. This is very similar to setting the phase delay in an analog lockin. In some systems, this phase is then set for the entire campaign. If the phase shift between the PEM drive signal and the actual PEM modulation changes this would decrease the amplitude of the signal detected at the desired harmonic in this "fixed phase" scheme. If this occurred for only one of the PEMs it would lead to errors that are modulo $\pi/2$ (for an identical analysis as discussed for a gain difference in the detector). The analysis system on C-MOD does not typically use a fixed phase and instead maximizes the signal at the desired harmonic at a precisely determined frequency, a scheme termed the "rms analysis". Alternately the fixed phase analysis can also be used.

The rms analysis scheme allows the system to monitor the phase between the PEM drive signal and the actual retardance imposed by the PEM (assuming the time-delay between the drive signal and the digitizer and the detected signal and the digitizer remains constant). Results for a single runday for each of the detectors are shown in Figure 156 which corresponds to the same runday shown in Figure 153. The phase is shown to be constant to $<\sim 0.03$ radians.

The choice of the windowing period in the phase-look loop is also important and is covered elsewhere [1].

C.18 CONCLUSIONS

These tests show that the MSE behaves nearly ideally in many ways. The results are summarized below:

1. The viewing geometry and periscope location do not move between campaigns, during a campaign, or during a runday.

2. The filter transmission functions are close to what is expected and respond properly to temperature tuning. The ovens operate correctly and can properly tune the filter location. The in-situ filter measurements are used to properly position the filters over the beam emission to avoid 3D source effects.
3. The periscope is not significantly vignetted and has approximately the proper transmission. It has the proper spectral throughput. Nominally, it is a properly operating optical system.
4. The periscope does not create spurious polarized light from unpolarized above the 1 percent level. The periscope has only a 1 percent transmission dependence on input polarization angle, and it depolarizes light at the < 1 percent level—it is nearly an ideal transmitter of polarized light during maintenance periods.
5. The periscope does not allow light from outside the viewing volume to scatter into the MSE sightlines and contaminate the measurement.
6. Only a very weak effect from stress at the vacuum window due to differential vacuum is present.
7. The heating of the objective lens by the plasma has a negligible effect on the measured angles.
8. The periscope and detector system have little effect on the polarization response as a function of wavelength.
9. The detector, detector gain, and amplifier characteristics have a $< 0.05°$ effect on the polarization measurement.
10. The diagnostic is only weakly sensitive to the temperature of the PEM optical heads or driver units.
11. The PEMs provide a mostly stable retardance.
12. The phase-shift between the PEMs and the detectors can be tracked and compensated for using phase-insensitive analysis techniques.

BIBLIOGRAPHY

[1] H.Y. Yuh. *The Motional Stark Effect diagnostic on Alcator C-Mod*. PhD, Massachusetts Institute of Technology, 2005.

[2] J. Ko. *Current profile measurements using Motional Stark Effect on Alcator C-Mod*. PhD, Massachusetts Institute of Technology, 2009.

[3] W. M. Solomon, K. H. Burrell, P. Gohil, R. Groebner, and D. Kaplan. Cross-calibrating spatial positions of light-viewing diagnostics using plasma edge sweeps in DIII-D. *Review of Scientific Instruments*, 74(12):5084, 2003.

[4] I. O. Bespamyatnov, W. L. Rowan, K. T. Liao, and R. S. Granetz. An integrated charge exchange recombination spectroscopy-/beam emission spectroscopy diagnostic for Alcator C-Mod tokamak. *Review of Scientific Instruments*, 81(10):10D709, 2010.

[5] M. F. M. De Bock, N. J. Conway, M. J. Walsh, P. G. Carolan, and N. C. Hawkes. Ab initio modeling of the motional stark effect on MAST. *Review of Scientific Instruments*, 79(10):10F524, 2008. Printed.

[6] Stephen C. McClain, Chanda L. Bartlett, J. Larry Pezzaniti, and Russell A. Chipman. Depolarization measurements of an integrating sphere. *Applied Optics*, 34(1):152–154, January 1995.

D

SOURCES AND CHARACTER OF POLARIZED LIGHT INSIDE C-MOD

Knowledge of the mechanism that polarizes the light upon reflection allows careful study of the different sources of background light that can contribute to the MSE polarized background inside the tokamak. These are detailed in these sections.

D.1 VISIBLE BREMSSTRAHLUNG

The most obvious and unavoidable source of background light is visible bremsstrahlung (VB), which creates quasi-broadband light throughout the visible spectrum and is always present in the plasma. At times, the partially-polarized MSE background light appears to correlate well with the visible bremsstrahlung measurement from the Z_{eff}-monitoring diagnostic, which measures the light in an impurity-line contamination-free region in the green wavelengths. Figure 157 shows an example of a plasma with large changes in density as it transitions in and out of H-mode. It is apparent that the total light detected by the MSE diagnostic is dominated by visible bremsstrahlung. The polarized component of the light also appears to track the visible bremsstrahlung. In this case, the different sightlines have been normalized to be the same intensity early in the discharge to show relative changes. It is clear that all three sightlines, center, middle, and edge, observe nearly the same time history of total light and polarized light.

In most plasmas, the polarized light does not track the visible bremsstrahlung exactly due to a deuterium emission component to be discussed in the next section. However, the partially-polarized light does correlate very well with visible bremsstrahlung in helium plasmas as shown in Figure 158. Panel A shows the polarized background for the MSE sightlines scaled to match early in the discharge. The core (tangency radius = 0.67cm) VB signal is scaled and plotted for comparison. Note that all the sightlines show nearly the same time behavior and are consistent with visible bremsstrahlung. The change from 1.1 to 1.3s is due to the plasma shifting from lower diverted to upper diverted and back again. Panels b and c show the linear polarization fraction and polarization angle respectively during the discharge. These traces are not normalized and are remarkably constant in time, consistent with the polarized light coming from a single, stationary source. Note that most sightlines measure polarization angles near

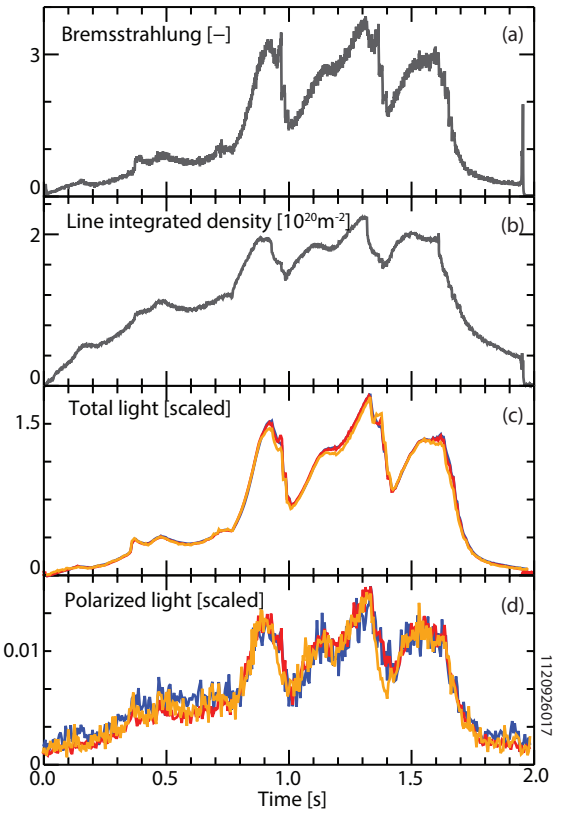

Figure 157: The contribution of visible bremsstrahlung to the MSE partially-polarized background. The signal from the Z_{eff} diagnostic measuring the bremstrahlung emission intensity (a) shows peaks due to the changes in plasma density as the plasma goes in and out of H-mode (b). The total light (c) and polarized light (d) from three MSE sightline. The MSE sightlines have been normalized to agree early in the shot.

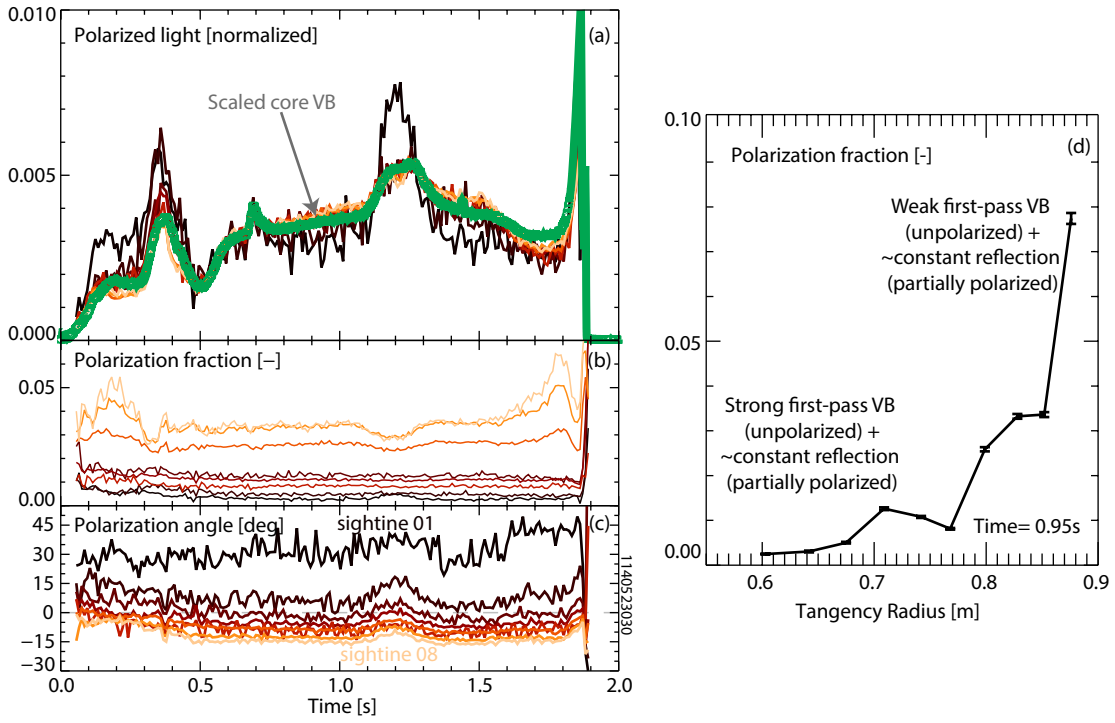

Figure 158: The time history of MSE partially-polarized background in a helium plasma. The polarized component of the MSE background for all the sightlines (a). The polarized light has been scaled to match at 0.5s and the core VB measurement has been similarly scaled and over-plotted. The polarization fraction (b) and polarization angle (c) for the sightlines. The polarization fraction as a function of sightline tangency radius at time 0.95s (d).

near 0°, which would indicate the light is coming from a source near the midplane. The lack of a chord or filter dependence likely implies the source is very spatially diffuse with little spectral structure, both qualities of visible bremsstrahlung.

There is an important qualitative difference between light that is observed upon first-pass, light that is observed only upon reflection, and light that is a combination of first-pass and reflection. The first-pass emission is collected unpolarized (thus only Stokes component I has any intensity) whereas the reflected light is partially-polarized (Stokes components U and Q also have intensity). Therefore, a source of light that is observed both on the first pass and upon reflection will have a lower polarization fraction than a source observed only upon reflection. The fact that the different sightlines all have different chord lengths through the plasma means those with tangency radii near the core see more first pass volumetric emission than those with tangency radii near the edge. Meanwhile, all the sightlines likely observe the volumetric source upon reflection with similar polarization amounts and fractions. Adding together the two contributions from a volumetric source leads to a spatially dependent polarization fraction with the edge sightlines having a higher polarization fraction than the core.

Figure 158 panel D plots the polarization fraction of the sightlines as a function of sightline tangency radius. The observed dependence of polarization fraction on tangency radius indicates this picture is consistent with the volumetric visible bremsstrahlung emission being seen both on first-pass and upon reflection. The data is extracted from $0.9 - 1.0$s, though is similar at all other times. The core sightlines have very low polarization fractions ($< 0.5\%$), while the edge sightlines have larger polarization fractions. Note the dip in the polarization fraction trend around tangency radius 0.78m (sightline o6). This is consistent with the dip in the polarization fraction in the polarization photos due to these sightlines terminating on the space between the D and E-port ICRF antennas. Assuming that the light reflecting from the antenna has a polarization fraction of 0.5 (consistent with the polarization photos of the ICRF antenna), then the core and edge sightlines observe the visible bremsstrahlung with a first-pass-to-reflected total intensity ratio of $\sim 100:1$ and $\sim 5:1$, respectively.

If visible bremsstrahlung was the only source present, the polarized background compensation strategy might be fairly simple. Since the polarization angle and polarization fraction are nearly constant, the background Stokes components could be simply scaled from an intensity measurement. This could be done by scaling the Stokes vector prior to the beam pulse by the change in the visible bremsstrahlung measured by the Z_{eff} diagnostic. Furthermore, since it relies on the particle transport into and out of the plasma, the visible bremsstrahlung emission does not change very rapidly (except during disruptions).

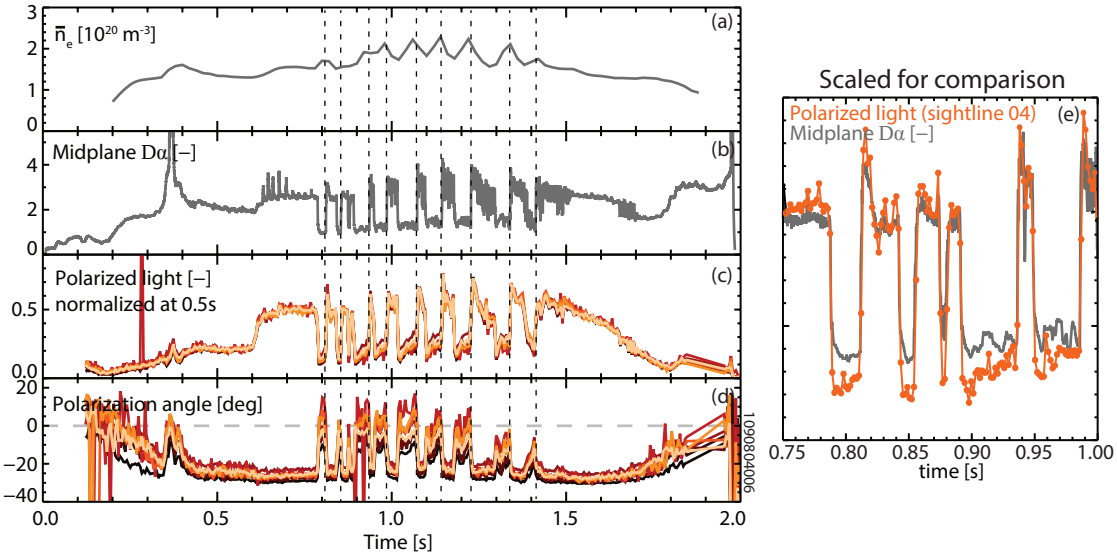

Figure 159: A lower-diverted discharge with many L to H-mode and H to L-mode transitions as indicated by the line average density (a) and midplane D_α (b) traces. The H to L-mode transitions are indicated with vertical dashed lines. The polarized light detected by the MSE system (c) and the polarization angle (d). Note the intensity is scaled to match at 0.5s. A comparison bewteen the midplane D_α (grey) and the polarized intensity from sightline 04 (orange) on the microbin timescale is shown in (e).

This makes time-interpolation a reasonable approach if the beam can be modulated quickly. However,rarely is the visible bremsstrahlung the only, or the dominant, contributor to the partially-polarized MSE background light.

D.2 DIVERTOR QUASI-CONTINUUM

Most times it is apparent that there is an additional source of light present that appears to be closely related to the D_α emission from the cold edge and divertor plasma. This partially polarized source has been previously noted on C-MOD [1, 2]. The polarized light from this source usually dominates the polarized light from the core visible bremsstrahlung and has been a long-term problem and mystery for the C-MOD diagnostic.

An example of this "D_α-correlated" source is shown in Figure 159. This lower diverted plasma undergoes many transitions between L and H-mode which is apparent in the change in slope of the line averaged density (a) and the step change in the midplane D_α (b). Every time the plasma enters H-mode, the density begins to rise and the D_α drops precipitously. Then when the plasma back transitions to L-mode, the density begins to decrease and the D_α quickly rises back to its L-mode value. These back-transitions are indicated with the dashed vertical lines. The visible bremsstrahlung (not shown) tracks

similar to the density squared; and when the D_α signal drops during H-mode, the visible bremsstrahlung signal starts to rapidly increase.

The polarized light intensity detected by MSE (c), which has been normalized at 0.5s to better show changes, has the same temporal behavior as the D_α. Note that all of the sightlines have the same behavior and nearly the same relative changes in polarized intensity at the transitions. Focusing on the time 0.75s to 1.00s (e) shows the D_α (grey) and the polarized intensity from sightline 4. It is very clear that the background follows the D_α trace during the L-mode phases when D_α is bright. The timing of the transitions is nearly identical with little to no phase lag; even bumps in wiggles in the D_α show up in the polarized intensity, particularly when the D_α is bright. The polarization angle is shown in panel D. Whenever the D_α and polarized intensity are high, the polarization angle is $< 20°$. When the D_α and polarized intensity decrease, the background moves toward 0°.

This behavior is very indicative of two competing sources of polarized light. One source is dominate in the L-mode phases and leads to more intense polarized light with angles consistent with a source located in the lower divertor. Then, in H-mode with decreased D_α, the source decreases significantly, leaving the dimmer source to dominate. This weaker source appears to be near the midplane and is likely visible bremsstrahlung.

Another example that illustrates even faster changes in the polarized background is shown in Figure 160. In this lower diverted discharge, the plasma experiences D_α "dithering". The midplane D_α (b) shows an oscillation at ~ 80Hz during the L-mode phase from 0.75s to 1.00s prior to an enhanced D_α H-mode. Note the line-integrated density (a) does not show this oscillation. Panel C shows that this dithering appears very strongly in the polarized light intensity of all the MSE sightlines, which have been normalized from 0.5s to 0.7s to show changes. The dithering also appears in the the polarization fraction (d) and polarization angle (e). This dithering was first noticed in the MSE background by Yuh [1]. Examining this dithering period more closely (right) shows that the peak in the polarized intensity corresponds to the peak in the midplane D_α, as indicated by the vertical blue lines. The polarized intensity changes by over a factor of two and has similar magnitude changes and timing in all sightlines. The peaks of the midplane D_α also appear in phase with the peak in the polarization fraction, which has an oscillation of $> 50\%$ of its value in the edge channels. Again, the polarization angle is most negative when the polarized intensity and D_α is brightest, though the data is noisier than the previous case with many H-modes.

D.2.1 *A problem due to filters?*

The strong correlation between D_α and the MSE partially-polarized background could indicate that the bandpass filters are not properly

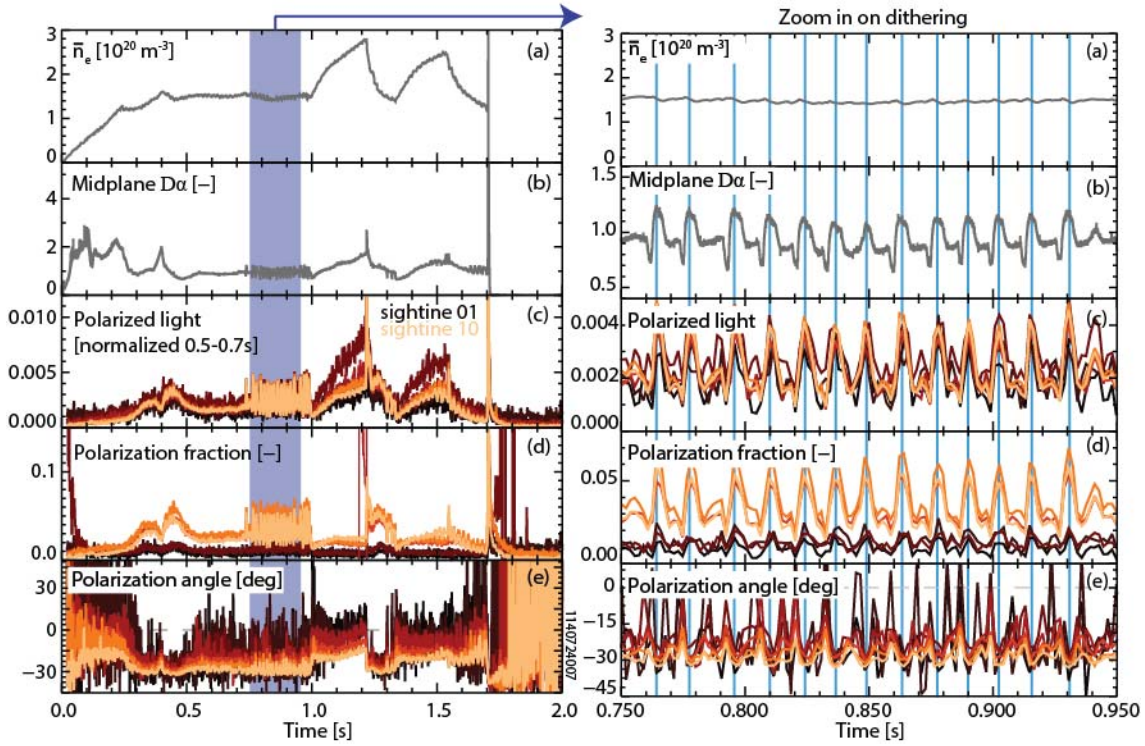

Figure 160: A lower diverted discharge with a D_α "dithering" phase from 0.75s to 1.00s. The line-averaged density (a) and midplane D_α (b). The polarized intensities of the MSE sightlines (c) normalized from 0.5s to 0.7s, the polarization fraction (d) and polarization angle (e). An expanded time-axis during the dithering phase in the blue shaded region is shown in the left with the peaks in the D_α indicated by vertical blue lines.

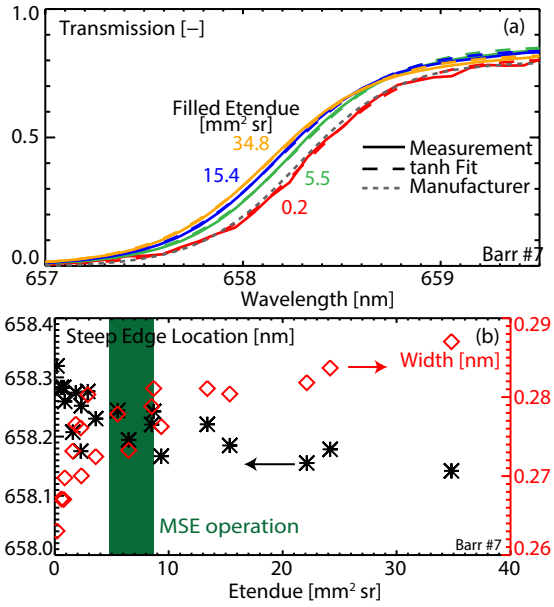

Figure 161: The transmission curves of the steep-edge filters designed to block D_α emission were measured in-situ (a). Measurements at different filled étendues were taken and compared to the manufacturer's measurement using a thin collimated beam (dashed). A tanh fit was performed and the resulting parameters are plotted vs the filled étendue (b).

blocking out the strong D_α emission from the cold edge of the plasma located just to the blue of the MSE light. These bandpass filters are supposed to pass $< 10^{-5}$ (OD5) of the light at the D_α wavelengths and their passbands have been measured in-situ. The fact that the same source shows up in each sightline with the same intensity indicates either that the emission is very spectrally broad or that all the filters are flawed in a similar manner. Steep-edge blocking filters were procured previously to decrease the transmission of the D_α line by an additional factor of 100 (OD2) to test whether the problem lies with improper blocking of the D_α line. However, installing these filters did not decrease the amount of MSE partially-polarized background or its correlation with the D_α measurements [2]. One conjecture was that these steep-edge filters were also fabricated improperly or that the large étendue passed through the filters by the MSE system significantly hampered the filter's blocking of the D_α wavelengths.

Therefore, the steep-edge filter pass-bands were tested in-situ in the same manner as the MSE narrow bandpass filters detailed in Appendix C. The results are shown in Figure 161. The étendue passed through the filter was varied using masks to set the field and aperture stops. The filter transmission curve was measured at each setting (a). The resulting location of the blocking band and width of the transition region are plotted in panel B. The manufacturer measurement at a single point in the middle of the filter with a highly collimated beam is plotted as the dashed line. It is apparent that the filters were fabricated correctly and operate correctly in the MSE optical system; increased étendue only shifts the bandpass to the blue ever so slightly. So it remains true that the "problem with D_α" is not due to D_α itself, and the emission exists in the MSE wavelengths. Further experiments that swapped out narrow bandpass filters showed that the source is

present in all the MSE wavelengths and is not strongly wavelength or sightline dependent.

D.2.2 *Separating components using magnetic geometry*

The fact that the source that scales with D_α and appears to be isolated to the divertor prompted a dedicated experiment. This experiment was a comparison between helium and deuterium discharges during a sweep through different magnetic geometries. The idea has two key components: (1) Scanning divertor geometries would move the divertor source, allowing the polarized component to be isolated by changes in polarization angle and (2) the contribution from visible bremsstrahlung could be subtracted using the identical helium discharge, which only has the visible bremsstrahlung source, thus yielding only the source correlated to D_α. The two discharges were executed and their gross characteristics are compared in Figure 162. The helium discharge (black) and the deuterium discharge (red) had very similar time histories. The location of the secondary seperatrix is shown with positive numbers indicating the plasma was upper diverted and negative numbers indicating the plasma was lower diverted (a). Prior to 0.35s, the plasma is limited, at which point a lower divertor is established until 1.00s. At that point the plasma becomes a double null, then is upper diverted by 1.2s, sweeping back through double null to become lower diverted by 1.40s. At that point the deuterium discharge disrupts. The line-integrated density (b) was well matched for the two discharges, leading to $\sim 2\times$ more visible bremsstrahlung emission in the helium discharge (c) due to the change in Z_{eff}. The deuterium discharge had $> 10\times$ more D_α emission than the helium discharge (d). The magnetic geometries from EFIT show that the magnetic geometry of the discharges were nearly identical in each phase (e). The unfiltered wide view camera images show the deuterium (f) and helium (g) plasmas had very similar emission patterns in each phase, with the helium plasma possibly having less divertor emission in the upper diverted phase (though the camera is mostly saturated in the divertor in all phases).

Figure 163 shows the background polarization measured with the MSE system at each phase for both the helium (black) and deuterium (red) discharges. The secondary seperatrix is shown to identify the phases (a). The total light detected by MSE (b) is significantly higher in the helium discharge due to the increased bremsstrahlung. However, the polarized component of the light (c), which has not been scaled, is significantly higher in the deuterium discharge. These two effects lead to a polarization fraction that is up to $3\times$ higher for the deuterium discharge for this sightline. The resulting polarization angle (e) is significantly more negative for most of the deuterium discharge. In the deuterium discharge, the polarization fraction and polarization angle are dynamic, clearly showing that mutliple sources are

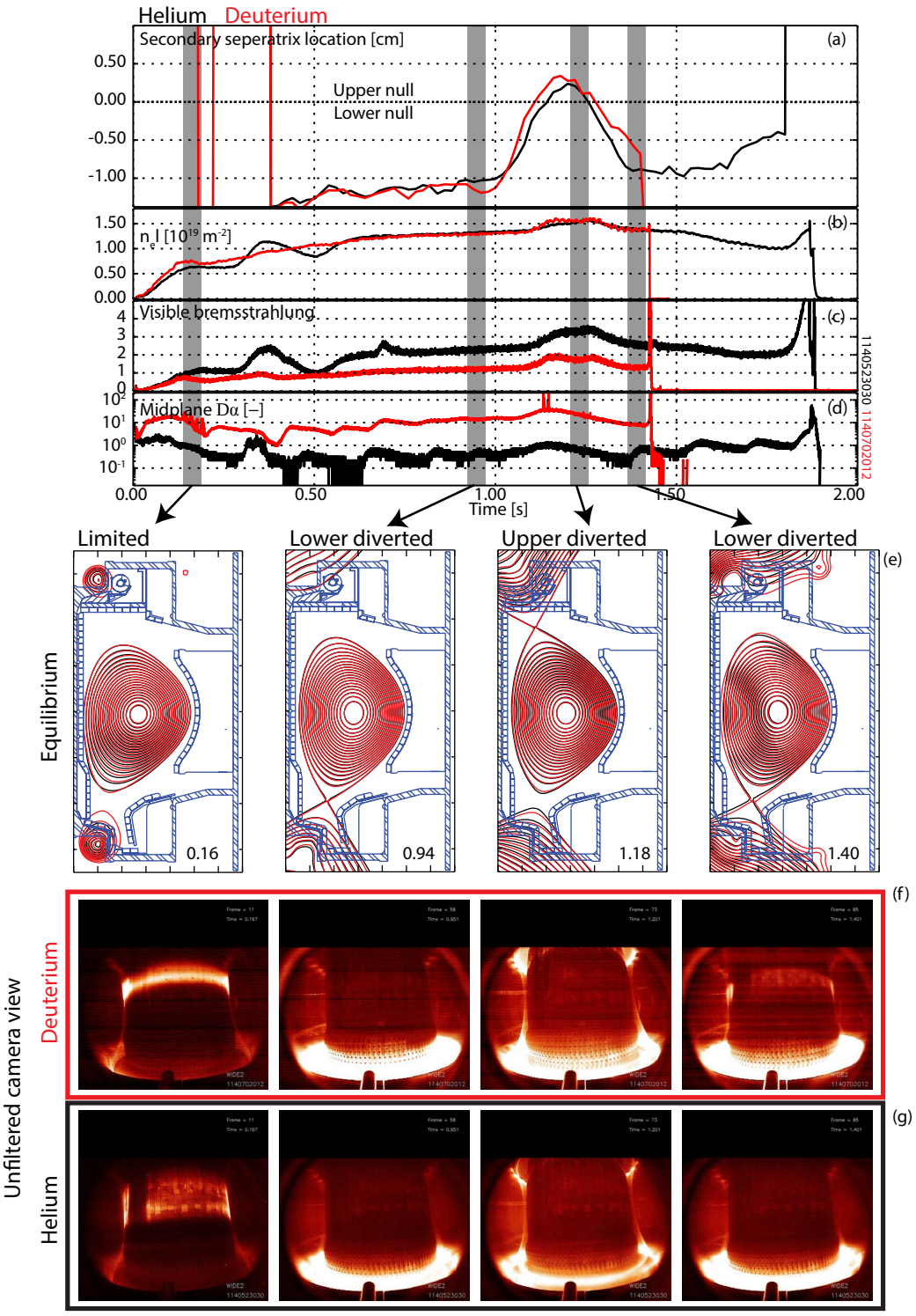

Figure 162: Identical discharges were taken in helium (black) and deuterium (red) plasmas. The plasma was swept from a limited configuration to a lower diverted configuration at 0.35s, then to upper diverted at 1.20s, then back to lower diverted at 1.40s as shown by the location of the secondary seperatrix (a). The density was well matched between the shots (b), leading the helium shot to have $\sim 2\times$ more visible bremsstrahlung (c) with $> 10\times$ less D_α. The magnetic geometry in each phase of the plasma was nearly identical (e). The unfiltered visible camera shows that the plasmas looked very similar in each phase (f and g) with the helium shot possibly having less divertor emission.

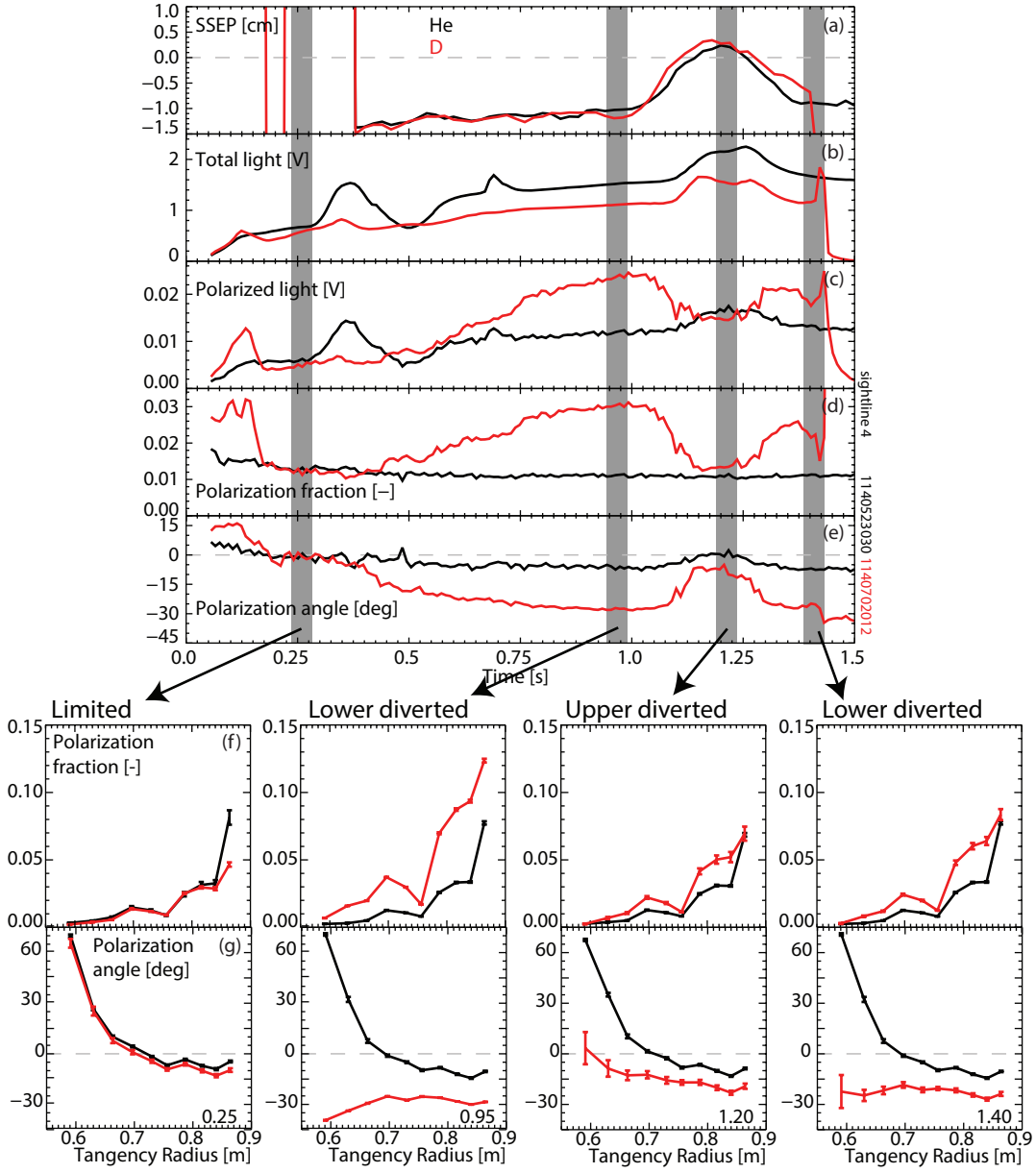

Figure 163: A magnetic configuration sweep (a) conducted in helium (black) and deuterium (red) produced different amounts of total light (b) and polarized light (c) with differing polarization fraction (d) and polarization angle (e). The profiles of the polarization fraction (f) and polarization angle (g) vs. sightline tangency radius at the four phases of the discharge: limited, lower-diverted, upper-diverted, and then back to lower-diverted.

competing. The polarization fraction and polarization angle profiles as a function of sightline tangency radius for each phase are shown at the bottom of the figure. Both profiles are in agreement during the limited stage. Throughout the rest of the shot, the polarization fraction in the deuterium discharge is higher than the helium profile, but with a similar profile shape. The polarization angle in the deuterium discharge is more negative than in the helium discharge after the establishment of a divertor.

The two discharges are nearly identical in density and magnetic geometry and other bulk plasma properties. Additionally, the helium discharge has only a single component of the background: visible bremsstrahlung. Thus the helium discharge and the ratios in visible bremsstrahlung between the two discharges can be used to decompose the two background sources in the deuterium discharge into a component from visible bremsstrahlung and a component from deuterium:

$$\begin{bmatrix} I \\ Q \\ U \\ V \end{bmatrix}^{\text{D shot}}_{\text{D component}} = \begin{bmatrix} I \\ Q \\ U \\ V \end{bmatrix}^{\text{D shot}}_{\text{measured}} - \begin{bmatrix} I \\ Q \\ U \\ V \end{bmatrix}^{\text{He shot}} \times \frac{VB(t)^{\text{D shot}}}{VB(t)^{\text{He shot}}} \quad (80)$$

Where $VB(t)$ is the visible bremsstrahlung intensity measured by the Z_{eff} diagnostic in each discharge. In practice, this decomposition is calculated using the intensity at the PEM harmonics which is proportional to the Stokes vectors with a proportionality constant that is the same in both discharges.

This decomposition yields a visible bremsstrahlung component and a deuterium component each with their own total intensity, polarized intensity, polarization fraction, and polarization angle. This process is be done for each sightline. It should be noted that the most error-prone part of this technique is the polarization fraction since it is composed of decomposed quantites in both the nominator and the denominator and involves subtracting I, Q, and U.

Figure 164 shows the results for sightline 4. The actual measurement is shown in red, the component from visible bremsstrahlung is shown in orange, and the component from deuterium is shown in blue. Panel A shows the decomposition of the total intensity; note that the deuterium component is substantially less than the visible bremsstrahlung component. Panel B shows the polarized intensity of the different components. Note the polarized deuterium component peaks early at 0.15s, decreases to zero, and then slowly rises throughout the discharge. The polarized deuterium component becomes substantially brighter than the visible bremsstrahlung component until the time that the discharge becomes upper diverted. At this time it decreases, then increases again after the plasma lower divertor is re-

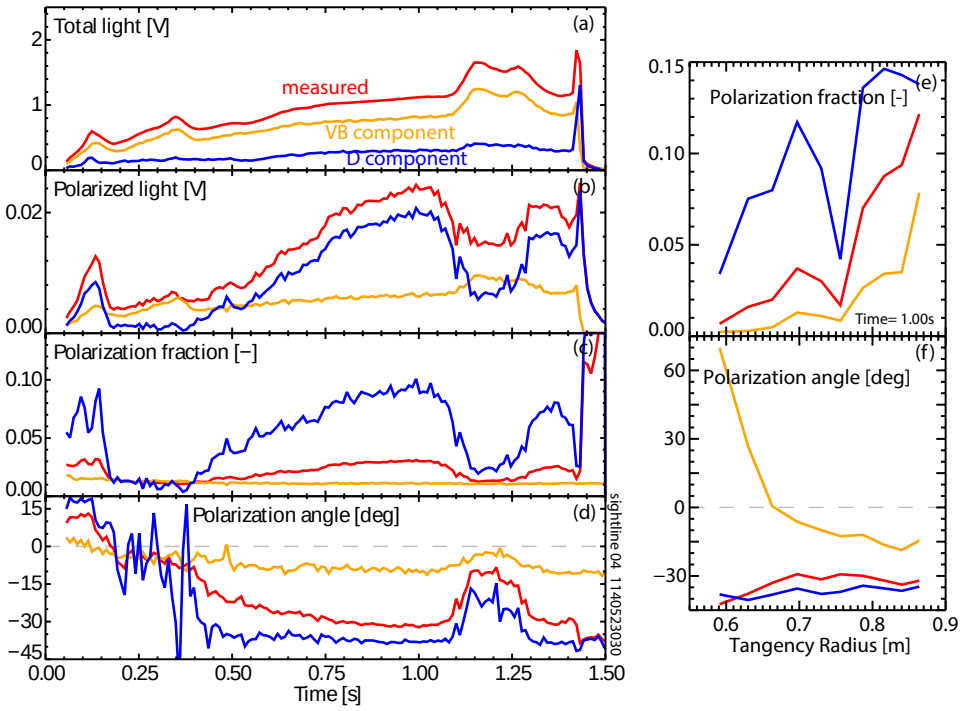

Figure 164: The background is decomposed into different components from the measured quantities (red) into a component due to visible bremsstrahlung (orange) and a component due to deuterium (blue). The decomposition of the total light (a), polarized intensity (b), polarization fraction (c), and polarization angle (d) for sightline 04 are shown. The spatial profiles of the polarization fraction (e) and polarization angle (f) decomposed into the components at 1.00s are also shown.

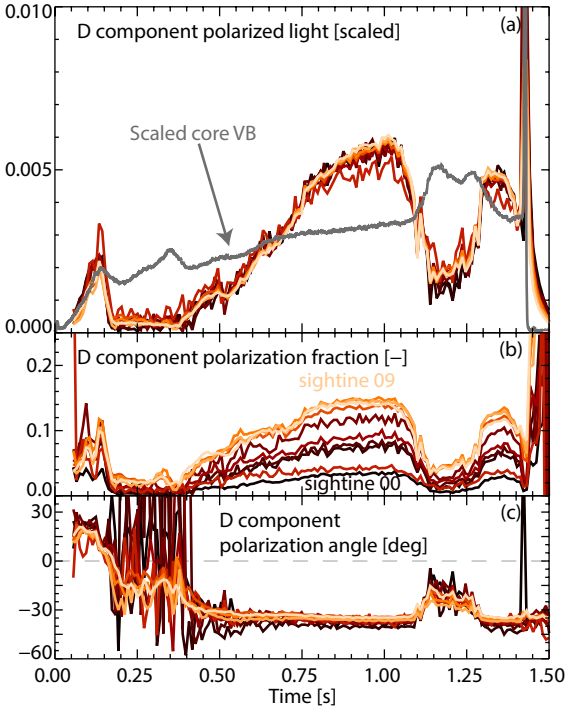

Figure 165: The deuterium component of the background (a) is scaled for comparison between sightlines. The core visible bremsstrahlung is overplotted for comparison (grey). The polarization fraction (b) and polarization angle (c) of the deuterium component are also shown.

established. Panel C shows the polarization fraction (c) of the deuterium component is relatively high early on and then high again when the lower divertor is established. Panel D shows that the polarization angle of the deuterium component has a positive polarization angle early in the discharge followed by constant and negative polarization angles until the plasma is upper-diverted, after which the polarization angle returns to negative. The spatial profiles at 1.00s of the polarization fraction are shown in panel E and are high for the deuterium component and polarization angle, shown in panel F, is negative across all sightlines.

Figure 165 shows the polarized intensity of the deuterium component for each of the sightlines. The polarized intensity has been scaled to show that they all have the same time behavior. This behavior is not consistent with the core visible bremsstrahlung (grey)—clearly it is from a separate emission source. Interestingly, the intensity of this polarized component goes to and stays near zero from 0.2s to 0.35s, indicating that the visible bremsstrahlung subtraction technique is operating well, with visible bremsstrahlung as the only component present at this time. The polarization fraction of the deuterium component (b) for all the sightlines shows the same time behavior shape. The polarization angle (d) of the deuterium component is also very similar for all the sightlines. The angle begins positive prior to the establishment of the divertor and then becomes negative, consistent with the source being in the lower divertor at later times. Such a constant angle as a function of time, even as the polarization intensity changes, indicates that there is indeed only a single, spatially station-

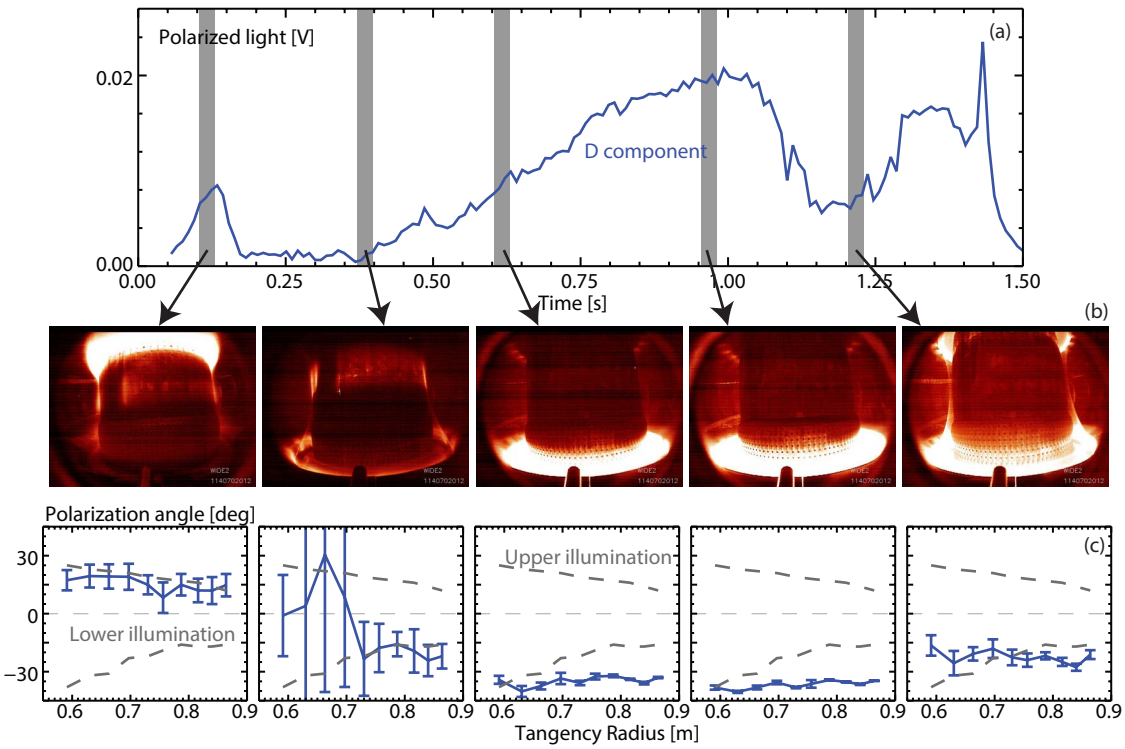

Figure 166: The polarized component from the deuterium as a function of time (a) correlates with the bright emission from the visible camera (b) during the MARFE and later in the diverted phase. The spatial profile of the deuterium component polarization angle is plotted (c) along with the polarization angle from the polarization photos taken invessel using lower and upper illumination.

ary source remaining after visible bremsstrahlung is subtracted. The angle increases when the plasma moves toward upper-diverted and returns afterwards.

Examining the polarization angle along with camera views of the plasma can help localize the deuterium component source. Figure 166 shows the polarized intensity of the deuterium component from one of the MSE sightlines (a), unfiltered camera images of the plasma (b), and the spatial profile of the deuterium component's polarization angle (c) at different times during the discharge. It is apparent that the early spike in polarized emission comes from the MARFE moving up the inner wall toward the upper divertor. This produces polarization angles similar to those seen in the polarization photos when a source high in the vessel is seen upon reflection (upper grey dashed lines). Later, in the diverted phase, the polarized emission comes from the lower divertor with the source possibly moving upward when the plasma moves to upper divertor. The polarization angle is consistent with the polarization angle observed in the polarization photos during illumination from the lower divertor (lower grey dashed lines).

Figure 167 shows the ratio between the polarized intensity of the deuterium and visible bremsstrahlung components. The deuterium component from the MARFE dominates early in the discharge. For

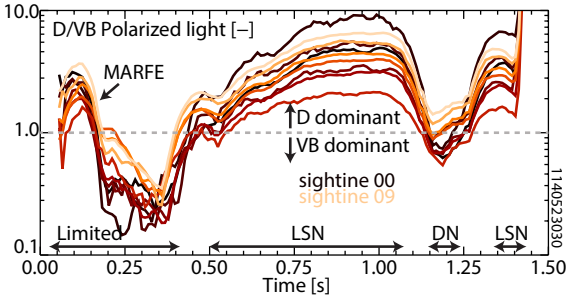

Figure 167: The ratio of the polarized intensity from the deuterium component to the polarized intensity from the visible bremsstrahlung component for each sightline. The different phases of the discharge are noted.

the remainder of the limited phase the visible bremsstrahlung component is dominant. The deuterium component dominates during the rest of the discharge, decreasing when the plasma is upper diverted or double null. This process clearly shows that the MSE background can be composed of multiple sources, each with a different location and different temporal characteristics.

D.2.3 *Spectroscopic studies in the divertor*

Once the source that correlates with D_α has been isolated and characterized, the next step is to identify the physical process that generates this source. The experimental results all hint that the source resides in the divertor and is fairly constant in wavelength across the passbands observed by the MSE system. Therefore, the divertor spectroscopy system was used to examine these wavelengths for such features that match the time history of this component. Figure 168 shows measurements in the lower divertor. The MSE narrow bandpass filter transmission curves are plotted over the measured spectrum using the CHROMEX spectrometer (a) from a chord through the lower divertor (b) at 1.00s. A 0.5nm portion of the spectra is integrated around each filter's center wavelength for each frame of the spectrometer. The resulting time histories are plotted in panel C for the ten sightlines. This is compared to the polarized intensity of the deuterium component from the previous analysis plotted in panel D; the intensities of this emission have been normalized to agree from 0.25s to 1.00s. Note the time histories are very similar between the polarized component and the emission in this wavelength from the divertor. Also, the small spike in the polarized component early in the discharge associated with the MARFE (t = 10ms) is not present in the spectral traces from the lower divertor.

The multi-chord divertor spectroscopy can also be used to locate the spectral feature as a function of space. Figure 169 shows four sightlines through the divertor plasma (left). The spectra prior to the time the lower divertor is established are shown in the top right. These are flat with little or no emission beyond the carbon impurity lines (these are likely near zero counts due to a datum error). After the divertor is established, the spectra show a substantial increase

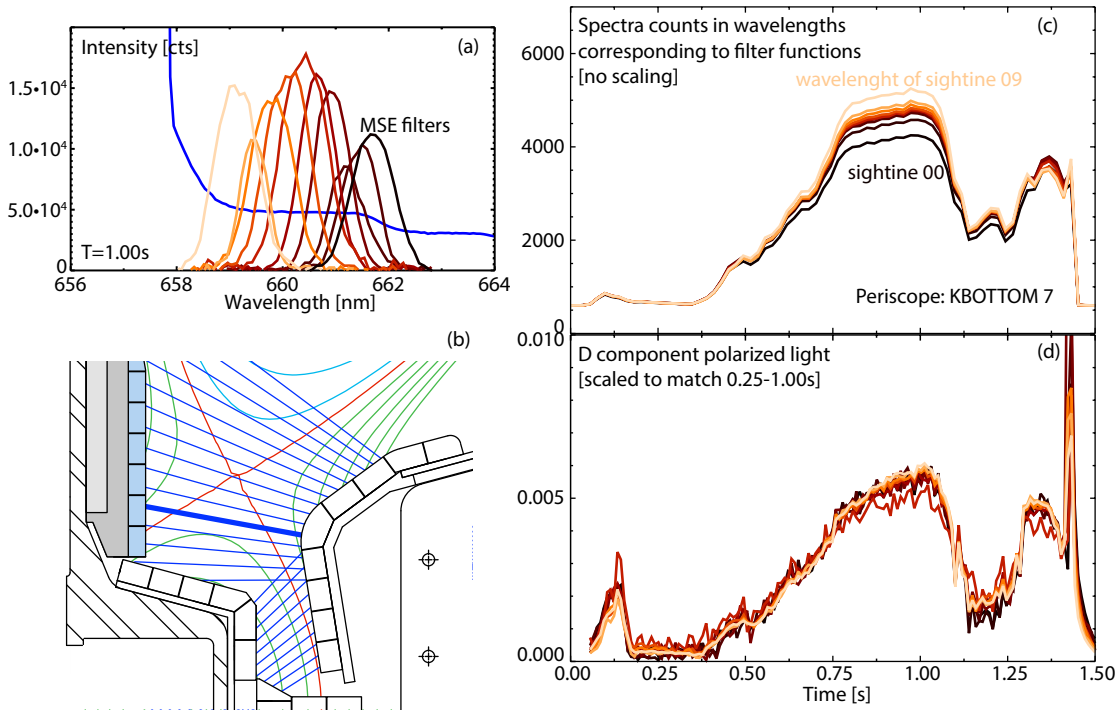

Figure 168: Divertor spectroscopy (a) with the MSE filter passbands overplotted. The chosen spectrometer sightline is located in the lower divertor below the x-point location (b). The time traces of the wavelength regions are overpotted (c). The deuterium component in the polarized background for the sightlines are plotted after normalizing (d).

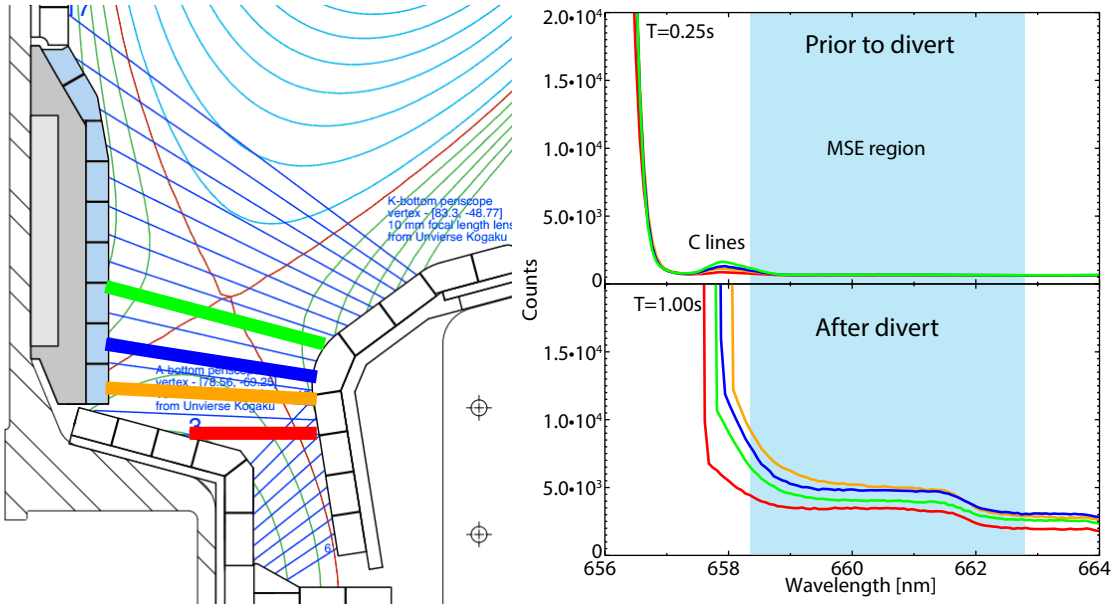

Figure 169: Multiple views through the lower divertor lower than the x-point using divertor spectroscopy (left). Spectra from the views prior to diverted (top right) and after the plasma becomes lower diverted (lower right).

in these wavelengths (lower right). It appears that the emission is brightest on the second and third of the chords, perhaps localizing the emission to the area below the x-point in the private flux region.

D.2.4 *A molecular source?*

In summary, there appears to be a strong source of emission that:

1. Is highly correlated with D_α, but not actually D_α
2. Is present in deuterium, but not helium discharges
3. Is located in the active divertor
4. Is often the dominate source
5. Changes on a very fast timescale (< 5ms)
6. Appears in all sightlines and spectral bandpasses used by MSE
7. Agrees with D_α"wing" in spectroscopy in the divertor
8. Appears in MARFEs

These observations lead to the conjecture that this component of the MSE polarized background comes from molecular deuterium in the edge-regions of the plasma. There are many molecular lines reported in this region that could lead a quasi-continuum "wing" on the D_α emission. However, further study is required to confirm this, possibly using high resolution spectroscopy in the divertor. Tests for determining if the emission is from molecular deuterium could include correlating to the Fulcher-alpha bands of molecular lines.

D.3 BLACKBODY RADIATION FROM GLOWING SURFACES

Under intense heat fluxes, tokamak material surfaces can become hot enough to glow in the visible. This is especially true on C-MOD, where the molybdenum tiles occasionally melt, indicating they reached temperatures over 2600°C. Figure 170 shows the spectral emission at 660nm for a blackbody surface with emissivity $\epsilon = 1$ when viewed through a spectral bandpass of 0.5nm. The melting temperature of various materials often found in the tokamak are indicated for reference. It is apparent that once a temperature of ~ 700K is reached, the surface starts to glow intensely and can produce photon rates that far exceed the brightness from the beam. This blackbody can glow much brighter than even the visible bremsstrahlung. This means that even a very small hot area can become the dominant source of light inside the tokamak in the MSE wavelengths. This light, emitted unpolarized [3], can then be reflected off the ICRF antenna and enter the MSE sightline as partially-polarized background. At the melting temperature of plasma-facing components, even small melt areas observed via mul-

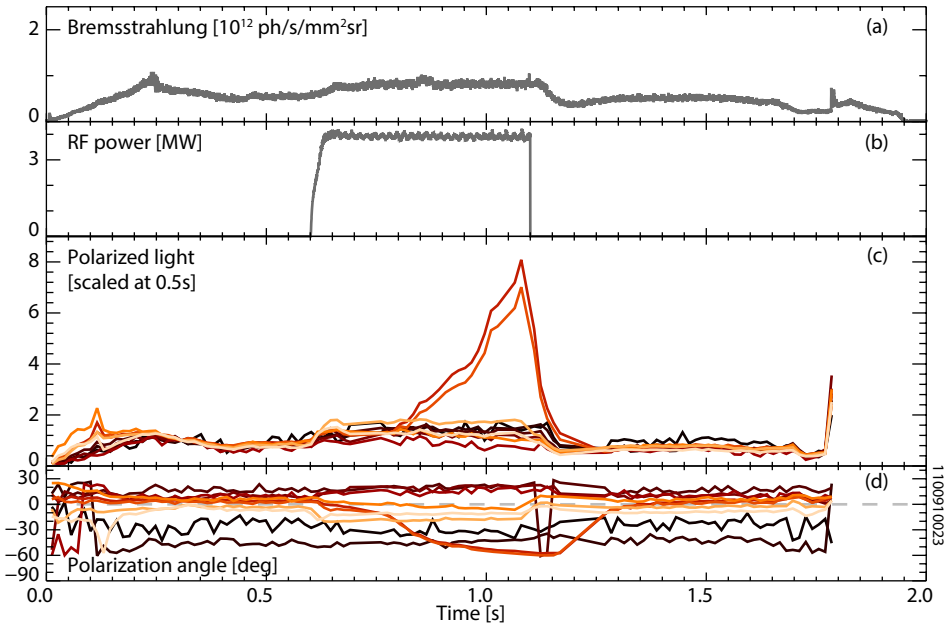

Figure 171: An example of a hot glowing surface contributing to the MSE partially-polarized background. ICRF power is applied to the plasma (b) without raising the visible bremsstrahlung appreciably (a). The polarized light detected by the MSE sightlines (c) (normalized at 0.5s to show changes). The polarization angle of the light (d).

tiple reflections can produce brightness on the order of the directly viewed beam emission.

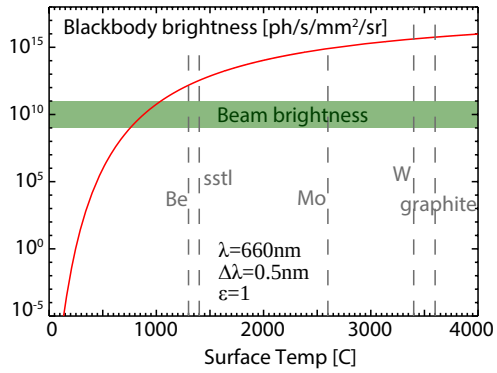

Figure 170: The emission of a blackbody as a function of temperature. Calculated at 660nm in a 0.5nm bandpass with emissivity=1. The melting points of various tokamak materials are shown, as is the typical brightness from the beam.

Figure 171 shows a discharge with significant ICRF heating where such a situation occurs. The visible bremsstrahlung stays relatively constant (a) while 4MW of ICRF power is applied (b). The polarized light detected by two adjacent MSE sightlines suddenly increases at 0.8s (c). Note the polarized intensities have been normalized at 0.5s to show sightline-to-sightline changes. Presumably this rapid increase is caused by some plasma-facing component receiving a significant power flux making it glow. During this time, the polarization angle of these two sightlines changes significantly while the other sightlines stay fairly constant (d). After the turn-off of the ICRF, system the polarized light in these two sightlines decays exponentially, presumably because the heat flux to the component is removed and the surface starts to radiatively and conductively cool. During this cooling phase the two sightlines are no longer dominated by the reflection from the glowing surface and their polarization intensity and polarization angle return to the level prior to the heating event. The polarization angle change to more negative values during

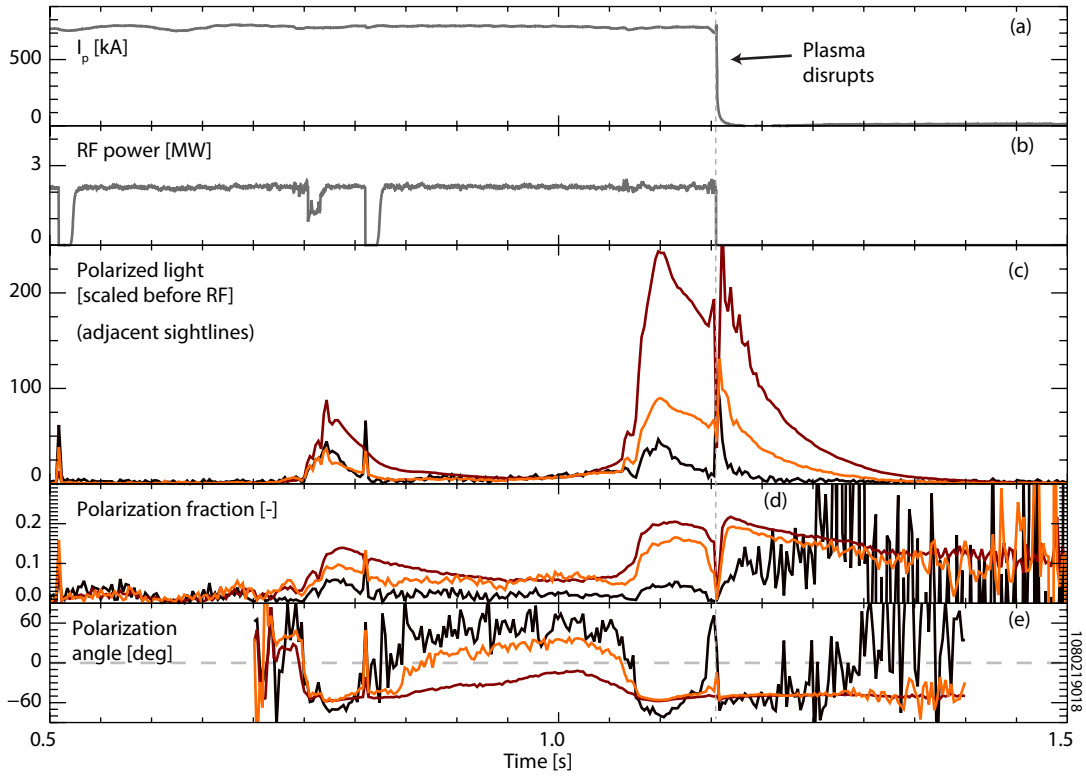

Figure 172: An example of hot glowing surface in the MSE partially-polarized background without plasma. The plasma disrupts at 1.15s. (a). ICRF power is applied to the plasma (b) causing elements to glow. The polarized light detected by three MSE sightlines (c) (normalized prior to the ICRF to show changes). The polarization fraction of the light (d) and the polarization angle of the light (e).

the event indicates the glowing source is likely located in the lower divertor.

Another example is presented in Figure 172. In this discharge the MSE diagnostic observes polarized light even in the absence of plasma. The plasma disrupts at 1.15s (a) during a ICRF heating period (b). The polarized light (c) in three adjacent sightlines has increased substantially during the ICRF pulse. There is an early increase in polarized light which is terminated at 0.75s due to a fault in one ICRF antenna. Later, starting at 1.05s, the polarized light suddenly increases an order of magnitude before starting to exponentially decrease prior to the disruption. The disruption occurs, temporarily increasing the polarized light, which then continues despite there no longer being plasma in the vacuum chamber. During this time the light intensity exponentially decays. The polarized light intensity is normalized prior to the start of ICRF to show sightline-to-sightline changes. The other sightlines (not shown) do not see these events and instead remain at the intensity level similar to the three sightlines prior to events. The other sightlines do not observe light after the disruption.

In this plasma the ICRF heats a surface in the vessel repeatedly. The different sightlines observe varying amounts of the resulting black-

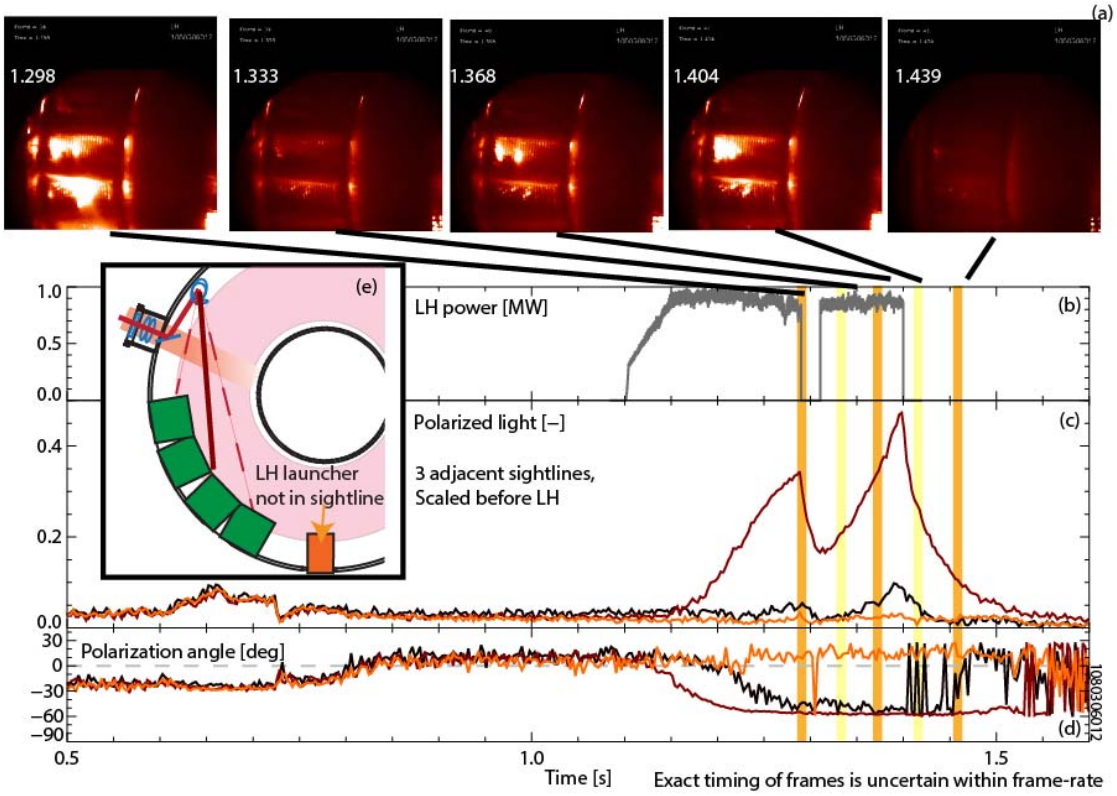

Figure 173: An example of hot glowing surface in the MSE partially-polarized background. The LHCD launcher overheats as seen in the visible camera observing it (a). LHCD power is applied to the plasma, but the overheating causes trips and restarts (b). The polarized light detected by three MSE sightlines (c), which is normalized prior to the LHCD, shows large changes in one sightline but not as large a change in the other sightlines. The polarization angle of the light (d).

body emission and thus have different mixes of sources and different polarization fractions (d) and angles (e). When the element is hottest and dominating the background, the polarization fractions are high and the angles are negative, which indicates that the source is in the lower divertor. The plasma disrupts, leaving the glowing element as the only source of emission, and it cools in place. This produces exponentially decreasing light that is reflected and polarized at a constant polarization angle and a nearly constant—and high—polarization fraction similar in all three sightlines. Note the small dip in the polarization fraction and momentary upward jump in the polarization angle at the time of the disruption is likely due to the saturation of the digitizer.

Figure 173 shows an example where the source is localized using visible cameras inside C-MOD. The LHCD launcher overheats during a discharge, saturating the camera that observes it (a). This heating causes the LHCD system to trip off once before restarting (b). The blackbody emission from the launcher is observed by the MSE diagnostic, as indicated by increasing polarized light (c) and a change in the polarization angle (d). The rise and falls of the polarized light

correspond to the glowing of the LHCD launcher in the camera view. The launcher glow is seen in two MSE sightlines (dark red, black), but not in an adjacent one (orange). This light is observed despite the launcher not being within the line of sight of the MSE diagnostic (e). This discharge had ICRF power, but this was constant throughout the time of interest, as were other plasma parameters.

Hot glowing surfaces present a substantial challenge to the diagnostic since they are highly localized and can become very bright, dominating the other sources of emission. The source can be as small as a region on an antenna or an edge in a divertor, but still be an ample radiator. This localized source is then reflected into only one or two MSE sightlines due to the highly complex nature of the ICRF antennas. So even though the MSE viewing volumes overlap on the antenna, the light that adjacent sightlines collect can differ by factors of up to 40(!) because one sightline is dominated by a single small reflective surface reflecting an extremely bright source.

Blackbody emission is quasi-continuum with no spectral features under the MSE filters, thus spectral effects cannot be the cause of the difference between adjacent MSE sightlines. This is further confirmed by the fact that similar heating-cooling time histories can appear in different sightlines with different spectral filters in different discharges. The time trajectory of the emission can change extremely fast with < 10ms doubling times. This causes problems with beam modulation time-interpolation. The time the surface transitions from heating to cooling can be very problematic because it produces a spike in the background that is misrepresented using time-interpolation, skewing the results and under predicting the measurement uncertainty. Additionally, there are no diagnostics that can measure the emission to provide correlation data to aid in background estimation.

D.4 ATOMIC LINE EMISSION

Atomic lines from impurities may become MSE partially-polarized background if they occur in the MSE filter passband and are bright enough to be observed upon reflection. C II lines at 657.80nm and 658.29nm, and a C I line at 658.76nm, are particularly problematic in other tokamaks with MSE systems using a Doppler red-shifted viewing geometry. However, this has not been observed on C-MOD, which has very little carbon in the plasma and a sufficient Doppler red shift, Stark shift, and MSE π triplet collection to avoid these lines.

Visible atomic line emission comes from low charge states that exist at relatively low plasma temperatures. Unlike visible bremsstrahlung, which is a volumetic source, this emission comes from a "shell" around the plasma and likely from the divertor region. If the line emission is within the MSE spectral bandpass, then it can be observed by the diagnostic both upon first-pass and reflection. Sightlines with the largest tangency radius observe a higher brightness from this emission on

first-pass since these sightlines pass through a longer path length when tangent to the shell. Sightlines with a small tangency radius, on the other hand, pass through the shell at near normal angles. These effects make interpretation of the polarization fraction difficult.

ALCATOR C-MOD seeds the plasma with impurities for various purposes: helium for edge diagnostics, argon for x-ray diagnostics, and nitrogen and neon for radiative power dissipation in the divertor. Each of these impurities has atomic lines near the MSE spectrum and could therefore be problematic. An experiment was conducted by puffing large amounts of these impurities into the plasma so they dominate the radiative power and Z_{eff} to absolutely calibrate other spectroscopy diagnostics. MSE observed these plasmas with the typical spectral filter positions to determine if partially-polarized light from the impurities is observed by the diagnostic.

Figure 174 shows the results for the four impurity species. The four plots each show the location of the species' atomic lines from the literature [4] relative to the normalized MSE filter transmission curves measured in-situ (top). The time history of the sightline polarization intensity is plotted along with the time history of the visible bremsstrahlung emission from the Z_{eff} diagnostic and the radiative power from a 2π integrating diode. The polarization fraction and polarization angle from the MSE sightlines are plotted below that. The time history of the polarized light and polarization fraction are normalized so that all sightlines agree from 0.5s to 0.7s to better show changes. The timing of the puff is indicated, as is the change in the radiative power and the Z_{eff} due to presence of the impurities in the plasmas.

Helium (top left) is not expected to impact the MSE diagnostic since the He I line at 663.19nm is barely overlapping only the reddest filter. This is a very weak line for this transition and may not actually be present. The polarization fraction and polarization angle do not change across the puff, indicating the helium seeding does not contaminate the MSE wavelengths. Also, the polarized intensity follows the change in VB across the puff very well, indicating that visible bremsstrahlung dominates.

The argon seeding (top right) also does not contaminate the MSE wavelengths. However, there are very bright Ar II lines right next to the red of the MSE emission at 663.82nm and 664.37nm. These lines may be problematic for some MSE geometries and beams with larger Doppler shifts.

The neon seeding (bottom left) does contaminate the MSE background due to the fairly bright Ne I line at 659.89. The four bluest filters overlap this line (dashed). These sightlines observe a large increase in polarized intensity during the gas puffing, which remains high after the puffing has ceased. Note that these sightlines also have a significantly different polarization fraction and polarization angle

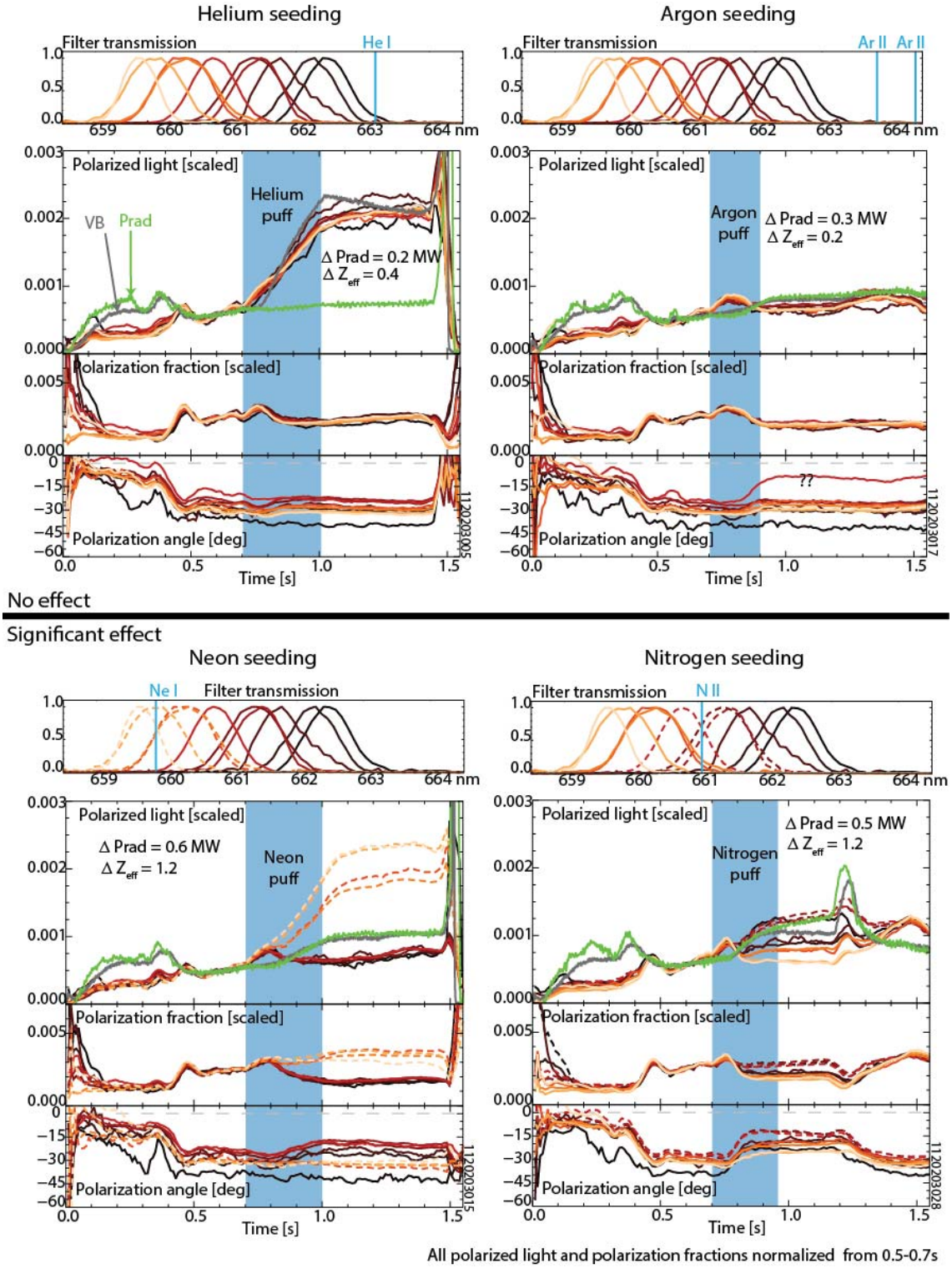

Figure 174: Impurity puffing to determine if atomic lines from common species are observed in the MSE partially-polarized background. Helium (upper left), argon (upper right), neon (lower left) and nitrogen (lower right) were puffed at levels large enough to raise the plasma Z_{eff} (grey) and radiative power (green). The change in these two quantities due to the puff (blue shaded region) is noted. The location of potential atomic lines for the puffed impurity is plotted with the normalized, in-situ measured, MSE filter transmission curves at the top of each plot. The polarized intensity, polarization fraction, and polarization angle time traces for each of the MSE sightlines are shown. The polarization intensity and polarization fraction have each been normalized at times prior to the puff to better identify changes due to the impurity.

time trajectory than the other sightlines after the puff. In this case the puffing was very significant, increasing the Z_{eff} by 1.2.

The nitrogen seeding (bottom right) causes a similar, though not as pronounced, effect due to the N II line at 661.06nm, which overlaps with the middle three filters (dashed). This line is very weak and only changes polarized intensity subtly despite being a very perturbative puff. The polarization fraction has a somewhat different time trajectory than the other sightlines.

Neon is the worst impurity for the diagnostic since it has several filters that overlap the line at 659.89nm and the line has a relatively large effect on the measurement. In the future, it may be advisable to tune the edge sightline filters more toward the red to avoid this line while still collecting the MSE π emission. Such disruptive neon puffing is unlikely in the future. However, even weak puffing may cause problems, and the effects should be monitored.

D.5 SYNCHROTRON EMISSION

Fast particles traveling in a magnetic field emit synchrotron light that is polarized in the direction of their acceleration. Relativistic electron beams can be created with energies of many MeV in a tokamak. This occurs at low densities and high electric fields when the fast electrons are not sufficiently collisional, such as during a disruption or in dedicated runaway-electron experiments. These runaway beams are accelerated by the toroidal electric field in the tokamak and can be quite localized. The beams emit synchrotron emission in the classical "headlight" pattern, beaming their radiation in a small cone in the forward direction. Recent work on C-MOD shows that this emission can be quite bright in the visible red due to the small size and high magnetic field. This was the first ever observation of polarized light from a runaway beam. This runaway electron synchrotron emission is a rare source of directly polarized light in the tokamak not requiring a reflection.

Figure 175 shows an example of MSE detecting this polarized synchrotron emission. When the plasma current direction is reversed on C-MOD, the runaway electrons travel toward the MSE objective lens and their headlight emission can be observed by the diagnostic (a). Two shots were taken with slightly different densities (b), resulting in the lower density discharge (blue) developing a large population of runaway electrons. This is indicated by the visible bremsstrahlung (c) and hard x-ray diagnostic (d) detecting the fast electron bremsstrahlung present in the lower density discharge (blue) but absent in the higher density discharge (red). **The polarized light observed by the MSE diagnostic is a factor of $\sim 100\times$ brighter in the discharge with runaways than in the discharge without runways.** The population of runaways is clearly present from 0.35s to 1.40s. The polarization fraction (f) is also much higher in the runaway discharge. The syn-

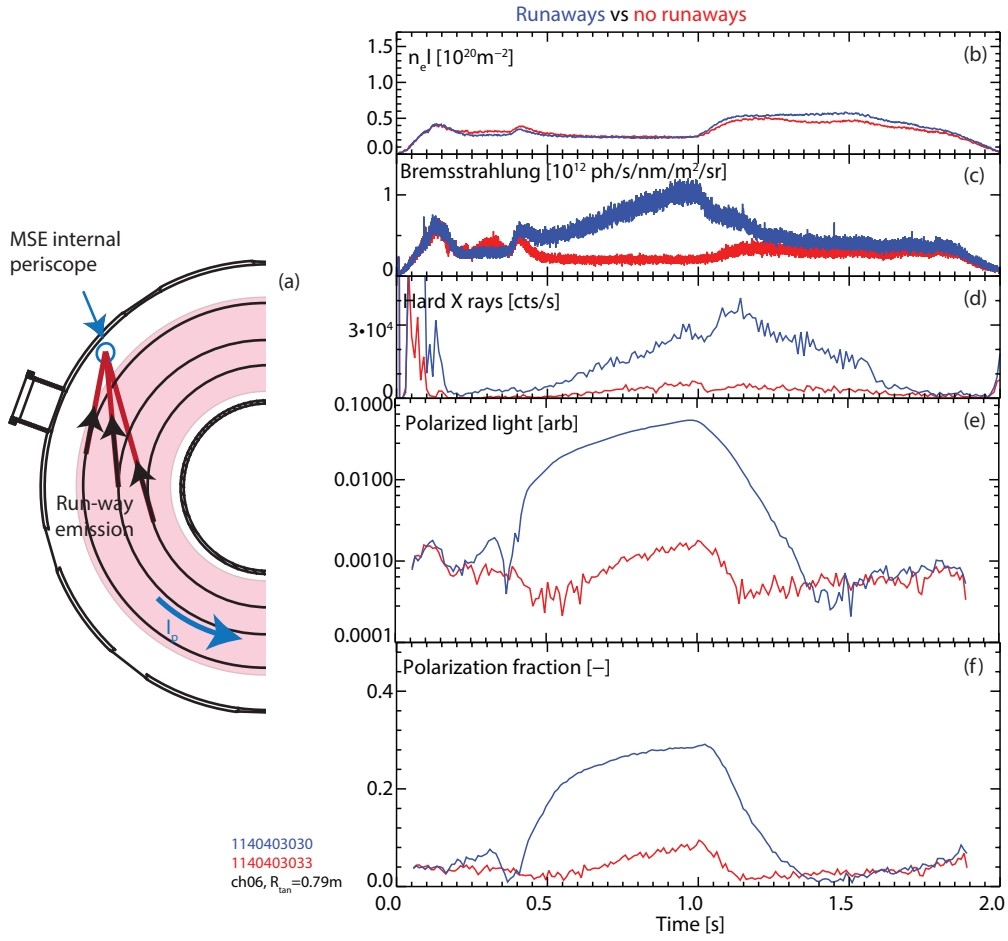

Figure 175: When C-MOD is operated in the "reverse" field direction, runaway electrons beam synchrotron emission toward the MSE objective lens (a). The emission can be compared between a discharge without runaways (red) and a slightly lower density (b) discharge with runaways (blue). The runaways are detected by increases in the visible bremsstrahlung (c) and hard x-ray (d) detectors. The MSE systems detects substantial increases in the polarized light (e, note log scale) and higher polarization fraction (f) in the presence of these runaways. This data was taken from a MSE sightline with a tangency radius of 0.79m.

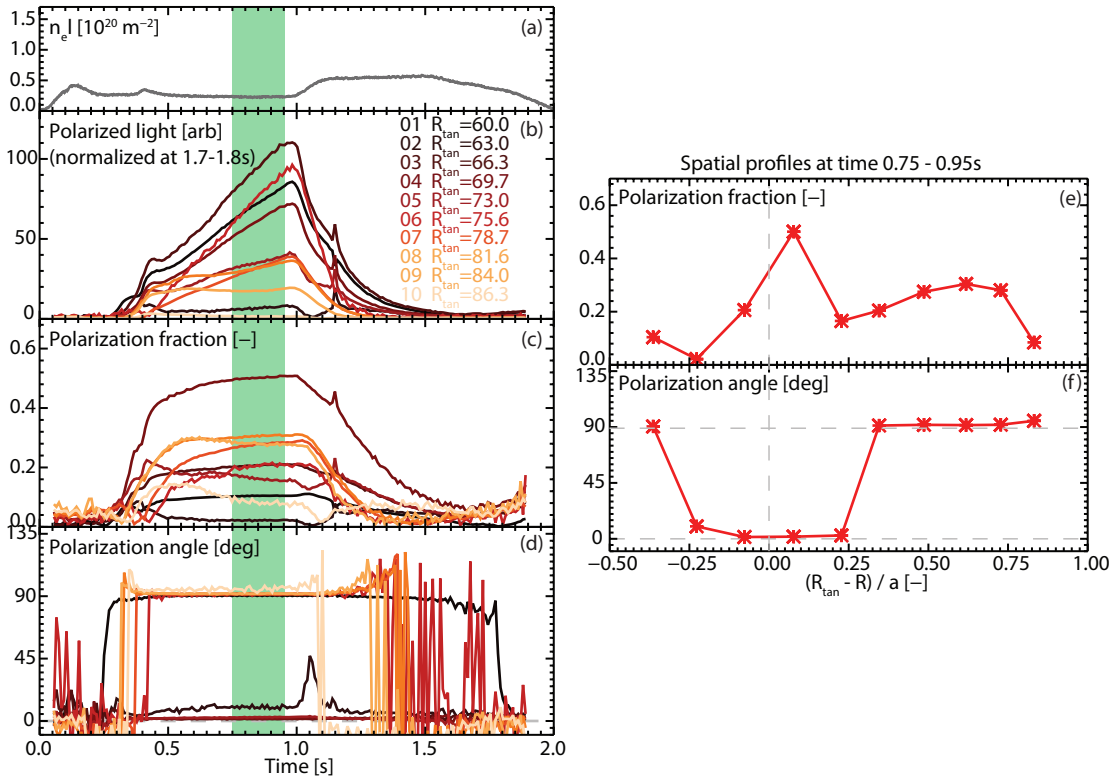

Figure 176: Runaway electrons are produced by decreasing the plasma density (a: line integrated), leading to polarized light in all the MSE sightlines (b). The polarized intensities have been normalized from 1.7s to 1.8s for plotting purposes. The polarization fraction (c) and polarization angle (d) are shown. The spatial profiles of these two quantities averaged from 0.75s to 0.95s are shown in figures (e) and (f), respectively.

chrotron emission is bright enough to blind the diagnostic and thus it has to be operated with much lower APD gain in these types of experiments. The MSE diagnostic operated in this manner is the most sensitive detector of runaway electrons on ALCATOR C-MOD. It might be the case that the lower density discharge has a small population of runaways that are detected by only the MSE system.

The runaway beam likely encodes information about its population distribution in the polarization properties of its emission. Changes in beam population, velocity distribution, and pitch angle can likely be detected as temporal and spatial changes in the polarization intensity, angle, and fraction. These properties can only be observed using the MSE diagnostic. Figure 176 shows the time histories of the line-integrated electron density (a) for a runaway discharge in reverse field. The polarized light shows sightline-dependent time dynamics (b). Note that the polarized intensities have been normalized late in the discharge for comparison. The polarization fraction (c) has sightline-to-sightline variation but less variation in time. The polarization angle (d) is split, some sightlines have vertical (0°) polarization angles while others have horizontal (90°) polarization angles throughout the runaway portion of the discharge. The spatial profiles of the

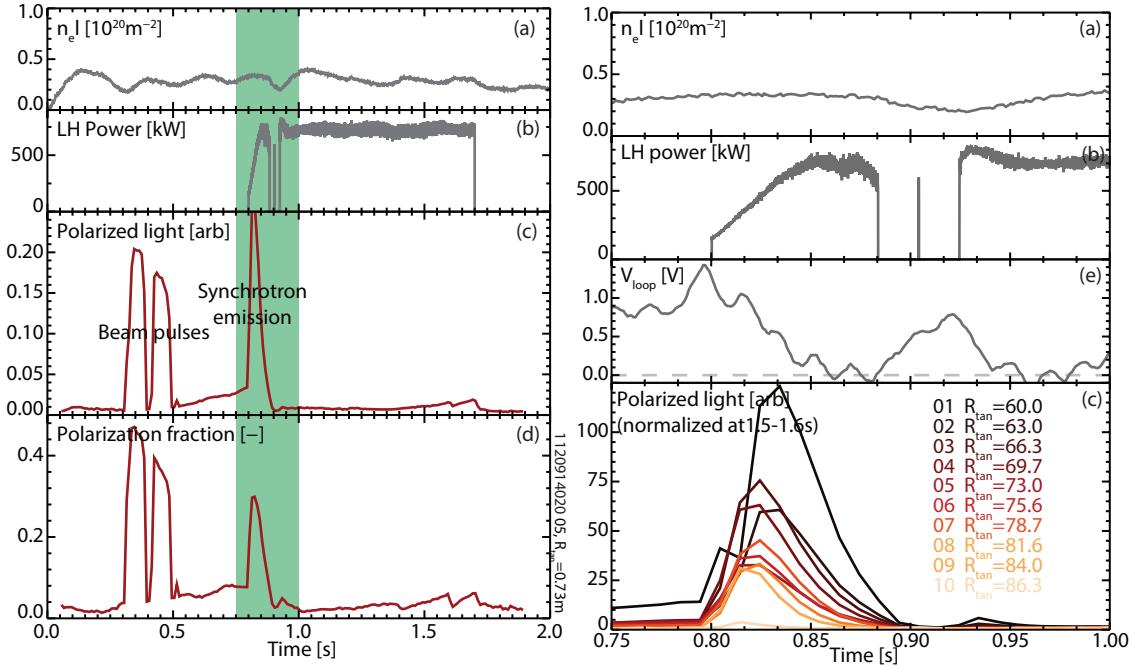

Figure 177: Runaway electrons triggered by LHCD at moderate line integrated densities (a). The LHCD power (b) causes strong polarized emission (c) at moderate polarization fractions (d). The right plots show a detailed time history of the pulse of synchrotron emission (highlighted in green), including the surface loop voltage (e). Two early beam pulses occur before the beam faults out at 0.5s.

polarization fraction (e) and angle (f) show trends, especially in the polarization angle. Detection of these spatial and temporal dynamics in the polarization properties opens new avenues to the study of runaway electron beams, a topic not covered in this thesis.

Dedicated runaway experiments are not the only instances that this polarized synchrotron emission is observed. Figure 177 shows how LHCD can create runaway electrons that can be detected by the MSE diagnostic. This occurs because LHCD seeds the plasma with fast electrons that interact with the background toroidal electric field. The runaway beam appears soon after the start of LHCD, creating polarized synchrotron light that is brighter than the light from the preceding beam pulses (c). Closely examining the pulse of synchrotron emission (right) shows that the polarized emission decreases despite the rising LHCD power and constant or decreasing density. This is because the applied loop voltage (e) (i.e., toroidal electric field) decreases as the LHCD drives a significant amount of the plasma current. The loop voltage rises after the fault in LHCD, and upon its restart at 0.935s and a small amount of synchrotron emission is created. There are other examples of coupling LHCD to an existing runaway beam and amplifying it as evidenced by a large increase of synchrotron emission.

Despite being very bright—to the point of blinding the diagnostic—the synchrotron emission is only a problem for MSE near the conditions where runaways are produced (conditions typically avoided

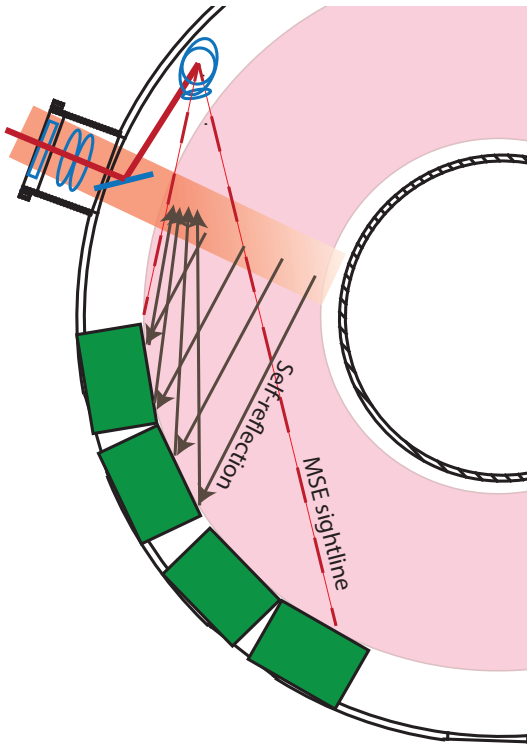

Figure 178: The beam and view geometry are illustrated. The core-most and edge-most MSE sightlines are shown in dashed red with the eight other sightlines equally spaced in between. Examples of rays that could reflect from the beam into a sightline with a red Doppler shift are shown in dark grey.

on most tokamaks). Furthermore, on C-MOD, these beams are only detected by the MSE diagnostic in the "reverse" magnetic field configuration. However, care must be taken to examine the background for problems with synchrotron emission at the start and end of LHCD in this magnet configuration.

D.6 BEAM SELF-REFLECTION

One potentially problematic source of unwanted polarized background light is emission from the beam that is reflected from the wall and then enters a MSE sightline. This would have a different polarization than beam emission collected by that sightline on first-pass because it originated from a different part of the plasma, with at a different Doppler shift or a different polarization projection. If this is not accounted for, the measurement could be systematically skewed.

A red Doppler shift is required for beam emission to be measured by a sightline on C-MOD. Figure 178 shows the beam and view geometry. The extent of the rays that can be accepted by the MSE system are shown as dashed lines. An example of light that has a red Doppler shift and also can reflect off the antenna and enter a sightline is shown in grey. This reflected emission would contaminate sightlines with polarized emission from deeper into the plasma. The beam cannot produce red Doppler shifted rays that could reflect into the core sightlines, especially rays which are sufficiently red-shifted to pass through the core sightlines' MSE filters. Therefore, the view and

beam geometry result in only the edge sightlines being susceptible to this contamination.

Unfortunately, this emission is very difficult to identify since it only occurs when the beam is firing. Beam-into-gas experiments cannot identify this source since they produce secondary emission that contaminates the measurement [5]. Additionally, spectral measurements in plasmas would be fairly insensitive to this light. Fortunately, the brightness would be reduced substantially due to the reflection (which would have to occur at an acute angle), the dim source, the spectral filtering requirement, and the longer path length between the source and the objective lens. Additionally, this effect would likely be reproducible since the geometry and source are fixed, so it would show up as a constant systematic error.

D.7 OTHER POSSIBLE SOURCES

Since any source of light in the tokamak can be reflected into the MSE sightlines, several other sources of light could potentially contribute to the MSE partially-polarized background:

BEAM CHARGE-EXCHANGE WITH IMPURITIES The presence of impurities in the plasma that generate light only when they charge-exchange with beam neutrals would be difficult to detect since this emission would be modulated by the beam. However, no impurities in the MSE wavelengths beyond those discussed above have been observed during large puffing experiments, natural impurity injections, and laser blow off experiments—situations which would also create charge-exchange light. The impurities ruled out thus far are: Fe, F, Ca, Mo, and W.

CHARGE EXCHANGE WITH FAST IONS Fast hydrogenic ions in the plasma can become neutrals via charge-exchange with species in the plasma or with a neutral beam. These fast ions produce a very Doppler-broadened H_α or D_α line that may be broad enough to substantially overlap with the Stark emission. The light could then be reflected, becoming partially-polarized and entering the diagnostic sightline. This is particularly true in beam-heated discharges where the fast ions can be a large fraction of the total plasma inventory. These ions have energies up to the beam energy and thus can overlap the Stark spectrum. In radio frequency heated plasmas, such as those typical on C-MOD, a fast ion tail can also be created at energies up to 1MeV. In C-MOD plasmas, this tail is typically not large enough to produce much light. However, this effect would be difficult to detect and compensate for since the source would be modulated by the beam, which provides the neutrals necessary to charge-exchange. No evidence of partially-polarized light via this mechanism has been observed on C-MOD, but further work

might be prudent to gain confidence in the MSE diagnostic in the scenarios where a hot ion tail is produced.

DIVERTOR VISIBLE BREMSSTRAHLUNG Bremsstrahlung from the core plasma is not the only source of bremsstrahlung present. The divertor, especially at low temperature, can also produce strong bremsstrahlung due to the very high densities. Like any other source, this light can then be reflected into the MSE sightlines. The signature of this effect would be a polarized background intensity which scales like the divertor density squared. Note that the divertor component associated with D_α is not due to divertor visible bremsstrahlung since it is not present in helium plasmas, which presumably have similar divertor densities. Furthermore, the fluctuations seen in this deuterium component do not correlate with divertor density fluctuations that would be detected by the interferometer chords passing through the divertor.

RADIATION INDUCED FLUORESCENCE The plasma produces strong neutron and x-ray emission. The neutrons induced further x-ray and gamma ray emission from the surrounding materials. It could be possible that some of these particles create radiation-induced florescence in the MSE wavelengths in the tokamak and in the diagnostic itself. In this case the background light would likely track the neutron rate, which is not observed to be the case on C-MOD.

STRAY LASER LIGHT If a laser line exists or is scanned through the MSE wavelengths, some of its light could be reflected and enter the MSE diagnostic. This may be important for laser-induced florescence experiments, but could be avoided by staggered timing of the MSE observation and the laser pulse.

To date none of these sources has been observed in the MSE partially-polarized background inside ALCATOR C-MOD. Hence, they won't be considered moving forward.

BIBLIOGRAPHY

[1] H.Y. Yuh. *The Motional Stark Effect diagnostic on Alcator C-Mod*. PhD, Massachusetts Institute of Technology, 2005.

[2] J. Ko. *Current profile measurements using Motional Stark Effect on Alcator C-Mod*. PhD, Massachusetts Institute of Technology, 2009.

[3] Daniel F. V. James. Polarization of light radiated by black-body sources. *Optics Communications*, 109(3-4):209–214, July 1994.

[4] A. Kramida, Yu Ralchenko, J. Reader, and NIST ASD Team. NIST atomic spectra database (version 5.2) [online]. available: http://physics.nist.gove/asd, 2014.

[5] Howard Y. Yuh, F. M. Levinton, S. D. Scott, and J. Ko. Simulation of the motional Stark effect diagnostic gas-filled torus calibration. *Review of Scientific Instruments*, 79(10):10F523, 2008.

The Alcator C-Mod team in the C-Mod control room during the FY12 campaign. The author is the first gray hard hat from the left.

The author inside the tokmaka working on the MSE diagnostic. The red glow is the LEDs from the MSE's ISC system.

The author and his advisor with the 10 MSE-MSLP polychromators in the setup lab prior to installation

The lower hybrid team on the LHCD mezzanine. The LHCD klystrons are the red tubes on the right. The copper waveguides transmit the waves to the tokamak's launcher

COLOPHON

This document was typeset using `classicthesis` developed by André Miede (although aspects were changed to comply with the MIT thesis standards and the author's personal preferences). The style was inspired by Robert Bringhurst's seminal book on typography "*The Elements of Typographic Style*". `classicthesis` is available for both LaTeX and LyX:

http://code.google.com/p/classicthesis/

Final Version as of June 23, 2015 (`classicthesis` version 4.1).

Hermann Zapf's *Palatino* and *Euler* type faces (Type 1 PostScript fonts *URW Palladio L* and *FPL*) are used. The "typewriter" text is typeset in *FPL*, originally developed by Bitstream, Inc. as "Bitstream Vera". (Type 1 PostScript fonts were made available by Malte Rosenau and Ulrich Dirr.)